

PERFORMANCE-BASED DESIGN IN EARTHQUAKE GEOTECHNICAL ENGINEERING—
FROM CASE HISTORY TO PRACTICE

Performance-Based Design in Earthquake Geotechnical Engineering— from Case History to Practice

Editors

Takaji Kokusho

*Department of Civil & Environmental Engineering,
Chuo University, Tokyo, Japan*

Yoshimichi Tsukamoto

*Department of Civil Engineering,
Tokyo University of Science, Tokyo, Japan*

Mitsutoshi Yoshimine

*Department of Civil and Environmental Engineering,
Tokyo Metropolitan University, Tokyo, Japan*



CRC Press

Taylor & Francis Group

Boca Raton London New York Leiden

CRC Press is an imprint of the
Taylor & Francis Group, an **informa** business

A BALKEMA BOOK

Cover photograph: Maturube Great Bridge fallen due to landslide during 2008 Iwate-Miyagi Nairiku earthquake: M = 7.2 was kindly provided by OYO CORPORATION, Japan.

CRC Press/Balkema is an imprint of the Taylor & Francis Group, an informa business

© 2009 Taylor & Francis Group, London, UK

Typeset by Vikatan Publishing Solutions (P) Ltd., Chennai, India

Printed and bound in Great Britain by Antony Rowe (A CPI Group company), Chippenham, Wiltshire

All rights reserved. No part of this publication or the information contained herein may be reproduced, stored in a retrieval system, or transmitted in any form or by any means, electronic, mechanical, by photocopying, recording or otherwise, without written prior permission from the publisher.

Although all care is taken to ensure integrity and the quality of this publication and the information herein, no responsibility is assumed by the publishers nor the author for any damage to the property or persons as a result of operation or use of this publication and/or the information contained herein.

Published by: CRC Press/Balkema

P.O. Box 447, 2300 AK Leiden, The Netherlands

e-mail: Pub.NL@taylorandfrancis.com

www.crcpress.com – www.taylorandfrancis.co.uk – www.balkema.nl

ISBN: 978-0-415-55614-9 (Hbk+CD-Rom)

Table of contents for Book and CD-ROM

Preface	XIX
Committees	XXI
<i>Keynote lectures</i>	
Performance based earthquake design using the CPT <i>P.K. Robertson</i>	3
Performance of foundation ground in Kashiwazaki-Kariwa Nuclear Power Station during 2007 Chuetsu-Oki earthquake <i>T. Kokusho</i>	21
Seismic performance based-design of large earth and tailing dams <i>R. Verdugo</i>	41
Gravel drains for the remediation of liquefiable sites: The Seed & Booker (1977) approach revisited <i>G.D. Bouckovalas, A.G. Papadimitriou & D. Niarchos</i>	61
Seismic soil-pile-structure interaction based on large shaking table tests <i>K. Tokimatsu & H. Suzuki</i>	77
<i>Theme lectures</i>	
Development of performance criteria for foundations and earth structures <i>S.L. Kramer, P. Arduino & H. Shin</i>	107
Evaluation of seismic performance of geotechnical structures <i>M. Cubrinovski & B.A. Bradley</i>	121
Outline of performance-based design for railway earth structures in Japan <i>M. Shinoda, K. Watanabe, K. Kojima & M. Tateyama</i>	137
Seismic performance of geosynthetic-reinforced soil retaining walls and their performance-based design in Japan <i>J. Koseki, S. Nakajima, M. Tateyama, K. Watanabe & M. Shinoda</i>	149
Evaluation of spatial variations in soil stiffness using stress wave propagations <i>D.S. Kim, H.J. Park, J.T. Kim, N.R. Kim & E.S. Bang</i>	163
Determining the undrained residual strength of soils from field penetration tests with some case history studies <i>Y. Tsukamoto</i>	179
The use of controlled blasting for evaluating seismic performance <i>S.A. Ashford, Y. Kawamata, K.M. Rollins, R.E. Kayen, T.J. Weaver & T. Juirnarongrit</i>	193
Lessons learned from sampling and CPT in silt/sand soils <i>A.B. Huang</i>	209
Satisfaction and dissatisfaction of port facilities designer facing to the performance based design methodology <i>T. Sugano & S. Miyata</i>	221

Academics and practitioners discussion session

Evaluating seismic performance of earth structures and soil-structure systems <i>R.W. Boulanger</i>	229
Geotechnical performance-based seismic design for bridge foundations—a Western Canada perspective <i>E. Naesgaard</i>	233
Prediction of behavior of underground structure and quay wall during earthquake <i>N. Yoshida</i>	235
Evaluation of the seismic performance of embankment dams and levees <i>R. Pyke</i>	237
Seismic design of shallow immersed tunnels and underground metro stations <i>K. Pitilakis</i>	239
The role of soil properties in performance-based design <i>M. Maugeri & S. Grasso</i>	241
Role of soil investigation in performance based design <i>A.M. Kaynia</i>	249
Role of soil investigation in performance-based design <i>S.L. Kramer</i>	253
Relevant soil investigations and laboratory tests to estimate liquefaction-induced deformation of structures <i>S. Yasuda</i>	259
Discussion session on performance criteria for designing geotechnical structures <i>S. Iai</i>	265
Risk measures in design of geotechnical structures <i>G.J. Rix</i>	269
Determining criteria for seismic performance of earth structures <i>I. Towhata</i>	273
Integrated design of structure-foundation systems and performance based design <i>M.J. Pender</i>	275
Learning from geotechnical earthquake engineering case histories <i>J.D. Bray</i>	277
The role of remote sensing in documenting landslide and ground failure case histories for performance-based seismic design <i>E.M. Rathje</i>	283
Landslides induced by Earthquake and their subsequent effects—lessons learned from the Chi-chi earthquake, 1999 <i>M.L. Lin, K.L. Wang & T.C. Kao</i>	287
 <i>2008 Wenchuan 8.0 earthquake of China</i>	
Characteristics of disasters induced by the Wenchuan 8.0 earthquake and lessons learnt from it <i>L.M. Wang, Z.J. Wu & X.M. Zhong</i>	295
Damage investigation and analysis of buildings in Southern Gansu province during 2008 Wenchuan earthquake <i>L. Chen, W. Liu, H. Ma & Z. Wu</i>	305
Earthquake damages of earth-wood buildings during the Wenchuan Ms 8.0 earthquake <i>R. Qiu, Z. Yuan & Q. Wang</i>	315

Review on geotechnical hazard caused by Wenchuan 8.0 earthquake <i>Z.X. Yuan</i>	319
Application of micro tremor observation on disaster investigation in the quake-hit area of Gansu province by the Wenchuan great earthquake <i>Z.J. Wu, J.J. Sun, H.Z. Wang, A.L. Che & L.Z. Chen</i>	323
Application of micro tremor observation on investigation of geological hazard induced by the great Wenchuan earthquake in Sichuan province <i>A.L. Che, J.H. Qi, X.P. Wu, T. Iwatate, M. Yoshimine, Y. Oda, Q.W. Ma, F. Zhang & Z.J. Wu</i>	331
 <i>Special discussion session—future directions of performance-based design</i>	
Perspectives in geotechnics for vastly strong earthquake shaking <i>K. Ishihara</i>	339
Seismic behaviour of geotechnical structures—Past, present and future <i>P.S. Séco e Pinto</i>	341
Some emerging issues in performance based design <i>W.D. Liam Finn</i>	349
Short comment on site specific earthquake ground motion characteristics for performance based design <i>A. Ansal & G. Tönük</i>	357
PBD in earthquake geotechnical engineering and energy-based design <i>T. Kokusho</i>	359
 General papers on CD-ROM only	
 <i>Ground motions and site effects</i>	
Site response study for urban areas of Chennai city, India—a geotechnical approach <i>G.P. Ganapathy & S. Rajarathnam</i>	365
A case study on dynamic site characterization of Delhi region <i>D. Neelima Satyam & K.S. Rao</i>	373
Site effects evaluation procedures for performance-based design <i>A. Ferraro, S. Grasso & M. Maugeri</i>	377
About consequences of Nevelsky earthquakes in Sakhalin Island <i>A.Zh. Zhusupbekov, V.J. Alperovich, O. Blinova, K.C. Un, I.N. Tikhonov, I.A. Yemelyanov, T.S. Mun & O.N. Cherba</i>	385
Site response of deep and shallow sediments in Bucharest—from microtremors to strong ground motions <i>A. Aldea, S. Demetriu, R. Vacareanu, H. Yamanaka & S. Fukumoto</i>	391
Synthesizing the Mw 6.2 Kojour earthquake of May 28, 2004 using empirical Green's function <i>A. Nicknam, R. Abbasnia, M. Bozorgnasab & Y. Eslamian</i>	401
Estimation of the characteristics of surface wave propagation using arrays of seismometers <i>D.L. Calderon, T. Sekiguchi & S. Nakai</i>	409
Amplification zoning based on grade-II methods of TC4 for Khuzestan province, SW-Iran <i>M. Saghafi, M. Ghorashi & H. Jamshidi</i>	413
Elastic demand spectra based on worldwide strong ground motion records <i>K. Pitilakis, D. Manou & A. Anastasiadis</i>	423

A uniform hazard design spectral shape for building codes <i>R.A. Green, W.I. Cameron, K.A. Gunberg & A. Hadjian</i>	431
Evaluation of amplification factors of soft soils through seismic response analyses <i>G. Biondi, P. Cacciola & E. Cascone</i>	437
Nonlinear earthquake response analysis considering dynamic soil stiffness with both frequency and strain dependencies <i>N. Nakamura</i>	445
PML absorbing boundary condition in numerical modeling of Rayleigh surface wave <i>W.F. Xu, J. Xu, Z.Z. Xie & Z.Q. Xiong</i>	453
Influence of water table depth on the ground surface response of soils <i>S.U. Dikmen & A.M. Turk</i>	457
A new principle for protection from seismic waves <i>S.V. Kuznetsov</i>	463
Nonlinearity in seismic soil-structure interaction <i>J. Yang & X.R. Yan</i>	469
 <i>Wall structures and foundations</i>	
Seismic retrofit of a historic bridge <i>J.R. Gingery, J.F. Meneses, K.W. Franke & Z. Zafir</i>	475
Characteristics of liquefaction induced damage to house and quantified degree of damage <i>A. Onoue</i>	483
Performance based design of Shahid Rajaei diaphragm wall: Pseudo-static and dynamic perspective <i>H. Alielahi, H. Nouri & B. Ebrahimian</i>	491
Long term economic benefits of ground improvement—Ford-Otosan plant case history <i>C.G. Olgun, J.R. Martin II & C.W. Zobel</i>	501
Various parallel quay walls with shore, Kish Commercial port case history <i>M. Jalili, M. Habibi, G.H. Roodi & M. AbadiMarand</i>	509
Evaluation of seismic earth pressure and wall friction acting on embedded footing based on centrifuge test <i>S. Tamura, T. Sakamoto, T. Hida & N. Maeda</i>	517
Performance of model piles in liquefiable soil during shaking tests <i>T.S. Ueng & C.H. Chen</i>	523
A study on deformation behavior of the pile foundation reinforced with ground solidification body by full scale field test and numerical analysis <i>Y. Adachi, K. Urano, M. Mihara & M. Kawamura</i>	531
Contribution Index—a new methodology in distribution of lateral force in pile groups behind quay walls subjected to liquefaction-induced lateral spreading <i>R. Motamed & I. Towhata</i>	541
Pressure dissipater panels for seismic mitigation of caisson quay walls <i>A.A. Mostafavi Moghadam, A. Ghalandarzadeh, P. Haji Alikhani & I. Towhata</i>	549
On seismic response of retaining structures <i>N. Sitar & L. Al Atik</i>	557
Instability of sand undergoing earthquakes after groundwater level rise <i>K. Yasuhara, K. Nishiwaki, H. Komine & S. Murakami</i>	565
Performance-based pseudo-static analysis of gravity retaining walls <i>G. Biondi, M. Maugeri & E. Cascone</i>	571

Experimental modelling of kinematic bending moments of piles in layered soils <i>L. Dihoru, S. Bhattacharya, C.A. Taylor, D. Muir Wood, F. Moccia, A.L. Simonelli & G. Mylonakis</i>	581
On design of retaining walls in seismic areas <i>Y. Wu, S. Prakash & V.K. Puri</i>	589
Influence of earthquake motion characteristics on settlement behavior of tank foundation due to liquefaction <i>S. Higuchi, N. Sento, M. Kazama, R. Uzuoka & H. Takahashi</i>	595
Significance of settlement on seismic stability of footing on slope <i>M. Okamura & T. Sugata</i>	603
Simplified modeling of wave absorbing concrete blocks for performance-based design <i>H. Ishida, K. Ichii & T. Mishima</i>	607
Large scale 1-g shaking table test of an unanchored earth-retaining RC diaphragm <i>R.C. Borg, M. Corigliano, C.G. Lai & A. Pavese</i>	613
Pushover analysis for piles subjected to liquefaction-induced flow pressure and ground displacement <i>J.H. Hwang, Y.D. Lyu & M.C. Chung</i>	621
Derivation of cyclic p - y curves from shaking table tests <i>S.S. Lin, K.J. Chiou, J.C. Liao, C.H. Chen & T.S. Ueng</i>	629
Nonlinear soil–foundation–structure interaction aiming in performance based design <i>D. Pitilakis</i>	635
Experimental and numerical evaluation of the effect of pile cracking to the performance-based design concept <i>E.M. Comodromos, M.C. Papadopoulou & I.K. Rentzeperis</i>	643
Energy oriented approach to take into account the effect of the seismic non-linear SSI on the performance-base design <i>E. Sáez, F. López-Caballero & A. Modaressi-Farahmand-Razavi</i>	651
Study of p - y curves for liquefiable soil <i>S.R. Dash, S. Bhattacharya & A. Blakeborough</i>	659
Evaluation chart of existing pile foundation against seismic soil displacements <i>S. Mori, K. Suga & T. Akaishi</i>	667
Prediction of the natural frequency in a gravity quay wall with saturated backfill during an earthquake <i>J.-I. Hwang, S.-R. Kim, J.-T. Han & M.-M. Kim</i>	675
Simulation of vertical cyclic loading tests for a pile in sand by accumulated damage theory <i>K. Abe, M. Koda, K. Horii & M. Kiguchi</i>	683
Effective stress based dynamic analysis on the interaction between pile foundation and liquefied ground <i>H. Yokawa, A. Tanabe, A. Yashima & K. Sawada</i>	689
Dynamic response of cantilever retaining walls <i>A. Evangelista, A. Scotto di Santolo & A.L. Simonelli</i>	697
An approach to the seismic design of embedded retaining walls based on the results of dynamic numerical analysis <i>F.M. Soccodato & L. Callisto</i>	705

Earthquake induced permanent displacements of shallow foundations— performance based design <i>M.J. Pender, J.C.W. Toh, L.M. Wotherspoon, T.B. Algie & M.C.R. Davies</i>	713
Seismic performance of anchored quay walls and numerical simulation techniques <i>B. Ebrahimian</i>	721
Numerical modeling of the seismic behavior of gravity type quay walls <i>B. Ebrahimian, A.A. Mostafavi Moghadam & A. Ghalandarzadeh</i>	731
Seismic active earth pressure with varying shear modulus in backfill— pseudo-dynamic approach <i>S. Kolathayar & P. Ghosh</i>	739
Analysis of laterally loaded pile groups in multi-layered grounds by hybrid elastic method <i>H. Hirai</i>	745
Dynamic behavior of liquefied sand around pile foundation: Model experiment and numerical simulation <i>A. Shimizu, Y. Ogata, T. Matsushima & Y. Yamada</i>	753
Influence of head connection type on seismic behaviour of inclined micropiles <i>R. Noorzad & G.R. Saghaee</i>	761
Nonlinear incremental analysis for the prediction of seismic performances of embedded retaining walls <i>C. Visone & F. Santucci de Magistris</i>	769
Kinematic pile bending in layered soils: Linear vs. equivalent-linear analysis <i>S. Sica, A.L. Simonelli & G. Mylonakis</i>	777
Dynamic response of surface foundation resting on sand by means of physical modeling <i>F. Jafarzadeh & H. Ghasemzadeh</i>	785
A dynamic load calculation for multi-anchored flexible walls <i>A.D. Garini</i>	791
Some remarks on the kinematic vs. inertial interaction for piled foundations <i>R. Di Laora & A. Mandolini</i>	795
Pseudo-static and dynamic analysis for an anchored diaphragm wall according to the performance-based design method <i>B. Ebrahimian</i>	801
Embedment effect on seismic performance of soil-structure system <i>G. Abate, M.R. Massimino & M. Maugeri</i>	811
Use of a fully coupled analysis for evaluation of performance of footings on liquefiable and densified subsoils <i>H. Shahir & A. Pak</i>	819
Kinematic interaction: A parametric study on single piles <i>F. Moccia, S. Sica & A.L. Simonelli</i>	827
 <i>Embankments and slopes</i>	
Peculiarities of formation and activation of landslide processes in Kyrgyzstan and Kazakhstan <i>K.Ch. Kojogulov, O.V. Nikolskaya, R.B. Baimakhan, G.R. Mirzakulova, A.M. Aliyeva, G.B. Yliasova, A.G. Tanirbergenov, N. Sakpanova & D. Chan</i>	837
Estimation of earthquake-related embankment crest settlements <i>R. Singh & D. Roy</i>	843

Stability of embankment and reclaimed land composed of industrial wastes during earthquake <i>H. Nagase, A. Hirooka, S. Nakamura & T. Monzen</i>	851
Importance of groundwater to the earthquake performance design of natural slope <i>S. Sakajo & N. Sakai</i>	859
Variations in threshold acceleration for seismic induced deformations of embankments <i>Y. Hata, K. Ichii, S. Kano & T. Tsuchida</i>	867
Model test and numerical analysis of slope stability during earthquake <i>K. Arai, Z.J. Wang & L. Lu</i>	873
Development of slope displacement evaluation method during earthquakes by energy approach—case study in 2004 Niigata-ken Chuetsu earthquake <i>T. Ishizawa & T. Kokusho</i>	881
The effect of vertical accelerations on seismic slope stability <i>S.K. Sarma & M.R. Scorer</i>	889
Calculating the factor of safety of the slope stability: A case study <i>M.X. Hou, C.G. Li, Y.Z. Liu & X.R. Ge</i>	897
Earthquake-induced shear deformation of slopes for performance-based engineering <i>M. Taiebat, B. Jeremić, Y.F. Dafalias & A.M. Kaynia</i>	907
Estimation of sliding of gentle slope on partially saturated fine sand subject to strong ground motion <i>J. Lee, K. Yoshizako, N. Ohbo & T. Sakanoue</i>	915
Consideration on fill slope failure in Takamachi developed residential land in 2004 Niigataken Chuetsu earthquake <i>S. Ohtsuka, K. Isobe & T. Takahara</i>	923
Two-dimensional seismic response analysis to evaluate permanent slope displacements <i>S. Rampello, L. Callisto & P. Fagnoli</i>	929
Performance-based design of potentially liquefiable embankments using a combined effective stress—total stress model <i>E. Naesgaard, M.H. Beaty & P.M. Byrne</i>	937
Analytical study for effect of uncertainty in soil parameters on seismic settlement of earth structure <i>A. Wakai, S. Nishimura & S. Tani</i>	947
Evaluation of seismic displacements of a natural slope by simplified methods and dynamic analyses <i>E. Ausilio, A. Costanzo, G. Tropeano & F. Silvestri</i>	955
Experimental study on seismic reinforcement method at crest of road embankment by geosynthetics <i>N. Tatta, J. Jang, K. Tokida, K. Oda & A. Nakahira</i>	963
<i>Dams and underground structures</i>	
Strategy of reduction of seismic risk for hydro-technical structures <i>T.R. Rashidov, V.A. Kondratiev, M.A. Akhmedov & A.I. Tuchin</i>	975
Longitudinal seismic response of Keddara dam: A comparison of observed records and analyzed results <i>S. Louadj, R. Bahar, N. Laouami, E. Vincens & B. Cambou</i>	981
Safety analyses of Srinagarind dam induced by earthquakes using dynamic response analysis method <i>S. Soralump & K. Tansupo</i>	987

Experimental assessment of performance-based methods for the seismic design of circular tunnels <i>G. Lanzano, E. Bilotta, G. Russo, F. Silvestri & S.P.G. Madabhushi</i>	995
Ultimate performance of GSET earth fill dam by shaking table tests <i>Y. Mohri, K. Matsushima, T. Tanaka & F. Tatsuoka</i>	1005
Settlement in friction soil due to vibrations from rock tunneling by blast method <i>M. Bahrekazemi, A. Fredriksson, H. Mattsson & D. Sennerby</i>	1013
Centrifuge modelling of normal fault-pipeline interaction <i>S. Nagaoka, M.F. Bransby & M.C.R. Davies</i>	1021
Dynamic performance of core in asphaltic concrete core dams by means of 1G shaking table <i>A. Mirdamadi, A. Ghalandarzadeh & S. Feizi-Khanakandi</i>	1027
1G Shaking table experiments on the effect of shaking and vertical shear displacement on buried instrumented pipes—implications for design <i>W.W. Sim, I. Towhata & M.A. Sakr</i>	1033
Centrifuge model tests on the uplift behavior of an underground structure during liquefaction and its numerical modeling <i>H. Uno, F. Oka, S. Tanizaki & A. Tateishi</i>	1041
Comparison of constitutive models through a case study on seismic response of tunnels <i>S. Kontoe, L. Zdravkovic, D.M. Potts & C.O. Menkiti</i>	1051
Observed and estimated sewer manhole uplifts during earthquakes <i>T. Tobita, S. Iai, G.C. Kang & Y. Konishi</i>	1061
Numerical analysis of uplift behavior of an underground structure due to liquefaction using an effective stress analysis method <i>A. Tateishi, F. Oka, Y. Kotani & R. Asai</i>	1071
Ground-motion asynchronism in the seismic response of earth dams <i>E. Bilotta, L. Pagano & S. Sica</i>	1081
Evaluation of seismic performance of a box culvert buried in saturated sand with centrifuge and its numerical simulation <i>T. Kawai, A. Asaoka & T. Noda</i>	1087
Seismic safety evaluation of Dapu-Road Tunnel <i>Z.Y. Chen, Y. Yong & H.T. Yu</i>	1095
Accelerogram construction of strong earthquakes in deep layers of a ground and an estimation of stability of underground constructions <i>R.B. Baimakhan, A.R. Baimakhan, N.K. Moldakunova, F.K. Yakhiyev, K.A. Kalymova, G.I. Salgarayeva, B.Zh. Zhakashbayev & S.A. Issayev</i>	1101
Research of the seismo-stressed condition of a complex system of the underground construction taking place in the anisotropic ground <i>R.B. Baimakhan, Sh. Altynbekov, G.P. Rysbayeva, S. Avdarsolkzy, A.S. Kozhebayeva, A.A. Takishov & K.A. Abdikalikov</i>	1107
Multiple non-circular tunnel linings design under seismic effects of Earthquakes <i>N.N. Fotieva, N.S. Bulychev & P.V. Deev</i>	1113
The application and research of stress-stain monitor of Central Division Wall in Double-arch Tunnel <i>F. Zhang, J.-P. Chen, C.-Q. Zuo, C. Zeng & W.-F. Xu</i>	1123
Appropriate countermeasures against liquefaction-induced uplift of existing manholes and pipes <i>S. Yasuda, S. Mayuzumi & H. Onose</i>	1127

Soil liquefaction and countermeasures

- A study on performance based design applied to liquefaction countermeasure
T. Kato, T. Hara, A. Yashima, H. Yokawa, A. Tanabe & Y. Otake 1135
- A liquefaction countermeasure grounded on performance based design
for Kisogawa-canal
K. Otsushi, H. Tanaka, T. Kato, T. Hara & A. Yashima 1145
- The effect of underground columns on the mitigation of the liquefaction in shaking table
model experiments
A. Bahmanpour, I. Towhata, M.A. Sakr, M.M.A. Hussein, Y. Yamamoto & S. Yamada 1153
- Shaking table test for partially improved ground considering the spatial locality
of liquefaction
K. Kasama, K. Zen, G. Chen, M. Kobayashi & K. Hayashi 1161
- Performance evaluation of lattice-shaped ground improvement for liquefaction mitigation
T. Namikawa & J. Koseki 1169
- A study on prediction accuracy of the dissipation of pore water pressure
and the settlement of soil surface for an actual case by the dynamic effective
stress analysis program
A. Suzuki, O. Ozutsumi, S. Iai & N. Yokoyama 1177
- Evaluation of liquefaction countermeasure effects on the performance of structures
F. López-Caballero, E. Sáez & A. Modaressi-Farahmand-Razavi 1185
- Model modification considering steady state for dynamic analysis with effective
stress response
*N. Fujii, S. Sawada, S. Iai, K. Ichii, N. Yokoyama, O. Ozutsumi,
T. Nakahara & K. Mizuno* 1193
- Coseismic and postseismic behavior of intermediate soil ground improved
by sand compaction pile method
H. Takeuchi, T. Noda & A. Asaoka 1199
- New Biot's equation for finite element analysis
N. Yoshida, Y. Ohya & T. Sugano 1207
- The effect of soil-mix panels on ground motions—a performance based approach
C.G. Olgun & J.R. Martin II 1217
- A numerical study on post liquefaction soil behavior by dynamic effective stress analysis
Y. Tamari, O. Ozutsumi, S. Iai & N. Yokoyama 1223
- A parametric study on the factors affecting the post-liquefaction
flow deformations of ground
R. Alchamaa, M. Yoshimine, R. Karasawa, K. Shiomi & Y. Hosono 1233
- Calibration chamber investigation into performance of TGC grouting
A.M. El-Kelesh, K. Tokida, T. Oyama, S. Shimada & T. Sasaki 1241
- Effects of spatial variability of cement-treated soil on liquefaction potential
N. Kataoka, K. Zen, G. Chen, K. Kasama & K. Hayashi 1249
- An evaluation of liquefaction potential of sands at low confining pressure
M.T. Manzari 1257
- Centrifuge modeling for performance evaluation of geotechnical
structures improved by earthquake resistant cushion
H. Hazarika, J. Kobayashi, H. Kanno & S.P.G. Madabhushi 1261
- Dynamic model tests in centrifuge on lattice-shaped DMM ground improvement
for restraining displacement of quay wall
H. Takahashi & K. Hayano 1269

Field testing

- Soil liquefaction hazard evaluation for performance-based earthquake engineering
S. Grasso & M. Maugeri 1279
- The advancement of the subterranean investigating method for basic assessment of aseismatic improvement of a line structure
K. Inoue, H. Nakazato & T. Unno 1287
- Geotechnical in situ investigation for seismic design of buildings in Romania
C. Arion, D. Lungu, C. Neagu & E. Calarasu 1293
- Spanning static properties of a normally consolidated silt with dynamic stiffness
Y.J. Mok, D.S. Park, J.W. Jung & H.S. Kim 1301
- Correlating qc and cyclic liquefaction resistance of sands through calibration chamber tests and simple shear tests
D.D. Porcino & V. Marciandò 1307
- Interrelationship between small strain modulus G_0 and operative modulus
P. Monaco, S. Marchetti, G. Totani & D. Marchetti 1315
- Estimation of S-wave velocity structure of vertical section orthogonal to the Fukui earthquake fault based on microtremor observation
K. Kojima & T. Noguchi 1325
- Characterization of earth-dam soil properties by in situ tests
L. Pagano, C. Mancuso & S. Sica 1333
- Seismic performance evaluation of ground improvement with composite effect using surface wave investigation
Y. Sato, K. Maeda, K. Hayashi, Y. Murata & T. Takahara 1339
- The role of site uncertainty of soil parameters on performance-based design in geotechnical earthquake engineering
A. Cavallaro, S. Grasso & M. Maugeri 1349
- In situ damping ratio profiling of cemented sandy and gravelly soils by surface wave measurements
A. Haddad & S. Ghazvinian 1357
- Application of micro tremor observation for ground liquefaction investigation in Tianjin Wangqingtu reservoir area
J.H. Qi, A.L. Che, X.R. Ge, Y.Z. Yang, X.Q. Luo, S.K. Feng & T. Kambara 1365
- Application of surface wave survey for ground liquefaction investigation
A.L. Che, X.Q. Luo, J.H. Qi, S.K. Feng & T. Kambara 1373

Laboratory testing

- Laboratory research on liquefaction characteristics of a sandy silt substratum in Shanghai
Y. Huang, C. Jin, Z.J. Zhuang, Y.L. Zheng, Z.Y. Chen & W.M. Ye 1381
- Characteristics of subsidence of unsaturated ground and subsidence mechanism in the Niigataken Chuetsu-oki Earthquake in 2007
H. Sato, K. Momose, T. Suehiro, T. Tani, M. Sato, K. Ozeki & T. Kitazume 1387
- Modeling of strain increase of liquefied soils in cyclic shear loading considering material characteristics
T. Mikami, K. Ichii, S. Iai, O. Ozutsumi, T. Nakahara & N. Yokoyama 1395
- Online earthquake response tests for evaluating deformation of river dykes founded on saturated sandy deposits
T. Fujii, M. Hyodo, T. Kaneko & R.P. Orense 1403

Correlation of cyclic triaxial and shear box test results to estimate CSR <i>Y. Yilmaz & M. Mollamahmutoglu</i>	1409
Experimental study on strength properties of slipping zone soil of the Qianjiangping landslide in the Three Gorges reservoir area under the wet-dry-cycle condition <i>X.Q. Luo, A.L. Che & L. Cao</i>	1415
Measurement of the small strain stiffness of Auckland natural clay <i>A. Ibrahim, R.P. Orense, M.J. Pender & N. Kikkawa</i>	1423
Importance of effects of partial saturation on undrained shear strength of soils <i>T. Kamata, Y. Tsukamoto & K. Ishihara</i>	1429
Comparison of stress and strain approaches for evaluation of liquefaction potential of sands <i>K. Hazirbaba & M. Omarov</i>	1435
Physical and mechanical properties of soils obtained from slope failure sites during epicentral earthquakes <i>H. Toyota, S. Takada & K. Nakamura</i>	1443
Anisotropy ratio of marine clays <i>S.L. Yang, K. Schjetne, T. Lunne & E. Solhjell</i>	1451
Seismic stability and deformation of river dyke founded on sand-clay soils <i>M. Hyodo, U.G. Kim, T. Kaneko, N. Yoshimoto & R.P. Orense</i>	1457
Post earthquake volumetric strain of cohesive soils due to undrained cyclic loadings <i>M. Hatanaka & S. Yokoji</i>	1465
Measuring excess pore-water pressure of an unsaturated silty soil in cyclic shear test <i>T. Nishimura</i>	1471
Assessment of liquefaction potential against long duration shaking and its application <i>K. Uemura, K. Ichii, T. Mikami & O. Ozutsumi</i>	1477
Effect of water content on dynamic properties of sand in cyclic simple shear tests <i>F. Jafarzadeh & H. Sadeghi</i>	1483
Research on coefficient of brittle stress drop of brittle-plastic rocks after failure <i>G.C. Shi, X.R. Ge & Y.D. Lu</i>	1491
Deformation behavior modeling in case of cyclic mobility <i>S. Lenart</i>	1497
Characterization of natural sand under complex dynamic loading <i>E. Rascol & L. Vulliet</i>	1505
Study on influence factors of silt liquefaction and corresponding prevention measures <i>D. Wang, X.Q. Luo & A.L. Che</i>	1513
Anisotropic behavior of silty sands by means of undrained monotonic triaxial tests <i>R. Rafiee Dehkharghani, A. Ghalandarzede & M. Moradi</i>	1519
Normalisation of cyclic undrained triaxial and simple shear strength of carbonate sand to monotonic shear strength <i>D.D. Porcino & A. Saccetti</i>	1527
<i>Methodology and codes</i>	
Study on utilizing 'performance-based design' in setting compaction improvement specifications <i>K. Harada, N. Shinkawa, S. Yasuda & Y. Ariyama</i>	1537
Seismic hazard analysis of Hanahan water treatment plant using geographic information systems (GIS) <i>K. Ofori-Awuah & J.R. Martin II</i>	1543

Performance-based evaluation of a massive liquefaction-induced lateral spread in a subduction zone <i>J.F. Meneses, K.W. Franke, B.R. Cox, A. Rodriguez-Marek & J. Wartman</i>	1551
Pile design practice and seismic performance concerns in Taiwan <i>D.W. Chang, T.Y. Yang, S.H. Cheng, C.T. Chin, T.C. Su & F.K. Huang</i>	1559
Earthquake induced kinematic bending moments on fixed-head piles <i>L. de Sanctis & R.M.S. Maiorano</i>	1567
An integrated seismic hazard framework for assessing the liquefaction triggering of dam foundation soils <i>S. Unsal, A. Yunateci & K.O. Cetin</i>	1575
Challenges to the quantitative assessment of liquefaction risks in High-Speed Railways <i>P.A.L.F. Coelho</i>	1581
Safety of assessment of old fill-dams considering the risk of strong earthquake motion <i>S. Tani, Y. Seshimo & M. Tsukini</i>	1591
Analysis of earthquake damaged sluice pipe supported by piles based on newly developed performance based design methodology <i>S. Nakajima, H. Sugita, S. Tanimoto & A. Takahashi</i>	1599
Seismic performance-based design of gravity quay walls. Application to Jeddah port <i>M. Alsuliman, M. Rouainia & S.M. Wilkinson</i>	1609
Procedures for evaluating pile-supported bridges affected by liquefaction-induced lateral ground displacements <i>C.A. Ledezma & J.D. Bray</i>	1615
The fragility analysis for pile-supported wharfs using capacity spectrum method <i>H.H. Yang, J.S. Chiou, C.H. Chen & Y.Y. Ko</i>	1625
Macroscopic aseismic assessment method of road embankment <i>K. Tokida, K. Oda, K. Hayashi & A. Nakahira</i>	1633
Advantage of performance based design for geotechnical structures undergoing seismic loading <i>I. Towhata, I. Yoshida, Y. Ishihara & S. Suzuki</i>	1639
Effect of uncertainty of seismic action and failure mechanism on the fragility characteristics of embankment <i>S. Nakamura, S. Sawada & N. Yoshida</i>	1645
Probabilistic evaluation of liquefaction-induced lateral spreading displacement for a site in south of Iran <i>A. Kavand & S.M. Haeri</i>	1653
Performance-based geotechnical aspects for seismic retrofit of a hospital complex <i>J.F. Meneses, J.R. Gingery & Z. Zafir</i>	1659
Method for calculating design bearing capacity of piles under various construction methods by statistical analysis of loading test database <i>H. Nishioka, M. Koda, M. Shinoda & M. Tateyama</i>	1667
Probabilistic pseudo-static analysis of pile foundations in liquefiable soils <i>B.A. Bradley & M. Cubrinovski</i>	1673
Numerical evaluation on the seismic permanent displacement of highway bridge shallow foundations <i>M. Shirato, S. Nakatani, T. Kouno & R. Paolucci</i>	1681

Calculation of seismic response of building with simplified estimation of sway and rocking springs and dashpots <i>M. Iiba, Y. Umemura, O. Kurimoto & T. Akita</i>	1691
The simultaneous failure probability of quay walls at multiple sites <i>K. Ichii, Y. Yamamoto, Y. Hata & R. Shibasaki</i>	1701
Consideration of loess ground in seismic design code of construction for Lanzhou urban areas <i>L.M. Wang & Z.X. Yuan</i>	1707
Basic procedures for performance-based design of earth structures considering effects of soil liquefaction <i>J. Obayashi, Y. Adachi, K. Harada, S. Ito, M. Okamura, W. Takanashi & Y. Tsukamoto</i>	1713
 <i>Big projects</i>	
Performance-based seismic design of structures connecting reclaimed island and piled-elevated platform in Tokyo International Airport re-expansion project <i>Y. Sunasaka, Y. Niihara, S. Tashiro, T. Asanuma, M. Miyata & T. Noguchi</i>	1719
Centrifuge modeling of liquefaction sites treated with prefabricated drains <i>R. Howell, E.M. Rathje, A. Marinucci, R. Kamai, R.W. Boulanger, C. Conlee & S. Kano</i>	1729
Liquefaction-induced lateral spreading behavior of large-size model ground with quay wall and pile-supported structure in the E-Defense shaking table test <i>K. Tabata & M. Sato</i>	1737
Earthquake response of huge structure for new runway of Tokyo International Airport <i>K. Tsujioka, M. Yoshida, S. Masuda, T. Murakami & T. Noguchi</i>	1745
Effects of ground displacement on piles with different strength during laterally spreading in centrifuge test <i>H. Suzuki, K. Tokimatsu & R.W. Boulanger</i>	1755
Centrifuge modeling for liquefaction mitigation using colloidal silica stabilizer <i>C.T. Conlee, P.M. Gallagher, R.W. Boulanger & R. Kamai</i>	1763
Seismic behavior of the high embankment airport island constructed by non-liquefiable material <i>K. Inoue, K. Kawamura, Y. Matsumoto, T. Sakaiya & T. Noguchi</i>	1771
Numerical prediction of the seismic behavior of pile foundation adjacent to a quay wall on the E-Defense shaking table <i>R. Uzuoka, N. Sento, F. Oka, A. Yashima, F. Zhang & K. Tabata</i>	1781
Nonlinear macroelements for performance-based design of pile-supported waterfront structures in liquefiable sites <i>D. Assimaki & Varun</i>	1791
Fragility and repair models for container wharves <i>L.M. Ivey, G.J. Rix & S.D. Werner</i>	1799
 <i>Structural design and analysis</i>	
A study of soil-structure interaction using in-situ tests of school buildings <i>Y.Y. Ko & S.-Y. Hsu</i>	1809
Structural and geotechnical seismic monitoring of the new Student House in Campobasso, Italy <i>G. Fabbrocino, C. Laorenza, C. Rainieri, F. Santucci de Magistris & C. Visone</i>	1817

Evaluation of modal pushover analysis procedure using concrete frames <i>P. Zarfam, M. Mofid & M. Ahmadiam</i>	1825
Behavior factor and non-linear behavior of knee braced steel frames with semi-rigid connections <i>M. Miri, H. Abbas zadeh & A. Zare</i>	1831
Comparison of retrofitting simple steel frames using steel shear walls and concentric braces by performance levels <i>M. Miri, H. Hemmati & M. Ghalehnovi</i>	1839
Comparison of seismic performance of the ordinary and chevron knee braced frames <i>A. Zare, M. Miri & H. Abbas zadeh</i>	1845
Assessment of historic residential buildings using fragility curves <i>P. Antl, G. Achs & H. Wenzel</i>	1853
Adaptive displacement-spectra-based pushover analysis procedure for estimating seismic performance for bridges <i>S.F. Qin, J.R. Tao, H.L. Wang, C.G. Liu & G. Lin</i>	1861
Modified DASPA procedure for estimating seismic performance for cable-stayed bridge <i>C.G. Liu, S.F. Qin, J.R. Tao, H.L. Wang & G. Lin</i>	1869
Survey of special steel moment frames in the way of performance based design by consideration of panel zone <i>M. Miri, A. Kashiryfar & M. Naghipour</i>	1875
Energy approach in performance-based optimization of steel moment resisting frames <i>M. Tehranizadeh & A. Moshref</i>	1883
Author index	

Preface

Performance-Based Design is increasingly employed recently in structural design of buildings and infrastructural facilities in many countries. The performance of foundation ground and soil structures under earthquake loading has long been a major topic of discussion since the beginning of TC4 in 1987 initiated by Professor Kenji Ishihara, the first Chairman. Professor Liam Finn, previous Chairman, emphasizing the importance of PBD in earthquake geotechnical engineering, held the Satellite Conference just before the 2005 ICSMGE in Osaka focusing on this problem.

Despite such long lasting efforts, PBD has not yet been established sufficiently in geotechnical engineering practice. Seismically induced ground deformation essential to performance design is not easy to evaluate mainly because, in contrast to superstructures, the ground is a 3-dimensional continuum with tremendous spatial variability and its stress-strain relationship is strongly nonlinear with dilatancy effect.

A rapid development in practical and reliable PBD is thus needed not only for foundation design but also for superstructures resting on incompetent soils. It is particularly true under circumstances where seismic ground motions observed during recent destructive earthquakes are getting larger. Such large motions often lead to intolerable results of foundational ground and superstructures resting on it, if they are designed by the conventional limit state design methodologies. Thus, we are urged to reconsider how to design new buildings and new civil engineering structures properly and also how to retrofit existing structures from the viewpoint of their performance under increasing seismic loads.

The first task toward this direction is to establish the performance criteria in the arena of earthquake geotechnical design to comply with the performance of buildings or civil engineering structures. The next major challenge for geotechnical engineering community is to shift from the limit state design to the strain/deformation evaluation based on time/frequency-domain calculations not only in research front but also in engineering practice as well.

More and more numerical analyses incorporating time-histories of input seismic motions and strong nonlinear response of soils are already in practice in this respect. However, in contrast to the conventional methods, uncertainties involved in the PBD become considerable in terms of seismic input, large-strain soil properties, optional parameters in numerical analyses, etc, which almost inevitably attracts designers' attention from the deterministic method to probabilistic approach.

What we need in judging their reliability and how to choose appropriate values for input parameters is a sort of benchmark case histories with well-documented geotechnical and seismic conditions. "Earthquake Geotechnical Case Histories for Performance-Based Design" published by TC4, ISSMGE, during this conference aims to serve as a common scale to measure the reliability of the analytical tools.

Also essential for PBD to be reliable enough is the improvement/innovation in soil investigation methodologies, in situ and in laboratory, and their data interpretations. In situ deformation properties, together with their statistical variability and strain-dependent nonlinearity need to be reevaluated in particular. Finally design codes, domestic and international, which support designers by stating the essence of PBD in geotechnical aspects without regulating too much detail in the scope of the performance of a total system are also very much desirable.

Under such current circumstances, it is really timely to hold IS-Tokyo 2009 "International Conference on Performance-based Design in Earthquake Geotechnical Engineering" to develop and share a common view on PBD in earthquake geotechnical engineering. In the conference, state-of-the-arts in PBD in earthquake geotechnical engineering are reviewed and discussed in keynote lectures, theme lectures and many technical sessions for typical problems including case histories, numerical methods, soil investigations. Discussion sessions will be held for case histories, performance evaluations, role of soil investigations and performance criteria/design codes. As one of the recent case histories during extremely strong earthquakes, Special Session on the 2008 Wenchuan Sichuan earthquake in China will also be held. At the end of Conference, Special Discussion Session on Future Directions of PBD will take place with panelists of honorable TC4 members.

About 240 technical papers including invited papers have been submitted from all over the world and printed in the proceedings. Among them, about 210 general papers have been peer-reviewed. I would like to show my

deep gratitude to the peer-reviewers who contributed their precious time. All the papers are accommodated in the CD-ROM of the proceedings in full color with the table of contents and serial page numbers, among which the invited papers and short papers concerning the discussion sessions are printed in black and white in the hard cover volume.

After agreeing to have this conference in TC4 meeting in Thessaloniki at the occasion of 4th ICEGE, an Organizing Committee including Special Task Team with the members given below have paid every effort to make this conference worthwhile. I would like to express my sincere gratitude to all the members for their great contribution. Among them, Professor Yoshimichi Tsukamoto, Secretary General, devoted a majority of his busy time and efforts in drafting the conference program, budgeting, serving as a liaison of general matters. Professor Michutoshi Yoshimine, Academic Secretary, made great effort in dealing with abstracts, full paper submissions, reviewing, etc. Professor Kenji Ishihara, the first Chairman of TC4, encouraged and advised the Committee members in constructing the conference program, the technical tour, etc. The organizing committee of IS-Tokyo 2009 would like to acknowledge that this conference is partly funded by Maeda Engineering Foundation. The cooperation to the Conference Exhibition by 17 engineering companies and 4 universities are also gratefully acknowledged.

Finally, it is my sincere hope that this conference will be able to serve as a milestone for international geotechnical engineers and researchers, in practically using and further developing Performance-Based Design methodologies in earthquake geotechnical engineering.

Takaji Kokusho
Professor of Chuo University,
Tokyo, Japan

Chairman of IS-Tokyo 2009

“International Conference on Performance-based Design in Earthquake Geotechnical Engineering”
Co-chairman of TC4, Geotechnical Earthquake Engineering and Associated Problems, ISSMGE.
June 2009

Committees

Conference Chairman

Prof. Takaji Kokusho

International Advisory Committee

Prof. A. Ansal (Turkey)

Prof. R.W. Boulanger (USA)

Prof. J.D. Bray (USA)

Prof. C.H. Chen (Taiwan)

Prof. M. Cubrinovski (New Zealand)

Prof. W.D.L. Finn (Canada)

Prof. I.M. Idriss (USA)

Prof. Myon-Mo Kim (Korea)

Prof. K. Pitilakis (Greece)

Prof. P. Seco e Pinto (Portugal)

Prof. F. Silvestri (Italy)

Prof. K.H. Stokoe II (USA)

Prof. R. Verdugo (Chile)

Prof. L. Wang (China)

Organizing Committee

Prof. T. Kokusho (Chairman)

Prof. S. Iai

Prof. K. Ishihara

Dr. M. Kanatani

Dr. O. Matsuo

Dr. T. Sugano

Dr. K. Takahashi

Dr. M. Tateyama

Prof. I. Towhata

Prof. S. Yasuda

Prof. N. Yoshida

Organizing Committee (Special Task Team)

Dr. Y. Tsukamoto (Secretary General)

Dr. M. Yoshimine (Academic Secretary)

Dr. H. Hazarika

Dr. J.L. Deng

Dr. K. Horikoshi

Dr. T. Ishizawa

Dr. T. Kawai

Dr. T. Kiyota

Dr. J.W. Lee

Dr. T. Matsushima

Dr. N. Sakai

Dr. S. Sawada

Dr. M. Shinoda

Dr. Y. Taji

Dr. Y. Yamada

Dr. K. Watanabe

Keynote lectures

Performance based earthquake design using the CPT

P.K. Robertson

Gregg Drilling & Testing Inc., Signal Hill, California, USA

ABSTRACT: Application of the Cone Penetration Test (CPT) for the evaluation of seismic performance is reviewed and updates presented. The role of the CPT in geotechnical earthquake engineering is presented. The use of the CPT to identify soil behavior type and the normalization of CPT parameters is also reviewed and updates presented. The case-history based method to evaluate the resistance of sand-like soils to cyclic loading is reviewed and compared with the expanded and re-evaluated case history database. The laboratory based method to evaluate the resistance of clay-like soils to cyclic loading is reviewed and modified for application using the CPT. A new combined CPT-based method to evaluate the resistance to cyclic loading is proposed that covers all soils and is evaluated using an expanded case history database. The CPT-based method is extended to estimate both volumetric and shear strains for all soils and evaluated using the expanded case history database.

1 INTRODUCTION

The seismic performance of geotechnical structures often requires an estimate of potential post-earthquake displacements. Historically, geotechnical earthquake design has focused extensively on evaluation of liquefaction in sandy soils since deformations tend to be large when soils experience liquefaction. Liquefaction analyses have traditionally focused on the evaluation of factor of safety and using this as an indicator of potential post-earthquake deformations. Recently there has been growing awareness that soft clays can also deform during earthquake loading.

In North American building codes (e.g. NBC 2005, FEMA 356 and SEAOC 1995), the design philosophy for earthquake loading is to accept some level of damage to structures, i.e. to accept some level of deformation. The acceptable level of damage and deformation is a function of the importance of the structure and the earthquake return period. The importance of the structure is a function of the risk. The evaluation of post-earthquake deformations is therefore a key element in any performance based earthquake design.

Due to size limitations, this paper will only discuss the application of the Cone Penetration Test (CPT) for the evaluation of post-earthquake deformations. The intent of this paper is not to imply that all earthquake geotechnical design can be accomplished using only the CPT; other in-situ tests along with sampling and laboratory testing also play a role, depending on the risk of the project.

2 ROLE OF CPT IN GEOTECHNICAL EARTHQUAKE ENGINEERING

Since this paper is focused on the application of CPT results for the evaluation of post-earthquake deformations, it is appropriate to briefly discuss the role of the CPT in geotechnical earthquake engineering practice. Hight and Leroueil (2003) suggested that the appropriate level of sophistication for a site characterization and analyses program should be based on the following criteria:

- Precedent and local experience
- Design objectives
- Level of geotechnical risk
- Potential cost savings

The evaluation of geotechnical risk was described by Robertson (1998) and is dependent on hazards (what can go wrong), probability of occurrence (how likely is it to go wrong) and the consequences (what are the outcomes). Earthquake loading can be a significant hazard, but the resulting risk is primarily a function of the probability of occurrence and the consequences. General recommendations for the appropriate level of sophistication for site investigation and subsequent design can be summarized in [Table 1](#). Although [Table 1](#) indicates only two broad outcomes, Robertson (1998) and Lacasse and Nadim (1998) showed that the level of risk cover a range from low to high and that the resulting site characterization program should vary accordingly.

Table 1. Appropriate level of sophistication for site characterization and analyses.

Rating	Criteria	Rating
Good	<i>Precedent & local experience</i>	Poor
Simple	<i>Design objectives</i>	Complex
Low	<i>Level of geotechnical risk</i>	High
Low	<i>Potential for cost savings</i>	High
Low risk project		High risk project
<i>Traditional</i>		<i>Advanced</i>
<i>(simplified) methods</i>		<i>(complex) methods</i>

For low risk projects, traditional methods, such as in-situ logging tests (e.g. CPT, SPT) and index testing on disturbed samples combined with conservative design criteria, are often appropriate. For the evaluation of liquefaction and post-earthquake deformations the Simplified Procedure, first proposed by Seed and Idriss (1971) and recently updated by Youd et al. (2001), is appropriate for low risk projects. For moderate risk projects, the Simplified Procedure should be supplemented with additional specific in-situ testing where appropriate, such as seismic CPT with pore pressure measurements (SCPTu) and field vane tests (FVT) combined with selective sampling and basic laboratory testing to develop site specific correlations. Sampling and laboratory testing is often limited to fine-grained soils where conventional sampling is easier and appropriate. For high risk projects, the Simplified Procedure can be used for screening to identify potentially critical regions/zones appropriate to the design objectives. This should be followed by selective high quality sampling and advanced laboratory testing. The results of laboratory testing should be correlated to in-situ test results to extend the results to other regions of the project. The Simplified Procedure for liquefaction evaluation should be used only as a screening technique to identify potentially critical regions/zones for high risk projects. Advanced techniques, such as numerical modeling, are often appropriate for more detailed evaluation of potential post-earthquake deformations for high risk projects.

One reason for the continued application of the Standard Penetration Test (SPT) as a basic logging test is that the test provides a soil sample suitable for index testing, even though the test can be unreliable. A common complaint about the CPT is that it does not provide a soil sample. Although it is correct that a soil sample is not obtained during the CPT, most commercial CPT operators have a simple push-in soil sampler that can be pushed using the CPT installation equipment to obtain a small (typically 25 mm diameter) disturbed sample of similar size to that obtained from the SPT. Often the most cost effective solution is to obtain a detailed continuous stratigraphic profile using the CPT, then to move over a short distance (<1 m)

and push a small diameter sampler to obtain discrete selective soil samples in critical layers/zones that were identified by the CPT. Continuous push samplers are also available to collect plastic-lined near continuous small diameter, disturbed soil samples. The push rate to obtain soil samples can be significantly faster than the 2 cm/s required for the CPT therefore making sampling rapid and cost effective for a small number of discrete samples. For low risk projects the efficiency and cost effectiveness of CPT, combined with adjacent discrete push-in soil samples, is usually superior to that of CPT plus adjacent boreholes with SPT.

Many of the comments and recommendations contained in this paper are focused on low to moderate risk projects where traditional (simplified) procedures are appropriate and where empirical interpretations tend to dominate. For projects where more advanced procedures are appropriate, the recommendations provided in this paper can be used as a screening to evaluate critical regions/zones where selective additional in-situ testing and sampling may be appropriate. Risk based site investigation and analysis is consistent with performance based design principles where the design criteria are in terms of deformation based on the risk of the structure.

3 BASIC SOIL BEHAVIOR UNDER EARTHQUAKE LOADING

Boulanger and Idriss (2004b, 2007) showed that, for practical purposes, soils can be divided into either 'sand-like' or 'clay-like' soils, where sand-like soils can experience 'liquefaction' and clay-like soils can experience 'cyclic failure'. In a general sense, sand-like soils are gravels, sands, and very-low plasticity silts, whereas clay-like soils are clays and plastic silts.

In general, all soils deform under earthquake loading. Earthquakes impose cyclic loading rapidly and soils respond undrained during the earthquake. In general, all soils develop some pore pressure during earthquake loading and at small strains these pore pressures are almost always positive. Sand-like soils can develop high positive pore pressures during undrained

cyclic loading and can reach a condition of zero effective confining stress. At the condition of zero effective stress, the initial structure of the soil is lost and the stiffness of the soil in shear is essentially zero or very small and large deformations can occur during earthquake loading. The condition of zero effective stress is often defined as 'liquefaction' or 'cyclic liquefaction'. Loose, young, uncemented sand-like soils are more susceptible to 'liquefaction' than dense sand-like soils. The ability of sand-like soils to liquefy is a function of in-situ state (relative density and effective confining stress), structure (age, fabric and cementation) and the size and duration of the cyclic loading. Most liquefaction cases occur in young uncemented sand-like soils. During earthquake loading, loose sand-like soils can experience very large shear strains which can result in large lateral and vertical deformations, depending on ground geometry and external static loads (e.g. buildings, embankments, slopes, etc.). Very loose sand-like soils can also experience strength loss after earthquake loading that can result in flow slides with very large deformations depending on ground geometry and drainage. Following earthquake loading, sand-like soils can also experience volumetric strains and post-earthquake reconsolidation settlements. The resulting volumetric strains can be large due to the loss of initial soil structure at zero effective stress and resulting small volumetric stiffness (constrained modulus) during initial reconsolidation. These settlements generally occur rapidly after the earthquake (i.e. in less than a few hours), depending on soil stratigraphy and drainage conditions.

Clay-like (cohesive) soils can also develop pore pressures during undrained cyclic loading, but generally do not reach zero effective stress and hence retain some level of stiffness during cyclic loading and generally deform less than sand-like soils. Traditionally, clay-like soils are considered not susceptible to liquefaction, since they generally do not reach a condition of zero effective stress. However, clay-like soils can deform during cyclic earthquake loading. The amount of pore pressure buildup is a function of in-situ state (overconsolidation ratio), sensitivity, structure (age, fabric and cementation) and size and duration of cyclic loading. Soft normally to lightly overconsolidated and sensitive clay-like soils can develop large positive pore pressures with significant shear strains during earthquake loading that can result in lateral and vertical deformations, depending on ground geometry and external static loads (e.g. buildings, embankments, slopes, etc.). Very sensitive clay-like soils can also experience strength loss after earthquake loading that can result in flow slides with very large deformations depending on ground geometry. Following earthquake loading, clay-like soils can also experience volumetric strains and post-earthquake reconsolidation settlements. However, these settlements generally occur slowly after the earthquake due to the lower

permeability of clay-like soils and are also a function of soil stratigraphy and drainage conditions. The volumetric strains during post-earthquake reconsolidation are generally small since clay-like soils often retain some original soil structure and hence, maintain a high value of volumetric stiffness during reconsolidation.

Following earthquake loading, pore-water redistribution can result in some sand-like soils changing void ratio and becoming looser. This can result in strength loss and the potential for instability.

Recent research has indicated that the transition from sand-like to clay-like soils can be approximately defined by Atterberg Limits (e.g. plasticity index) of the soil (Seed et al, 2003; Bray and Sancio, 2006; Boulanger and Idriss, 2007). Sangrey et al. (1978) suggested that the transition was controlled by the compressibility of the soil, where, in general, clay-like soils have a higher compressibility than sand-like soils. In a general sense, soft normally consolidated clay-like fine grained soils respond in a similar manner to loose sand-like soils in that they are both contractive under shear and develop positive pore pressures in undrained shear. Highly sensitive clay-like soils are similar to very loose sand-like soils in that both can experience a large increase in pore pressure under undrained shear and can experience significant strength loss (i.e. strain soften). Stiff overconsolidated clay-like fine grained soils respond in a similar manner to dense sand-like soils in that they both dilate under shear at high strains. Soil response in fine grained soils is controlled partly by the amount and type of clay minerals. The plasticity index is an approximate measure of the mineralogy of the soil, where the amount and type of clay mineral influences soil behavior.

Traditionally, the response of sand-like and clay-like soils to earthquake loading is evaluated using different procedures. It is common to first evaluate which soils are sand-like, and therefore susceptible to liquefaction based on grain size distribution and Atterberg Limits, and then to determine the factor of safety (FS_{liq}) against liquefaction. A key element in performance based geotechnical earthquake design is the evaluation of post-earthquake deformations. The challenge is to develop procedures that capture the correct soil response as soil transitions from primarily sand-like to clay-like in nature. The objective of this paper is to outline a possible unified approach for all soils using CPT results with the ultimate goal to evaluate possible post-earthquake deformations.

4 CPT SOIL BEHAVIOUR TYPE

One of the major applications of the CPT has been the determination of soil stratigraphy and the identification of soil type. This has been accomplished using charts that link cone parameters to soil type. Early charts using q_c and friction ratio (R_f) were proposed

by Douglas and Olsen (1981), but the charts proposed by Robertson et al. (1986) have become popular. Initially these charts were based on empirical correlations, but theoretical studies have supported the general concepts. Robertson et al. (1986) and Robertson (1990) stressed that the charts were predictive of Soil Behaviour Type (SBT) since the cone responds to the mechanical behaviour of the soil and not directly to soil classification criteria based on grain-size distribution and soil plasticity. Fortunately, soil classification criteria based on grain-size distribution and plasticity often relate reasonably well to soil behaviour and hence, there is often good agreement between soil classification based on samples and SBT based on the CPT. Several examples can be given when differences arise between soil classification and SBT based on CPT. For example, a soil with 60% sand and 40% fines may be classified as 'silty sand' using the unified classification system. However, if the fines are composed of a highly active clay mineral with high plasticity, the soil behaviour may be controlled more by the clay and the SBT from the CPT will reflect this behaviour and predict a more clay-like behaviour, such as 'clayey silt'. If the fines were non-plastic the soil behaviour may be controlled more by the sand, the CPT SBT would predict a sand like soil type, such as 'silty sand'. Saturated loose silts often behave like soft clay in that their undrained strength is low and undrained response often governs geotechnical design. Hence, SBT based on CPT in soft saturated silts is often defined as clay. Very stiff heavily overconsolidated fine-grained soils tend to behave similar to coarse-grained soil in that they dilate at large strains under shear and can have high undrained shear strength compared to their drained strength. These few examples illustrate that the SBT based on the CPT may not always agree with traditional classification based on samples. Geotechnical engineers are usually interested in the behaviour of the soil rather than a classification based only on grain-size distribution and plasticity, although knowledge of both is useful.

The corrected cone (tip) resistance (q_t) responds to the average shear strength (depending on soil sensitivity, heterogeneity and macro fabric) of the soil ahead and behind the advancing cone, whereas the sleeve friction (f_s) and measured pore pressure (u_2) responds to the larger strain behaviour of the soil in contact with the cone. There is also a small scale effect and physical offset between the q_t and f_s measurements. Typically most commercially available CPT data acquisition systems adjust the two readings to present them at the same depth in the soil profile (i.e. the f_s reading is recorded when the center of the sleeve has reached the same depth/elevation as the cone tip). Soils with gravel particles can produce rapid unrepresentative variations in sleeve friction due to large particles touching the friction sleeve.

Robertson (1990) updated the CPT SBT charts using normalized (and dimensionless) cone parameters, Q_{t1} , F_r , B_q , where:

$$Q_{t1} = (q_t - \sigma_{v0})/\sigma'_{v0} \quad (1)$$

$$F_r = [(f_s/(q_t - \sigma_{v0}))] 100\% \quad (2)$$

$$B_q = \Delta u/(q_t - \sigma_{v0}) \quad (3)$$

where:

σ_{v0} = pre-insertion in-situ total vertical stress

σ'_{v0} = pre-insertion in-situ effective vertical stress

u_0 = in-situ equilibrium water pressure

Δu = excess penetration pore pressure.

In the original paper by Robertson (1990) the normalized cone resistance was defined using the term Q_t . The term Q_{t1} is used here to show that the cone resistance is the corrected cone resistance, q_t with the stress exponent for stress normalization $n = 1.0$. Note that in clean sands, $q_c = q_t$, but the more correct q_t is used in this paper.

In general, the normalized charts provide more reliable identification of SBT than the nonnormalized charts, although when the in-situ vertical effective stress is between 50 kpa to 150 kpa there is often little difference between normalized and non-normalized SBT. The term SBTn will be used to distinguish between normalized and non-normalized SBT. Robertson (1990) suggested two charts based on either $Q_{t1} - F_r$ or $Q_{t1} - B_q$ but recommended that the $Q_{t1} - F_r$ chart was generally more reliable, especially for onshore geotechnical investigations where the CPT pore pressure results are more problematic and less reliable.

Jefferies and Davies (1993) identified that a Soil Behaviour Type Index, I_c , could represent the SBTn zones in the $Q_{t1} - F_r$ chart where I_c is essentially the radius of concentric circles that define the boundaries of soil type. Robertson and Wride (1998) modified the definition of I_c to apply to the Robertson (1990) $Q_{t1} - F_r$ chart, as defined by:

$$I_c = [(3.47 - \log Q_{t1})^2 + (\log F_r + 1.22)^2]^{0.5} \quad (4)$$

Contours of I_c are shown in [Figure 1](#) on the Robertson (1990) $Q_{t1} - F_r$ SBTn chart. The contours of I_c can be used to approximate the SBT boundaries.

Jefferies and Davies (1993) suggested that the SBT index I_c could also be used to modify empirical correlations that vary with soil type. This is a powerful concept and has been used where appropriate in this paper.

Robertson and Wride (1998) and updated by Zhang et al. (2002) suggested a normalized cone parameter, using normalization with a variable stress exponent, n , where:

$$Q_{tn} = [(q_t - \sigma_v)/p_a](p_a/\sigma'_{v0})^n \quad (5)$$

where:

$(q_t - \sigma_v)/p_a$ = dimensionless net cone resistance,

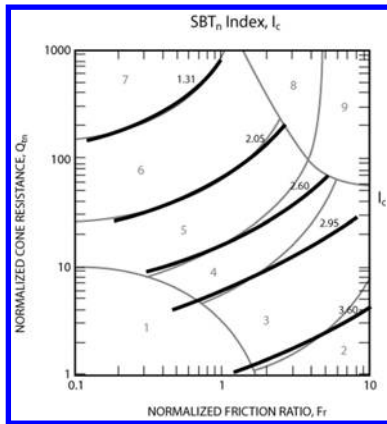


Figure 1. Contours of soil behaviour type index, I_c on normalized SBT $Q_{tn} - F_r$ chart.

$(p_a/\sigma'_{vo})^n$ = stress normalization factor
 n = stress exponent that varies with SBTn
 p_a = atmospheric pressure in same units as q_t and σ_v .

Robertson and Wride (1998) and Zhang et al. (2002) use the term, q_{c1N} instead of Q_{tn} . This paper will use the more general term, Q_{tn} . Where the term 'Q_t' denotes normalized corrected cone resistance and the subscript 'n' denotes normalization with a variable stress exponent. Note that, when $n = 1$, $Q_{tn} = Q_{t1}$. Zhang et al. (2002) suggested that the stress exponent, n , could be estimated using the SBTn Index, I_c , and that I_c should be defined using Q_{tn} .

Robertson (2008) recently updated the stress normalization by Zhang et al. (2002) to allow for a variation of the stress exponent with both SBTn I_c and effective overburden stress using:

$$n = 0.381(I_c) + 0.05(\sigma'_{vo}/p_a) - 0.15 \quad (6)$$

where $n \leq 1.0$.

Robertson (2008) suggested that the above modification to the stress exponent would capture the correct state response for soils at high stress level and would avoid the need for a further stress level correction (K_σ) in liquefaction analyses.

There have been several publications regarding the appropriate stress normalization (Olsen and Malone, 1988; Robertson, 1990; Jefferies and Davies, 1991; Robertson and Wride, 1998; Zhang et al., 2002; Boulanger and Idriss, 2004a; Moss et al., 2006; Cetin and Isik, 2007; Robertson, 2008). The contours of stress exponent suggested by Cetin and Isik (2007) are very similar to those first suggested by Robertson and Wride (1998), updated by Zhang et al. (2002) and further modified slightly by Robertson (2008). The contours by Moss et al. (2006) are similar to those first suggested by Olsen and Malone (1988). The normalization suggested by Boulanger and Idriss (2004a)

only applies to sands where the stress exponent varies with relative density with a value of around 0.8 in loose sands and 0.3 in dense sands. Figure 2 shows a comparison of the stress exponent contours suggested by Robertson (2008) for $\sigma'_{vo}/p_a = 1.0$, Moss et al. (2006), and Boulanger and Idriss (2004a) on the normalized SBTn chart of $Q_{tn} - F_r$. The regions where the three methods provide similar values are highlighted and show that the methods agree on or close to the normally consolidated zone suggested by Robertson (1990). Wroth (1984) showed that the stress exponent is 1.0 for clays based on Critical State Soil Mechanics (CSSM) theory, which is reflected in the Robertson (1990 & 2008) contours. The contours suggested by Olsen and Malone (1988) and Moss et al. (2006) are not supported by CSSM.

Robertson (1990) stated that the soil behaviour type charts are global in nature and should be used as a guide for defining Soil Behaviour Type (SBT). Caution should be used when comparing CPT-based SBT to samples with traditional classification systems based only on grain size distribution and plasticity. Factors such as changes in stress history, in-situ stresses, macro fabric, cementation, sensitivity and void ratio/water content will also influence the CPT response and resulting SBT. The rate and manner in which the excess pore pressures dissipate during a pause in the cone penetration can significantly aid in identifying soil type.

Robertson (1990) and others have suggested that soils that have a SBTn index $I_c < 2.5$ are generally cohesionless where the cone penetration is generally drained and soils that have $I_c > 2.7$ are generally cohesive where the cone penetration is generally undrained. Cone penetration in soils with $2.5 < I_c < 2.7$ is often partially drained.

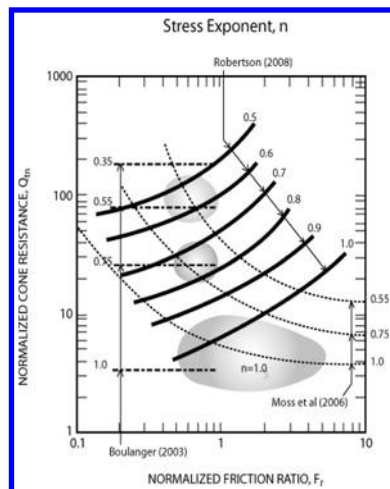


Figure 2. Comparison of contours of stress exponent 'n' on normalized SBTn chart $Q_{tn} - F_r$.

5 SOIL STRATIGRAPHY—TRANSITION ZONES

Robertson and Campanella (1983) discussed how the cone tip resistance is influenced by the soil ahead and behind the cone tip. Ahmadi and Robertson (2005) illustrated this using numerical analyses and confirmed that the cone can sense a soil interface up to 15 cone diameters ahead and behind, depending on the strength/stiffness of the soil and the in-situ effective stresses. In strong/stiff soils, the zone of influence is large (up to 15 cone diameters), whereas, in soft soils, the zone of influence is rather small (as small as 1 cone diameter). Ahmadi and Robertson (2005) showed that the zone of influence decreased with increasing stress (e.g. dense sands behave more like loose sands at high values of effective stress).

For interbedded soil deposits, the thinnest stiff soil layer for which the measured cone resistance represents a full response is about 10 to 30 cone diameters. Hence, as described by Robertson and Campanella (1983), soil parameters may be under-estimated in thin stiff layers embedded within a softer soil (e.g. thin sand layers in a softer clay). Fortunately, the cone can sense a thin soft soil layer more precisely than a thin stiff soil layer. The fact that the cone can underestimate the soil resistance in thin stiff layers has led to the thin layer correction for liquefaction analyses (Robertson and Wride, 1998, Youd et al., 2001).

The zone of influence ahead and behind a cone during penetration will influence the cone resistance at

any interface (boundary) between two soil types of significantly different strength and stiffness. Hence, it is often important to identify transitions between different soils types to avoid possible misinterpretation. This issue has become increasingly important with software (or spreadsheets) that provide interpretation of every data point from the CPT. When CPT data are collected at close intervals (typically every 20 to 50 mm) several data points are ‘in transition’ when the cone passes an interface between two different soil types (e.g. from sand to clay and vice-versa). For thin stiff layers the two interface regions can join such that the cone resistance may not represent the true value of the thin layer.

It is possible to identify the transition from one soil type to another using the rate of change of either I_c or Q_{tn} . When the CPT is in transition from sand to clay, the SBTn I_c will move from low values in the sand to higher values in the clay. Robertson and Wride (1998) suggested that the approximate boundary between sand-like and clay-like behaviour is around $I_c = 2.60$. Hence, when the rate of change of I_c is rapid and is crossing the boundary defined by $I_c = 2.60$, the cone is likely in transition from a sand-like to clay-like soil, or vice-versa. Profiles of I_c provide a simple means to identify these transition zones. Figure 3 illustrates a CPT profile through a deposit of interbedded sands and clays and shows how computer software (CLiq, 2008) can identify transition zones on the I_c profile based on the rate of change of I_c as I_c crosses the value 2.60. There are clear transitions from clay to

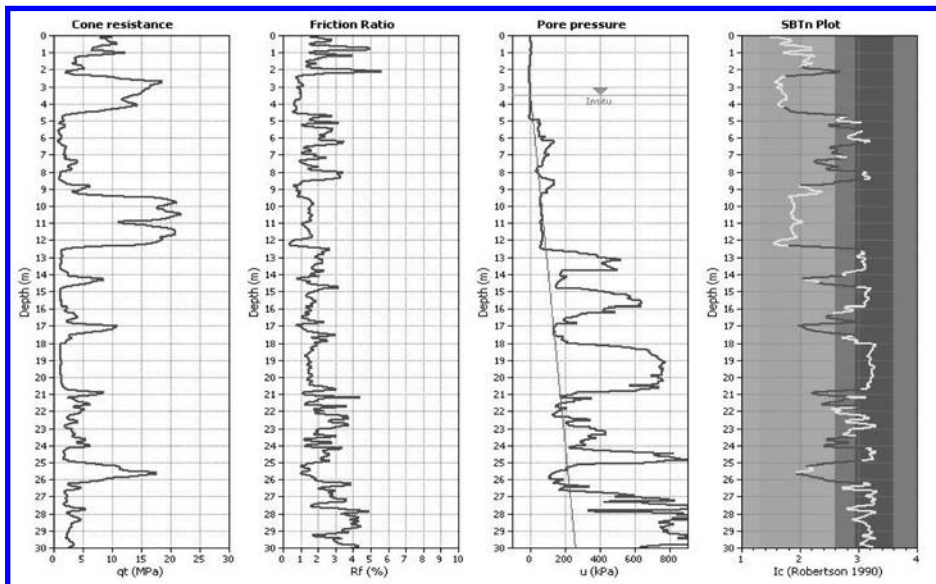


Figure 3. Example of interbedded soil profile with transition zones identified (in red) on SBTn I_c plot (CLiq Software, Geologismiki).

sand (and vice-versa) at depths of 4.5, 8.5, 12.5, 14.1, 14.5, 16.9, 17.5, and 20.5 m. The region between 5.0 to 8.0 m, and again between 20.5 to 21.8 m, represent soils close to the boundary of $I_c = 2.60$. Although these transitions could be identified from combinations of Q_{tn} , F_r and B_q , the algorithm (software) that identifies the zones on the profile of I_c appears to be more effective. Figure 3 also illustrates that the pore pressure measurements are less effective at shallow depths where saturation of the CPT sensor may be less effective. At depths of about 14 m, 17 m and 21 m there are thin sand layers where the maximum values in the sand are likely too low due to the adjacent transition zones. Hence, identification of transition zones aids in the recognition of thin layers that may require correction (Youd et al., 2001).

6 RESISTANCE TO EARTHQUAKE LOADING

Idriss and Boulanger (2008) present a summary of the history and background on the evaluation of liquefaction resistance to earthquake loading. They describe in detail how the Factor of Safety (FS_{liq}) against triggering of liquefaction in sand-like soils can be computed as the ratio of the soils CRR to the earthquake-induced CSR, with both the CRR and CSR values pertaining to the design earthquake magnitude (M) and in-situ effective overburden stress (σ'_{vo}):

$$FS_{liq} = CRR_{M,\sigma'_{vo}} / CSR_{M,\sigma'_{vo}} \quad (7)$$

Alternately, it is common to convert the earthquake-induced CSR into the reference condition applicable to $M = 7.5$ and $\sigma'_{vo} = 1$ atm. (i.e. $\sigma'_{vo}/p_a = 1$).

$$FS_{liq} = CRR_{M=7.5, \sigma'_{vo}=1} / CSR_{M=7.5, \sigma'_{vo}=1} \quad (8)$$

where:

$CRR_{M=7.5, \sigma'_{vo}=1}$ = Cyclic Resistance Ratio applicable to $M = 7.5$ and an effective overburden stress of $\sigma'_{vo} = 1$ atm., sometimes presented as simply $CRR_{7.5}$.

$CSR_{M=7.5, \sigma'_{vo}=1}$ = earthquake induced Cyclic Stress Ratio adjusted to the equivalent CSR for the reference values of $M = 7.5$ and an effective overburden stress of $\sigma'_{vo} = 1$ atm., sometimes presented as simply $CSR_{7.5}$.

For low-risk projects, CSR is typically estimated using the Simplified Procedure first described by Seed and Idriss (1971), using:

$$CSR_{7.5} = 0.65[a_{max}/g][\sigma_{vo}/\sigma'_{vo}]r_d[1/MSF][1/K_\sigma] \quad (9)$$

Alternate methods have been suggested for estimating the correction factors, r_d , MSF and K_σ .

Boundary lines have been developed that separate case histories in which 'liquefaction' was observed, from case histories in which liquefaction was not observed. This boundary line is used to provide the relationship between in-situ $CRR_{7.5}$ and an in-situ test

index. Due to space limitations, this paper will only present CPT-based methods to estimate $CRR_{7.5}$.

6.1 Sand-like (cohesionless) soils

$CRR_{7.5}$ for sand-like soils is generally defined in terms of 'triggering' liquefaction (i.e. reaching zero effective stress) although laboratory testing often uses a critical shear strain level (e.g. $\gamma = 3\%$). Triggering of 'liquefaction' in loose sands is the onset of large strains. Therefore, since $CRR_{7.5}$ is traditionally used to define 'liquefaction' it can also be used to define the onset of large deformations. If the factor of safety against 'liquefaction' is less than 1 (i.e. $FS_{liq} < 1$) shear strains can be large and tend to increase as the factor of safety decreases, especially for loose sands.

The evaluation of CRR has evolved primarily from case histories of past earthquakes. The earliest efforts began with attempts to use SPT data (Kishida, 1966, Seed et al, 1984). In the early 1980's efforts were made to use CPT data (Zhou, 1980; Robertson and Campanella, 1985). In 1996–97, a workshop by NCEER and NSF provided a summary and recommendations on SPT-, CPT-, and V_s -based correlations and procedures (Youd et al., 2001). Following the NCEER workshop several major earthquakes provided new case histories. Moss et al. (2006) produced a compilation of the expanded database.

The NCEER/NSF workshop provided a set of recommendations by over 20 leading experts and was summarized by Youd et al. (2001). Youd et al. (2001) recommended the Robertson and Wride (1998) method for the CPT-based approach to evaluate CRR for cohesionless soils ($I_c < 2.60$). However, since 1997 there have been several publications attempting to update these recommendations. These updates have led to some confusion in practice, since changes were suggested to both CSR and CRR, which often resulted in minor changes to the calculated FS_{liq} .

Traditionally, case history data have been compiled by identifying the combination of the earthquake-induced cyclic stress ratio, CSR, and in-situ test results that best represents the 'critical zone' where liquefaction was estimated to have occurred for each site. It has been common to adopt a magnitude $M = 7.5$ earthquake, an effective overburden stress of $\sigma'_{vo} = 1$ atm and case histories with modest static shear stress (i.e. essentially level ground conditions). The resulting $CSR_{7.5}$ values are plotted against the in-situ test results normalized to $\sigma'_{vo} = 1$ atm. The resulting plots are then used to develop boundary lines separating cases of 'liquefaction' from cases of 'non-liquefaction' and, therefore, a method to estimate the $CRR_{7.5}$. This paper will focus only on the approaches that use CPT results, since the CPT is generally considered more repeatable and reliable than the SPT and provides continuous data in a cost effective manner.

Although this traditional approach of using case history data has resulted in significant developments, the approach has some limitations. The following is a short description of the main limitations.

'Liquefaction' and 'Non-liquefaction': field evidence of 'liquefaction' generally consists of surface observations of sand boils, ground fissures or lateral spreading. Sites that show no surface features may have experienced either liquefaction or the development of significant pore pressures in some soil layers, but no sand boils resulted, either due to the depth of the layer or the overlying deposits. Also, sites that show no surface deformation features may have experienced significant pore pressure development in some soil layers, but showed limited post-earthquake deformations due to ground geometry and lack of any significant static loads. Few case histories have well documented deformation records where deformations were recorded with depth.

Selecting the 'critical zone': the depth where 'liquefaction' was assumed to have occurred requires considerable judgment. Occasionally, this is based on linking sand boil material to a specific soil layer, but often the selection is more subjective.

Average data points to represent each site: considerable judgment is required to select an appropriate average value for the in-situ test. For SPT results this was simpler because there were often only 1 or 2 SPT values in the critical zone. However, for CPT results this is more difficult, since there can be many CPT values within a layer. CPT results often show that a soil layer is not uniform either in terms of consistency (i.e. density/state) or grain characteristics (e.g. fines content/plasticity). In critical soil layers, where the soil is non-uniform and the cone resistance is variable, an 'average' value can be misleading.

Although the SPT- and CPT-based design methods were developed using average values, the methods are generally applied to all data points for design. CPT data are generally recorded at 5 cm depth intervals to provide a near continuous profile. Hence, application of case-history based design methods, using the near continuous CPT profile, incorporate some level of conservatism. Applying the CPT-based methods to average in-situ test values for design requires judgment in selecting appropriate representative average values, and details in the near continuous profile can be lost.

Although the traditional approach has limitations, it has resulted in relatively simple approaches to evaluate a complex problem. Moss et al. (2006) (based on Moss, 2003) compiled a comprehensive database based on CPT records. For this paper, the Moss (2003) database has been re-evaluated using the continuous digital CPT records, where available, to confirm or modify the estimated average in-situ test values. The re-evaluation focused primarily on case histories that plot close to the boundary lines, since these play a more important role in defining the boundary line.

The near continuous CPT records were processed through software that incorporates the updated Robertson and Wride (1998); Zhang et al. (2002) and Zhang et al. (2004) CPT-based method as well as transition zone detection and the updated Robertson (2008) stress normalization (equation 6) (CLiq www.geologismiki.gr). The re-evaluation showed that the Robertson and Wride (1998) method performed extremely well on the database of near continuous CPT records. Some sites that appeared to have 'liquefaction' average data points on the 'non-liquefaction' side of the boundary line actually predicted 'liquefaction' (i.e. had regions in the critical layer where the computed $FS_{liq} < 1$) when using the near continuous CPT data. Hence, at sites where the Robertson and Wride (1998) method would appear to have incorrectly predicted performance based on the case history results using Moss et al. (2006) average values, the method predicted the correct performance using the measured near continuous values in terms of liquefaction (i.e. $FS_{liq} < 1.0$) and post-earthquake deformations. Some key sites, where the average values selected by Moss et al. (2006) were considered inappropriate, are the sites at Whiskey Springs (1983 Borah Peak earthquake). These sites were composed of gravelly sands to sandy gravels and the CPT results showed significant rapid variation caused by the gravel content. The CPT measurements at these sites were less reliable due to the gravel content, and the average values selected by Moss et al. (2006) were considered too high and unrepresentative of the loose sand matrix that likely dominated the buildup of pore pressures during the earthquake. Other key sites are Balboa Blvd. and Malden St. (1994 Northridge, USA) and Kornbloom (1982 Westmorland, USA). Average values can be misleading in interbedded soils and may not adequately represent the various individual soil layers.

Moss et al. (2006) and Juang et al. (2003) have used the expanded case history database based on average values to provide criteria based on probability. The re-evaluation, using near continuous CPT records, suggest some uncertainty on proposed levels of probability, due to the highly subjective nature of the average values selected and the observation that some 'liquefaction' and 'non-liquefaction' sites were incorrectly classified when using only the Moss et al. (2006) average values. It is recommended that the near continuous CPT data be used to evaluate various CPT-based liquefaction methods and not average values that were subjectively selected. It is also interesting to note that, to the authors knowledge, none of the more recent CPT-based methods (i.e. post-Youd et al., 2001) used the recorded near continuous CPT records from the case histories to confirm the accuracy of the proposed new methods.

The Moss et al. (2006) database included 182 case history results (146 'liq' and 36 'non-liq'). However,

30 cases (23 'liq' and 7 'non-liq') were described as 'Class C' data that were case histories where the CPT results were obtained using either 'non-standard or mechanical cone' or 'no friction sleeve data available'. The Class C data are clearly less reliable than the rest of the data, especially for methods that make use of the friction sleeve results in the form of either friction ratio, R_f (Moss et al., 2006) or soil behavior type, I_c (Robertson and Wride, 1998; Juang et al., 2003). Robertson and Campanella (1983) showed that mechanical cone friction sleeve values can be significantly different from standard electric cone values in the same soil.

The database, (with Class C data removed) where liquefaction was observed, had earthquake magnitudes in the range $5.9 < M_w < 7.7$ and vertical effective stress in the range $15 \text{ kpa} < \sigma'_v < 135 \text{ kpa}$. The average vertical effective stress in the liquefied layers was 60 kpa. No liquefaction, based on surface observations, was considered to have occurred at a depth greater than 16 m. The average depth for the critical liquefiable layers was around 5 to 6 m.

All the CPT-based methods (to determine $CSR_{7.5}$) typically include corrections for depth (r_d), magnitude scaling factors (MSF) and overburden correction factor (K_σ). The variations in these correction factors when applied to the database are generally small. Hence, the database is insufficient to clarify which correction methods are appropriate for design. Most methods specify that consistency is required when applying the methods to design problems (i.e. use the same correction factors on which the method was based). This paper uses the correction factors (r_d , MSF, K_σ) suggested by the NCEER workshop (Youd et al., 2001), with $K_\sigma = 1.0$.

Figure 4 shows a summary plot of the reevaluated expanded database in terms of CPT results in the form of $CSR_{7.5}$ versus normalized cone resistance (Q_{tn}). The Class C data are not included in Figure 4. Figure 4 includes some case history data where the soil was not considered to be 'clean sand', however, the resulting boundary line is unaffected, because the 'liq' data in soils that are not 'clean sands' have lower cone resistance (i.e. located to the left of the boundary line). The resulting boundary line is often referred to as the 'clean sand' boundary line.

Figure 4 also shows some of the most recent published correlations superimposed over the updated database. The comparison in Figure 4 is not strictly correct, since the various published procedures include different normalization procedures for the CPT results. Fortunately, the differences, when applied to the case history data, are generally small (less than 20%), since all of the case history data are from sites where the range in vertical effective stress was small ($15 \text{ kpa} < \sigma'_v < 135 \text{ kpa}$). The various correlations are similar in the region of maximum data ($20 < Q_{tn} < 100$). When Q_{tn} is larger than 100 the correlations differ,

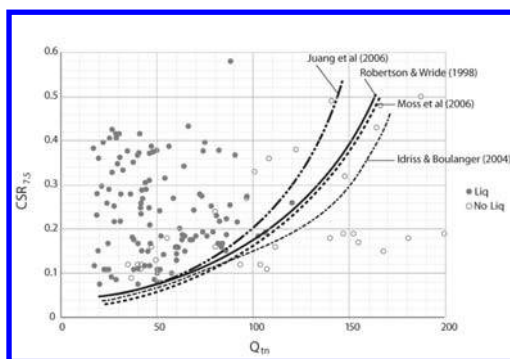


Figure 4. Updated case history database in terms of $CSR_{M=7.5, \sigma'_{vo}=1}$ VS Q_{tn} (Class C data excluded).

mainly due to the form of the suggested correlations. Hence, for 'clean sands' the baseline correlation to estimate $CRR_{7.5}$ from CPT results is reasonably well established, especially in the region defined by $20 < Q_{tn} < 100$. It is likely that there will be little gained from further evaluation of current case history data using average values for clean sands in the form of $CSR_{7.5} - Q_{tn}$ plots. It is also recommended that further fine-tuning of the $CRR_{7.5}$ relationships using average values will be ineffective, since the location of the boundary is sensitive to the judgment used to select appropriate average in-situ test values. The form of the relationship controls $CRR_{7.5}$ for $Q_{tn} > 100$, since very little field data exists in this range. The form of the relationship becomes important when the method is extended to estimate post-earthquake displacements.

For soils that are not 'clean sands', the traditional approach has been to adjust the in-situ penetration results to an 'equivalent clean sand' value. This evolved from the SPT-based approach where samples could be obtained and the easiest parameter to quantify changes in grain characteristics was the percent fines content.

Research has clearly shown that fines content alone does not adequately capture the change in soil behavior. Also, the average fines content of an SPT sample may not always reflect the variation in grain characteristics in heterogeneous soils, since it is common to place the full SPT sample into a container for subsequent grain size analyses, with resulting misleading 'average' fines content. The recent Idriss and Boulanger (2008) CPT-based approach that uses only fines content from samples to make adjustments to cone resistance is a retrograde step and is not recommended.

Several recent CPT-based liquefaction methods use modified CPT results to estimate clean sand equivalent values based on either SBT I_c (e.g. Robertson and Wride, 1998; Juang et al., 2006) or friction ratio, R_f , (Moss et al., 2006). Figure 5 shows a summary plot of

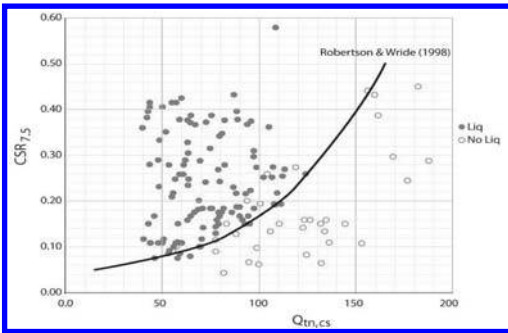


Figure 5. Updated case history database in terms of $CSR_{M=7.5, \sigma'_{vo}=1}$ vs $Q_{tn,cs}$ (Class C data excluded).

the reevaluated expanded database, in terms of CPT results in the form of $CSR_{7.5}$ versus normalized clean sand equivalent cone resistance ($Q_{tn,cs}$), based on the corrections suggested by Robertson and Wride (1998) using I_c .

Good agreement exists between the expanded database and the original Robertson and Wride (1998) CPT-based method.

Figures 6 and 7 show the updated database plotted on the normalized SBTn chart ($Q_{tn} - F_r$), where Q_{tn} and F_r were calculated using the method suggested by Zhang et al. (2002) and recently modified slightly by Robertson (2008). Figure 6 shows the case history data where $0.20 < CSR_{7.5} < 0.50$. Figure 7 shows the data where $CSR_{7.5} < 0.20$. The case history database is insufficient to subdivide the data into smaller divisions in the $Q_{tn} - F_r$ format, since both are on log scales. Presenting the case history data, in terms of the full CPT data (Q_{tn} and F_r) on the SBT chart, provides a different view of the influence of changing soil type on the correlations. Superimposed on the SBTn chart are the contours for $CRR_{7.5}$ suggested by Robertson and Wride (1998) in the region where $I_c < 2.60$. The Class C data are also included in Figures 6 and 7 but are identified using a different symbol. The Moss et al. (2006) corrections using friction ratio (R_f), appear to be influenced by the questionable Class C data. It is also interesting to note that, excluding the questionable Class C data, there are no case histories of observed 'liquefaction' based on average CPT values where $I_c > 2.60$. It is useful to remember that each data point, in terms of Q_{tn} and F_r , represents an average value for the critical layer.

Figure 8 shows the data where $CSR_{7.5} < 0.20$ with the correlations suggested by Olsen and Koester (1995); Suzuki et al. (1995); Robertson and Wride (1998) and Moss et al. (2006), for comparison. This format provides a way to compare the different 'correction' factors to adjust CPT results for soil type. The correlations suggested by Moss et al. (2006) appear

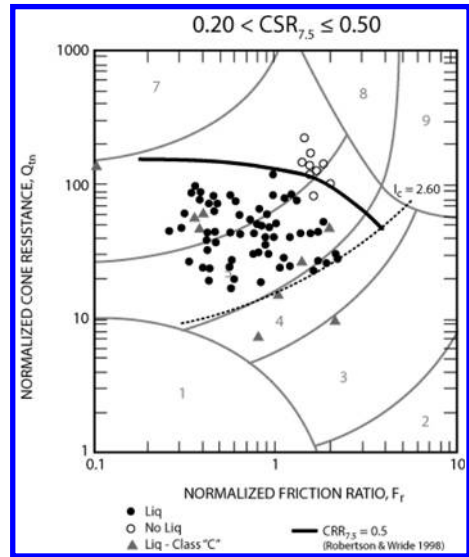


Figure 6. Updated database on SBTn $Q_{tn} - F_r$ chart for $0.20 < CRR_{7.5} < 0.50$ and Robertson and Wride (1998) contour for $CRR_{7.5} = 0.50$ ($I_c < 2.60$).

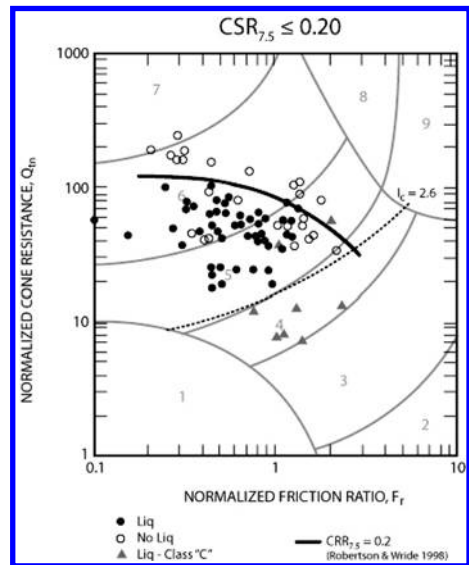


Figure 7. Updated database on SBTn $Q_{tn} - F_r$ chart for $CRR_{7.5} < 0.20$ and Robertson and Wride (1998) contour for $CRR_{7.5} = 0.20$ ($I_c < 2.60$).

to be too conservative at high values of either friction ratio or I_c . This was partly a result of using the unreliable Class C data, as well as inappropriate average values for some key sites, especially the sites from Whiskey Springs. The correlations suggested

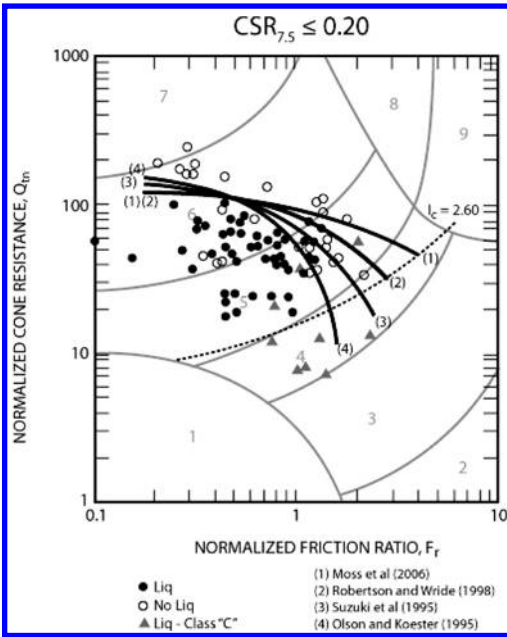


Figure 8. Comparison of published correlations on SBT $Q_{th} - F_r$ chart for $CRR_{7.5} < 0.20$.

by Suzuki et al. (1995) and Olsen and Koester (1995) appear to be unconservative at high values of I_c , which was also pointed out by Robertson and Wride (1998).

6.2 Clay-like (cohesive) soils

Since cohesive clay-like soils are not susceptible to ‘liquefaction’, the criteria used to define CRR is deformation, which is often assumed to be a shear strain of $\gamma = 3\%$. Since detailed deformation records are uncommon in many case histories, much of our understanding regarding the response of cohesive soils to earthquake loading derives from undrained cyclic laboratory testing. Fortunately, it is also possible to obtain high quality undisturbed samples in many clay-like soils.

Sangrey et al. (1978) showed that fine-grained soils tend to reach a critical level of repeated loading that is about 80% of the undrained shear strength (s_u). Boulanger and Idriss (2006, 2007) provided a summary of the response of cohesive soils to cyclic loading. There is a strong link between the cyclic undrained response of fine-grained soils and their monotonic undrained response. The monotonic response of fine-grained soils is generally defined in terms of their peak undrained shear strength, s_u . Although the undrained shear strength is not a unique soil parameter, since it varies with the direction of loading, it does provide a simple way to understand the behavior of cohesive soils and captures many features (e.g. stress

history, age and cementation). During earthquake loading, the predominant direction of loading is simple shear; hence, the undrained strength in simple shear is often the most appropriate parameter to link with CRR. Since earthquake loading is best defined in terms of CSR (τ_{cy}/σ'_v), it is appropriate to compare this with the undrained strength ratio (s_u/σ'_v). In simple terms, if the earthquake imposes a shear stress ratio that is close to the undrained strength ratio of the soil, the soil will deform. Since earthquake loading is rapid and cyclic, the resulting deformations may not constitute ‘failure’ (i.e. unlimited deformations). However, shear deformations can be large and tend to progress during the earthquake. Boulanger and Idriss (2004) used the term ‘cyclic softening’ to describe the progression of shear strains during cyclic undrained loading in fine-grained soils.

Boulanger and Idriss (2004b) presented published data that showed that, when the CSR ratio approaches about 80% of s_u/σ'_v , deformations tend to become large. Wijewickreme and Sanin (2007) showed that the $CRR_{(\gamma=3\%)}$ in low plastic silts is also controlled by their peak undrained shear strength ratio (s_u/σ'_v). Although it is common to treat low plastic silts as ‘sand-like’, their CRR is controlled by their undrained strength ratio. Hence, soft low plastic silts tend to ‘behave’ similar to soft clays, where their response is controlled by the undrained strength ratio.

Boulanger and Idriss (2007) suggested that the $CRR_{7.5}$ (for a shear strain of 3%) could be estimated using either:

$$CRR_{7.5} = 0.8(s_u/\sigma'_{v0}) \quad (10)$$

or

$$CRR_{7.5} = 0.18(OCR)^{0.8} \quad (11)$$

Both methods are equivalent, since Ladd (1991) showed that:

$$s_u/\sigma'_{v0} = 0.22(OCR)^{0.8} \quad (12)$$

Boulanger and Idriss (2004b) suggested a further reduction factor (K_α) to $CRR_{7.5}$, based on the static shear stresses existing at the time of the earthquake. Therefore, the factor of safety against cyclic softening (3% shear strain), for cases in which the static shear stresses are small (i.e. $K_\alpha = 1.0$), can be expressed as:

$$FS_{\gamma=3\%} = CRR_M/CSR_M = CRR_{7.5}/CSR_{7.5} \quad (13)$$

Boulanger and Idriss (2007) showed that the MSF for clays is different than that for sands. They also showed that the $CRR_{7.5}$ of saturated clays and plastic silts can be estimated by three approaches:

- Directly measuring CRR by cyclic laboratory testing on undisturbed samples.
- Empirically estimating CRR based on s_u profile.
- Empirically estimating CRR based on consolidation stress history (i.e. OCR) profile.

Boulanger and Idriss (2007) described that the first approach provides the highest level of insight and confidence, whereas the second and third approaches use empirical approximations to gain economy. For low risk projects, the second and third approaches are often adequate. Based on the work of Wijewickreme and Sanin (2007) it would appear that the $CRR_{7.5}$ for soft low plastic silts can also be estimated using the same approach.

Robertson (2008) showed that CPT results in fine-grained soils are influenced primarily by both stress history (OCR) and soil sensitivity (S_t) and that the normalized cone resistance (Q_{tn}) is strongly influenced by OCR and almost unaffected by S_t , whereas, the normalized friction ratio (F_r) is strongly influenced by S_t and almost unaffected by OCR. Hence, Robertson (2008) suggested that the peak undrained shear strength ratio in cohesive soils can be estimated from:

$$(s_u/\sigma'_{vo}) = \frac{q_t - \sigma_{vo}}{\sigma'_{vo}} (1/N_{kt}) = Q_{tn}/N_{kt} \quad (14)$$

when $I_c > 2.60$ and $n \sim 1.0$)

where N_{kt} = empirical cone factor with an average value of 15.

Hence, when $K_{\alpha} = 1.0$:

$$CRR_{7.5} = 0.8 Q_{tn}/15 = 0.053 Q_{tn} \quad (15)$$

Alternately, the OCR of clay can be estimated using (Kulhawy and Mayne, 1990):

$$OCR = 0.33 Q_{tn} \quad (16)$$

Hence, when $K_{\alpha} = 1.0$:

$$CRR_{7.5} = 0.074 (Q_{tn})^{0.8} \quad (17)$$

For values of $Q_{tn} < 10$ (i.e. $CRR_{7.5} < 0.5$), both approaches produce similar values of $CRR_{7.5}$.

Hence, estimates of $CRR_{7.5}$ can be made from CPT results using the normalized cone resistance Q_{tn} , since $CRR_{7.5}$ is controlled primarily by the peak undrained shear strength ratio. Note that in clays and silts where $I_c > 2.60$, $Q_{tn} = Q_{t1}$.

6.3 All soils

By combining the Robertson and Wride (1998) approach for cohesionless sand-like soils with the Boulanger and Idriss (2007) recommendations for cohesive clay-like soils, it is possible to provide a simple set of recommendations to estimate $CRR_{7.5}$ from CPT results for a wide range of soils.

The recommendations can be summarized, as follows:

When $I_c \leq 2.60$, assume soils are sand-like:

Use Robertson and Wride (1998) recommendation based on $Q_{tn,cs} = K_c Q_{tn}$, where K_c is a

function of I_c . Robertson and Wride (1998) set a minimum level for $CRR_{7.5} = 0.05$.

When $I_c > 2.60$, assume soils are clay-like where:
 $CRR_{7.5} = 0.053 Q_{tn} K_{\alpha}$ (18)

Boulanger and Idriss (2007) suggested that, in clay-like soils, the minimum level for $CRR_{7.5} = 0.17 K_{\alpha}$ for soft normally consolidated soils.

For a more continuous approach, it is possible to define a transition zone between sand-and clay-like soils:

When $I_c \leq 2.50$, assume soils are sand-like:

Use Robertson and Wride (1998) recommendation based on $Q_{tn,cs} = K_c Q_{tn}$, where K_c is a function of I_c .

When $I_c > 2.70$, assume soils are clay-like, where:
 $CRR_{7.5} = 0.053 Q_{tn} K_{\alpha}$ (19)

When $2.50 < I_c < 2.70$, transition region:

Use Robertson and Wride (1998) recommendations based on $Q_{tn,cs} = K_c Q_{tn}$, where:

$$K_c = 6 \times 10^{-7} (I_c)^{16.76} \quad (20)$$

The recommendations where $2.50 < I_c < 2.70$ represent a transition from drained cone penetration to undrained cone penetration where the soils transition from predominately cohesionless to predominately cohesive.

Figures 9 and 10 show the proposed combined relationships for $CRR_{7.5} = 0.5$ and 0.2 , respectively, compared to the expanded database. Additional non-liquefaction data points (28 in total) have been added from the published case history records. The 'non-liquefaction' points reflect soil layers (predominately clay-like soils) that did not 'liquefy' and did not show any observable/recorded deformations (i.e. no cyclic failure). As noted above, the criteria to define $CRR_{7.5}$ in clay is a shear strain of 3%. Figure 9 includes two data points (Yalova Harbour and Soccer Field sites, Kocaeli earthquake, Turkey, 1999) where cyclic softening may have occurred in the soft clay layer during earthquake shaking but no significant post-earthquake deformations within the clay layers were observed or noted. The lack of observed deformation in the clay layers at the two sites in Turkey may have been due to small static shear stresses at the depth of the clay. Figure 10 includes one data point from the Moss Landing site (Sandholt Rd., Loma Prieta, 1995) where a soft silty clay ($Q_{tn} = 4$ to 5 , $F_r = 3$ to 4%) appears to have been close to cyclic failure and where a small amount of post-earthquake lateral deformation (approximately $\gamma = 0.5\%$) was observed from slope indicator measurements (Boulanger et al., 1995) and where the $CSR_{7.5}$ was about 0.25 .

Data from three sites (Marina District, Treasure Island Alameda) with deposits of soft, sensitive San

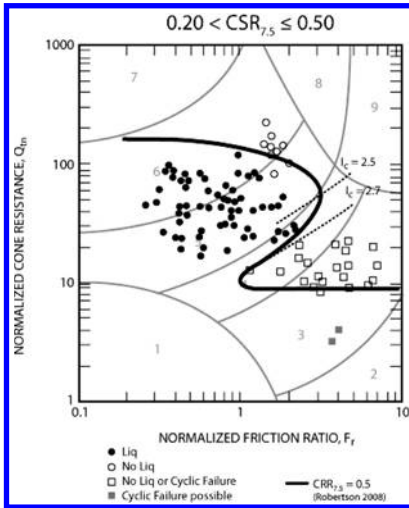


Figure 9. Proposed relationship to estimate $CRR_{7.5} = 0.50$ for a wide range of soils compared to updated database.

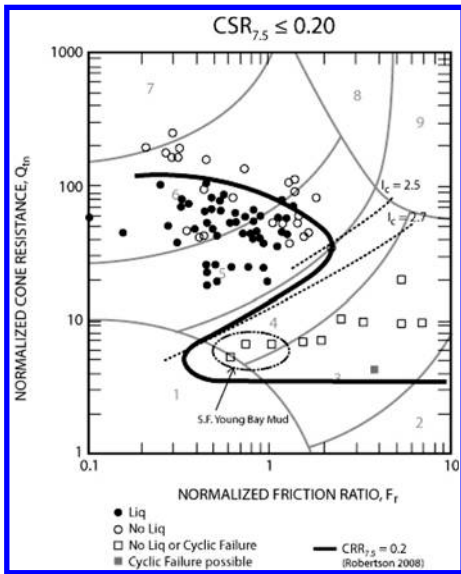


Figure 10. Proposed relationship to estimate $CRR_{7.5} = 0.20$ for a wide range of soils compared to updated database.

Francisco (SF) young Bay Mud are also identified in Figure 10. These sites likely experienced a $CSR_{7.5}$ of about 0.15 during the Loma Prieta earthquake but showed no reported signs of deformations within the clay layer. This may have been, in part, due to the rather small static shear stress at these sites within the soft clay. The less reliable Class C data have not been included in Figures 9 and 10.

Boulanger and Idriss (2004) showed that high static shear stresses in soft clays can initiate cyclic failure during earthquake loading. They presented results from sites that experienced ground failure during the Kocaeli 1999 earthquake in soft clays where the static shear stresses were high. The above CPT-based approach to estimate CRR also correctly predicts ground failure at the sites presented by Boulanger and Idriss (2004) when $K_{\alpha} < 1.0$.

Typically, when $I_c > 2.60$ the soils are generally fine-grained and more easily sampled. Therefore, in this region ($I_c > 2.60$), selective sampling and laboratory testing can be appropriate, depending on the risk of the project.

7 POST-EARTHQUAKE DEFORMATIONS

Estimating deformations in soils is generally difficult, due to the non-linear, stress dependent stress-strain response of soils. Estimating deformation after earthquake loading is more difficult, due in part to the complex nature of earthquake loading and the role of soil stratigraphy and variability.

Idriss and Boulanger (2008) present a summary of alternate approaches to estimating post-earthquake deformations depending on the risk and scope of the project. For low to moderate risk projects it is common to estimate post-earthquake deformations by estimating strains and then integrate those strains over depth to estimate deformation. The estimated deformations may also be empirically adjusted on the basis of calibration to case history observations. For high risk projects it is appropriate to perform complex non-linear dynamic numerical analyses if initial screening indicates a need.

7.1 Vertical settlements due to reconsolidation

Post-earthquake vertical displacements can develop in two ways: (1) settlement caused by reconsolidation, and (2) vertical displacement caused by shear deformation associated with lateral deformation. This section addresses only settlements caused by reconsolidation.

7.1.1 Volumetric strains—cohesionless sand-like soils

Post-earthquake reconsolidation volumetric strains are generally estimated using relationships derived primarily from laboratory studies. Methods are then evaluated using case history observations. One of the primary laboratory studies used is that by Ishihara and Yoshimine (1992) for cohesionless soils. Ishihara and Yoshimine (1992) observed that volumetric strains of sand samples were directly related to the maximum shear strain during undrained cyclic loading and to

the initial relative density of the sand. Ishihara and Yoshimine (1992) showed that when $FS_{liq} > 1$ some shear and volumetric strains still occur and that as the FS_{liq} decreases ($FS_{liq} < 1$), shear and volumetric strains increase but reach maximum values depending on the relative density. When $FS_{liq} < 1.0$, loose cohesionless soils have reached zero effective stress with a loss of structure/fabric, the stiffness of the soil is then very small during reconsolidation that can result in large volumetric strains.

Zhang et al. (2002) coupled the Robertson and Wride (1998) CPT-based method using clean sand equivalent values to determine FS_{liq} with the Ishihara and Yoshimine (1992) volumetric strain relationships, to provide a method to estimate the post-earthquake vertical reconsolidation settlements. Zhang et al. (2002) evaluated the approach using case history observations and showed that the approach provided reasonable predictions of settlements, although details on site geometry and soil stratigraphy play an important role. Since most cohesionless soils have relatively high permeability, the post-earthquake reconsolidation settlements occur relatively soon after the earthquake, but depend on soil stratigraphy and drainage.

7.1.2 Volumetric strains—cohesive clay-like soils

Factors affecting vertical (1-D) settlement caused by post-earthquake reconsolidation of clay layers are discussed in Ohara and Matsuda (1988), Matsuda and Ohara (1991) and Fiegel et al. (1998). The limited laboratory data indicate that reconsolidation volumetric strains are controlled primarily by the max. shear strain which is function of the factor of safety ($FS_{\gamma=3\%}$) and stress history (OCR) of the soil. During undrained cyclic loading, pore pressures develop that result in a decrease in effective confining stress. However, the effective stresses generally do not reach zero and the soil retains some structure and stiffness. Wijewickreme and Sanin (2007) showed that, on average, for a wide range of fine-grained soils, when $FS_{liq} = 1$ the excess pore pressure represents about 80% of the effective confining stress (i.e. $\Delta u/\sigma'_{vo} = r_u = 0.8$). Volumetric strains occur as the soil reconsolidates back to the in-situ effective confining stress. The volumetric strains in cohesive soils during reconsolidation after earthquake loading are generally much smaller than those observed in cohesionless coarse-grained soils because cohesive soils retain some level of stiffness during reconsolidation. Case history field observations have also shown that post-earthquake settlements, due to reconsolidation, are generally small at sites with thick deposits of cohesive soils. For example, the San Francisco Bay area in California has extensive thick deposits of soft (young) Bay Mud (essentially normally to lightly overconsolidated clay) but very few observations of measurable post-earthquake settlements within the clay deposits were made following

the Loma Prieta earthquake. The re-evaluation of post-earthquake reconsolidation settlements at the Marina District, Treasure Island and Moss Landing sites following the Loma Prieta earthquake and sites in Taiwan following the Chi-Chi earthquake, suggest an average volumetric strain of less than 1% in fine-grained soils.

Volumetric strains for cohesive soils can be estimated using the 1-D constrained modulus, M , and the change in effective stress due to the earthquake loading where,

$$\varepsilon_{vol} = (\Delta\sigma'_v/M) \quad (21)$$

$$\Delta\sigma'_v = r_u\sigma'_{vo} \quad (22)$$

The buildup in pore pressure and hence, change in effective stress, is a function of the factor of safety (FS) and the OCR of the soil. Laboratory test results indicate that r_u is a function of FS. When $FS = 1.0$, $r_u = 0.8$ and when $FS = 2$, $r_u = 0$. Assuming a linear relationship between FS and r_u and an inverse relationship with OCR gives:

$$r_u = [0.8 - 2.66 \log (FS)]/OCR \quad (23)$$

where: $r_u \leq 1.0$, when $FS = 0.84$

Kulhawy and Mayne (1990) showed that OCR can be estimated from the CPT using:

$$OCR = 0.33 Q_{tn} \quad (24)$$

Hence,

$$\Delta\sigma'_v = [0.8 - 2.66 \log (FS)] \sigma'_{vo}/0.33 Q_{tn} \quad (25)$$

Assuming the 1-D constrained modulus during reconsolidation is generally larger than the initial constrained modulus estimated from the CPT:

$$M = A M_{CPT} \quad (26)$$

The 1-D constrained modulus estimated from the CPT is equivalent to the modulus from the in-situ stress to a higher stress, whereas during reconsolidation the cohesive soil has become overconsolidated due to the decrease in effective stress and the reconsolidation modulus is stiffer. For soft normally consolidated cohesive soils the reconsolidation stiffness is about $10 M_{CPT}$. Whereas, in stiff overconsolidated cohesive soils, the reconsolidation stiffness is approximately equal to M_{CPT} . Therefore, assume that A varies with OCR as follows:

$$A = 10 - 9 \log (OCR) \quad (27)$$

$$\text{Since } OCR = 0.33 Q_{tn}$$

$$A = 10 - 9 \log (0.33 Q_{tn}) \quad (28)$$

Robertson (2008) showed that in soft clays:

$$M_{CPT} = (Q_{tn})^2 \sigma'_{vo} \quad (29)$$

Hence:

$$\varepsilon_{vol} = [0.8 - 2.66 \log (FS)]/[0.33A(Q_{tn})^3] \quad (30)$$

When $FS \leq 0.84$ set $r_u = 1.0$ & limit $\varepsilon_{vol} \leq 1\%$.

The above procedure provides an approximate estimate of the post-earthquake reconsolidation volumetric strains in clay-like soils based on CPT results. The re-evaluation of the expanded case history database shows good agreement between observed post-earthquake settlements and those calculated using the Zhang et al. (2002) CPT-based method with the continuous CPT records incorporating the above method to estimate volumetric strains in clay-like soils.

7.2 Lateral displacements due to shear deformation

7.2.1 Shear strains—cohesionless soils

Zhang et al. (2004) coupled the Robertson and Wride (1998) CPT-based method to determine FS_{liq} with the Ishihara and Yoshimine (1992) maximum shear strain relationships to provide a method to estimate the post-earthquake lateral displacement index (LDI). Zhang et al. (2004) used case history observations to modify the LDI based on ground geometry to estimate actual lateral displacements. Zhang et al. (2004) evaluated the approach using case history observations and showed that the approach provided reasonable predictions of settlements. Chu et al. (2007) showed that the Zhang et al. (2004) CPT-based method provided reasonable but generally conservative estimates of lateral displacements from the 1999 Chi-Chi (Taiwan) earthquake. Chu et al. (2007) also showed that shear strains at a depth more than twice the height of the free face should not be included in the method, since static shear stresses are likely too small to contribute to the lateral deformation.

7.2.2 Shear strains—cohesive soils

The potential for shear deformations or instability in clay-like cohesive soils depends heavily on the static shear stresses (which can be captured via K_α) and the sensitivity of the soil.

Boulanger and Idriss (2004) have shown that high static shear stresses in soft clays can initiate high shear strains during earthquake loading. The CPT-based approach described here captures the decrease in FS in clay-like soils when an appropriate value of K_α is used.

If clays are sensitive and show significant strain softening in undrained shear (i.e. high sensitivity, S_t), strength loss can lead to significant deformations and instability. Boulanger and Idriss (2007) stated that the magnitude of strain, or ground deformation, that will reduce the clay's undrained shear strength (s_u) to its fully remolded value (s_{ur}) is currently difficult to assess, but it is generally recognized that it would require less deformation to remold very sensitive clays than more ductile relatively insensitive clays. Based on the assumption that the CPT sleeve friction (f_s) measures the remolded shear strength of the soil

(i.e. $s_{ur} = f_s$), it is possible to estimate the sensitivity of clays using CPT results (Robertson, 2008); where:

$$S_t = s_u/s_{u(r)} = 7.1/F_r \quad (31)$$

It is also possible to estimate the remolded undrained shear strength ratio (s_{ur}/σ'_{vo}) using (Robertson, 2008):

$$s_{ur}/\sigma'_{vo} = f_s/\sigma'_{vo} = (F_r \cdot Q_{tn})/100 \quad (32)$$

As soil sensitivity increases, CPT data moves to the left on the $Q_{tn} - F_r$ SBTn chart, as F_r decreases with increasing S_t .

In a general sense, the $FS_{(y=3\%)}$ is controlled by the OCR and peak undrained shear strength of the clay (i.e. Q_{tn} , equation 18) whereas the potential for strength loss and large deformations is controlled by the sensitivity of the clay (i.e. F_r , equation 31).

8 EVALUATION OF POST-EARTHQUAKE DEFORMATIONS USING CASE HISTORY OBSERVATIONS

Zhang et al. (2002; 2004) showed that CPT results could be used to provide reasonable estimates of post-earthquake reconsolidation settlements and lateral spread deformations. However, at that time there were limited case history records that had CPT profiles. The earthquakes in Turkey and Taiwan in 1999 have now added to the case history records with CPT profiles and recorded deformations. The following is a brief summary of a comparison between shear deformations observed at sites in Taiwan and Turkey and those predicted using the Zhang et al. (2004) CPT-based method but with the updates described in this paper. Four sites experienced lateral spreading during the Kocaeli earthquake, Turkey in 1999, namely: Police Station, Soccer Field, Yalova Harbour and Degirmendere Nose sites. Several sites also experienced lateral spreading during the Chi-Chi earthquake in Taiwan in 1999. As noted earlier the sites at Yalova Harbour and Soccer Field have deposits of soft clay that would be predicted to have been close to cyclic failure, but appear to have had little influence on the lateral spread deformations due to the low static shear stress at the depth of the soft clay. Hence, these sites do not assist in our estimate of probable post-earthquake shear strains in clays. Figure 11 shows a summary of the predicted post-earthquake lateral displacements compared to the measured lateral displacements at the sites in Turkey and Taiwan based on the Zhang et al. (2004) CPT-based method with the updates described in this paper. The updated CPT-based method to estimate liquefaction and cyclic softening appears to provide reasonable estimates of lateral deformations.

The updated CPT-based method, including the addition for estimating cyclic softening in clay-like soils, was used to re-evaluate the available case history

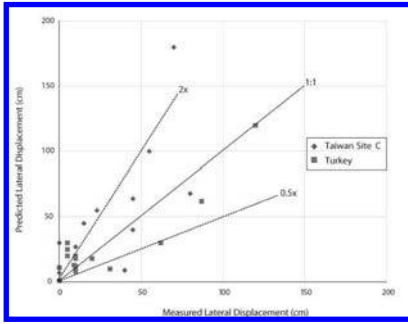


Figure 11. Measured post earthquake lateral displacements compared to predicted values using Zhang et al. (2004) CPT-based method.

CPT records and showed that clay-like soils generally play a minor role in almost all the available case history records. Although some clay-like soils likely experienced some cyclic softening during the earthquake, they generally appear to contribute little to the observed deformations, except the few cases where high static shear stresses contributed to ground failure (Boulanger and Idriss, 2004). In a general sense, cyclic softening and ground failure during seismic loading for clay-like soils is confined to soft, normally to lightly overconsolidated and/or sensitive fine-grained soils.

9 SUMMARY

This paper has presented an update of the Robertson and Wride (1998) CPT-based method to evaluate both liquefaction and cyclic softening in cohesionless and cohesive soils. Case history records have been carefully reviewed to re-evaluate the CPT-based method. Where possible, the near continuous CPT records have been used in the re-evaluation. The original Robertson and Wride (1998) method has been updated using a new stress normalization procedure that captures the change in soil response with increasing overburden stress and avoids the need for the K_σ correction for high overburden stresses. A transition zone detection feature has also been included to identify zones where the near continuous CPT data may incorrectly interpret soil type, due to rapid variation at soil boundaries. The method has also been extended to include cohesive clay-like soils using the concepts described by Boulanger and Idriss (2004). The extension into the clay-like region avoids the need for a SBTn I_c cut off to separate sand-like from clay-like soils.

Figure 12 presents a summary of the CPT SBTn $Q_{tn} - F_r$ chart to identify zones of potential liquefaction and/or cyclic softening. The chart in Figure 12

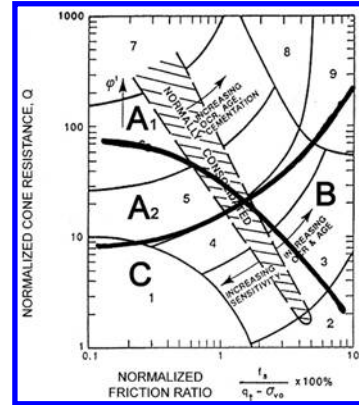


Figure 12. CPT Soil Behavior Type (SBTn) chart for liquefaction and cyclic softening potential.

can be used as a guide for the choice of engineering procedures to be used in evaluating potential deformation and strength loss in different types of soils during earthquakes. Zones A₁ and A₂ correspond to cohesionless or sand-like soils for which it is appropriate to use existing CPT case-history based liquefaction correlations. Soils in Zones A₁ and A₂ are both susceptible to cyclic liquefaction, while the looser soils in zone A₂ are more susceptible to substantial strength loss. Zones B and C correspond to cohesive or clay-like soils for which it is more appropriate to use procedures similar to, or modified from, those used to evaluate the undrained shear strength of clays (e.g., field vane tests, CPT, and shear strength tests on high-quality thin-walled tube samples). Soils in Zones B and C are both susceptible to cyclic softening (e.g. accumulation of strains if the peak seismic stresses are sufficiently large), but the softer soils in Zone C are more sensitive and susceptible to potential strength loss. For moderate to high risk projects, undisturbed sampling of soils in Zones B and C is recommended to determine soil response, since soils in these zones are more suitable for conventional sampling and laboratory testing. Loose, saturated, non-plastic silts often fall in Zone C, however, their CRR is strongly controlled by undrained shear strength and the methods described for clay-like soils also apply. However, the resulting shear and volumetric strains should be evaluated based on either, undisturbed sampling and laboratory testing for moderate to high risk projects, or, assumed conservative values for low risk projects. For low risk projects, disturbed samples should be obtained for soils in Zones B and C to estimate if the soils will respond either more sand-like or clay-like, based on Atterberg Limits and water content.

The CPT is a powerful in-situ test that can provide continuous estimates of the potential for either liquefaction or cyclic softening and the resulting

post-earthquake deformations in a wide range of soils. However, the CPT-based approach is a simplified method that should be used appropriately depending on the risk of the project. For low risk projects, the CPT-based method is appropriate when combined with selective samples to confirm soil type as well as conservative estimates of soil response. For moderate risk projects, the CPT-based method should be combined with appropriate additional in-situ testing, as well as selected undisturbed sampling and laboratory testing, to confirm soil response, where thin-walled tube sampling is generally limited to fine-grained soils in Zones B and C. For high risk projects, the CPT-based method should be used as an initial screening to identify the extent and nature of potential problems, followed by additional in-situ testing and appropriate laboratory testing on high quality samples. Advanced numerical modeling is appropriate for high risk projects where initial screening indicates a need.

Cohesionless soils (A_1 & A_2)—Evaluate potential behavior using CPT-based case-history liquefaction correlations.

A_1 Cyclic liquefaction possible depending on level and duration of cyclic loading.

A_2 Cyclic liquefaction and post-earthquake strength loss possible depending on loading and ground geometry.

Cohesive soils (B & C)—Evaluate potential behavior based on in-situ or laboratory test measurements or estimates of monotonic and cyclic undrained shear strengths.

B Cyclic softening possible depending on level and duration of cyclic loading.

C Cyclic softening and post-earthquake strength loss possible depending on soil sensitivity, loading and ground geometry.

ACKNOWLEDGMENTS

This research could not have been carried out without the support, encouragement and input from John Gregg, Kelly Cabal and other staff at Gregg Drilling and Testing Inc. Additional input and assistance was provided by John Ioannides.

REFERENCES

Ahmadi, M.M., and Robertson, P.K., 2005. Thin layer effects on the CPT qc measurement. *Canadian Geotechnical Journal*, 42(9): 1302–1317.

Bray, J.D., and Sancio, R.B., 2006. Assessment of liquefaction susceptibility of fine-grained soils. *Journal of Geotechnical and Geoenvironmental Engineering*, ASCE, 132(9): 1165–1177.

Boulanger, R.W., Idriss, I.M., and Mejia, L.H., 1995. Investigation and Evaluation of Liquefaction Related ground displacements at Moss landing during 1989 Loma Prieta Earthquake. *Report No. UCD/CGM-95/02*. Center for Geotechnical Modeling, Department of Civil and Environmental Engineering, University of California, Davis.

Boulanger, R.W., and Idriss, I.M., 2004a. State normalization of penetration resistance and the effect of overburden stress on liquefaction resistance. *Proceedings 11th International Conference on Soil Dynamics and Earthquake Engineering*. Berkeley, 484–491.

Boulanger, R.W., and Idriss, I.M., 2004b. Evaluating the potential for liquefaction or cyclic failure of silts and clays. *Report No. UCD/CGM-04/01*. Center for Geotechnical Modeling, Department of Civil and Environmental Engineering, University of California, Davis.

Boulanger, R.W., and Idriss, I.M., 2006. Liquefaction susceptibility criteria for silts and clays. *Journal of Geotechnical and Geoenvironmental Engineering*, ASCE, 132(11): 1413–426.

Boulanger, R.W., and Idriss, I.M., 2007. Evaluation of cyclic softening in silts and clays. *Journal of Geotechnical and Geoenvironmental Engineering*, ASCE, 133(6): 641–52.

Cetin, K.O., and Isik, N.S., 2007. Probabilistic assessment of stress normalization for CPT data. *Journal of Geotechnical and Geoenvironmental Engineering*, ASCE, Vol. 133(7): 887–897.

Chu, D.B., Stewart, J.P., Youd, T.L., and Chule, B.L., 2006. Liquefaction induced lateral spreading in near-fault regions during the 1999 Chi-Chi, Taiwan earthquake. *Journal of Geotechnical and Geoenvironmental Engineering*, ASCE, Vol. 132(12): 1549–565.

CLiq, 2008, Geologismiki: Geotechnical liquefaction software at <http://w.w.geologismiki.gr/>

Douglas, B.J., and Olsen, R.S., 1981. Soil classification using electric cone penetrometer. In *Proceedings of Symposium on Cone Penetration Testing and Experience*, *Geotechnical Engineering Division*, ASCE, St. Louis, Missouri, October 1981, pp. 209–227.

FEMA 356. Federal Emergency Management Agency, Washington, DC, Nov., 2008.

Fiegel, G.L., Kutter, B.L., and Idriss, I.M., 1998. Earthquake-induced settlement of soft clay. *Proceedings Centrifuge 98*. Balkema, Rotterdam (1): 231–36.

Hight, D., and Leroueil, S., 2003. Characterization of soils for engineering purposes. *Characterization and Engineering Properties of Natural Soils*, Vol.1, Swets and Sitlinger, Lisse, pp. 255–360.

Idriss, I.M. and Boulanger, R.W., 2004. Semi-empirical procedures for evaluating liquefaction potential during earthquakes. *Proceedings 11th International Conference on Soil Dynamics and Earthquake Engineering*. Berkeley, 32–56.

Idriss, I.M. and Boulanger, R.W., 2008. Soil Liquefaction During Earthquakes. Earthquake Engineering Research Institute. MNO-12.

Jefferies, M.G., and Davies, M.O., 1991. Soil Classification by the cone penetration test: discussion. *Canadian Geotechnical Journal*, 28(1): 173–176.

Jefferies, M.G., and Davies, M.P., 1993. Use of CPTU to estimate equivalent SPT N_{60} . *Geotechnical Testing Journal*, ASTM, 16(4): 458–468.

- Juang, C.H., Yuan, H., Lee, D.H., and Lin, P.S., 2003. Simplified Cone Penetration Test-based Method for Evaluating Liquefaction Resistance of Soils. *Journal of Geotechnical and Geoenvironmental Engineering*, ASCE, Vol. 129(1): 66–80.
- Kishida, H. 1966. Damage to reinforced concrete buildings in Niigata City and Special reference to foundation engineering. *Soils and Foundations*. Japanese Society of Soil Mechanics and Foundation Engineering, 6(1), 71–86.
- Kulhawy, F.H., and Mayne, P.H., 1990. Manual on estimating soil properties for foundation design, *Report EL-6800*. Electric Power Research Institute, EPRI, August 1990.
- Lacasse, S., and Nadim, F., 1998. Risk and reliability in geotechnical engineering. State-of-the-Art paper. *Proceedings of 4th International Conference on Case Histories in Geotechnical Engineering*. St. Louis, Missouri, Paper No. 50.A.-S.
- Ladd, C.C., 1991. Stability evaluation during staged construction (22nd Terzaghi Lecture). *Journal of Geotechnical Engineering*, 117(4): 540–615.
- Lunne, T., Robertson, P.K., and Powell, J.J.M., 1997. *Cone penetration testing in geotechnical practice*. Blackie Academic, EF Spon/Routledge Publ., New York, 1997, 312 p.
- Matsuda, H., and Ohara, S., 1991. Settlement calculations of clay layers induced by earthquake. *Proceedings 2nd International Conference on Recent Advances in Geotechnical Earthquake Engineering and Soil Dynamics*. St. Louis, M.O. pp. 473–79.
- Moss, R., 2003. CPT-based Probabilistic Assessment of Seismic Soil liquefaction initiation. PhD. Thesis. University of California, Berkeley.
- Moss, R.E.S., Seed, R.B., and Olsen, R.S., 2006. Normalizing the CPT for overburden stress. *Journal of Geotechnical and Geoenvironmental Engineering*, 132(3): 378–387.
- NBC 2005. National Building Code of Canada. National Research Council Canada.
- Ohara, S., and Matsuda, H., 1988. Study on the settlement of saturated clay layer induced by cyclic shear. *Soil and Foundations*. Japanese Society for Soil Mechanics and Foundation Engineering 28(3): 103–13.
- Olsen, R.S., and Malone, P.G., 1988. Soil classification and site characterization using the cone penetrometer test. *Penetration Testing 1988*, ISOPT-1, Edited by De Ruiter, Balkema, Rotterdam, Vol. 2, pp. 887–893.
- Olsen, R.S., and Koester, J.P. 1995. Prediction of liquefaction resistance using the CPT. *Proceedings of the International Symposium on Cone Penetration Testing*, Vol. 2, Swedish Geotechnical Society, Linköping, pp. 257–262.
- Robertson, P.K., 1990. Soil classification using the cone penetration test. *Canadian Geotechnical Journal*, 27(1): 151–158.
- Robertson, P.K., 1998. Risk-based site investigation. *Geotechnical News*: 45–47, September 1998.
- Robertson, P.K., 2008. Interpretation of the CPT: a unified approach. Manuscript submitted to the *Canadian Geotechnical Journal*.
- Robertson, P.K., and Campanella, R.G., 1983. Interpretation of cone penetration tests—Part I (sand). *Canadian Geotechnical Journal*, 20(4): 718–733.
- Robertson, P.K. and Campanella, R.G., 1985. Liquefaction Potential of sands using the cone penetration test. *Journal of Geotechnical Engineering Division*, ASCE, 111(3): 384–406.
- Robertson, P.K. and Wride, C.E., 1998. Evaluating cyclic liquefaction potential using the cone penetration test. *Canadian Geotechnical Journal*, Ottawa, 35(3): 442–459.
- Robertson, P.K., Campanella, R.G., Gillespie, D., and Rice, A., 1986. Seismic CPT to measure in-situ shear wave velocity. *Journal of Geotechnical Engineering Division*, ASCE, 112(8): 791–803.
- Sangrey, D.A., Castro, G., Poulos, S.J., and France, J.W., 1978. Cyclic loading of sands, silts and clays. *Proceedings of ASCE Specialty Conference Earthquake Engineering and Soil Dynamics*, Pasadena, Vol. 2 836–851.
- SEAOC 1995 VISION 2000. Structural Engineers Association of California (SEAOC).
- Seed, H.B., Tokimatsu, K., Harder, L.F. Jr., and Chung, R., 1984. The influence of SPT Procedures on Soil Liquefaction Resistance Evaluation. *Report No. UCB/ERC-84/15*, Earthquake Engineering Research Center, University of California, Berkeley.
- Seed, H.B., and Idriss, I.M., 1971. Simplified Procedure for evaluating soil liquefaction potential. *Journal Soil Mechanics and Foundations Div.*, ASCE 97(SM9), 1249–273.
- Seed, R.B., Cetin, K.O., Moss, R.E.S., Kammerer, A., Wu, J., Pestana, J., Riemer, M., Sancio, R.B., Bray, J.D., Kayen, R., and Faris, A., 2003. Recent advances in soil liquefaction engineering: a unified and consistent framework. Keynote presentation, *26th Annual ASCE Los Angeles Geotechnical Spring Seminar*; Long Beach, CA.
- Suzuki, Y., Tokimatsu, K., Taya, Y., and Kubota, Y., 1995. Correlation between CPT data and dynamic properties of insitu frozen samples. *Proceedings 3rd International Conf. on Recent Advances in Geotechnical Earthquake Engineering and Soil Dynamics*. Vol. 1, St. Louis, M.O.
- Wroth, C.P., 1984. The interpretation of in-situ soil tests. Rankine Lecture, *Geotechnique* (4).
- Wijewickreme, D., and Sanin, M.V., 2007. Effect of Plasticity on the laboratory cyclic shear resistance of fine-grained soils. *Proceedings 4th International Conf. on Earthquake Geotechnical Engineering*, Thessaloniki, Greece.
- Youd, T.L., Idriss, I.M., Andrus, R.D., Arango, I., Castro, G., Christian, J.T., Dobry, R., Finn, W.D.L., Harder, L.F., Hynes, M.E., Ishihara, K., Koester, J.P., Liao, S.S.C., Marcuson, W.F., Martin, G.R., Mitchell, J.K., Moriwaki, Y., Power, M.S., Robertson, P.K., Seed, R.B., and Stokoe, K.H., 2001. Liquefaction Resistance of soils: summary report from 1996 NCEER and 1998 NCEER/NSF workshop on evaluation of liquefaction resistance of soils. *J. Geotechnical and Geoenvironmental Eng.*, ASCE 127(10): 817–33.
- Zhang, G., Robertson, P.K., and Brachman, R.W.I., 2002. Estimating Liquefaction induced Ground Settlements From CPT for Level Ground, *Canadian Geotechnical Journal*, 39(5): 1168–1180.
- Zhang, G., Robertson, P.K., and Brachman, R.W.I., 2004. Estimating Liquefaction induced Lateral Displacements using the SPT or CPT. *J. Geotechnical and Geoenvironmental Eng.*, ASCE 130(8): 861–71.
- Zhou, S., 1980. Evaluation of the liquefaction of sand by static cone penetration tests. *Proceedings 7th World Conference on Earthquake Engineering*, Istanbul, Turkey, Vol. 3, 156–162.

Performance of foundation ground in Kashiwazaki-Kariwa Nuclear Power Station during 2007 Chuetsu-Oki earthquake

T. Kokusho

Civil Engineering Department, Chuo University, Tokyo, Japan

ABSTRACT: The Kashiwazaki-Kariwa NPS located near the focal region of the 2007 Niigataken-Chuetsu-Oki earthquake ($M_J = 6.8$) was attacked by a fierce seismic motion which far exceeded the design motion. All the reactors stopped safely without major release of radioactive materials. The seismic effect on important nuclear facilities embedded directly on rock was limited, while backfill soils around them suffered considerable settlement of more than 1 m. Strong ground motions were recorded by a number of seismometers deployed in the NPS, including a down-hole array which clearly indicated soil nonlinearity effect in surface soil layer. In this paper, time histories, response spectra and Fourier spectrum ratios of the recorded motions are shown and their characteristics are discussed. Then, soil properties exhibited during the earthquake are back-calculated to indicate a great degree of strain-dependent nonlinearity in sand dune layers. Based on the results, seismic wave energy propagating upward is quantified. Finally, geotechnical performance of building foundations and surrounding ground is explained focusing on large settlement of the backfill soils including the soil properties, indicating the great impact of the seismic motion. Considering the damage caused by the subsidence, criteria for geotechnical performance specifically for NPS is discussed.

1 INTRODUCTION

During recent earthquakes, more and more strong seismic records have been obtained. Table 1 shows representative high values of peak ground accelerations (PGA) and peak ground velocities (PGV) recorded in seismometers during major earthquakes in the past 7 decades.

Fig. 1 illustrates the plots of PGA and PGV versus the years of earthquakes based on Table 1. For PGA of Fig. 1(a) in particular, it is quite interesting that the acceleration gets higher and higher as years go by. The PGA over 1 G, which used to be inconceivable 3 or 4 decades ago and was embarrassing first found in the Pacoima dam record during the 1971 San Fernando earthquake, is now getting quite common and further increasing beyond 2.5 G. Quite probably, recent high-density deployments of strong motion seismometers in high-seismicity countries/areas have enabled the detection of near-source ground motions (possibly site-dependent anomalies too), which used to be overlooked in old times. In parallel with that, the values of PGV are also increasing as depicted in Fig. 1(b), and those exceeding 100 m/s have been observed quite often in several events since 1994 Northridge earthquake.

It should be pointed out that the high accelerations in recent earthquakes did not necessarily result in high structural or geotechnical damage. For instance, during the 1971 San Fernando earthquake earthquake

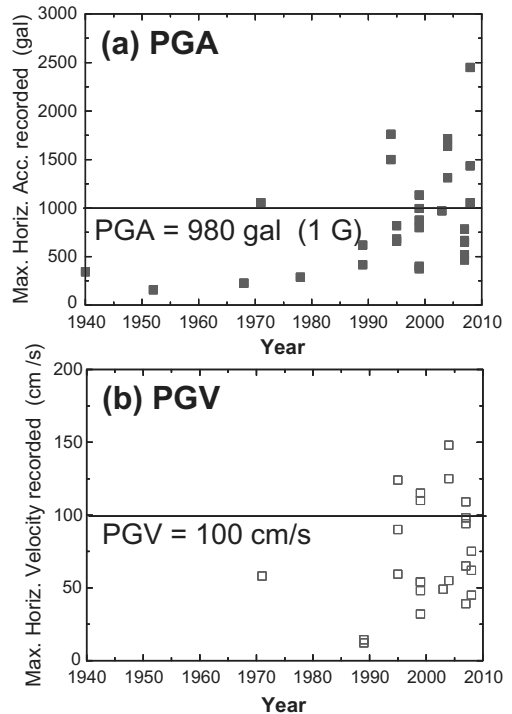


Figure 1. Variation of PGA (a) and PGV (b) recorded by seismometers in years since 1940.

Table 1. Maximum acceleration and velocity in strong motion records in past 7 decades.

Year	Earthquake (M) (Depth)	Observation site	Epicenter distance: e Hypocenter distance: R	Maximum Acceleration (gal = cm/s ²)	Maximum Velocity (cm/s)
1940	Imperial Valley EQ. (USA) (M _S = 7.1)	El Centro		342	
1952	Kern County EQ. (USA) (M _S = 7.7)	Taft		155	
1968	Tokachi-Oki EQ. (M _J = 8.0)	Hachinohe Harbor		225	
1971	San Fernando EQ. (USA) (M _S = 6.6) (8 km)	Pacoima Dam	$e = 11$ km	1055	58
1978	Miyagiken-Oki EQ. (M _J = 6.8)	Kaihoku Bridge		287	
1989	Loma Prieta EQ. (USA) (M _S = 7.1) (18 km)	Corralitos	$e = 7$ km, $R = 19$ km	620	55
		Capitola-Fire Station	$e = 9$ km, $R = 20$ km	460	36
1994	North Ridge EQ. (USA) (M _w = 6.7) (19 km)	Tarzana	$e = 5$ km, $R = 20$ km	1780	110
		Pacoima Dam	$R = 19$ km	1500	
1995	Hyogoken Nambu (Kobe) EQ. (M _J = 7.2) (16 km)	JMA-Kobe NS	$e = 17$ km, $R = 23$ km	818	90
		JR-Takatori EW	$e = 11$ km, $R = 19$ km	656	124
		Port Island (GL-83.4 m: NS)	$e = 18$ km, $R = 24$ km	679	59
1999	Kocaeli (Turkey) (M _S = 7.8) (18 km)	Adapazari(Sakarya) EW	$e = 7$ km, $R = 19$ km	398	48
		Duzce NS	$e = 15$ km, $R = 23$ km	374	54
1999	Chi-Chi (Taiwan) (M _S = 7.6) (7 km)	TCU065 EW	$e = 27$ km, $R = 28$ km	797	110
		TCU084 EW	$e = 9$ km, $R = 11$ km	1133	115
		TCU0129 EW	$e = 14$ km, $R = 16$ km	995	54
2003	Tokachi-Oki EQ. (M _J = 8.0) (45 km)	Hiroo k-net EW	$e = 85$ km, $R = 96$ km	970	49
		Makubetsuchou JMA EW	$e = 139$ km $R = 146$ km	875	32
2004	Niigataken Chuetsu EQ. (M _J = 6.8) (13 km)	Ojija k-net EW	$e = 7$ km, $R = 15$ km	1311	125
		Kawaguchi JMA EW	$e = 3$ km, $R = 13$ km	1637	148
		Tokamachi k-net NS	$e = 21$ km, $R = 25$ km	1715	55
2007	Noto Hanto EQ. (M _J = 6.9) (11 km)	Wajima JMA NS	$e = 27$ km, $R = 29$ km	463	94
		Wajima K-net NS	$e = 28$ km, $R = 30$ km	519	39
		Anamizu K-net EW	$e = 20$ km, $R = 22$ km	782	98
2007	Niigataken Chuetsu-Oki EQ. (M _J = 6.8) (17 km)	Kashiwazaki K-net NS	$e = 21$ km, $R = 27$ km	665	109
		Kashiwazaki-Kariwa NPP Service Hall PEW (GL-99.4 m)	$e = 16$ km, $R = 23$ km	646	65
2008	Iwate-Miyagi Nairiku EQ. (M _J = 7.2) (8 km)	Higashi-Naruse kik-net EW	$e = 21$ km, $R = 23$ km	2448	75
		Ichinoseki-Nishi kik-net EW	$e = 3$ km, $R = 8$ km	1434	62
		Ichinoseki-Higashi kik-net EW	$e = 13$ km, $R = 15$ km	1053	45

in USA, the acceleration (PGA) of 1 G and 1.8 G measured in Pacoima dam and in Tarzana, respectively, did not make significant structural damage in the surrounding area. During the 2004 Niigataken Chuetsu earthquake in Japan, PGA of 1.7 G in Tokamachi again did not produce so much damage as anticipated. Other than these, there are quite a few similar cases where no significant damage occurred under PGA larger than 1 G. It indicates that the acceleration may not be a proper parameter to govern the deterioration of structures or soils if it is used alone without referring to other parameters such as particle velocity or seismic wave energy (Kokusho et al., 2007).

Recent strong motion records also indicate significant spectral characteristics which may have strong

impact on seismic damage. Figs. 2(a) and 2(b) summarizes acceleration and velocity response spectra (5% damping ratio), respectively, of strong motion records obtained in near-source stations. Note that, in many of the acceleration spectra of destructive earthquakes (i.e., 1995 Kobe, 1999 Chi-Chi, 2004 Chuetsu, 2007 Chuetsu-Oki) peak frequencies are relatively low (around 1 Hz). It is interesting that some earthquakes which show very high response accelerations in frequencies much higher than 1 Hz did not inflict heavy structural damage as exemplified in Hiroo during the 2003 Tokachi-Oki EQ. and also in Higashi-Naruse during the 2008 Iwate-Miyagi Nairiku EQ.

In accordance to that, the velocity spectra of many destructive earthquakes have very high peaks at periods

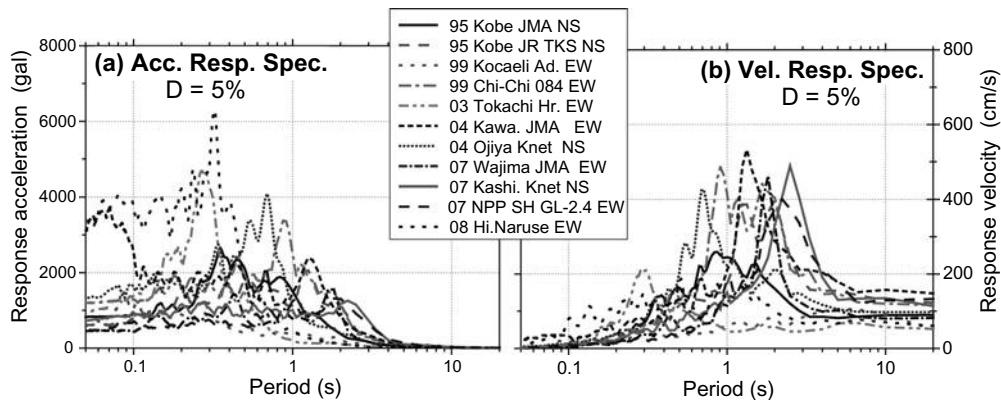


Figure 2. Response spectra of Acceleration (a) and Velocity (b) of strong ground motion records.

around 1 s or longer. At JR Takatori specifically where numerous human lives were lost during the 1995 Kobe earthquake due to collapse of old wooden houses, the peak period was about 2 s and the peak response velocity was as high as 400 cm/s. The 1999 Chi-Chi earthquake in Taiwan causing devastation in buildings, slopes, etc. show the peaks exceeding 400 m/s at 1–2 seconds. At Kawaguchi during the 2004 Niigataken Chuetsu earthquake which triggered several thousands of failures in natural slopes and embankments, the peak period was around 2 s and the response velocity was as high as 500 cm/s. At 2 near-source sites during the 2007 Chuetsu-Oki earthquake, which will be discussed in detail later, the peak periods are longer than 2 s with peak velocities 400–500 m/s.

Thus, the recent dramatic increase of PGA and PGV urges us to reevaluate how to design new buildings and new civil structures properly and also how to retrofit existing structures particularly from the viewpoint of their performance during design earthquakes. One of the major challenges for geotechnical engineers in particular is to shift from the force-equilibrium concept based on deformation or its modified seismic coefficients to the deformation-energy concept based on time/spectrum-domain calculations.

With the considerable increase of PGA in highly seismic areas, many of the conventional design schemes based on the force-equilibrium are not realistic and intolerable in terms of economy. If high PGA is directly used for stability calculation of structures, slope stability evaluations or liquefaction susceptibility evaluations of foundation soils, the solution is not allowable in many cases.

More and more numerical analyses incorporating time-histories of input seismic motions and strong nonlinear response of soils are already in practical use. It is preferable for such numerical tools to be as simple as possible so that it can capture the essential aspect

of seismic behavior without employing too many parameters. However, uncertainties involved in such analytical methodologies seems to become enormous as seismic input motions get stronger and soil nonlinearity gets greater. What we need in judging their reliability and how to choose appropriate values for input parameters is a sort of benchmark case histories with well-documented geotechnical and seismic conditions. “Case History Volume for Performance-Based Design in Earthquake Geotechnical Engineering” published by TC4, ISSMGE, during the International Conference IS-Tokyo 2009 aims to serve as such benchmarks for geotechnical engineers and researchers.

With what has been mentioned above as a background, a performance of a nuclear power station (NPS) which experienced one of the strongest seismic shaking during recent earthquakes and unexpected geotechnical damage there is addressed in this paper. Dynamic ground response and soil subsidence due to immensely strong ground motions and their impact on the performance of the NPS will be discussed.

First, strong motion records obtained by a set of accelerometers installed in the NPS are incorporated to characterize ground motions and soil response. Vertical array records in the site are back-calculated to optimize soil properties and to examine the degree of soil nonlinearity exhibited during the earthquake. Furthermore, seismic wave energy is evaluated based on the records and the back-calculated properties to characterize the incident wave of the earthquake in terms of energy. Next, the effect of the seismic motion on the NPS is addressed focusing on the subsidence of the backfill soils. Soil investigations carried out after the earthquake are reviewed and the cause of the subsidence and associated structural damage are discussed. Finally, based on this case history, performance criteria for such critical facilities as NP stations are considered from a geotechnical engineering point of view.

2 NIIGATAKEN CHUETSU-OKI EARTHQUAKE

2.1 Earthquake and nuclear power plant

The Niigataken Chuetsu-Oki earthquake ($M_J = 6.8$), which occurred in July 16, 2007 along the coast of Sea of Japan, attacked a relatively narrow region encompassing Kashiwazaki city and Kariwa village of Niigata prefecture with very strong intensity of shaking. Although the epicenter was about 10 kilometers off the coast, the fault rupture (the reverse thrust with the strike $N 30^\circ E$) seems to have reached inland.

Fig. 3 is the satellite photograph of the area strongly affected by the earthquake. The Kashiwazaki-Kariwa Nuclear Power Station (KK-NPS), the largest capacity NPS in the world with 7 reactors belonging to Tokyo Electric Power Company (TEPCO), was situated in the focal area along the coast and about 6 km far from the center of Kashiwazaki city. It experienced strong shaking exceeding the design acceleration spectra by 2–3 times at the maximum. Despite that, all the nuclear reactors during operation were stopped safely and cooled down without significant leakage of radioactive materials. In a good contrast to that, considerable settlement occurred in backfill soils placed around important buildings (embedded on bedrock), buried conduits and pipes, causing damage in facilities not critical in terms of nuclear safety. The seismic design of these non-nuclear facilities was regulated in accordance to conventional criteria for general civil engineering structures.

Strong motion records were obtained by a set of accelerometers installed at the ground surface and in deeper levels in the NPS site. Besides those, a K-net



Figure 3. Damaged area along the coast of Sea of Japan (from Google Map).

station near the center of Kashiwazaki city which had been deployed by NIED (National Research Institute for Earth Science and Disaster Prevention in Tsukuba, Japan) obtained the record at the ground surface. The surface soil layer of the K-net site consists of relatively dense dune sand of about 18 m thick followed by Pleistocene stiff clay of 45 m thick, which are underlain by Tertiary mudstone. Fig. 4 shows the acceleration time histories of the K-net Kashiwazaki in EW and NS directions. A very peculiar shape of waves can be recognized in the acceleration, which presumably reflects the cyclic mobility of saturated sand sheared by seismic wave in undrained condition, indicating that the dune sand was not loose enough to fully liquefy there.

Fig. 5 shows a plan view of the KK-NPS with the area of about 3 km by 1.5 km, in which 7 units of the power station (5 Boiled Water Reactors and 2

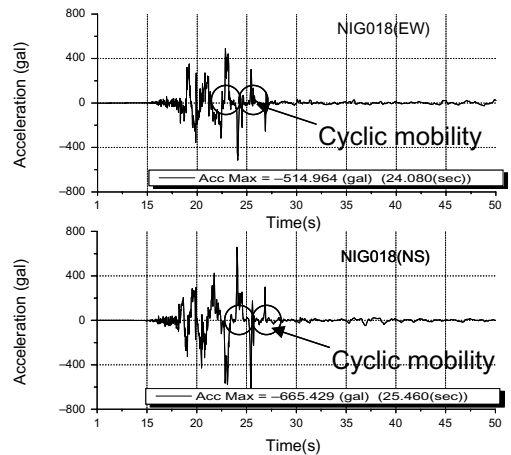


Figure 4. Acceleration records of K-net at Kashiwazaki city showing cyclic mobility.

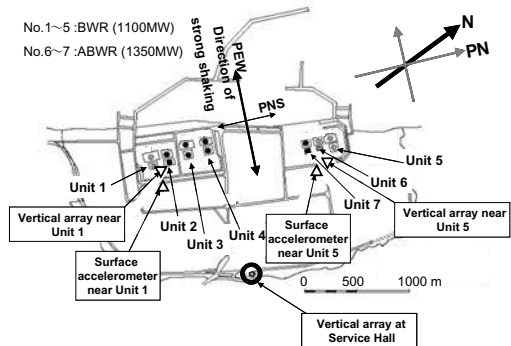


Figure 5. Plan view of Kashiwazaki-Kariwa NPS having 7 Units of power stations with installed accelerometers and vertical arrays.

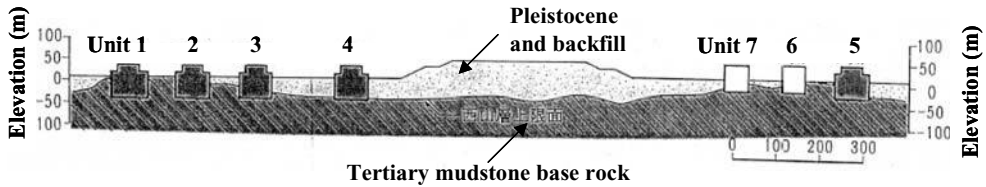


Figure 6. Geological cross section of 7 RB buildings embedded on bedrock in Kashiwazaki-Kariwa NPS.

Advanced Boiled Water Reactors) are situated along the coast. Each unit consists of a reactor building (RB) on the inland side and a turbine building (TB) on the seaside. Fig. 6 shows the typical geological profile of the 7 units. The geological setting of the site is basically the same in this area including the Kashiwazaki K-net and consists of dune sand at the top underlain by Pleistocene soil and Tertiary mudstone. Nuclear-related important facilities, such as reactor buildings (RBs) and turbine buildings (TBs), were all embedded directly on the Tertiary rock and backfilled by the dune sands.

2.2 Earthquake records

The accelerometers had been installed at many locations in the NPS, on the ground surface, in boreholes and inside the buildings, though not all of them could record the time history of the main shock. All accelerometers plotted in Fig. 5 are 3-dimensional, EW, NS and UD, though the horizontal directions are not the true EW/NS directions but modified by 19 degrees according to the plant alignment (named here as PEW/PNS) as shown in Fig. 5. It should be pointed out that the ground motion was obviously larger in the PEW direction than in the PNS direction presumably due to the fault rupture mechanism. Also noted is that the motions of Units 1–4 were apparently larger than those of Units 5–7 which are located by 1 km north. The measured spectra exceeded corresponding design spectra in all the units as already mentioned, although no significant damage occurred with respect to nuclear safety of critical facilities (Sakai et al., 2009). It was also found that the maximum accelerations on the RB foundations were greater than those given by empirical equations previously proposed on the PGA attenuation with distance (Sakai et al., 2009).

There were multiple down-hole vertical arrays deployed in the site to monitor the seismic amplification in the ground. In the arrays indicated in Fig. 5 near Unit 1 (about 100 m apart) and Unit 5 (about 200 m apart), the acceleration time histories of the main shock were unfortunately lost but its maximum values (A_{\max}) could be retained. Variations of A_{\max} -values for the two arrays are shown in Figs. 7(a)

and 7(b) along the ground depth for PEW and PNS directions and compared with those of aftershocks. In the same charts, the soil profiles, S-wave velocities (V_s) and the installation depths of accelerometers are also depicted. For both arrays, the top 20–30 m is Pleistocene deposits underlain by the Tertiary mudstone base rock. Note that the acceleration was as high as 1 G at the depth of 250 m and evidently deamplified in the surface soil layer, quite different from the aftershocks, presumably due to soil nonlinearity near Unit 1. In contrast to that, the A_{\max} -value near Unit 5 was comparatively smaller (about 0.4 G) in the base rock and amplified in the surface layer in the same manner as the aftershocks.

The array at Service Hall (shown in Fig. 5) distant from the power units and on the top of a sand dune was only one which could successfully record the down-hole acceleration time histories. In the next section, the records will be analyzed in detail to discuss how the foundation soil of the NPS behaved during strong shaking.

3 ANALYSIS OF VERTICAL ARRAY RESPONSE AND SOIL PROPERTIES

3.1 Vertical array records

The vertical array installed at Service Hall (SH) consists of 4 down-hole accelerometers at the depth of GL-2.4 m, GL-50.8 m, GL-99.4 m and GL-250 m as depicted in Fig. 8. The top 2 are in the sand dune layer of 83 m thick and the bottom 2 are in the Tertiary mudstone. The water table is judged to be at GL-45 m because the P-wave velocity shown in the figure jumps from 650 m/s to the value exceeding $V_p = 1500$ m/s, there.

Fig. 9 shows the acceleration response spectra in the two horizontal directions near the ground surface (GL-2.4 m) at the vertical array, which are compared with those of the K-net records. The peak periods are about 2 seconds, indicating a great contribution of long period motions to the shaking. The spectra in the two sites about 6 km far look similar as a whole, but if the spectrum of the Service Hall and that of the K-net are compared, the former is larger in the period longer than around 0.5 s. This may reflect the dynamic response

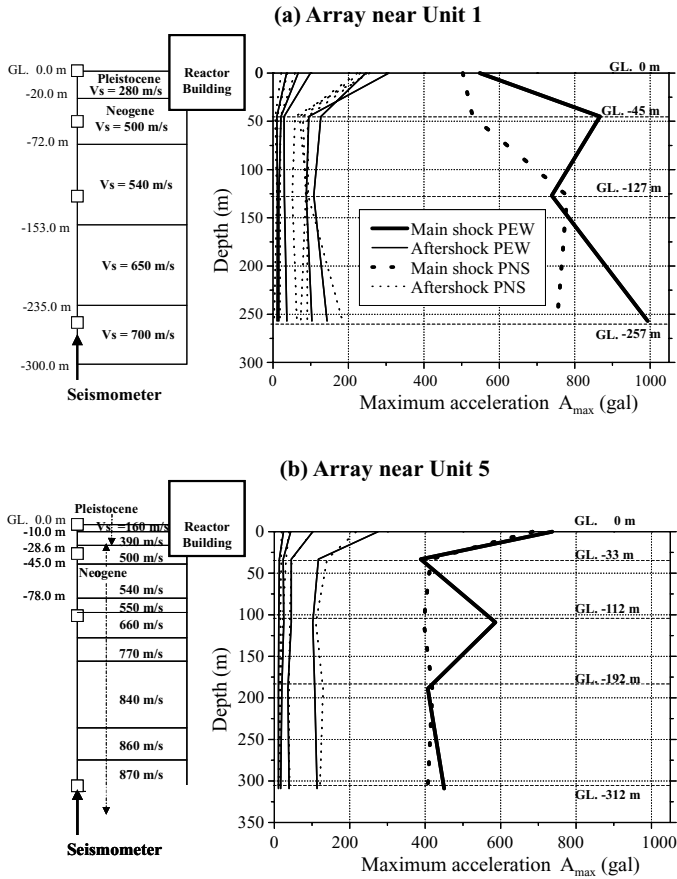


Figure 7. Maximum acceleration along depth for vertical arrays near Unit 1 (a) and Unit 5 (b).

of sand dune soils of Service Hall much thicker than the K-net site as will be mentioned later.

Acceleration time histories at the 4 levels in PEW direction during the main shock are shown in Fig. 10. Note that the recorded motions at the ground surface here show no indication of cyclic mobility unlike the K-net record shown in Fig. 4. The greater depth of the ground water table at the Service Hall than at the K-net may be one of the reasons.

Corresponding acceleration response spectra for $D = 5\%$ are shown in Fig. 11(a), indicating that the long period motion of $T > 0.5$ s tends to amplify in the interval of 250 m thick, whereas the motion shorter than that clearly deamplify in the soil layer. The velocity response spectra for $D = 5\%$ of PEW direction in Fig. 10(b) indicate that the peak period is longer than 2 s and the peak value is considerably amplified from the bottom to the top. The similar trend can be recognized also in the spectra in the PNS direction shown in Figs. 11(c) and (d).

The down-hole distributions of maximum acceleration and maximum velocity in the horizontal direction are depicted in Fig. 12. In accordance to the characteristics in the response spectra in Fig. 11, a clear trend of deamplification in acceleration in contrast to amplification in velocity can be seen.

Fourier spectrum ratios were calculated between the surface motion (at GL-2.4 m) and the down-hole motions of deeper levels. The Parzen window of 0.3 Hz is used in calculating the Fourier spectra. Figs. 13(a) and 13(b) exemplify those between the surface and GL-99.4 m for the PEW and PNS directions, respectively. In the charts, not only the main shock but also 8 small shocks before the main shock are shown with the curves of average \pm standard deviation. An obvious difference in the amplification can be recognized between the two types of shocks. The frequency of the first peak in the spectrum ratio tends to be lower in the main shock, and the higher order peaks clearly identified in the small shocks become obscure in the main

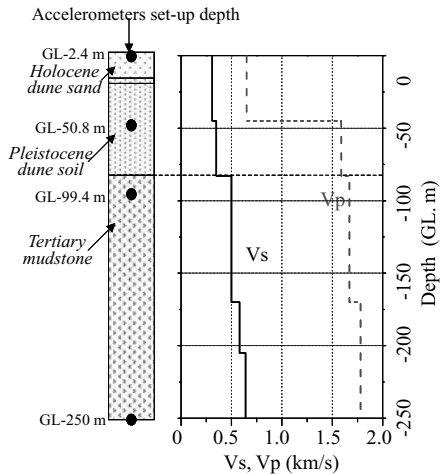


Figure 8. S-wave velocity and other profiles at the vertical array site.

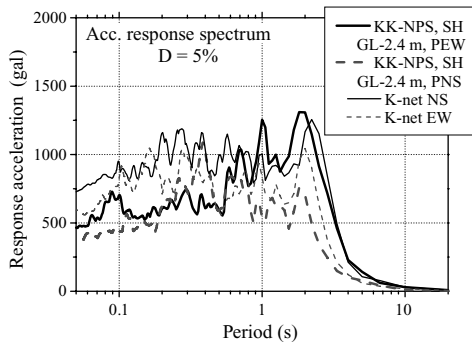


Figure 9. Comparison of acceleration response spectra at ground surface between Service Hall of KK-NPS and K-net Kashiwazaki.

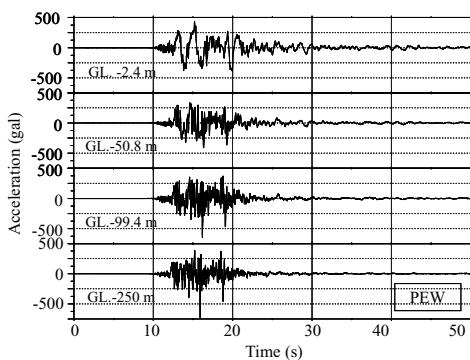


Figure 10. Acceleration time history of vertical array in PEW direction.

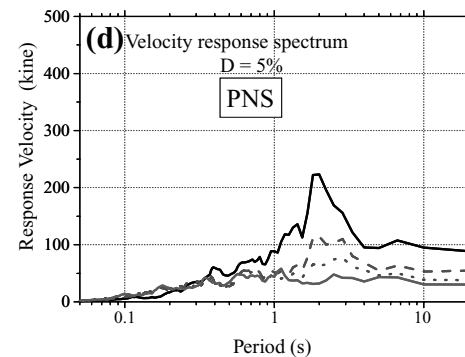
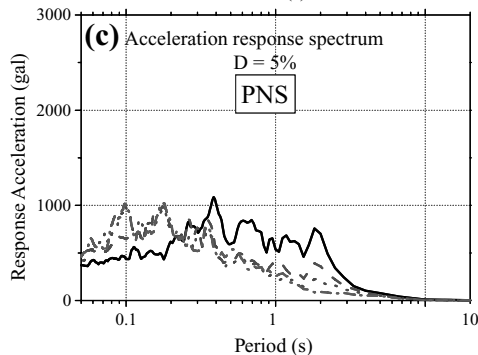
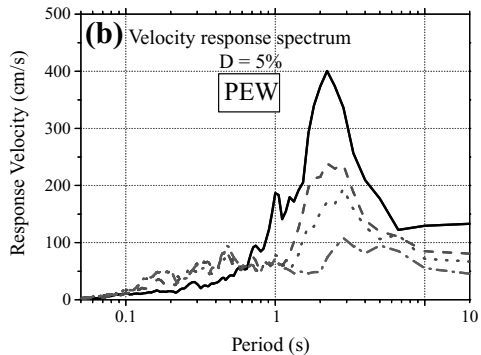
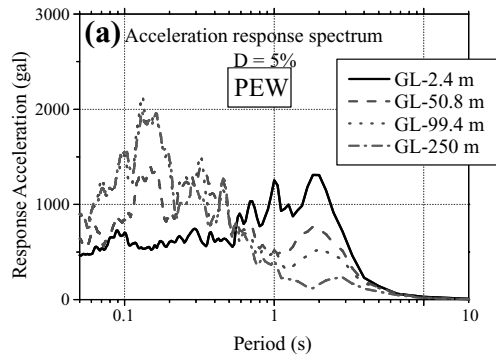


Figure 11. Response spectrum for acceleration (a), (b) and velocity (b) of vertical array records in PEW direction.

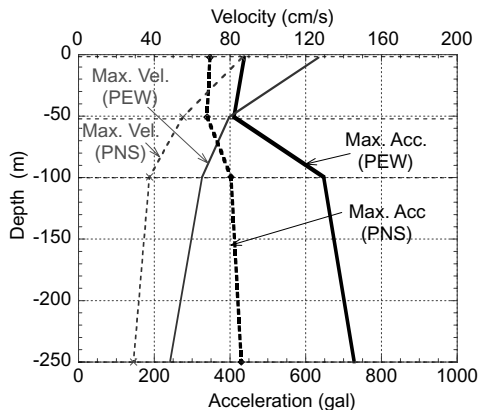


Figure 12. Maximum acceleration and velocity along depth in vertical array.

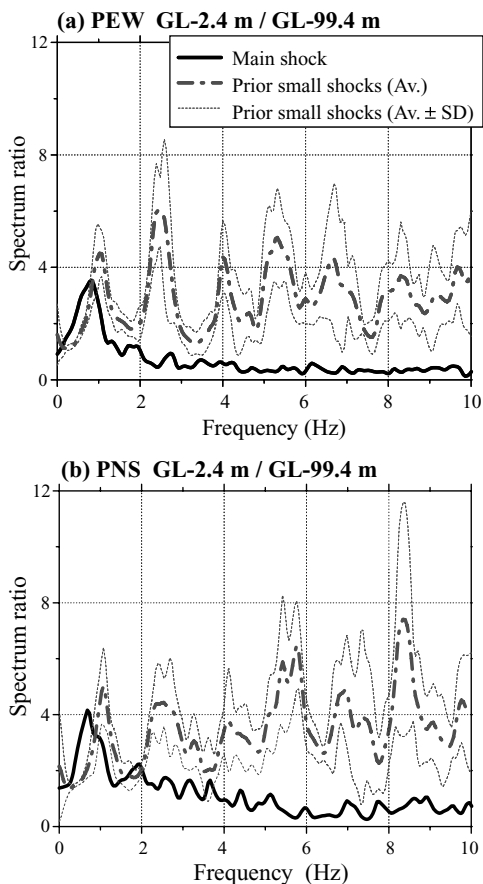


Figure 13. Spectrum ratio between surface and GL-99.4 m; comparison between main shock and small shocks before main shock in PEW(a) and in PNS (b).

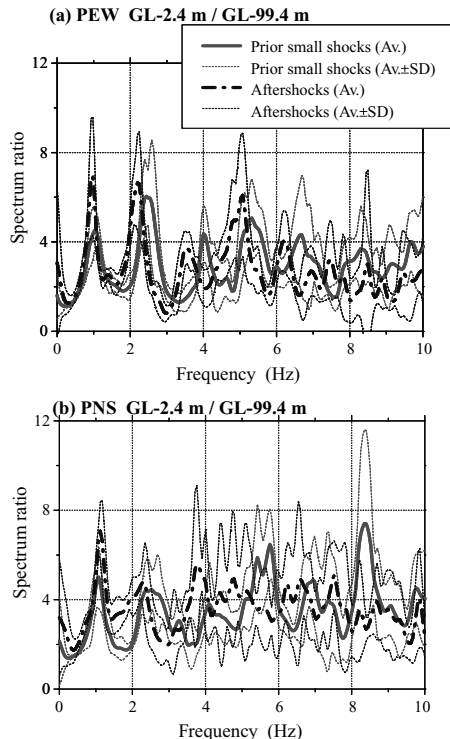


Figure 14. Spectrum ratio between surface and GL-99.4 m in PEW direction; comparison between small shocks before main shock and aftershocks in PEW(a) and in PNS (b).

shock. These differences may be largely attributable to strain-dependent soil properties in the layers above the mudstone bedrock.

Also noted is the comparison depicted in Fig. 14 between the 8 small shocks before the main shock (maximum acceleration at GL-2.4 m is 1–19 gal) and 5 aftershocks (maximum acceleration at GL-2.4 m is 18–77 gal) with the average \pm standard deviation between the surface (GL-2.4 m) and GL-99.4 m in the PEW and PNS directions. There are slight but obvious differences in peak frequencies in the spectrum ratios between the two shocks, where those in the aftershocks are evidently lower. Considering that the induced soil strain was smaller than 10^{-4} in both shocks, these differences may presumably reflect the disturbance of soil micro-fabrics due to strong ground motion during the main shock (Kokusho and Suzuki 2008b).

3.2 Back-calculation of soil properties

Back-calculation was carried out to optimize the soil properties so that the spectrum ratios explained above are best reproduced by using Extended Bayesian

Method. Based on a 1D soil model constructed from soil profiles provided by TEPCO, S-wave velocity V_s and damping ratio D of individual layers are optimized from initial values of guess to have the best fit with the observed spectrum ratios (Kokusho and Suzuki 2008a, 2008b). Values of V_s and D are postulated to be independent of frequency as in the normal geotechnical engineering practice.

Soil properties shallower than the second deepest seismometer (GL-99.4 m) are first optimized by utilizing spectrum ratios between the surface and that level. Then, properties deeper than that are optimized based on spectrum ratios between the surface and the deepest level. The frequency range for minimizing the residuals of spectrum ratios is chosen as 0.3 Hz to 10 Hz in this analysis. Frequency increment used in the computation is constant in the logarithmic scale so that spectrum ratios in lower frequencies contribute more to the computed residuals than those in higher frequencies. Further details of the back-calculation procedures are available in other literatures (Suetomi 1997 and Kokusho et al., 2005).

Fig. 15 shows the optimized transfer functions of GL-2.4 m/GL-99.4 m and GL-2.4 m/GL-250 m in PEW and PNS directions compared to the corresponding spectrum ratios by observation for the main shock.

In the same chart, transfer functions based on V_s by wave logging tests are also superposed. Though the optimized spectrum ratio does not match the observation so perfectly, it is definitely closer than that using the small-strain properties in all cases.

In Fig. 16(a), as the result of the back-calculation, the optimized values of V_s in the PEW and PNS directions are shown versus the ground depth for the main shock as well as the small shocks prior to the main shock and the aftershocks. Compared to the small strain V_s -logging values superposed in the chart, the back-calculated values of V_s for the main shock decrease by 37–23% in the soil layers and by 2–0.4% in the Tertiary mudstone. The damping ratios D shown in Fig. 16(b) are evaluated as 17–14% in the soil layers, which are considerably larger than the initial guess corresponding to small strain values, while in the base rock they are as small as 1.5–1% not so different from the initial guess. Fig. 16(a) also indicates that the V_s -value for the small shocks which occurred prior to the main shock is evaluated nearly identical to the V_s -logging values, while that for the aftershocks is slightly lower than the V_s -logging results.

Thus, it is certain from the back-calculation that a obvious reduction of V_s took place during the main shock in the soil layer, while the Tertiary base rock

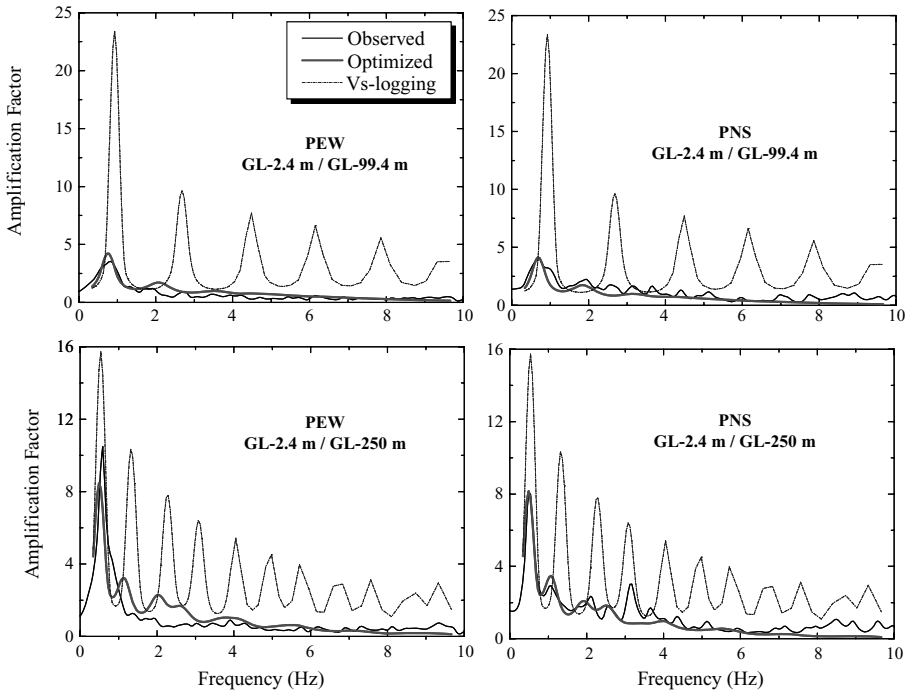


Figure 15. Optimized spectrum ratio between surface and GL-99.4 m in PEW and PNS directions for main shock compared to observations.

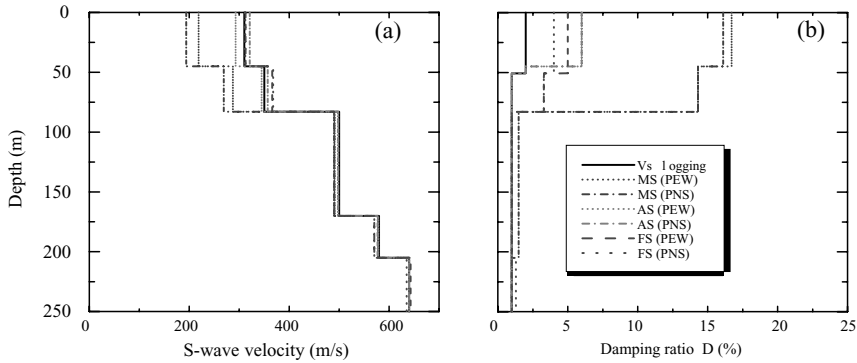


Figure 16. Optimized S-wave velocity (a) and damping ratio (b) for main shock, aftershocks and small shocks before main shock along depth compared with initial small-strain values.

behaved almost as a linear material with a minimal V_s reduction of less than a few percent. The maximum induced strain calculated by a forward multiple reflection analysis of SH-wave using the optimized properties was 0.27% for the soil deposits consisting of Pleistocene and Holocene natural soil.

As will be mentioned later, the V_s -value of the artificially backfilled soil was 100–200 m/s down to around GL-10 m, considerably smaller than that of the natural soil layer of the vertical array. Considering that induced shear strain γ by a unilaterally propagating wave is expressed as $\gamma = \dot{u}/V_s$, much larger strain is estimated to have occurred in the backfill even under the same particle velocity \dot{u} and the linear V_s -values, leading to much more nonlinearity effect and volume change there.

4 EVALUATION OF INCIDENT SEISMIC WAVE ENERGY

4.1 Calculation of wave energy

Considering that the incident wave energy is directly related to induced strain or damage in superstructures in general (Kokusho et al., 2007), it is worthwhile here to evaluate a seismic input not only by acceleration or velocity but also by energy. The seismic wave energy E , if its major portion is assumed to be transmitted by SH-wave, can be calculated simply as

$$E = \rho V_s \int (\dot{u})^2 dt \quad (1)$$

where \dot{u} is particle velocity of horizontal motion and ρV_s is the seismic impedance of a layer where the wave is defined. Note that \dot{u} in Eq. (1) is the particle velocity not directly of recorded motions but of traveling waves in either upward or downward direction. Therefore, it is essential to separate a measured motion at a point

into upward and downward waves in order to evaluate the individual energies (Kokusho and Motoyama 2002).

If a site consists of a set of horizontal soil layers and they behave as linear materials, upward and downward waves at any point can be calculated from a surface record based on the multiple reflection theory (e.g. Schnabel et al., 1972) from which the flow of the energy there is readily evaluated. During strong earthquakes, though, seismic motions at the ground surface are very much affected by the soil nonlinearity. However, the deeper the soil is, the more linearly soil behaves even during strong earthquakes (Kokusho et al., 1996). If vertical array records are available, the energy flow in deeper ground can be evaluated by using earthquake records at deeper levels where seismic wave is less contaminated by soil nonlinearity. The separation of upward and downward waves from measured motions at two different underground levels is readily made using the multiple reflection theory as explained in another literature (Kokusho and Motoyama, 2002). On the other hand, the incident energy at a ground surface can be calculated by substituting a half of particle velocity there into \dot{u} in Eq. (1).

The upward energy thus calculated using the optimized properties in PEW and PNS directions and summed up in the two directions at GL-250 m, GL-99.4 m, GL-50.8 m and at GL-2.4 m are 453 kJ/m², 434 kJ/m², 384 kJ/m² and 377 kJ/m², showing a gradually decreasing trend with decreasing depth. Among them, the energies evaluated at GL-99.4 m, almost the same elevation as the embedded foundations of the reactor buildings (RBs), are exemplified in Fig. 17 together with the corresponding velocity time histories. The upward energies increases monotonically with time and amounts to be 351 kJ/m² in PEW direction and 83 kJ/m² in PNS direction eventually. Compared with the downward energy

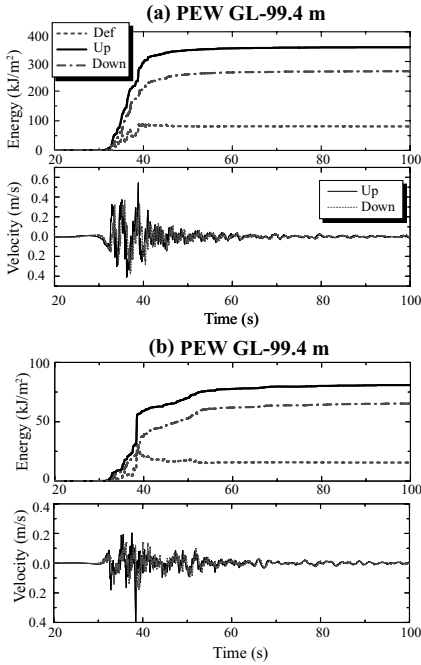


Figure 17. Time histories of wave energies and particle velocities of upward & downward waves at GL-99.4 m. in the directions of PEW (a) and PNS (b).

similarly calculated, the difference between them can be calculated as shown in the chart, the final value of which indicates the dissipated energy in the ground above that particular depth (Kokusho and Motoyama 2002).

4.2 Energy spectrum

Though seismically induced strain or damage of structures is highly dependent on the incident wave energy, another important damage-related parameter is the frequency content of the incident energy in view of resonance of structures. In order to know the frequency-dependent energy distributions, “energy spectrum” is proposed herein as the power spectrum of the particle velocity times the seismic impedance ρV_s . Thus, the total energy E defined in Eq. (1) can be expressed as the sum of energy spectra, $\rho V_s T(A_k^2 + B_k^2)/2$ corresponding to frequencies, $f_k = K \Delta f$; as

$$E = \rho V_s \int (\dot{u})^2 dt = \rho V_s \Delta t \sum_{m=0}^{N-1} x_m^2 \quad (2)$$

$$= \rho V_s T \left[\left(\frac{A_0}{2} \right)^2 + \frac{1}{2} \sum_{k=1}^{N/2-1} (A_k^2 + B_k^2) + \left(\frac{A_{N/2}}{2} \right)^2 \right]$$

where a velocity time history consisting of m discrete data is expressed by the finite Fourier series with coefficients A_k and B_k , and $\Delta f = 1/(N \Delta t)$, $k = 0, 1, 2, \dots, N/2$, $\Delta t =$ time increment of the velocity time history, $N =$ the total data points in the time history, and $T = N \Delta t$.

The energy spectrum of the incident wave at GL-99.4 m is shown in Fig. 18, where, needless to say, the sum of the individual spectrum amplitudes is equal to the total energy (434 kJ/m²) in the PEW and PNS directions at GL-99.4 m. Note that a major portion (73%) of the incident wave energy during the 2007 Chuetsu-Oki earthquake is in the frequency range lower than 1.0 Hz, indicating that the earthquake gave much stronger impact on the soil ground and the backfill soils, which is greatly affected by long period cyclic shearing, than on superstructures having higher resonant frequencies.

4.3 Comparison of incident energy

In Fig. 19, the total energy at GL-99.4 m is plotted with a star symbol versus the hypocenter distance $R = 23$ km of the main shock. The solid line in the chart indicates the energy per unit area calculated by a simple equation assuming spherical energy radiation with R as

$$E_{IP}/A = E_0/(4\pi R^2) \quad (3)$$

where E_0 is the total wave energy assumed to radiate from the hypocenter and is determined using the empirical equation by Gutenberg (1955):

$$\log E_0 = 1.5M + 11.8 \quad (4)$$

Here, E_0 has the unit of erg (1 erg = 10⁻¹⁰ kJ), and M is the earthquake magnitude using the Richter scale. Here the Japanese Earthquake Magnitude, M_J , was used to compute E_0 because the Richter and Japanese magnitude scales are almost equivalent. Thus, input energies E_{IP} at bedrock during the earthquake may be

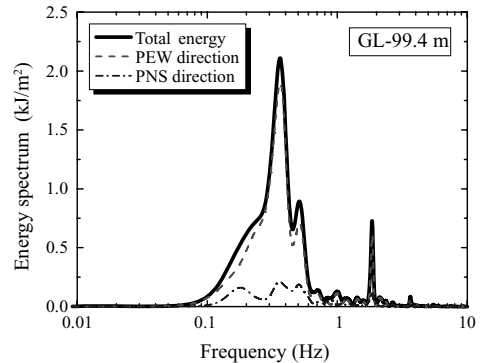


Figure 18. Energy spectrum of incident wave at GL-99.4 m.

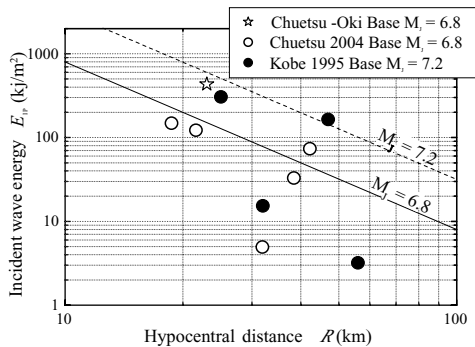


Figure 19. Incident wave energy versus hypocentral distance evaluated from vertical array records compared with simple calculation based on spherical energy dissipation.

readily computed by Eqs. (3) and (4), if the earthquake magnitude M and the focal distance R is given.

Incident energies at base layers 100–300 m deep from GL computed from the KiK-net down-hole array records (Kokusho et al., 2006) during the 2004 Niigataken Chuetsu earthquake ($M_J = 6.8$) are also compared in Fig. 19 with the same theoretical solid line. In the same chart, incident energies at base layers around 100 m deep during the 1995 Kobe earthquake ($M_J = 7.2$) are also plotted and compared with the dashed line by Eqs. (3) and (4) (Kokusho et al., 2006). The energy during the Chuetsu-Oki earthquake was evidently higher in the near fault region than the 2004 Chuetsu earthquake of the same seismic magnitude $M_J = 6.8$. Also obvious is that the energy in the NPS site was as high as in the Kobe earthquake despite that the magnitude was smaller. One of the reasons seems to be attributable to the fault mechanism of the Chuetsu-Oki earthquake such as directivity and asperity and their direction/location relative to the NPS.

5 DYNAMIC RESPONSE AND GEOTECHNICAL PERFORMANCE

5.1 Response of building foundations and backfill

As explained above, the incident wave energy was found large in long period motions in particular from the seismic records in the NPS. In this section, the performance of soils and foundations under the high incident wave energy is explained with an emphasis on ground subsidence in the backfill area.

As previously mentioned, the reactor buildings, turbine buildings and other important structures were embedded directly on foundation rock of Nishiyama

mudstone of Neogene, which was covered with Pleistocene dense dune sand. The details of the embedment of the foundations and backfilling around them are available in the case history paper by Sakai et al. (2009). Fig. 20 illustrates the cross-sections of Units 1–4. The building foundations are deeply embedded in the excavated base rock directly or a man-made rock as stiff as the natural rock. The four sides of the buildings are backfilled by the dune sand, the maximum thickness of which is 30 m and 25 m on the left (sea) and right (inland) side, respectively, being thicker on the seaside for most of the units. During the construction, the quality of the backfill soil was controlled by a set of compaction machineries to achieve a prescribed compaction rate of 95% given by the dry density divided by the maximum density by 1 E_c (the standard energy by Procter). As regulated in all reactor buildings in Japan, the ground water here was designed to stay always at the foundation bottom by pumping up (sub-drainage) in order to secure the greatest possible shear resistance of the building foundation without the buoyant effect. Hence, the backfill soils near the buildings were unsaturated, although a gradual increase of the phreatic level with increasing horizontal distance from the buildings may have occurred.

Fig. 21(a) shows the acceleration response spectra of 5% damping ratio in the PEW direction obtained on the deeply embedded concrete RB foundations of the 7 units superposed on the same chart. As previously mentioned, the response of Units 1–4 is apparently larger than that of Units 5–7, which are located by 1 km north. As a whole, the peak periods of the acceleration spectra are unexpectedly long indicating a great involvement of long period ground motions. Actually, the velocity response spectrum of the same motion shown in Fig. 21(b) indicates that the peak period is as long as 3 seconds and the response is again larger for Units 1–4 than for Units 5–7.

There were no accelerometers recording the ground motion directly on the backfill soils. However, there were 2 seismometers near Units 1 and 5, about 200 m eastward from the reactor buildings (See Fig. 5), which recorded acceleration time histories on the ground surface. Fig. 22(a) compares the acceleration spectra between the embedded RB foundations and the neighboring ground surface for Units 1 and 5. Obviously, the response acceleration of the ground surface near the RBs takes much higher value than that at Service Hall in the period shorter than 1 s if compared between Figs. 22(a) and 11(a) presumably due to the shallower thickness of the surface soil layer overlying the Tertiary base rock.

The spectrum is obviously larger on the ground surface than on the foundation, demonstrating the effect of the embedded concrete foundation directly resting on the base rock. This effect is particularly

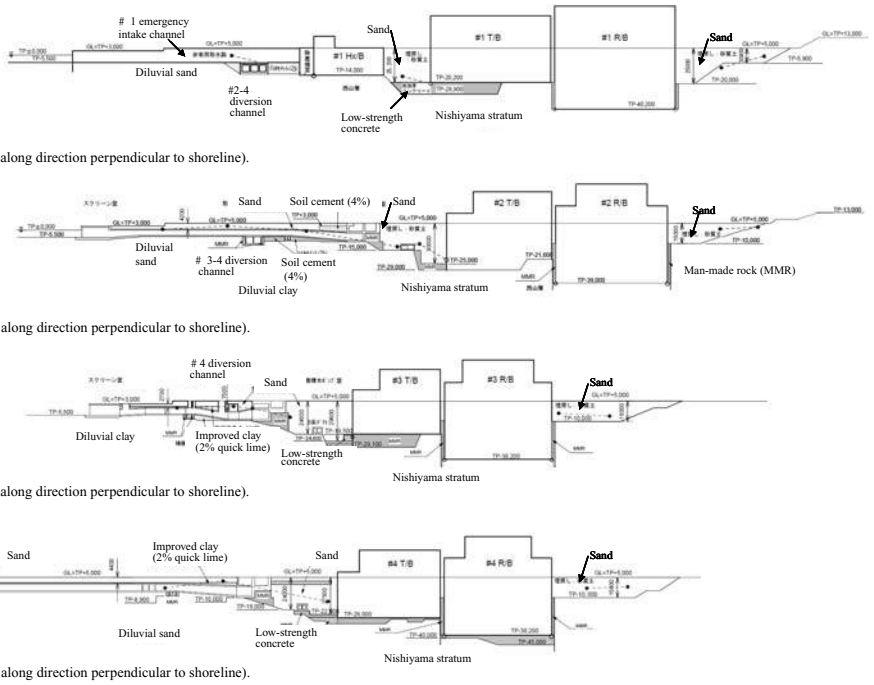


Figure 20. Cross-sectional view of RB and TB embedded in base rock and backfilled (Sakai et al., 2009).

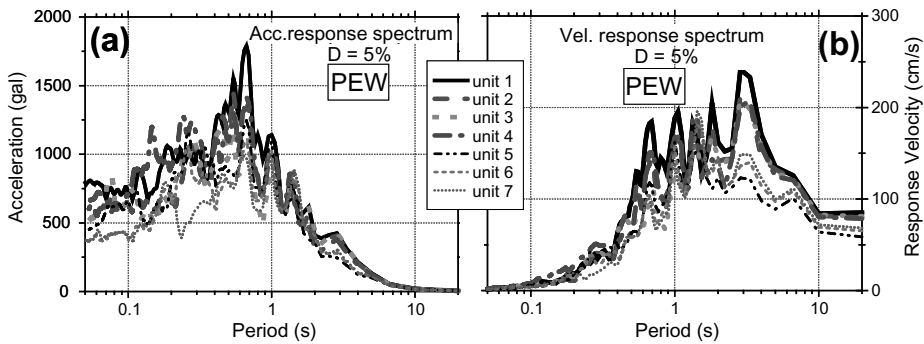


Figure 21. Acceleration response spectra (a) and velocity response spectra (b) of $D = 5\%$ in PEW direction on RB foundations of 7 units.

clear for short period range of $T \approx 0.5$ s or less, which seems beneficial to mechanical equipments of the plant facilities. The corresponding velocity response spectra shown in Fig. 22(b) indicate that the response velocity has a high value of about 300 m/s in a wide period range of 0.5–3 s on the ground surface. The long period motion seems responsible for the large subsidence of backfill soils, because the longer the period, the larger effect of cyclic shear stress can propagate to deeper level of the ground.

5.2 Subsidence of backfill

Fig. 23 depicts the subsidence contour map of the ground surface around Units 1–4 (suffering greater subsidence than Units 5–7), which was developed by comparing two survey results before and after the earthquake. It can be recognized first that the post-earthquake ground subsidence tends to concentrate in backfilled areas near the buildings except for near-shore or inland areas where subsidence occurred

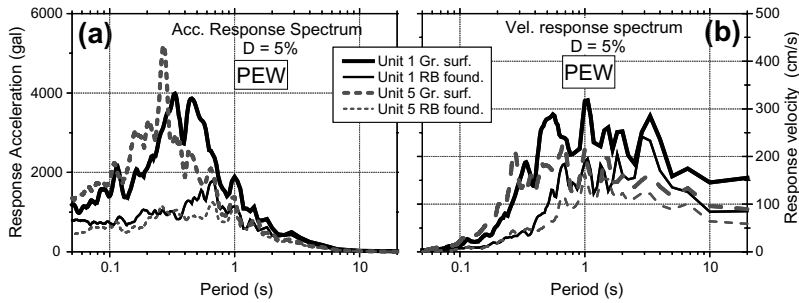


Figure 22. Acceleration response spectra (a) and velocity response spectra (b) of $D = 5\%$ in the PEW direction compared between RB foundation and neighboring ground surface for Units 1 and 5.

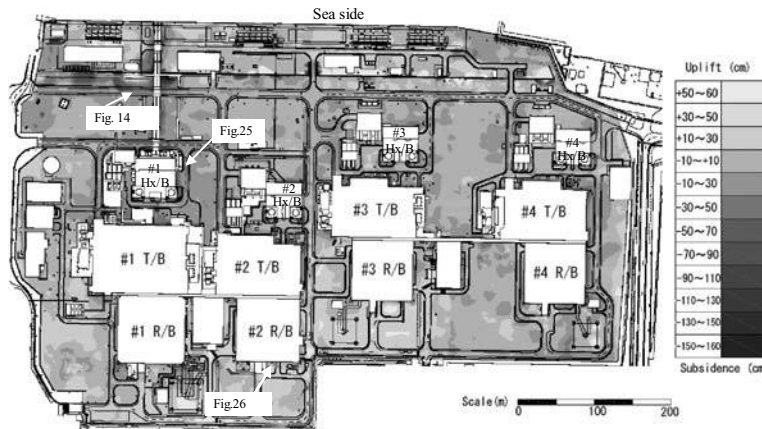


Figure 23. Spatial distribution of ground subsidence due to earthquake for Unit 1-4 (Sakai et al., 2009).

by liquefaction of loose sand or embankment instability. Fig. 24 shows examples of photographs of backfill area of the heat exchange building of Unit 1 after the earthquake. Also noted is that there are wide areas where no measurable subsidence occurred despite such a strong ground motion except those where buried ducts were backfilled. Two photographs in Fig. 25 show clear difference of ground behavior with and without backfilling around buried ducts.

Based on the detailed observations reported by Sakai et al. (2009), subsidence around the important buildings may be summarized as follows.

- a. Subsidence of the backfill was particularly large immediately beside the buildings and decreases with increasing distance from them.
- b. The maximum subsidence of 1.6 m occurred at Unit 1 where the backfill thickness was 25 m, indicating the average compression strain larger than 6%. For other units, too, the strain was evaluated more than a few percent just beside the buildings. This large subsidence can be explained not by

liquefaction but by the interaction of unsaturated backfill soils with the buildings.

- c. In the area slightly distant from the buildings, the compression strain was evaluated as 1-2%, which may be explained by cyclic straining of backfill soils.

In addition to the above summary, a further observation concerning (b) above may be made from Fig. 23 in which the subsidence looks greater on the seaside (west) than the inland side (east) of the buildings for all Unit 1-4. Fig. 26 shows the backfill area of Unit 2, in which the seaside of the turbine building was considerably larger than the inland side of the reactor building where the settlement was smaller and even some compression failure of corner stones could be seen. This may be partly attributed to the fact that the backfill soil thickness was smaller on the inland side in most of the units. However, Fig. 27 demonstrates the similar difference of ground subsidence on the two sides having almost identical backfill condition at the heat exchange building of Unit 2.



Figure 24. Subsidence of backfill ground near unit 1 heat exchanger building (Sakai et al., 2009).



Figure 26. Subsidence of backfill of Unit 2; seaside (right) of turbine building with large subsidence (top) and inland side (left) of reactor building with little subsidence or even some effect of compression (bottom).



Figure 25. Subsidence of backfill soil beside buried duct (top: Sakai et al., 2009) and no visible subsidence where nothing buried (bottom).

Relative horizontal displacement between the buildings and the surrounding backfill during earthquake shaking may have something to do with this. In Fig. 28(a), velocities and displacements of the RB

foundation and the surrounding ground surface of Unit 1 are shown, which are calculated by integrating the acceleration time histories once and twice in terms of time, respectively. Similarly, Fig. 28(b) shows the corresponding results for Unit 5. The velocity at ground surface in Unit 1 looks apparently strange after 9 seconds as shown in the top row of Fig. 28(a), reflecting the residual displacement which occurred to the base mat of the accelerometer and actually confirmed after the earthquake. Hence, the corresponding displacement in the bottom row of Fig. 28(a) is not reliable in the latter part.

Note that the major ground motion with high acceleration and velocity finished by the end of the first 12 seconds, although larger displacement is calculated thereafter contributed presumably by very long period motions, tectonic movements or possibly some errors involved in the integration. It may be justified to assume that the subsidence of the backfill occurred due to shaking effect and mostly in the first 12 seconds. During that interval, the displacements of the foundation and the ground in Unit 5 fluctuate almost in parallel, resulting in only a minimal relative displacement between them. In contrast to that, a large difference between the displacements is calculated from the first part of the motions (before 9 seconds), which is exempt from the subsequent residual offset, indicating that a



Figure 27. Subsidence of backfill soil beside heat-exchange building of Unit 2; seaside (right) of the building with large subsidence (top) and inland side (left) with little subsidence or even some compression heave (bottom).

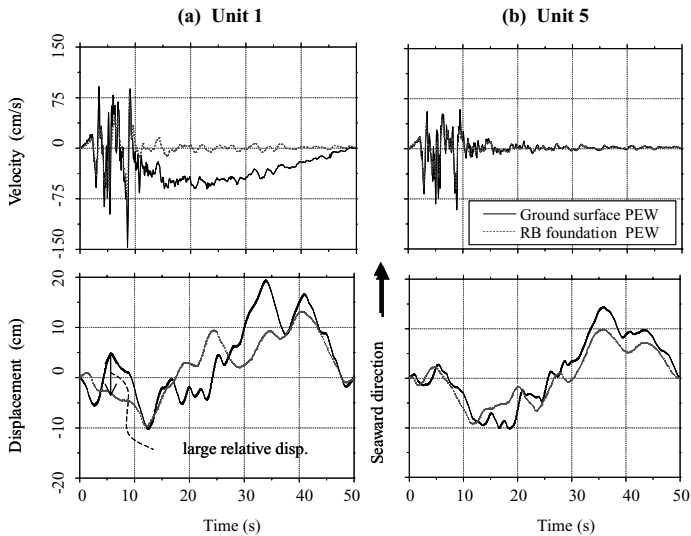


Figure 28. Velocity and displacement for ground surface compared to RB foundation in Unit 1 (a) and Unit 5 (b) in PEW direction.

distinct relative displacement between foundation and ground may have occurred during the major shaking.

Though its absolute value may not be accurate because the ground surface motion was measured at a place about 200 m far from the RB foundation outside

the backfilled area, the qualitative trend seems sufficiently reliable, implying that a relative displacement occurred by the ground movement westward (seaward) relative to the foundation. This relative horizontal displacement may have made a significant contribution

to the settlement of the backfill soils in addition to the effect of the cyclic shear stress by the long period motion previously mentioned.

As already explained, the settlement was particularly large (1.6 m maximum) at the seaside of the buildings compared to the inland side probably because the ambient soil tended to separate from the structure, while in the inland side, even some compression heave could be observed at some locations.

Similar direction-dependent difference of soil subsidence could be observed in some of pile-supported buildings in Kashiwazaki city, about 6 km far from the NPS. Fig. 29 exemplifies the case in a large public sports compound, where sea-side backfill area settled considerably in contrast to inland side. These case histories seem to give us a valuable lesson on how soil-structure interaction possibly occur in near-source regions of destructive earthquakes, which may lead to very different settlement of backfill soil depending on the directions.

5.3 Soil properties of backfill

After the earthquake, soil survey was densely implemented by TEPCO to investigate the physical and mechanical properties of the backfill soil. Bore holes were drilled at several locations around the reactor buildings of Unit 1–5 where substantial ground



Figure 29. Subsidence of backfill soil beside a sport compound in kashiwazaki city; seaside of the building with large subsidence (top) and inland side with little subsidence (bottom).

settlement occurred, and P/S-wave logging, RI density logging, Standard Penetration Test and soil sampling were carried out there (Sakai et al., 2009).

The grain size curves obtained are illustrated in Fig. 29, indicating that the backfill soil was quite uniform in its particle gradation. It is essentially uniform sandy soil consisting of 60–80% sand, 5–15% fines and 0–20 fine gravels. The dry density is 1.5–1.7 t/m³ and the wet density is 1.75–1.9 t/m³ on average and no clear increasing trend is observed with depth. The saturation ratio is 40–70% in the unsaturated fill.

Figs. 31(a) and 31(b) shows the variation of SPT N-value (not modified by overburden stress) along the depth measured at Unit 1 and Unit 4 at 3 different distances (2, 11.5, 22.5 m for Unit 1, and 1.6, 6.7, and 24.2 m for Unit 4) from the buildings. The N-values are 5–15 for the depth shallower than 15 m and show gradual increase with depth, which are almost the same trends for all the distances. However, the absolute N-values are obviously smaller in the immediate vicinity of the building than the distant points.

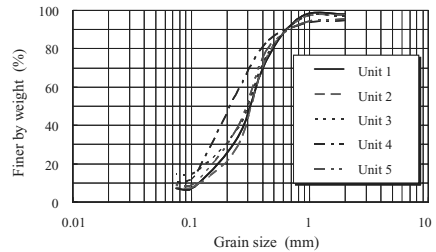


Figure 30. Grain size curves of backfill soils (Sakai et al., 2009).

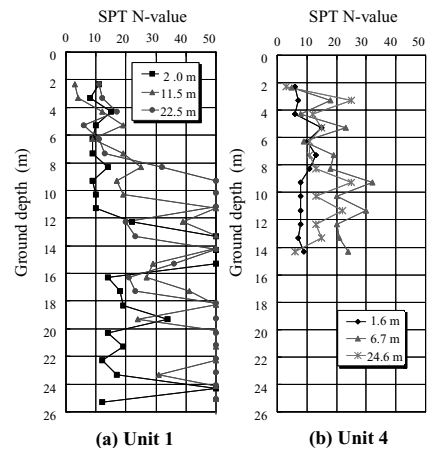


Figure 31. Variations of SPT N-value in backfill soil along depth measured at 3 distances from RB wall for Unit 1 (a) and Unit 4 (Sakai et al., 2009).

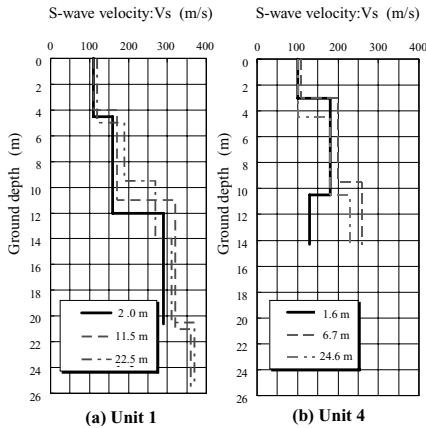


Figure 32. Variations of S-wave velocity in backfill soil along depth measured at 3 distances from RB wall for Unit 1 (a) and Unit 4 (Sakai et al.,).

Figs. 32(a) and 32(b) shows the variation of S-wave velocity along the depth measured at Unit 1 and Unit 4 at 3 different distances (2, 11.5, 22.5 m for Unit 1 and 1.6, 6.7, and 24.2 m for Unit 4) from the buildings. It is distinctly smaller than that in the natural soil ground of the vertical array shown in Fig. 8. The V_s -value is about 100 m/s near the surface and clearly increases with depth, the trend of which is almost the same for all the distances. However, the absolute V_s -values are again smaller in the immediate vicinity of the building than the distant locations. These trends may reflect that the soil had been less compacted near the buildings than at distant locations due to difficulty in carrying out heavy compaction near the building wall during the construction (Sakai et al., 2009).

Although the soil was essentially unsaturated near the buildings, liquefaction tests (undrained cyclic tri-axial tests) were also conducted for saturated backfill soils of dry density 1.6 t/m^3 (relative density 85%). The stress ratio under the effective confining stress 98 kPa was $R_L = 0.26$ for 5% double amplitude strain for 20 cycles of loading (Sakai et al., 2009).

6 DAMAGE CAUSED BY SUBSIDENCE OF BACKFILL SOILS AND PERFORMANCE CRITERIA

6.1 Damage due to subsidence

As mentioned previously, the RB/TB foundations had been directly based on the Neogene mudstone and suffered literally no settlement. In contrast, some of non-crucial structures had been constructed on pile foundations or shallow foundations in the backfill soil. The considerable soil subsidence in the backfill described previously did nothing wrong to the

important buildings but resulted in uneven settlement in structures supported by shallow foundations and buried pipes near the buildings.

A typical failure of this kind occurred adjacent to the Unit 3 turbine building, where a power connection bus supported by direct shallow foundation on the backfill subsided by 20 to 25 cm as shown in Fig. 33. The bus had connected a house transformer supported by piles driven in the backfill down to the base rock and the turbine building directly on the rock, both of which did not experience measurable settlement. The settlement of the bus support caused a breakage of a joint and consequent oil leak from the transformer, eventually leading to fire as explained in detail in Fig. 33.

Another failure case is shown in Fig. 34, in which considerable ground settlement occurred around an oil tank of Unit 1. The tank, classified as a critical structure for nuclear safety, was supported by the base rock, and did not settle, the backfill soil adjacent to the tank subsided considerably so that a large gap was generated around the tank foundation. This might have caused deformations of a concrete duct with oil pipes inside connecting the tank and the RB building if the duct were not properly supported.

A typical damage to pipes occurred to fire protection pipe lines buried directly in backfill soil around the buildings. Subsidence of the backfill soil relative to the buildings caused rupture of threaded and coupling joints near the building wall where the deformation exceeded their rupture limit as shown in Fig. 35.

6.2 Consideration on performance criteria

Thus, the soil subsidence in the backfill area and associated structural failures gave various impacts in considering the performance of the nuclear power plant during the severe earthquake, though the critical performance concerning the nuclear safety was secured. Hence, some considerations may be made with respect to the design criteria of the backfilling from the viewpoint of the performance based design.

First, the design earthquake load for non-nuclear non-critical structures (named Class C in NPS Regulatory Guide) was regulated to use a seismic coefficient of the same standard as normal industrial facilities and engineers followed that regulation. Unfortunately, the actual earthquake far exceeded even the severest design earthquake to be incorporated for critical nuclear structures (named S2), that almost nobody had dreamed of. This resulted in the considerable soil subsidence in backfill areas. So, the problem here is what kind of performance criteria for backfill should be considered for future earthquakes attacking nuclear power plants.

Provided that all important buildings or facilities associated with nuclear-safety (named Class As, A and B) are strictly regulated to rest directly on

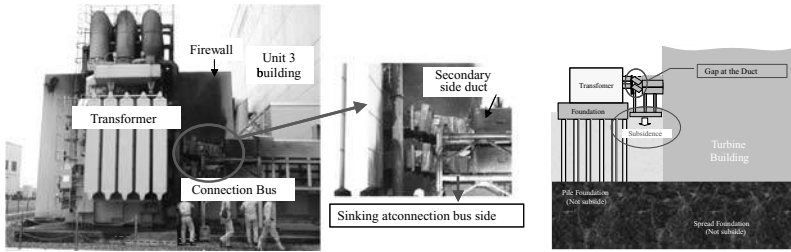


Figure 33. Transformer supported by pile foundation driven in the backfill down to the base rock and the turbine building based on the rock. The settlement of the bus support caused a breakage of a joint and an oil leak from the transformer and resulted in a fire (Sakai et al., 2009).



Figure 34. Ground settlement occurred around an oil tank of Unit 1 (Sakai et al., 2009).



Figure 35. Damage to buried pipes occurred to fire protection pipe lines buried in backfill soil around the buildings (Sakai et al., 2009).

seismically stable stratum such as cemented rock, and that the subsidence of the backfill soil has little to do with the stability of the important facilities, the performance criteria to be considered here for the backfill is not directly related to nuclear-safety. However, the backfill of NP facilities may have a big difference from that of other industrial facilities, simply because the definitions on serviceability, reparability and so forth may be quite different. The case of the KK-NPS clearly indicated that.

In any country in the world, nuclear power plants are considered quite special to general public and our society in the context of nuclear safety. Once it suffers

earthquake damage, no matter whether the damage is significant or not, it takes really long time to make clear that the safety is again secured. In the performance criteria of the backfilling, this very special condition of NPS should be considered and associated performance criteria should be introduced by taking account the probability of even the severest seismic load to be used in seismic design of nuclear power plants.

7 CONCLUSIONS

The ground motions obtained at KK-NPS during the Chuetsu-Oki earthquake and some analyses based on

them yielded the following major findings;

1. Main shock motions measured in the vertical array at the top of the sand dune indicates deamplification in acceleration and amplification in velocity with decreasing depth. Back-calculation of the motions indicates that remarkable nonlinearity in properties took place in soil layers whereas the effect remained marginal in the underlying base rock.
2. Peak periods of the acceleration spectra are unexpectedly long indicating a great involvement of long period motions with the peak period of 3 seconds in the velocity response spectrum, which seems responsible for the large subsidence of backfill soils in the NPS by introducing large cyclic shear stress or strain into deeper soils.
3. The incident wave energies evaluated at almost the same elevation as the RB foundations amounts to be 434 kJ/m². The energy spectrum proposed and evaluated here indicates that a major portion (73%) of the incident wave energy was in the frequency range lower than 1.0 Hz, indicating the major energy involved in long period motions gave great impact on soil ground and backfill.
4. The incident wave energy at the level of RB foundations was larger than that of the 2004 Chuetsu earthquake of the same magnitude and also almost equivalent to that of the 1995 Kobe earthquake of the larger magnitude.
5. Displacements calculated from the motions on the RB foundation resting on the bedrock and neighboring soil surface indicate that horizontal ground displacement occurred westward (seaward) relative to the foundation, which may have contributed to considerable settlement of the backfill soils around important buildings particularly large at the seaside compared to the inland side. This gives us a lesson on how backfill soil behaves in a near source region during destructive earthquakes.
6. In the performance criteria of the backfilling, although it is not critical to nuclear safety, special conditions of NPS should be considered, and associated performance criteria in serviceability, reparability, etc. should be introduced by taking account even the severest seismic load to be used for nuclear power plants.

ACKNOWLEDGMENTS

TEPCO (Tokyo Electric Power Company) is gratefully acknowledged for disseminating the valuable strong motion records during the 2007 Niigataken Chuetsu-Oki earthquake as well as other associated data set. NIED (National Research Institute for Earth Science and Disaster Prevention) in Tsukuba, who generously provided K-net and KiK-net data through the internet, is gratefully acknowledged. The great

efforts in data reduction of voluminous KiK-net records by graduate and undergraduate students of Civil Engineering Department in Chuo University are also very much appreciated. The author also expresses his deep gratitude to Dr. I. Suetomi who generously provided the computer code for Extended Bayesian Method.

REFERENCES

- Gutenberg, B. (1955): The energy of earthquakes, *Quarterly Journal of the Geological Society of London*, Vol. CXII, No. 455, 1–14.
- Kokusho, T., Matsumoto, M. and Sato, K. (1996): “Non-linear seismic properties back-calculated from strong motions during Hyogoken-Nambu EQ.” *Proc. World Conference on Earthquake Engineering (Acapulco)*, CD-publication.
- Kokusho, T. and Motoyama, R. (2002): “Energy dissipation in surface layer due to vertically propagating SH wave.” *Journal of Geotechnical and Geoenvironmental Engineering*, ASCE, Vol. 128, No. 4: 309–318.
- Kokusho, T., Aoyagi, T. and Wakunami, A. (2005): In situ soil-specific nonlinear properties back-calculated from vertical array records during 1995 Kobe Earthquake, *Journal of Geotechnical and Geoenvironmental Engineering*, ASCE, Vol. 131, No. 12, 1509–1521.
- Kokusho, T., Motoyama, H. and Ishizawa, T. (2006): Seismic wave energy in surface layers and energy-based damage evaluation”, *Proc. 8th National Conference on Earthquake Engineering in commemorate of 100th San Francisco Earthquake*, San Francisco, 8NCEE-133, CD-publication.
- Kokusho, T., Motoyama, R. and Motoyama, H. (2007): Wave energy in surface layers for energy-based damage evaluation, *Soil Dynamics & Earthquake Engineering* 27, 354–366.
- Kokusho, T. and Suzuki, T. (2008a): Vertical array records during 2007 Niigata-Ken Chuetsu-Oki earthquake and incident wave energy, *Proc. 14th World Conference on Earthquake Engineering*, Paper No. S26-13, CD publication.
- Kokusho, T. and Suzuki, T. (2008b): Soil properties optimized from vertical array records during 2007 Niigata-Ken Chuetsu-Oki earthquake, *Proc. 3rd Taiwan-Japan Symposium on Natural Hazards Mitigation*, Paper No., CD publication.
- Sakai, T., Suehiro, T., Tani, T. and Sato, H. (2009): Geotechnical performance at the Kashiwazaki-Kariwa Nuclear Power Station caused by the 2007 Niigataken Chuetsu-oki Earthquake, *Case History Volume for Performance-Based Design in Earthquake Geotechnical Engineering*, Technical Committee No. 4, ISSMGE, Balkema.
- Schnabel, P.B., Lysmer, J. and Seed, H.B. (1972): “SHAKE, A computer program for earthquake response analysis of horizontally layered sites.” *Report EERC 72-12*, University of California Berkeley.
- Suetomi, I. (1997): A program manual for optimization of soil structure by Bayesian Method. *Report by Central Research Institute of Sato Kogyo Co. Ltd.*, (in Japanese).

Seismic performance based-design of large earth and tailing dams

R. Verdugo

University of Chile, Chile

ABSTRACT: The actual capability of predicting the seismic performance of earth structures is limited and it is important to recognize that the real application of PBSD in professional practice is still years away. However, it is important to admit that PBSD is attractive and efforts have to be done to make it closer to practitioners. In the seismic design of tailings dams there are two main factors that control the liquefaction resistance of tailings sands: density and fines content. Accordingly, test results showing the effect of these two factors are presented. In the case of large earth dams, the use of coarse materials is common because of their good mechanical behavior. However, the evaluation of their properties is difficult due to the lack of equipment to test large particles. An alternative procedure to evaluate mechanical properties of coarse soils is presented. Additionally, the long term deformations of three large dams are analyzed and an empirical expression to estimate these deformations is proposed.

1 PERFORMANCE BASED SEISMIC DESIGN

In a broad sense performance-based seismic design (PBSD) can be understood as a design criteria which goal is the achievement of specified performance targets when the structure is subjected to a defined seismic hazard. The specified performance target could be a level of displacements, level of stresses, maximum acceleration, mobilized strength, or a limit state, among others. In this respect, the limit state design can be seen as a particular case of the PBSD, where the performance target is the accomplishment of a resisting force.

The PBSD is being strongly promoted by structural engineers, probably encouraged by the heavy financial losses resulting after recent earthquakes. This comes from the fact that the main investments in building construction are the non-structural components and contents (Astrella & Whittaker, 2004). For example, in the case of office buildings, hotels and hospital structures, the investment in structural framing is only around 18, 13 and 8%, respectively; of the total cost (Miranda & Taghavi, 2003). This clearly indicates that the fundamental objective of building code provisions to guaranty structure integrity, in terms of no collapse against strong ground motion, is definitely insufficient to be considered a successful seismic behavior to the society. Accordingly, efforts are now being conducted to reduce the financial losses associated with the non-structural components and contents throughout a design that considers specific performance structural targets, such as maximum displacements, maximum accelerations, or inter-story drift, especially in those parts where the main investments are located. In this scenario, it seems naturally that building owners

and insurers, among others, should be involved in making informed decisions regarding the expected performance of the structures.

It is important to recognize that the formal use of performance-based design is definitely less widespread in geotechnical engineering than in structural engineering. Nevertheless, since the 60s the earthquake geotechnical community is applying methods of analysis for predicting permanent displacements in earth structures, which is basically a performance criterion as opposed to the classical concept of limit equilibrium (Newmark, 1965; Seed 1966, Makdisi & Seed, 1977). In addition, the design of foundations placed on granular soils is normally controlled by settlements rather than bearing capacity, which is also a performance criterion. In this sense, although it is not formally stated, the performance-based design is reasonably familiar for geotechnical engineers.

Since the middle 90s, geotechnical engineers from different countries have been promoting the development and application of PBSD, following to some extent the tendency that is observed in structure seismic design. Although some efforts have been oriented to standardize and improve the use of PBSD, as it is now conceived, it is flawed in crucial elements. Our present capability of predicting the mechanical seismic performance of earth structures inherently involves an important level of uncertainty. Starting with the prediction of the seismic event, continuing with the ability of ground characterization (such as geometry, heterogeneities, properties) and ending up with the real skills to model the dynamic soil response when it goes well beyond the linear behavior. Considering these fundamental uncertainties, it is commonly suggested that PBSD should be conducted on a

probabilistic basis, indicating the probability of exceeding a certain desired performance and the confidence of this probability. Unfortunately, the probabilistic approach is not accessible for most of practitioners and it does not really improve the final outcome which is the performance prediction.

Likely the most important issues behind the PBSO are the following:

- The intention of involving stakeholders (owners, insurers and regulators) in the decisions concerning the choice of target performances for a earth structure during and after seismic events, sharing in this way the decision-making process.
- The premise that seismic performance levels can be predicted analytically, so the cost associated with each level of performance can be rationally evaluated.

In spite of the benefit of involving stakeholders in the decision-making process of choosing a specific set of performance targets, it is important to be aware of the potential problems and consequences associated with this idea. To combine appropriately both, complex technical solutions and investment decision based on risk analysis, is also risky. This necessarily introduces another source of uncertainty which could be even more important than the technical uncertainties. This statement is written just when the financial crisis is striking the whole world, and it is strongly influenced by this fact.

On the other hand, the actual capability of predicting the seismic response of earth structures is a more fundamental issue. From a scientific point of view, there is a reasonable knowledge of soil and rock mechanical behavior that has been incorporated into numerical models that are basically able to reproduce a variety of laboratory test results. However, in engineering practice, the real situation is less promising, especially when the earth structures have singular geometries that need, for example, three dimensional analysis, or when several different geotechnical materials are involved, being necessary a deep geotechnical characterization of each one.

In the case of dam engineering, additionally, practitioners have to face the geotechnical characterization of rockfill materials constituted by large size particles. Normally there is a lack of available testing apparatuses for these coarse materials, therefore geotechnical properties have to be estimated to properly design a earth dam of this type.

In addition, there are several factors that are well recognized that affect the stress-strain relationship, but they are not included in the current models used in practice. Among these factors, it is possible to indicate that the most relevant are the following:

- Stress rotations that take place during seismic loading.

- Variation of the intermediate principal stress, σ_2 .
- Seismic pore water pressure generation.
- Redistribution of pore water pressure.
- Densification due to particle rearrangement.

In this context, the actual capability of predicting the seismic performance is quite limited. Consequently, it is important to recognize that the real application of the PBSO in professional practice is years away, but it is also important to admit that this design criterion is attractive and more efforts have to be done in order to improve it.

In this paper key geotechnical properties of copper tailings materials are presented, which are necessary to consider if performance based seismic design is carried out in tailings dam projects.

For the case of earth dams constructed with coarse materials, a test procedure using parallel grain size curves is proposed to estimate the mechanical properties of the coarse fills. Additionally, the variation of the deformation modulus with time obtained from the analysis of measured settlements of three Chilean dams is presented. For the application of the performance based seismic design of earth dams with coarse fills these results are considered relevant.

2 TAILINGS DEPOSITS

2.1 *General framework*

The waste products resulting from mining operations are called tailings. Typically in copper, gold and zinc mines, the extracted ore is crushed to the size of fine sand to clay from where the minerals are recovered. In the case of copper mines it is important to mention that, as an order of magnitude, around one percent in weight corresponds to the valuable minerals that are retrieved from the milled ore. Therefore, the mining operations have to manage large quantities of tailings which are around 99 times the weight of the copper, gold or zinc production. In addition, it is necessary to mention that due to the mining processes associated to the removal of the minerals, the resulting tailings are fully saturated.

In countries with a substantial mining industry, such as Australia, Canada, Chile, China, Peru, Poland, South Africa, and USA, among others, the design and construction of enormous tailing disposals is a crucial necessity that has been continuously imposing new geotechnical challenges. The mining industry generates everyday millions of cubic meters of waste that has to be disposed safely and inexpensively. In Chile, for instance, there are in operation tailings dams with a height of 150 meters and reservoirs with more than one thousand million tones of slimes, and there are projects under construction that will end up with tailings dams of 220 meter in high (Valenzuela et al., 1995). This trend indicates that conventional tailings

dams with large dimensions in terms of height and extension are accepted solutions for disposing mining waste products, and the assessment of their mechanical stability is one of the main concerns. Additionally, in all those regions with a high seismic activity, the stability and liquefaction resistance requirements are the main issues to be analyzed and satisfied. Furthermore, because all tailings disposals will exist well after the mining operation is ended, the seismic stability has to be ensured for a large period of time after closure of the mine.

In spite of these requirements, there are several case histories associated to the total failure of tailings dams due to the occurrence of liquefaction. In general, saturated deposits of loose cohesionless soils have shown to be susceptible to liquefaction during the occurrence of earthquakes. This phenomenon has been observed in tailing dams, hydraulic fills, as well as in natural slopes of sandy soils. It is important to bear in mind that a failure of a tailings dam has catastrophic results from economical and environmental points of view, and also can be associated with human casualties. Consequently, a failure has to be avoided by all means, but at the same time it is necessary to keep in mind that over design it is just a waste of resources.

For an appropriate design of conventional tailings dams that ensures stability at a minimum cost of construction, operation and abandon, the conditions of the storage site as geomorphology, geology and seismic activity of the area have to be considered. On the other hand, the geotechnical properties of the involved tailings play a predominant role in the selection of the most convenient design. In this paper the liquefaction strength of tailings materials is discussed at the light of new experimental data considering a wide range of fines content and densities.

2.2 Tailings disposals

Depending on how the tailings are processed, transported, discharged and stored, the resulting tailings disposals can be divided in two different systems: thickened tailings (or paste) disposals and conventional tailings dams. There are also others procedures, for example, filtered tailings, but they are less used due to their high cost.

In the case of thickened tailings disposal system, the main goal is to create a self-supporting tailings mass, so confining dikes can be eliminated or at least minimised. To accomplish this, the water content of the initial tailings slurry is reduced as much as possible prior to discharge by mean of high-density thickeners, resulting in a tailings deposit of a gently-sloping conical shape, with typical angles between 2 to 6 percent. The concept of thickened tailings was introduced by Robinsky in the late 60's and actually used since the beginning of the 90's (Robinsky 2000; Salvas et al., 1989).

The conventional as well as the thickened tailings disposal systems have to be designed and analysed in order to guarantee the appropriate level of stability. However, the pass experience has shown that conventional tailings disposals are susceptible to undergo seismic failure due to the occurrence of liquefaction. In the case of the thickened tailings disposals there is no sufficient information about their actual seismic behaviour due to its recent widespread application and the lack of important earthquakes in any of the existing thickened tailings facilities. Nevertheless, the following three factors can be used to argue that this type of disposal is intrinsically more stable against seismic disturbances than the conventional one. First, an increment in the density of the deposited tailings at the surface tends to occur due to its natural desiccation and the associated shrinkage of the tailings mass. Second, a quite limited saturated zone can be developed at the bottom of the disposed tailings and third, the driving shear stresses are low due to the reduced slopes reached by the surface of the disposal. In spite of this reasoning, there is no much information about the static and cyclic strength of thickened tailings and in this context new experimental evidence is presented below.

The oldest procedure for tailings disposal corresponds to the conventional tailings dams with the formation of a basin through the construction of a confining perimeter with one or several dams according to the topography of the site. The dikes or dams are usually made with the sand fraction of the tailings because, in general, it is the solution that provides the lowest cost. The sandy tailings are obtained by cycloning the natural tailings, resulting a material that classifies as sandy soil with fines contents usually in the range of 10 to 30%. The saturated finer tailings (slimes) are discharged and stored into the basin that is the disposal site. According to the construction procedure, it is possible to identify three different structures of tailings dams, so-called, upstream, downstream and center-line method of construction, which are sketched in Fig. 1.

It can be observed that the upstream method of construction requires the minimum volume of coarse tailings for dikes construction, but the geotechnical properties of the slimes are involved in the overall stability of the dikes. On the other hand, the dams constructed following the downstream method

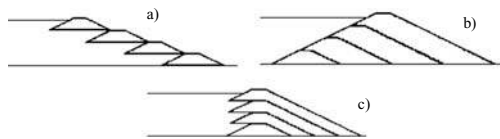


Figure 1. a) Upstream, b) downstream and c) center-line methods of construction.

produce dikes with the largest need of coarse tailings, but at the same time there are no fines tailings involved in the mechanical resistance of the resulting dam body. As can be expected, the tailings dams constructed with the upstream procedure have shown to be more vulnerable against both static and seismic failures, while the downstream dams have presented the safer behaviour. The tailings dams constructed by the center-line method have exhibited an intermediate behaviour in terms of stability. Consequently, in seismic regions the upstream dams, although attractive from an economical point of view, are avoided in favor of the downstream and center-line tailings dams. The seismic stability of these dams is basically controlled by the liquefaction resistance of the sandy tailings that constitute the dikes, which is mainly governed by the fines content and density of these sandy tailings.

Some singularities that make the conventional tailings dams different from others soil structures are the following:

- Tailings dams do not retain water, instead they contain saturated slimes, so from stability considerations, the most permeable the dam the better. Therefore, to ensure the drainage through and below the tailings dam body, it is common to build a drainage system at the bottom of the basin, in the natural ground, that passes through the base of the tailings dam. This drainage decreases the water level in the dam to a quite low position, what it is an important factor to reduce the zone with a potential occurrence of liquefaction.
- From economical considerations, only low efforts in compaction are accepted and therefore, the tailings dams tend to be in a loose to medium state of density.
- The period of construction of the embankments follows the mining operation, so the period of construction can be quite large, being possible to re adjust the original design.
- Tailings dams remain as a soil structure well after the mining operation is ended, which imply that stability must be ensured well beyond the period of the mining activity, to the so-called abandon period of the tailings dam.

These singularities have to be considered in the tailings dam design. For example, since the sand fraction of the tailings are placed with a high amount of water, a significant segregation takes place and a notable stratification is created, which has to be considered when the geotechnical properties are evaluated. However, in new projects, no information associated with the actual resulting fabric in the field is available and therefore, only reasonable estimations of properties can be done. This situation is overcome from the fact that the construction of tailings dams takes time according to the mine operation, which allows to carry out site investigations and laboratory

tests to evaluate material properties and optimize the design under the light of actual data.

2.3 Seismic failures of conventional tailings dams

The engineering practice have registered catastrophic failures of tailings dams triggered by the dynamic forces of earthquakes, causing severe losses to the private property, important destruction of agricultural lands and in many cases loss of human lives. Most of the seismic failures of tailings dams are attributed to increase in pore water pressure and to the occurrence of liquefaction (Dobry et al., 1967; Ishihara 1984; Finn, 1980; Finn 1996). In Fig. 2 is shown one of the oldest flow failure that has been reported in a tailings dam that took place at El Teniente copper mine in Chile, following the earthquake of October 1, 1928 (Agüero, 1929). The Barahona dam of 65 m in high collapsed 3 minutes after the main shock, releasing 4 millions tons of material that flowed along the valley, killing 54 persons. The cross section of the remaining tailings after the failure is sketched in Fig. 2, where the existence of several almost horizontal terraces are observed. This configuration is attributed to the low post liquefaction strength developed by weak layers of the typical strongly horizontal stratified structure of the tailings disposed in the basin.

Later on, during the earthquake of March 28, 1965, El Cobre tailings dam located in Chile failed catastrophically and more than 2 millions tons of material flowed around 12 km in a few seconds, killing more than 200 people and destroying El Cobre town. At the time of the failure, the dam was about 33 m high and it had a downstream slope as steep as 35° to 40° , respect to the horizontal (Dobry et al., 1967). A cross section of the tailings dam before and after the failure is shown in Fig. 3, where it is possible to observe the final profile of the tailings consisting also of several terraces with 1° slope towards the valley (Dobry et al., 1967).

Another well documented seismic failure of a tailings dam took place after the earthquake of January 14, 1978, at the dikes No. 1 and 2 of Mochikoshi gold mine in Japan. The dike No. 1 collapsed around 10 seconds after the main shock, releasing 60 thousands cubic meters of slimes. The dike No. 2 failed 24 hours after the main earthquake, at the time when there was not any ground shaking and a total volume of 3 thousand

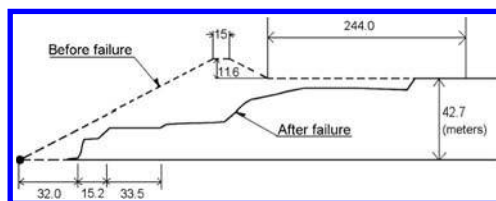


Figure 2. Failure of Barahona tailings dam, (Agüero, 1929).

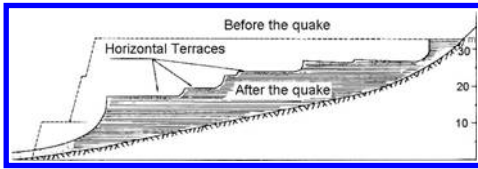


Figure 3. Failure of El Cobre tailings dam, (Dobry et al., 1967).

cubic meters of material flowed into the valley to a distance of about 240 m. The cross sections of these two dikes showing the situation before and after the failure are presented in Fig. 4 (Ishihara 1984).

Site investigation indicated that the remaining tailings in the pond adopted an average slope of 8° towards the valley. Part of the failure can be appreciated in Fig. 5.

Furthermore, during the Chilean earthquake of March 3, 1985, with a Magnitude 7.8, two tailings dams failed by liquefaction. Cerro Negro dam of 30 m in height failed and about 130 thousand tons of tailing material flowed into the valley for a distance of about 8 Km, (Castro et al., 1989). Due to this earthquake another failure occurred in Veta de Agua No. 1 dam, which at the time of the shaking had a maximum height of 15 m. According to a witness, the failure took place in the central part of the dam few seconds after the shaking had finished. The fines tailings stored in the pond moved along the El Sauce creek for about 5 km (Castro et al., 1989).

These failures, added to many others seismic failures that have occurred around the world, emphasise the importance of carrying out studies concerning the seismic response of tailings dams, with special focus on the liquefaction phenomena. However, it is also important to understand that these catastrophic failures have brought in many countries an over reaction from the community that has resulted in strong and rigid legal regulations, unnecessarily increasing the costs of tailings disposal. This situation may become more and more complicated as the tailings dams need to be larger and the construction costs grow exponentially. Therefore, studies supporting the actual liquefaction strength of tailings materials are of a paramount importance for the rational design of tailings disposals.

2.4 Cyclic mobility and flow failure

The term liquefaction was coined by Hazen (1920) to describe the failure of the hydraulic fill sand of Calaveras Dam on March 24th, 1918. In this failure, the up-stream toe of the under construction Calaveras dam, located near San Francisco in California, suddenly flowed moving approximately $700,000 \text{ m}^3$ of material for around 90 m. Apparently at the time of

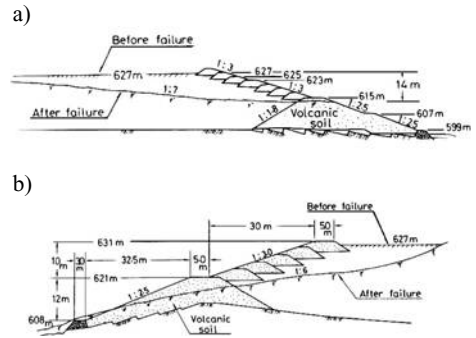


Figure 4. Failure of Mochikoshi tailings dams. (a) Dike N° 1 and (b) Dike N° 2, (Ishihara, 1984).

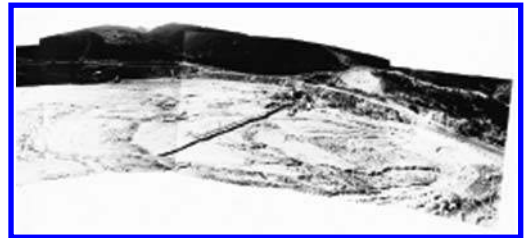


Figure 5. View of part of the Mochikoshi tailings dam failure (courtesy of Prof. K. Ishihara).

the failure none special disturbance was noticed, indicating that this phenomenon can occur in the absence of earthquakes.

Since that failure, the term liquefaction has been used in a broad sense for describing two different phenomena that may occur in saturated cohesionless soils, which have in common a significant pore pressure build-up and large deformations of the ground. Nevertheless, to understand the actual soil behaviour it is of a great importance to distinguish between the so-called flow failure, where a sudden lost of strength takes place, and the term cyclic mobility that is essentially associated to a progressive strain softening without any lost of strength.

The term cyclic mobility was proposed by Casagrande (1975) to conceptualise the continuous development of strains that is observed during undrained cyclic loading, when the occurrence of a significant pore water pressure has been reached. Typical experimental results on loose and dense sands showing this phenomenon are presented in Fig. 6, where it is important to observe that the soil mass does not undergo any loss in strength, but important deformations are progressively developed indicating a clear degradation of stiffness.

The rate of this degradation increases after each cycle when the material is loose and it decreases when the material is dense (Ishihara 1985).

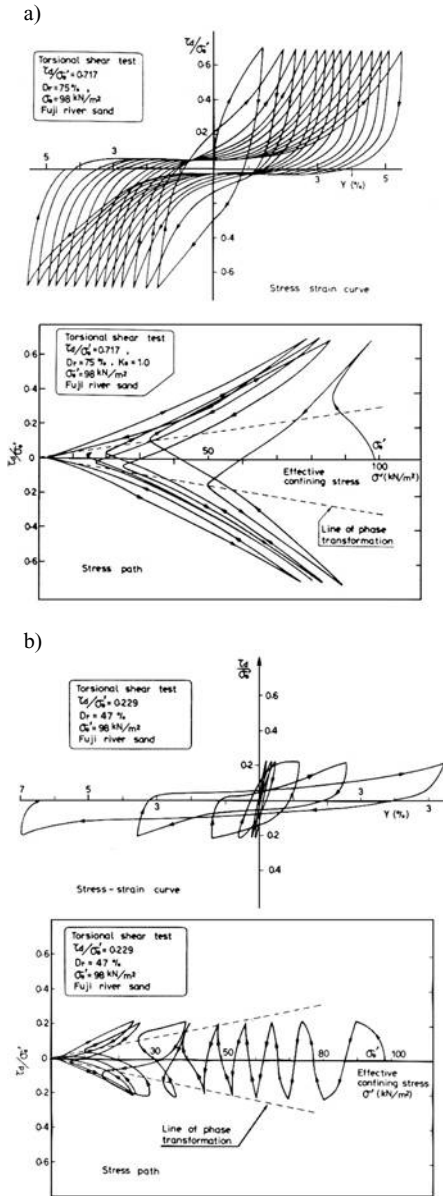


Figure 6. Typical experimental results for sands under a cyclic loading condition, (a) dense and (b) loose sand (Ishihara, 1985).

On the other hand, Casagrande (1975) proposed the term true liquefaction or flow failure for the phenomenon where a sudden loss in strength to a residual value takes place in a loose cohesionless soil (Castro, 1969). When the existing driving forces, or permanent forces, are larger than the mobilised residual strength, the failure is triggered and the soil mass deforms and flows resembling a viscous fluid. After failure has

occurred, the soil mass involved in the collapse tends to reach very gentle slopes. Typically, flat angles of 1° to 8° have been observed. This failure can be triggered not only by earthquakes, but also by disturbances that are fast enough to induce an undrained response of the initially loose soil mass.

True liquefaction or flow failure is the phenomenon that has been observed in the catastrophic failures of tailings dams, causing adverse scenarios with a significant amount of soil mass flowing hundred of meters in a few minutes. Consequently, seismic analysis of tailing dams must include the evaluation of the eventual occurrence of flow failure. The condition of flow failure generates a large level of deformation where the steady state or ultimate state of the soil is reached, so the use of this concept in the evaluation of a potential flow failure is suitable.

The ultimate response of the specimen has been referred to as the steady state of deformation (Poulos, 1981). Experimental results of undrained triaxial tests performed on samples at different effective confining pressure and at the same void ratio after consolidation are shown in Fig. 7 (Verdugo, 1992; Ishihara, 1993; Verdugo et al., 1996). It can be seen that regardless the initial level of confining pressures, the same ultimate state or steady state strength is achieved.

Additionally, the effect of the stress history is shown in Fig. 8 in terms of stress strain curves on loose and dense specimens loaded monotonically and cyclically.

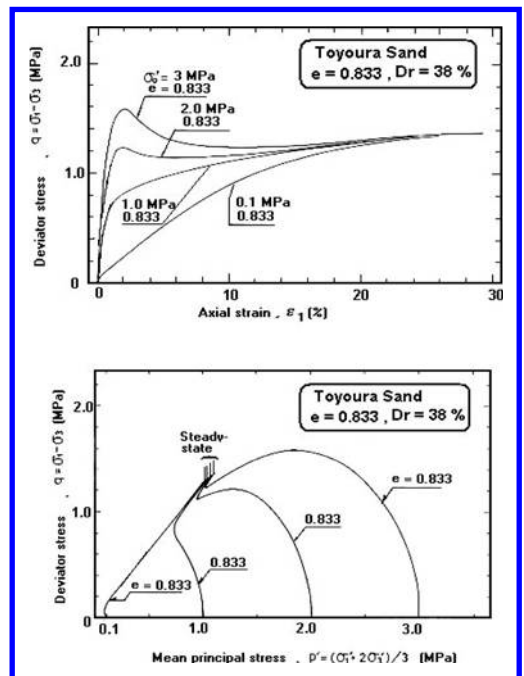


Figure 7. Steady state strength (Ishihara, 1993).

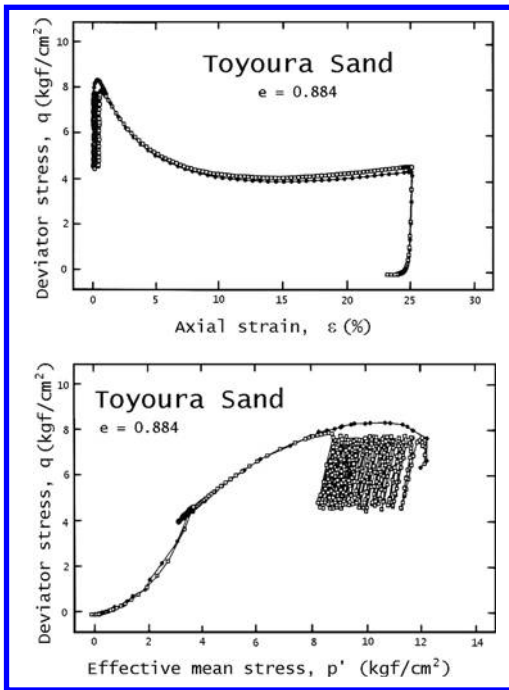


Figure 8a. Effect of stress history on loose sand (Verdugo, 1992).

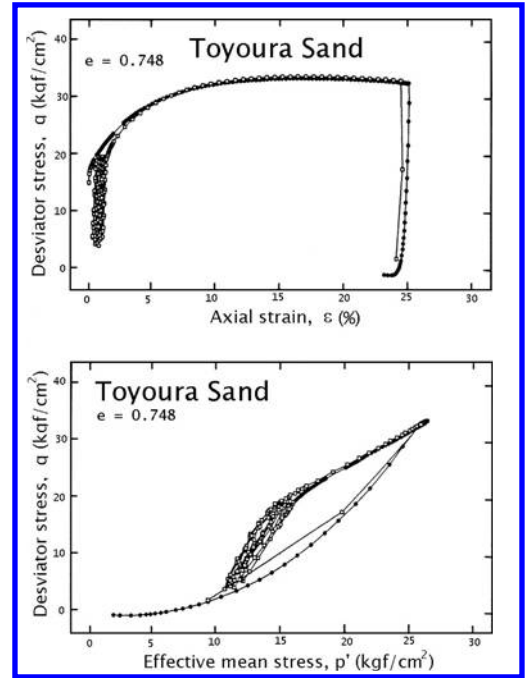


Figure 8b. Effect of stress history on dense sand (Verdugo, 1992).

As it is observed, the ultimate condition or steady state strength achieved at large deformations is independent of the previous cyclic loading indicating that the stress history does not affect the strength developed at large deformation (Verdugo, 1992). These experimental results suggest that the steady state strength is mainly a function of the void ratio. Therefore, the analysis of a flow failure basically needs to establish the level of static shear stresses and the undrained strength, which would be only dependent on the void ratio of the soil mass. The seismic action has to be seen as a trigger of the undrained strength.

To guaranty the stability of a tailing dam, the analysis of liquefaction has to be done in terms of both cyclic mobility and flow failure, and therefore an experimental program of tests covering these two phenomena has been performed. During the operation of a conventional tailing disposal there are mainly two parameters that can be modified (intentionally or incidentally), and which are directly associated with the static as well seismic strength of the dikes; density and fines content. Accordingly, the effect of these parameters in the tailings strength has been investigated.

2.5 Maximum and minimum void ratios

In the evaluation of the degree of compaction, or densification, of tailing sands it is important to take into

account the fines content, because the maximum and minimum densities are influenced by the fine particles. Besides, the procedure to determine the maximum density is also dependent on the fines content of the sand, being recommended the use of vibration when the fines content is less than 12 to 15%, whereas for higher fines contents the use of Proctor compaction test is used. To investigate the effect of fines on the maximum and minimum densities a comprehensive series of tests was carried out by Verdugo & Viertel (2004) on copper tailings sands retrieved from the main dike of a Chilean tailings dam. The original sample was separated in two batches: clean sand free of fines and tailings with 100% of particles passing mesh # 200 (0.074 mm). The grain size curves are shown in Fig. 9 and the particle shapes can be appreciated in the photos presented in Fig. 10.

The angularity in all the particles is readily apparent, especially in the case the finer particles. The fine-grained tailings are from the dike and they classify as non-plastic soil.

Using these two batches of tailings homogeneous mixtures of tailings with 2, 5, 10, 28, 40, 50, 60 and 100% of fines contents were prepared. The original tailings sand existing in the embankment with 18% of fines was also included as another homogeneous mixture. In all these mixtures the maximum and minimum densities were evaluated and in some of them Modified Proctor tests were also carried out. Placing the soil

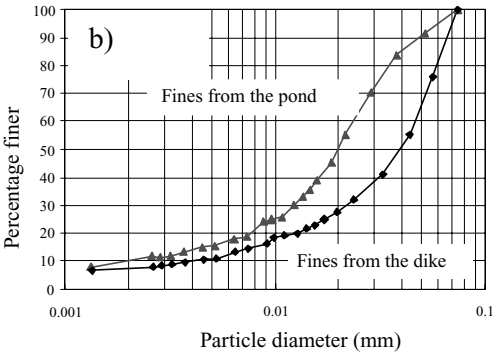
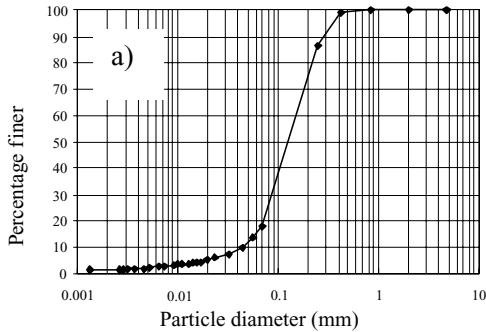


Figure 9. Grain size distribution curves. a) Sand fraction, b) fine-grained tailings.

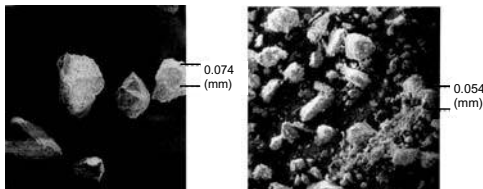


Figure 10. Particle shape of sand fraction and fines from the dike.

in a container using a paper funnel of conical shape the minimum densities were determined (Verdugo et al. 1996). The results of these tests are shown in Fig. 11 and summarized in Table No. 1.

It is interesting to observe that up to fines contents in the range of 60 to 70%, the maximum dry densities obtained by vibration are slightly higher than the values obtained by the Modified Proctor. Therefore, in the case of non-plastic fines the concept of relative density holds valid well above 15% of fines content, confirming previous results reported by Verdugo (1997).

A study related to the characteristics of maximum and minimum void ratios of natural sands reported by Cubrinovski et al. (2002) indicates the existence of a good correlation between these two indices.

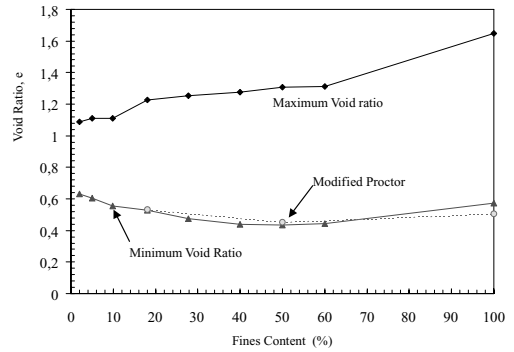


Figure 11. Maximum and minimum void ratios as function of fines content.

The maximum and minimum void ratios obtained in the present investigation are plotted in Fig. 12 together with the proposed correlations established by Cubrinovski et al., (2002). It can be seen that tailings sandy soils develop lower minimum void ratios or higher maximum void ratio than natural sands. According to the presented data, it is possible to point out that, tailings sands containing non-plastic fines achieve particular values of maximum and minimum void ratios that differ from the values reported by natural sandy soils. It is important to remark that these non-plastic fines are constituted mainly by particles with sizes in the range associated with silty soils. However, they have been created artificially by crushing fresh rocks, and therefore, in terms of behaviour they are closer to a fine sand than to a silty soil.

2.6 Cyclic resistance ratio

The experimental evidence indicates that mechanical properties of silty sands are largely controlled by the amount of fines and by the plasticity of these fines (Verdugo & Viertel 2004; Polito & Martin, 2001; Ni et al., 2004). For cooper tailings, Troncoso & Verdugo (1985) studied the effect of fines content on the cyclic strength of tailings sands testing reconstituted samples compacted at the same initial void ratio. Test results associated with the number of cycles required to 100% of pore water pressure build-up are shown in Fig. 13, evidencing the degradation of cyclic resistance exhibited by the tailing sands with the presence of low plastic tailing fines. It is important to mention that these results have been obtained for samples compacted at the same initial void ratio, which means that each series of soil batch has different relative density, or degree of compaction.

Ishihara et al. (1980) reported the results of a series of cyclic triaxial tests conducted on different tailings sands at different void ratios. The test results are summarized in Fig. 14, where it is possible to observe that

Table 1. Maximum and minimum dry densities.

Fines Content (%)	γ_{\min} (t/m ³) (Cone paper)	γ_{\max} (t/m ³) (vibration)	γ_{\max} (t/m ³) (M. Proctor)	ω_{opt} (%) (M. Proctor)
2	1.298	1.659		
5	1.284	1.689		
10	1.283	1.744		
18	1.216	1.773	1.767	14.0
28	1.203	1.839		
40	1.191	1.882		
50	1.174	1.887	1.868	11.7
60	1.171	1.877		
100	1.023	1.724	1.802	14.0

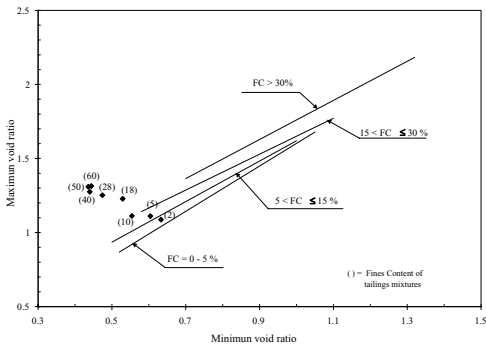


Figure 12. Maximum and minimum void ratios of tailings and natural sands.

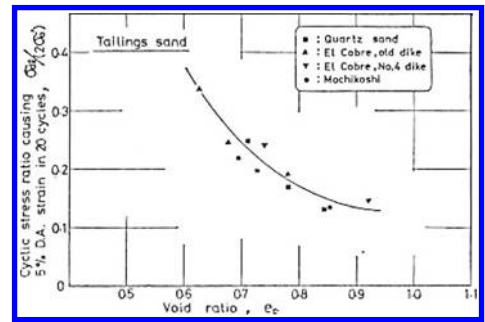


Figure 14. Variation of cyclic strength with void ratio (Ishihara et al., 1980).

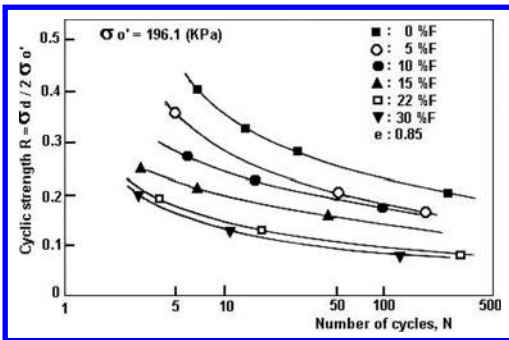


Figure 13. Effect of fines on the cyclic strength (Troncoso & Verdugo, 1985).

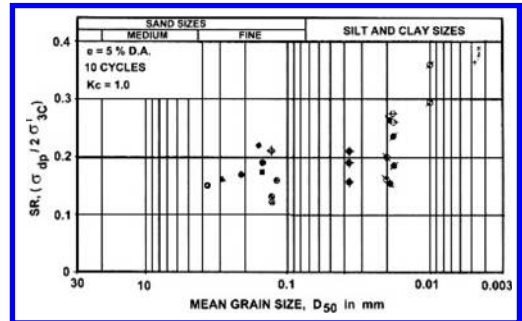


Figure 15. Variation of cyclic stress ratio with grain size in Tailings (Garga, 1984).

the cyclic strength decreases consistently with increase in the void ratio, confirming the effect of density.

Test results obtained in “undisturbed” samples of tailings with different particle sizes were compiled by Garga et al., (1984). The cyclic stress ratio to cause 5% double amplitude strain in ten cycles is shown in Fig. 15. For sand-sized materials, these data have been normalized to 50% relative density, but for the fine-grained materials no adjustment has been made.

According to these data, the normalized cyclic strength of the sand-sized materials falls within a relatively narrow range, and it increases for the clayey tailings.

Using the same tailings described in section 2.5, a comprehensive series of cyclic triaxial tests on compacted samples was carried out by Verdugo & Viertel (2004), some of which results are presented in Figs. 16, in terms of cyclic stress ratio and number of cycles associated with 100% of pore water pressure build-up for the tailings mixture of 18% fines content.

The general trend observed in each of these curves follows what has been reported in the literature for other sandy soils. For practical purposes, the cyclic strength associated with 20 cycles of loading, R_{20} , can be considered an appropriate value for representing the cyclic strength of each curve. Accordingly, R_{20} is plotted in Fig. 17 for each fines content and relative density.

It is observed that in the range of fines content that has been studied, the cyclic strength consistently decreases as the fines content increases, independently of the degree of densification.

Furthermore, for fines contents of 2 and 10%, the cyclic strength as a function of relative density follows a similar trend. There is a sharp increase in the cyclic strength from approximately a relative density of 50%. While for fines contents of 28%, the cyclic strength increases monotonically with the relative density. On the other hand, the mixture of 18% of fines shows an intermediate behavior with a rather pronounced increase in strength approximately from a relative density of 80%. The existence of a threshold value of relative density above which the cyclic strength increases drastically has been reported by Tatsuoka et al. (1982) for Toyoura sand samples tested on cyclic torsional simple shear tests. Considering the

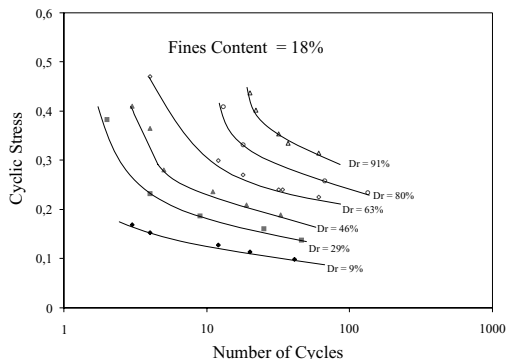


Figure 16. Cyclic strength for different relative densities. Mixture of 18% of fines content.

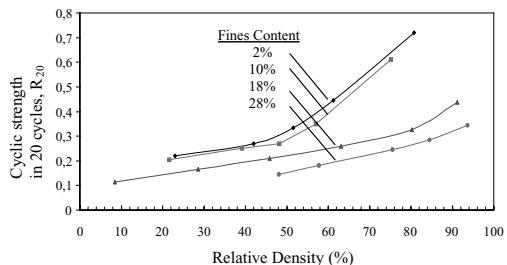


Figure 17. Cyclic strength as a function of relative density for different fines content.

cyclic strength associated with a 15% of shear strain in double amplitude achieved in 20 cycles, Tatsuoka et al. (1982) reported for Toyoura sand a threshold value of relative density around 83%. This value is quite close to the threshold relative density exhibited by the tailing mixture of 18% of fines content. It is also interesting to indicate that the tailings mixtures with less fine-grained material present a cyclic strength higher than Toyoura sand in the complete range of relative density. These results are suggesting that copper tailings materials with low amount of non-plastic fines develop a high cyclic strength, probably associated with the considerable angularity and hardness of the particles.

Although it has been shown that relative density is a suitable parameter when non-plastic fines are involved, the previous results are presented again, but using just the sample void ratios, which is a straightforward representation of the effect of density on these experimental results as shown Fig. 18.

It can be seen that similar conclusions can be drawn, confirming that in the wide range of non-plastic fines content that has been used, the cyclic strength consistently increases as the void ratio decreases, and as the fines content increases the cyclic strength decreases.

These results suggest that the mixtures containing non-plastic fines are always affected by the presence of these fines, regardless of how small is the amount of fines. A possible explanation is related to the actual location of the fines in a rather homogeneous mixture. It is possible to hypothesize that part of the fines will cover the larger sand particles and therefore, some of the contacts between sand grains would be contaminated with fines, which would affect to some extent the resulting overall mechanical response. Obviously, a very small amount of fines would affect only few contacts and the resulting effect would be small. On the other hand, when the amount of fines is large enough, so that the voids are completely filled with fines, the contacts

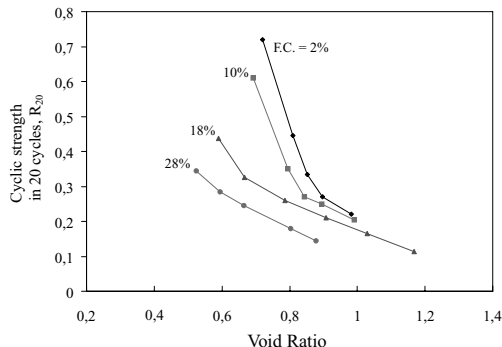


Figure 18. Cyclic strength as a function of void ratio for different fines contents.

between particles will take place mainly throughout the fines matrix, and the overall behavior would be controlled by the fine fraction. Hence, it is possible to indicate that the concept of sand skeleton usually used to model the effect of fines is inappropriate because always a part of the existing fines will contaminate some of the contacts between larger particles, which will definitely alter the mechanical response.

These experimental results resume the effects of density and fines content on the cyclic strength of tailing sands, which has a tremendous practical application on the design and operation of a conventional tailing dam. First, the seismic analysis permits to establish the cyclic strength that ensure the required stability, then using the above-presented results all the possible combinations of fines content and relative density that satisfy the needed cyclic strength can be obtained. Therefore, during the tailing dam construction it is possible to have a flexible design playing with the requested density according to the fines content produced by the cycloning process.

2.7 Undrained steady state strength

Series of CIU triaxial tests were carried out on the same tailings sand described above. The steady state lines defined by these tests are shown in the e - p' plane in Fig. 19. It can be seen that as the fines content increases the location of the steady state lines move down, suggesting an increase in the compressibility of the mixture. Nevertheless, the slope of the steady state lines is maintained unaffected by the presence of fines in the mixtures.

On the other hand, all the data fall in a rather unique straight line in the q - p' plane that is associated to an angle of internal friction of 35° , which means that the frictional resistance of these soils is not affected by

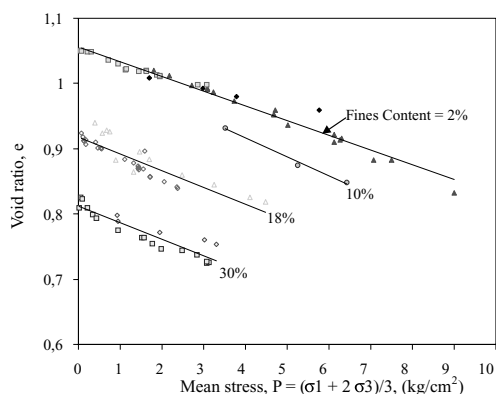


Figure 19. Steady state lines for mixtures of different fines content.

the finer fraction. Therefore, it is possible to conclude that the non-plastic fines affect the general structure of the tailing sandy mixtures, at least, in the range of 2 to 30%, making them more contractive as the fines content increases.

2.8 Monotonic drained strength

During monotonic drained loading conditions, the mobilized strength of a cohesionless material can be well characterized by the angle of internal friction. For cohesionless copper tailings, at the same initial value of void ratio, $e = 0.90$, the variation of the angle of internal friction with fines content is presented in Fig. 20 (Troncoso & Verdugo, 1985).

It is interesting to notice that for the range of confining pressure used, 1 to 5 kg/cm^2 , the angle of internal friction mobilized at the peak failure is rather high, suggesting that tailing sands can develop high frictional resistance due to the angularity and hardness of the particles. Similar results have been reported by Pettibone et al. (1971) and others researchers. Furthermore, it can be observed that keeping the same initial void ratio, the angle of internal friction decreases as the fines content increases, suggesting that the lower the fines content the higher the strength.

2.9 Shear modulus and damping ratio

Provided that there is no generation of pore water pressure during seismic disturbances (dense sands, non-saturated sand), an alternative to model the seismic response of tailings dams is using the Equivalent Linear Method. In this condition both the shear modulus degradation curve and the variation of the damping ratio with the level of deformations are needed.

Test results of these parameters obtained in copper tailings sands using resonant column have been reported by Rojas et al. (1985) and they are presented in Figs. 21 and 22. It can be seen that in tailings sands the degradation of the shear modulus with the level of strain is less pronounced than the one reported for

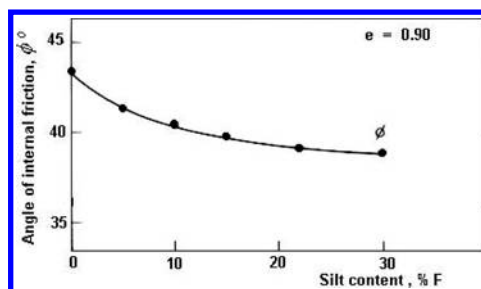


Figure 20. Angle of friction and fines content (Troncoso et al., 1985).

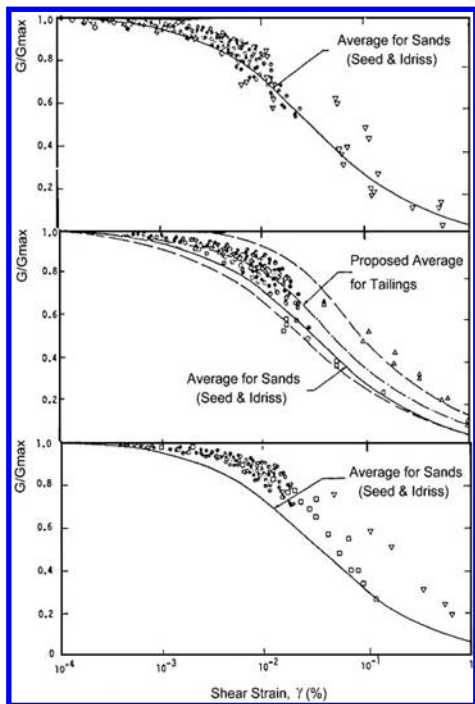


Figure 21. Degradation of shear modulus (Rojas et al., 1985).

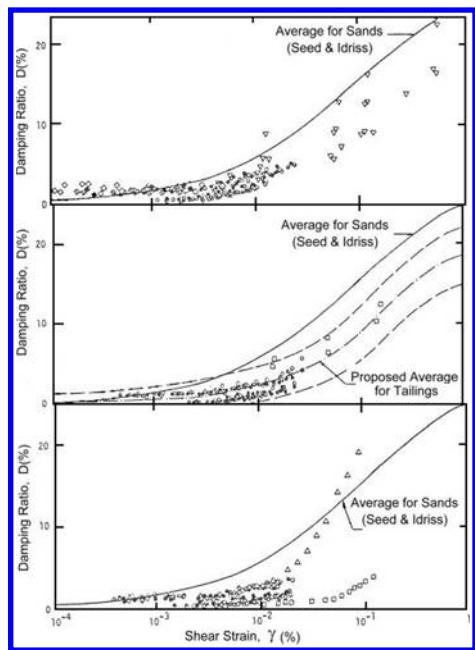


Figure 22. Damping ratio (Rojas et al., 1985).

natural sandy soils and the damping ratio achieves less values than natural sandy soils.

On the other hand, the effect of fines content on the degradation of the shear modulus has been reported by Troncoso & Verdugo (1985) and shown in Fig. 23. It is noticeable that, for any level of strain, shear modulus decreases as the fines content increases. Therefore, higher stiffness can be expected in cycloned tailings sands as the fines content decreases.

2.10 Effect of initial fabric

During the genesis of any soil deposit, the sedimentation and placement of soil particles is affected by the gravity force, which generates a preferential particle orientation that makes anisotropic soil structures. Casagrande et al. (1944) named this initial anisotropy caused by the geological process of deposition Inherent Anisotropy. Depending upon the environmental conditions existing during the sedimentation process, the inherent anisotropy may affect significantly the soil response. This situation is particularly important in hydraulic fills as the case of tailing dams, where there is not only a preferential orientation of particles, but also a segregation that results in a heterogeneous structure. Hence it is strongly recommended the evaluation of geotechnical properties using samples with the actual structure generated in the field.

Nevertheless, in saturated tailing sands, the field operation to retrieve “undisturbed” samples for being tested in the laboratory is complicated and expensive. Furthermore, at the beginning of the projects, when the tailing dams are not yet constructed, “undisturbed” samples are not available. Consequently, the alternative of testing reconstituted specimens compacted at the same density expected in the field it is always attractive, but it can not be ignored that the initial fabric or structure may have an important effect on the soil parameters, and therefore efforts has to be done in order to reproduce the expected actual soil structure.

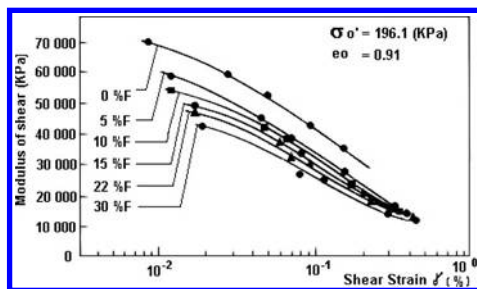


Figure 23. Shear modulus and fines content, (Troncoso & Verdugo, 1985).

Regarding the undrained steady state strength developed at large strains, there is experimental evidence showing that this parameter is independent of the initial inherent anisotropy or initial particle arrangements. However, it has been also shown that the steady state strength of non-homogeneous samples is strongly dependent on the initial configuration of particles, which suggests that even pretty large deformations are not able to erase the initial heterogeneity (Verdugo, 1992; Verdugo et al., 1995). Hence, it is proposed to divide the initial arrangement of soil particle in two groups as indicated in Fig. 24.

Firstly, it is possible to identify those homogeneous initial arrangements of soil particles that can be completely broken down at large deformation, and therefore can mobilize a unique steady state line. In the second group are those particle configurations of heterogeneous distribution of grains that can not be fully erased by large deformations, independently of how large the strains are. Tailing sand deposits are in this second group.

Triaxial tests data obtained from both reconstituted and “undisturbed” samples of tailing sands have been reported by Castro et al. (1989), and shown in Fig. 25. It is readily apparent that there is a significant difference between the undrained strength of “undisturbed” and reconstituted samples.

These experimental results confirm that an initial heterogeneous structure is not erased at large deformation and it develops a different undrained steady

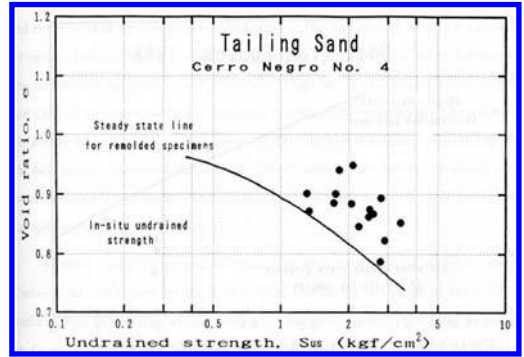


Figure 25. Undrained steady state strength from reconstituted and “undisturbed” samples (Castro et al., 1989).

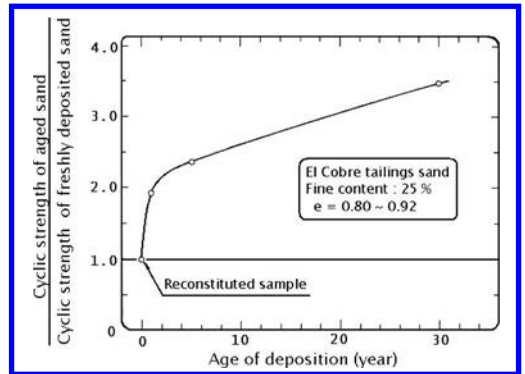


Figure 26. Aging effect on the cyclic strength of tailing sands (Troncoso et al., 1988).

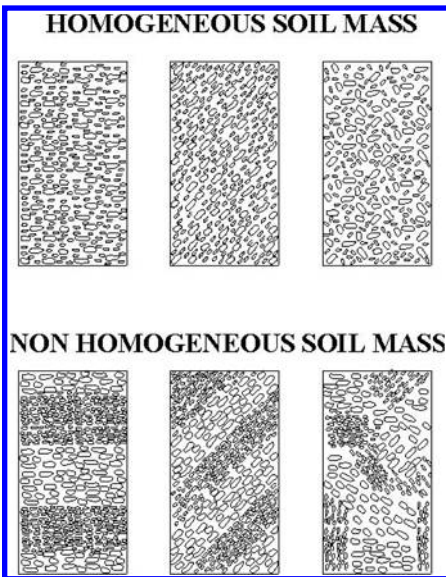


Figure 24. Proposed division of initial arrangement of soil particle.

state strength respect to the one reached by the homogeneous soil mass. Then, for the geotechnical characterization of tailing deposits the use of “undisturbed” samples is strongly recommended.

2.11 Liquefaction and aging

It has been generally recognized that the liquefaction resistance (cyclic mobility) tends to increase with the age of the deposit, what can be associated to the development of light cementation or some welding at points of grain contact. To study the effect of the time of deposition in the cyclic strength of tailing sands, series of cyclic triaxial tests have been performed on “undisturbed” samples retrieved from an old tailing dam at different depth, which basically means different age of the samples. In addition, tests on fresh samples reconstituted in the laboratory were carried out (Troncoso et al., 1988). The test results are summarized in Fig. 26, indicating that the cyclic stress ratio required to produce a state of softening with 5% double amplitude strain tends to increase by a factor of 3.5, 2.4 and 2

for the samples of 30, 5 and 1 years of sustained deposition, respectively.

Therefore, it is strongly recommended to estimate the effect of aging for stability analysis during the abandon period. This type of study can be done when the tailings dam has been in operation for several years, so it is possible to retrieve samples at different depths, which are associated to different years of deposition. Testing this batch of “undisturbed” samples, it is possible to establish the variation of the cyclic strength with the age of deposition, which allows an estimation of the improvement of the cyclic resistance with time.

3 LARGE EARTH DAMS

3.1 *Rockfill and gravel-fill dams*

Because of the intrinsic exceptional geotechnical properties of coarse materials, they are normally used in the construction of large earth dams. These materials are used in Concrete Face Rockfill Dam (CFRD) and Concrete Face Gravel-fill Dam (CFGD). These types of dams have increased in number throughout the world mainly because of the following two reasons: modern CFRD is a high quality dam type from all technical standpoints and the CFGD is often the lowest-cost dam type when the material is readily available at site (Sherard & Cooke, 1987).

However, coarse materials as rockfill, cobbles and gravel always present difficulties in the evaluation of their properties, commonly due to the lack of sufficiently large equipment to test large size particles. Hence in rockfill and gravel-fill dam projects, the available information related to mechanical properties of the coarse material of the fill is quite limited. Additionally, an important aspect to bear in mind is associated with the post construction deformations, which might affect the concrete face.

Therefore, evaluation of mechanical properties and long term deformations are two important issues that have to be faced on the design of a rockfill and gravel-fill dams. These topics are addressed in the following sections.

3.2 *Evaluation of mechanical properties of coarse soils*

Different methods to evaluate mechanical properties of coarse soils have been proposed, which involve testing of “equivalent” soil samples, free of oversized particles. The matrix model method, the parallel gradation method and the scalping and replacement method are the most commonly used methods. In the matrix model, the original coarse soil is divided in two parts: oversized particles and matrix material. The definition of oversize is arbitrary, and it is related

to the maximum particle size that can be tested in the available equipment. It is assumed in this method that the oversized particles are in a “floating” state, meaning that these particles have little or no contact between them. The matrix material to be tested is compacted to a density that has to be estimated, corresponding to the actual density of the soil matrix in the field (Siddiqi et al., 1987; 1991; Fragaszy et al., 1990; 1992). Therefore, the use of this procedure is limited by the validity of the assumption that the oversized particles are “floating” and the accuracy of the procedure to estimate the actual density of the soil matrix in the field.

In the scalping-replacement method, all those particles that are considered oversized with respect to the available testing equipment are scalped and replaced with an equal weight of a smaller particle range (Donaghe & Torrey, 1979). This procedure changes drastically the original soil gradation and, although some experimental data have shown promising results, there is no real evidence to support the equivalence between the original soil and the artificially created batch of soil scalped and replaced.

In the parallel gradation method, the oversized particles are scalped and a new batch of soil is prepared using the original material, which has a grain size distribution curve parallel (in the common semi log scale) to that of the original sample (Lowe, 1964; Marachi et al., 1972; Verdugo et al., 2003; Varadajan et al., 2003). The main advantage of this procedure is that the soil gradation is maintained. However, depending upon the particular characteristics of each soil, the mineralogy and hardness of grains, particle shape, and particle roughness, may be different and function of the particle size (Al-Hussaini, 1983; Cho et al., 2005; Lee et al., 1967; Santamarina et al., 2003 & 2004). In granular soils where these factors are similar for all particle sizes, the parallel gradation method can be seen as an attractive alternative.

Verdugo & De La Hoz (2006) reported test results of gravelly soils using the parallel gradation method. The grain size distribution curves and the maximum and minimum densities of one of the material tested are presented in Fig. 27. It is interesting to observe that the maximum and minimum densities are rather similar, regardless of the mean grain size, D_{50} . All tests were performed on samples compacted to an initial relative density of 70% and in a range of confining pressure between 20 and 600 kPa.

The stress-strain curves and the volumetric strains of these batches are presented in Fig. 28.

It can be observed that both peak strength and stiffness are similar for the different batches.

The stress-strain curves present an initial linear portion that can be represented by the deformation modulus, E_{50} (stiffness associated with a stress level equal to half of the peak strength), which results are presented in Fig. 29. It is observed that the parallel

gradations are able to capture the essential mechanical response of the soils, showing the same expression for E_{50} :

$$E_{50} = 175(\sigma_3)^{0.79} \quad (\text{MPa}) \quad (1)$$

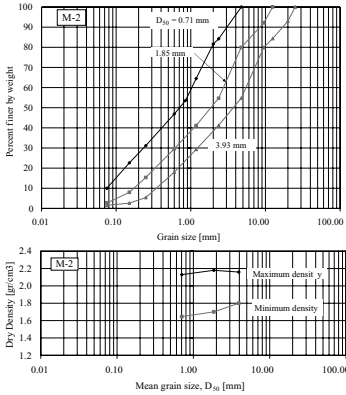


Figure 27. Grain size distribution curves and maximum and minimum densities of samples M-2.

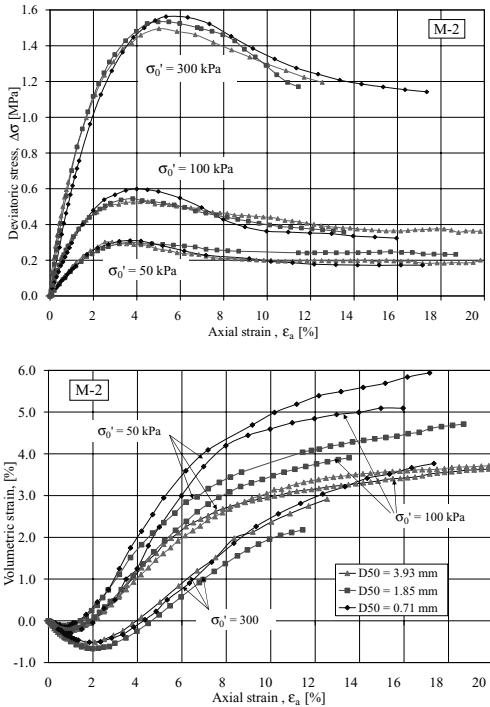


Figure 28. Stress-strain curves and volumetric strains obtained in samples M-2.

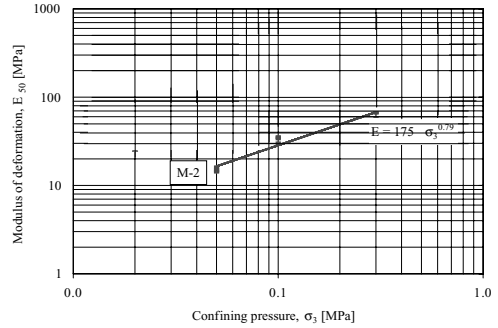


Figure 29. Deformation Modulus, E_{50} for samples M-2.

3.3 Post-construction deformations

A study of the behavior of the Chilean largest earth dams conducted for the Ministry of Public Work permitted the analysis of the variation of the static deformation modulus of rockfill and gravel-fill dams. In this study, long term post-construction settlements monitored on three Chilean earth dams were used to estimate the time variation of the deformation modulus these coarse materials. Basic information of the analyzed dams is indicated in Table 2.

The static dam response was modeled using a perfect elasto-plastic stress-strain relationship, implemented in the computer stress code FLAC. The evaluation of the deformation modulus was performed by a try and error process until the calculated and observed dam settlements matched.

The main body of Cogoti dam was finished in 1938 and the vertical deformations have been monitored since that time. The dam was finally completed in 1940.

This dam was constructed with blasted rock without compaction. In its first 15 meters, rockfill with a maximum size of 1.5 meters were just dumped in the dam site by gravity. In the following raises, rockfill with a maximum size of 1.3 meters was placed by mechanical means and it was slightly compacted by the construction procedure associated to the traffic

Table 2. Monitored Chilean dams.

Dam	Cogoti	Conchi	Santa Juana
Completion year	1940	1975	1995
Foundation type	Rock	Rock	Rock fluvial
Dam type	CFRD	CFRD	CFGD
Height (m)	82.7	66.0	113.4
Crest length (m)	160	200	390
Upstream Slope (H:V)	1.45:1	1.5:1	1.5:1
Downstream Slope (H:V)	1.5:1	1.5:1	1.6:1



Figure 30. General view of Cogoti dam.

of trucks. Consequently this dam is a good example of a coarse material dam on a very loose state of compaction. A general view of Cogoti dam is shown in Fig. 30.

Conchi dam, completed in 1975, was constructed with rockfill of a maximum size of 0.65 m. Great effort to compact the rockfill was applied. The available information indicates that the compacted fill reached a degree of compaction associated with a relative density greater than 90%. Fig. 31 presents a general view of Conchi dam.

Santa Juana dam, completed in 1995, was constructed with rockfill and gravely particles with maximum sizes of 1 and 0.65 m in the upstream and downstream supporting shoulders, respectively. Compaction was also applied to the fill. A general view of Santa Juana dam is shown in Fig. 32.

The settlements along the crest of Cogoti dam for different years are shown in Fig. 33. It is interesting to observe that the maximum settlements do not take place at the location of the maximum height of the dam, but they systematically occur above the point where a change in the slope of the bedrock exists.

The maximum static vertical deformations measured at different time and for the three dams are shown in Fig. 34. It can be observed, that Cogoti dam presents the greatest settlements compared to the others two dams. According to the study, this can be attributed to the uncompacted fill of Cogoti dam.



Figure 31a. General view of Conchi dam.



Figure 31b. General view of Conchi dam.



Figure 32. General view of Santa Juana dam.

In the numerical analysis of these settlements, an elasto-plastic constitutive law with the Mohr-Coulomb failure criterion was selected. This model was considered to be a reasonable approximation of the mechanical behavior of these dams in view of the fact that the analyzed dams have developed a mechanical response that is far from failure. A constant Poisson's ratio equal to 0.3 was assumed for all the cases.

The computed values of the deformation modulus at different time after completion the dams were normalized by the computed deformation modulus at 1 year of dam completion, E_1 . The resulting variation of

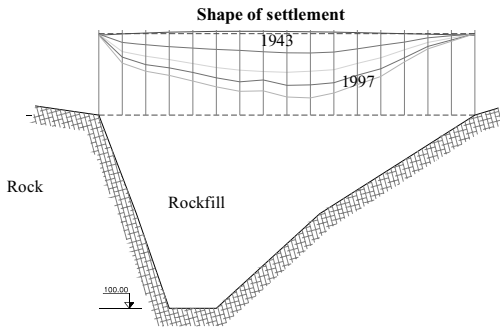


Figure 33. Vertical settlements along the crest of Cogoti Dam.

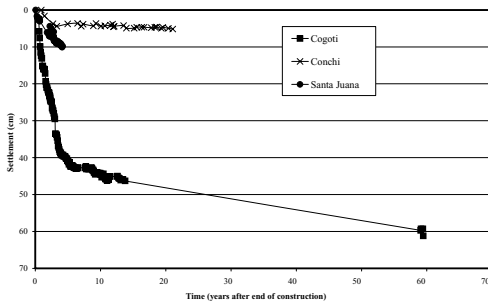


Figure 34. Development of the static maximum vertical deformation.

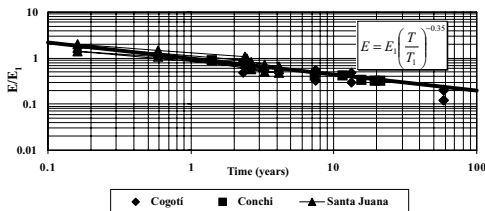


Figure 35. Normalized deformation modulus as a function of time.

the normalized deformation modulus (E/E_1) with the number of years after completion is shown in Fig. 35. These results indicated that the time effect on the static deformation modulus can be expressed as follows:

$$E = E_1 (t/t_1)^{-0.35} \quad (2)$$

Where, t represents time in years after completion and t_1 is 1 year after the end of construction. This deformation modulus is associated to the total accumulated settlements. Therefore, the use of this expression is related to the long term settlement evaluation.

4 SUMMARY

The performance-based seismic design is strongly encouraged by structural engineers that have observed heavy financial losses in recent earthquakes. Structures designed according to current codes performed well in terms of life safety, but financial losses have been surprisingly high. This comes from the fact that the main investments in building construction are made in the non-structure components and contents. Therefore, it is evident that the fundamental issue of building code provisions to guaranty structures integrity, in terms of no collapse against strong ground motion, is definitely insufficient to be considered a successful seismic behavior to the society. In this context the performance-based seismic design would help to reduce the financial losses associated with the non-structure components and contents.

Formally, the use of PBSO is less common in geotechnical engineering. However, the earthquake geotechnical community is quite familiar in predicting permanent displacements of earth structures, which basically mean a criterion of performance as opposed to the classical concept of limit equilibrium.

One important issue of PBSO is associated with the intention of involving stakeholders (owners, insurers and regulators) in the decisions concerning the choose of target performances of an earth structure during and after seismic events, sharing in this way the decision-making process. In spite of the benefits, it is important to take into account that the results of combining both complex technical solutions and investment decision are at least risky.

The second important issue of PBSO is related to the premise that seismic performance levels can be predicted analytically, permitting that the cost associated with each level can be rationally evaluated. From a scientific point of view, there is a reasonable knowledge of soil and rock mechanics behavior that has been incorporated into numerical models. However, in engineering practice the real situation is less promising, especially when three dimensional analysis is needed. Additionally, in the case of dam engineering, practitioners have to face the geotechnical characterization of rockfill materials, but, normally there is a lack of available testing apparatuses for these coarse soils, which means that in the design, geotechnical properties have to be estimated.

In this context, the actual capability of predicting the seismic performance is quite limited. Consequently, it is important to recognize that the real application of the PBSO in professional practice is years away, but it is also important to admit that this design criterion is attractive and efforts have to be done in order to make it closer to practitioners.

In the PBSO of tailings dams, the liquefaction resistance of the tailings sands play an important role, and this resistance is affected by density and

the fines content. Therefore, these effects have to be understood. On the hand, the PBSD of concrete face rockfill dams needs the mechanical properties of the coarse fill used in these dams. However, sufficiently large machines to test these materials are not usually available, so alternative procedures to obtain the required properties are needed. As can be expected, material properties are an important issue in the application of the PBSD and their evaluation and understanding is strongly needed.

In the design of tailings dams there are two important issues that control the liquefaction strength of the tailings; density and fines contents. Accordingly, results of a comprehensive study carried out on different mixtures of sand and fines compacted at different densities have been presented.

The maximum density obtained by the Modified Proctor test is only slightly lower than the maximum density achieved by vibration, even for a 50% of fines. Hence, it is possible to indicate that the concept of relative density holds valid for this tailings sand even with 50% fines or more.

The experimental results show that the cyclic strength decreases as the fines content increases. Mixtures with 2 and 10% of fines content present a sharp increase in cyclic strength from a relative density around 50%, while mixtures with 18 and 28% of fines content present only a gradual increase of cyclic strength with relative density.

A rather unique steady state line in the q - p' plane was obtained for all the mixtures, indicating a constant residual angle of internal friction of 35° , regardless the fines content.

Fines content affect the position of the steady state lines in the e - p' plane. The higher the fines content the lower the position of the steady state line. However, the fines do not affect the slope of the steady state lines.

The amount of non-plastic fines used in this study affect the soil structure making it more contractive, and therefore, more sensitive to liquefaction.

From the seismic analysis, the required cyclic strength can be established and from the presented results, the possible combinations of fines content and relative density that satisfy the required cyclic strength can be obtained. Therefore, during the tailing dam construction it is possible to have a flexible design playing with the requested density according to the fines content produced by the cycloning process.

In the case of large earth dam, these days the most common adopted design corresponds to Concrete Face Rockfill Dam and Concrete Face Gravel-fill Dam. These types of dams have increased in number throughout the world mainly because of the good behavior from all technical standpoints and also due to the lower cost. Coarse materials as rockfill, cobbles and gravel always present difficulties in the evaluation of their properties, commonly due to the

lack of available equipment to test large particles. An alternative procedure to evaluate the mechanical properties is the parallel gradation method. The oversized particles are scalped and a new batch of soil is prepared using the original material, which has a grain size distribution curve parallel (in the common semi log scale) to that of the original sample. The main advantage of this procedure is that the soil gradation is maintained.

Experimental results indicate that the parallel gradation method provides a quite reasonable procedure to evaluate the geomechanical response of coarse granular materials.

Another issue of Concrete Face Rockfill and Gravel-fill dams is associated with the long term deformation which might affect the concrete face. Using a simple elasto-plastic stress-strain relationship, the measurements of three Chilean dams were reproduced and the deformation modulus computed. The relationship that reproduced the calculated values of the deformation modulus can be expressed in the form: $E = E_1 (t/t_1)^b$, where E_1 (deformation modulus associated to the settlement of the dam at 1 year after construction) depends upon the dam material, and the parameter b has shown to be a constant value for rockfill dams; $b = -0.35$.

ACKNOWLEDGMENTS

The author wants to acknowledge the very useful comments done by Dr. Claudia Medina and Dr. Javier Ubilla. Also, thanks are due to Dirección de Obras Hidráulicas of the Chilean Ministry of Public Work and IDIEM (Institute for research and testing of materials) of the Faculty of Engineering, University of Chile.

REFERENCES

- Al-Hussaini, M. 1983: Effect of particle size and strain conditions on the strength of crushed basalt. *Canadian Geotechnical Journal*, 20(4): 706–717.
- Agüero, G. 1929. Formation of Tailings Deposits in El Teniente Mine. *Anales del Inst. de Ingenieros de Chile*. pp. 164–187.
- Astellera, M. and Whittaker, A. 2004. Changing the paradigm for performance based design. *Proc. Intern. Workshop on Performance-Based Seismic Design Concept and Implementation*. Slovenia.
- Casagrande, A. 1975. Liquefaction and Cyclic Deformation of Sands—A Critical Review. *V Panamerican Conference on Soil Mech. & Foundation Eng.* Buenos Aires, Argentina.
- Casagrande, A. and Carrillo, N. 1944. Shear Failure of Anisotropic Materials. *Proc. Boston Soc. of Civil Eng.* Vol. 31, pp. 74–87.
- Castro, G. 1969. Liquefaction of Sands. *Doctoral Thesis*, Harvard University, Cambridge, Mass. USA.

- Castro, G. and Troncoso, J. 1989. Effects of Chilean Earthquake on three tailing dams. *Int. Sem. on Dynamic Behavior of Clays, Sands & Gravel*. Kitakyushu, Japan.
- Conlin, B. 1987. A Review of the Performance of Mine Tailings Impoundments Under Earthquake Loading Conditions. *Proceedings Vancouver Geotechnical Society Seminar on Earthquake*. Geot. Canada.
- Cubrinovski, M. and Ishihara, K. 2002. Maximum and minimum void ratio characteristics of sands. *Soils and Foundations*, Vol. 42, No. 6, pp. 65–78.
- Cho, G., Dodds, J. and Santamarina, J. (2005): "Particle Shape effects on parking density, stiffness and strength: Natural and Crushed sands," *Internal report*. Georgia Institute of Technology.
- Dobry, R. and Alvarez, L. 1967. Seismic Failures of Chilean Tailings Dams. *Journal of Soil Mechanics and Foundation Division*, ASCE, Vol. 93, SM6, pp. 237–260.
- Donaghe, R. and Torrey, V. 1979. Scalping and replacement effects on strength parameters of earth-rock mixtures. *Proc. Conf. on Design Parameters in Geotechnical Engineering*, London, Vol. 2, pp. 29–34.
- Finn, W. 1980. Seismic Response of Tailings Dams. *Proceeding Seminar on Design and Construction of Tailings Dams*. Colorado School of Mines. USA.
- Finn, W. 1996. Seismic Design and Evaluation of Tailings Dams: State of the Art. Int. Symposium on Seismic and Environmental Aspects of Dam Design: Earth, Concrete and Tailing Dams. Chile.
- Fragaszy, R., Su, W. and Siddiqi, F. 1990 Effects of oversize particles on the density of clean granular soils. *Geotechnical Testing Journal*, 13(2): 106–114.
- Fragaszy, R., Su, W., Siddiqi, F. and Ho, C. (1992): "Modeling strength sandy gravel." *Journal of Geotechnical Engineering*, 118(6): 920–935.
- Garga, V. and McKay, L. 1984. Cyclic Triaxial Strength of Mine Tailings. *Journal of Geotechnical Engineering*, ASCE, Vol. 110, No. 8, pp. 1091–1105.
- Hazen, A. 1920. Hydraulic-Fill Dams. *ASCE Transactions*, Vol. 83, pp. 1713–1745.
- Ishihara, K. 1984. Post-Earthquake Failure of a Tailings Dam Due to Liquefaction of the Pond Deposit. *Int. Conference on Case Histories in Geotechnical Engineering*. St. Louis. USA.
- Ishihara, K. 1985. Stability of Natural Deposits During Earthquakes. *XI International Conference on Soil Mechanics and Foundation Engineering*. Vol. 2, pp. 321–376.
- Ishihara, K. 1993. Liquefaction and Flow Failure During Earthquakes. *33rd Rankine Lecture. Geotechnique*, Vol. 43, No. 3, pp. 351–415.
- Ishihara, K., Troncoso, J. and Kawase, Y. 1980. Cyclic Strength Characteristics of Tailings Materials. *Soils and Foundations*, Vol. 20, No. 4, pp. 128–142.
- Lee, K. and Seed, H. 1967. Drained strength characteristics of sands. *Journal of the Soil Mechanics and Foundations Division*, 93(6): 117–141.
- Lowe, J. 1964. Shear Strength of coarse embankment dam material. *Proceedings, 8th Congress on Large Dams*, pp. 745–761.
- Makdisi, F. and Seed, H.B. 1977. A simplified procedure for estimating earthquake-induced deformations in dams and embankments, *EERC Report No. 77/19*.
- Marachi, D., Chan, C. and Seed, H. 1972. Evaluation of properties of rockfill materials. *Journal of the Soil Mechanics and Foundations Division*, 98(1): 95–114.
- Miranda, E. and Taghavi, S. 2003. Response assessment of nonstructural building elements. *PEER Report 2002/03, Pacific Earthquake Engineering Research Center*, University of California, Berkeley, USA.
- Newmark, N.M. 1965. Effects of earthquakes on dams and embankments, *Geotechnique*, Vol. 5, No. 2.
- Ni, Q., Tan, T., Dasari, T. and Hight, D. 2004. Contribution of fines to the compressive strength of mixed soils. *Geotechnique* 54, No. 9.
- Pettibone, H. and Kealy, C. 1971. Engineering Properties of Mine Tailings. *Journal of Soil Mechanics and Foundations Division*, ASCE, Vol. 97, SM9, pp. 1207–1225.
- Polito, C. and Martin, J. 2001. Effects of nonplastic fines on the liquefaction resistance of sands. *Journal of Geotechnical and Geoenvironmental Engineering*. Vol. 127, No. 5.
- Poulos, S. 1981. The Steady State of Deformation. *J. of Geot. Eng. Division*, ASCE, Vol. 107, No. GT5, pp. 553–562.
- Poulos, S., Castro, G. and France, J. 1985. Liquefaction Evaluation Procedure. *J. of Geot. Eng.*, ASCE. Vol. 111, No. 6.
- Poulos, S., Robinsky, E. and Keller, T. 1985. Liquefaction Resistance of Thickened Tailings. *J. of Geotechnical Engineering*, ASCE. Vol. 111, No. 12, pp. 1380–1394.
- Robinsky, E. 2000: Sustainable Development in Disposal of Tailings. *Proceedings Tailings and Mine Waste '00*, Colorado State University. USA.
- Rojas-González, L., Ben-Khalal, H. and Lewis, K. 1985. Dynamic Properties and Behavior of Copper Tailings. *XI Int. Conf. on Soil Mechanics and Foundation Eng.* Vol. 3, pp. 1289–1292.
- Salvas, R. 1989. Beneficial Characteristics of Sloped Tailings Deposits. *International Symposium on Tailings and Effluent Management, Metallurgical Society of the Canadian Institute of Mines and Metallurgy*. Vol. 14. Pergamon Press.
- Santamarina, J. and Cho, G. 2004. Soil Behaviour: The role of particle shape. *Proceedings Skempton Conference*. London. <http://www.ce.gatech.edu/~carlos/laboratory/tool/ParticleShape/ParticleShape.htm>
- Santamarina, J. and Díaz-Rodríguez, J. 2003. Friction in Soils: Micro and Macroscale Observations. *Pan-American Conference*, Boston, 2003.
- Seed, H.B. 1966. A method for earthquake-resistant design of earth dams, *Journal of the Soil Mechanics and Foundations Division*, ASCE, Vol. 92, No. SM1.
- Sherard, J. and Cooke, B. 1987. Concrete-face rockfill dam: I. Assessment. *Journal of Geotechnical Engineering*, Vol. 113, No. 10.
- Siddiqi, F. and Fragaszy, R. 1991. Strength evaluation of coarse grain dam material. *IX Pan-American Conference*, Viña del Mar, Chile, pp. 1293–1302.
- Siddiqi, F., Seed, R., Chan, C., Seed, H. and Pyke, R. 1987. Strength evaluation of coarse-grained soils. *Earthquake Engineering Research Center, University of California*, Berkeley, California. Report N° UCB/EERC-87/22.
- Tatsuoka, F., Muramatsu, M. and Sasaki, T. 1982. Cyclic undrained stress-strain behaviour of dense sands by torsional simple shear test. *Soils and Foundations*, Vol. 22, No. 2, pp. 55–70.
- Troncoso, J. and Verdugo, R. 1985. Silt Content and Dynamic Behavior of Tailings Sands. *XI Int. Conf. on Soil Mechanics and Foundation Engineering*. Vol. 3, pp. 1311–1314.
- Troncoso, J., Ishihara, K. and Verdugo, R. 1988. Aging Effects on Cyclic Shear Strength of Tailings Materials. *IX World Conference on Earthquake Engineering*, Vol. 3, pp. 121–126. Tokyo, Japan.

- Valenzuela, L., and Barrera, S. 1995. Large Tailings Dams: Current Practice in Chile. *X Panamerican Conf. on Soil Mech. and Found. Eng.* Mexico. Vol. 3, pp. 1556–1569.
- Varadajan, A., Sharma, K., Venkatachalam, K. and Gupta, K. 2003. Testing and Modeling two rockfill materials. *Journal of Geotechnical and Geoenvironmental Engineering*, 129(3): 206–218.
- Verdugo, R. 1992. Characterization of Sandy Soil Behavior Under Large Deformations. *Doctoral Thesis*, University of Tokyo.
- Verdugo, R. 1997. Tailings Compaction. *IV Chilean Congress on Geotechnical Engineering*. Vol. 1, pp. 29–41.
- Verdugo, R. and Ishihara, K. 1996. The Steady State of Sandy Soils. *Soils and Foundations*. Vol. 36, No. 2, pp. 81–91.
- Verdugo, R. and Bard, E. 1996. Maximum and Minimum Densities in Cohesionless Soils. *X Panamerican Conference on Soil Mechanics and Foundation Engineering*, Guadalajara, Mexico. Vol. 1, pp. 582–592.
- Verdugo, R., Castillo, P. and Briceño, L. 1995. Initial Soil Structure and Steady State. *I International Conf. on Earthquake Geotechnical Eng.* Japan. Vol. 1, pp. 209–214.
- Verdugo, R., Gesche, R. and De La Hoz, K. 2003. Metodología de evaluación de parámetros de resistencia al corte de suelos granulares gruesos. *12th Pan American Conference on Soil Mechanics & Geotechnical Engineering*, Cambridge, MA, pp. 691–696.
- Verdugo, R. and De La Hoz, K. 2006. Strength and stiffness of coarse granular soils. *Soil Stress-Strain Behavior: Measurement, Modeling and Analysis. Geotechnical Symposium in Rome*, March 16–17, 2006. Springer.
- Verdugo, R. and Viertel, P. 2004. Effect of density and fines content on the cyclic strength of copper tailings. V Congreso Chileno de Geotecnia.

Gravel drains for the remediation of liquefiable sites: The Seed & Booker (1977) approach revisited

G.D. Bouckovalas

National Technical University of Athens, Greece

A.G. Papadimitriou

University of Thessaly, Greece

D. Niarchos

Massachusetts Institute of Technology, USA

ABSTRACT: This paper revisits the seminal work of Seed & Booker (1977) on the design of gravel drains for liquefaction mitigation. It shows that their basic mathematical assumption for the earthquake-induced excess pore pressure generation process overlooks the shake-down effects of fabric evolution during cyclic loading and eventually leads to an underestimation of the gravel drain effectiveness. Hence, a new implementation of the equation for the rate of undrained excess pore pressure generation, with insight to the mechanism of the soil deformation, leads to a more realistic estimation of the effectiveness of gravel drains, that is backed by experimental measurements from shaking table tests and numerical simulations with appropriate constitutive modeling. The paper ends with the proposal of a new set of charts for a more realistic design of gravel drains for liquefaction mitigation.

1 INTRODUCTION

The installation of gravel piles accompanied by vibratory compaction of the surrounding loose sand deposits (Fig. 1) is one of the most widely used methods for liquefaction mitigation worldwide. In such cases, the main function of the gravel piles is twofold: they increase the liquefaction strength of the sand by increasing the insitu density, and also retard the excess pore pressure build-up by triggering radial drainage, from the sandy ground towards the more permeable gravel piles. In principle at least, the presence of the relatively stiffer gravel piles may also lead to redistribution of the shear stresses and strains induced by seismic shaking, so that the stresses and strains applied to the improved ground are reduced and the margins of safety against liquefaction are thus enhanced (Priebe, 1989 & 1991, Baez & Martin, 1993, Adalier et al., 2003). Nevertheless, for the gravel pile configurations which are usually employed in practice (i.e. with area replacement ratios $a_s = 10$ to 25%), the reduction in ground stresses and strains is marginal and may even be overshadowed by the possible amplification of the seismic shaking within the improved ground (Adalier et al., 2003, Bouckovalas et al., 2006, Papadimitriou et al., 2006).

When this method is applied within an urban environment, or in order to improve existing foundations, vibration is partially or totally avoided during pile installation, so that ground improvement relies solely upon the drainage function of the gravel piles (Saito et al., 1987, Mitchell & Wentz, 1991, Mitchell et al., 1995, TC4, 2001, Adalier & Elgamal, 2004, Towhata, 2007, Yasuda, 2007). Thus, it has been recently proposed that prefabricated plastic or metal pipe drains replace the traditional gravel piles in such applications, as they cause limited environmental impact, while they require simpler mechanical equipment and less working space (Rollins, 2004, Rollins et al., 2004, Harada et al., 2006, Kamai et al., 2007, Marinucci et al., 2008). Furthermore, they are much more permeable than gravel piles, and better protected against clogging due to sand and silt infiltration, so that they diffuse concerns expressed in the past (e.g. Onoue, 1988, Boulanger et al., 1998) about the actual capacity of gravel piles to trigger drainage in the field.

Seed & Booker (1977) were pioneers in proposing an analytical method for the evaluation of radial drainage effects on earthquake induced excess pore pressures, for the case of uniform ground and for drain wells of infinitely large permeability. Their method can be handily applied via design charts which

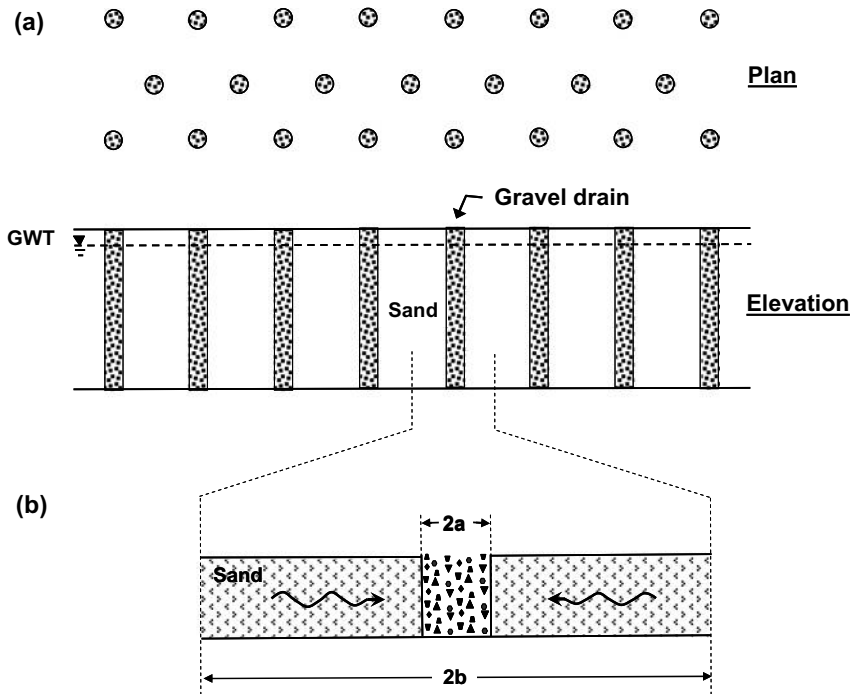


Figure 1. (a) Arrangement of gravel drain system, (b) Gravel drain with radial drainage only (Seed and Booker, 1977).

account consistently for soil properties and seismic motion characteristics. As such, it has been established in practice today, having been adopted by a number of contemporary design handbooks and guidelines worldwide (e.g. JGS, 1998, USACE, 1999, INA, 2001).

Although, for many years, the relevant research was not given priority over the investigation of methods for liquefaction-induced hazard assessment, a number of valuable studies have succeeded to lift some of the simplifying assumptions introduced by Seed & Booker (1977) and improve the accuracy of analytical predictions. Of these newer method variants, one that has attracted considerable attention is the work of Onoue (1988), who used the drain permeability k_d as a design parameter that created the so-called dimensionless drain resistance L , which reduces the dissipating capability of drains if the k_d value is not significantly larger than that of the natural soil k_s . Furthermore, Onoue (1988) studied the problem of combined horizontal (towards the drains) and vertical upward dissipation of excess pore pressures through the sand layer to the ground surface that may occur if the layer in question is not covered by a low-permeability layer (e.g. a clay cap). In parallel, Matsubara et al. (1988) and Iai & Koizumi (1986) proposed similar method variants, with relatively small differences on the dissipating capacity

of the drains, as a function of the drain resistance L factor. More recently, Madhav & Adapa (2007) studied the effects of radially variable ground densification, as well as of the possible dilation of the gravel pile material.

Apart from the applied refinements, the basic differential equations which are used in all previous methods to describe the build up and dissipation of excess pore pressures in the liquefiable sand are essentially common. In this paper, we show that one of these common assumptions, namely that concerning the rate of excess pore pressure build up in the natural ground, may have been misinterpreted in the mathematical formulation of the problem, leading to overrated predictions of excess pore pressures. Consequently, new design charts are produced for the same conditions examined in the pioneering work of Seed & Booker (1977) and examples are given for the potential benefit from their use in practice.

2 BASIC EQUATIONS

To aid the reader focus upon the proposed changes, we quote hereafter (in italics) the derivation of the basic governing equations from the original paper by Seed & Booker (1977). It should be noted in advance, that the same equations are also adopted by this study, with

the exception of Eq. 8 for the rate of pore pressure build up in the soil due to seismic shaking which is re-examined in the next section.

"In developing the basic equations governing the generation and dissipation of pore water pressure throughout a granular material, it will be assumed that the flow of the pore water is governed by Darcy's Law, so that the usual considerations of continuity of flow lead to the equation:

$$\frac{\partial}{\partial x} \left(\frac{k_h}{\gamma_w} \frac{\partial u}{\partial x} \right) + \frac{\partial}{\partial y} \left(\frac{k_h}{\gamma_w} \frac{\partial u}{\partial y} \right) + \frac{\partial}{\partial z} \left(\frac{k_v}{\gamma_w} \frac{\partial u}{\partial z} \right) = \frac{\partial \varepsilon}{\partial t} \quad (1)$$

in which u is the excess hydrostatic pore pressure; k_v , k_h are coefficients of permeability in the vertical and the horizontal directions; γ_w is the unit weight of water; and ε is the volumetric strain, with volumetric reduction being considered positive.

During an interval of time, dt , the pore water pressure in an element of soil will undergo a change, du , while the element will also be subjected to dN cycles of alternating shear stress which will cause an additional increase in pore pressure $(\partial u_g / \partial N) dN$, in which u_g is the pore pressure generated by the alternating shear stresses for the appropriate conditions of prior strain history. It therefore follows, considering that the change in bulk stress is negligible, that the volume change $d\varepsilon$ of the element in time dt is given by:

$$d\varepsilon = m_{v,3} \left(du - \frac{\partial u_g}{\partial N} dN \right) \quad (2a)$$

in which $m_{v,3}$ is the coefficient of volume compressibility, i.e.

$$\frac{\partial \varepsilon}{\partial t} = m_{v,3} \left(\frac{\partial u}{\partial t} - \frac{\partial u_g}{\partial N} \frac{\partial N}{\partial t} \right) \quad (2b)$$

Combining Eqs. 1 and 2b it is found that:

$$\begin{aligned} \frac{\partial}{\partial x} \left(\frac{k_h}{\gamma_w} \frac{\partial u}{\partial x} \right) + \frac{\partial}{\partial y} \left(\frac{k_h}{\gamma_w} \frac{\partial u}{\partial y} \right) + \frac{\partial}{\partial z} \left(\frac{k_v}{\gamma_w} \frac{\partial u}{\partial z} \right) \\ = \left(\frac{\partial u}{\partial t} - \frac{\partial u_g}{\partial N} \frac{\partial N}{\partial t} \right) m_{v,3} \end{aligned} \quad (3)$$

If the coefficients of permeability and $m_{v,3}$ are constant and the problem exhibits radial symmetry, Eq. 3 becomes

$$\begin{aligned} \frac{k_h}{\gamma_w m_{v,3}} \left(\frac{\partial^2 u}{\partial r^2} + \frac{1}{r} \frac{\partial u}{\partial r} \right) + \frac{k_v}{\gamma_w m_{v,3}} \frac{\partial^2 u}{\partial z^2} \\ = \frac{\partial u}{\partial t} - \frac{\partial u_g}{\partial N} \frac{\partial N}{\partial t} \end{aligned} \quad (4)$$

and for purely vertical drainage reduces to the form developed by Seed, Martin and Lysmer (1975)

$$\frac{k_v}{\gamma_w m_{v,3}} \frac{\partial^2 u}{\partial z^2} = \frac{\partial u}{\partial t} - \frac{\partial u_g}{\partial N} \frac{\partial N}{\partial t} \quad (5)$$

Under conditions of purely radial drainage, as considered in the following section, Eq. 4 reduces to

$$\frac{k_h}{\gamma_w m_{v,3}} \left(\frac{\partial^2 u}{\partial r^2} + \frac{1}{r} \frac{\partial u}{\partial r} \right) = \frac{\partial u}{\partial t} - \frac{\partial u_g}{\partial N} \frac{\partial N}{\partial t} \quad (6)$$

In order to evaluate the extent of pore pressure generation and dissipation using this equation, it is necessary to determine $\partial u_g / \partial N$ and $\partial N / \partial t$ as well as the soil properties k_h and $m_{v,3}$. The effective horizontal permeability coefficient can best be determined by means of a pumping testing in the field, and the value of $m_{v,3}$ by means of a cyclic loading triaxial compression test as described by Lee and Albaisa (1974). In fact, $m_{v,3}$ is not constant but varies with the pore pressure ratio r_u . However, it is essentially constant for values of r_u up to about 0.5, and since the object of the drains is to keep the value of r_u to a reasonably low value, the assumption of the constant value is justified in this case.

The values of $\partial u_g / \partial N$ can be found from undrained tests as described by Seed, Martin and Lysmer (1975). For many soils the relationship between u_g and N can be expressed for practical purposes in terms of the number of cycles N_1 required to cause initial liquefaction under the given stress conditions in the following form (Seed et al., 1975):

$$\frac{u_g}{\sigma'_o} = \frac{2}{\pi} \sin^{-1} \left(\frac{N}{N_1} \right)^{1/2A} \quad (7)$$

for which σ'_o is the initial mean bulk effective stress for triaxial test conditions or the initial vertical effective stress for simple shear conditions; and A is an empirical constant that has a typical value of 0.70 (see Fig. 2). Thus

$$\frac{\partial u_g}{\partial N} = \frac{\sigma'_o}{A\pi N_1} \frac{1}{\sin^{2A-1} \left(\frac{\pi}{2} r_u \right) \cos \left(\frac{\pi}{2} r_u \right)} \quad (8)$$

in which $r_u = u / \sigma'_o$ is the pore pressure ratio.

For practical purposes, the irregular cyclic loading induced by an earthquake may be converted to an

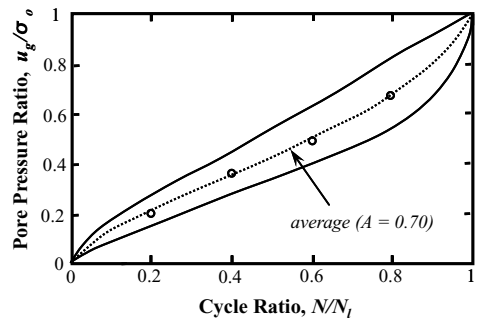


Figure 2. Excess pore-water pressure build up in cyclic undrained simple shear tests (DeAlba et al., 1975).

equivalent number, N_{eq} , of uniform stress cycles at a stress ratio τ_h/σ'_o , occurring in some duration of time t_d of earthquake shaking (Seed et al., 1975). Thus

$$\frac{\partial N}{\partial t} = \frac{N_{eq}}{t_d} \quad (9)$$

In using these results it must be noted that the rate of pore pressure generation, $\partial u_g/\partial N$, depends on the previous cyclic history of the soil and this may be represented approximately by the accumulated pore pressure u . Thus, for any given point at time, t_i , the appropriate rate of pore pressure generation $(\partial u_g/\partial N)_{t_i}$, must be determined by Eq. 8 corresponding to a value of u existing in the soil at that time. By this means the past history of strain cycles may be taken into account with a reasonable degree of accuracy. Note, however, that the soil will increase slightly in density due to any pore pressure dissipation that has already occurred and this will influence the pore pressure generation function. It is considered that this effect is of minor importance in the overall development of pore pressures and for practical purposes can be neglected."

3 REVISED RATE OF EXCESS PORE PRESSURE GENERATION

To gain insight to the factors affecting the rate of excess pore pressure build up, one needs to re-examine the derivation of Eq. 8. Namely, differentiation of Eq. 7 with respect to N , leads to the following expression of the excess pore pressure generation rate in terms of the normalized number of cycles, N/N_i :

$$\frac{\partial u_g}{\partial N} = \frac{\sigma'_o}{A\pi N_i} F_1 F_2 \quad (10a)$$

where

$$F_1 = \frac{1}{(N/N_i)^{1-1/2A}} \quad (10b)$$

and

$$F_2 = \frac{1}{\sqrt{1 - (N/N_i)^{1/A}}} \quad (10c)$$

Eq. 10a is plotted in Figure 3a, while Eqs. 10b and 10c are plotted in Figure 3b. It can now be observed that the rate of excess pore pressure build up is not a monotonic function of N/N_i . On the contrary, it decreases rapidly at the initial stages of cyclic loading (e.g. for $N/N_i < 0.3$), then it remains more or less constant (e.g. for $N/N_i = 0.3$ to 0.6), and finally it increases rapidly (e.g. for $N/N_i > 0.6$) to lead the sand to initial liquefaction. The response at the initial stages of loading is almost exclusively controlled by F_1 , while that at the final stages by F_2 .

From a physical point of view, at the initial stages of loading the sand exhibits the typical "shake-down"

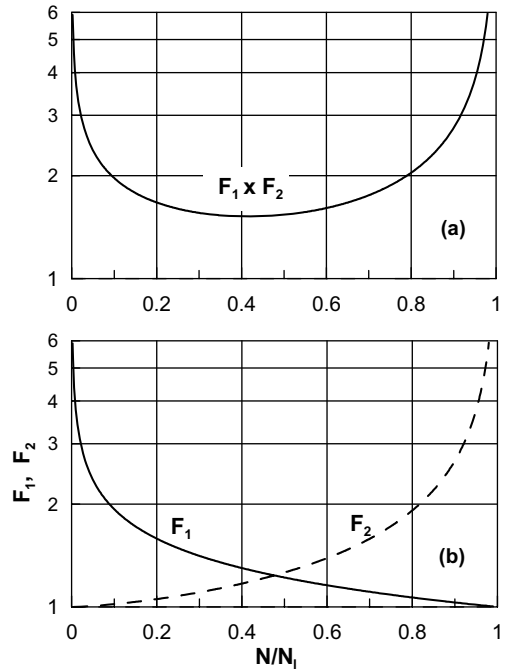


Figure 3. (a) Rate of excess pore-water pressure build up in cyclic simple shear tests (b) Decoupling of competing effects of fabric (F_1) and cyclic shear strain (F_2) evolution.

response generally observed during cyclic loading, where each subsequent loading cycle induces less plastic volumetric strain under drained cyclic loading or less excess pore pressure increase under undrained cyclic loading of constant strain amplitude (e.g. Fig. 4). The mechanism behind this response is the gradual evolution of the sand fabric towards a more stable state, a process which continues with time t or with number of cycles N , as long as cyclic stresses do not cross the phase transformation line, i.e. the limiting state between shear-induced contraction and dilation (e.g. Ishihara et al., 1975, Ladd et al., 1977, Nemat-Nasser & Tobita, 1982, Papadimitriou & Bouckovalas, 2002).

To this extent, it is realized that function F_1 should remain a function of N/N_i , rather than change to a function of excess pore pressure ratio r_u as suggested by Eq. 8. Taking further into account that $N = t/T$, with T being the (predominant) period of shaking, Eq. 10b becomes:

$$F_1 = \frac{1}{(t/TN_i)^{1-1/2A}} \quad (11a)$$

The above response is reversed at the final stages of loading, where the rate of excess pore pressure build up becomes higher with each subsequent loading cycle. This is because the basic relationship used to obtain

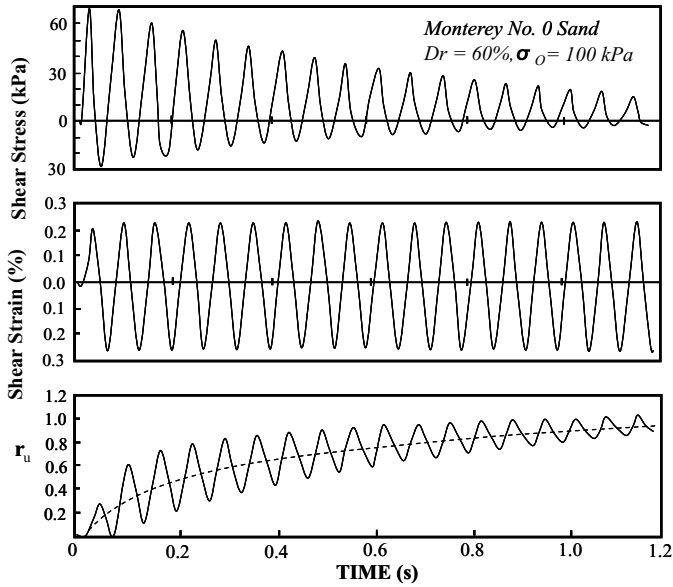


Figure 4. Typical results from triaxial liquefaction tests with constant cyclic strain amplitude (Ostadan et al., 1996).

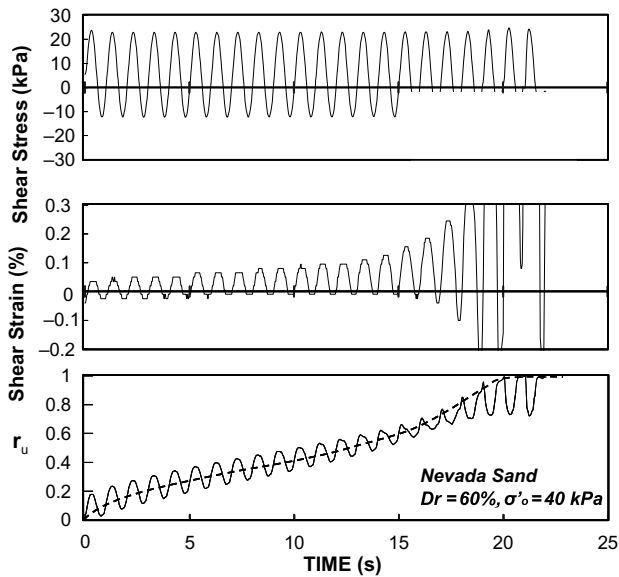


Figure 5. Typical results from triaxial liquefaction tests with constant cyclic stress amplitude (The Earth Technology Corp., 1992).

excess pore pressures in terms of the number of cycles N (see Fig. 2 and Eq. 7) comes from cyclic liquefaction tests under constant shear stress amplitude (e.g. Fig. 5). In such tests, the continuous decrease in effective confining stresses leads to a gradual increase in the cyclic

shear strain amplitude, which has long been acknowledged as the direct mechanism behind the plastic strain and excess pore pressure accumulation during cyclic loading. For instance, observe that in the liquefaction test of Fig. 4, where the cyclic shear strain amplitude

remains constant, the rate of excess pore pressure build up does not increase at later stages of cyclic loading but continues to decrease throughout the test.

In view of the above mechanism, it appears reasonable to adopt the choice of the initial formulation with regard to function F_2 , which prevails at these late stages of cyclic loading, i.e. relate it to the ever current value of the excess pore pressure ratio r_u . Thus, Eq. 10c remains as in Seed & Booker (1977):

$$F_2 = \frac{1}{\cos\left(\frac{\pi}{2}r_u\right)} \quad (11b)$$

Combination of Eqs. 11a and 11b with Eq. 10a provides the final expression for the rate of excess pore pressure build up in the sand, which replaces Eq. 8 in the proposed solution:

$$\frac{\partial u_g}{\partial N} = \frac{\sigma'_o}{\pi AN_I} \frac{1}{(t/TN_I)^{1-1/2A} \cos\left(\frac{\pi}{2}r_u\right)} \quad (12)$$

To appreciate the practical implications of this change, one could consider the right hand side of differential Eq. 6 which describes the pore water flow towards the gravel drain. At the beginning of shaking, excess pore pressures in the sand are low, so that the rate of excess pore pressure dissipation, $\partial u/\partial t$, is less than the initially high rate of excess pore pressure build up due to cyclic shearing, $\partial u_g/\partial t$.

As a result, excess pore pressures in the sand eventually increase, leading to a gradual increase of the dissipation rate $\partial u/\partial t$. This process continues until the rates of excess pore pressure build up and dissipation eventually become equal. In the case of Eq. 8, which suggests that the rate of excess pore pressure build up depends exclusively upon the ever current excess pore pressure ratio r_u , no further change in the excess pore pressure should be observed from that point on (Seed & Booker, 1977). On the contrary, according to Eq. 12, excess pore pressures in the sand should gradually decrease thereafter, for one main reason: the rate of excess pore pressure build up will decrease as time passes, forcing a new equilibrium between the rates of pore pressure build up and dissipation, at lower r_u values.

Experimental and theoretical evidence in support of the above conceptual finding is presented in Figures 6 and 7. Namely, Fig. 6 shows time histories of excess pore pressure ratios recorded during a shaking table test simulating the seismic response of a pile supported model footing on liquefiable ground treated with prefabricated vertical drains (Harada et al., 2006). All recordings refer to the mid-depth of the 400 mm thick treated zone (Silica sand, $D_r = 40\%$), and depict the response of the natural ground (free field) as well as the treated ground below the footing (internal and external side of corner pile). The prefabricated drains had

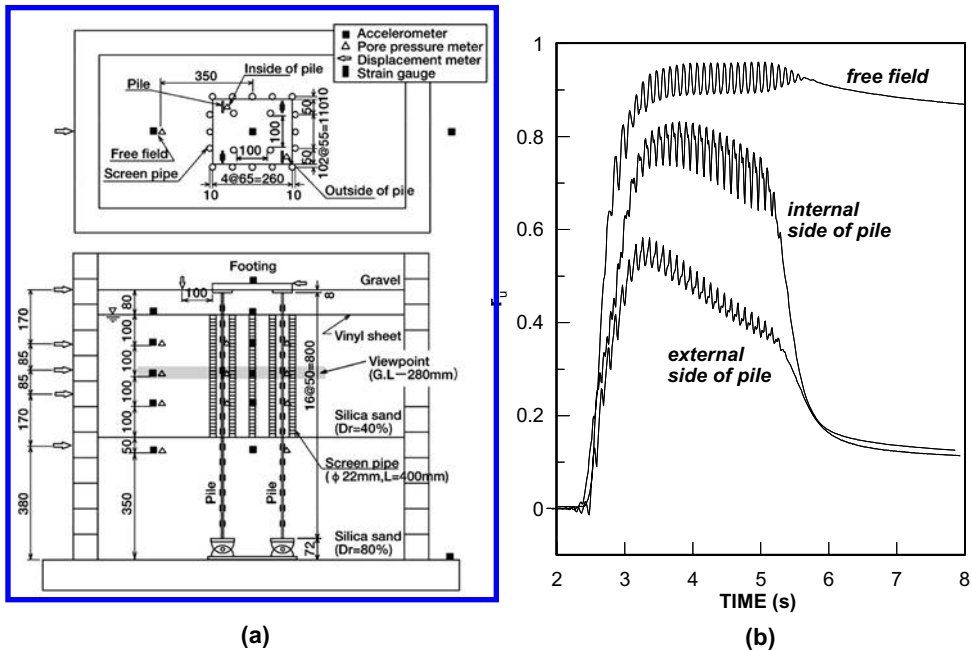


Figure 6. Effect of drains on excess pore pressure buildup (from Harada et al., 2006): (a) Plan view and cross section of test arrangement and instrumentation. (b) Time histories of excess pore pressure ratio r_u in the free field, as well as within the improved ground.

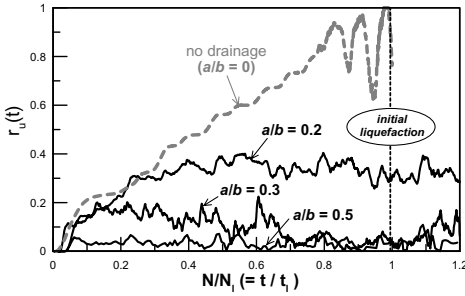


Figure 7. Excess pore pressure buildup for various spacing ratios a/b of gravel drains from 2D fully coupled non-linear numerical analyses (Papadimitriou et al., 2007).

a 22 mm diameter and were placed 60 mm apart (corresponding to a spacing ratio $a/b \cong 0.20$) inside the footing area and 100 mm apart ($a/b \cong 0.30$) along the footing perimeter. Shaking consisted of a main body of twenty two sinusoidal acceleration cycles with 10 Hz frequency and uniform (200 gal) amplitude. Observe that, in the free field, the average excess pore pressure ratio r_u rises fast to little below unity, and remains constant for the rest of shaking, indicating that any effects of radial or vertical drainage are minimal in this area. On the contrary, under the footing, average pore pressure ratios r_u remain well below unity, as a result drain induced radial drainage. Most importantly, the peak r_u values occur at the early stages of loading and are followed by a steady pore pressure decrease at the later stages, just as foreseen by the revised formulation proposed herein.

Fig. 7 shows similar evidence from 2-D fully coupled non-linear dynamic analyses, where gravel drains were simulated as equivalent gravel walls having a thickness smaller than their diameter (Papadimitriou et al., 2007). In order to establish that the flow is purely horizontal towards the drains, the liquefiable sand layer (of 1 m thickness) was set between clayey layers having a 1000 times lower permeability. Similar to the experimental study, the seismic excitation was sinusoidal, with constant acceleration amplitude and period. It is observed again that, as the drain configuration becomes denser (especially for $a/b \leq 0.30$) the numerically predicted excess pore pressure time histories attain a peak at the early stages of cyclic loading, and subsequently decrease smoothly, despite that shaking continues with undiminished intensity.

4 EXCESS PORE PRESSURE PREDICTION

In the sequel, Eq. 6 is combined with Eqs. 9 and 12 and is re-written in non-dimensional form as:

$$T_{ad} \left(\frac{\partial^2 r_u}{\partial R^2} + \frac{1}{R} \frac{\partial r_u}{\partial R} \right) = \frac{\partial r_u}{\partial t^*} - B \quad (13a)$$

where

$$B = \frac{1}{\pi A} \left(\frac{N_{eq}}{N} \right)^{1/2A} \frac{1}{(t^*)^{1-1/2A} \cos\left(\frac{\pi}{2} r_u\right)} \quad (13b)$$

$R = r/a (\geq 1)$, $t^* = t/t_d (\geq 0)$ and T_{ad} is the normalized time factor given by:

$$T_{ad} = \frac{k_h t_d}{\gamma_w m_{v,3} a^2} \quad (14)$$

Solution of the above equation is achieved numerically, via the Finite Difference method, for the following initial and boundary conditions:

$$r_u(R, t^* = 0) = 0 \quad (15a)$$

$$r_u(R = 1, t^*) = 0 \quad (15b)$$

$$\frac{\partial r_u}{\partial R}(R = b/a, t^*) = 0 \quad (15c)$$

Before proceeding to the solution of Eq. 13, the finite difference solution setup has been verified against the original results of Seed & Booker (1977). Hence, Fig. 8 presents a comparison of simulations for various values of the spacing ratio a/b and $N_{eq}/N_i = 2$ to their counterparts as they appeared in the original publication. This comparison verifies the accuracy of the finite difference solution setup, and also enables comparisons between the original and the revised method predictions. Exemplary comparisons between the results of the two methods are presented in Figs. 9 to 12.

Specifically, Fig. 9 shows typical time histories of the excess pore pressure ratio r_u for an exemplary spacing ratio $a/b = 0.10$ and various shaking intensities ($N_{eq}/N_i = 1$ to 4) and drainage capacities ($T_{ad} = 5$ to 50). More specifically, the original predictions are denoted by the solid lines, the revised by the solid lines enhanced with symbols and the shaded regions denote the differences between the two methods for each exemplary case. Observe that the difference between

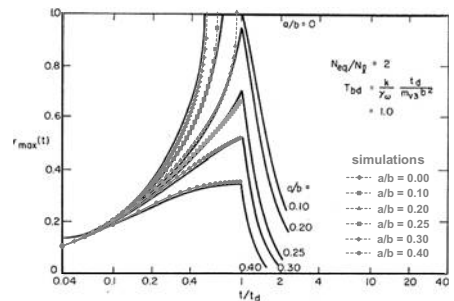


Figure 8. Verification of numerical solution algorithm: reproduction of the Seed & Booker (1977) time histories of the excess pore pressure ratio r_u for various spacing ratios a/b and $N_{eq}/N_i = 2$ (continuous lines).

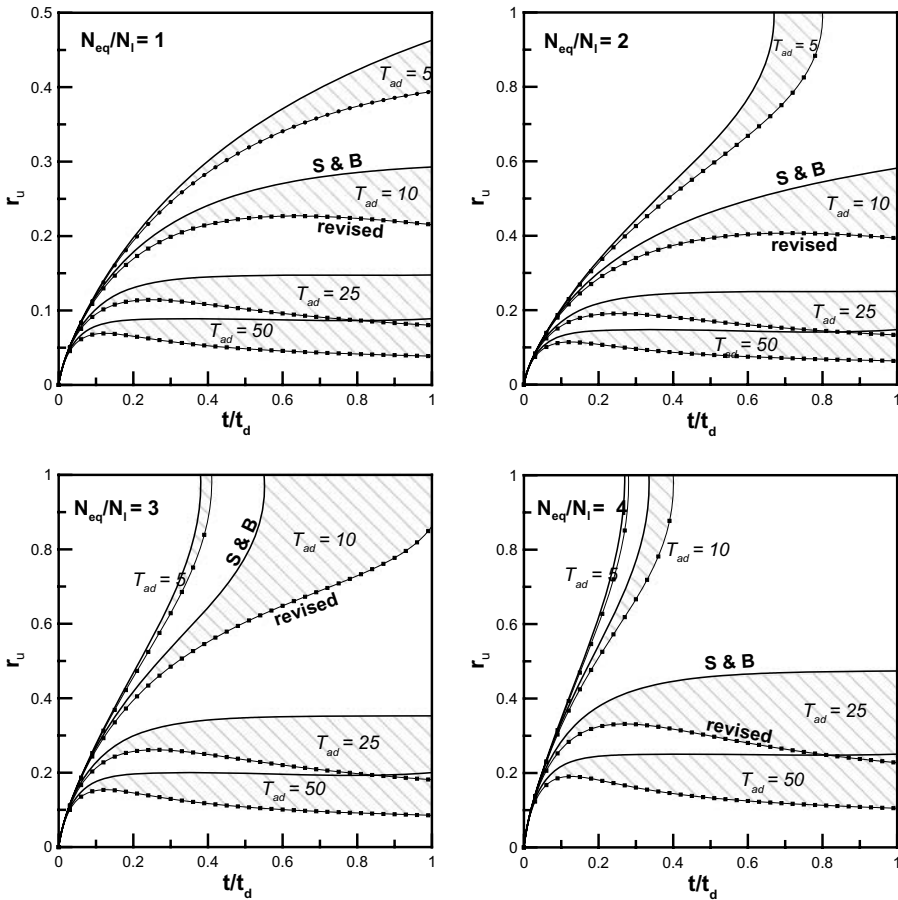


Figure 9. Effect of shaking intensity (N_{eq}/N_l) and drainage potential (T_{ad}) on the time history of excess pore pressure ratio (r_u) for drains at spacing ratio $a/b = 0.1$, as predicted by the revised and the original Seed & Booker (1977) methods.

the two methods increases as the intensity of shaking N_{eq}/N_l and the drainage capacity T_{ad} increase, with the revised predictions of r_u being systematically lower than the original ones. Furthermore, observe that for the case of successful liquefaction mitigation (i.e. when $r_{u,max} < 1.0$), the revised predictions of r_u attain a peak value at the early stages of shaking and then decrease smoothly. On the contrary, the original predictions always increase asymptotically towards their peak value. In qualitative terms, the response of the revised predictions is consistent with the experimental and numerical results shown earlier in Figs. 6 and 7. As such, the proposed change of Eq. 8 with Eq. 12 seems to offer more realistic results for the effectiveness of the gravel drains.

The original as well as the revised charts for the computation of the peak excess pore pressure ratio $r_{u,max}$ in terms of the gravel pile spacing ratio ($a/b = 0$ to 0.5), the drainage capacity ($T_{ad} = 2$ to 200) and the

intensity of shaking ($N_{eq}/N_l = 1$ to 4) are shown in Fig. 10. To aid in the comparison between the two sets of design charts, Fig. 11 presents the ratio of the revised over the original $r_{u,max}$ values [denoted as $(r_{u,max})_{rev.}/(r_{u,max})_{S\&B}$] as a function of the spacing ratio ($a/b = 0$ to 0.5), the drainage capacity ($T_{ad} = 2$ to 200) and the intensity of shaking ($N_{eq}/N_l = 1$ to 4).

Observe that this ratio is smaller or equal than 1.0 (following the qualitative observations from Fig. 9) and that the minimum value of the ratio seems to be mostly a function of the intensity of shaking (decreases with N_{eq}/N_l) and not so much of the spacing ratio (a/b) and the drainage capacity T_{ad} .

In addition, to explore the potential benefit from the proposed revisions, Fig. 12 shows the ratio of revised over original $r_{u,max}$ values obtained from Fig. 11, in terms of the original predictions of $r_{u,max}$ (Fig. 12a) as well as of the revised predictions (Fig. 12b). Apart from verifying in a more systematic manner that the

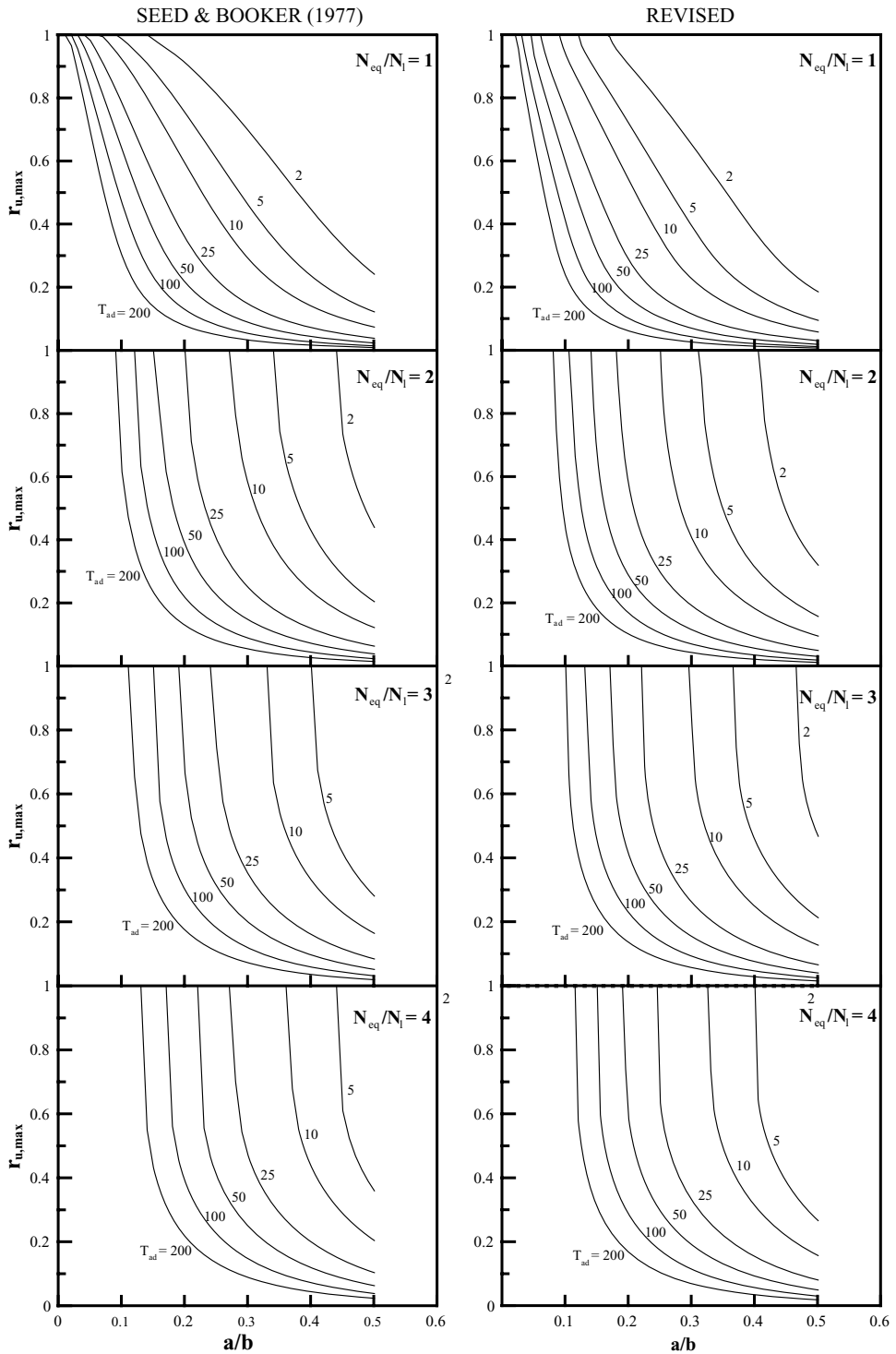


Figure 10. Peak excess pore pressure ratios ($r_{u,max}$) versus gravel pile spacing (a/b) and drainage potential (T_{ad}), for various intensities of seismic shaking (N_{eq}/N_l), based on the revised and the original methodology of Seed & Booker (1977).

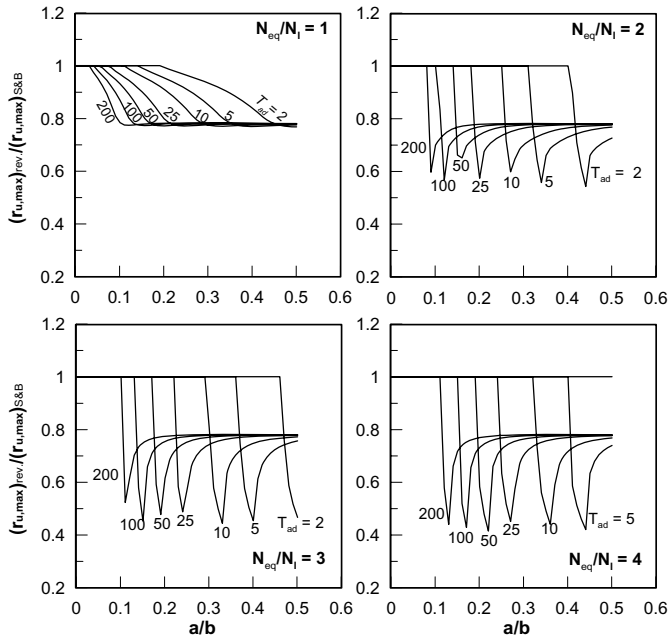


Figure 11. Ratio of revised over original (Seed & Booker, 1977) peak excess pore pressure ratios $r_{u,max}$ versus gravel pile spacing (a/b) and drainage potential (T_{ad}), for various intensities of seismic shaking (N_{eq}/N_l).

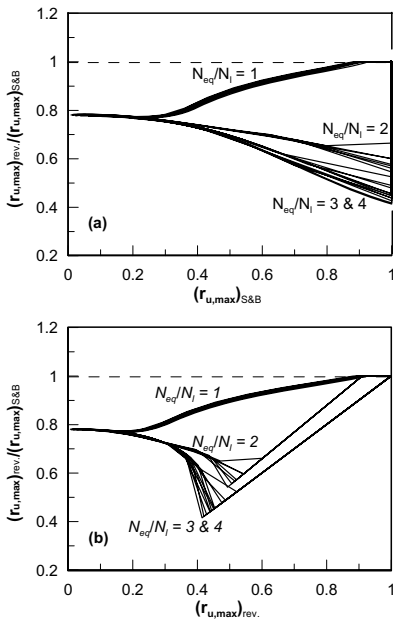


Figure 12. Ratio of revised over original predictions of peak excess pore pressure ratios ($r_{u,max}$) for $a/b = 0$ to 0.5 , $T_{ad} = 2$ to 200 , $N_{eq}/N_l = 1$ to 4 , versus: (a) the original $(r_{u,max})_{S\&B}$ predictions, (b) the revised $(r_{u,max})_{rev}$ predictions.

revised formulation leads to smaller values of $r_{u,max}$, this figure also depicts more clearly the factors that affect the $(r_{u,max})_{rev.}/(r_{u,max})_{S\&B}$ ratio, i.e.

- The ratio in question is mainly a function of the intensity of shaking (N_{eq}/N_l) and the anticipated value of maximum excess pore pressure ratio ($r_{u,max}$). The spacing ratio (a/b) and the drainage potential (T_{ad}) do not have a direct effect, but only an indirect one through the value of $r_{u,max}$.
- For moderate shaking with $N_{eq}/N_l = 1$ (and associated factor of safety against liquefaction $FS_l = 1.0$), the $(r_{u,max})_{rev.}/(r_{u,max})_{S\&B}$ ratio decreases gradually with the anticipated $r_{u,max}$ value, from 1.0 for $r_{u,max} = 0.9$ – 1.0 down to 0.78 (22% decrease) for $r_{u,max} < 0.2$ to 0.3 .
- For more intense shaking with $N_{eq}/N_l = 2$ to 4 (and associated factor of safety against liquefaction $FS_l < 1.0$), the $(r_{u,max})_{rev.}/(r_{u,max})_{S\&B}$ ratio dips more abruptly at high to medium values of the anticipated $r_{u,max}$, before it gradually increases again towards the limiting value of 0.78 for $r_{u,max} < 0.2$ to 0.3 . The minimum values attained for intermediate $r_{u,max}$ levels is about 0.6 (40% decrease) for $N_{eq}/N_l = 2$ and 0.45 (55% decrease) for $N_{eq}/N_l \geq 3$.

The implications of the proposed revisions on the design of gravel pile systems in practice are explored in [Fig. 13](#), in terms of the area replacement ratio a_s which

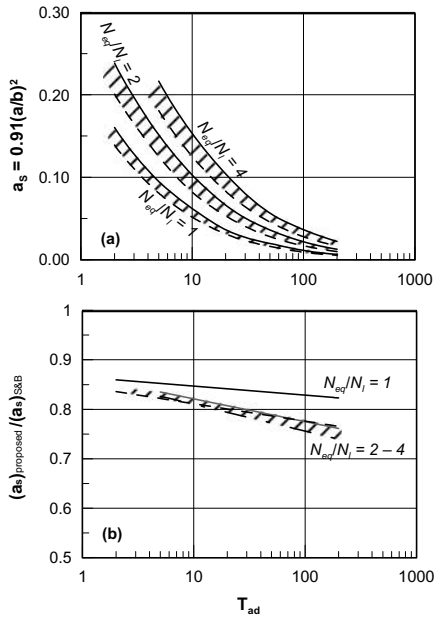


Figure 13. (a) Area replacement ratio a_s required for $r_{u,max} = 0.4$, versus drainage potential (T_{ad}) and seismic shaking intensity (N_{eq}/N_l), as predicted by the revised (dashed lines) and the original (solid) methods, (b) Comparison of the respective area replacement ratios $[(a_s)_{rev.} \text{ and } (a_s)_{S\&B}]$.

is required to improve a liquefiable site. Computations have been performed with the revised as well as with the original method of Seed & Booker (1977), assuming that the gravel pile arrangement will be triangular (e.g. as in Fig. 1a) with $a_s \cong 0.91(a/b)^2$ and that the design peak excess pore pressure ratio during shaking is $r_{u,max} = 0.40$.

The variation of computed a_s values with T_{ad} and N_{eq}/N_l is shown in Fig. 13a, with the solid and dashed lines depicting the values of a_s stemming from the original and the revised design methods, respectively.

To make the comparison even clearer, Fig. 13b shows the respective variation for the ratio of revised over original a_s predictions [denoted as $(a_s)_{rev.}/(a_s)_{S\&B}$], as a function of T_{ad} for the various N_{eq}/N_l values. As expected, both the revised and the Seed & Booker (1977) predictions for a_s are strongly affected by T_{ad} and N_{eq}/N_l , with the revised values of a_s being systematically lower than those from the original method.

Nevertheless, their relative difference is much less dependent on the above factors, especially T_{ad} , with the a_s ratio being approximately equal to 0.85 (15% decrease) for moderate shaking with $N_{eq}/N_l = 1$, and 0.75 to 0.85 (i.e. 15% to 25% decrease) for stronger shaking with $N_{eq}/N_l > 2$. In view of the comparisons

shown previously in Figs 11 and 12, it is reasonable to expect a larger decrease in revised a_s values for tolerable excess pore pressure ratios higher than the $r_{u,max} = 0.40$ limit.

5 REVISED DESIGN CHARTS

Application of the revised methodology in practice may rely on the charts of Fig. 9 which resemble the ones which are currently in use. Nevertheless, one additional advantage from the proposed revisions is that the number of necessary charts may now be reduced to cases of seismic intensity with $N_{eq}/N_l \leq 2$.

To substantiate this simplification, Fig. 14 shows the effect of N_{eq}/N_l on the peak excess pore pressure ratio ($r_{u,max}$) and the time that this peak occurs relative to the duration of shaking required to cause liquefaction in the unimproved ground t_l , denoted by the ratio $(t/t_l)_{max}$ in Fig. 14. In addition, Fig. 15 shows the effect of N_{eq}/N_l on the whole excess pore pressure time history $r_u - t/t_l$, the results of which were used to construct the preceding Fig. 14. In order to be able to focus upon the effect of seismic shaking intensity alone, independently from the gravel drain diameter and the soil characteristics, the time factor T_{ad} was decoupled from N_{eq}/N_l , by introducing t_l as the reference time in place of the duration of shaking t_d :

$$T_{ad} = T_{al} \left(\frac{N_{eq}}{N_l} \right) \quad (16)$$

where

$$T_{al} = \frac{k_h t_l}{\gamma_w m_{v,3} a^2} \quad (17)$$

is a seismic shaking intensity-independent problem variable.

The results shown in Figs 14 and 15 were obtained for constant $T_{al} \cong 5.7$, six different gravel drain configurations with $a/b = 0.10, 0.15, 0.20, 0.25, 0.30$ and 0.50 , and four different seismic shaking intensities with $N_{eq}/N_l = 1, 2, 3$ and 4 . Observe in Fig. 14a that, for sparse configurations with $a/b \leq 0.25$, $r_{u,max}$ gradually increases with N_{eq}/N_l but remains constant after $N_{eq}/N_l \cong 3.0$. For denser gravel drain configurations ($a/b \geq 0.30$), $r_{u,max}$ remains practically constant for all N_{eq}/N_l values.

This seemingly unexpected response with regard to the effect of seismic shaking intensity is explained with the aid of Fig. 15. Observe here that, for the same ground conditions and gravel drain system, the r_u time histories obtained for the different N_{eq}/N_l values are part of a common backbone curve which peaks at $(t/t_l)_{max}$. Consequently, as long as the duration of shaking t_d/t_l is less than $(t/t_l)_{max}$, $r_{u,max}$ is equal to the excess pore pressure ratio at the end of shaking, and increases as $N_{eq}/N_l = t_d/t_l$ increases. However, when t_d/t_l exceeds the $(t/t_l)_{max}$, the excess pore

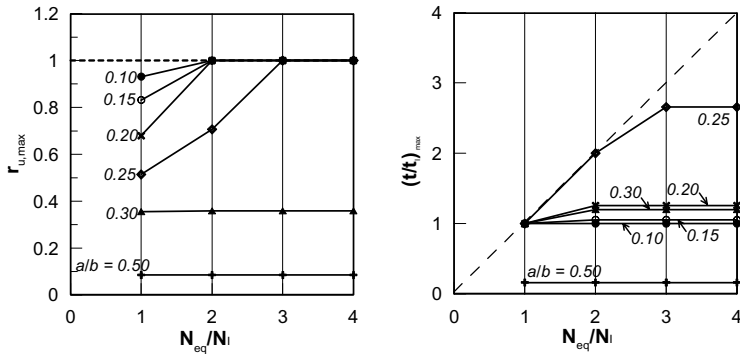


Figure 14. Effect of seismic intensity N_{eq}/N_l on: (a) the peak excess pore pressure ratio ($r_{u,max}$), and (b) the corresponding normalized time potential $(t/t_1)_{max}$, for various drain spacings a/b and $T_{al} = 5.7$, based on the revised method.

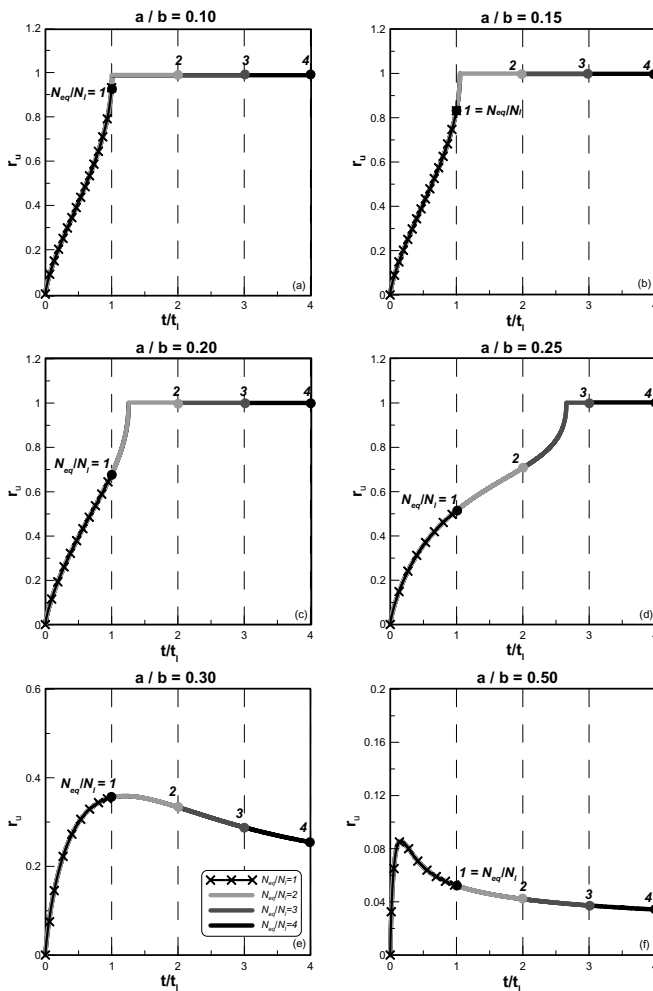


Figure 15. Effect of seismic intensity N_{eq}/N_l on the time history of excess pore pressure ratio r_u for various drain spacings a/b and $T_{al} = 5.7$, based on the revised method.

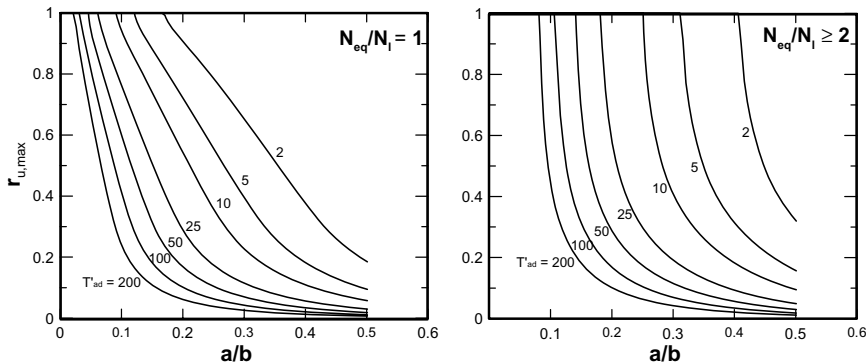


Figure 16. Revised design charts for improvement of liquefiable sites using infinitely permeable gravel drains.

pressure ratio at the end of shaking is either equal or less than the peak, which now becomes the constant $r_{u,max}$ value. Note that the former response is related to sparse drain arrangements (e.g. $a/b \leq 0.25$) and peak $r_{u,max}$ values near 1.0, while the latter is related to the more commonly used dense drain arrangements ($a/b \geq 0.30$) where the peak $r_{u,max}$ values are significantly less than 1.0.

Focusing upon design cases of practical interest, where the aim is to keep peak $r_{u,max}$ values low (e.g. below 0.60), it is observed that the effect of seismic shaking intensity is essentially diminished after $N_{eq}/N_l = 2.0$. Note that this limiting value of N_{eq}/N_l , has also been verified against the results of the much larger set of parametric analyses which were performed in order to produce the charts shown in Fig. 10.

The physical meaning of this value is that when the number of cycles exceeds about $2N_l$, the tendency of the rate of excess pore pressure build up to decrease due to sand fabric evolution (function F_1 in Fig. 3) overcomes the tendency for increase due to increased cyclic shear strain (function F_2 in Fig. 3), leading to a gradual overall decrease of the excess pore pressures. Thus, it is reasonable to expect that the exact value of this limit does not only depend upon the target $r_{u,max}$ value, but also on the form of the equation used to describe the excess pore pressure build up in the un-improved ground (Eq. 7), and specifically on the value of the exponent A which was taken here as 0.70, following the original recommendation by Seed & Booker (1977).

Hence, in practice, it is possible to ignore any loading cycles beyond $2N_l$ and use the charts for $N_{eq}/N_l = 2$ for the computation of $r_{u,max}$. In that case, the duration of shaking will have to be reduced as well to $t'_d = t_d(2/n)$, where $n = N_{eq}/N_l$. In this way, the four design charts of Fig. 10 may be reduced to only two (Fig. 16): one for $N_{eq}/N_l = 1$ and the other for $N_{eq}/N_l \geq 2$. Yet, the timefactors which are compatible with these charts

are as follows:

$$T_{ad} = C \frac{k_h t_d}{\gamma_w m_{v,3} a^2} \quad (18)$$

where $C = 1$ for $N_{eq}/N_l = 1$, and $C = 2/(N_{eq}/N_l)$ for $N_{eq}/N_l \geq 2$.

6 CONCLUDING REMARKS

The pioneering work of Seed & Booker (1977) for liquefaction mitigation using infinitely permeable gravel drains has been revised with respect to the assumed rate of excess pore pressure buildup $\partial u_g / \partial N$ in the unimproved ground. Specifically, in the original publication it was assumed that this rate depends solely upon the excess pore pressure ratio r_u at any given instant of time. It is now recognized that this rate is the final outcome of two competing effects. The first is the effect of cyclic strain amplitude, which increases with r_u and leads in turn to gradually increasing rates of excess pore pressure buildup. The second effect of sand fabric evolution towards a more stable state, which leads to gradually decreasing rates of excess pore pressure buildup and is a function of the number of cycles N_{eq} or the time elapsed from the beginning of shaking.

In summary, the basic alterations to the original solution of the problem, which resulted from the aforementioned revision, are the following:

- Unless the improved ground liquefies, excess pore pressures reach a peak value at the early stages of seismic shaking and then decrease, while shaking continues. Note that the original formulation predicts a steady asymptotic increase of excess pore pressures reaching the peak value at the end of shaking.
- The revised predictions of peak excess pore pressure $r_{u,max}$ in the improved ground are systematically

lower than the original ones. For moderate seismic shakings with $N_{eq}/N_f = 1$, the maximum difference is a little higher than 20% and occurs at the low range of excess pore pressure ratio i.e. for $r_{u,max} < 0.3$. For stronger shakings with $N_{eq}/N_f \geq 2$ the maximum difference is of the order of 50% and occurs at the intermediate range of excess pore pressure ratio values (i.e. $r_{u,max} = 0.3-0.7$).

- c. For a typical value of the maximum excess pore pressure ratio in the improved ground, such as $r_{u,max} = 0.4$, the difference in the volume of required gravel drains is approximately equal to 15% for moderate shakings ($N_{eq}/N_f = 1$) and 15 to 25% for stronger events ($N_{eq}/N_f = 2$ to 4). Larger differences are likely to occur when the target value of $r_{u,max}$ is increased.
- d. Due to (a) above, the intensity of shaking has no effect on the peak value of anticipated excess pore pressures for $N_{eq} > 2N_f$. Thus, in practical applications, when the target $r_{u,max}$ is less than about 0.50, it is possible to ignore any loading cycles beyond $2N_f$ and use the design charts for $N_{eq}/N_f = 2$ with proper adjustment to the value of the time factor T_{ad} .

Note that, although the revised solution presented herein refers to the basic case of uniform ground, radial drainage and infinitely permeable gravel drains, the above conclusions are relevant to all newer method variants referred in the introduction. This is because, they may have effectively removed some of the simplifying assumptions of the original Seed & Booker (1977) solution, but maintained the same assumption for the rate of excess pore pressure build up $\partial u_g / \partial N$, as expressed by Eq. 8.

REFERENCES

- Adalier, K., Elgamal, A., Meneses, J. & Baez, I.J. 2003. Stone columns as liquefaction counter-measure in non-plastic silty soils. *Soil Dynamics and Earthquake Engineering*, 23(7): 571–584.
- Adalier, K. & Elgamal, A. 2004. Mitigation of liquefaction and associated ground deformations by stone columns. *Engineering Geology*, 72, 275–91.
- Baez, J.I. & Martin, G.R. 1993. Advances in the design of vibro-systems for the improvement of liquefaction resistance. *Proceedings, Symposium of Ground Improvement*, Vancouver Geotechnical Society, Vancouver, B.C., Canada.
- Boukvalas, G.D., Papadimitriou, A.G., Kondis, A. & Bakas G.J. 2006. Equivalent-uniform soil model for the seismic response analysis of sites improved with inclusions. *Proceedings, 6th European Conference on Numerical Methods in Geotechnical Engineering*, Graz, 6–8 September.
- Boulanger, R., Idriss, I., Stewart, D., Hashash, Y. & Schmidt, B. 1998. Drainage capacity of stone columns or gravel drains for mitigating liquefaction. *Proceedings, Geotechnical Earthquake Engineering and Soil Dynamics III, Special Publication No. 75*, vol. I, 678–690.
- Harada, N., Towhata I., Takatsu T., Tsunoda, S. & Sesov, V. 2006. Development of new drain method for prediction of existing pile foundations from liquefaction effects. *Soil Dynamics and Earthquake Engineering*, 26 (4): 297–312.
- Iai, S. & Koizumi, K. 1986. Estimation of earthquake induced excess pore pressure for gravel drains. *Proceedings, 7th Japan Earthquake Symposium*, 679–684.
- INA 2001. Seismic design guidelines for port structures. Working Group No. 34 (eds), Maritime Navigation Commission, International Navigation Association, A.A. Balkema, Rotterdam, The Netherlands.
- Ishihara, K., Tatsuoka, F. & Yasuda, S. 1975. Undrained deformation and liquefaction of sand under cyclic stresses. *Soils and Foundations* 15(1): 29–44.
- JGS 1998. Remedial measures against soil liquefaction. *The Japanese Geotechnical Society (ed)*, A.A. Balkema, Rotterdam, The Netherlands.
- Kamai, R., Kano, S., Conlee, C., Marrinucci, A., Rathje, E., Boulanger, R., Rix, G. 2007. Evaluation of the effectiveness of prefabricated vertical drains for liquefaction remediation—Centrifuge data report for SSK01. *Center for Geotechnical Modelling Data Report*, University of California Davis, U.S.A.
- Ladd, C.C., Foott, R., Ishihara, K., Schlosser, F. & Poulos, H.G. 1977. Stress deformation and strength characteristics. State-of-the-art report. *Proceedings, 9th International Conference on Soil Mechanics and Foundation Engineering*, Tokyo, 2: 421–494.
- Madhav, M.R. & Adapa M.K. 2007. Liquefaction mitigation of sand deposits by granular piles: densification and dilation effects. *Proceedings, 4th Intern. Conference on Geotech. Earthq. Engineering, Thessaloniki, Greece, June*.
- Marinucci, A., Rathje E., Kano S., Kamai, R., Conlee, C., Howell, R., Boulanger, R. & Gallagher, P. 2008. Centrifuge testing of prefabricated vertical drains for liquefaction mitigation. *Proceedings, Geotechnical Earthquake Engineering and Soil Dynamics IV*, Sacramento, U.S.A., May.
- Matsubara, K., Mihara, M. & Tsujita M. 1988. Analysis of gravel drain against liquefaction and its application to design. *Proceedings, 9 World Conference on Earthquake Engineering*, Vol. III 249–254.
- Mitchell, J.K. & Wentz, F.K. 1991. Performance of improved ground during Loma Prieta earthquake. *Report No. 91/12*, EERC, University of California, Berkeley, U.S.A..
- Mitchell, J.K., Baxter, C.D.P. & Munson, T.P. 1995. Performance of improved ground during earthquakes. *Proceedings, Soil Improvement for Earthquake Hazard Mitigation*, ASCE Special Publication, vol. 49, 1–36.
- Nemat-Nasser, S. & Tobita, Y. 1982. Influence of fabric on liquefaction and densification potential of cohesionless soils. *Mechanics of Materials* 1: 43–62.
- Onoue, A. 1988. Diagrams considering well resistance for designing spacing ratio of gravel drains. *Soils and Foundations* 28(3): 160–168.
- Ostadan, F., Deng N. & Arango I. 1996. Energy based method for liquefaction potential evaluation, Phase I—Feasibility Study. Research Report, Bechtel Corporation, San Francisco, CA, August.
- Papadimitriou, A.G., & Boukvalas, G.D. 2002. Plasticity model for sand under small and large cyclic strains: a

- multiaxial formulation. *Soil Dynamics & Earthquake Engineering* 22(3): 191–204.
- Papadimitriou, A.G., Vytiniotis, A.C., Bouckovalas, G.D. & Bakas G.J. 2006. Equivalence between 2D and 3D numerical analyses of the seismic response of improved sites. *Proceedings, 6th European Conference on Numerical Methods in Geotechnical Engineering*, Graz, 6–8 September.
- Papadimitriou, A.G., Moutsopoulou M.-E., Bouckovalas G. & Brennan A. 2007. Numerical Investigation of Liquefaction Mitigation using Gravel Drains. *Proceedings, 4th International Conference on Earthquake Geotechnical Engineering*, Thessaloniki, Greece, June.
- Priebe, H.J. 1989. The prevention of liquefaction by vibro-replacement. *Proceedings, Earthquake Resistance Construction and Design*, Berlin, Germany.
- Priebe, H.J. 1991. Vibro-replacement design criteria and control. *Deep Foundation Improvements: Construction and Testing*. Esrig, Bachus (Eds), ASTM STP 1089, 62–72, Philadelphia, U.S.A..
- Rollins, K. 2004. Liquefaction mitigation using vertical composite drains: Full scale testing. NCHRP-IDEA Project 94 Report, Transportation Research Board, Washington D.C..
- Rollins, K., Anderson, J., Goughnour, R. & McCain, A. 2004. Liquefaction hazard mitigation using vertical composite drains. *Proceedings, 13th WCEE*, Vancouver, B.C., Canada, Paper No. 2880.
- Saito, A., Taghawa, K., Tamura, T., Oishi, H., Nagayama, H. & Shimaoka, H. 1987. A countermeasure for sand liquefaction: Gravel drain method. *Technical Report, Overseas No. 51*, Nippon Kokan, Japan.
- Seed, H.B., Idriss, I.M., Makdisi F. & Banerjee, N. 1975. Representation of irregular stress time histories by equivalent uniform stress series in liquefaction analyses. *Report No. EERC 75-29*, Earthquake Engineering Research Center, University of California, Berkeley, CA.
- Seed, H.B. & Booker, J.R. 1977. Stabilization of potentially liquefiable sand deposits using gravel drains. *Journal of the Geotechnical Engineering Division, ASCE* 103(GT7): 757–768
- Seed, H.B., Martin, P.P. & Lysmer, J. 1975. The generation and dissipation of pore water pressures during soil liquefaction. *Report No. EERC 75-26*, Earthquake Engineering Research Center, University of California, Berkeley, CA.
- TC4 2001. Case histories of post-liquefaction remediation. *Report, Technical Committee for Earthquake Geotechnical Engineering*, ISSMGE, The Japanese Geotechnical Society, Tokyo, Japan.
- The Earth Technology Corporation 1992. VELACS—laboratory Testing Program. *Soil Data Report*, prepared for the NSF, Irvine, CA, March.
- Towhata, I. 2007. Developments of soil improvement technologies for mitigation of liquefaction risk. *Chapter 15, Earthquake Geotechnical Engineering*, K.D. Pitilakis (ed), 355–384.
- USACE 1999. Engineering and design guidelines on structure improvement for structures and facilities. Publ. No. ETL 1110-1-185, US Army Corps of Engrs, Enginrng Division, Directorate of Civil Works, Washington DC, U.S.A.
- Yasuda, S. 2007. Remediation methods against liquefaction for existing structures. *Chapter 16, Earthquake Geotechnical Engineering*, K.D. Pitilakis (ed), 384–406.

Seismic soil-pile-structure interaction based on large shaking table tests

K. Tokimatsu & H. Suzuki

Tokyo Institute of Technology, Tokyo, Japan

ABSTRACT: Field performance of various pile foundations that experienced the recent earthquakes are summarized together with the effects of ground displacement as well as those of inertial force of superstructures on pile damage in non-liquefiable and liquefiable deposits. Large shaking table tests conducted on soil-pile-structure models with dry and saturated sands for examining and quantifying the effects of inertial and kinematic forces are demonstrated, in addition to the effects of earth pressure acting on the embedded foundation and of horizontal subgrade reaction of piles. Pseudo-static analysis for estimating pile stress in liquefiable and non-liquefiable sand is presented in which inertial and kinematic effects observed in large shaking table tests are incorporated and the effectiveness of the method has been demonstrated through the comparison of observed and computed pile stresses in the shaking table tests. Sensitivity analysis is also made to differentiate crucial factors affecting pile stress in a liquefied soil.

1 INTRODUCTION

Extensive soil liquefaction that occurred in the Hyogoken-Nambu (Kobe) earthquake ($M = 7.2$) of January 17, 1995, induced geotechnical-related damage to various structures in the reclaimed land area along the coastline of Kobe city. Not only many buildings with spread foundations but also numerous pile-supported buildings settled and/or tilted without significant damage to their superstructures. Such foundation distress was particularly extensive near the waterfronts where lateral ground movements occurred due to quay wall failures caused by soil liquefaction. Similar foundation distress without any significant damage to superstructure also occurred at quite a few pile-supported buildings located outside the liquefied area.

There was a serious concern that the piles of those buildings might have been damaged. Excavation surveys after the quake showed that the pile heads in most tilted buildings in the non-liquefied area did fail, suggesting strong effects of inertial force from their superstructures. This, however, may not be the case in the liquefied area where the piles were often damaged at depths other than the pile head, suggesting the effects of increased cyclic and/or permanent ground displacement of liquefied and/or laterally spreading ground. This in turn suggests that the effects of both dynamic and permanent ground movements on piles should be properly taken into account in foundation design. Little was known, however, about the actual failure mode and process of those piles as well as their relation to ground displacements, since

they occur and progress in the ground. Extensive field investigations using newly invented techniques to identify pile damage and/or deformation were, therefore, performed on pile foundations that experienced strong ground shaking, liquefaction or lateral ground spreading during the Kobe earthquake (e.g., Kansai Branch of Architectural Institute Japan (AIJ), 1996; AIJ et al., 1998; BTL Committee, 1998). In addition, many studies using centrifuge and large shaking tables have been made (e.g., Boulanger, 1999; Wilson et al., 2000; Abdoun, 2003; Mizuno, 1997), the later of which include two large-scale shaking tables of the National Institute of Earth Science and Natural Disaster Prevention (NIED) in Tsukuba and Miki, Japan.

The objective of this paper is to summarize the failure and deformation modes of piles that experienced the Kobe earthquake, and to examine the inertial and kinematic effects on pile stresses based on large shaking table tests. Pseudo-static analyses using p - y curves are then performed for the large shaking table tests and well-documented case histories of pile foundations that experienced the Kobe earthquake.

2 SUMMARY OF FIELD OBSERVATION AFTER 1995 KOBE EARTHQUAKE

A large number of case histories of pile foundations during the Kobe earthquake have been examined, based on field investigation including excavation of pile heads (e. g., Kansai Branch of Architectural Institute Japan (AIJ), 1996; AIJ et al., 1998).

The main findings from the field investigation (Tokimatsu, 2003a) are summarized below.

1. In the non-liquefied area where damage to superstructures concentrated, quite a few buildings tilted with their superstructures remaining intact, due to shear failure of their pile heads.
2. In the liquefied area, many buildings supported on non-ductile piles suffered foundation distress with their superstructures remaining intact, due mainly to failures of the piles at the interface between liquefied and non-liquefied layers.
3. In the laterally spreading area, similar but more extensive foundation distress occurred in which the piles of a building near the waterfront often showed different failure modes in the direction perpendicular to the waterfront, while those away from the waterfront showed similar deformation patterns.

The significant difference in damage pattern of piles among non-liquefied, liquefied, and laterally spreading areas is considered to be due mainly to the following:

1. The non-liquefied surface soil amplified the ground motions significantly, leading to the extensive damage to buildings or otherwise the shear failure at the pile heads.
2. Soil liquefaction de-amplified the ground motions particularly in the period range less than 1s, reducing the damage to superstructure in the liquefied and laterally spreading areas.
3. Soil liquefaction and lateral spreading increased the ground displacement and thus kinematic effects, leading to the damage to pile foundations, which concentrated not only at the pile head but also near the boundary between liquefied and non-liquefied layers.
4. Spatial variation of ground displacement in the laterally spreading area had a significant effect on the difference in failure modes of piles within a building.

The field case histories from the Kobe earthquake strongly suggest that not only the inertial force but also the kinematic force due to ground displacement, overlooked in the design specification at that time, might have significant effects on pile damage.

3 SOIL-PILE-STRUCTURE INTERACTION STUDIES USING SHAKING TABLE TESTS

In view of the extensive pile damage in the Kobe earthquake, numerous research projects were initiated to investigate the effects of soil-pile-structure interaction on pile damage during the earthquake. Along these lines, soil-pile-structure interaction studies were conducted using large shaking table facilities at Tsukuba, Japan, and subsequently at E-Defense, Miki near

Kobe, Japan, under several research projects. These included mainly Special Project for Earthquake Disaster Mitigation in Urban Areas, supported by the Ministry of Education, Culture, Sports, Science and Technology (MEXT), which is so called “Dai-Dai-Toku” project (2002–2006). Both shaking table facilities are owned and operated by the National Research Institute for Earth Science and Disaster Prevention (NIED). In addition to the larger size and payload capacity, the E-defense shaking table is a tri-axial one that contrasts well with the one-dimensional one at Tsukuba. Described in the following are some of the test results and findings from these shaking tables and other related centrifuge tests.

3.1 Soil-pile structure interaction in level ground using large shaking table at Tsukuba

Several series of shaking table tests were conducted for soil-pile-structure interaction studies during 2000–2005, using the shaking table facility at Tsukuba, NIED (e.g., Tamura et al., 2000; Tokimatsu et al., 2005a, 2005b), as shown in Figure 1. Figure 2 illustrates fifteen soil-pile-structure models, the results of which are used in this study. The dimensions of the shear box were 4.6 or 6.1 m in height, 12.0 m in width and 3.5 m in length. The dry sand deposit prepared in the laminar box consisted of a homogeneous layer of 4.0 or 4.5 m. The soil used for dry sand deposit shown in Figure 2 was Nikko Sand ($e_{\max} = 0.98$, $e_{\min} = 0.65$, $D_{50} = 0.42$ mm). The relative densities were about 80% for the tests. The liquefiable saturated sand deposit consisted of three layers including a top dry/unsaturated sand layer of 0.5 m in thickness (if a foundation was embedded), a saturated sand layer of 3 to 4 m in thickness and an underlying dense sand or gravel layer of about 1.5 m in thickness. The sand used was Kasumigaura Sand ($e_{\max} = 0.961$, $e_{\min} = 0.570$, $D_{50} = 0.31$ mm, $F_c = 5.4\%$).

A 2×2 pile group was used in all the tests. All the piles had a diameter of 16.52 cm with a 0.37 cm wall

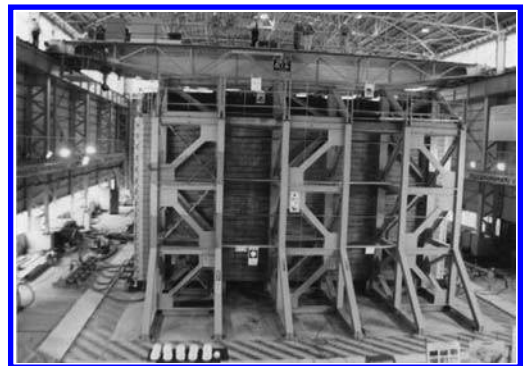


Figure 1. Laminar shear box on shaking table facility.

	without embedment		with embedment			
	without superstructure	with superstructure	without superstructure	with superstructure		
Dry sand	Model layout					Flexible pile: D = 165.2 mm, t = 3.7 mm
	Test ID & T _b	DAN	DAS (0.06s, T _b < T _g) DAL (0.7s, T _b < T _{gl})	DBN	DBS (0.06s, T _b > T _g) DBL (0.7s, T _b > T _{gl})	
Saturated sand	Model layout					Flexible pile: D = 165.2 mm, t = 3.7 mm
	Test ID & T _b	SAN	SAS (0.2s, T _b < T _g < T _{gl}) SAL (0.8s, T _g < T _b < T _{gl})	SBN	SBS (0.2s, T _b < T _g < T _{gl}) SBL (0.8s, T _g < T _b < T _{gl})	
	Model layout	/				Stiff pile: D = 318.5 mm, t = 6.0 mm
	Test ID & T _b			SBNR	SBRS (0.2s, T _b < T _g < T _{gl}) SBLR (0.8s, T _g < T _b < T _{gl})	

T_s: Natural period of superstructure T_g: Natural period of non-liquefied ground (=0.3s)
T_{gl}: Natural period of liquefied ground (>1.0s)

Figure 2. Soil-pile-structure models.

thickness and their tips were connected to the container base with pin joints. The piles were set up with a horizontal space of about ten-pile diameters center to center. Their heads were fixed to a foundation with or without a superstructure. A model ID consisting of three or four alphabets specifies the test conditions. The first one indicates soil condition (D: dry sand; and S: saturated sand), the second one the presence of foundation embedment (A: no; and B: yes), and the third one the presence of a superstructure and its natural period (T_b) relative to that of the ground at a small strain level (T_g) (N: no; S: T_b < T_g; and L: T_b > T_g). The natural period of the superstructure with ID containing S was 0.08 or 0.2s, which was shorter than that of the ground. The natural period with ID containing L was 0.7 or 0.8s, which was longer than that of the non-liquefied ground but shorter than that of the liquefied ground. The fourth one, if exists (R), indicates that the piles are stiffer than others. Series ID containing l at the end had a foundation of a weight 16.7 kN, while ID containing L or S at the end had a foundation of 20.6 kN and a superstructure of 139.3 kN.

Prior to each shaking table test, cone penetration tests were conducted to estimate density distribution of the deposit with depth. Either artificial accelerogram called Rinkai or the one recorded during the 1940 El Centro Earthquake was used as an input motion to the shaking table. In total, thirty-one tests were conducted on the soil-pile-structure models with the two input motions having a maximum acceleration adjusted to 1.2–2.4 m/s². The soil-pile-structure system was heavily instrumented with accelerometers, displacement transducers, strain gauges, and, if saturated, pore

pressure transducers. Particularly, the accelerometers of all piles and the ground were measured at every 50 cm with depth and the bending strains of all piles at every 10–25 cm.

3.2 Effects of inertial and kinematic forces on piles in level ground using shaking table at Tsukuba

Figure 3 (Tokimatsu et al., 2005b) shows the maximum pile stresses including shear forces, bending moments and axial forces at pile heads with respect to the maximum inertial forces in all the tests. There is a definite trend in which the pile stresses increase with increasing inertial force. The increase in pile stresses with respect to the inertial force in non-liquefied ground is more significant in tests without foundation embedment (tests models DAS and DAL) than in tests with foundation embedment (tests models DBS and DBL).

It is interesting to note that the shear force in the test models DBS and DBL is smaller than the inertial force from the superstructure and the foundation, while that in the test models DAS and DAL is as large as the inertial force (Figure 3a). This suggests that the presence of foundation embedment did have a significant effect on reducing shear force transmitted from the superstructure to the piles. In addition, the pile stresses become larger for a short-period superstructure (test models DAS and DBS) than for a long-period superstructure (test models DAL and DBL). This is because the inertial force and ground displacement are in phase in the tests with a short-period superstructure but out of phase in the tests with

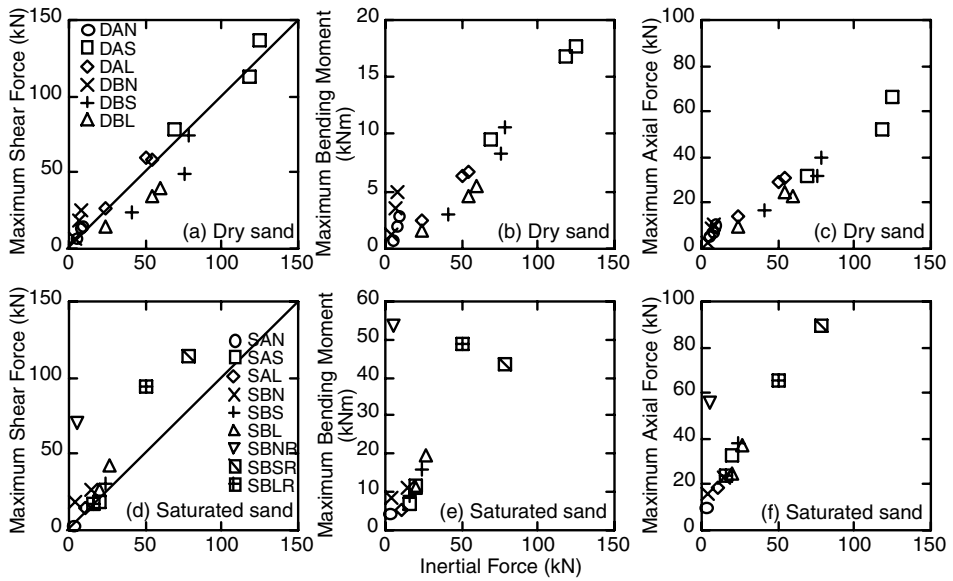


Figure 3. Relation of maximum pile stresses with maximum inertial force in large shaking table tests.

a long-period superstructure. These findings confirm that the factors other than the inertial force, i.e., the presence of foundation embedment and whether the natural period of the superstructure is greater than that of the ground, significantly affect the pile stress.

The increase in pile stresses with increasing inertial force in liquefied ground is more significant with foundation embedment (model IDs starting with SB) than without it (model IDs starting with SA). Namely, the shear force at the pile head is larger than the inertial force (Figure 3d). This suggests that the presence of foundation embedment does have an opposite effect on pile stresses before and after liquefaction in such a way that it reduces the shear force transmitted to piles before liquefaction but may increase it after liquefaction. It is interesting to note that, if the foundation is embedded, stresses in piles without a superstructure become as large as those with a superstructure after liquefaction, despite their different inertial forces (Figures 3d, e).

A comparison of pile stresses in different soil conditions indicates that an increase in pile stress with increasing inertial force is larger in liquefied sand (Figures 3d–f) than in dry sand (Figures 3a–c). This is probably caused by drastic change in soil resistance due to liquefaction. The non-liquefied soil near the ground surface can resist most of the inertial force from the superstructure, reducing shear force transmitted to the piles. The non-liquefied crust overlying liquefied layer as well as the liquefied upper soil layer, in contrast, cannot bear most of the inertial force and may even push the foundation to increase the shear

force in piles when the ground displacement exceeds that of the foundation.

3.3 Estimation of kinematic forces on piles in laterally spreading ground using shaking table at Tsukuba

To investigate kinematic force acting on piles during liquefaction-induced lateral spreading, shaking table tests were conducted using the large shaking table facility in Tsukuba in 2004, under US-Japan collaboration research (Suzuki & Tokimatsu, 2009). Figure 4 shows two soil-pile systems prepared in a laminar shear box, 5.5 m in height, 12.0 m in width and 3.5 m in length, which was set on the shaking table with a slope angle of 2 degrees, as shown in Figure 4. The sand deposit constructed in the laminar shear box had a thickness of 5 m with an inclined surface having a slope angle of 2 degrees, in which two single piles 6 m in length were set apart.

The two single piles had the same diameter but different wall thickness and different stiffness. The one located downstream was a steel pipe with a diameter of 318.5 mm and a wall thickness of 6 mm. The other located upstream was a stainless steel pipe with a diameter of 318.5 mm and a wall thickness of 3 mm. The downstream pile is hereby called the stiff pile (PS-1 and PS-2) and the upstream pile the flexible pile (PF-1 and PF-2). Both piles had a free rotational condition at their heads and a fixed boundary with the laminar shear box base at their tips.

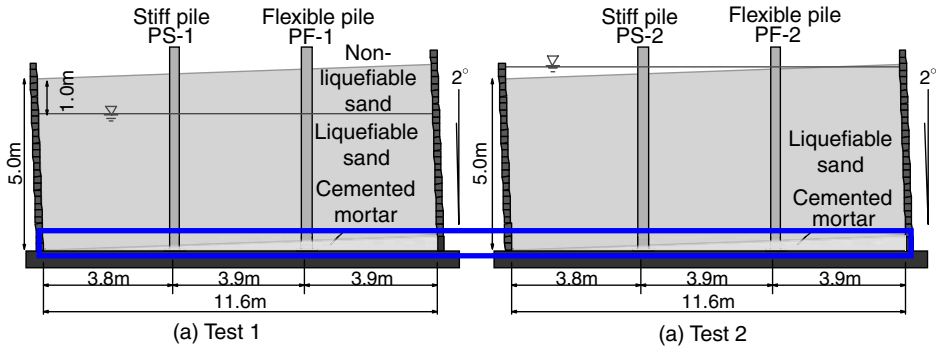


Figure 4. Inclined soil-pile models.

As shown in Figure 4, the water table was at 1.0 m below the lowest ground surface for Test 1 or at the same level as the highest ground surface for Test 2. To prepare the sand deposit for Test 1, after fixing the piles in the inclined base layer of cemented mortar, the laminar shear box was filled with water to a certain level (4.0 m high from the base) and wet Kasumigaura Sand was pluviated into the water. Dry sand was, then, air-pluviated to form the top non-liquefiable layer above the water table. After conducting Test 1, the entire sand deposit was saturated with poring the water from the laminar box base to prepare the sand deposit for Test 2. For both the tests, a sinusoidal wave with a frequency of 2 Hz was used as an input base motion, with a maximum acceleration of 2.0 m/s^2 . Before each shaking event, a geophysical test and cone penetration test were conducted to characterize soil profile.

The test models were densely instrumented with accelerometers, displacement transducers, strain gauges, pore water pressure transducers and earth pressure transducers. In particular, to investigate factors influencing subgrade reaction of piles during lateral spreading, pore pressure transducers were installed on both downstream and upstream sides of the two piles.

Figure 6 shows the laminar shear box after Test 2. The permanent deformation of the laminar box after the test, induced by lateral ground spreading, was more than 1 m at the top.

The pore water pressure reaches the initial effective stresses, causing soil liquefaction within 5 s after the start of shaking. The ground displacement increases downstream with cyclic fluctuation, increasing pile displacement and bending strain in the initial stage of shaking.

Figure 7 compares distributions of bending strains of the stiff and flexible piles in two instants, i.e. 5.6 s and 20 s, for Tests 1 (Figs. 7a, b) and 2 (Figs. 7c, d). The bending strains of the stiff pile in both tests are larger at 5.6 s than at 20.0 s (Figs. 7a, c), while those of the flexible pile are almost the same between the two



Figure 5. Laminar box before shaking.



Figure 6. Laminar box after shaking.

instants (Figs. 7b, d). This suggests that the effects of kinematic forces depend on pile stiffness, resulting in the difference in pile behavior during laterally spreading. The bending strain of the stiff pile is slightly larger in Test 1 than in Test 2, indicating that the presence of the non-liquefied crust layer might have affected an increase in bending strains. The bending strain near the tip of the flexible pile, in contrast, is significantly

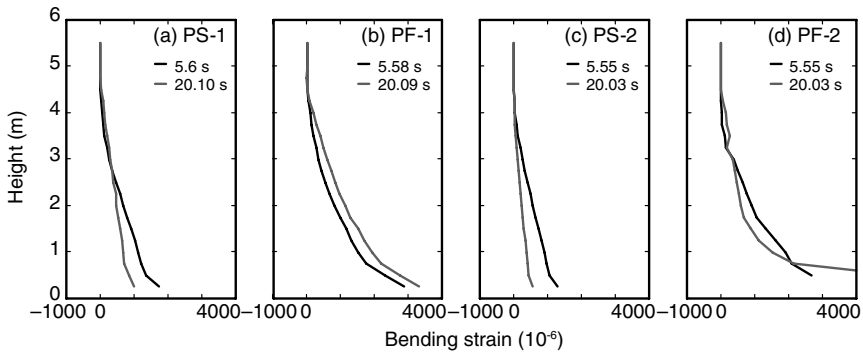


Figure 7. Distributions of bending strains of stiff and flexible piles in two tests.

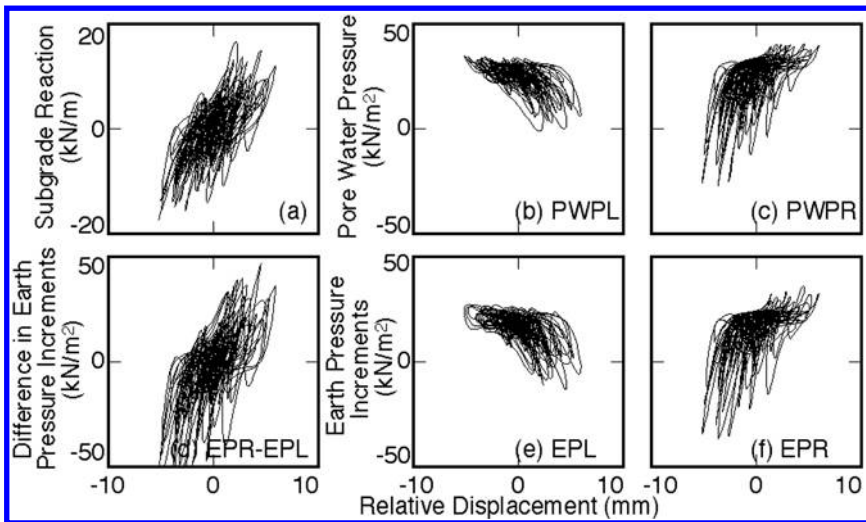


Figure 8. Relations of relative displacement with subgrade reaction, pore water pressures and earth pressure increments at 3 m depth in test with level ground.

larger in Test 2 than in Test 1, probably due to cyclic degradation after yielding.

3.4 Factors affecting horizontal subgrade reaction of pile during soil liquefaction and lateral spreading

To evaluate the mechanism of subgrade reaction development in liquefied level ground, the subgrade reaction of a pile is calculated from the double differentiation of observed bending moment with depth and the displacements of the ground and pile from the double integration of their observed accelerations (Suzuki et al., 2005). Figure 8 shows the relation of relative displacement with subgrade reaction and the pore water pressures and earth pressure increments measured on both sides of the pile during liquefaction. The positive

relative displacement in the figures indicates that the pile pushes the soil on the right or the soil pushes the pile from the right. The negative relative displacement, conversely, indicates that the pile pushes the soil on the left or soil pushes the pile from the left.

When the positive relative displacement develops, the subgrade reaction increases sharply (Fig. 8a). At this stage, the pore water pressure on the left side of the pile decreases significantly, whereas that on the right side maintains almost constant (Figs. 8b, c). When the negative relative displacement develops, the pore water pressures on both sides are reversed. The earth pressure increments measured on both sides of the pile show a similar trend to that of the pore water pressures on the same sides (Figs. 8e, f). The difference in the two earth pressures on both sides of the pile with relative displacement, shown in Figure 8d, shows the same

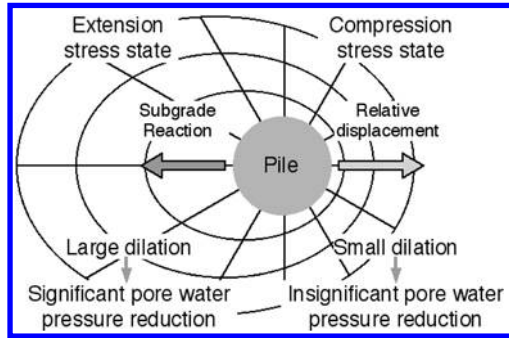


Figure 9. Stress states in soil around pile in liquefied ground.

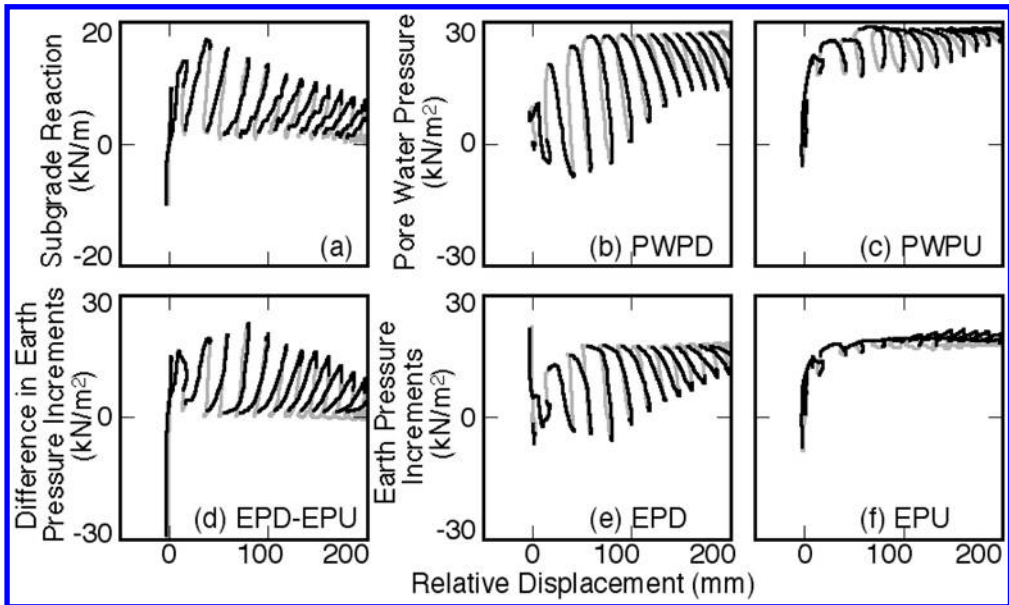


Figure 10. Relations of relative displacement with subgrade reaction, pore water pressures and earth pressure increments for stiff pile at 3.0 m depth in test with inclined ground.

trend as the subgrade reaction shown in Figure 8a. This indicates that the subgrade reaction could be induced by the pore water pressure changes around the pile.

Figure 9 shows a schematic diagram indicating how the subgrade reaction of a pile develops during soil liquefaction. When the pile pushes the soil on the right or the soil pushes the pile from the right, the compression stress state develops on the right and the extension stress state develops on the left of the pile. On the extension side, the pore water pressure reduction becomes pronounced due to the combined effects of decrease in normal stress and soil dilation induced by the shear stress. On the compression side, in contrast, the pore water pressure reduction becomes small due to the adverse effects of increase in normal stress

and soil dilation induced by the shear stress. As a result, the pile is pulled back by the soil on the extension side. Such mechanism of p - y behavior in liquefied soil is different from that in dry sand where horizontal subgrade reaction is induced by the increase in soil pressure on the compression side of the pile.

To estimate the effects of pore water pressure variation around the pile during lateral spreading, Figure 10 shows the relation of relative displacement with subgrade reaction and the pore water pressures and earth pressure increments observed on both sides of the stiff pile in Test 1 (Suzuki et al., 2005). Black lines in the figures indicate that the ground and pile move downstream and gray lines indicate that they move upstream. When the pile and ground move downstream, shown in

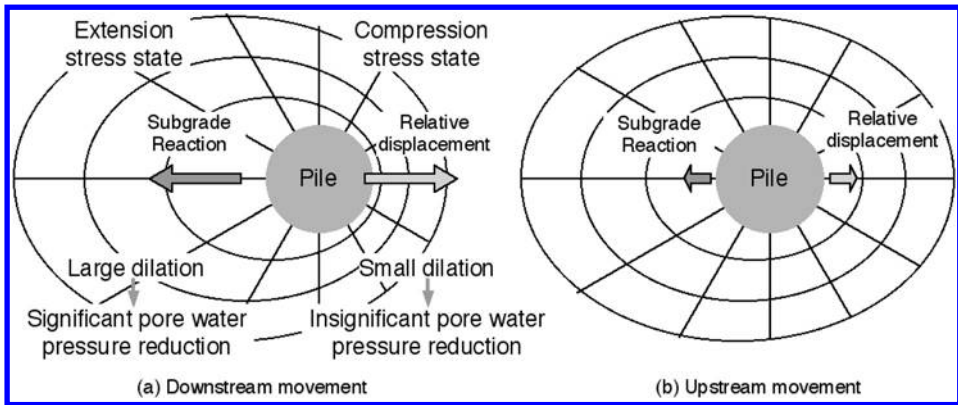


Figure 11. Stress states in soil around pile in laterally spreading ground.

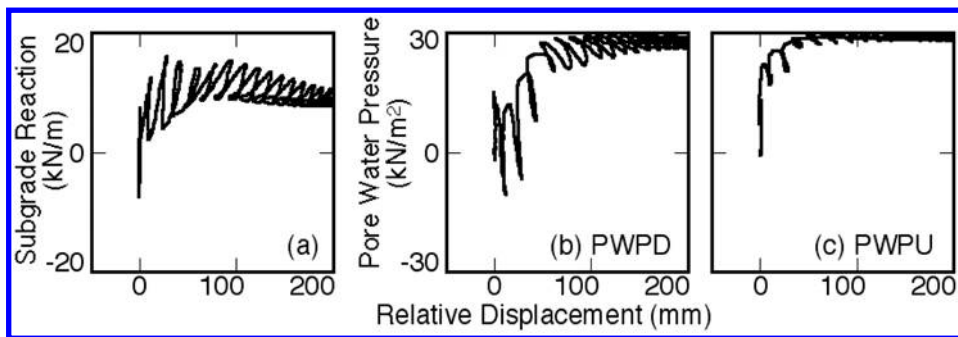


Figure 12. Relations of relative displacement with subgrade reaction, pore water pressures for flexible pile at 3.0 m depth in test with inclined ground.

black lines, the pore water pressure and earth pressure increment on the downstream side of the pile decrease significantly with those on the upstream side almost constant (Figs. 10b, c, e, f). At this stage, the subgrade reaction becomes large (Fig. 10a). When the pile and ground move upstream, shown in gray lines, the pore water pressures and earth pressure increments on both sides of the pile increase or maintain almost constant (Figs. 10b, c, e, f). At this stage, the subgrade reaction decreases (Fig. 10a). The difference in two earth pressure increments shows good agreement in trend with the subgrade reaction (Fig. 10d). This indicates that the subgrade reaction in laterally spreading ground is also induced by the pore water pressure changes in soil around a pile.

Figure 11 shows a schematic diagram indicating how the subgrade reaction of a pile develops during lateral spreading. When the pile and ground move downstream, the compression stress state develops on the upstream side of the pile with insignificant pore water pressure reduction and the extension stress state develops on the downstream side with significant pore water

pressure reduction. As a result, the pile is pulled by the soil on the downstream side. When the pile and ground move upstream, the relative displacement does not increase but decrease due to the accumulated downstream ground displacement. Therefore, the stress states developed on both sides of the pile are considered to be unloading, leading to a decrease in subgrade reaction. This indicates that the subgrade reaction development in laterally spreading ground is caused by the difference in stress states on both sides of a pile, as in the case of level ground. The pile in laterally spreading ground, however, is pulled only by the downstream soil, which is different from that in liquefied level ground where the pile is pulled by the soil on both sides alternately.

Figure 12 shows the relations of relative displacement with subgrade reaction and pore water pressures on both sides for the flexible pile. A comparison of trends between the stiff and flexible piles shows that a decrease in pore water pressure on downstream side as well as an increase in subgrade reaction with increasing relative displacement is more significant

in the test with the stiff pile than with the flexible pile (Figs. 10a–c and 12a–c). It is also interesting to note that the value of subgrade reaction of the stiff pile is back to almost zero at every cycle, while that of the flexible pile is not (Figs. 10a and 12a). This indicates that the subgrade reaction consists of cyclic and permanent components. The cyclic component, which might have been induced by the cyclic ground deformation with pore water pressure reduction, is larger in the stiff pile than in the flexible pile. The permanent component, which might have been induced by the permanent ground deformation, on the other hand, is larger in the flexible pile than in the stiff pile. The difference in subgrade reactions between stiff and flexible piles is probably induced by the difference in behavior between the two piles. The stiff pile, that can resist ground movement more than the flexible pile, yields larger relative displacement but smaller permanent displacement. The flexible pile, on the other hand, that can follow ground movement, yields smaller relative displacement but larger permanent displacement. As a result, the cyclic subgrade reaction becomes larger in the stiff pile but the permanent one becomes larger in the flexible pile.

3.5 Soil-pile-structure interaction in dry sand using E-Defense shaking table

The E-Defense shaking table platform has a dimension of 15 m long and 20 m wide. It is supported on fourteen vertical hydraulic jacks and connected to five hydraulic jacks each in the two orthogonal horizontal directions. Figures 13 and 14 show the shaking table with a cylindrical laminar box, with a height of 6.5 m and a radius of 8.0 m, made especially for geotechnical-related studies (Tokimatsu et al., 2007a, 2007b). The cylindrical laminar box consists of forty-one stacked ring flanges, enabling shear deformation of the inside soil during two-dimensional horizontal shaking.

The first soil-pile-structure interaction studies using the facilities were made with dry sand in FY2005. Preparation of soil-pile-foundation model in the laminar box was made in the preparation building next to the main building that accommodates the large shaking table. A 3 × 3 steel pile group was used for the test. The piles are labeled A1 to C3 according to their locations within the pile group, as shown in Figure 14. Each pile had a diameter of 152.4 mm and a wall thickness of 2.0 mm. The piles were set up with a horizontal space of four-pile diameters center to center. Their tips were jointed to the laminar box base with pins and their heads were fixed to the foundation of a weight of 10 tons.

After setting the pile group in the laminar box, the sand was air-pluviated and compacted to a relative density of about 70% to form a uniform sand deposit

with a thickness of 6.3 m. Albany sand, imported from Australia, was used for preparing the sand deposit. The sand had a mean grain size D_{50} of 0.31 mm and a coefficient of uniformity U_c of 2.0. The natural period of the ground is about 0.2 s throughout the test.

The laminar box with the built-in soil-pile-foundation mode was then moved to the main building with a lorry (Fig. 15) and on to the shaking table with two gigantic cranes. Several superstructures were in turn connected with four columns to the foundation and shaking tests were repeated.

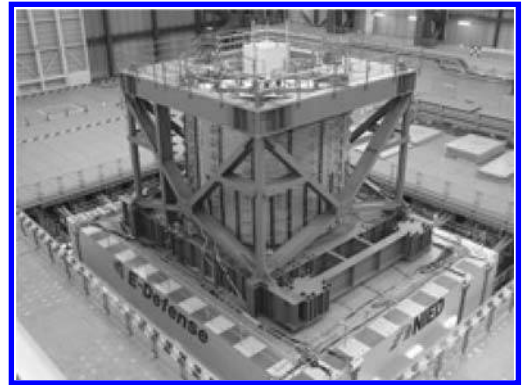


Figure 13. Test model on E-Defense large shaking table.

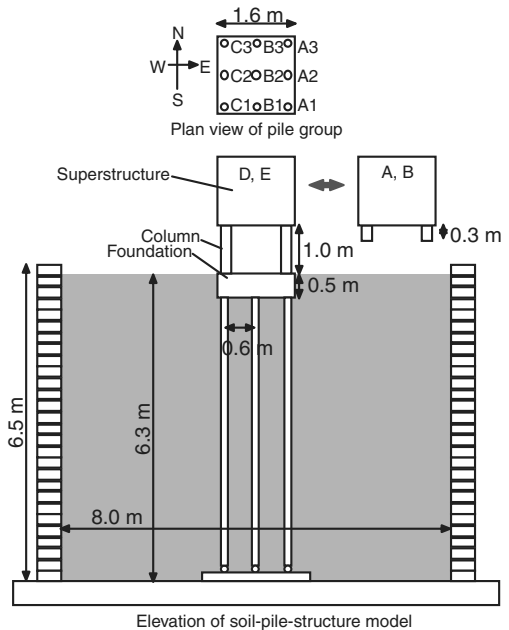


Figure 14. Soil-pile-structure model.

Table 1. Test series.

Embedment	Superstructure	Natural period (s)	Maximum input acceleration (m/s ²)										
			JR Takatori				Taft and Tottori						
			X	Y	XY	XYZ	X	Y	XY	XYZ			
A	Yes	Yes	0.1										
B	Yes	Yes	0.6										
C	Yes	No	–	0.3, 0.8					–				0.3, 0.8
D	Yes	Yes							0.3, 0.8				
E	No	Yes	0.2	0.3, 0.8			0.3, 0.8, 6.0, 8.0		–				



Figure 15. Test model moved by lorry.

A total of five test series named A to E was conducted as shown in Table 1, in which the presence of foundation embedment and superstructure, and the natural period of the superstructure, as well as the type of input motions including predominant period and maximum acceleration were varied. The foundation carried the superstructure of a weight of 28 tons in all series except for series C and had embedment except for series E. The superstructure had a natural period of 0.1, 0.2 or 0.6 s. This was achieved by changing the height and/or the rigidity of the four columns supporting the superstructure. The superstructure in series A was carried on steel columns 0.3 m high, that in series B on four rubber columns 0.3 m high, and those in series D and E on steel columns 1.0 m high. The natural period of the superstructure is smaller than that of the ground in series A, but close to that of the ground in series D and E and larger than that of the ground in series B.

A large number of strain gauges, accelerometers, velocity meters, earth pressure transducers, displacement transducers, settlement meters and load cells,

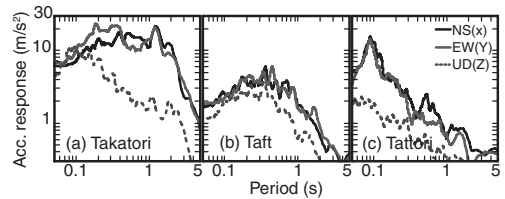


Figure 16. Acceleration response spectra of input motion.

about 900 sensors in total, were placed in the deposit as well as on the pile-structure model.

The tests were conducted under one-, two- or three-dimensional shaking with three different ground motions recorded at Takatori in the 1995 Kobe earthquake, at Lincoln School in the 1952 Taft earthquake and at Akasaki in the 2000 Tottori earthquake (hereby named Takatori, Taft, and Tottori). Figure 16 shows their acceleration response spectra with a damping ratio of 5%. The acceleration response spectra of the horizontal motions at Tottori dominate only in a short period range with a sharp spectral peak at about 0.1 s, whereas those at Takatori and Taft dominate over a wide period range covering from 0.1 s to 1.0 s.

In each test series, either the two horizontal or three-component motions, or both, were used as input to the shaking table with the largest horizontal acceleration being scaled to one listed in Table 1. The NS and EW components of the ground motion were applied to the NS (X) and EW (Y) directions as shown in Figure 14, with the UD (Z) component to the vertical direction. This paper describes inertial and kinematic effects on deformation and failure mode of piles based on test series E with Takatori motion having maximum input accelerations of 0.8 m/s² and 6.0 m/s². The piles were within the elastic range under the maximum input acceleration of 0.8 m/s², whereas they failed with a maximum input acceleration of 6.0 m/s². Further

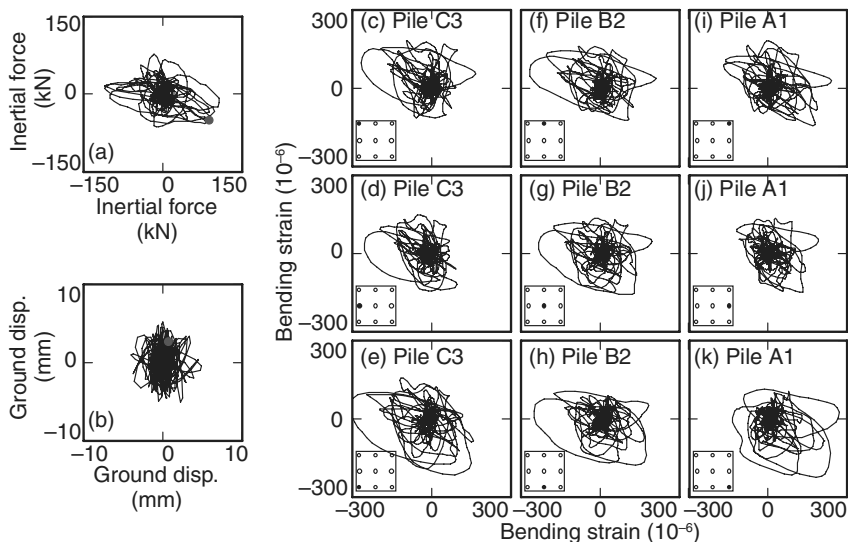


Figure 17. Loci of inertial force, ground surface displacement and bending strains.

details of the test apparatus and procedure have been described elsewhere (Tabata & Sato, 2006).

3.6 Inertial and kinematic effects on bending stress and failure mode of pile group in dry sand

To investigate the variation of bending strain within the pile group, Figure 17 shows loci of the inertial force of the structure, ground surface displacement and bending strain of each of the nine piles on the horizontal plane. The horizontal axis corresponds to the EW direction and the vertical one to the NS direction. The inertial force is larger in the EW direction than in the NS direction and its two-dimensional locus shows a spindle shape with its longer axis in the EW direction (Fig. 17(a)). The loci of bending strain show the same trends as those of the inertial force. In addition, whenever the inertial force acts southeastward, the bending strain becomes the largest in Pile A1 located at the southeast side of the pile group (Fig. 17(k)). In contrast, whenever the inertial force acts northwestward, the bending strain becomes the largest in Pile C3 located at the northwest side (Fig. 17(c)). This indicates that the bending strain is the largest at the leading pile within the pile group. The ground displacement is significantly small and its locus shows a different shape from those of inertial force and bending strains (Fig. 17(b)). This suggests the ground displacement plays an insignificant role in an increase in pile stresses in the test with small shaking.

To estimate the difference in bending strain within the pile group, Figure 18 shows the distributions with

depth of bending strains computed by a sum of NS and EW components for the nine piles when the inertial force takes the largest peak on the southeast, as shown by a circle in Figures 17 a, b. At this instant, Pile A1 is the leading corner pile and Pile C3 is the trailing corner pile. The bending strains at the pile head as well as at a depth of about 1.0 m become the largest in the leading corner pile, i.e., Pile A1 (Fig. 18i), and become the smallest at the trailing corner pile, i.e., Pile C3 (Fig. 18a). In addition, the depth at which the bending strain takes the inflection tends to be smaller in the leading pile, i.e., Pile A1 (Fig. 18i) than in any other trailing pile. These trends confirm that the pile stresses vary within the pile group and that bearing load is the largest in the leading corner pile.

To investigate inertial and kinematic effects on deformation and failure mode of piles, Figure 19 shows the distributions with depth of bending strains of the nine piles at about 6 s after the start of shaking at which the piles start yielding. The inertial force and ground surface displacement increase northeastward, making Pile A3 the leading corner pile. The figure shows that the bending strains at about 1 m depth in Piles A1, A2, and A3 exceed the elastic limit because of the combined effects of inertial and kinematic forces acting on the same directions at this moment (Figs. 19g–i). This indicates that the leading piles including Pile A3 bear larger forces than others and might have failed first.

After the test with a maximum acceleration of 6.0 m/s^2 , a higher input motion with a maximum acceleration of 8.0 m/s^2 was applied to the test model.

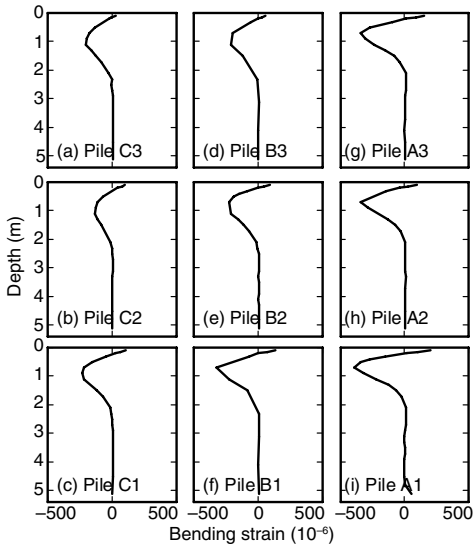


Figure 18. Distributions of bending strain in test with maximum acceleration of 0.8 m/s^2 .

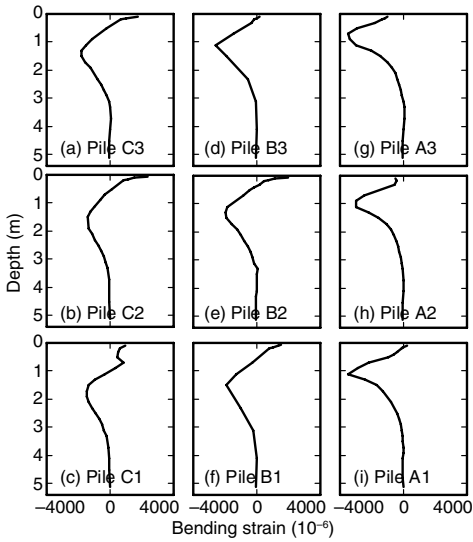


Figure 19. Distributions of bending strain in test with maximum acceleration of 6.0 m/s^2 .

The ground deformed significantly along the strong axis oriented in the northeast-southwest direction. The superstructure began to incline toward northeast. Figure 20 shows the residual deformation of the foundation, indicating that it not only moved northeastward but also rotated clockwise. Figure 21 shows the inclined superstructure after the test, and Figure 22 shows the pile damage to pile after excavation. Piles

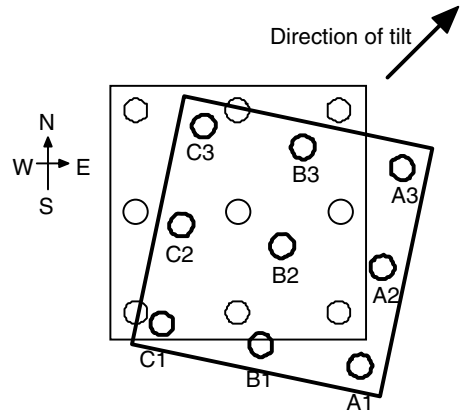


Figure 20. Residual deformation of foundation.

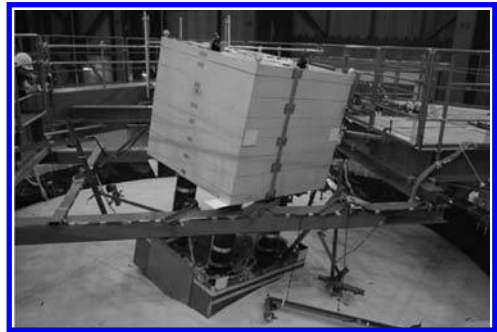


Figure 21. Inclined structure after test with high input motion.

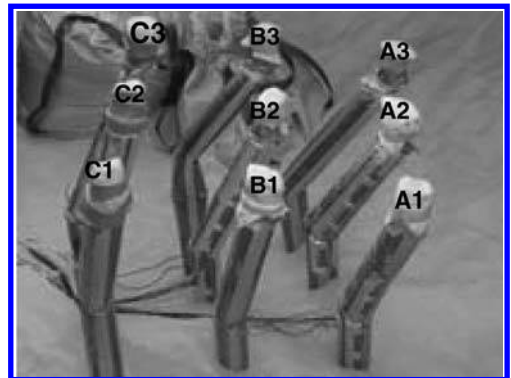


Figure 22. Damage to piles.

A1–A3 buckled at 1.2 m below their pile heads, the depth of which corresponds to the depth at which the measured bending strains take a peak (Figs. 19g–i). In contrast, Piles C1–C3 deform at 0.7 m below their pile

heads, the depths of which is shallower than the depth at which the measured bending strain take a peak, i.e., a depth of 1.0 m (Fig. 19a–c). This is probably because the failure firstly occurred in Piles A1–A3, which led to the redistribution of bearing load within the pile group, causing the buckling of the other piles at a smaller depth.

3.7 Soil-pile-structure interaction in liquefiable sand using E-Defense shaking table

The soil-pile-structure interaction studies with liquefiable sand using E-defense shaking table was made in late FY2006 (Suzuki et al., 2008). The sand, piles and foundation used for the tests were identically the same as those used for the tests with dry sand, made in the preceding fiscal year. The sand deposit prepared in the laminar box consisted of two layers, including a liquefiable layer with a thickness of 5.4 m and an underlying non-liquefiable layer with a thickness of 0.8 m. After setting a pile group in the laminar box, the bottom non-liquefiable layer around the pile group was made with cement-mixing sand and that away from the pile group with air-pluviation and compaction of the sand. The dry sand was also air-pluviated to form the liquefiable layer. The relative densities of the compacted and liquefiable sand layers were about 90% and 60%, respectively.

To minimize the occupation time of the shaking table platform, the above preparation processes were made outside the shaking table platform, and the



Figure 24. Laminar box being covered for saturation.

laminar box including the dry-sand-pile-foundation system was then moved on to the shaking table by two gigantic cranes, as shown in Figure 23. The dry sand was then saturated by percolating water from the bottom of the laminar box under a vacuum on the shaking table to avoid unexpected soil disturbance after saturation. Figure 24 shows that the laminar box was being covered with a large bell-shaped cap to form a vacuum. The groundwater table was set at a depth of 0.4 m below the ground surface.

Table 2 summarizes the test conditions. Model A did not carry any superstructure, whereas Model B carried a superstructure of 12 tons with four steel columns of 1.0 m height. About 900 sensors including strain gauges, accelerometers, velocity meters, earth pressure transducers, pore water pressure transducers, displacement transducers, settlement meters and load cells were placed in the sand deposit as well as on the pile-structure model.

The tests were conducted with two different ground motions, Takatori and Tottori, as defined in section 3.5. Two horizontal component motions were used as the input to the shaking table with the largest horizontal acceleration adjusted from 0.3 m/s^2 to 3.0 m/s^2 , as shown in Table 3. The final three tests were run with Model B in turn using Tottori with a peak acceleration of 0.8 m/s^2 , Takatori with 0.8 m/s^2 , and Takatori with 3.0 m/s^2 . These tests are hereby called as Tottori-80, Takatori-80 and Takatori-300. Further details of the test apparatus and procedure have been described elsewhere (Tabata et al., 2007).



Figure 23. Laminar box carried by two cranes.

Table 2. Test conditions.

Test model	Superstructure	Input motion	Maximum input acceleration
Model A	No	Tottori	0.3 m/s ² , 0.8 m/s ²
		Takatori	0.3 m/s ² , 0.8 m/s ²
		Tottori	0.3 m/s ² , 0.8 m/s ²
Model B	Yes	Takatori	0.3 m/s ² , 0.8 m/s ² , 3.0 m/s ²

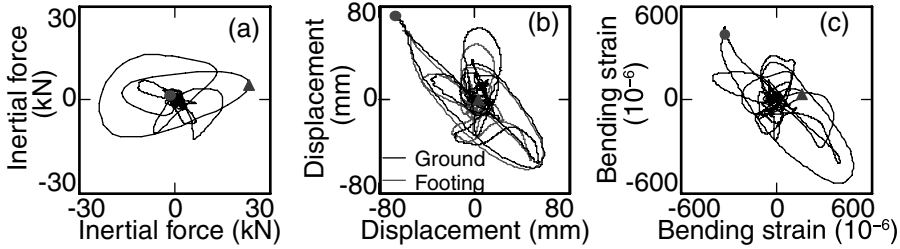


Figure 25. Horizontal loci of inertial force, displacement and bending moment in Takatori-80.

Although pore pressure built up slightly, soil liquefaction did not occur in Tottori-80. In contrast, it did occur in Takatori-80 with the same peak acceleration as well as in Takatori-300 with a greater input acceleration. The pore water pressures in Takatori-300 rose abruptly leading complete liquefaction at only 4 s. The ground displacement becomes larger and the de-amplification of the superstructure becomes more pronounced than those in Takatori-80. This led to a larger bending strain of about 3000 μ , leading to the yielding of the pile heads as well as residual foundation displacements of 66 mm on the east and of 43 mm on the south and foundation settlements of 16 mm on the southeast side and of 8 mm on the northwest sides of the foundation.

3.8 Inertial and kinematic effects on pile stress and failure mode in liquefiable sand

To investigate distribution of pile stresses within the pile group in the liquefaction test, Figure 25 shows the loci on the horizontal plane of the inertial force, the displacements of the ground surface and foundation, and the bending strain at the head of Pile A1 in Takatori-80. Figure 26 shows the distributions with depth of bending and axial strains for the nine piles at two instants (i.e., at 2.9 s (before liquefaction) and at 7.9 s (after liquefaction)) in Takatori-80, which correspond to the instants marked by square and circle symbols on the loci shown in Figure 25.

A large inertial force acts eastward at 2.9 s (the square symbol in Fig. 25a), accompanied by a very small ground displacement. This not only induces bending strains that decrease rapidly with depth

(Figs. 26a–c) but also creates the largest bending strain at the heads of the leading piles (Piles A1, A2 and A3), probably due to the pile group effects, in which the leading piles attract the largest earth pressure among others, such as that shown in section 3.6.

In addition, the largest axial compression (negative) strain develops on the leading side of the pile group (Piles A1, A2 and A3), with the largest axial extension (positive) strain on the rear piles (Piles C1, C2 and C3) (Figs. 26g–i). The axial strain in this case decreases with depth. In contrast, a large ground displacement occurs northwestward with a small inertial force at 7.9 s, as indicated with the circle symbol (Figs. 25a, b). At this instant, large bending strains occur not only at the pile heads but also at the bottom of the liquefied layer. The bending strain at the pile heads is the smallest in Pile A1 located at the following side (the southeast side) among others (Figs. 26d–f). The axial strains on both compression and extension sides do not seem to decrease with depth (Figs. 26j–l), the trend of which is different from that before liquefaction, and suggest that the positive friction having reduced the axial stress in piles becomes smaller after liquefaction.

Figures 27 and 28 show loci of horizontal plane of the inertial force, ground surface and foundation displacements, bending strain at the head of Pile A1 and distributions of bending and axial strains for the nine piles at 4.2 s in Takatori-300. The ground displacement and the inertial force increase southeastward at 4.2 s as indicated with a circle symbol (Fig. 27), causing large bending strains at the pile heads. The bending strain at the pile head takes the largest value in the leading pile (Piles A1, A2 and A3), (Figs. 28a–c) but the pile

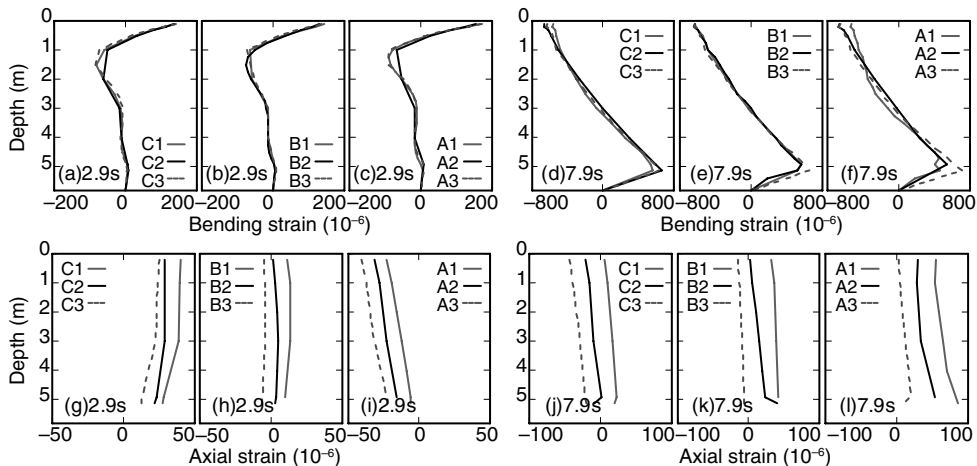


Figure 26. Distribution of bending and axial strains in Takatori-80.

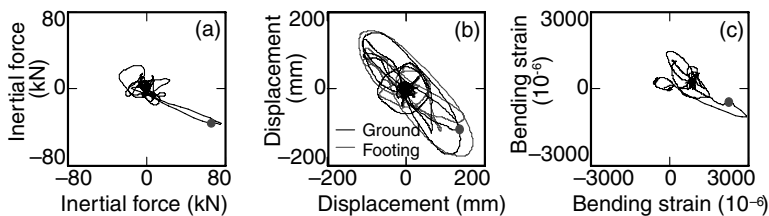


Figure 27. Horizontal loci of inertial force, displacement and bending strain in Takatori-300.

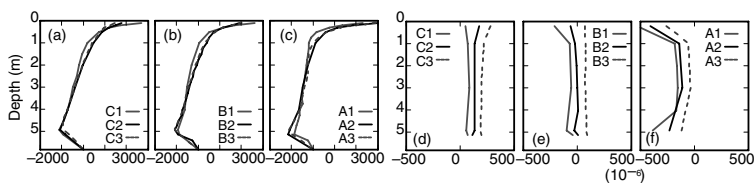


Figure 28. Distribution of bending and axial strains in Takatori-300.

group effects are less significant compared with those observed in dry sand. The axial strain also increases significantly at the pile heads on the leading side (Piles A1, A2 and A3) (Figs. 28d–f).

3.9 Pile group effects in centrifuge shaking table tests

Suzuki et al., (2006) investigated seismic behavior of pile group through the centrifuge model tests on pile groups with different pile spacing in both dry and liquefiable sands. They further showed that the pile group effects are different between dry and liquefiable sands and dependent on pile spacing. [Figure 29](#)

summarises their test results in which the distribution of shear force at pile head within three pile groups subjected to leftward movement is plotted for different pile spacing (7.5, 3.75, and 2.5 diameter spacing center to center). The shear force ratio in the figure is the measured shear force of each pile normalized with respect to the average shear force in the pile group. The test results lead to the followings:

1. In the non-liquefied ground, the shear forces at the pile heads tend to become larger in the leading row than in the trailing rows with decreasing pile spacing. This is because the subgrade reaction in non-liquefied ground is induced by an increase

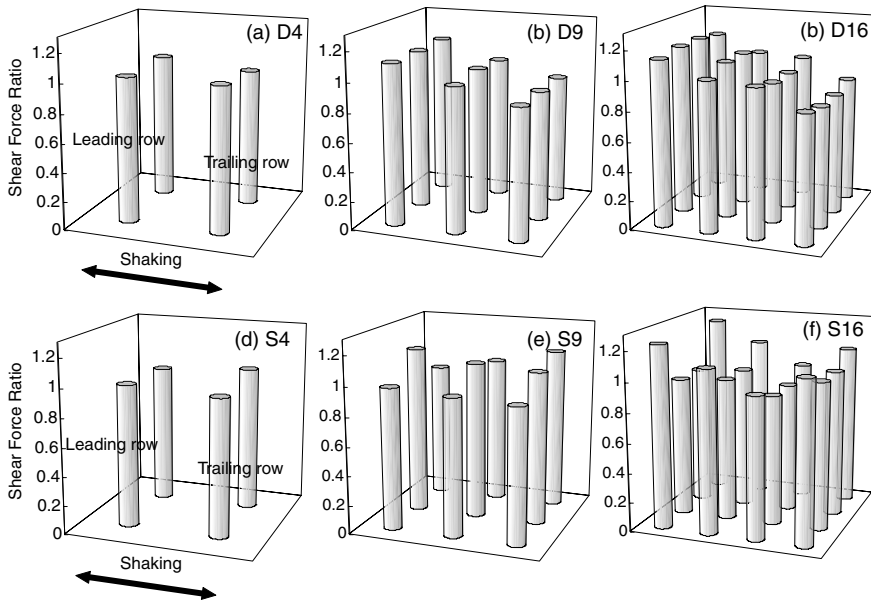


Figure 29. Distribution of shear forces at pile heads.

in normal stress on the compression side of a pile and such an increase is the largest in the leading piles due to shadowing effects of pile group. Such pile group effects are apparent at a pile spacing of 3.75.

2. In the liquefied ground, the shear forces at the pile heads tend to become larger in the outside piles than in the inside piles as the pile spacing decreases. This is probably because, in the liquefied ground, the subgrade reaction is induced by the difference in pore water pressure changes between compression and extension sides of a pile, as shown in section 3.5. This condition is well developed in the perimeter piles but may not be the case in the inside piles. This is because the compression stress induced by one pile may be reduced by the extension stress by the adjacent pile in soil inside a pile group. This could lead to a decrease in the difference in pore water pressures on both sides of the inside piles as well as the smaller subgrade reaction in the inside piles. Such pile group effects are apparent only at a pile spacing of 2.5.
3. The distributions of shear force at the pile head in both dry and liquefiable sand with pile spacing of 7.5 and 3.75 are consistent with the moment distributions obtained from the large shaking table tests described in sections 3.1–3.6.
4. The critical pile spacing beyond which pile group effects become notable appears to be smaller in dry sand than in liquefied sand, probably due to the difference in strain level between the two.

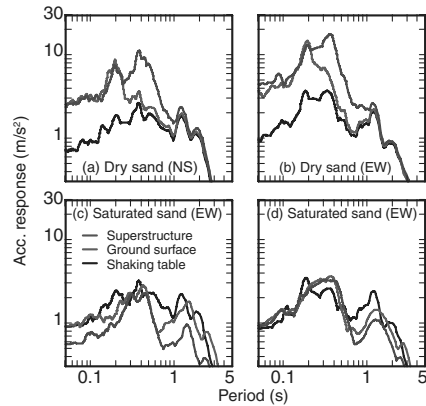


Figure 30. Acceleration response of superstructure, ground surface and input motion.

3.10 Structural response in non-liquefied and liquefied grounds in shaking table tests

Figure 30 shows the acceleration responses of the superstructure, ground and shaking table, which are computed from the observed acceleration. The figure confirms that the field evidence in which soil liquefaction de-amplified the ground motions particularly in the period range less than 1s, reducing the response of structures as well as the damage to superstructure in the liquefied and laterally spreading areas.

4 PSEUDO-STATIC ANALYSIS FOR EVALUATING PILE PERFORMANCE

4.1 Beam-on-Winkler-springs method

Seismic design of foundations may be made using either dynamic response analysis or pseudo-static analyses. In this chapter, the later based on Beam-on-Winkler-springs method is described, with emphasis placed on how the kinematic effects determined in the preceding chapters with recent other findings are incorporated.

Figure 31 schematically illustrates the soil-pile-structure interaction in non-liquefiable and liquefiable soils during and after an earthquake (Tokimatsu, 2003a). Only the inertia force from the superstructure dominates in dry or non-liquefied sand where both cyclic and permanent ground displacements are negligibly small (Case I: Fig. 31a). Not only the inertial force but also the kinematic force induced by cyclic ground displacement comes to play an important role when soil liquefies (Cases II: Fig. 31b) and the kinematic force due to permanent ground displacement may have a dominant effect when lateral ground spreading occurs (Case III: Fig. 31c). These loading conditions should be properly considered in stress and deformation analysis of piles.

Simplified pseudo-static design methods using p-y curves for pile foundations (AIJ, 1988, 2001; Railway Technical Research Institute, 1997), i.e., a single pile supported on nonlinear Winkler springs as shown in Figure 32, are based on the following equation (Nishimura, 1978; Tokimatsu & Nomura, 1991):

$$EI \frac{d^4 y}{dz^4} = k_h B \{f(z) - y\} \quad (1)$$

in which E and I are Young's modulus and moment of inertia of pile, y is horizontal displacement of pile, z is depth, k_h is coefficient of horizontal subgrade reaction, B is pile diameter, and $f(z)$ is either zero throughout the depth (Case I), cyclic ground displacement (Case II), or permanent ground displacement (Case III), to be applied to the pile through p-y springs as shown in Fig. 31b or 31c. The value of $\{y-f(z)\}$ in the equation is the relative displacement between soil and pile. The combination of inertial force and ground displacement may be determined based on the natural period of the superstructure (T_b) relative to that of the ground (T_g), according to the following method:

Method I ($T_b < T_g$): The pile stress may be estimated, provided that the maximum (design) inertial force and ground displacement are applied to the pile at the same time (Fig. 32a).

Method II ($T_b > T_g$): The pile stress may be given by the square root of the sum of the squares of the two values estimated, provided that the maximum (design) inertial force and ground displacement are applied to the pile separately (Fig. 32b).

To make the simplified pseudo-static analysis, one should know the following information that could control the kinematic effects concerning: (1) cyclic ground deformation profile and/or permanent ground deformation profile, (2) seismic earth pressure acting embedded foundation, and (3) horizontal subgrade reaction of pile, i.e., p-y spring.

4.2 Cyclic and permanent ground displacement

Tokimatsu & Asaka (1998) proposed a preliminary chart for estimating cyclic ground displacement to be developed in liquefied ground during earthquakes, which is similar to the one for the liquefaction evaluations using SPT N-values. The method consists of the following steps:

1. Determine adjusted SPT N-values, N_a , and equivalent cyclic stress ratios during earthquake, τ_{av}/σ'_{vo} , with depth.
2. Estimate γ_{cy} from Figure 33a, with depth.
3. Estimate a cyclic ground displacement profile, $f_{cy}(z)$, by integrating γ_{cy} with depth, assuming γ_{cy} develops in the same horizontal direction.

$$f_{cy}(z) = \int_z^H \gamma_{cy}(z) dz \quad (2)$$

Similarly, Tokimatsu & Asaka (1998) proposed preliminary charts for estimating permanent ground displacement to be developed near a waterfront area with a horizontally stratified deposit subjected to lateral spreading, as follows:

1. Estimate the horizontal ground surface displacement at the waterfront, D_o , by:

$$D_o = \min(f_{\max}(0), D_w) \quad (3)$$

in which D_w is displacement of the quay wall and $f_{\max}(z)$ is maximum possible ground surface displacement of the liquefied soil determined by integrating γ_{\max} with depth, using Equation 2 with γ_{cy} , $f_{cy}(z)$, and Figures 33a replaced by γ_{\max} , $f_{\max}(z)$, and Figure 33b.

2. Evaluate the horizontal permanent ground displacement, D, at a distance of X from the waterfront based on Figure 34 or by:

$$D(x) = (1/2) \frac{x}{10D_o} D_o \quad (4)$$

3. Estimate a ground displacement profile with depth as:

$$f_{pm}(x, z) = D(x) \frac{f_{\max}(z)}{f_{\max}(0)} \quad (5)$$

in which x is distance from the waterfront.

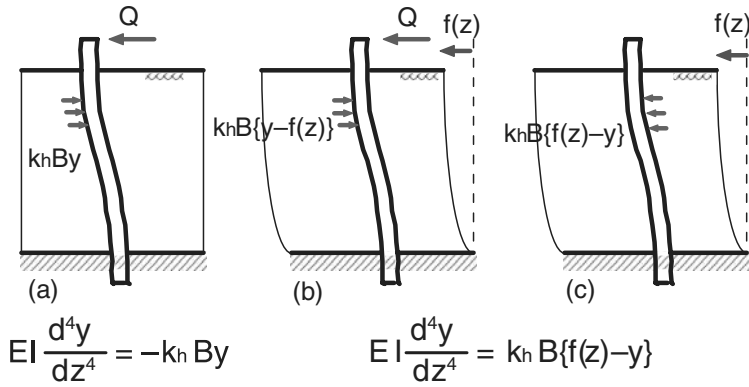


Figure 31. Simplified pseudo-static design methods using p–y curves for pile foundations.

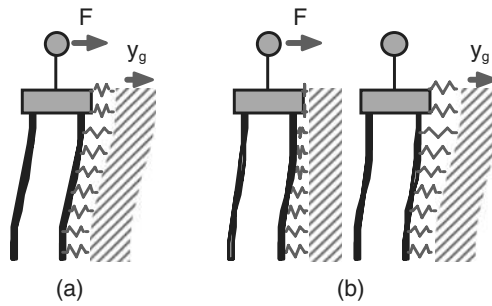


Figure 32. Combination of inertial force and ground displacement.

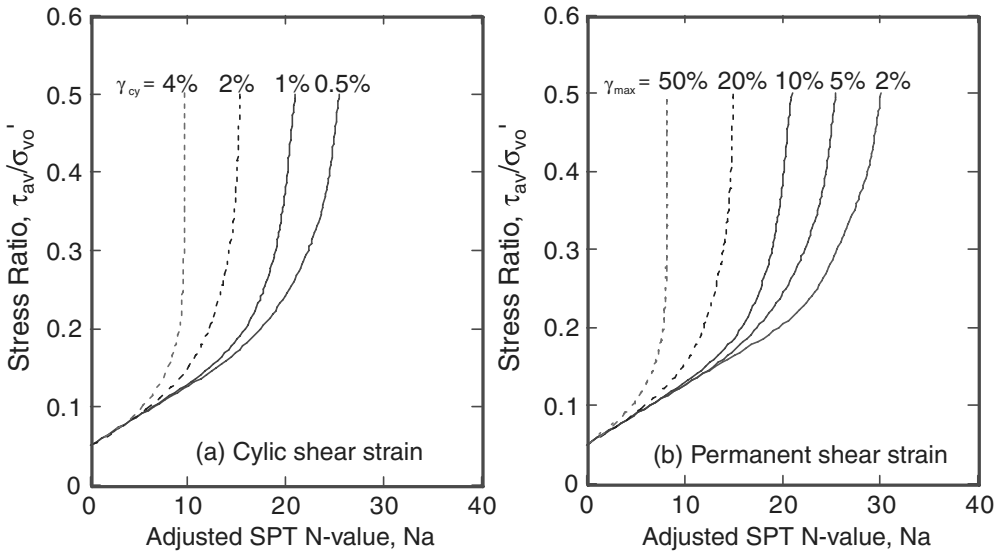


Figure 33. Maximum cyclic and permanent shear strains to be developed in liquefied and laterally spreading ground during and after earthquakes.

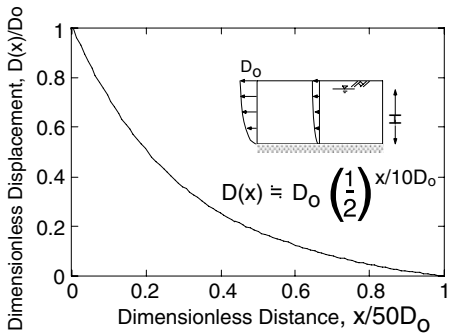


Figure 34. Relation of horizontal ground displacement with distance from waterfront.

4.3 Seismic earth pressure acting on embedded foundation

The total seismic earth pressure, P_E , acting on the embedded foundation/pile cap, as shown in Figure 35, may be defined as (Tamura et al., 2002):

$$P_E = P_{Ep} - P_{Ea} = \frac{1}{2} \gamma H^2 B (K_{Ep} - K_{Ea}) \quad (6)$$

in which γ is unit weight of soil, H and B are height and width of foundation and K_{Ea} and K_{Ep} are the coefficients of seismic earth pressure in active and passive sides and may be expressed by the following equations (Mononobe, 1924; Okabe, 1924; Zhang et al., 1998):

$$K_{Ea} = \frac{2 \cos^2(\phi - i)}{\cos^2(\phi - i)(1 + R) + \cos i \cos(\delta_{mob} + i)(1 - R)I_{E.1}} \quad (7)$$

$$K_{Ep} = 1 + \frac{1}{2}(R - 1) \left[\frac{\cos^2(\phi - i)}{\cos i \cos(\delta_{mob} + i)I_{E.2}} - 1 \right] \quad (8)$$

$$\left(\frac{I_{E.1}}{I_{E.2}} \right) = \left[1 \pm \sqrt{\frac{\sin(\phi + \delta_{mob}) \sin(\phi - i)}{\cos(\delta_{mob} + i)}} \right]^2 \quad (9)$$

$$\tan i = k_i \quad (10)$$

$$R = \max \left[-1, - \left(\frac{|\Delta_r|}{\Delta_a} \right)^{0.5} \right] \quad (\text{Active side}) \quad (11)$$

$$R = \min \left[3, 3 \left(\frac{|\Delta_r|}{\Delta_p} \right)^{0.5} \right] \quad (\text{Passive Side}) \quad (12)$$

$$\delta_{mob} = \frac{1}{2}(1 - R)\delta_a \quad (\text{Active Side}) \quad (13)$$

$$\delta_{mob} = \frac{1}{2}(R - 1)\delta_p \quad (\text{Passive Side}) \quad (14)$$

in which ϕ is internal friction angle of sand, i is angle of seismic coefficient in the horizontal direction (k_i), R is lateral strain constraint and is somewhere between -1 and 0 in the active side and 0 and 3 in

the passive side (Fig. 36), Δ_r is relative displacement between soil and foundation, δ is friction angle of the surface of the foundation, δ_a and δ_p are friction angles of sand at the active and passive states, and Δ_a and Δ_p are reference relative displacements at active and passive states, expressed as:

$$\Delta_a = aH \quad (15)$$

$$\Delta_p = bH \quad (16)$$

in which $a = 0.001-0.005$ and $b = 0.05-0.1$.

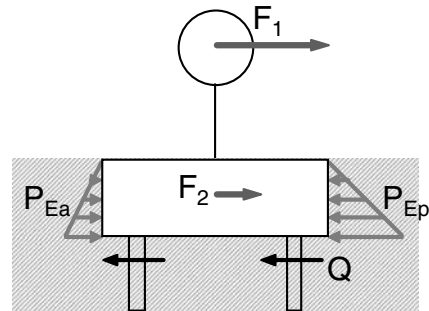
The effectiveness of the proposed method has been described elsewhere (Tokimatsu et al., 2003b).

4.4 Subgrade reaction of pile

The relation between subgrade reaction and relative displacement is given by:

$$p = k_h B y_r \quad (17)$$

in which p is subgrade reaction, B is diameter of pile and y_r is relative displacement, and k_h is coefficient subgrade reaction given by:



F: Inertial force ($= F_1 + F_2$)
P_E: Total earth pressure ($= P_{Ep} - P_{Ea}$)
Q: Shear force at pile head

Figure 35. Earth pressure acting on embedded foundation.

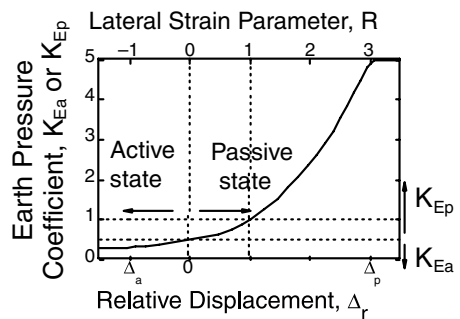


Figure 36. Relation of relative displacement and earth pressure coefficient.

$$K_h = K_{h1} \frac{2}{1 + |y_r/y_1|} (1 - U)^\alpha \quad (18)$$

in which U is pore water pressure ratio and α is constant being equal to 0.5–1.0, y_1 is reference value of y_r , and k_{h1} is reference value of k_h and can be estimated by (Architectural Institute of Japan, 2001):

$$k_{h1} = 80E_0B_0^{-0.75} \quad (19)$$

$$E_0 = 0.7N \quad (20)$$

in which E_0 (MN/m²) is modulus of deformation, N is SPT N-value, and B_0 is pile diameter in cm.

From Equations 17 and 18, the subgrade reaction is given by:

$$p = \frac{2K_{hl}}{1 + |y_r/y_1|} (1 - U)^\alpha B y_r \quad (21)$$

In Equation 21, with y_r enlarged to infinite, the maximum subgrade reaction, p_{\max} , is given by:

$$p_{\max} = 2K_{hl}(1 - U)^\alpha B y_1 \quad (22)$$

To estimate pile performance in the field where the recovery in effective stress is unknown, both P_{y1} and k_{o1} of liquefied soils may be assumed, for example, according to the following equations, as illustrated in Figure 37 (AIJ, 2001).

$$K_{h1} = \beta_1 K_{ho} \quad (23)$$

$$P_{y1} = \alpha_1 P_{yo} \quad (24)$$

in which p_y is ultimate lateral resistance defined as:

$$p_{yo} = 3K_p \sigma'_{vo} \quad (25)$$

in which σ'_{vo} is the initial effective confining pressure, K_p is the Rankine passive earth pressure coefficient and α_1 and β_1 are scaling factors in terms of SPT

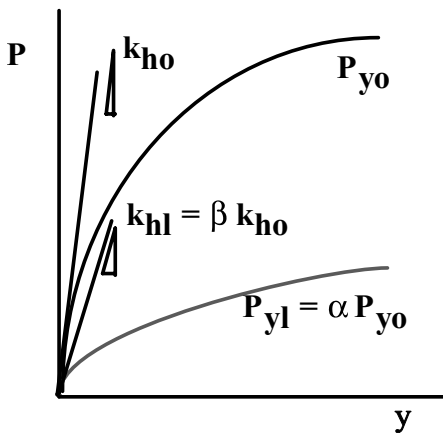


Figure 37. Analytical model for p-y spring.

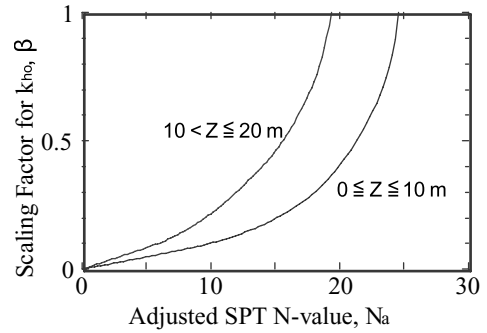


Figure 38. Scaling factor for p-y spring.

N-value as shown in Figure 38 where α_1 is tentatively equal to β_1 (AIJ, 2001). The scaling factor in the figure is 0.05, 0.10, and 0.40 for loose, medium, and medium dense sands, respectively, which are equivalent to the recovery in effective stress ratio around a pile in liquefied soil having a similar soil density and at a relative displacement of about 3–5% of pile diameter (Japan Road Association, 1997; Tokimatsu et al., 2002).

5 EFFECTIVENESS OF PSEUDO-STATIC ANALYSIS FOR ESTIMATING PILE PERFORMANCE

Tokimatsu and Asaka (1998) and Tokimatsu (2003a) applied the abovementioned pseudo-static analysis to well-documented case histories. They concluded that it could reproduce qualitatively the significant features of the pile damage in the field and could be used to explain the effects of lateral spreading on pile damage in the field. In addition, they suggested that the difference in deformation modes observed within a building in the laterally spreading zone was presumably induced by the difference in spatial variations of lateral spreading. The accumulation of data from the large shaking table tests further offers an opportunity to examine the effectiveness of the pseudo-static analysis. Described in the following is a comparison of such analytical results with the shaking table test results shown in Chapter 3.

5.1 Simulation of stresses in piles in level ground

To demonstrate the effectiveness of the pseudo-static analysis, the maximum bending moment, shear force and axial force in all the thirty-one tests described in Section 3.1 were computed (Tokimatsu et al., 2005b). It is assumed that the inertial force is equal to the observed maximum and that the ground displacement above the base of the foundation is equal to the observed maximum at the ground surface and

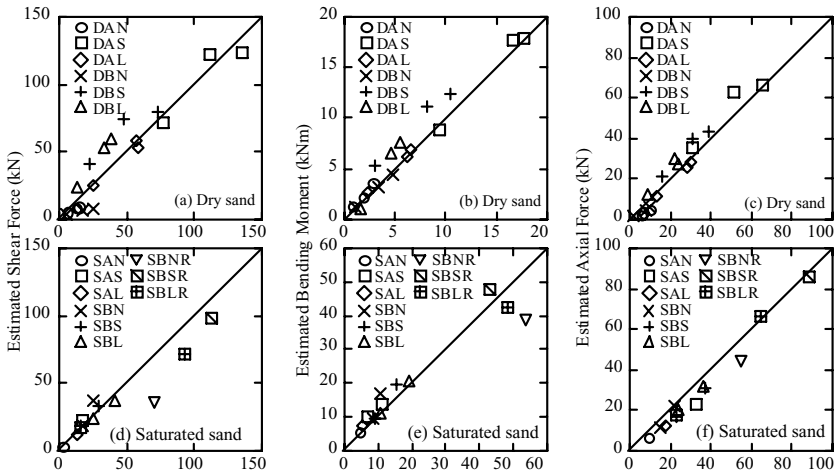


Figure 39. Comparison of estimated pile stresses with observed pile stresses.

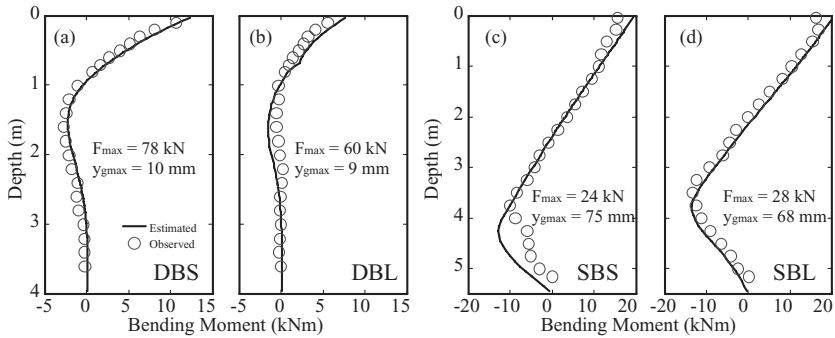


Figure 40. Distributions of observed and estimated bending moment in shaking table tests.

decreases linearly to zero at the base of the laminar box in dry sand or at the bottom of the liquefied layer in saturated sand. The N-value to be used in Equation 20 is estimated from the CPT resistance measured prior to each shaking table test. It is also assumed that α is 0.1 for liquefied sand and 1.0 for the non-liquefied sand and gravel, y_1 in Equation 18 is 1.0% of the pile diameter, ϕ is 30 degrees and that δ_a and δ_p are 0.5% and 5% for the height of the foundation.

Figure 39 compares the estimated maximum bending moments, shear forces, and axial forces at the pile heads with observed ones. The computed pile stresses agree reasonably well with the observed values irrespective of such factors as input acceleration, ground displacement, pile stiffness, natural periods of structure and ground, and presence of embedment. The good agreement indicates that the proposed pseudo-static analysis considering such factors as the combination of inertial and kinematic effects, earth pressure acting on embedded foundation and scaling

factor for p-y spring is promising for estimating pile stress during earthquakes.

Figure 40 compares the observed and computed moment distributions of the four tests (DBS, DBL, SBS, and SBL). The computed moment distributions agree reasonably well with the observed ones. The good agreement indicates that the proposed pseudo-static analysis considering such factors as the combination of inertial and kinematic effects, earth pressure acting on embedded foundation and scaling factor for p-y spring is promising for estimating stresses in piles in level ground during earthquakes.

5.2 Simulation of stresses in pile in laterally spreading ground

To estimate the stresses in the stiff and flexible piles in the laterally spreading ground in Section 3.3, it is assumed that the ground displacement is equal to the observed one, the value of which is 200 mm at 5.5 s and

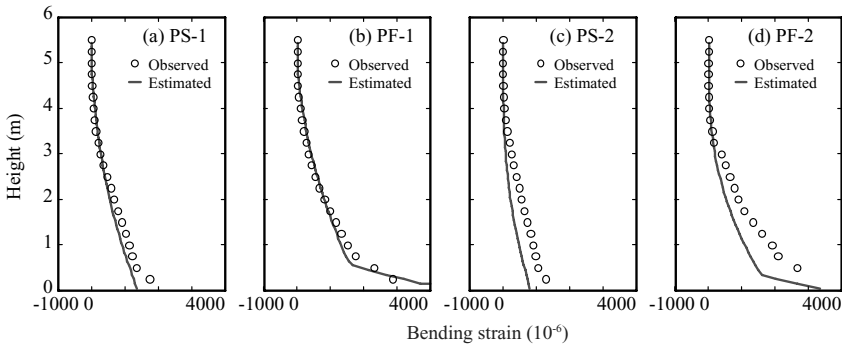


Figure 41. Distributions estimated and observed bending strains in initial stage of laterally spreading.

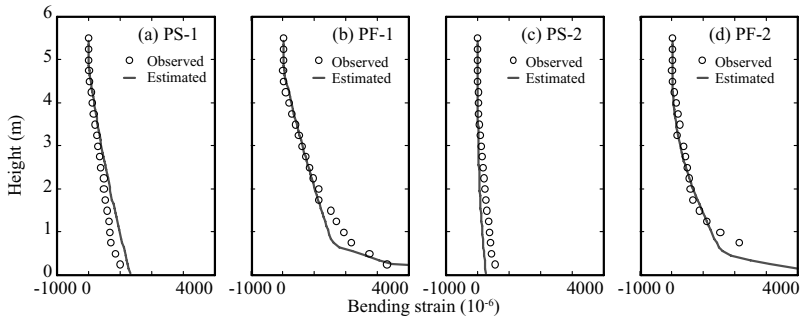


Figure 42. Distributions estimated and observed bending strains in later stage of laterally spreading.

400 mm at 20 s. k_{h1} is given by the N-value computed from the CPT resistances measured prior to each shaking table tests and γ_1 is one percent of a pile diameter. β is assumed to change from 0.1 in 5.5 s to 0.02 in 20 s, to take into account the degradation of soil stiffness during lateral spreading (Suzuki & Tokimatsu, 2009).

Figures 41 and 42 compare the estimated and observed bending strains of the stiff and flexible piles for the two instants, i.e. 5.5 s and 20 s, in Tests 1 and 2. The estimated bending strains of both flexible and stiff piles agree reasonably well with the observed ones. Namely, that of the flexible pile is almost the same between the two instants (Figures 41b, d and 42b, d), while that of the stiff pile is smaller at 20 s than at 5.5 s, despite the increased ground displacement at 20 s. The decrease in bending strain of the stiff pile is due probably to the degradation of soil stiffness induced by the large relative displacement. Probably, the subgrade reaction of the stiff pile reaches the ultimate value due to large relative displacement before the large strain enough to cause pile yielding to develop. In contrast, the flexible pile yields before the subgrade reaction reaches the ultimate value. In addition, the estimated bending strain of the stiff pile is

larger in Test 1 than in Test 2, while that of the flexible pile is almost the same between the two. This suggests that the effects of non-liquefied crust layer are more significant on the stiff pile than on the flexible pile. The abovementioned trends in estimated bending strains are in good agreement with the observed ones.

5.3 Simulation of stresses in pile group in dry sand

To estimate the stresses in the pile group in both dry and liquefied sands described in Section 3.5–3.8, it was assumed that the inertial force and the ground surface displacement were equal to the observed ones when the bending moment and axial force become the maxima, and that the ground surface decreased linearly to zero at the base of the laminar box for dry sand or at the bottom of the liquefied layer for saturated sand. The coefficient of horizontal subgrade reaction of each pile in liquefied sand was assumed to be 0.1 times that in dry sand, regardless of the location of the pile. Such a scaling factor in dry sand, on the contrary, was assumed to vary depending on the location, i.e., 1.0 in the front row, 0.7 in the second row, and 0.4 in the third row. The bending moment and

axial force in piles subjected to the two-dimensional shaking were then estimated as the sum of those obtained by applying the two orthogonal components separately.

Figures 43 and 44 compare the computed maximum bending moment distributions for nine piles with the observed ones. Figure 45 compares the maximum axial force at pile head with the observed ones. The computed bending moment and axial force are in good agreement with the observed ones in the two tests. This suggests that the bending moment and axial force in both non-liquefied and liquefied ground can be estimated by considering the combined effects of inertial and kinematic forces in the two-dimensional horizontal plane.

5.4 Sensitivity analysis

To investigate crucial factors for reasonably estimating pile stress, Tokimatsu et al., (2005b) made a sensitivity study of the moment at the pile head using the same pseudo-static analysis on soil-pile-structure models shown in Figure 46.

The sensitivity of the moment at the pile head may be estimated through the following moment ratio:

$$D = \frac{M_c}{M_0} \quad (26)$$

in which M_0 is the reference moment computed for a test with the maximum inertial force, F_{max} , and ground displacement, $y_{g,max}$, observed in the test as well as with a scaling factor of 0.1 for p-y spring and the earth pressure model described in the previous

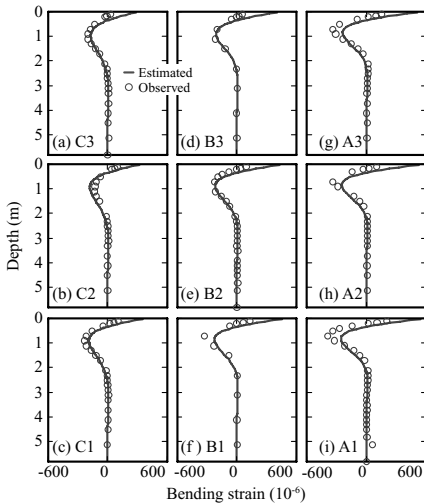


Figure 43. Distributions estimated and observed bending strains in dry sand.

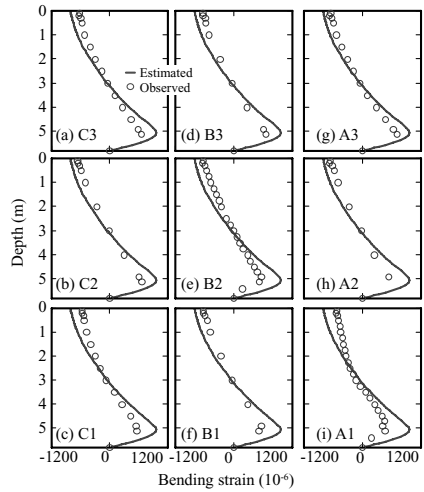


Figure 44. Distributions estimated and observed bending strains in saturated sand.

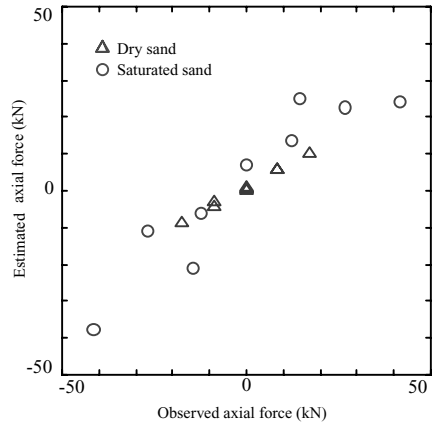


Figure 45. Comparison of estimated and observed axial forces.

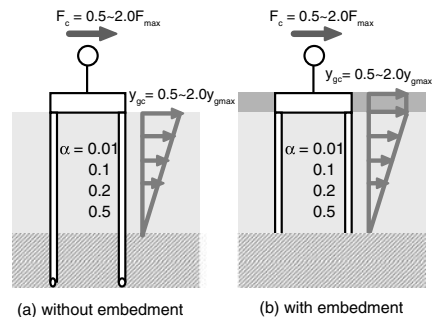


Figure 46. Soil-pile-structure models in sensitive analysis.

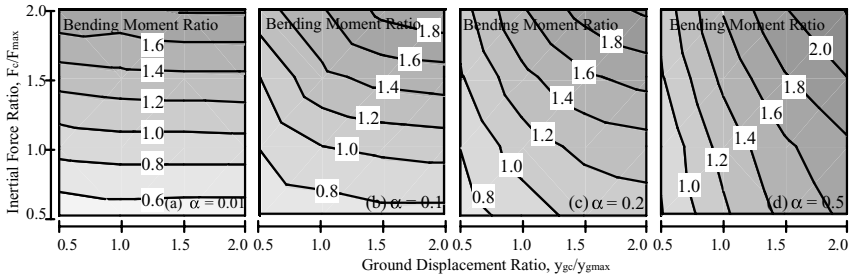


Figure 47. Contour of bending moment ratios of pile without foundation embedment.

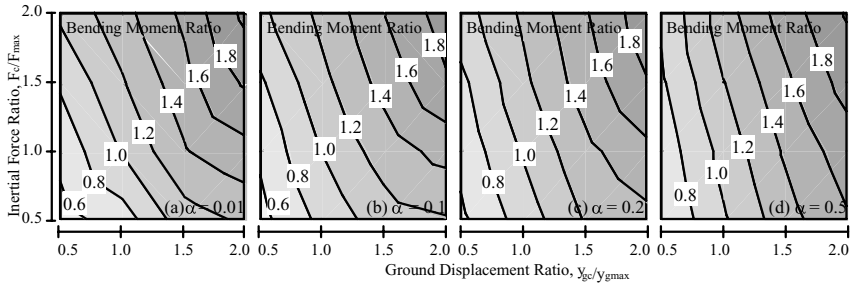


Figure 48. Contour of bending moment ratio of pile with foundation embedment in non-liquefiable crust.

chapter; and M_c is the one computed for the same test but with different values of the parameters. In the computation of M_c , the magnitudes of inertial force and ground surface displacement are varied from 0.5 to 2.0 times the observed maximum ones, with a scaling factor for p–y spring from 0.01 to 0.5. The ratios of the assumed inertial force, F_c , and ground displacement, y_{gc} , with respect to the observed maxima, F_{max} and y_{gmax} , are hereby called inertial force ratio ($= F_c/F_{max}$) and ground displacement ratio ($= y_{gc}/y_{gmax}$). It is assumed that the ground displacement is constant above the bottom of the foundation, decreasing linearly to zero at the bottom of the liquefied layer, and that the pile is always elastic. Two test models SAS (without foundation embedment) and SBS (with foundation embedment in a non-liquefiable crust) that were subjected to a maximum input acceleration of about 2.4 m/s^2 were considered in the analysis.

Figures 47 and 48 show contours of the moment ratio in a two-dimensional plane, the vertical and horizontal axes of which are the inertial force ratio and ground displacement ratio. Figure 47 shows that the contours with a scaling factor less than 0.1 tend to be horizontal but that those with a larger scaling factor incline from the upper left to the lower right and becomes more vertical than horizontal when $\alpha = 0.5$. This is because the liquefied soil with a small scaling factor (with low stiffness) can neither resist inertial

force from superstructure nor push piles while that with a large scaling factor (with high stiffness) can do both. This suggests that the inertial force effects dominate over the ground displacement in controlling stress in piles without foundation embedment when $\alpha < 0.1$ but that both inertial and kinematic effects have strong effects when $\alpha > 0.2$ and may dominate when $\alpha > 0.5$.

Figure 48 indicates that the contour lines with any scaling factor incline from the upper left to the lower right and are more vertical than horizontal irrespective of α . The larger the value of α , the more vertical the contour line. This suggests that the effect of ground displacement becomes dominant when the foundation is embedded in a non-liquefiable crust. This is because the earth pressure acting on the embedded foundation, which does not exist in the case shown in Figure 47, could play an important role in controlling pile stresses.

Figures 49 and 50 show the variation of the moment ratio against either inertial force or ground displacement ratio with the other fixed to unity for $\alpha = 0.01, 0.1, 0.2$ and 0.5 in the two test models. For the piles without foundation embedment (Fig. 49), the moment ratio for $\alpha = 0.01$ is linearly proportional to the inertial force ratio (Fig. 49b) but almost constant against the ground displacement ratio (Fig. 49a). The moment ratio for $\alpha = 0.5$, in contrast, is insensitive to the inertial force ratio (Fig. 49b) but sensitive to the ground displacement ratio (Fig. 49a). This suggests

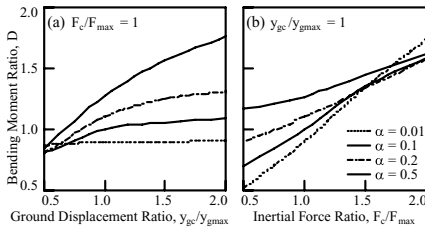


Figure 49. Relation of bending moment ratios with ground displacement or inertial force for pile with foundation embedment.

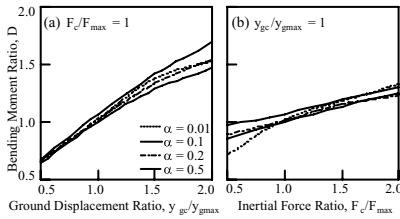


Figure 50. Relation of bending moment ratios with ground displacement or inertial force for pile with foundation embedment in non-liquefiable crust.

that the error in inertial force is crucial but the error in ground displacement may not be equally crucial in the liquefied soil with low stiffness, but that the error in ground displacement may become critical in the liquefied soil with high stiffness.

Unlike the case without foundation embedment as shown in Figure 50, the pile moment ratio with foundation embedment in a non-liquefiable crust in Figure 50 is more sensitive to ground displacement ratio than inertial force ratio. This suggests that the ground displacement may be significant and, in some cases, more crucial than the inertial force. It is interesting to note that the computed moment ratios at the pile head with foundation embedment in a non-liquefiable crust layer are almost the same regardless of α in Figure 50. This is probably because the earth pressure acting on the embedded foundation becomes dominant, masking the effects of scaling factor for p - y spring. This suggests that the scaling factor for liquefied sand seems less important in estimating stress at the pile head with foundation embedment in a non-liquefiable crust layer. It is noted that this may not be the case for pile stress at the bottom of the liquefied soil.

6 CONCLUSIONS

The field investigation of pile foundations that experienced the 1995 Hyogoken-Nambu earthquake has shown the significant effects of cyclic and permanent

ground displacement in both liquefied and lateral spreading grounds on damage to pile foundations. Soil liquefaction that deamplified the ground motions particularly in the period range less than 1s, in contrast, lessened the damage to superstructure in the liquefied and laterally spreading areas, compared with the extensive superstructure damage in non-liquefied area.

The large shaking table tests conducted to estimate the effects of dynamic soil-pile-structure interaction in both dry and saturated sands have shown the following:

1. If the natural period of the structure is less than that of the ground, the kinematic force tends to be in phase with the inertial force, increasing the stress in piles. The maximum pile stress tends to occur when both inertial force and ground displacement take the peaks in the same direction.
2. If the natural period of the structure is greater than that of the ground, the kinematic and inertial forces tend to be out of phase, restraining the pile stress from increasing. The maximum pile stress hardly occurs when both inertial force and ground displacement take the peaks at the same time.
3. The above findings are valid for both dry and saturated liquefied deposits. The maximum pile stress may be estimated by applying both the inertial and kinematic forces on the pile at the same time, if the natural period of the structure is less than that of the ground. It may be estimated as the square root of the sum of the squares of the two moments estimated by applying the inertial and kinematic forces on the pile separately, if the natural period of the structure is greater than that of the ground.

Effects of stress states in soil around piles on subgrade reaction development in liquefied and laterally spreading ground have been investigated through large shaking table tests with both level ground and inclined ground. Discussions on the test results have shown the following:

1. In both liquefied level ground and laterally spreading ground, the extension and compression stress states develop on the rear and front sides of a pile with increasing relative displacement between soil and pile. The pore water pressure on the extension side decreases due to the combined effects of extension and shear stresses, while that on the compression side maintains almost constant due to the adverse effects of compression and shear stresses.
2. The increase in horizontal subgrade reaction of a pile in liquefied and laterally spreading ground is caused by the difference in pore water pressures on both sides of the pile. The pile may be pulled by the soil on the extension side. Such mechanism of p - y behavior in liquefied soil is different from that in dry sand where horizontal subgrade reaction

is induced by the increase in soil pressure on the compression side of the pile.

3. In liquefied level ground, the extension and compression stress states alternately develop on both sides of a pile. As a result, the pile is pulled by the soil on the right and left sides alternately. In laterally spreading ground, the extension stress state develops on the downstream side of the pile only when the ground moves downstream. As a result, the pile is pulled only by the downstream soil when the ground moves downstream.
4. The subgrade reaction in laterally spreading ground consists of two components. One is induced by the cyclic ground deformation, which becomes large in a stiff pile. The other is induced by the permanent ground deformation, which becomes large in a flexible pile. This is because the stiff pile resists ground movement, while the flexible pile follows ground movement.

The results of the shaking table tests at E-Defense, have led the following:

1. In the E-Defense shaking table test with a 3×3 pile group having a pile spacing of 3.75 in dry sand, the bending strain is larger in the leading piles than in the trailing piles probably due to pile group effects and the depth at which the inflection of bending strains occurs is shallower in the leading piles than in the trailing piles. The piles failed, accompanied by tilt of the superstructure under the high input motion. The piles not only suffered local buckling at their heads but also in the ground. The depth of the later failure varied from 0.7 to 1.0 m below the pile heads, probably due to pile group effects and the redistribution of pile stress following the preceding failure of the leading piles. The direction of permanent pile deformation corresponds to those of the strong axis of inertial force and ground displacement.
2. In the E-Defense shaking table test with a 3×3 pile group having a pile spacing of 3.75 in liquefiable sand, the bending strain also becomes the largest in the leading pile, with its variation within the pile group is, however, quite small, compared to the test with dry sand. All the pile heads yielded under the largest input acceleration, causing residual deformation and settlement of the foundation in the direction of the strong axis of the inertial force and ground displacement.
3. The axial strain in piles decreases with depth in non-liquefied ground but is almost constant or even increases with depth in liquefied ground, probably due to the reduction in positive frictional resistance of the pile during soil liquefaction.

The results of the E-defense shaking table tests together backup centrifuge shaking table tests regarding

pile group effects have further shown the following:

1. In the non-liquefied ground, the shear forces at the pile heads tend to become larger in the leading row than in the trailing rows with decreasing pile spacing. This is because the subgrade reaction in non-liquefied ground is induced by an increase in normal stress on the compression side of a pile and such an increase is the largest in the leading piles due to shadowing effects of pile group. Such pile group effects are apparent at a pile spacing of about 4.
2. In the liquefied ground, the shear forces at the pile heads tend to become larger in the outside piles than in the inside piles as the pile spacing decreases. This is probably because, in the liquefied ground, the subgrade reaction is induced by difference in pore water pressure changes between compression and extension sides of a pile, as shown in section 3.5. This condition is well developed in the perimeter piles but may not be the case in the inside piles. This could lead to a decrease in the difference in pore water pressures on both sides of the inside piles as well as the smaller subgrade reaction in the inside piles. Such pile group effects are apparent only at a pile spacing less than about 3.
3. The critical pile spacing beyond which pile group effects become notable, appears to be smaller in dry sand than in liquefied sand, probably due to the difference in strain level between the two.
4. The estimated bending moment based on pseudo static analysis is in fairly good agreement with the observed values both in dry and saturated liquefied sands for both single and pile group. This suggests that pseudo-static analysis is promising to estimate pile stress with a reasonable degree of accuracy.

Pseudo-static analysis for estimating pile stress in liquefiable and non-liquefiable sand has been presented in which inertial and kinematic effects observed in large shaking table tests are incorporated, and its effectiveness has been demonstrated through the comparison of observed and computed pile stresses in the shaking table tests. Sensitivity analysis has been made to differentiate from crucial and less crucial factors affecting pile stress in liquefied soil. The following conclusions may be made based on the test results, analytical results, and their discussions:

1. The pseudo-static analysis can estimate the pile stresses in large shaking table tests with a reasonable degree of accuracy, regardless of the pile stiffness, the presence of foundation embedment and the occurrence of soil liquefaction.
2. The pseudo-static analysis can also reproduce qualitatively the significant features of the pile damage in the field as well as in laterally spreading ground.
3. The difference in deformation modes observed within the pile foundation in dry sand was induced

by the pile group effects; whereas that in the laterally spreading zone was presumably induced by the difference in spatial variations of lateral spreading.

4. The pile stress in liquefied soil with low stiffness is governed by inertial force from the superstructure, while that with high stiffness is governed by the ground displacement. The effects of inertial force on pile stress become less significant when the foundation is embedded in a non-liquefiable crust overlying a liquefiable/soft layer.
5. The bending moment at the pile head without embedment is sensitive to scaling factor for p - y spring but becomes insensitive when the foundation is embedded in a non-liquefiable crust.
6. The bending moment and axial force in piles caused by the two-dimensional shaking can be estimated by the sum of those obtained by applying the two orthogonal components separately. The bending moment depends only on the magnitude of combined external (inertial and kinematic) force in the two-dimensional horizontal plane, regardless of the direction of its strong axis, resulting in almost the same value within the pile group. In contrast, the axial force depends not only on the magnitude of combined external force but also on the direction of its strong axis, inducing different axial forces within the pile group.
7. In dry sand, the soil near the foundation tends to act against the inertial force from the superstructure. The axial force is almost controlled by the overturning moment that is induced by the inertial force in the horizontal plane, with its rotational axis near the bottom of the foundation. In liquefied sand, in contrast, the kinematic force arising from the ground displacement tends to act with the inertial force. The axial force is controlled by the overturning moment that is induced by the combined inertial and kinematic force in the horizontal plane, with its rotational axis near the bottom of the liquefied layer.

ACKNOWLEDGMENTS

The study described herein was made possible through the post-earthquake field investigation and their compilation conducted by various organizations including the Committee on Building Foundation Technology against Liquefaction and Lateral Spreading, Japan Association for Building Research Promotion, as well as three research projects related to soil-pile-structure interaction using the large shaking tables at the National Research Institute for Earth Science and Disaster Prevention (NIED), including Special Project for Earthquake Disaster Mitigation in Urban Areas, supported by Ministry of Education, Culture, Sports, Science and Technology (MEXT) and

US-Japan collaboration research among NIED, Rensselaer Polytechnic Institute, University of California, San Diego, Tokyo Soil Research Co. and Tokyo Institute of Technology. The authors express their sincere thanks to the above organizations.

REFERENCES

- Abdoun, T., Dobry, R., O'Rourke, T.D. and Goh, S.H. (2003): Pile response to lateral spreads: centrifuge modeling, *Journal of Geotechnical and Geoenvironmental Engineering*, ASCE, 129 (10), pp. 869–878.
- Boulanger, R.W., Curras, J.C., Kuter, B.L., Wilson, D.W. and Abghari, A. (1999): Seismic soil-pile-structure interaction experiments and analyses, *Journal of Geotechnical and Geoenvironmental Engineering*, ASCE, 125 (9), pp. 750–759.
- Architectural Institute of Japan (1988, 2001): Recommendations for design of building foundations, 430 p. (in Japanese).
- Architectural Institute of Japan et al., (1998): Report on the Hanshin-Awaji Earthquake Disaster, Building Series Volume 4, Wooden Structure and Building Foundations (in Japanese).
- BTL Committee (1998): Research Report on liquefaction and lateral spreading in the Hyogoken-Nambu earthquake (in Japanese).
- Japan Road Association (1997): Specifications for road bridges, Vol. IV (in Japanese).
- Kansai Branch of Architecture Institute of Japan (1996): Report on case histories of damage to building foundations in Hyogoken-Nambu earthquake, Report presented by Committee on Damage to Building Foundations (in Japanese).
- Mizuno, H., Sugimoto, M., Iiba, M., Hirade, T. and Mori, T. (1997): Evaluation of seismic behavior of pile foundations and seismic action on piles by shaking table tests of large-scale shear box (Part 5 Plan and intention of shear box shaking table tests (liquefaction) and soil characteristics), *Proc. of Japan National Conference on Architecture and Building Engineering*, B-2, pp. 377–378 (in Japanese).
- Mononobe, N. (1924): Notes on the Vertical Motion of an Earthquake and on the Vibration of Structures, *Journal of the civil engineering society*, 10 (5), pp.1063–1094. (in Japanese).
- Nishimura, A. (1978): Design of structures considering ground displacement, *Kisoko*, 6(7), pp. 48–56 (in Japanese).
- Okabe, S. (1924): General Theory on Earth Pressure and Seismic Stability of Retaining Wall and Dam, *Journal of the civil engineering society*, 10(6), pp. 1277–1323.
- Railway Technical Research Institute (1997): Foundation design codes for railway structures (in Japanese).
- Suzuki, H., K. Tokimatsu, Sato, M. and Abe, A. (2005): Factor affecting horizontal subgrade reaction of piles during soil liquefaction and lateral spreading, *Geotechnical Special Publication*, ASCE, 145, pp. 1–10.
- Suzuki, H., Tokimatsu, K. and Ozawa, G. (2006): Estimation of Group Pile Effects in Non-liquefied and Liquefied Ground Based on Centrifuge Model Tests, *Proc., Eighth National Conference on Earthquake Engineering*, 9 p.
- Suzuki, H., Tokimatsu, K., Sato, M. and Tabata, K. (2008): Soil-pile-structure interaction in liquefiable ground

- through multi-dimensional shaking table tests using E-Defense Facility, *Proc., 14th World Conference on Earthquake Engineering*, 8 pp.
- Suzuki, H. and Tokimatsu, K. (2009): Estimation of Kinematic Force Acting on Piles in Laterally Spreading Ground *Proc., 6th International Conference on Urban Earthquake Engineering*, in press.
- Tabata, K. and Sato, M. (2006): Report of special project for earthquake disaster mitigation in urban areas, Ministry of Education, Culture, Sports Science and Technology, pp. 489–554, (in Japanese).
- Tabata, K., Sato, M. and Tokuyama, H. (2007): Report of special project for earthquake disaster mitigation in urban areas, Ministry of Education, Culture, Sports Science and Technology, pp. 466–546, (in Japanese).
- Tamura, S., Tsuchiya, T., Suzuki, Y., Fujii, S., Saeki, E. and Tokimatsu, K. (2000): Shaking table tests of pile foundation on liquefied soil using large-scale laminar box (Part 1 Outline of test), *Proc., Thirty-fifth Japan National Conference on Geotechnical Engineering*, pp. 1907–1908 (in Japanese).
- Tamura, S., Tokimatsu, K., Uchida, A. Funahara, H. and Abe, A. (2002): Relation between seismic earth pressure acting on embedded footing and inertial force based on liquefaction test using large scale shear box, *Journal of Structural and Construction Engineering*, 559, pp. 129–134 (in Japanese).
- Tokimatsu, K. and Nomura, S. (1991): Effects of ground deformation on pile stresses during soil liquefaction, *Journal of Structural and Construction Engineering*, 426, pp. 107–113 (in Japanese).
- Tokimatsu, K. and Asaka, Y. (1998): Effects of Liquefaction-induced ground displacements on Pile Performance in the 1995 Hyogoken-Nambu Earthquake, *Soils and Foundations*, Special Issue, pp. 163–177.
- Tokimatsu, K., Suzuki, H. and Saeki, E. (2002): Modeling of horizontal subgrade reaction of pile during liquefaction based on large shaking table, *Journal of Structural and Construction Engineering*, 559, pp. 135–141 (in Japanese).
- Tokimatsu, K. (2003a): Behavior and design of pile foundations subjected to earthquakes, *Proc. of Twelfth Asian Regional Conference on Soil Mechanics and Geotechnical Engineering*, pp. 1065–1096.
- Tokimatsu, K., Tamura, S., Miyazaki, M. and Yoshizawa, M. (2003b): Evaluation of seismic earth pressure acting on embedded footing based on liquefaction test using large scale shear box, *Journal of Structural and Construction Engineering*, 570 (in Japanese).
- Tokimatsu, K., Suzuki, H. and Sato, M. (2005a): Effects of Inertial and Kinematic Interaction on Seismic Behavior of Pile with Embedded Foundation, *International Journal of Soil Dynamics and Earthquakes Engineering*, Special Issue, Vol. 25, pp. 753–762.
- Tokimatsu, K., Suzuki, H. and Sato, M. (2005b): Influential factors affecting pile stress in liquefiable soils, *Proc., Satellite Conference on Recent Developments in Earthquake Geotechnical Engineering*, pp. 38–45.
- Tokimatsu, K., Suzuki, H., Sato, M. and Tabata, K. (2007a): Three-dimensional shaking table tests on soil-pile-structure models using E-Defense facility, *Proc. of 4th International Conference on Earthquake Geotechnical Engineering*, 11 p.
- Tokimatsu, K., Suzuki, H., Sato, M. and Tabata, K. (2007b): Soil-Pile-Structure Interaction during Multi-Dimensional Shaking through Physical Model Tests Using E-Defense Facility, *Proc. of Fourth International Conference on Urban Earthquake Engineering*, pp. 849–856.
- Zhang, J.-M., Shamoto, Y. and Tokimatsu, K. (1998): Evaluation of earth pressure under any lateral displacement, *Soils and Foundations*, 38 (2), pp. 143–163.
- Wilson, D.W., Boulanger, R.W. and Kutter, B.L. (2000): Observed seismic lateral resistance of liquefying sand, *Journal of Geotechnical and Geoenvironmental Engineering*, 126 (10), pp. 898–906.

Theme lectures

Development of performance criteria for foundations and earth structures

S.L. Kramer & P. Arduino

University of Washington, Seattle, Washington, USA

H. Shin

Kleinfelder, Inc., Bellevue, Washington, USA

ABSTRACT: Performance-based seismic design offers the potential for more rational and consistent design of structures in different seismic environments. Although implemented in different ways in different regions of the world at this early stage of its development, all performance-based design procedures require the definition and quantitative characterization of performance. Performance can be defined in different ways, and different performance metrics may be optimal for different purposes and different stakeholders. This paper reviews some of the basic concepts and principles of performance-based earthquake engineering, and discusses different ways of defining performance. The notion of damage limit states as measures of performance is discussed, and different ways of implementing performance-based design in that system are introduced. The need for improved procedures for specifying limit state capacities, and methods for doing so ranging from case history analysis to expert opinion, are discussed. An example of a performance evaluation of a potential bridge design is presented.

1 INTRODUCTION

The development of performance-based earthquake engineering (PBEE) concepts offers the promise of more rational and consistent design of structures in various seismic environments. While these concepts are developing rapidly in many areas of the world, their implementation has taken different forms so no uniformly accepted procedures exist at this time. Nevertheless, there are a number of unifying concepts beneath all performance-based approaches, and these concepts require that certain criteria be satisfied.

Among the most fundamental concepts behind performance-based design (PBD) procedures is the notion that a system of interest is being designed to achieve a certain level of *performance* during (and after) earthquake shaking. Therefore, the quantity (or quantities) used to characterize performance must be identified and quantified. The engineer has many choices for measures of performance—some are more effective than others and some are more difficult to characterize than others. This paper reviews the nature of performance and quantities used to characterize it, and describes some of the procedures and challenges faced by geotechnical earthquake engineers in the implementation of performance-based seismic design concepts.

2 PERFORMANCE IN EARTHQUAKES

The move toward PBD requires that engineers be able to define performance in terms that are understandable and useful to the wide range of technical and non-technical people who make decisions on the basis of performance predictions. The term “performance” can mean different things to different people. An engineer might consider maximum interstory drift of a building or settlement of a footing as a good descriptor of performance. To an estimator preparing a bid for repairs, the width and spacing of cracks in columns or floor slabs could be more useful measures of performance. Finally, to an owner, the economic loss or downtime associated with earthquake damage could be the best measure of performance.

These different notions of performance lead to a relatively simple, but helpful, way of viewing the process that leads to losses. As illustrated in [Figure 1](#), an earthquake produces ground motion, which leads to dynamic response of a structure. That response can lead to physical damage, and that damage can lead to loss. The prediction of losses, or at least the likelihood of a certain level of loss, therefore requires that we also be able to predict ground motion intensity, system response, and physical damage. Losses can be viewed as the ultimate measure of performance since

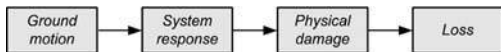


Figure 1. Illustration of the process that leads to earthquake losses.

they are usually of greatest importance to those who make the final decisions on seismic design, repair, and retrofitting efforts. Losses, however, can be very difficult to quantify so other measures of performance must also be considered.

2.1 Terminology

In order to describe the process illustrated in Figure 1, the notation developed by the Pacific Earthquake Engineering Research (PEER) Center will be used in this paper. The level of ground motion produced by earthquake shaking can be characterized by one or more *Intensity Measures*, or *IMs*, which could be any of a number of ground motion parameters (e.g., a_{\max} , S_a , Arias intensity, etc.). The response of the system of interest (e.g., interstory drift, ground settlement, etc.) to the ground motion can be described by *Engineering Demand Parameters*, or *EDPs*. The physical damage associated with the response (e.g., column, beam, or slab cracking, etc.) is expressed in terms of *Damage Measures*, or *DMs*. Finally, the losses associated with the physical damage (e.g., casualties, repair cost, downtime, etc.) are expressed in a form that is useful to decision-makers by means of *Decision Variables*, or *DVs*.

2.2 Intensity measures

Many ground motion parameters have been used as *IMs* in seismology and earthquake engineering. The merits of a particular *IM* relative to others that might be used to describe the intensity of shaking lies in its relationship to the response measure(s), or *EDP(s)*, of interest. An *efficient IM* is one that is closely related to the most useful *EDP*, i.e. one for which the uncertainty in *EDP* given *IM* is small. A *sufficient IM* is one that captures all of the useful information about the ground motion's potential to produce response, i.e., one for which additional ground motion information provides no reduction of uncertainty in *EDP*. A *predictable IM* is one that can be predicted relatively accurately from earthquake source parameters, i.e., one for which the error term in its ground motion prediction equation (or attenuation relationship), $\sigma_{\ln IM}$, is low. Performance predictions can be made most accurately when using *IMs* that are efficient, sufficient, and predictable.

2.3 Engineering demand parameters

EDPs describe the response of a system of interest. The most useful *EDPs* are those to which physical damage is most closely related. The ideas of

efficiency and sufficiency described in the preceding paragraph can also be applied to *EDPs*—desirable *EDPs* are efficient and sufficient predictors of physical damage. For many years, the primary measures of response utilized by geotechnical engineers were force—or stress-based. Quantities such as factors of safety were defined as ratios of capacities to demands, which were defined as resisting and driving forces, or as shear strengths and shear stresses. Over the past 10–20 years, increasing recognition of the relationship between deformations and serviceability, coupled with the increased ability to compute deformations, has led to deformation-based design. In this sense, deformations are replacing forces as useful measures of seismic response. With the development of new computational models and more powerful computers, practicing engineers can perform sophisticated numerical analyses with much greater ease than in the past. The ease of performing these calculations must, however, be tempered with a solid understanding and recognition of their limitations, the uncertainty of the data that goes into them, and the sensitivity of the response to that data.

2.4 Damage measures

The characterization of physical damage in continuous, quantitative terms is, at present, a very difficult task. If system response is to be characterized in terms of deformations, then damage (or damage levels) must be related to deformations. Optimum *DMs* should be efficient and sufficient predictors of loss, so the best *DMs* are those that a loss estimator would use to quantify losses.

Some aspects of geotechnical design have been characterized in terms of deformations for many years. The design of shallow foundations on dense, granular soil, for example, is rarely controlled by the strength of the soil; rather, it is controlled by the amount of footing displacement required to mobilize resistance to the applied footing load. Their design, therefore, has been controlled by the concept of *allowable settlement*, a term that is easily explained but difficult to define accurately for general conditions. The allowable settlement can be thought of as a capacity associated with a particular limit state—the state of “excessive settlement.” The consequences of being in this state of excessive settlement, however, are usually not clear. The implication is that something bad will happen if settlements are excessive, but the details and extent of that “badness” are not specified. This situation leads to one of the most pressing needs for further development and implementation of PBD, as will be discussed later in the paper.

There are ways in which physical damage can be quantified, i.e. expressed in terms of one or more *DMs*. The number, spacing, and widths of cracks in a floor slab, for example, could be used as *DMs* for

a warehouse in an area underlain by liquefiable soils. These *DM*s could provide an indication of the amount of epoxy that might be needed to repair or overlay the floor slab, and could be efficient and sufficient predictors of the costs of that repair. For other situations, however, quantitative measures of damage are difficult to characterize or may not be used by loss estimation professionals. In such cases, qualitative limit states, such as “negligible” or “severe” damage may be defined in terms of various levels of deformation.

2.5 Decision variables

Losses can take many forms—casualties, repair costs, and losses associated with lack of utility of important systems. The prevention of casualties has been one of the most fundamental principles of seismic design since engineers began designing for earthquakes, and it must continue to be treated as such. With preservation of life safety accepted as a minimum design objective, the level of performance that controls design will generally be one that limits economic losses to some acceptable value. What is acceptable will naturally vary from one structure to another, and from one owner/operator to another.

3 HISTORICAL AND CURRENT DESIGN PROCEDURES

Procedures for seismic design of foundations and earth retaining structures have grown out of procedures used for design under static loading conditions. Following the development of earthquake engineering, most early procedures accounted for the effects of earthquakes by adding pseudo-static loads to the static loading imposed by gravity. Design criteria were typically expressed in the same manner as static design criteria—in terms of minimum acceptable factors of safety under pseudo-static conditions. For foundations, the factors of safety were against bearing failure, sliding, etc. Factors of safety for earth structures were typically applied to stability mechanisms.

These early procedures treated earthquake loading in a very simplistic way and interpreted the adequacy of a particular design in a binary manner—the design was considered acceptable if the minimum factor of safety was exceeded, and unacceptable if it was not. The actual physical consequences of an unacceptably low factor of safety were not specified or explicitly considered, although they were usually implicitly considered in selection of the minimum factor of safety. The use of pseudo-static loading required specification of an appropriate pseudo-static acceleration, which was addressed differently by different engineers. Many engineers took the pseudo-static acceleration to be equal to the peak ground acceleration

with the logic that such a value would be conservative. Of course, the problem of determining the appropriate peak ground acceleration was also significant. Ground shaking hazards have moved from being specified deterministically to probabilistically, and it is now common to define loading by an *IM* value corresponding to a particular return period.

3.1 Foundations

The seismic design of foundations generally remains primarily force-based, although LRFD procedures allow for consideration of uncertainties in both loading and resistance. Such designs are usually decoupled from design of the structure supported by the foundation, generally due to the difficulty of performing soil-foundation-structure interaction (SFSI) analyses. The effects of foundation performance on structural performance can only be reliably predicted when the interaction of the structure and the foundations are explicitly accounted for. Doing so properly, however, requires analyses that are beyond the limitations of time and budget associated with most design projects. Further limitations come from the paucity of analytical codes that are capable of modeling both soils and structures with the level of detail and accuracy required for quantitative damage prediction. The relatively recent development of macroelement foundation models (e.g., Cremer et al., 2001, 2002; Chatsigogos, 2007) offer the potential for more computationally efficient prediction of foundation deformations under dynamic loading.

3.2 Earth structures

Over time, geotechnical earthquake engineers have increasingly recognized the close relationship between serviceability and deformations of earth structures. They also began, spurred by the development of sliding block analyses (Newmark, 1965) to recognize that large, high-frequency peak accelerations would not necessarily cause large deformations. Pseudo-static analyses, due primarily to their simplicity and convenience, remained popular so attempts at relating the results of pseudo-static analyses to deformations began to develop. Hynes-Griffin and Franklin (1984), for example, stated that earth dams with pseudo-static factors of safety greater than 1.0 using pseudo-static accelerations of half of the expected peak ground acceleration would not develop “dangerously large” deformations. These conclusions were based on an extensive series of Newmark analyses, but neither the distributions of displacement nor the definition of dangerously large deformations were provided.

Sliding block analyses have been used to develop convenient graphical and analytical models for estimation of permanent displacements of earth structures. The graphs produced by Makdisi and Seed (1978),

for example, have been used for many years, and improved analytical expressions (e.g., Bray and Travasarou, 2007) are now available.

Modern earth structures are commonly designed for deformations being limited to some allowable value for one or more hazard levels. The allowable deformation values vary from one situation to another, but are usually based more on judgment and experience than on an explicit relationship between response and physical damage.

4 PERFORMANCE PREDICTION

The Pacific Earthquake Engineering Research Center (PEER) has proposed a framework for PBEE. The framework makes use of the previously described notation, and recognizes the fact that IM s, EDP s, DM s, and DV s, as well as the relationships between them, are all uncertain. The PEER framework is encapsulated in a “framing equation” formally presented in its most general form as

$$\lambda(\mathbf{DV}) = \iiint G(\mathbf{DV}|\mathbf{DM})|dG(\mathbf{DM}|\mathbf{EDP})| \times |dG(\mathbf{EDP}|\mathbf{IM})||d\lambda(\mathbf{IM})| \quad (1)$$

In Equation (1), $G(a|b)$ denotes a complementary cumulative distribution function (CCDF) for a conditioned upon b (the absolute value of the derivative of which is the probability density function for a continuous random variable) and the bold type denotes vector quantities. From left to right, the three CCDFs result from loss, damage, and response models; the final term, $d\lambda(\mathbf{IM})$ is obtained from the seismic hazard curve. The framing equation implicitly assumes that the quantities used to describe \mathbf{IM} , \mathbf{EDP} , and \mathbf{DM} are sufficient predictors of \mathbf{EDP} , \mathbf{DM} , and \mathbf{DV} , respectively.

4.1 Continuous variables

This triple integral can be solved directly only for an idealized set of conditions, so it is solved numerically for most practical problems. When all variables are continuous, the numerical integration can be accomplished (assuming scalar parameters for simplicity) as

$$\lambda_{DV}(dv) = \sum_{k=1}^{N_{DM}} \sum_{j=1}^{N_{EDP}} \sum_{i=1}^{N_{IM}} P[DV > dv|DM = dm_k] \times P[DM > dm_k|EDP = edp_j] \times P[EDP > edp|IM = im_i] \Delta \lambda_{IM}(im_i) \quad (2)$$

where $P[a|b]$ describes the probability of a given b , and where N_{DM} , N_{EDP} , and N_{IM} are the number of increments of DM , EDP , and IM , respectively.

The PEER framework has the useful benefit of being modular. The discretized framing equation (Equation 2) can be broken down into a series of components, e.g.,

$$\lambda_{EDP}(edp) = \sum_{i=1}^{N_{IM}} P[EDP > edp|IM = im_i] \times \Delta \lambda_{IM}(im_i) \quad (3a)$$

$$\lambda_{DM}(dm) = \sum_{j=1}^{N_{EDP}} P[DM > dm|EDP = edp_j] \times \Delta \lambda_{EDP}(edp_j) \quad (3b)$$

$$\lambda_{DV}(dv) = \sum_{k=1}^{N_{DM}} P[DV > dv|DM = dm_k] \times \Delta \lambda_{DM}(dm_k) \quad (3c)$$

which means that hazard curves can be computed for EDP , DM , and DV and interpreted in the same manner as the more familiar seismic hazard curve (for IM) produced by a PSHA.

4.2 Discrete damage and loss states

Equations (3) assume the availability of continuous IM s, EDP s, DM s, and DV s. IM s are generally computed from recorded ground motions and are therefore nearly always continuous (an exception could be when a categorical quantity such as Modified Mercalli Intensity is used in lieu of a quantitative IM). Response quantities are usually predicted from IM s and expressed as forces, displacements, rotation, etc.; such quantities used as EDP s are also continuous. In some cases, however, continuous DM s may not be available or practical. Discrete DM s, and even discrete DV s, can also be incorporated into the PEER PBEE methodology. For example, damage could be divided into five damage states described in qualitative terms—say, negligible, minor, moderate, severe, and catastrophic—each defined in a manner related to prediction of losses. In this approach, ranges of EDP s corresponding to each damage state must be determined. A damage probability matrix, \mathbf{X} , can be defined such that its elements represented the probabilities of being in damage state k given that the EDP is in EDP range j .

$$X_{jk} = P[DM = dm_k|EDP = edp_j] \quad (4)$$

For the case of the previously listed five damage states, the damage probability matrix is represented in

Table 1. Damage probability matrix.

Damage State, DM	Description	EDP range				
		edp_1	edp_2	edp_3	edp_4	edp_5
dm_1	Negligible	X_{11}	X_{12}	X_{13}	X_{14}	X_{15}
dm_2	Slight	X_{21}	X_{22}	X_{23}	X_{24}	X_{25}
dm_3	Moderate	X_{31}	X_{32}	X_{33}	X_{34}	X_{35}
dm_4	Severe	X_{41}	X_{42}	X_{43}	X_{44}	X_{45}
dm_5	Catastrophic	X_{51}	X_{52}	X_{53}	X_{54}	X_{55}

tabular form as shown in Table 1. The EDP ranges can be defined by four EDP threshold values (accepting that $EDP = 0$ corresponds to the lower bound of negligible damage, and that $EDP = \infty$ corresponds to the upper bound of catastrophic damage).

Because a given value of the DM can come from different EDP ranges (i.e. there is uncertainty in the EDP - DM relationship), multiple non-zero terms are present in each row of the damage probability matrix shown in Table 1; what is required of this matrix is that the values in vertical columns sum to unity, i.e. that $\sum X_{jk} = 1.0, j = 1, N_{DM}$ for all k ; this is equivalent to saying that the damage for a given EDP must fall into one of the five damage states. The total probability theorem can then be used to compute the probability of being in a given damage state using the conditional distribution of $DM|EDP$ and the distribution of EDP ranges, i.e.

$$P[DM = dm_k] = \sum_{j=1}^{N_{EDP}} P[DM = dm_k|EDP = edp_j] \times P[EDP = edp_j] \quad (5)$$

A series of loss states, each of which were described by discrete DV values, can also be defined; the DV selected for loss evaluation could be taken as the fraction of replacement cost of the system under consideration, a quantity referred to subsequently as the repair cost ratio, RCR . A loss probability matrix, Y , can be defined such that the individual elements

$$Y_{kl} = P[DV = dv_l|DM = dm_k] \quad (6)$$

The loss probability matrix can be illustrated in tabular form as shown in Table 2.

Because uncertainty exists in the cost associated with a given damage state, a given value of DV can result from different damage states. Therefore, the total probability theorem can again be used to compute the probability of a particular loss level given the different damage states.

Table 2. Loss probability matrix.

Loss state, DV	Damage state				
	dm_1	dm_2	dm_3	dm_4	dm_5
dv_1	Y_{11}	Y_{12}	Y_{13}	Y_{14}	Y_{15}
dv_2	Y_{21}	Y_{22}	Y_{23}	Y_{24}	Y_{25}
dv_3	Y_{31}	Y_{32}	Y_{33}	Y_{34}	Y_{35}
dv_4	Y_{41}	Y_{42}	Y_{43}	Y_{44}	Y_{45}
dv_5	Y_{51}	Y_{52}	Y_{53}	Y_{54}	Y_{55}

$$P[DV = dv_l] = \sum_{k=1}^{N_{DM}} P[DV = dv_l|DM = dm_k] \times P[DM = dm_k] \quad (7)$$

Substituting Equation (5) into Equation (7) allows calculation of losses directly from response

$$P[DV = dv_l] = \sum_{k=1}^{N_{DM}} \sum_{j=1}^{N_{EDP}} P[DV = dv_l|DM = dm_k] \times P[DM = dm_k|EDP = edp_j]P[EDP = edp_j] \quad (8)$$

or, substituting Equations (4) and (6) into (8),

$$P[DV = dv_l] = \sum_{k=1}^{N_{DM}} \sum_{j=1}^{N_{EDP}} X_{jk} Y_{kl} P[EDP = edp_j] \quad (9)$$

From this, the exceedance probability for a given cost level can be written as

$$P[DV > dv_l] = \sum_{l=l+1}^{N_{DV}} \sum_{k=1}^{N_{DM}} \sum_{j=1}^{N_{EDP}} X_{jk} Y_{kl} P[EDP = edp_j] \quad (10)$$

4.3 Discussion

The methodology described in the preceding paragraphs allows estimation of performance at the loss level; the ultimate result of a complete PBEE evaluation could be expressed in terms of a loss curve, i.e., a relationship indicating the return periods (or annual probabilities) associated with different levels of loss. Loss modeling is, at the present state of PBEE development, a relatively unrefined subject. Combining losses due to casualties with economic losses is an extremely difficult problem. Estimating indirect losses, i.e., the losses associated with loss of utility, has also proven to be very difficult. Due to uncertainties in quantities and unit costs, which can be affected by uncertain factors such as future material and labor costs, interest rates, repair times, etc., considerable uncertainty also exists in loss modeling. As a result of all of these difficulties, PBEE is more effectively implemented at this point in time at the damage level.

5 DAMAGE LIMIT STATE DESIGN

Modern geotechnical design has been migrating toward load and resistance factor design (LRFD) for some years. This terminology, however, is inconsistent with the ongoing transition from force- to deformation-based design. Following the structural engineering nomenclature of using the term “demand” to describe system response (for either force- or deformation-related quantities) and the term “capacity” to describe resistance (also in terms of forces or deformations), a more general design procedure called demand and capacity factor design (DCFD) can be formulated (Cornell et al., 2002; Jalayer, 2003). In this formulation, demand and capacity factors are analogous to the load and resistance factors used in LRFD.

The development of DCFD procedures for geotechnical seismic design will require consideration of seismic loading, geotechnical response to seismic loading, and damage resulting from geotechnical response. When an earthquake occurs, the resulting ground motions cause structures, foundations, and the soils that support them to respond dynamically. That response may be weak or strong, depending on the level of ground motion and the nature of the structure, foundations, and soil. Geotechnical engineers use response models to predict the response of soils and foundations to ground motions. The response, in turn, can lead to physical damage. The damage may be low or high, depending on the level of response and the nature of the soil, foundations, and structure. A damage model is required to relate damage to response.

One approach to developing demand and capacity factors can be described using the PEER notation described previously. The response model is used to compute the *EDP* resulting from a given *IM*, i.e. $EDP = \mathcal{R}(IM)$, and the damage model is used to estimate the *DM* resulting from a given *EDP*, i.e. $DM = \mathcal{D}(EDP)$. It should be noted that these elements have both randomness (inherent) and uncertainty (lack of knowledge) associated with them; the development of demand and capacity factors will need to characterize all of these sources of randomness and uncertainty.

From Equation (3a), the mean annual rate of exceeding an *EDP* level, edp_j , can be expressed as

$$\lambda_{EDP}(edp_j) = V \sum_{i=1}^{N_{IM}} P[EDP > edp_j | IM = im_i] \times P[IM = im_i] \quad (11)$$

where ν is the mean annual rate of earthquakes exceeding some minimum magnitude. If the maximum allowable damage level for a given damage state is denoted as $DM = dm^*$, the damage function (assumed deterministic for the time being) can be inverted to compute the corresponding maximum acceptable response

level, edp^* . Note that edp^* is a measure of resistance, or capacity (e.g. maximum allowable displacement for the given damage state). For simplicity, the allowable response capacity will be described hereafter by the random variable, C , so

$$edp^* = \mathcal{D}^{-1}(dm^*) = c \quad (12)$$

Assuming the *IM* hazard curve can be expressed as $\lambda_{IM}(im) = k_o(im)^{-k}$ (after Sewell et al., 1991) and that the response model can be expressed in the form, $edp = a(im)^b$, a closed-form solution for a response hazard curve can be obtained (Jalayer, 2002), as illustrated in Figure 2.

The mean annual rate of exceeding some known capacity level, $C = c$, is therefore given by

$$\lambda_{EDP|C}(c) = k_0 \left(\frac{c}{a}\right)^{-k/b} \exp\left[\frac{1}{2} \frac{k^2}{b^2} \sigma_{\ln EDP|IM}^2\right] \quad (13)$$

Recognizing that the capacity is also uncertain (due to randomness and uncertainty in soil and foundation properties and uncertainty in response), the *EDP* hazard curve considering uncertainty in capacity can be expressed as

$$\lambda_{EDP}(edp) = \int_0^{\infty} \lambda_{EDP|C}(c) f_c(c) dc \quad (14)$$

Inverting the median response and damage models, we can find the value of *IM* that would produce the median limiting damage state, dm^* , as

$$im^* = \mathcal{R}^{-1}(c) = \mathcal{R}^{-1}[\mathcal{D}^{-1}(dm^*)] \quad (15)$$

If the capacity is assumed to be lognormally distributed with median, $\mu_{\ln C}$, and standard deviation, $\sigma_{\ln C}$, the mean annual rate of exceeding the capacity can be expressed as

$$\lambda_{EDP}(c) = \lambda_{IM}(im^{\mu_{\ln C}}) \exp\left[\frac{1}{2} \frac{k^2}{b^2} \sigma_{\ln EDP|IM}^2\right] \times \exp\left[\frac{1}{2} \frac{k^2}{b^2} \sigma_{\ln C}^2\right] \quad (16)$$

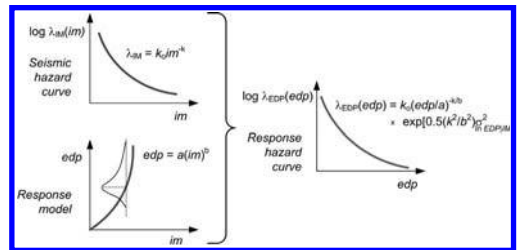


Figure 2. Closed-form expression for response hazard curve.

This equation can be rearranged to be expressed in the form

$$\mu_{\ln EDP}(im_p) \cdot \gamma = \mu_{\ln C} \cdot \phi \quad (17)$$

where $\mu_{\ln EDP}(im_p)$ is the natural logarithm of the median EDP for a given $IM = im_p$, p is an acceptable probability of capacity exceedance, $\mu_{\ln C}$ is the natural logarithm of the median capacity, and

$$\gamma = \exp \left[\frac{1}{2} \frac{k}{b} \sigma_{\ln EDP|IM}^2 \right] \quad (18)$$

$$\phi = \exp \left[-\frac{1}{2} \frac{k}{b} \sigma_{\ln C}^2 \right] \quad (19)$$

In this form, therefore, γ and ϕ represent demand and capacity factors (analogous to load and resistance factors), respectively. Both are influenced by the ground motion hazard (through the variable, k) and the response model (through the variable, b), and by uncertainties in both response (loading) and capacity (resistance). The demand factor can be seen to increase with increasing uncertainty and the capacity factor to decrease with increasing uncertainty. The factored demand (left side of equation) depends on the design probability level, but the factored capacity (right side) does not.

The preceding paragraphs have described a framework for an LRFD-like implementation of performance-based design. This basic framework was developed and has been implemented for steel moment frames (Cornell et al., 2002). It requires identification and quantitative characterization of one or more damage limit states that define performance. It recognizes that such limit states are uncertain and accounts for that uncertainty in the design process.

6 EVALUATION OF LIMIT STATE CAPACITIES

A PBD system based on damage limit states requires definition of the limit states and establishment of the boundaries between the limit states. These boundaries can be expressed in terms of allowable levels of response, and thought of as describing the capacity of the system of interest to resist different levels of response with various levels of damage. The boundaries themselves must be recognized as being uncertain, therefore knowledge of the distributions of the limit state boundaries is required. There are several ways in which limit state boundaries can be determined.

6.1 Case histories

The ideal way in which limit state boundaries could be defined would be through interpretation of damage levels observed in a large database of well-documented case histories. Such case histories would have detailed

surface and subsurface geometry and material property data, nearby recorded ground motions, and detailed records of the nature, amount, and distribution of observed damage. Unfortunately, such databases do not exist at this time. Large, damaging earthquakes occur relatively rarely, and site-specific geometric, material, and ground motion data are not usually available even when they do occur. The types of field reconnaissance investigations frequently led by U.S. and Japanese engineers following strong earthquakes, however, adds greatly to the geotechnical engineering profession's ability to characterize earthquake damage.

An example of a case history-based geotechnical damage state methodology is the Liquefaction Potential Index (Iwasaki et al., 1978). The Liquefaction Potential Index is defined as

$$LPI = \int_{z=0}^{z=20m} w(z)Fdz \quad (20)$$

where $w(z) = 10 - 0.5z$ with z in meters and $F = \max(0, 1-FS_L)$. LPI therefore can vary from 0 to 100; Iwasaki et al. (1982) determined that surficial effects of liquefaction (ground cracking, structural distress, etc.) were not observed for $LPI < 5$ and that severe effects were likely when $LPI > 15$. Toprak and Holzer (2003) used CPT data to compute LPI values in the Monterey Bay area of California and found general agreement with the effects expressed by Iwasaki et al. (1982); they also found that lateral spreading occurred for $LPI > 12$. By quantifying boundaries between different damage levels, LPI can be used to define limit states.

Structural engineers have made use of the Park-Ang (Park and Ang, 1985) damage index for reinforced concrete structures. This index is defined as a linear combination of maximum deformation and dissipated energy.

$$DI = \frac{u_{\max}}{u_{\text{mon}}} + \beta \frac{E_h}{F_y u_{\text{mon}}} \quad (21)$$

where u_{\max} is the peak displacement, u_{mon} is the ultimate monotonic displacement, F_y is the yield force, E_h is the dissipated energy, and β is a model parameter usually on the order of 0.10–0.15. The Park-Ang index has been applied to laboratory component tests and field observations. Damage limit states have been proposed (Table 3) based on ranges of Park-Ang damage index values.

6.2 Model test

Model tests are frequently used to study the response of soil-foundation-structure systems to earthquake shaking. Geotechnical centrifuges have seen increasing use in research investigations over the past 20 years. While

Table 3. Proposed relationship between Park-Ang damage index and damage limit states (after Golaifshani et al., 2005; Ang et al., 1993).

Degree of damage	Physical appearance	Damage index	State of building
Slight	Sporadic occurrence of cracking	<0.1	No damage
Minor	Minor cracks: partial crushing of concrete in columns	0.1–0.25	Minor damage
Moderate	Extensive large cracks: spalling of concrete in weaker elements	0.25–0.4	Repairable
Severe	Extensive cracking of concrete; disclosure of buckled reinforcement	0.4–1.0	Beyond repair
Collapse	Partial or total collapse of building	>1.0	Loss of building

they allow the modeling of complex systems with realistic boundary conditions, the small model scale usually requires the use of materials other than those that would be used in the prototype structure. Pile foundations, for example, are usually constructed of aluminum tubing; although the dimensions and thickness of the tubing may be controlled to match that of, say, a prototype-scale prestressed concrete pile, the mechanisms of damage will be very different. Nevertheless, centrifuge model tests do allow insight into damage mechanisms and inferences about damage states can usually be drawn more accurately with the results of such tests than without.

Large-scale shaking tables (e.g., Tamura et al., 1999; Tamura et al., 2001; Cubrinovsky et al., 2006) offer the potential for testing of much larger physical models under 1-g conditions. Model foundations constructed of concrete can be used in large shaking tables, which allow damage in the form of cracking to be observed and investigated. The enormous volumes of soil involved in such tests, however, makes their performance much more time-consuming and costly than model tests using centrifuges.

6.3 Numerical analysis

Numerical analyses can be used to simulate the response of soil-foundation-structure systems, and their results can be used to draw inferences about damage. Direct computation of damage can be achieved for some damage mechanisms (e.g., yielding and plastic deformation of metallic elements) but remains difficult for others (e.g., concrete cracking). Nevertheless, damage can be estimated from other parameters—for example, experimental databases (e.g., Berry et al., 2004) can be used to relate concrete cracking, spalling,

and failure to drift ratio, a quantity that can be calculated through numerical analyses.

Many textbooks provide values for quantities such as allowable settlement, in many cases without reference to the type of structure that is potentially damaged by the settlement. By analyzing soil-foundation-structure systems with advanced models capable of capturing the nonlinear, inelastic response of soils, structures, and the interfaces between them, site- and structure-specific estimates of damage can be developed. Such analyses, however, must be recognized as being relatively difficult and time-consuming.

6.4 Expert opinion

In the absence of the preceding sources of damage state information, damage states can be defined using expert opinion. Based on observations of ground failure following the 1999 Kocaeli earthquake, Bray and Stewart (2000) defined a four-level Ground Failure Index (Table 4). The four indices can be interpreted as damage states and the values listed in the interpretation of each can provide some rough guidance as to bounding values of response (e.g., settlement and/or lateral movement).

Table 4. Geotechnical damage index (Bray and Stewart, 2000).

Index	Description	Interpretation
GF0	No observable ground failure	No settlement, tilt, lateral movement, or boils
GF1	Minor ground failure	Settlement, $D < 10$ cm; tilt of > 3 -story buildings < 1 degree; no lateral movements
GF2	Moderate ground failure	$10 < D < 25$ cm; tilts of 1–3 degrees; small lateral movements (< 10 cm)
GF3	Significant ground failure	$D > 25$ cm; tilts of > 3 degrees; lateral movements > 25 cm.

Table 5. Damage state displacement ranges (Upsall, 2006).

Damage state	Horizontal displacement (cm)	Vertical displacement (cm)
Negligible	0–1	0–1
Minor	1–4	1–6
Moderate	4–12	6–20
Severe	12–50	20–60
Catastrophic	50+	60+

Upsall (2006) polled a group of practicing geotechnical engineers in the Seattle, Washington area and another group of experienced earthquake reconnaissance experts for their opinions on the amounts of vertical and horizontal soil movement required to produce damage states that would be described as negligible, minor, moderate, severe, and catastrophic. The group of practitioners suggested displacement values that were considerably lower than those suggested by the reconnaissance experts, particularly for the higher damage states. Combining the results with greater weight given to the values from the reconnaissance experts produced the displacement ranges shown in Table 5, which are not inconsistent with the limit states of Bray and Stewart (2000).

Although conducted informally, the damage states information in Tables 3 and 4 illustrate the type of information that can be developed based on expert opinion and used for implementation of damage limit state design. Improved versions of these damage state definitions could be obtained by gathering groups of engineering and loss estimation experts and formally eliciting their opinions on damage state boundaries.

7 EXAMPLE—PERFORMANCE OF A HIGHWAY BRIDGE IN LIQUEFIABLE SOIL

An example of a performance evaluation using different criteria has been developed by a team of PEER researchers. Shin et al. (2008) described the evaluation of a highway bridge typical of that designed and construction by the California Department of Transportation (Caltrans). The bridge is underlain by liquefiable soil susceptible to lateral spreading (Figure 3). The bridge consists of a five-span reinforced concrete structure with a post-tensioned reinforced concrete box girder deck section. The pier columns are circular with a 1.2 m (4 ft) diameter. Details on the bridge structure design are presented by Mackie and Stojadinovic (2007). The bridge columns are supported by 3 × 2 pile groups with center-to-center spacing of 1.83 m (6 ft). The individual piles are open-ended steel pipe piles with a diameter of 0.61 m (2 ft) and wall thickness of 0.0127 m (0.5 inch). The same pile type is used for the 6 × 1 abutment foundations with center-to-center spacing of 2.44 m (8 ft).

Accurate estimation of performance required development of a detailed model of the soil-foundation-structure system. The bridge piers and pile groups are labeled from the left abutment as Pier 1, Pier 2, Pier 3, Pier 4, and Pile 1, Pile 2, Pile 3, Pile 4, respectively. The pile groups at the left and right abutments are labeled as Pile 0 and Pile 5.

7.1 Soil conditions

The soil below the left embankment consists of a medium stiff clay crust underlain by a thin, loose to medium dense sand, a layer of stiff clay, and a dense sand layer underlain by rock. The soil beneath the right embankment consists of the same clay crust underlain by a thicker layer of loose sand, followed by a dense sand layer underlain by rock. The lower clay layer below the left abutment becomes thinner toward the center of the bridge and does not exist below the right embankment. The embankments are 8.53 m (28 ft) high with 2:1 side slopes. The groundwater table is located at the bottom of the surface clay layer. The soil types and properties are shown in Table 6. The configuration of the bridge structure and abutment is shown in Figure 4.

7.2 Numerical model

The soil-foundation-structure system was modeled in OpenSees. The Pressure Dependent Multi-Yield (PDMY) elasto-plastic material model developed by Yang et al. (2003) was used to model sandy soils. To account for saturated conditions, the PDMY material was coupled with a Fluid Solid Porous Material (FSPM) model that allows the generation of pore pressures. Clays were modeled with a Pressure Independent

Table 6. Soil types and properties.

Soil layer	Soil type	Unit weight (kN/m ³)	Strength parameters
1	Dense sand	21.2	$\phi = 45^\circ$
2	Medium stiff clay	17.3	$c = 36.58 \text{ kPa}$
3	Loose sand	18.0~20.2	$\phi = 33.36^\circ$
4	Medium stiff clay	17.3	$c = 40.58 \text{ kPa}$
5	Dense sand	21.2	$\phi = 40^\circ$

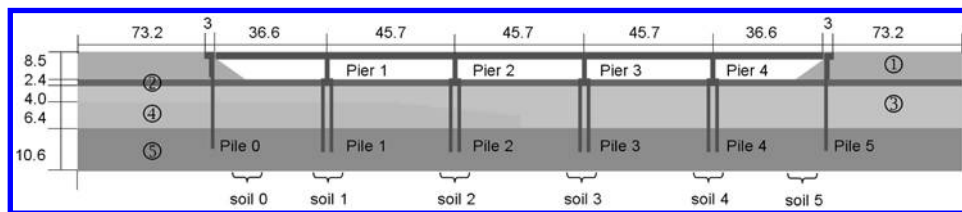


Figure 3. Target bridge system (dimensions in meters).

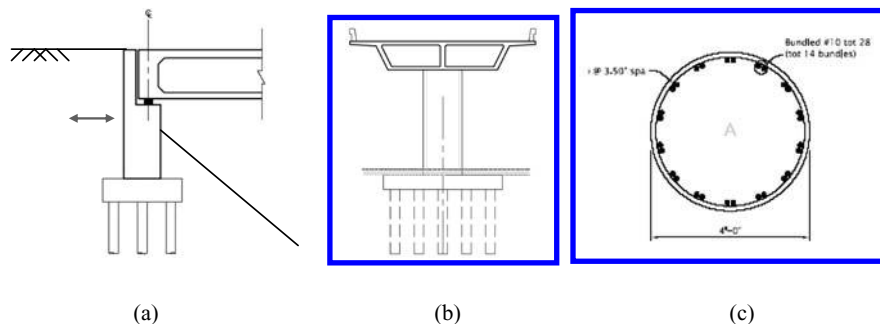


Figure 4. Structural configurations (a) abutment structure (b) bridge structure, and (c) bridge column section.

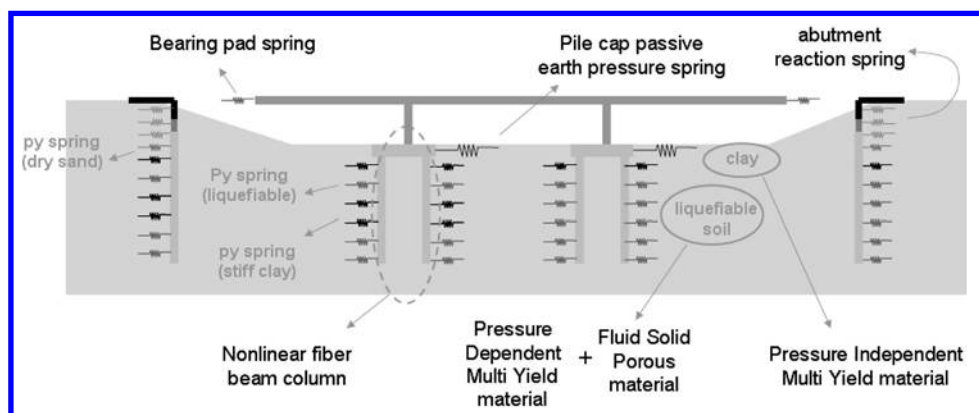


Figure 5. Modeling of soil-structure interaction in OpenSees.

Multi-Yield (PIMY) material. The soil parameters used in this study were based on recommendations (<http://cyclic.ucsd.edu/openses>) for typical soil conditions. The embankment side soil was extended outward 73.2 m (240 ft) from the crest of each slope.

Several types of interface springs were used to capture important soil-structure interaction effects. The parameters of these interface elements reflect the existence of different soil types, ground water conditions, pile group effects, and passive earth pressures in the pile caps and abutments. The 3×2 pile groups that support the piers were simplified using equivalent two-dimensional 1×2 pile group models that combined the three piles in each out-of-plane row to produce an equivalent single pile. In OpenSees, the equivalent pile was generated by patching three individual pile sections without changing the diameter or pile wall thickness. The pile group spring parameters were factored (using *p-multipliers*) to consider pile group effects. The *p-y* springs in the liquefiable soils were modeled using the *pyLiql* model (Boulanger et al. 1999 and 2004) available in OpenSees. The

pyLiql material was coupled with adjacent soil elements that provide porewater pressure information. The spring resistance forces were based on API (1993) criteria and were factored by the porewater pressure ratio to approximate the liquefaction effect on soil-pile structure interaction. Residual strengths after liquefaction were calculated based on correlations to Standard Penetration Test (SPT) values. Passive earth pressure springs were used to capture the response of pile caps and abutment backwalls. The envelope of the pile cap passive earth pressure for clay followed the approach ($\phi = 0$ sliding wedge method) suggested by Mokwa (1999). For the abutment wall resistance, the resultant force-displacement envelope was based on Caltrans' Seismic Design Criteria (2004).

The abutment backwall was 1.8 m (6 ft) high and 13.7 m (45 ft) wide. The interaction between the bridge deck and abutment was decomposed into components that explicitly accounted for the bearing pad, expansion joint gap, and the abutment backwall, which was modeled as a structural "fuse" that would break in shear to avoid transmitting high axial loads

to the bridge girders. For the selected abutments, the initial stiffness and ultimate resistance used were 164,300 kN/m (20 kips/in/ft) and 6,258 kN (1290 kips), respectively.

7.3 Computed response

The response of the system was computed for 40 input motions corresponding to four different return periods. A total of 23 EDPs (Table 7) were used to describe the response of the system. Figure 6 shows an exaggerated view of the permanent deformations of the system for one particular input motion; the movement of both approach embankments toward the center, accompanied by bending of piles and columns, and the extent of liquefaction are apparent from the figure. Figure 7 shows the variation of two EDPs with peak ground velocity.

7.4 Damage modeling

Two approaches to damage modeling were taken in this investigation. The first involved definition of discrete damage and loss states for the foundations alone, and the second treated those quantities as continuous variables for the entire bridge system.

7.4.1 Discrete damage and loss states

Five discrete foundation damage states were correlated to lateral foundation displacement—negligible, minor,

moderate, severe, and catastrophic. Using the result of a poll of experienced earthquake reconnaissance experts and a degree of judgment, a damage probability matrix (Table 8) was established; note that the damage states refer only to the foundation. Uncertainty in the damage limit states is reflected in the distributions of potential DMs for each EDP range.

The EDP hazard curves for the horizontal displacement of each of the pile caps were used, along with the damage probability matrix shown in Table 8, to estimate damage levels associated with the computed response. Since the damage levels were expressed in terms of discrete, qualitatively described damage states, the exceedance rates (and associated return periods) are presented in tabular form in Table 9.

Table 7. Performance groups and associated EDPs.

Performance group	Engineering demand parameter, EDP
Column (4)	Maximum and residual tangential drift ratios
Expansion joint (2)	Longitudinal abutment displacement
Bearings (2)	Bearing displacement (absolute)
Back wall (2)	Back wall displacement
Approach slab (2)	Vertical abutment displacement
Deck segment (5)	Depth of spalling
Abutment pile groups (2)	Horizontal displacement
Interior pile groups (4)	Horizontal displacement

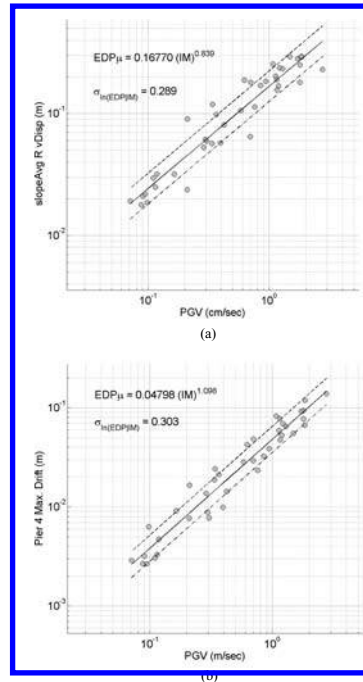


Figure 7. Variation of (a) settlement of the right approach embankment and (b) maximum drift of Pier 4 with peak ground velocity.

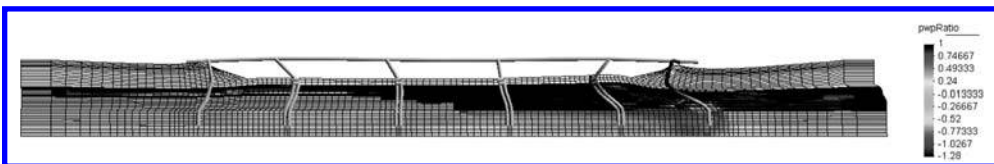


Figure 6. Displacement and pore water pressure ratio in soil (after shaking)—Erzincan, Turkey 1992, $a_{max} = 0.70$ g (displacement magnification factor = 20).

Table 8. Damage probability matrix.

Damage state, <i>DM</i>	Description	EDP range				
		<4 cm	4– 10 cm	10– 30 cm	30– 100 cm	> 100 cm
<i>dm</i> ₁	Negligible	0.95	0.05	0.00	0.00	0.00
<i>dm</i> ₂	slight	0.05	0.80	0.20	0.05	0.00
<i>dm</i> ₃	Moderate	0.00	0.10	0.60	0.25	0.05
<i>dm</i> ₄	Severe	0.00	0.05	0.15	0.55	0.10
<i>dm</i> ₅	Catastrophic	0.00	0.00	0.05	0.15	0.85

Table 9. Tabular listing of mean annual rates of exceedance and return period for various damage states.

Foundation	Damage state	Damage state				
		<i>dm</i> ₁	<i>dm</i> ₂	<i>dm</i> ₃	<i>dm</i> ₄	<i>dm</i> ₅
Left abutment	λ_{DV}	1.061	0.100	0.033	0.0004	0
	T_R	0.9	10	30	2279	∞
Pier 1	λ_{DV}	0.280	0.028	0.009	0.0002	0
	T_R	3.6	35	106	6112	∞
Pier 2	λ_{DV}	0.039	0.005	0.002	0.0001	0
	T_R	25	214	640	1919	∞
Pier 3	λ_{DV}	0.101	0.014	0.005	0.0003	0
	T_R	10	70	204	2885	∞
Pier 4	λ_{DV}	0.110	0.017	0.006	0.0003	0
	T_R	9.1	60	178	2870	∞
Right abutment	λ_{DV}	0.211	0.035	0.012	0.0012	0
	T_R	4.7	29	82	809	∞

The values shown in Table 9 indicate that a moderate level of damage is much more likely to be exceeded at the left abutment ($T_R = 30$ yrs) and much less likely to be exceeded at Pier 2 ($T_R = 640$ yrs) than at the other foundation locations. The relatively low damage rate for Pier 2 results from its location at a point where lateral spreading displacements (see Figure 6) are lower than those of the other piers. A severe level of damage is much more likely to be exceeded at the right abutment ($T_R = 809$ yrs) than at the other locations.

A total of 11 loss states were defined for the foundations; the loss states corresponded to estimated foundation repair cost ratios of 0.0, 0.1, . . . , 1.0. The loss probabilities assigned to each loss state are shown in Table 10. Combining these loss probabilities with the preceding damage rates produces the loss estimates shown in Table 11.

7.4.2 Continuous damage and loss states

In order to evaluate performance of the entire bridge system in terms of losses, performance-based analyses were performed using continuous damage states for all of the previously described performance groups. The EDP levels corresponding to the different damage

Table 10. Foundation loss probability matrix.

Decision variable, <i>DV</i>	Repair cost ratio	Damage state				
		<i>dm</i> ₁	<i>dm</i> ₂	<i>dm</i> ₃	<i>dm</i> ₄	<i>dm</i> ₅
<i>dv</i> ₁	0.0	0.95	0.00	0.00	0.00	0.00
<i>dv</i> ₂	0.1	0.05	0.15	0.20	0.00	0.00
<i>dv</i> ₃	0.2	0.00	0.50	0.60	0.00	0.00
<i>dv</i> ₄	0.3	0.00	0.20	0.15	0.00	0.00
<i>dv</i> ₅	0.4	0.00	0.15	0.05	0.15	0.00
<i>dv</i> ₆	0.5	0.00	0.00	0.00	0.50	0.00
<i>dv</i> ₇	0.6	0.00	0.00	0.00	0.25	0.00
<i>dv</i> ₈	0.7	0.00	0.00	0.00	0.10	0.00
<i>dv</i> ₉	0.8	0.00	0.00	0.00	0.00	0.10
<i>dv</i> ₁₀	0.9	0.00	0.00	0.00	0.00	0.20
<i>dv</i> ₁₁	1.0	0.00	0.00	0.00	0.00	0.70

Table 11. Estimated loss levels at 100 and 1,000 yr return periods.

Foundation	100-yr RCR	1,000-yr RCR
Left abutment	0.62	0.77
Pier 1	0.46	0.71
Pier 2	0.24	0.53
Pier 3	0.35	0.67
Pier 4	0.37	0.69
Right abutment	0.52	0.93

states were assumed to be lognormally distributed; an example for column damage based on maximum drift ratio is shown in Table 12. These damage levels were based on experimental observations as tabulated in a column performance database (Berry et al., 2004). An additional lower level damage state was defined for the onset of column cracking.

Losses were expressed in terms of repair costs. The repair cost data was initially estimated from various Caltrans documents (Caltrans 2004; 2005) and then updated based on discussions with Caltrans personnel. Using the bridge column performance group again as an example, repair methods included injecting cracks with epoxy, replacing minor concrete spalls, steel jacketing, and column replacement; the repair quantities and unit costs associated with each of these methods are summarized in Table 13. Similar tabulations were made for each of the other performance groups listed in Table 6.

The response, damage, and loss relationships were condensed into a single relationship for loss given ground motion intensity, i.e., $DV|IM$. The total $DV|IM$ relationship, considering all performance groups and normalized by the replacement cost of the entire bridge, is shown in Figure 8. This relationship was

then combined with the *IM* hazard curve to produce the loss curve shown in Figure 9.

One of the advantages of the PBEE methodology used in this example is the ability to deaggregated the loss curve at different return periods. Figure 10 shows an example of the deaggregated contributions to loss at the 475-yr hazard level. Such information allows the engineer and owner to examine sources of the expected losses in detail, and to see how changes in the design affect the amount and distribution of the expected losses.

Table 12. Column damage states based on maximum tangential drift ratio.

Damage state	Median EDP (Maximum drift ratio, %)	Dispersion ($\sigma_{\ln DMEDP}$)
Cracking	0.23	0.30
Spalling	1.64	0.33
Bar buckling	6.09	0.25
Failure	6.72	0.35

Table 13. Column repair methods and costs.

Damage state	Repair method	Unit	Repair Unit quantity	Unit cost
Cracking	Inject cracks with epoxy	ft	200	\$80
	Replace minor spalls	ft ²	10	\$100
Spalling	Inject cracks with epoxy	ft	200	\$80
	Replace minor spalls	ft ²	94	\$100
Bar buckling	Inject cracks with epoxy	ft	200	\$80
	Replace minor spalls	ft ²	236	\$100
	Steel column casing	kg	50	\$2000
	Bridge bar reinforcement	kg	1562	\$200
Failure	Replace column	ft ²	6728	\$120

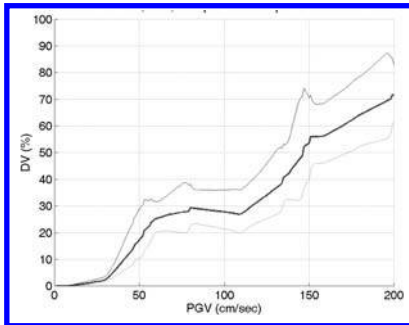


Figure 8. Distribution of $DV|IM$ (16th, 50th, and 84th percentile curves shown) for highway testbed bridge site for liquefaction case.

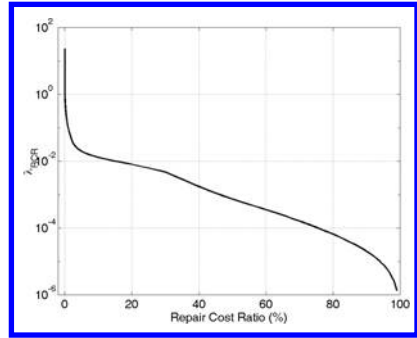


Figure 9. Total repair cost ratio hazard curve.

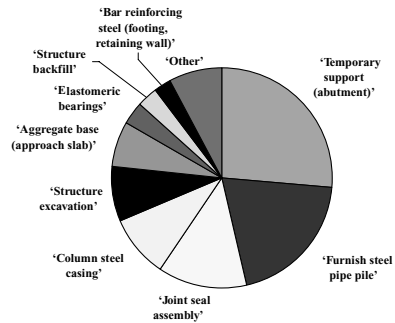


Figure 10. Deaggregated conditional repair costs for testbed highway bridge for 475 yr return period in liquefaction case.

8 SUMMARY

Performance-based design frameworks that allow performance to be expressed in many different ways are emerging in both research and practice. Implementation of PBD requires that performance criteria be identified and unambiguously characterized. In order to achieve designs with reliably predictable levels of performance, the uncertain nature of earthquake ground motions, response, damage, and loss must be recognized and accounted for. This requires that performance criteria be characterized probabilistically.

While PBEE frameworks capable of expressing performance in financial terms are available, difficulties in loss estimation render their implementation difficult at this time. Damage-based performance criteria are currently more practical, but their probabilistic characterization is at an early stage of development. This paper has reviewed several ways in which damage limit states could be identified and characterized, allow which differ in generality and complexity. It seems likely that more than one of these approaches will see use in practice, and that the simpler and more general approaches will define limit states with a

higher level of uncertainty than more detailed and specific procedures. Such different approaches all have merit and can all work within a comprehensive PBD framework to provide risk-consistent designs—provided that the uncertainties in each are accurately and objectively characterized.

REFERENCES

- Ang, A.H-S., Kim, W. J., & Kim, S.B. 1993. Damage estimation of existing bridge structures, *Structural Engineering in Natural Hazards Mitigation, Proc. ASCE Structures Congress, Irvine CA*, 2, 1137–1142.
- Berry, M., M. Parish, & M.O. Eberhard 2004. PEER Structural Performance Database. *Pacific Earthquake Engineering Research Center, Berkeley, CA*.
- Boulanger, R., Curras, C., Kutter, B., Wilson, D., & Abghari A. 1999. Seismic soil-pile-structure interaction experiments and analysis, *Journal of Geotechnical and Geoenvironmental Engineering, ASCE*, 125 (No. 9), 750–759.
- Boulanger, R., D. Wilson, B. Kutter, S. Brandenberg, & D. Chang. 2004. Nonlinear FE analysis of soil-pile-interaction liquefying sand, *Proceedings, Geotechnical Engineering for Transportation Projects, Geotechnical Special Publication*, No. 126, 470–478.
- Bray, J.D. & Stewart, J.P. 2000. Chapter 8: Damage patterns and foundation performance in Adapazari. Kocaeli, Turkey Earthquake of August 17, 1999 Reconnaissance Report, Editors T.L. Youd, J.P. Bardet, & J.D. Bray, *Earthquake Spectra*, Supplement A to Vol. 16, 163–189.
- Bray, J.D. & Travarasou, T. 2007. Simplified Procedure For Estimating Earthquake-Induced Deviatoric Slope Displacements, *J. of Geotech. Geoenv. Eng.*, ASCE, Vol. 133, No. 4, 381–392.
- Chatzigogos, C.T., Pecker, A., & Salencon, J. (2007). “A macro-element for dynamic soil-structure interaction analyses of shallow foundations,” *Proceedings, Fourth International Conference on Earthquake Geotechnical Engineering*, Thessaloniki, Greece, Paper No. 1387, 10 p.
- Cremer, C., Pecker A., & Davenne L. “Cyclic macro - element of soil-structure interaction: material and geometrical non-linearities”, *International Journal of Numerical and Analytical Methods in Geomechanics*, 25, 1257–1284, 2001.
- Cremer, C., Pecker A., & Davenne L. “Modelling of non linear dynamic behaviour of a shallow foundation with macro-element”, *Journal of Earthquake Engineering*, 6, Issue 2, 175-212, 2002.
- Coburn, A., & Spence, R. 1992. *Earthquake protection*, John Wiley & Sons, West Sussex, England, 420 p.
- Cornell, C.A., Jalayer, F., Hamburger, R.O., & Foutch, D.A. 2002. Probabilistic basis for 2000 SAC Federal Emergency Management Agency steel moment frame guidelines, *Journal of Structural Engineering*, 128(4), 526–533.
- Cubrinovski, M., Kokusho, T., & Ishihara, K. 2006. Interpretation from large-scale shake table tests on piles undergoing lateral spreading in liquefied soils, *Soil Dynamics and Earthquake Engineering*, 26, 275–286.
- Golafshani, A., Bakhshi, A., & Tabeshpour, M.R. 2005. Vulnerability and damage analysis of existing buildings, *Asian Journal of Civil Engineering (Building and Housing)*, 6(1–2), 85–100.
- Iwasaki, T., Tatsuoka, F., Tokida, K., & Yasuda, S. 1978. A practical method for assessing soil liquefaction potential based on case studies at various sites in Japan, *Proceedings of the 2nd International Conference on Microzonation*, San Francisco, Vol. 2, pp. 885–896.
- Iwasaki, T., Arakawa, T., & Tokida, K. 1982. Simplified procedures for assessing soil liquefaction during earthquakes, *Proceedings of the Conference on Soil Dynamics and Earthquake Engineering*, Southampton, UK, pp. 925–939.
- Mackie, K., & Stojadinovic, B. 2007. Performance of Benchmark Bridge Structures, *ASCE Structures Congress*, Long Beach, CA.
- Makdasi, F.I. & Seed, H.B. 1978. Simplified procedure for estimating dam and embankment earthquake-induced deformations, *Journal of the Geotechnical Engineering Division*, ASCE, Vol. 104, No. GT7, pp. 849–867.
- Mokwa, R. 1999. Investigation of the Resistance of Pile Caps to Lateral Loading, *Ph.D thesis, Virginia Polytechnic Institute*.
- SDC. 2004. Caltrans Seismic Design Criteria 2004. (http://www.dot.ca.gov/hq/esc/earthquake_engineering/SDC/SDCPage.html.)
- Sewell, R.T., Toro, G.R., & McGuire, R.K. 1991. Impact of ground motion characterisation on conservatism and variability in seismic risk estimates, *NUREG/CR-6467*, U.S. Nuclear Regulatory Commission, Washington, D.C.
- Shin, H., Arduino, P., Kramer, S.L. & Mackie, K. 2008. Seismic response of a typical highway bridge in liquefiable soil, *Proceedings, Geotechnical Earthquake Engineering and Soil Dynamics IV, ASCE Geo-Institute, Geotechnical Special Publication* 181, 11 p.
- Tamura, S., Miyazaki, M., Fujii, S., Tsuchiya, T., & Tokimatsu, K. 2001. Earth pressure acting on embedded footing during soil liquefaction by large-scale shaking table test, *Proceedings, 4th International Conference on Recent Advances in Geotechnical Earthquake Engineering and Soil Dynamics, Paper No. 6.19*.
- Tamura, S., Minowa, C., Fujii, S., Funahara, H., Sugimoto, M., Tsuchiya, T., & Abe, A. 1999. Shaking Table Test of a Reinforced Concrete Pile Foundation on Liquefied Sand Using a Large-scale Laminar Shear Box, *Technical Note of the National Research Institute for Earth Science and Disaster Prevention*, 190(111).
- Toprak, S., & Holzer, T.L., 2003. Liquefaction potential index: field assessment. , *Journal of Geotechnical and Geoenvironmental Engineering, ASCE* 129 (4), 315–322.
- Upsall, S.B. (2006). “Instrumental Intensity Scales for Geotechnical and Structural Damage,” *Ph.D. Dissertation*, University of Washington, Seattle, Washington, 403 p.
- Yang, Z., Elgamal, A. & Parra E. 2003. Computational model for cyclic mobility and associated shear deformation, *Journal of Geotechnical and Geoenvironmental Engineering, ASCE*, 129 (No. 12), 1119–1127.

Evaluation of seismic performance of geotechnical structures

M. Cubrinovski & B.A. Bradley

University of Canterbury, Christchurch, New Zealand

ABSTRACT: Three different approaches for assessment of seismic performance of earth structures and soil-structure systems are discussed in this paper. These approaches use different models, analysis procedures and are of vastly different complexity. All three methods are consistent with the performance-based design philosophy according to which the seismic performance is assessed using deformational criteria and associated damage. Even though the methods nominally have the same objective, it is shown that they focus on different aspects in the assessment and provide alternative performance measures. Key features of the approaches and their specific contribution in the assessment of geotechnical structures are illustrated using a case study.

1 INTRODUCTION

Methods for assessment of the seismic performance of earth structures and soil-structure systems have evolved significantly over the past couple of decades. This involves improvement of both practical design-oriented approaches and advanced numerical procedures for a rigorous dynamic analysis. In parallel with the improved understanding of the physical phenomena and overall computational capability, new design concepts have been also developed. In particular, the Performance Based Earthquake Engineering (PBEE) concept has emerged. In broad terms, this general framework implies engineering evaluation and design of structures whose seismic performance meets the objectives of the modern society. In engineering terms, PBEE specifically requires evaluation of deformations and associated damage to structures in seismic events. Thus, the key objective in the evaluation of the seismic performance is to assess the level of damage and this in turn requires detailed evaluation of the seismic response of earth structures and soil-structure systems. Clearly this is an onerous task since the stress-strain behaviour of soils under earthquake loading is very complex involving effects of excess pore-water pressures and significant nonlinearity. The ground response usually involves other complex features such as:

- Modification of the ground motion (earthquake excitation for engineering structures)
- Large ground deformation and excessive permanent ground displacements
- A significant loss of strength, instability and ground failure, and
- Soil-structure interaction effects.

The assessment of seismic performance of geotechnical structures is further complicated by uncertainties

and unknowns in the seismic analysis. Particularly significant are the uncertainties associated with the characterization of deformational behaviour of soils and ground motion itself. Namely, the commonly encountered lack of geotechnical data for adequate characterization of the soil profile, in-situ soil conditions and stress-strain behaviour of soils results in uncertainties in the modelling and prediction of ground deformation. Even more pronounced are the uncertainties regarding the ground motion (earthquake excitation to be used in the analysis) arising from the inability to predict the actual ground motion that will occur at the site in the future.

The above uncertainties affect key elements in the analysis, the input load (ground motion or earthquake load) and constitutive model (stress-strain curve or load-deformation relationship). Clearly, the output of the analysis will be adversely affected by these uncertainties and would therefore require careful interpretation. One may argue that, strictly speaking, a prediction of the seismic response is not possible under these circumstances; instead, the aim should be an assessment of the seismic performance. This argument is not in the realm of semantics, but it rather implies difference in philosophy. It alludes to the importance of the process and engineering interpretation rather than the outcome alone, which is in agreement with the traditional role that engineering judgement has played in geotechnical engineering.

In this paper, three approaches for assessment of seismic performance are applied to a case study of a bridge on pile foundations. Conventional methods of seismic analysis are used in the assessment and comparatively examined. Key features in the implementation of the methods, their advantages and disadvantages are discussed. It is demonstrated that the examined approaches focus on different aspects and make different contribution in the assessment.

2 METHODS FOR ASSESSMENT OF SEISMIC PERFORMANCE

2.1 Analysis methods

There are various approaches for seismic analysis of earth structures and soil-structure systems ranging from relatively simple approximate methods to very rigorous but complex analysis procedures. These approaches differ significantly in the theoretical basis, models they use, required geotechnical data and overall complexity. The simplest methods are based on the pseudo-static approach in which an equivalent static analysis is used to estimate the dynamic response induced by the earthquake. The pseudo-static analysis is based on routine computations and use of relatively simple models, and hence is easy to implement in practice. For this reason, it is the commonly adopted approach in seismic design codes. On the other hand, the most rigorous analysis procedure currently available for evaluation of the seismic response of soil deposits and earth structures is the seismic effective stress analysis. This analysis permits detailed evaluation of the seismic response while considering the complex effects of excess pore water pressures and highly nonlinear behaviour of soils in a rigorous dynamic (time history) analysis. Despite its complexity, the seismic effective stress analysis is now frequently used in geotechnical practice for assessment

of the seismic performance of important structures. As indicated in Figure 1, a large number of alternative analysis methods are available in the range between these two benchmark approaches.

2.2 Deterministic versus probabilistic approaches

Generally speaking, the seismic response can be evaluated either deterministically or probabilistically. Figure 2 illustrates the three approaches scrutinized in this study in this regard: (i) Deterministic approach (DA) in which a single scenario is considered; in this case, only one analysis is conducted and respectively a single response of the system is computed; (ii) Deterministic approach (DA_P) in which a series of analyses are conducted in a parametric manner in order to account for the uncertainties and unknowns in the analysis; as indicated in Figure 2, this approach results in a range of different responses for the analyzed system; (iii) Probabilistic approach (PA) in which “all possible” earthquake scenarios are considered for the site in question; this approach also results in a range of different responses for the system and, in addition, provides an estimate for the likelihood of each response.

The key difference between these three approaches is in the treatment of the uncertainties. The deterministic approach with a single scenario (DA) effectively ignores

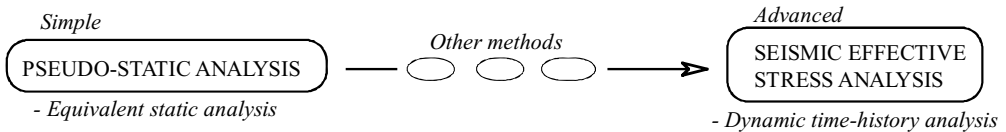


Figure 1. Methods for seismic analysis of earth structures and soil-structure systems.

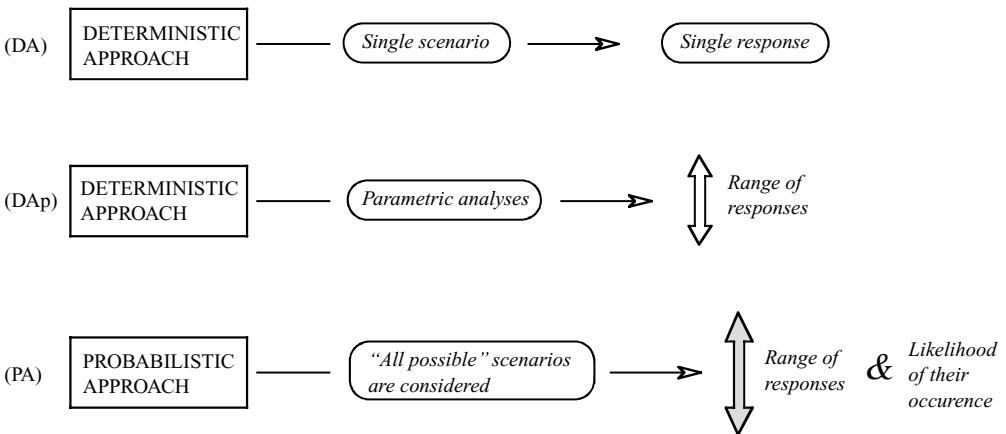


Figure 2. General approaches for assessment of seismic performance of geotechnical structures.

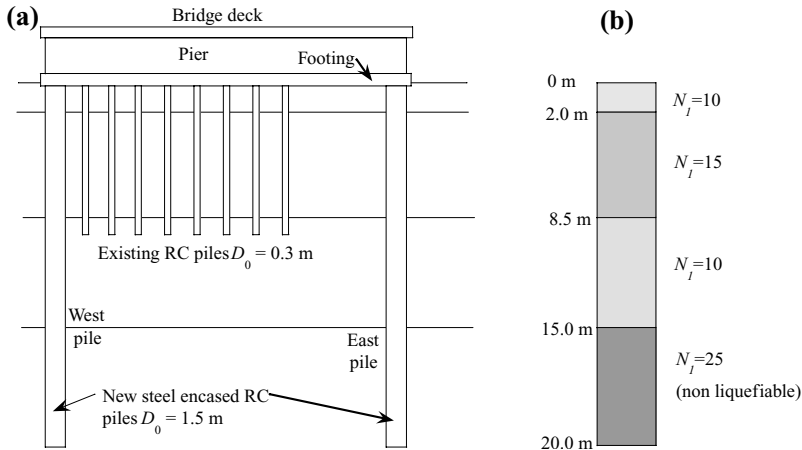


Figure 3. Central pier of the bridge: (a) cross section; (b) simplified soil profile used in seismic effective stress analyses (Bowen and Cubrinovski, 2008).

the uncertainties in the analysis while the probabilistic approach (PA) offers the most rigorous treatment of uncertainties and quantifies their effects on the computed seismic response.

2.3 Adopted approaches

This paper examines three approaches for assessment of the seismic performance in the context outlined above as follows:

1. Pseudo-static analysis within a deterministic approach incorporating parametric evaluation (DA_p)
2. Seismic effective stress analysis using a single scenario (DA)
3. Probabilistic approach based on the so-called PEER framework (Cornell and Krawinkler, 2000) using the seismic effective stress analysis as a computational method (PA)

These assessment approaches can be applied to various earth structures and soil-structure systems, but here they are applied to the assessment of seismic performance of pile foundations in liquefiable soils.

2.4 Case study

The Fitzgerald Avenue Bridge over the Avon River in Christchurch, New Zealand, will be used as a case study. It is a small-span twin-bridge that has been identified as an important lifeline for post-disaster emergency services. Hence, the bridge has to remain operational in the event of a strong earthquake. To this goal, a structural retrofit has been considered involving widening of the bridge and strengthening of the foundation with new large diameter piles. A cross section at the mid span of one of the bridges is shown

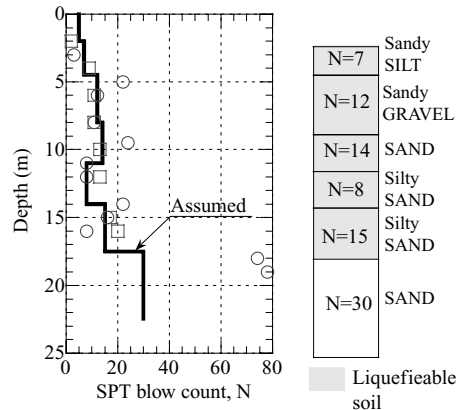


Figure 4. SPT blow count and soil profile at the north-east abutment.

in Figure 3 where both existing piles and new piles are shown.

Figure 4 depicts the SPT blow count and soil profile at the northeast corner of the bridge. This soil profile was adopted in the pseudo-static analyses. The soil deposit consists of relatively loose liquefiable sandy soils with a thickness of about 15 m overlying a denser sand layer. The sand layers have low fines content predominantly in the range between 3% and 15% by weight. Detailed SPT and CPT investigations revealed a large spatial variability of the penetration resistance at the site. Hence, a rigorous investigation of the seismic response of the bridge and its foundation would require consideration of 3-D effects and spatial variability of soils. These complexities are beyond the scope of this paper, however, and rather a simplified scenario will be considered herein with the principal

objective being to examine the response of the pile foundation shown in Figure 3. Here, we will focus on the cyclic response of the foundation during the intense ground shaking; effects of lateral spreading are beyond the scope of this study.

3 PSEUDO-STATIC ANALYSIS

3.1 Objectives

As a practical approach, the pseudo-static analysis should be relatively simple, based on conventional geotechnical data and applicable without requiring significant computational resources. In addition, in order to satisfy the PBEE objectives in the seismic performance assessment, the pseudo-static analysis of piles should:

- Capture the relevant deformational mechanism for piles in liquefying soils
- Permit estimation of the inelastic response and damage to piles, and
- Address the uncertainties associated with seismic behaviour of piles in liquefying soils.

Not all available methods for simplified analysis satisfy these requirements. In particular, in the current practice the treatment of uncertainties in the simplified analysis is often inadequate; commonly, the uncertainties are either ignored or poorly addressed in the analysis. In what follows, a recently developed method for pseudo-static analysis of piles in liquefying soils (Cubrinovski and Ishihara, 2004; Cubrinovski et al., 2009) is used to assess the seismic performance of the new piles of Fitzgerald Bridge. Key features of the simplified analysis and effects of uncertainties on the pile response are discussed.

3.2 Computational model and input parameters

Although in principle the pseudo-static analysis could be applied to a pile group, typically it is applied to a single-pile model. This is consistent with the overall philosophy for a gross simplification adopted in this approach. A typical beam-spring model representing the soil-pile system in the simplified pseudo-static analysis is shown in Figure 5. The model can easily incorporate a stratified soil profile (multi-layer deposit) with different thickness of liquefied layers and a crust of non-liquefiable soil at the ground surface. Since one of the key requirements of the analysis is to estimate the inelastic deformation and damage to the pile, in the proposed model simple but non-linear load-deformation relationships are adopted for the soil-pile system. The soil is represented by bilinear springs in which degraded stiffness and strength of the soil are used to account for effects of non-linear behaviour and liquefaction. The pile is modelled

using a series of beam elements with a tri-linear moment-curvature relationship. Parameters of the model are illustrated in Figure 5 for a typical three-layer configuration in which a liquefied layer is sandwiched between a surface layer and a base layer of non-liquefiable soils. All model parameters are based on conventional geotechnical data (SPT blow count) and concepts (subgrade reaction coefficient, Rankine passive pressure). In the model, two equivalent static loads are applied to the pile: a lateral force at the pile-head (F) representing the inertial load due to vibration of the superstructure, and a horizontal ground displacement (U_G) applied at the free end of the soil springs (Fig. 5b) representing the kinematic load on the pile due to lateral movement of the free field soils.

3.3 Uncertainties in the parameters of the model

The pseudo-static analysis aims at estimating the maximum response of the pile under the assumption that dynamic loads can be idealized as static actions. Since behaviour of piles in liquefying soils is extremely complex involving very large and rapid changes in soil stiffness, strength and lateral loads on the pile, the key question in the implementation of the pseudo-static analysis is how to select appropriate values for the soil stiffness, strength and lateral loads on the pile for the equivalent static analysis. In other words, what are the appropriate values for β , $p_{L-\max}$, U_G and F in the model shown in Figure 5? The following discussion illustrates that this choice is not straightforward and that all these parameters may vary within a wide range of values.

In the adopted model, effects of liquefaction on stiffness of the soil are taken into account through the degradation parameter β . Observations from full-size experiments and back-calculations from case histories indicate that for cyclic liquefaction (excluding lateral spreading), β typically takes values in the range between 1/10 and 1/50 (Cubrinovski et al., 2006).

Similar uncertainty exists regarding the ultimate pressure from the liquefied soil on the pile or the value of $p_{L-\max}$ in the model. The ultimate lateral pressure $p_{L-\max}$ can be approximated using the residual strength of liquefied soils (S_r) as $p_{L-\max} = \alpha_L S_r$. There are significant uncertainties regarding both α_L and S_r values. The latter is illustrated by the scatter of the data in the empirical correlation between the residual strength of liquefied soils and normalized SPT blow count (N_1)_{60cs} (Seed and Harder, 1991) shown in Figure 6. For example, for a normalized equivalent sand blow count of (N_1)_{60cs} = 10, the residual strength varies approximately between 5 kPa and 25 kPa.

The selection of appropriate equivalent static loads is probably the most difficult task in the pseudo-static analysis. This is because both input loads in the pseudo-static analysis (U_G and F) are in effect

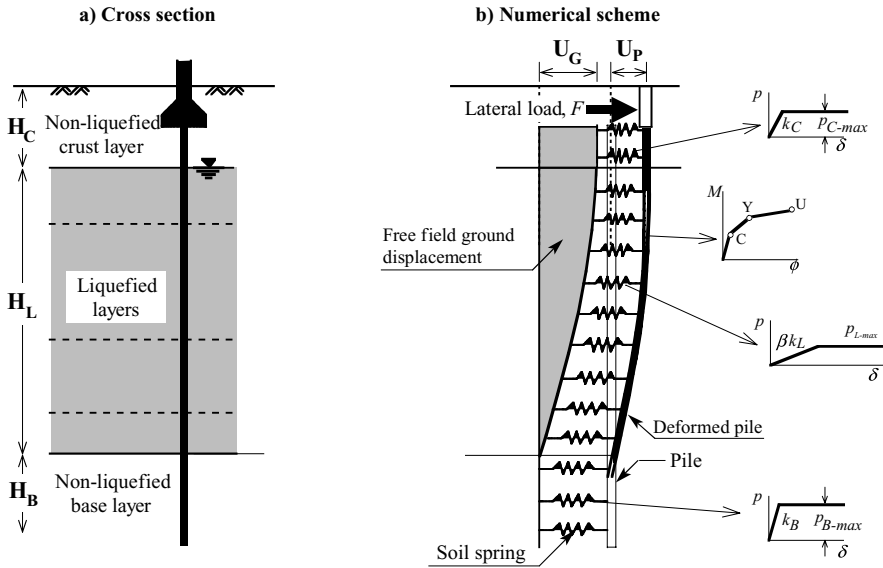


Figure 5. Beam-spring model for pseudo-static analysis of piles (model parameters and characterization of nonlinear behaviour).

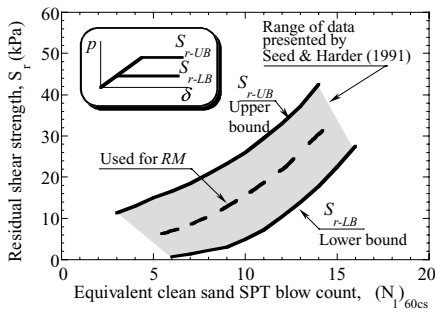


Figure 6. Residual shear strength of liquefied sandy soils (after Seed and Harder, 1991).

estimates for the seismic responses of the free field ground and soil-pile-structure system respectively. The magnitude of lateral ground displacement U_G can be estimated using simple empirical models based on SPT charts such as that proposed by Tokimatsu and Asaka (1998). Using this method, a value of $U_G = 0.36$ m was estimated for the maximum cyclic ground displacement at Fitzgerald Bridge site. Note that since U_G is an estimate for the free field response at the site, it is reasonable to expect a considerable variation in the value of U_G around the above estimate based on an empirical model.

As mentioned earlier, the objective of the pseudo-static analysis is to estimate the peak response of the pile that will occur during an earthquake. The peak loads on the pile due to ground movement and

vibration of the superstructure do not necessarily occur at the same time, and hence, there is no clear and simple strategy how to combine these loads in a static analysis. Recently, Boulanger et al. (2007) suggested that the maximum ground displacement should be combined with an inertial load from the vibration of the superstructure proportional to the peak ground acceleration a_{max} using the following expression: $F = I_c m_s a_{max}$. Here, m_s is the mass of the superstructure whereas I_c is a factor that depends on the period of the earthquake motion and practically provides a rule for combining the kinematic (U_G) and inertial (F) loads on the pile. Again, a wide range of values have been suggested for this parameter: $I_c = 0.4, 0.6$ and 0.8 for a short, medium and long period ground motions respectively (Boulanger et al., 2007).

3.4 Computed response for a reference model (RM)

Based on the procedures outlined above, a so-called *reference model* (RM) was defined for the pile foundation of Fitzgerald Bridge. RM is a single pile model for the new piles (1.5 m in diameter) in which a ‘mid range’ values were adopted for the parameters of the model, as summarized in Table 1. Here, the S_r values of 14 and 36 were derived using the broken line in Figure 6 and normalized blow counts of $(N_1)_{60cs} = 10$ and 15 respectively, for the liquefiable layers. The pile was subjected to a free field ground displacement with a peak value at the ground surface of $U_G = 0.36$ m, indicated in Figure 7a, and a lateral load at the pile head corresponding to a peak ground acceleration of

Table 1. Characteristic values of model parameters.

Parameter	RM	Range of values			
		LB*	—	UB**	
β	—	1/20	1/50	—	1/10
$S_r(N_1 = 10)$ (kPa)	14	6	—	—	22
$S_r(N_1 = 15)$ (kPa)	36	24	—	—	48
I_c	—	0.6	0.4	—	0.8
U_G	(m)	0.36	0.29	—	0.43

* Lower Bound (minimum value);
 ** Upper Bound (maximum value).

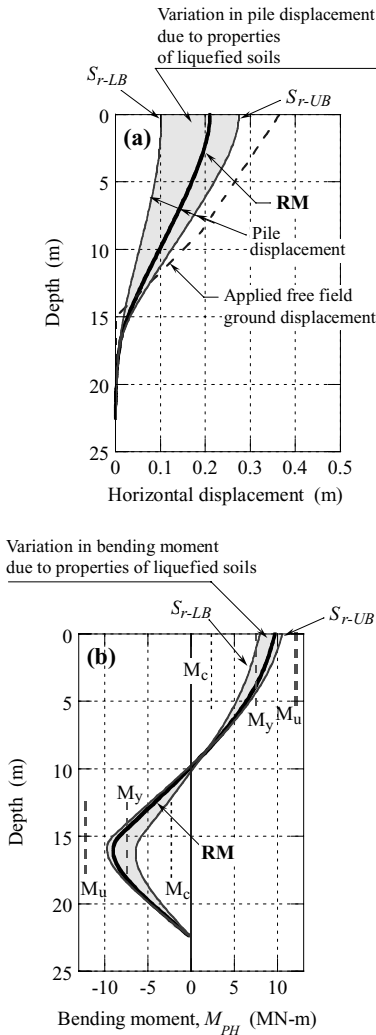


Figure 7. Effects of properties of liquefied soils on the pile response computed in the pseudo-static analysis: (a) pile displacements; (b) bending moments.

$a_{max} = 0.4$ g and an inertial coefficient of $I_c = 0.6$. The computed pile displacement and bending moment for the reference model (RM) are shown with solid lines in Figures 7a and 7b respectively. A pile head displacement of 0.21 m and a peak bending moment at the pile head of 9.6 MN-m were computed. The bending moment exceeded the yield level both at the pile head and at the interface between the liquefied layer and underlying base layer.

3.5 Effects of uncertainties on the pile response

To examine the effects of uncertainties associated with the liquefied soil and lateral loads on the pile, parametric analyses were carried out in which the above parameters were varied within the relevant range of values listed in Table 1. For example, an analysis was conducted in which RM values were used for all parameters except for the stiffness degradation (β) and residual strength (S_r) of the liquefied soil, for which instead the lower bound or minimum values of $\beta = 1/50$, $S_r = 6$ kPa ($N_1 = 10$) and $S_r = 24$ kPa ($N_1 = 15$) were used. Similarly, another analysis was conducted in which the upper bound or maximum values of $\beta = 1/10$, $S_r = 22$ kPa ($N_1 = 10$) and $S_r = 48$ kPa ($N_1 = 15$) were used in conjunction with the RM values for all other parameters. Results of these two analyses are shown in Figure 7 indicating significant effects of the spring properties for the liquefied soil on the pile response.

Figure 8 shows results from a similar pair of analyses in which the value for the applied ground displacement was either decreased ($U_G = 0.29$ m) or increased ($U_G = 0.43$ m) for 20% with respect to the RM displacement of 0.36 m. Again, a large difference in the pile response is seen resulting from a relatively small variation in the ground displacement applied to the pile.

Results of the parametric analyses are summarized in Table 2 and are depicted in tornado charts for the pile head displacement and bending moment (at the pile head) respectively in Figures 9a and 9b. The response of the reference model (RM) is also indicated in these plots for comparison purpose. The results clearly indicate that the pile response is significantly affected by the adopted values for stiffness and strength of the liquefied soil, and to a lesser extent by the adopted values for loads, U_G and F (due to variation of I_c between 0.4 and 0.8). Note that the size of these effects will change with the properties of the soil-pile system (especially with the stiffness of the pile relative to that of the soil), degree of yielding in the soil and pile, and the size of lateral loads from a non-liquefied crust at the ground surface.

3.6 Discussion

The above results clearly illustrate a high sensitivity of the pile response on the parameters of the simplified

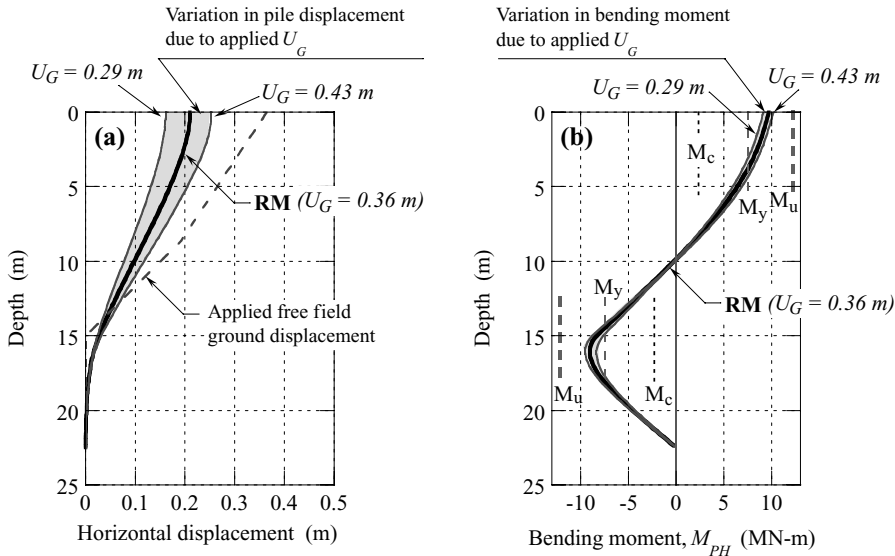


Figure 8. Effects of applied lateral ground displacement on the pile response computed in the pseudo-static analysis: (a) pile displacements; (b) bending moments.

Table 2. Results of parametric analyses.

Model	Pile response	
	U_{PH}^*	M_{PH}^{**}
<i>RM with S_r-LB and β2-LB</i>	0.10	7.8
<i>RM with $U_G = 0.29$ m</i>	0.16	8.9
<i>RM with $I_{s-LB} = 0.4$</i>	0.18	8.9
RM	0.21	9.5
<i>RM with $U_G = 0.43$ m</i>	0.25	9.9
<i>RM with $I_{s-UB} = 0.8$</i>	0.23	10.0
<i>RM with S_r-UB and β2-UB</i>	0.27	10.3

* Pile-head displacement;

** Bending moment at pile head.

model. This sensitivity is not specific to the adopted approach in this study, but rather is a common feature of simplified methods of analysis. It simply reflects the significant uncertainties associated with the complex phenomena considered and their gross simplification in the pseudo-static method of analysis. The results also clearly emphasize the need for a parametric evaluation of the seismic response when using simplified methods of analysis. In terms of the previously introduced assessment approaches, a deterministic approach including parametric analyses (DA_p) would be required when using simplified methods of analysis for seismic performance assessment.

In the current practice, various methods for simplified (pseudo-static) analysis are used. These methods are similar in principle however they all have distinct

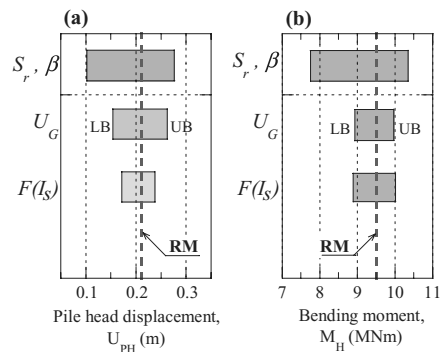


Figure 9. Tornado charts depicting pile response computed in parametric pseudo-static analyses: (a) pile-head displacement; (b) bending moment at pile head.

modelling features and use different load-deformation relationships, geotechnical data and empirical correlations. For this reason, they all require an independent process of ‘calibration’ in which model parameters will be rigorously examined and their relevant range of values identified. Note that this calibration is both model-specific and problem-specific. For example, the pseudo-static analysis method presented herein when applied to the assessment of piles subjected to lateral spreading will need different set of reference values for the model parameters, e.g. magnitude of U_G , load combination rule for U_G and F , and stiffness degradation factor β .

4 SEISMIC EFFECTIVE STRESS ANALYSIS

4.1 Implementation steps

Unlike the simplified analysis procedure where the response of the pile is evaluated using a beam-spring model and equivalent static loads as input, the seismic effective stress analysis incorporates the soil, foundation and superstructure in a single model and uses an acceleration time history as a base excitation for this model. This analysis aims at a very detailed modelling of the ground response and soil-structure system in a rigorous dynamic analysis. The seismic effective stress analysis is difficult to implement in practice because it requires significant computational resources and specialists knowledge from the user. In concept, the effective stress analysis could be considered as the opposite approach to that of the practical pseudo-static analysis.

The implementation of the effective stress analysis generally involves three steps (Fig. 10):

1. Determination of the parameters of the constitutive model
2. Definition of the numerical model
3. Dynamic analysis and interpretation of results.

In the first step, parameters of the constitutive model for the soil are determined using results from laboratory tests on soil samples and data from in-situ investigations. The required types of laboratory tests are model-specific and are generally used for determination of stress-strain relationships and effects of excess pore pressures on the soil response (liquefaction tests). Whereas most of the constitutive model parameters can be directly evaluated from data obtained from laboratory tests and in-situ investigations, some parameters are determined through a calibration process in which best-fit values for the parameters are identified in simulations of laboratory tests (so-called element test simulations).

In the second step, the numerical model is defined by selecting appropriate element types, dimensions of the model, mesh size, boundary conditions and initial stress state. The last two requirements often receive less attention, even though they have pivotal influence on the performance of the constitutive model and numerical analysis. Namely, one of the key advantages of the advanced numerical analysis is

that no postulated failure and deformation modes are required, as these are predicted by the analysis itself. In this context, the selection of appropriate boundary conditions along end-boundaries and soil-foundation-structure interfaces are critically important in order to allow unconstrained response and development of relevant deformation modes. Similarly, stress-strain behaviour of soils and liquefaction resistance are strongly affected by the initial stress state of the soil, and therefore, an initial stress analysis is required to determine gravity-induced stresses in all elements of the model resembling those in the field.

In the final step, an acceleration time history (ground motion) is selected which is used as a base excitation for the model. Considering the geometry of the problem and anticipated behaviour, numerical parameters such as computational time increment, integration scheme and numerical damping are adopted, and the dynamic effective stress analysis is then executed. The analysis is quite demanding on the user in all steps including the final stages of post-processing and interpretation of results since it requires an in-depth understanding of the phenomena considered, constitutive model used and particular numerical procedures adopted in the analysis. Benchmarking exercises imply that these rigorous requirements are not always satisfied in the profession even when dealing with static problems (Potts, 2003).

In cases when the analysis is used for a rigorous assessment of the seismic performance of important structures, high-quality geotechnical data from field investigations and laboratory tests are needed in order to model the particular deformational characteristics (stress-strain relationships) of the soils in questions. Such data are rarely available, however, and this has been often used as an excuse to avoid using the seismic effective stress analysis in geotechnical practice. However, even when conventional data is used as input, this analysis still provides an important and unique contribution in the seismic performance assessment of earth structures and soil-foundation-structure systems, as illustrated below.

4.2 Numerical model

The 2-D finite element model adopted for the effective stress analysis of the pile foundation of Fitzgerald

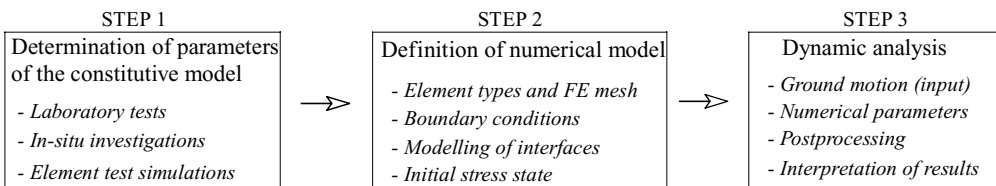


Figure 10. Key steps in the implementation of seismic effective stress analysis.

Bridge is shown in Figure 11. The model includes the soil, pile foundation (both existing piles and new piles) and the superstructure. Four-node solid elements were employed for modelling the soil and bridge superstructure while beam elements were used for the piles and pile cap. Lateral boundaries of the model were tied to share identical displacements in order to simulate a free field ground motion near the boundaries. Along the soil-pile interface, the piles and the adjacent soil were connected at the nodes and were forced to share identical horizontal displacements.

The footing, bridge deck and pier were all modelled as linear elastic materials with an appropriate tributary mass to simulate inertial effects from the superstructure. Nonlinear behaviour of the piles was modelled with a hyperbolic moment-curvature ($M-\phi$) relationship while the soil was modelled using an elastic-plastic constitutive model developed specifically for modelling sand behaviour and liquefaction problems (Cubrinovski and Ishihara, 1998a; 1998b). Details of the constitutive law and numerical procedures will not be discussed herein, but rather modelling of the liquefaction resistance based on conventional geotechnical data will be demonstrated.

The model shown in Figure 11 was subjected to an earthquake excitation with similar general attributes (magnitude, distance and PGA) to those relevant for the seismic hazard of Christchurch. An acceleration record obtained during the 1995 Kobe earthquake ($M = 7.2$) was scaled to a peak acceleration of 0.4 g and used as a base input motion. Needless to say, the adopted input motion is neither representative of the source mechanism nor path effects specific to Canterbury, but rather it was considered a relevant excitation typical for the size of the earthquake event considered in the analysis.

4.3 Modelling of liquefaction resistance

For a rigorous determination of parameters of the employed constitutive model, about 15 to 20 laboratory tests are required including monotonic and cyclic,

drained and undrained shear tests. In the absence of laboratory tests for the soils at the Fitzgerald Bridge site, the constitutive model parameters were determined by largely adopting the parameters of Toyoura sand (Cubrinovski and Ishihara, 1998a) and modifying the dilatancy parameters as described below.

Borelogs, penetration resistance data from CPTs and SPTs and conventional physical property tests were the only geotechnical data available for the soils at Fitzgerald Bridge site. A rudimentary modelling of stress-strain behaviour of soils considering liquefaction would require knowledge or assumption of the initial stiffness of the soil, strength of the soil and liquefaction resistance. Since none of these were directly available for the soils at this site they were inferred based on the measured penetration resistance. The liquefaction resistance was determined using the conventional procedure for liquefaction evaluation based on empirical SPT charts (Youd et al., 2001). After an appropriate correction for the fines content and the magnitude of the earthquake (using magnitude scaling factor), these charts provided the cyclic stress ratios required to cause liquefaction in 15 cycles, which are shown by the solid symbols in Figure 12. Using these values as a target liquefaction resistance, the dilatancy parameters of the model were determined and the liquefaction resistance was simulated for the two layers, as indicated with the lines in Figure 12. These two lines represent the simulated liquefaction resistance curves for the soils with $N_1 = 10$ and $N_1 = 15$ respectively. To illustrate better this process, results of element test simulations for the sand with $N_1 = 10$ are shown in Figure 13 where effective stress paths and stress-strain curves are shown for three different cyclic stress ratios of 0.12, 0.18 and 0.30 respectively. The number of cycles required to cause liquefaction in these simulations and the corresponding stress ratios are indicated with open symbols in Figure 12, depicting the simulated liquefaction resistance. Thus, only conventional data were used for determination of model parameters. While this choice of material parameters practically eliminates

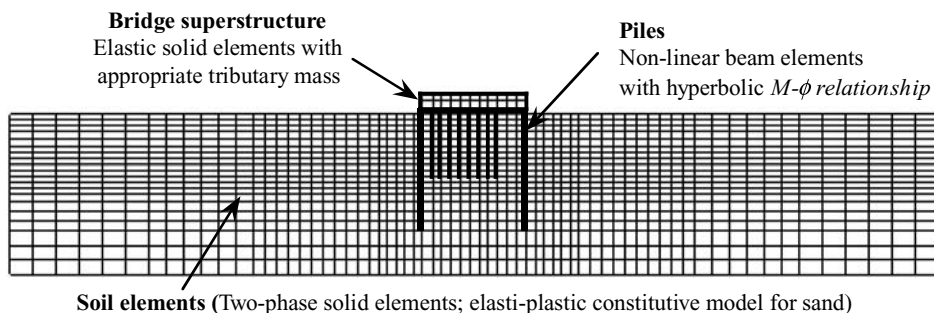


Figure 11. Numerical model used in the seismic effective stress analysis of Fitzgerald Bridge.

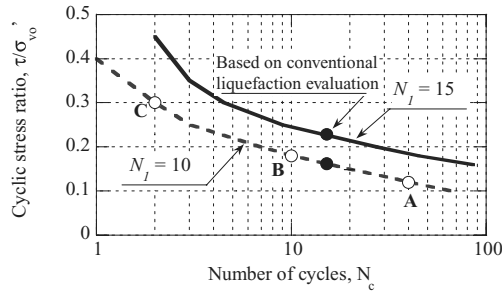


Figure 12. Liquefaction resistance curves adopted in the seismic effective stress analysis (curves represent model simulations).

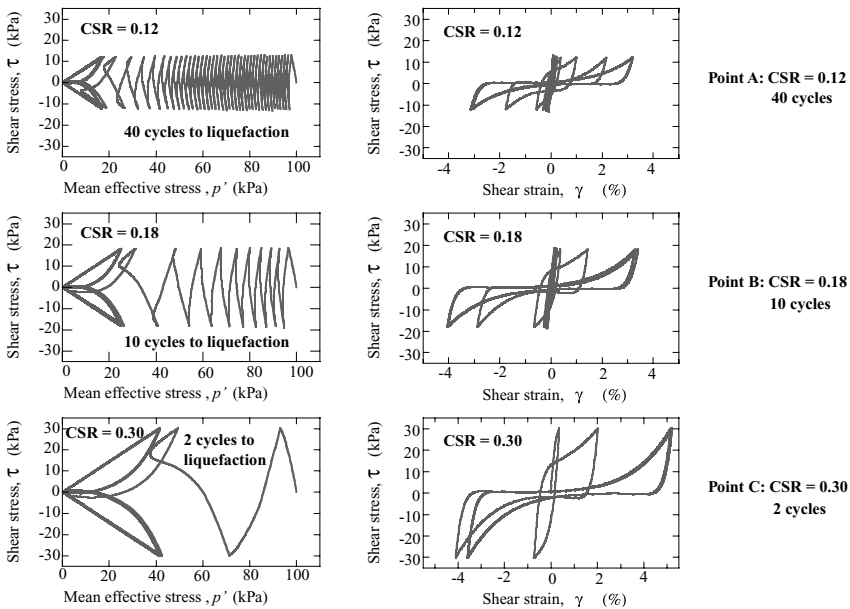


Figure 13. Effective stress paths and stress-strain curves obtained in element test simulations for the soil layer with $N_1 = 10$.

the possibility for a rigorous quantification of the seismic response of the soil-pile-structure system, one may argue that the parameters of the model defined as above are at least as consistent and credible as those used in a conventional liquefaction evaluation.

4.4 Computed ground response

Figure 14a shows time histories of excess pore water pressure computed at two depths corresponding to the mid depth of layers with $N_1 = 10$ and $N_1 = 15$ ($z = 13.2$ m and 7.0 m respectively). In the weaker layer, the pore water pressure builds-up rapidly in only one or two stress cycles until a complete liquefaction of this layer was reached at approximately

15 seconds. In the denser layer ($N_1 = 15$), the pore water pressure build up is slower and affected by the liquefaction in the underlying looser layer. The latter is apparent in the reduced rate of pore pressure increase after 15 seconds on the time scale. Clearly, the liquefaction of the loose layer at greater depth produced “base-isolation” effects and curtailed the development of liquefaction in the overlying denser layer. Figure 14b further illustrates the development of the excess pore water pressure throughout the depth of the deposit with time. Note that part of the steady build up of the pore pressure in the upper layer ($N_1 = 15$) is caused by “progressive liquefaction” or upward flow of water from the underlying liquefied layer. Needless to say, the pore pressure characteristics outlined

in Figure 14 will be reflected in the development of transient deformation and permanent displacements of the ground. The seismic effective stress analysis can simulate these complex features of the ground response and their effects on structures.

4.5 Computed pile response

The computed time history of horizontal displacement of the pile is shown in Figure 15a together with the corresponding displacement of the ground in the free field. The peak pile displacement reached

about 0.18 m at the pile head, which is significantly smaller than the peak free field displacement at the ground surface of 0.30 m indicating relatively stiff pile behaviour (the pile is resisting the ground movement). The response shown in Figure 15a indicates that the peak displacements of the pile and free field soil occurred at different times, at approximately 19 seconds and 32 seconds, respectively. The peak bending moment of the pile was attained at the pile head (M_{Ht}) with values slightly below the yield level (Figure 15b). This time history indicates not only the peak level of the response but also the number of

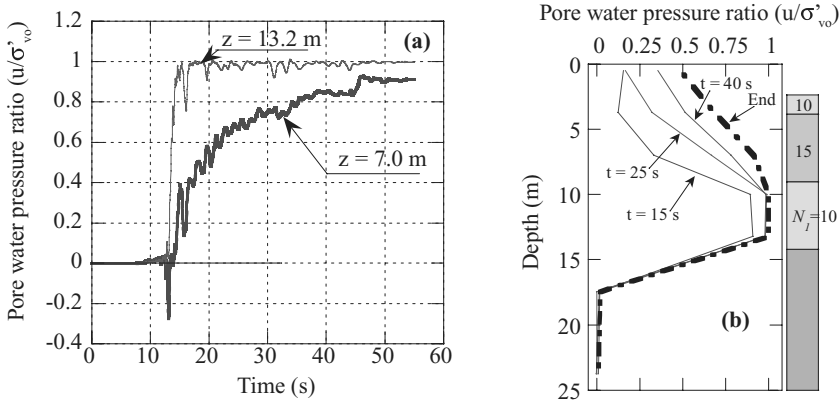


Figure 14. Computed excess pore water pressure in the free field soil: (a) time histories at mid-depths of layers with $N_1 = 10$ and $N_1 = 15$; (b) distribution of excess pore water pressures throughout the depth of the deposit and time.

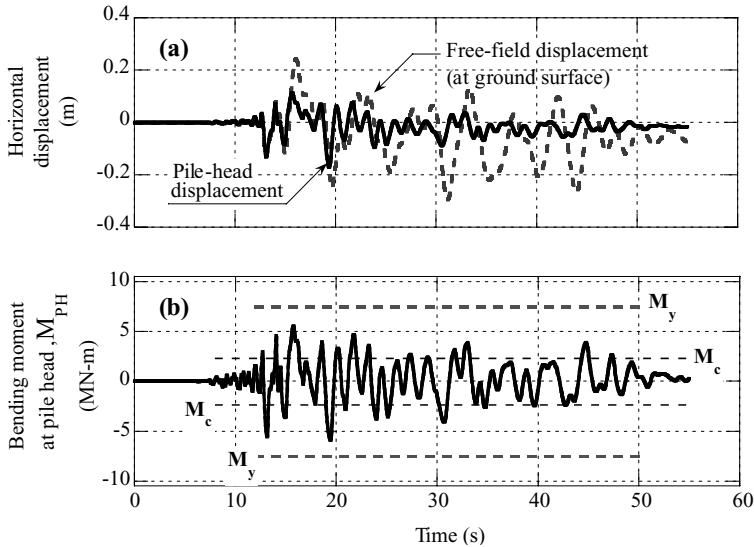


Figure 15. Computed response of the pile in seismic effective stress analysis: (a) horizontal displacement at pile head; (b) bending moment at pile head.

significant peaks exceeding cracking level which in turn provides additional information on the damage to the pile. Similar level of detail is available for other components of the numerical model including the foundation soil, old and new piles, and response of the superstructure.

4.6 Discussion

As illustrated in the above application, the seismic effective stress analysis allows realistic and detailed simulation of the seismic response of geotechnical structures induced by strong earthquakes. Effects of soil-structure interaction are easily included in the analysis, in which sophisticated nonlinear models can be used both for soils and for structural members. The analysis permits a rigorous assessment of the seismic performance of the soil-structure system as a whole and each of its components.

Effects of excess pore water pressure are often a key factor in the seismic response of ground and earth structures. Hence, the ability of this analysis to capture details of pore pressure build-up, development of liquefaction and consequent loss of strength and stiffness in the soil is of great value. The method simulates the most salient features of seismic behaviour of soils including peculiar effects from individual layers and cross interaction amongst them such as “base-isolation effects” or progressive liquefaction due to upward flow of water.

Because of its complexity and high-demands on the user, the seismic effective stress analysis is typically applied in a deterministic fashion using a single scenario (DA) or input ground motion. However, this analysis also provides an excellent tool for assessment of alternative design solutions, effectiveness of structural strengthening and soil remediation (countermeasures against liquefaction) on a comparative basis by quantifying their effects on the ground deformation, structural response and reduction (control) of damage.

5 PROBABILISTIC APPROACH

5.1 Background

A probabilistic approach (PEER framework) for Performance-Based Earthquake Engineering (PBEE) has been recently developed for a robust assessment of seismic performance of structures (Cornell and Krawinkler, 2000; Krawinkler 1999). This approach employs an integrated probabilistic treatment of all uncertainties that apply to the prediction of ground motion and evaluation of system response and associated damage (uncertainties associated with characteristics of ground motion, material properties, modelling approximations, seismic response and associated physical damage for a given response measure). Hence, it provides an alternative and more

rigorous way for assessment of seismic performance of engineering structures. Recently, attempts have been made to expand the application of this approach to geotechnical problems (Kramer, 2008; Ledezma and Bray, 2007; Bradley et al., 2008). Details of the probabilistic PBEE assessment are beyond the scope of this paper, and instead key features and implementation of this procedure will be outlined in the following using the case study considered.

5.2 Analysis procedure

Christchurch is located in a region of relatively high seismicity and Fitzgerald Bridge is expected to be excited by a number of earthquakes during its lifespan. Considering all possible earthquake scenarios, the response of the bridge and its pile foundation needs to be evaluated for earthquakes with different intensities ranging from very weak and frequent earthquakes to very strong but rare earthquakes. Characteristics of ground motions caused by these earthquakes are very difficult to predict because of the complex and poorly understood source mechanism, propagation paths of seismic waves and surface-soil effects. In order to account for these uncertainties in the ground motion characteristics, the following procedure was adopted.

A suite of 40 ground motions recorded during strong earthquakes was first selected, as indicated in Figure 16a. Next, each of these records was scaled to ten different peak amplitude levels, i.e. peak ground accelerations of $a_{\max} = 0.1, 0.2, 0.3, 0.4, 0.5, 0.6, 0.7, 0.8, 0.9$ and 1.0 g. Thus, 400 different ground motions were generated in this way, as indicated in Figure 16b, having very different amplitudes, frequency content and duration. Using each of these time histories as a base input motion, 400 effective stress analyses were conducted using the model shown in Figure 11 and procedures outlined earlier, as schematically depicted in Figure 16c.

5.3 Computed response

The next challenge to overcome is how to present results from 400 time history analyses in a meaningful way. Obviously, some relaxation in the rigorous treatment of time histories and evaluation of the response is needed here. In the probabilistic PBEE approach, this is achieved through the following reasoning:

1. First, the object of assessment is identified. Thus, instead of examining the entire soil-pile-structure system, for example, the attention is focused on the response of the pile.
2. Next, a representative measure for the response of the pile is identified, i.e. a parameter that describes and quantifies the pile response efficiently (“Engineering Demand Parameter”, EDP in the PBEE terminology). Hence, instead of using the entire time history of the pile response, the peak value of the

(a) 40 Earthquake Records

EQ1: Northridge 1994
EQ2: Imperial Valley 1979
•
•
•
•
EQ40: Kobe 1995

(b) 400 Ground Motions

GM1: EQ1, $a_{\max} = 0.1 \text{ g}$
GM2: EQ1, $a_{\max} = 0.2 \text{ g}$
•
•
•
•
GM10: EQ1, $a_{\max} = 1.0 \text{ g}$
GM11: EQ2, $a_{\max} = 0.1 \text{ g}$
•
•
•
•
GM399: EQ40, $a_{\max} = 0.9 \text{ g}$
GM400: EQ40, $a_{\max} = 1.0 \text{ g}$

(c) 400 Time History Analyses

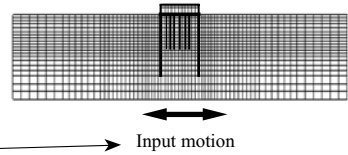


Figure 16. Schematic illustration of multiple effective stress analyses used in the probabilistic approach.

- response parameter (EDP) is used as a measure for the size of the response.
3. Similarly, a single parameter is used to describe the input motion or measure the intensity of the ground motion (“Intensity Measure”, IM).
 4. Finally, the results of the analyses are presented by correlating the parameter representing the size of the response (EDP) with the intensity of the ground motion (IM).

For example, one way of presenting the results from the 400 analyses with respect to the pile response for Fitzgerald Bridge is shown in Figure 17a where the peak displacement at the pile head (U_{PH}) computed in the analysis is plotted against the peak acceleration of the input motion (a_{\max}). Here, U_{PH} represents a measure for the size of the pile response (EDP) while a_{\max} is a measure for the intensity of the ground motion (IM). Each open symbol in Figure 17a represents the result (peak response of the pile) from one of the 400 seismic effective stress analyses while the solid line is an approximation of the trend from a regression analysis.

The scatter of the data in Figure 17a is quite large indicating a significant uncertainty in the prediction of the peak response of the pile based on the peak acceleration of the ground motion (input PGA). Clearly one issue in this approach is the need to identify an efficient intensity measure that reduces the uncertainty and hence improves the predictability of the pile response. However, there is no wide-ranging intensity measure that is appropriate for all problems but rather the intensity measure is problem-dependent and is affected by the particular deformational mechanism and features of the phenomena considered. Based on detailed numerical studies, Bradley et al. (2008) have identified that velocity-based intensity measures correlate the best with the seismic response of piles, and that in particular the velocity spectrum

intensity (VSI) is the most efficient intensity measure for piles. This is illustrated in Figure 17b where the same results for U_{PH} from the 400 analyses shown in Figure 17a are re-plotted using VSI as the intensity measure for the employed input motions. The improved efficiency and predictability of the pile response is evident in the reduced uncertainty as depicted by the smaller dispersion of the data. The plots shown in Figure 17 provide means for estimating the peak response of the piles of Fitzgerald Bridge for all levels of earthquake excitation, from elastic response to failure.

5.4 *Assessment of seismic performance: Demand hazard curve*

A conventional output from Probabilistic Seismic Hazard Analysis (PSHA) is the so-called seismic hazard curve which expresses the aggregate seismic hazard at a given site by considering all relevant earthquake sources contributing to the hazard. A seismic hazard curve for Christchurch (Stirling et al., 2001) is shown in Figure 18a where a relationship between the peak ground acceleration (a_{\max}) and mean annual rate of exceedance of a given a_{\max} is shown. For example, this hazard curve indicates that an earthquake event generating an $a_{\max} = 0.28 \text{ g}$ in Christchurch has a recurrence interval or return period of 475 years (or 10% probability of exceedance in 50 years).

By combining the seismic hazard curve expressed in terms of a_{\max} (Fig. 18a) and the correlation between the peak pile response (U_{PH}) and a_{\max} established from the results of the effective stress analyses (Fig. 17a), a so-called “Demand Hazard Curve” was produced, shown in Figure 18b for the existing and new piles respectively. In this way, the probability for exceedance of a certain level of peak pile displacement in any given year (annual rate of exceedance) could be estimated for the piles of Fitzgerald Bridge. A unique

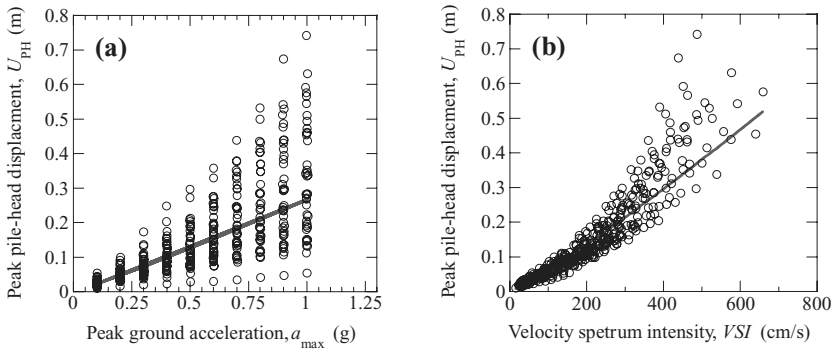


Figure 17. Computed pile-head displacements (U_{PH}) in 400 effective stress analyses: (a) correlation between (U_{PH}) and a_{max} of input motion; (b) correlation between (U_{PH}) and velocity spectrum intensity (VSI) of input motion.

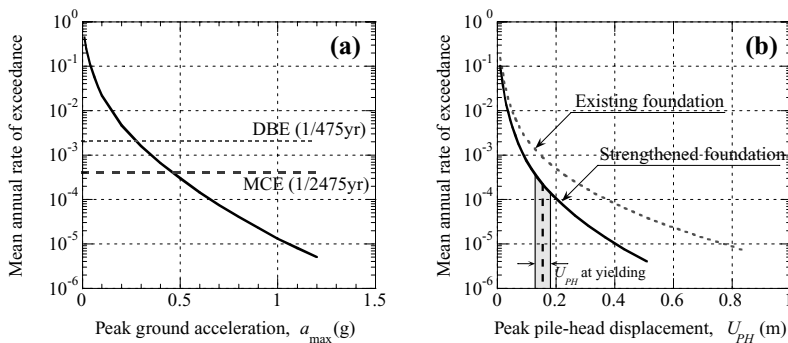


Figure 18. Probabilistic assessment of seismic performance of pile foundation: (a) seismic hazard curve for Christchurch; (b) Demand hazard curve for piles of Fitzgerald Bridge.

feature of the demand hazard curve is that it provides an assessment of the seismic performance of the pile foundation by considering all earthquake scenarios for the site in question and associated uncertainties in the characterization of the ground motion.

In the above interpretation, the peak pile displacement was adopted as a measure for the size of the pile response because it is a good indicator of the peak deformation and damage to the pile (Bradley et al., 2008). Thus, U_{PH} can be converted to a parameter directly correlating with the damage to the pile (the peak curvature of the pile), and then the demand hazard curve can be easily expressed in terms of a damage measure, thus providing likelihood of characteristic damage levels for the pile (cracking, yielding, failure). Furthermore, the physical damage of the pile foundation will lead to losses, and hence, the demand hazard curve can be also used to quantify the seismic performance in terms of economic measures (dollars). This in turn will provide an economic basis for decisions on seismic design, repair and retrofit, and will facilitate communication of the design outside the profession.

Clearly, the probabilistic assessment provides alternative measures of the seismic performance of the pile while rigorously accounting for the uncertainties associated with the seismic hazard and phenomena considered. This approach can be applied to seismic performance assessment of any other component of the soil-pile-structure system and to the bridge as a whole. Also, other sources of uncertainty such as those related to modelling, soil and site characterization can be easily incorporated in the analysis and their effects on the response can be quantified.

6 SUMMARY AND CONCLUSIONS

Three different approaches for assessment of the seismic performance of earth structures and soil-structure systems have been presented. These approaches use different models, analysis procedures and are of vastly different complexity. All are consistent with the performance-based design philosophy according to which the seismic performance is

Table 3. Methods for seismic performance assessment of soil-structure systems: Key features and contributions in the assessment.

Method of assessment	Key features	Specific contributions in the assessment	Shortcomings
Pseudo-static analysis	<ul style="list-style-type: none"> • Simple • Conventional data and engineering concepts 	<ul style="list-style-type: none"> • Evaluates the response and damage level for the pile (parametric evaluation is needed) • Enhances foundation design 	<ul style="list-style-type: none"> • Does not consider the response of the soil-foundation-structure system
Seismic effective stress analysis	Realistic simulation of ground response & seismic soil-foundation-structure interaction	<ul style="list-style-type: none"> • Detailed assessment of seismic response of pile foundations including effects of liquefaction and SSI • Integral assessment of inelastic behaviour of soil-foundation-structure systems • Enhances communication of design concepts between geotechnical and structural engineers 	<ul style="list-style-type: none"> • Ignores uncertainties in the ground motion
Probabilistic PBEE framework	<ul style="list-style-type: none"> • Considers all earthquake scenarios • Quantifies seismic risk 	<ul style="list-style-type: none"> • Addresses uncertainties associated with ground motion characteristics on a site specific basis • Provides engineering measures (response and damage) and economic measures (losses) of performance • Enhances communication of design outside profession 	<ul style="list-style-type: none"> • Ignores details of the seismic response

assessed using deformational criteria and associated damage; however, they focus on different aspects and make different contribution in the assessment. Key features of the examined approaches and their specific contribution in the seismic performance assessment are summarized in Table 3.

6.1 Pseudo-static analysis

The pseudo-static analysis is a practical approach based on conventional geotechnical data, engineering concepts and relatively simple computational models. It postulates a specific deformational mechanism and aims at estimating the peak response of the pile due to an earthquake under the assumption that dynamic loads can be represented as static actions. The method is easy to implement in practice and provides a suitable tool for evaluation of the seismic response of piles and associated damage to piles. This approach focuses on the pile itself (enhances foundation design) while it ignores the response of the system and other components of the system.

In addition to the uncertainties associated with the complex seismic behaviour and ground motion, there are significant uncertainties related to modelling arising from unknown variables and inaccurate model form. These modelling uncertainties are very pronounced in the simplified analysis because of the significant approximations and gross simplification of the problem adopted in this approach. Thus, when using simplified methods of analysis in the assessment, it is critically important to address these uncertainties through systematic parametric studies.

6.2 Seismic effective stress analysis

The seismic effective stress analysis aims at a very realistic simulation of the seismic behaviour of earth structures and soil-structure systems. It incorporates

sophisticated nonlinear models for the soil, foundation and structure in a rigorous dynamic analysis. The key contribution of this analysis is that it allows examining in detail the performance of the soil-structure system under a strong earthquake excitation. Even results from a single analysis (such as that presented herein) illustrate the benefit of a detailed soil-pile-structure analysis.

The experience from recent strong earthquakes suggests that design concepts in which pile foundations are considered to remain within the elastic range of deformation during strong earthquakes are not economical. The PBEE philosophy also suggests accepting damage in seismic events, if this proves the most economic solution (Krawinkler, 1999). Hence, there is a need to consider inelastic deformation concurrently in both the superstructure and pile foundation, and to assess the performance both on a system level and at a component level (Gazetas and Mylonakis, 1998). Advanced numerical analyses provide this capability and methods based on the effective stress principle further permit consideration of important ground response features such as effects of excess pore pressures and liquefaction.

Since this approach focuses on a detailed evaluation of the seismic response, it is not appropriate for parametric evaluation including large number of analyses. In this context, the selection of an appropriate input motion is problematic in cases when rigorous assessment and quantification of the seismic performance of important structures is needed.

6.3 Probabilistic approach

The probabilistic approach offers a unique perspective in the assessment of seismic performance, first through a rigorous treatment of the single most important source of uncertainty in seismic studies, the ground

motion, and then by providing alternative performance measures in the assessment, engineering and economic ones. It allows us to combine geotechnical and structural design aspects and to evaluate their effects on the performance of the entire system (soil-foundation-structure system) and each of its components. It is worth noting that in spite of the use of an effective stress analysis as a basic computational tool in the probabilistic approach employed herein, details of the response were not considered in the seismic performance assessment.

6.4 Future needs

The examined approaches address different aspects in the assessment and, in essence, are complimentary in nature. It is envisioned that these approaches will be used in parallel in the future, and hence, they all require further development and improvement. The pseudo-static approach requires establishment of improved models depicting multiple deformational mechanisms and in particular more rigorous and systematic procedures for parametric evaluation of the seismic response. Methods based on seismic effective stress analysis require improvement in the simulation of large ground deformation and more emphasis on use of sophisticated nonlinear models for an integrated analysis of the soil-foundation-structure system. Finally, further development of the probabilistic approach is needed including efforts towards simplification of procedures and identification of representative response measures (EDPs) and ground motion measures (IMs) for various specific problems.

All of these analysis procedures improve our understanding of complex seismic behaviour and enhance engineering judgement, which is probably one of the most significant contributions that one can expect from such an exercise.

ACKNOWLEDGEMENTS

The authors would like to acknowledge the financial support provided by the Earthquake Commission (EQC), New Zealand.

REFERENCES

Bradley, B., Cubrinovski, M. & Dhakal, R. 2008. Performance-based seismic response of pile foundations. *ASCE Geotechnical Special Publication* 181: 1–11.

Boulanger, R. Chang, D., Brandenberg, S. & Armstrong, R. 2007. Seismic design of pile foundations for liquefaction effects. *4th Int. Conference on Earthquake Geotechnical Engineering-Invited Lectures*, Ed. Pitilakis, 277–302.

Bowen, H.J. & Cubrinovski, M. 2008. Effective stress analysis of piles in liquefiable soil: A case study of a bridge

foundation,” *Bulletin of the NZ Society for Earthquake Engineering*, 41(4): 247–262.

Cornell, C.A. & Krawinkler, H. 2000. Progress and challenges in seismic performance assessment. *PEER Center News*, 3(2): 1–4.

Cubrinovski, M. & Ishihara, K. 1998a. Modelling of sand behaviour based on state concept. *Soils and Foundations* 38(3): 115–127.

Cubrinovski, M. & Ishihara, K. 1998b. State concept and modified elastoplasticity for sand modelling. *Soils and Foundations* 38(4): 213–225.

Cubrinovski, M. & Ishihara, K. 2004. Simplified method for analysis of piles undergoing lateral spreading in liquefied soils. *Soils and Foundations*, 44(25): 119–133.

Cubrinovski, M., Kokusho, T. & Ishihara, K. 2006. Interpretation from large-scale shake table tests on piles undergoing lateral spreading in liquefied soils. *Soil Dynamics and Earthquake Engineering*, 26: 275–286.

Cubrinovski, M., Ishihara, K. & Poulos, H. 2009. Pseudostatic analysis of piles subjected to lateral spreading. *Special Issue, Bulletin of NZ Society for Earthquake Engineering*, 42(1): (in print).

Gazetas G. & Mylonakis, G. 1998. Seismic soil-structure interaction: new evidence and emerging issues. *ASCE Geotechnical Special Publication* 75: 1119–1174.

Kramer, S.L. 2008. Performance-Based Earthquake Engineering: opportunities and implications for geotechnical engineering practice. *ASCE Geotechnical Special Publication* 181: 1–32.

Krawinkler, H. 1999. Challenges and progress in performance-based earthquake engineering. *Int. seminar on seismic engineering for Tomorrow—In Honour of Professor Hiroshi Akiyama* Tokyo, Japan, November 26, 1999: 1–10.

Ledezma, C. & Bray, J. 2007. Performance-based earthquake engineering design evaluation procedure for bridge foundations undergoing liquefaction-induced lateral spreading. *PEER Report 2007*: 1–136.

Potts, D.M. 2003. Numerical analysis: a virtual dream or practical reality? *The 42nd Rankine Lecture, Geotechnique* 53(6): 535–573.

Seed, R.B. & Harder, L.F. 1991. SPT-based analysis of cyclic pore pressure generation and undrained residual strength. *H. Bolton Seed Memorial Symposium Proc.*, 2: 351–376.

Stirling, M.W., Pettinga, J., Berryman, K.R. & Yetton, M. 2001. Probabilistic seismic hazard assessment of the Canterbury region. *Bulletin of NZ Society for Earthquake Engineering* 34: 318–334.

Tokimatsu K. & Asaka Y. 1998. Effects of liquefaction-induced ground displacements on pile performance in the 1995 Hyogoken-Nambu earthquake. *Special Issue of Soils and Foundations*, September 1998: 163–177.

Youd, T.L. & Idriss, I.M. 2001. Liquefaction resistance of soils: summary report from the 1996 NCEER and 1998 NCEER/NSF workshops on evaluation of liquefaction resistance of soils. *Journal of Geotechnical and Geoenvironmental Engineering*, 127(4): 297–313.

Outline of performance-based design for railway earth structures in Japan

M. Shinoda, K. Watanabe, K. Kojima & M. Tateyama

Railway Technical Research Institute, Tokyo, Japan

ABSTRACT: The design standard for railway earth structures was recently revised under the leadership of a technical committee that consisted of universities and railway companies. This design standard is based on a performance-based design method, and revises the standard that was established about fourteen years ago. This paper introduces the basis for this new design standard, which includes design flow, design life, required performance, and verification. As an example of this new performance-based design standard, the residual deformation from a level-2 seismic event was verified.

1 INTRODUCTION

In the past, embankments, earth slopes, cut slopes, retaining walls, and abutments in Japan were constructed using specification-based designs on the basis of an engineer's experience, without any advanced design method. Therefore, it was accepted that such structures would collapse when subjected to an earthquake or heavy rain and would need to be rebuilt as soon as possible. This was because the deformation and strength characteristics of soil are complex and have potential variability as compared to those of concrete or steel, so that it was considered to be unreasonable to apply an advanced design method to such structures. Here, it is important to define structures constructed with soil or rock, including track beds, embankments, cut slopes, reinforced soil, drainage structures, slope protection, and related structures as earth structures.

Table 1 shows the revisions that have been made to the technical standard for railway earth structures in Japan. The first design standard for railway earth

structures was established in 1961, which was only for Japan's super express system, Shinkansen. This standard was revised in 1967, making it a design and construction specification for earth structures. It was revised again in 1978 when the Japanese National Railways (JNR) was privatized. In 1987, the JNR was divided into several companies collectively called the Japan Railway (JR) Group. After the privatization of the JNR and the establishment of the JR Group, the above revised design standard was applied until 1991. In 1992, this design standard was revised again to introduce a new construction method and to take another look at the design and construction method described in the 1978 design standard. In 1995, the Hyogo-ken Nambu earthquake occurred near the city of Kobe, Japan. This earthquake caused over 5,000 deaths and extensive property damage in a highly urbanized area of Japan. Many railway structures were also severely damaged. After this earthquake, in 1999, the new seismic design standard for railway structures, including earth structures, bridge piers, frame structures, bridge support structures, foundations, and open cut tunnels, was established to take into consideration the earthquake motion caused by inland active faults. It was the first to adopt a performance-based design and was mainly composed of a dynamic analysis to calculate a structure's behavior when subjected to an earthquake. In 2001, the ministerial ordinance describing technical standards for railway structures was revised from a specification-based design method to a performance-based design method. Based on the above revision, the design standard for concrete structures was revised to adopt the performance-based design method in 2004.

With this background, the design standard for earth structures was revised to adopt the performance-based design method in 2007. This paper outlines the performance-based design method for earth structures.

Table 1. Revision of technical standard for railway earth structures in Japan.

Year	Name of standard
1961	Design standard for super express structures.
1967	Design and construction specification for earth structures.
1987	Establishment of JR Group.
1992	Design standard for earth structures.
1999	Seismic design standard for railway structures.
2001	Revision of ministerial ordinance.
2004	Design standard for concrete structures revised, adopting a performance-based design.
2007	Design standard for earth structures revised, adopting a performance-based design.

2 DESIGN BASIS

2.1 Scope

This design standard for railway earth structures can be used to create a performance-based design. This performance-based design method considers the individual conditions of structures and newly developed techniques and evaluates them from the viewpoint of performance. This standard can be applied to the construction of new structures on the main line, but can also be applied to the verification of existing earth structures, the construction of side tracks, the replacement of railway tracks due to river improvements or overhead crossings, and the reinforcement of existing earth structures.

2.2 Definitions

This design standard for railway earth structures defines terminology related to a performance-based design. The following definitions apply:

Earth structures: structures constructed with soil or rock, including track beds, embankments, cut slopes, reinforced soil, drainage structures, slope protection, and related structures.

Performance of structures: the ability exhibited by the structures.

Performance of requirement: the required performance of structures based on the objectives and functions.

Verification of earth structures: judgment as to whether the required performance of a design is satisfied for the entire earth structure, track bed, slope protection, drainage structure, etc. Verification methods use experiments with a full-scale structure, numerical analysis after theoretical verification, and empirical specifications defined with empirical knowledge.

Safety: performance ensuring that structures do not threaten the lives of users or others.

Serviceability: performance ensuring that users or others are comfortable with the structures, and that the structures perform the required functions.

Restorability: the ability of structures to have their performance easily restored when the structures are damaged.

Durability: the ability of the structures to resist changes in material properties over time.

Verification index: the replacement of a performance item with a physical quantity that can be evaluated quantitatively.

Pre-verified specification: specification of a construction method, material, geometry, etc. already verifying the satisfaction of the required performance level.

Static condition: condition of application of permanent load or ground deformation.

Seismic condition: condition of application of seismic action in addition to the action of the static condition.

Rainy condition: condition of application of rainy action in addition to the action of the static condition.

2.3 Design flow

Figure 1 shows the design flow for an embankment. According to the performance-based design method, performance requirements should be determined that consider the importance of the structure, track structure, and difficulty of restorability by a railway company. After that, a response value should be calculated with the preliminary sizing using the limit state design method. Subsequently, this response value should be verified to satisfy the performance limit value determined from the performance requirement.

However, since earth structures are essentially simple, it is not always appropriate to spend too much labor designing them, from the viewpoint of cost or the design and construction schedule. In particular, the above design process is practically difficult for a small scale or urgent construction project. Moreover, it becomes impractical or dangerous to design a structure without sufficient investigation or knowledge.

Therefore, to increase the convenience of the design method and consider the variability of the soil properties with a view to safety, a pre-verified specification classified into three performance levels according to the required performance is included in the performance-based design method. This method allows a conventional specification to be subdivided

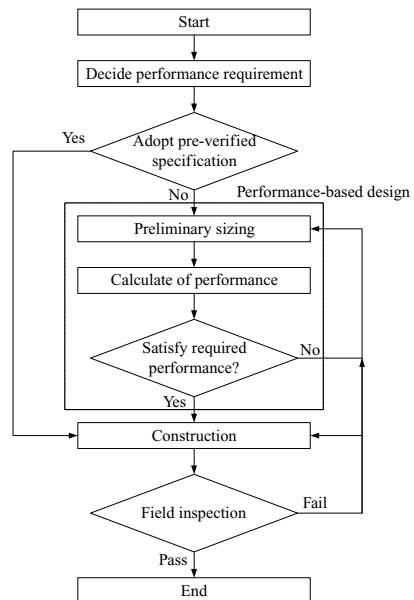


Figure 1. Design flow for embankment.

according to the required performance level, resulting in a more practical method. This is why the pre-verified specification is expected to be generally applied in designing structures.

In the case of applications of nonstandard specifications due to field conditions, the desire for a reasonable design rather than a standard design in a large scale construction project, or the adoption of a new type of earth structure, the performance-based design method is expected to be applied in the design work.

2.4 Design life

In principle, the design life is determined from the required service life, maintenance, environmental conditions, and life cycle cost. The design life is the length of time that the structure is expected to exhibit the required performance and is generally essential when considering the durability of the material used in the design. However, an earth structure, especially an embankment, becomes more stable over time, in contrast with other structures, such as a bridge pier. Therefore, it is not essential to determine the design life from the point of view of material durability or the necessity of replacement.

However, a design service life should be determined in relation to set actions caused by earthquakes or heavy rain in the design work. In this case, the design service life can be set at 100 years, which is a standard design life value for other structures.

2.5 Required performance

2.5.1 Required performance of earth structures

The required performance of earth structures should generally be set as safety, serviceability, and restorability. Tables 2 to 4 show the performance items and examples of the performance index for each required performance, such as safety, serviceability, and restorability.

2.5.2 Performance rank

For a practical design, it is necessary to classify the required performance level. In this standard, the required performance is given a performance rank of

Table 2. Performance item and safety index.

Performance item	Example of performance index
Failure	Internal stability of earth structure, displacement, deformation
Stability	Stability of foundation, including global stability and deformation of consolidation, displacement, deformation.
Train running	Displacement, deformation.

Table 3. Performance item and index for serviceability.

Performance item	Example of performance index
Riding quality	Displacement, deformation
Track maintenance	Displacement, deformation
Vibration or noise	Vibration level, noise level
Exterior	Deformation, cracking

Table 4. Performance item and index for restorability.

Performance item	Example of performance index
Deformation, damage, remaining resistance	Displacement, deformation

1 to 3. An earth structure with a performance rank of 1 exhibits little deformation under a static load and does not exhibit excessive deformation under extremely rare accidental action. An example of a performance rank of 1 is the earth structure that is used to support the ballastless track generally used in Japan for the Shinkansen super express system. An earth structure with a performance rank of 2 exhibits deformation that can be repaired by normal maintenance under the static condition and does not exhibit devastating deformation under extremely rare accidental action. An example of a performance rank of 2 is an earth structure supporting the ballast track of an important line. An earth structure with a performance rank of 3 exhibits deformation under a static load and does not exhibit deformation with no collapse under frequently occurring action.

It is important that these performance ranks be determined, not only from the viewpoint of the importance of the railway structure but also because of the necessity of a railway corporation to manage its business. Here, the performance rank for the required performance can originally be set by the railway corporation.

2.5.3 Principle of verification

Basically, a limit state based on the required performance should be determined for each earth structure. It should then be confirmed that the whole or part of the structure does not reach the limit state. For an earth structure constructed according to the pre-verified specification established in each performance rank, this structure is identified with that having the required performance. This pre-verified specification is already verified as satisfying the required performance by numerical analysis or past experience. This specification is considered to be a safety design. Therefore, in order to create a reasonable design for

a large scale construction project, the performance-based design method should be employed based on this standard.

2.6 Verification

2.6.1 Verification method

In the case of using a verification formula, the following formula can be used for each performance index:

$$\gamma_i \cdot \frac{I_{Rd}}{I_{Ld}} \leq 1.0 \quad (1)$$

where I_{Rd} is the design response value, I_{Ld} is the design limit value, and γ_i is the structure coefficient. This structure coefficient is generally set at a value of 1.0 to 1.2, considering the importance of the structure, social influence of the limit state of the structure, and importance of mitigation. The performance-based design method in this standard compares the response value with the limit value to verify each performance index after setting the limit state equivalent to the required performance. It is necessary to verify the structure's performance under the most severe conditions in the design life, considering the time-dependent characteristics of the structure.

2.6.2 Basis of safety verification

An earth structure's safety is verified to set the limit value of failure, residual displacement, and dynamic displacement amplitude of the structure subjected to actions during the construction and design life. The deformation and strength characteristics of soil can change due to various actions, including earthquakes or heavy rain. For example, in an earthquake, the stability of an earth structure decreases due to the softening of the saturated sand foundation supporting the structure because of an increase in the pore pressure in the foundation. Likewise, in a heavy rain, the stability of an earth structure decreases due to a decrease in the shear resistance because of a decrease in the suction or an increase in the pore pressure. Therefore, it is very important to set characteristic values related to strength or deformation while considering such actions in the design life.

2.6.3 Basis of serviceability verification

An earth structure's serviceability is verified to set limit values for track maintenance workability, riding quality, noise, vibration, and exterior within the design life. An earth structure exhibits excessive deformation or settling after the track construction, leading to an extreme increase in track maintenance. In particular, in the case of ballastless track applied for the purpose of low maintenance, large settlement or deformation causes a huge maintenance cost without functioning. Therefore, the limit value of an earth structure for serviceability should be determined as a residual settlement below the roadbed that is less than the limit

value considering the total cost of maintenance. The limit value for stiffness can be set so as not to exhibit excessive stress or strain in the railway structure, as the need arises.

If necessary, the limit values for noise and vibration should be determined for a super express or conventional line. For a super express, there is a special need to set an environmental standard related to noise and vibration. For a conventional line, the limit value should be set appropriately, especially for an embankment on soft ground. These verifications require the use of measured data and numerical analyses of this data because a prediction method for noise and vibration has not yet been established.

Table 5 can be referenced when the limit value for ground settlement is set. There is a correlation between the progression rate of undulation displacement and maintenance work. In addition, there is a correlation between the progression rate of undulation displacement and the residual displacement of the ground. Based on the above correlation, an allowable residual displacement can be set by considering the possible maintenance work for the specific line. Here, the possible maintenance work should be considered economically, as compared to the initial investment for ground settlement and the usual maintenance cost. The limit value criterion for ground settlement is identical to the settlement on the top of the embankment because a residual displacement of the embankment is not exhibited due to the stabilization of the embankment.

2.6.4 Basis of restorability verification

An earth structure's restorability is verified as not reaching the limit state of the following deformation level by considering the restorability of the structure when subjected to an accidental action, such as an earthquake or heavy rain. The deformation level should be set based on the following performance in relation to the residual deformation of the structure when subjected to an earthquake or heavy rain:

Deformation level 1: there is little deformation, there is no impairment of function, and it is possible to use the structure without any maintenance.

Deformation level 2: there is a small deformation, but the function can be restored quickly by a small amount of maintenance.

Deformation level 3: there is a large deformation, but the function can be restored by partial reconstruction.

Table 5. Limit value criterion of ground settlement for serviceability.

Residual displacement (cm)	Limit value of progression rate of settlement
10 cm	3 cm/year

Deformation level 4: there is an extremely large deformation. Therefore, the function cannot be restored without total reconstruction in some cases.

A damage level for an earth structure subjected to an earthquake or heavy rain should be set as follows, considering the restorability of the entire earth structure or its structural characteristics:

Damage level 1: there is little damage.

Damage level 2: there is damage that makes maintenance necessary in some cases.

Damage level 3: there is damage that makes maintenance necessary.

Damage level 4: maintenance is necessary. The replacement of part of the earth structure is necessary in some cases.

Table 6 shows the standard relationships between performance rank, deformation level, and damage level. The embankment consists of incidental structures, such as the track bed, slope protection, and drainage structure, in addition to the foundation and embankment itself. Each part has an influence that is different from the embankment itself, with a different allowable damage level and design life. Therefore, the relationships shown in Table 6 are a general standard. This means the deformation level and damage level can be set based on the performance rank to consider the individual condition. This standard provides the standard limit values for settlement as shown in Table 7 for practical design work.

2.7 Pre-verified specification

In the past, numerical design work for embankments had not been performed because specification-based design work was conducted based on the slope angle,

compaction method, required degree of compaction, and soil properties of the foundation, as determined from past records or experience. There were mainly two reasons for this. One is that a numerical design method is not appropriate for considering the variability of backfill soil or foundation properties. The other is that it is relatively easy to repair a damaged embankment. In fact, it is not appropriate to conduct numerical design work for an embankment in a small scale construction project, but would negate the merit of the structural simplicity. Therefore, in this standard, the pre-verified specification is provided to conduct the conventional specification-based design.

Table 8 shows the basic pre-verified specification for embankments. The following discusses 6.0 m high embankments as representative examples for each performance rank. An embankment with a performance rank of 1 is specified with an inclination of more than 1:1.8 and the installation of primary and secondary reinforcements with spacings of 1.5 m and 0.3 m, respectively, as shown in Figure 2a. An embankment with a performance rank of 2 is specified with an inclination of 1:1.8 or 1:1.5 and the installation of

Table 8. Basic pre-verified specification for embankments.

Performance rank	Inclination	Primary reinforcement	Secondary reinforcement
1	More than 1:1.8	Essential	Essential
2	More than 1:1.5	If necessary	Essential
3	More than 1:1.5	Basically not	Essential

Table 6. Standard relationships between performance rank, deformation level, and damage level.

Item	Performance rank 1	Performance rank 2	Performance rank 3
Deformation level	1	2–3	3–4
Damage level	1–2	2–3	3–4

Table 7. Standard limit values for settlement.

Deformation level	Vertical displacement
1	No displacement
2	Less than 20 cm
3	More than or equal to 20 cm and less than 50 cm
4	More than or equal to 50 cm

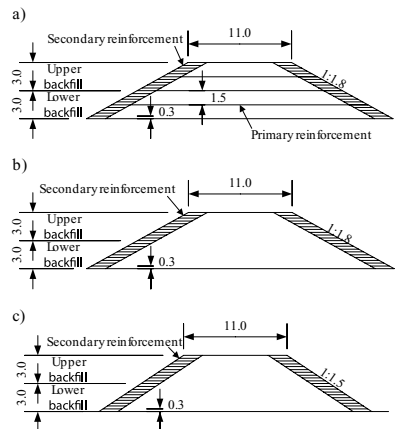


Figure 2. Representative geometries of embankment in each performance rank: a) performance rank 1, b) performance rank 2 and c) performance ranks 2 and 3.

secondary reinforcements with a spacing of 0.3 m, as shown in Figures 2b and 2c. An embankment with a performance rank of 3 is specified with an inclination of 1:1.5 and the installation of secondary reinforcements with a spacing of 0.3 m, as shown in Figure 2c.

The quality of the backfill soil is different in each performance rank. The backfill soil property for each performance rank will be explained later.

2.8 Action

For the performance-based design of earth structures, an appropriate combination of possible actions during the construction and design life should be considered. These actions include permanent, variable, and accidental actions.

A permanent action affects the earth structure continuously with negligible variation. For an earth structure, such permanent actions are dead loads, such as self weight or track weight. The earth pressure due to the self weight can be treated as a permanent action. A variable action is of frequent or continuous occurrence without negligible variation. These include train load, impact load, wind load, earth pressure due to train load, roadbed pressure, and especially earthquakes and rain, which will be explained later. An accidental action is of rare occurrence but causes significant damage to the earth structure. These actions include heavy earthquakes or rain.

2.8.1 Seismic action

The seismic standard prescribes Level-1 and Level-2 earthquake motions as design earthquake motions. These Level-1 and Level-2 earthquake motions are set at the bedrock and their properties are represented by acceleration response spectra. Level-1 earthquake motion has been used in combination with the elastic design method. In addition to being treated as a static load (for the seismic coefficient method), it is also provided as a seismic wave form for dynamic analysis. The intensity of this earthquake motion is determined by referring to the earthquake risk for a return period of 50 years. Level-2 earthquake motion is considered to occur in regions near faults, including hypocenters, and to be as severe as the strong earthquake motions experienced during the 1995 Hyogoken-Nambu Earthquake. The acceleration response spectra of Level-2 earthquake motion as standard earthquake motion considers the following:

- i. The acceleration response spectrum (Spectrum I) targeting near-land interpolate earthquakes that has been considered in a conventional design.
- ii. The acceleration response spectrum (Spectrum II) determined according to a statistical analysis based on past earthquake observation records targeting earthquakes produced by inland active faults. The

seismic standard also prescribes the ground surface design earthquake motion for each ground classification, and the characteristics of that earthquake motion are outlined by the acceleration response spectra. Since the characteristics of the surface ground must be expressed as accurately as possible, the ground is classified into eight types, as shown in Table 8. This classification corresponds to the natural period of the ground computed based on the initial velocity of the shear wave of the ground surface. Ground surface design earthquake motions are determined to be Level-1, Spectra I of Level-2, or Spectra II of Level-2 earthquake motions. As representative examples, the elastic acceleration response spectrum (Spectrum II) of Level-2 earthquake motions and the time history waveform (Spectrum II) of ground surface design earthquake motions (Level-2 earthquake motions) are shown in Figures 3 and 4, respectively.

2.8.2 Rain action

In contrast to RC or steel structures, the stability of an earth structure decreases when rain penetrates into the backfill soil of the embankment, potentially causing the collapse of the earth structure. Therefore, a verification of an earth structure subjected to rain should be conducted. If there is accumulated precipitation data for a long period near the concerned construction area, this can be used to calculate the probabilistic precipitation with a specific return period. If there is no accumulated precipitation data near the concerned construction area, the probabilistic precipitations with specific return periods for ten minute, hourly, daily, and annual rainfalls provided by this standard can be used. These probabilistic rainfalls with specific return periods should be selected for the respective verifications. For example, the design of a drainage structure is conducted using a 10 minute probabilistic rainfall with a return period of 5 years against

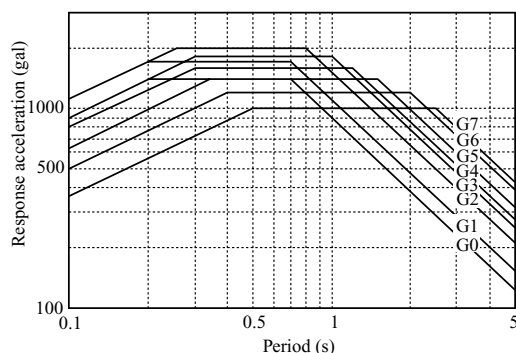


Figure 3. Elastic acceleration response spectra of ground surface design earthquake motions (Spectrum II of Level-2 earthquake motion).

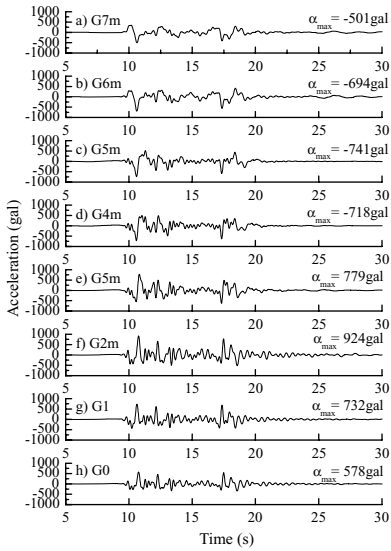


Figure 4. Time-history waveform of ground surface design earthquake motion (Spectrum II).

a localized torrential downpour. These probabilistic precipitations with specific return periods were calculated using the accumulated precipitation data for 40 years. Therefore, these probabilistic precipitations will be updated when additional precipitation data is accumulated.

On the other hand, the stability of an embankment decreases due to the penetration of rainfall over a long time. There are mainly two effects on the stability of an embankment subjected to rain. One is a decrease in the suction in the embankment due to the increase in the degree of saturation of the backfill soil. The other is a decrease in the effective pressure due to the decrease in the pore pressure in the backfill soil of the embankment in the case of long-term rainfall penetration. To ensure the stability of an embankment subjected to rain, a verification should be conducted.

To verify the performance of an embankment subjected to rain, an unsaturated seepage analysis can be conducted to consider all of the water characteristics, including the degree of saturation in the backfill soil of the embankment. To conduct an unsaturated seepage analysis, the maximum precipitation and time-history of the precipitation are necessary. This standard provides hourly, daily, or annual probabilistic rainfall with two specific return periods for the verification. The two probabilistic precipitations were provided as Action-1 and Action-2 with return periods of 100 and 1,000 years, respectively, as simulated rainfall of frequent or rare occurrence. Figures 5 and 6 show representative examples of probabilistic daily precipitation maps with a return period of 100 and 1,000 years

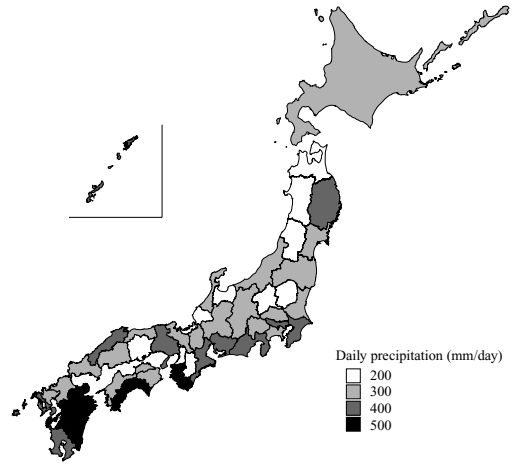


Figure 5. Probabilistic hourly precipitation map with a return period of 100 years for the whole country of Japan.

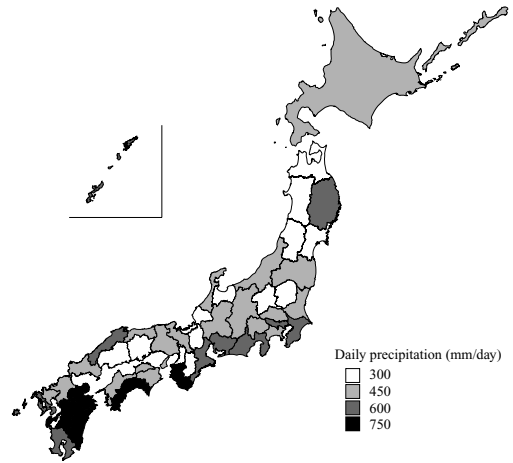


Figure 6. Probabilistic daily precipitation map with a return period of 1000 year for the whole country of Japan.

(Action-1 and Action-2), respectively. The maximum precipitation can be set by referring to the provided probabilistic precipitation, as shown in Figures 5 and 6, if there is no accumulated precipitation data near the concerned area. If it is necessary to set local probabilistic hourly or daily precipitations with a return period of 100 years, the local probabilistic precipitation maps proposed by Shinoda & Honjo (2007) can be referenced. Figure 7 shows a proposed probabilistic daily precipitation map with a return period of 100 years for Kanto region. This standard also provides two types of precipitation time-histories for short and long durations.

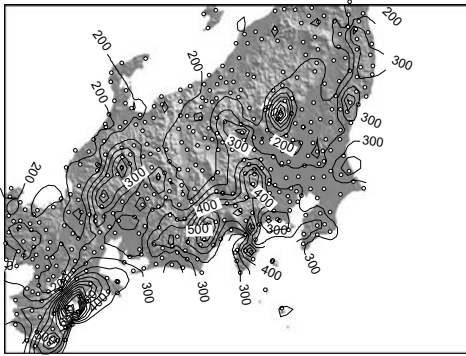


Figure 7. Probabilistic daily precipitation with a return period of 100 year in Kanto region (after Shinoda and Honjyo 2007).

2.9 Design value

2.9.1 Design value of backfill and surface soil

It is recommended that a laboratory test be conducted, such as a triaxial compression test, to determine a design value for the soil material of the embankment. To verify the stability of an embankment under static or seismic conditions, appropriate laboratory tests are the drained triaxial compression test for sand and the undrained triaxial compression test for clay. To verify the stability of an embankment under rainy conditions, the appropriate laboratory test is an unsaturated triaxial compression test to determine the water content of the backfill. It is important when conducting the above triaxial compression tests to set an appropriate confining pressure in accordance with the actual conditions.

Soil materials for embankments are classified as backfill and surface soils in this standard, as shown in Figure 8. This is because, in practice, the surface soil along a slope is generally very difficult to compact, thus requiring a lower friction angle. Moreover, the cohesion of unsaturated surface soil generally depends on the degree of saturation. The degree of saturation of the surface soil is usually higher due to the effects of rainfall. This indicates that the cohesion of surface soil may become lower than that of backfill soil. Thus, the properties of surface soil were modeled by using a relatively lower friction angle and cohesion than backfill soil.

Due to a limited budget or small scale construction, there may be a case where it is difficult to conduct the above triaxial tests. In this case, design values for backfill and surface soils for an embankment are provided in this standard, as shown in Tables 9 to 14. These design values were determined for each soil group, A to D. These soil groups were classified using the geotechnical classification of the Japanese Geotechnical Society. Tables 9 to 14 show backfill and surface soil design values that can be used for

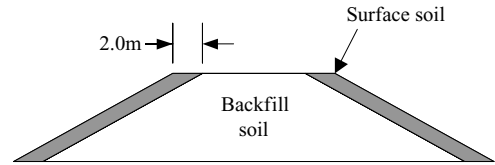


Figure 8. Classification of backfill and surface soil of embankment.

Table 9. Ground classification for seismic design.

Ground classification	Natural period (s)	Description
G0	–	Hard rock
G1	–	Bedrock
G2	0.25 and shorter	Diluvium
G3	0.25 to 0.5	Dense soil
G4	0.5 to 0.75	Dense to soft soil
G5	0.75 to 1.0	Soft soil
G6	1.0 to 1.5	Very soft soil
G7	1.5 and longer	Extremely soft soil

Table 10. Design values for the backfill soil of an embankment for stability verification under static, seismic, and rainy condition.

Soil group	γ (kN/m ³)	c (kN/m ²)	ϕ (degree)
A	18	6	45
B	17	6	40
C	16	6	35
D	14	20	25

Note: For rainy conditions, the degree of saturation of the backfill is less than 80%.

Table 11. Design values for the surface soil of an embankment for stability verification under static, seismic, and rainy conditions.

Soil group	γ (kN/m ³)	c (kN/m ²)	ϕ (degree)
A	18	3	40
B	17	3	35
C	16	3	30
D	14	10	20

Note: For rainy conditions, the degree of saturation of the backfill is less than 80%.

stability verifications under static, seismic, and rainy conditions. For rainy conditions, the design values of the backfill and surface soils are classified using the degrees of saturation.

If the compaction of the backfill soil is considered to be insufficient and causes a loose condition for the backfill, the design value of the backfill soil should be set the same as the design value of the surface soil. If the compaction of the backfill soil is confirmed to be

Table 12. Design values for the unsaturated backfill soil of an embankment under rainy conditions.

Soil group	γ (kN/m ³)	c (kN/m ²)	ϕ (degree)
A	19	3	45
B	18	3	40
C	17	3	35
D	15	10	25

Note: The degree of saturation of the backfill is less than 100% and greater than or equal to 80%.

Table 13. Design values for the unsaturated surface soil of an embankment under rainy conditions.

Soil group	γ (kN/m ³)	c (kN/m ²)	ϕ (degree)
A	19	1.5	40
B	18	1.5	35
C	17	1.5	30
D	15	5	20

Note: The degree of saturation of the backfill is less than 100% and greater than or equal to 80%.

Table 14. Design values for the saturated backfill soil of an embankment under rainy conditions.

Soil group	γ (kN/m ³)	c (kN/m ²)	ϕ (degree)
A	20	0	45
B	19	0	40
C	18	0	35
D	16	10	25

Note: The degree of saturation of the backfill is equal to 100%.

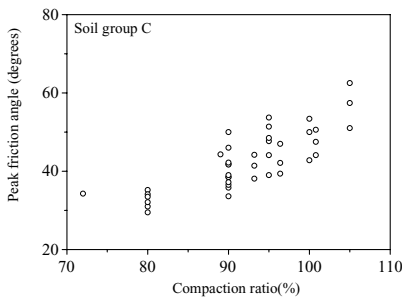


Figure 9. Sensitivity of peak friction angle to the ratio.

sufficient by field inspection, with a degree of compaction of more than 90%, the friction angle of the backfill soil increases, as shown in Figure 9. When the higher friction angle of the backfill soil is used, an appropriate judgment is essential on the results of the field or laboratory tests.

Table 15. Design values for the saturated surface soil of an embankment under rainy conditions.

Soil group	γ (kN/m ³)	c (kN/m ²)	ϕ (degree)
A	20	0	40
B	19	0	35
C	18	0	30
D	16	5	20

Note: The degree of saturation of the surface soil is equal to 100%.

2.9.2 Design value for ground

A design value for the ground is calculated by multiplying the characteristic value of the soil property by the ground inspection factor. The ground inspection factor should be determined to consider the accuracy and reliability of the ground inspection.

The design friction angle or design cohesion of the ground soil property is important for designing earth structures. Therefore, the design friction angle or design cohesion should be determined by the standard penetration test (SPT) or a laboratory test.

3 VERIFICATION EXAMPLE

As mentioned before, the performance-based design of an embankment is conducted according to the flow chart shown in Figure 1. Practically, an appropriate combination of actions should be considered, including static, rainy, or seismic conditions. In the following, as a representative example, the performance of an embankment under the level-2 seismic condition is verified by the performance-based design method.

3.1 Model configuration

Figure 10 shows a model for performance verification when a structure is subjected to a level-2 seismic load. The soil property is set as soil group C, as shown in Tables 9 and 10. The foundation is assumed to be an improved soil having high stiffness and strength. The performance requirement of this model is assumed to have performance rank 2. This indicates that the deformation level of this embankment is 2 to 3, according to Table 6. In this example, the required deformation level is assumed to be level 3. Accordingly, referring to Table 7, the design limit value for settlement can be set to 50 cm.

3.2 Verification equation of level-2 seismic residual deformation

The verification of level-2 seismic residual deformation is conducted to ensure that the response value for settlement at the top of the embankment is less than

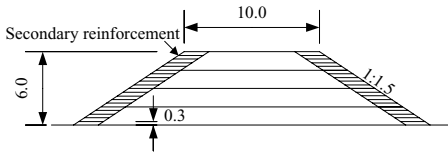


Figure 10. Model configuration for the performance verification of an embankment subjected to a level-2 seismic load.

the design limit value for settlement, based on Equation (1). In this verification, the following equation can be used:

$$\gamma_i \cdot \frac{S_{Rd}}{S_{Ld}} \leq 1.0 \quad (2)$$

where S_{Rd} is the design response value for settlement, S_{Ld} is the design limit value for settlement, and γ_i is a structure coefficient, which is generally set as 1.0. The design response value for settlement is a summation of the deformation along a circular slip surface, settlement due to the densification of the embankment and foundation. Generally, the settlement along the circular slip surface is the largest and most important in practice. Therefore, in this paper, the deformation along the circular slip surface is explained in the following. This deformation can be calculated by Newmark's sliding block analysis (Newmark, 1965), which will be explained in the following section.

3.3 Newmark's sliding block analysis

In this standard, Newmark's sliding block analysis (Newmark 1965) was adopted for the verification of the seismic deformation. It is a simplified procedure employed in the design code of railway structures in Japan (RTRI 2007), in which the seismic deformation of earth slopes or GRS slopes subjected to a strong ground motion can be calculated by integrating the equation for the rotational motion of a soil mass contained within the critical circular slip surface by assuming the failure mass as a rotational rigid block. The equation for rotational motion is solved for the rotation caused by the difference between the driving and resisting moments. The critical slip surface is determined by the conventional modified Fellenius method (Fellenius 1927), using a specific acceleration or seismic coefficient to yield a safety factor of 1.0. Hereafter, this acceleration and seismic coefficient will be referred to as the yield acceleration and yield seismic coefficient, respectively. Requisites for such an analysis are the unit weight, friction angle, and cohesion of the soil, along with the design strength of the reinforcement. For calculating the seismic deformation, it is not necessary to consider input parameters in addition to those mentioned above. The best feature of this analysis is that it is practically useful and less

time consuming in terms of calculation. Newmark's sliding block analysis will be hereafter referred to as the Newmark analysis.

Figure 11 shows the flow chart of the standard deterministic Newmark analysis based on the RTRI design code. The seismic stability analysis is conducted with the conventional modified Fellenius method to determine the center and radius of the critical circular slip surface and yield acceleration.

The safety factor in the above seismic stability analysis can be obtained from the following equation:

$$FS = \frac{M_r}{M_d} = \frac{M_{rw} + M_{rc} + M_{rt} - k_h M_{rk}}{M_{dw} + k_h M_{dk}} \quad (3)$$

where FS is the safety factor; k_h , seismic coefficient; M_r , overall resisting moment; M_d , overall driving moment; M_{rw} , resisting moment due to the self-weight of the soil; M_{rc} , resisting moment due to soil cohesion; M_{rt} , resisting moment due to the design strength of reinforcement; M_{rk} , decrease in the resisting moment

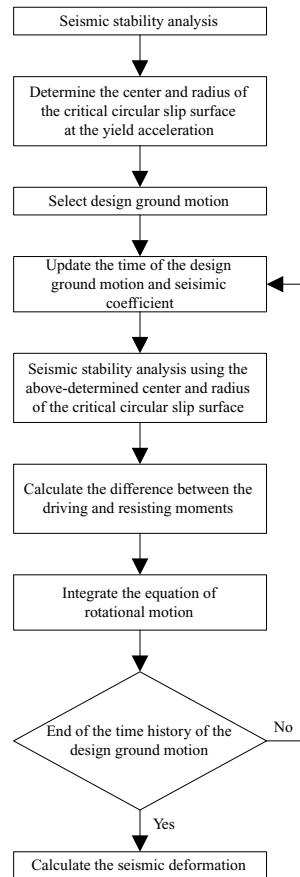


Figure 11. Flow chart for the standard Newmark analysis employed in the RTRI design code (2007).

per unit seismic coefficient due to the self-weight of the soil subjected to a seismic inertia force; M_{dw} , driving moment due to the self-weight of the soil; and M_{dk} , driving moment per unit seismic coefficient due to the seismic inertia force. By substituting $FS = 1.0$ and rearranging Eq. (3), the yield seismic coefficient is obtained as follows:

$$k_y = \frac{M_{rw} + M_{rc} + M_{rt} - M_{dw}}{M_{dk} + M_{rk}} \quad (4)$$

Each component of Eq. (3) and Eq. (4) can be calculated as follows:

$$M_{rw} = R \sum (W_i \cdot \cos \alpha_i \cdot \tan \phi) \quad (5)$$

$$M_{rc} = R \sum (c \cdot l_i) \quad (6)$$

$$M_{rt} = R \sum \{T_i \cdot (\sin \alpha_i \cdot \tan \phi + \cos \alpha_i)\} \quad (7)$$

$$M_{rk} = R \sum (W_i \cdot \sin \alpha_i \cdot \tan \phi) \quad (8)$$

$$M_{dw} = \sum \{(x_{g,i} - x_c) \cdot W_i\} \quad (9)$$

$$M_{dk} = \sum \{(y_c - y_{g,i}) \cdot W_i\} \quad (10)$$

The notations are defined in Figure 12, where R is the radius of the critical circular slip surface; W_i , soil weight of the i -th slice; α_i , angle between the critical slip surface and x coordinate of the i -th slice; ϕ , soil friction angle; c , soil cohesion; l_i , length of the critical slip surface of the i -th slice; $x_{g,i}$ and $y_{g,i}$, the x and y coordinates of the center of gravity of the i -th slice, respectively; and x_c and y_c , the x and y coordinates of the center of the critical slip surface, respectively. Subsequently, after selecting the design ground motion, a seismic stability analysis is conducted by using the above-determined center and radius of the critical slip surface. The seismic coefficient is updated as follows:

$$k_h(t) = \frac{A(t)}{g} \quad (11)$$

where $A(t)$ is the acceleration time history of the design ground motion, and g is the gravitational acceleration.

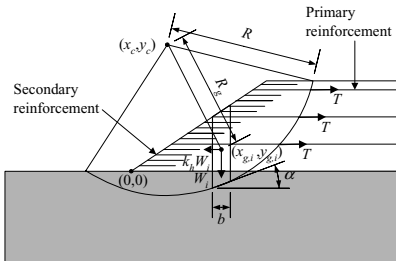


Figure 12. Notations for the geosynthetic-reinforced soil slope.

The above seismic stability analysis is performed up to the end of the time history of the design ground acceleration. During the seismic stability analysis, the difference between the overall driving and resisting moments is calculated, and the equation of rotational motion is obtained as follows:

$$\begin{aligned} J\ddot{\theta}(t) &= M_d(t) - M_r(t) \\ &= M_{dw} + k_h M_{dk} - M_{rw} + k_h M_{rk} - M_{rc} - M_{rt} \end{aligned} \quad (12)$$

where θ is the rotational angle of the soil mass and J is the moment of inertia expressed as follows:

$$J = \sum \left(J_{g,i} + \frac{1}{g} \cdot R_{g,i}^2 \cdot W_i \right) \quad (13)$$

where $J_{g,i}$ is the polar moment of inertia of the i -th slice and $R_{g,i}$ is the distance between the center of the slice and that of the critical circular slip surface of the i -th slice, as shown in Fig. 2. The angular acceleration, angular velocity, and rotation of the soil mass are obtained as follows:

$$\ddot{\theta}_{t+\Delta t} = \frac{1}{J} \Delta M_{t+\Delta t} \quad (14)$$

$$\dot{\theta}_{t+\Delta t} = \dot{\theta}_t + \frac{1}{2} \cdot (\ddot{\theta}_t + \ddot{\theta}_{t+\Delta t}) \cdot \Delta t \quad (15)$$

$$\theta_{t+\Delta t} = \theta_t + \dot{\theta}_t \cdot \Delta t + \frac{1}{6} \cdot (2 \cdot \ddot{\theta}_t + \ddot{\theta}_{t+\Delta t}) \cdot \Delta t^2 \quad (16)$$

The accumulated rotation of the soil mass is computed using Eq. (16) only when the angular velocity is positive. Finally, the seismic deformation is obtained as follows:

$$d_t = R \cdot \theta_t \quad (17)$$

In this paper, the seismic deformation is defined as a rotational displacement along the critical slip surface of the failure mass according to the RTRI design code.

3.4 Verification of level-2 seismic residual deformation

The seismic deformation analysis was conducted to obtain the design response value for settlement using Equation (2). The settlement due to the densification of the embankment was obtained based on the RTRI design code. Moreover, the settlement due to the densification of the foundation was negligible due to the improvement. Each settlement was obtained as shown in Table 16. Consequently, the design response value for settlement became 185 mm, by adding the individual settlements shown in Table 16.

Table 16. Classification of the properties of soil material.

Soil group	Engineering classification
A	G, G-S, GS, G-F, G-FS, GS-F, Low exfoliative excavated rock of tunnel construction
B	S, S-G, SG, S-F, S-FG, SG-F, High exfoliative excavated rock of tunnel construction
C	GF, GF-S, GFS, SF, SF-G, SFG
D	M, C, O, Pt, Mk, V

Note: X-Y = X containing Y equal to or more than 5% and less than 15%; XY = X containing Y equal to or more than 15%; G = Gravel; G-S and GS = Sandy gravel, G-F and GF = Gravel containing fine soil; G-FS, GF-S, GS-F, and GFS = Sandy gravel containing fine soil; S = Sand; S-G and SG = Gravelly sand; S-F and SF = Sand containing fine soil; S-FG, S-GF, SF-G, and SFG = Gravelly sand containing fine soil; M = Mo; C = Clay; O = Organic soil; Pt = Highly organic soil or Peat; Mk = Muck; V = Volcanic cohesive soil; Source—RTRI design specification.

Table 17. Result of seismic deformation analysis.

Item	Settlement (mm)
Settlement along the circular slip surface	109
Settlement due to the densification of the embankment	76
Settlement due to the densification of the foundation	0

The verification of level-2 seismic residual deformation is conducted as follows:

$$\gamma_i \cdot \frac{S_{Rd}}{S_{Ld}} = 1.0 \cdot \frac{185}{500} = 0.37 \leq 1.0. \quad (18)$$

The verification value is less than 1.0, therefore the required performance for level-2 seismic residual deformation is satisfied in this model, as shown in Figure 12.

4 CONCLUSIONS

This paper outlined the performance-based design method for railway earth structures. It introduced the design basis for the performance-based design of railway earth structures, including design flow, design life, required performance, and verification. As an example of the performance-based design method, a practical verification of a level-2 seismic residual deformation was conducted. Additional research

is required to investigate an economic cost-benefit evaluation with the life-cycle cost obtained from the limit state exceedance probability, considering the occurrence rate of different levels of seismic motions.

REFERENCES

- Kojima, K., Tateyama, M., Nishihara, S. & Hashimoto, K. 2006. Saturated degree contour models used rainfall design for embankment, RTRI report, Vol. 20, No. 12, pp. 37–42 (in Japanese).
- Newmark, N.M. 1965. Effect of earthquakes on dams and embankment, *Geotechnique*, Vol. 15, No. 2, pp. 139–160.
- Railway Technical Research Institute (RTRI). 2007. Design standard for railway earth structures. *Railway Technical Research Institute*, Maruzen (in Japanese).
- Shinoda, M., Horii, K., Yonezawa, T., Tateyama, M. and Koseki, J. 2006. Reliability-based seismic deformation analysis of reinforced soil slopes. *Soils and Foundations*, Vol. 46, No. 4, pp. 477–490.
- Shinoda, M. and Honjo, Y. 2008. Probabilistic precipitation map by the extreme value model based on meteorological data, Proceedings of Application of Statistics and Probability in Civil Engineering, 2008.
- Tarumi, H. & Murata, O. 1991. Outline of new design standard for railway earth structures, RTRI report, Vol. 5, No. 11, pp. 1–7 (in Japanese).
- Tateyama, M., Horii, K. and Kojima, K. 1999. Study on seismic performance and design of embankment, RTRI report, Vol. 13, No. 3, pp. 43–48 (in Japanese).
- Tateyama, M. 2006. Outline of new design standard for railway earth structures, RTRI report, Vol. 20, No. 12, pp. 9–12 (in Japanese).
- Tateyama, M., Shinoda, M., Horii, K. and Kojima, K. 2006. Calculation method of residual deformation of embankment subjected to cyclic loading due to running trains, RTRI report, Vol. 20, No. 12, pp. 43–48 (in Japanese).
- Watanabe, K., Tateyama, M. and Shinoda, M. 2007. Statistical property of soil parameters for performance-based design of embankment, Proceedings of the 13th Asian Regional Conference on Soil Mechanics and Geotechnical Engineering.

Seismic performance of geosynthetic-reinforced soil retaining walls and their performance-based design in Japan

J. Koseki

Institute of Industrial Science, The University of Tokyo, Japan

S. Nakajima

Public Works Research Institute, Japan

M. Tateyama, K. Watanabe & M. Shinoda

Railway Technical Research Institute, Japan

ABSTRACT: Focusing on seismic performance of geosynthetic-reinforced soil retaining walls in Japan and their performance-based design, case histories on their use for railway structures and relevant model test results are briefly summarized, and several features of a newly-revised Japanese design standard for railway earth structures are reported. Based on good performances that have been observed in a case history and confirmed by relevant model tests, geosynthetic-reinforced soil retaining walls have been frequently applied to both new construction and retrofit work after recent large earthquakes in Japan. In the design standard, three ranks of seismic performance against level 1 and 2 earthquakes are assigned, and a recommendation of their verification procedures is made.

1 INTRODUCTION

Recently, Japan suffered from several large earthquakes which caused extensive damage to earth structures. In some of them, geosynthetic-reinforced soils (GRSs) performed very well (e.g., Tatsuoka et al., 1997 and Koseki et al., 2008 among others), and thus they were considered more frequently for the replacement of conventional earth structures in reconstruction works (Koseki et al., 2006a, 2008 and Shinoda et al., 2007 among others).

Since the 1995 Hyogoken-Nanbu (Kobe) earthquake, in particular, the level of the design seismic load has been raised significantly, while introducing the concept of so-called level 2 earthquake load, which is defined as the maximum possible level over the design life of civil engineering structures (JSCE 2006). Meanwhile, the principle of performance-based design has been introduced as well. Under such circumstances, several design guidelines for new construction works of civil engineering structures in Japan have been revised or are under revision process, and reinforced soils are not the exceptions.

In view of the above, in this paper, by updating the information as compiled by Koseki et al., 2008, Japanese case histories are overviewed on the seismic performance of GRS structures and their use in reconstruction works as replacement of conventional earth

structures that have been damaged by earthquakes. Then, results from relevant model shaking tests are summarized, focusing on ductile behavior of GRS structures. Lastly, several features of a newly-revised design standard for railway earth structures in Japan (RTRI, 2007 and Koseki et al., 2007) are reported, focusing on performance-based seismic design of GRS structures.

2 JAPANESE CASE HISTORIES

2.1 1995 Hyogoken-Nanbu (Kobe) earthquake

In the severely shaken area by the January 17, 1995 Hyogoken-nanbu earthquake, conventional type retaining walls (RWs) without foundation, such as cantilever, gravity and leaning-type ones, suffered overall tilting and/or failure of the wall body, as typically shown in Fig. 1. Most of them had to be removed and reconstructed after the earthquake.

In contrast to the above, as shown in Fig. 2, one GRS RW with full-height rigid facing, which was located at Tanata within the severely shaken area, survived with minor residual lateral displacements of about 10 to 20 cm that are measured relative to the neighboring culvert box structure. The standard procedures for staged construction of this type of GRS RWs with a full-height rigid facing is illustrated in Fig. 3.

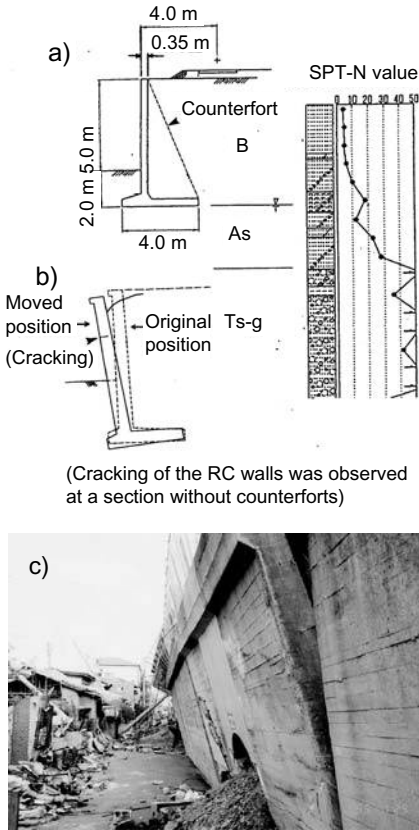


Figure 1. Failure of railway cantilever-type retaining wall at Ishiyagawa due to 1995 Hyogoken-nanbu earthquake (Tatsuoka et al., 1996).

On the other side of the culvert structure, as shown in Fig. 4, a cantilever-type RW with bored-pile foundation suffered similar amounts of residual lateral displacement, suggesting that this wall and the previous GRS RW without foundation exhibited almost the same seismic resistance.

Refer to Tatsuoka et al. (1995, 1996, 1997, 1998) and Koseki et al. (1999) for the details of the damage investigation and its back-analysis. The results from a series of relevant model tests conducted on the different types of RWs have been reported by Watanabe et al. (2003) and will be partly explained later.

2.2 2004 Niigataken-Chuetsu earthquake

Many embankments for roads, railways and housing estates were damaged by the October 23, 2004 Niigataken-chuetsu earthquake (Tatsuoka et al., 2006, JSCE 2006, JGS 2007a). For example, the traffic along national highways and prefectural roads were

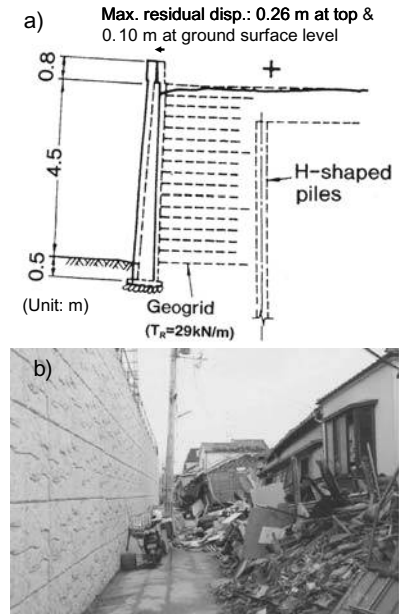


Figure 2. Residual displacement of railway geosynthetic-reinforced soil retaining wall at Tanata due to 1995 Hyogoken-nanbu earthquake (Tatsuoka et al., 1996).

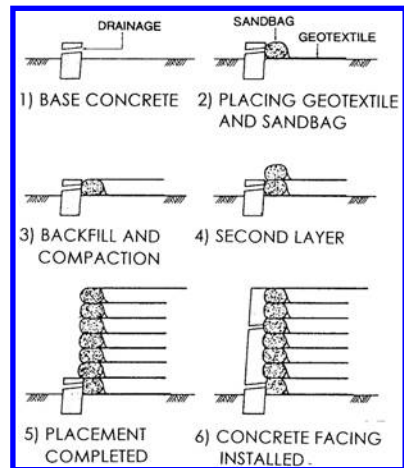


Figure 3. Staged construction procedures for geosynthetic-reinforced soil retaining walls with full-height rigid facing (Tatsuoka et al., 1995).

suspended at 101 sites (Koseki et al., 2006b), and most of them were caused by failure of embankments.

Figure 5 shows a case history where both a national highway retaining wall and a railway embankment were severely damaged by the same slide. The highway retaining wall was repaired using GRS RW with

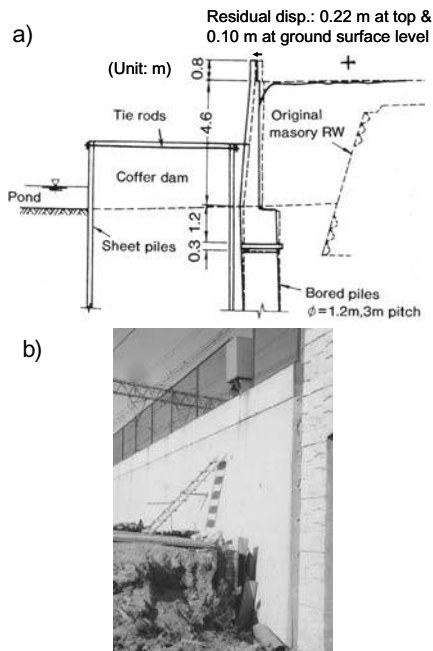


Figure 4. Residual displacement of railway cantilever-type retaining wall with pile foundation at Tanata due to 1995 Hyogoken-nanbu earthquake (Tatsuoka et al., 1996).

segmental facing panels made of pre-cast concrete (Fig. 6), while the railway embankment on the down slope side was reconstructed using GRS RW with a full-height rigid facing and rock bolts (Fig. 7). Such different repair decisions were made based on ground conditions, construction time and available backfill material.

Figure 8 shows another reconstruction case history of a collapsed railway embankment using a combination of GRS RW and earth anchors (Kitamoto et al., 2006).

Figure 9 shows reconstruction of a collapsed railway embankment by re-using the collapsed fill material. As illustrated in the figure, the fill material was improved by adding a cement-origin stabilizer at a mixing ratio of 150 kg/m^3 for the upper embankment and 105 kg/m^3 for the lower embankment. It was further reinforced with geogrid sheets that were placed at a vertical spacing of 1.5 m as secondary reinforcement. In order to ensure the drainage, a gravel mat was placed at the bottom of the embankment.

2.3 2007 Noto-Hanto earthquake

The March 25, 2007 Noto-hanto earthquake caused severe damage to embankments of Noto toll road.

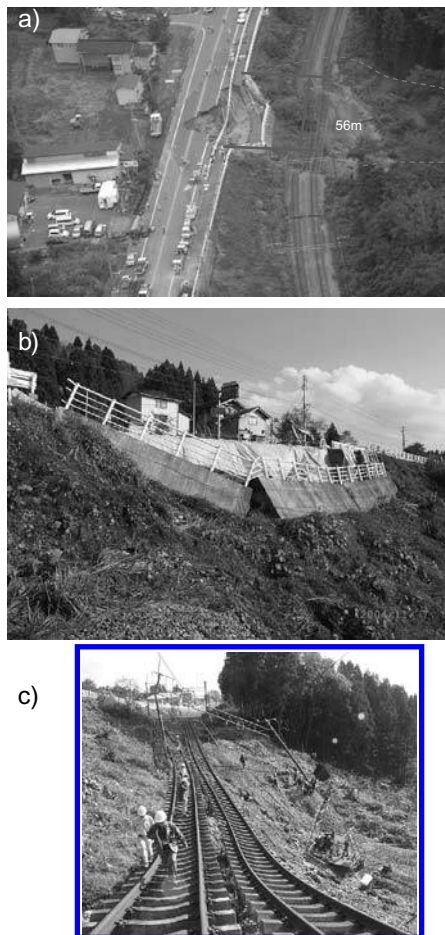


Figure 5. Failure of highway gravity-type retaining wall and railway embankment at Tenno due to 2004 Niigataken-chuetsu earthquake (Koseki et al., 2006a).

The north part of this toll road runs through a mountainous area for a length of 27.0 km, which was opened in 1978 to 1980.

The damage concentrated into this part, where eleven embankments filling valleys were extensively collapsed as typically shown in Figure 10. In this case, the fill material from the collapsed embankment flowed down the valley for a distance exceeding 100 meters. The fill material was a weathered tuff.

After temporary rehabilitation work, the road could be re-opened on April 27, 2007 in about a month, while the full re-construction will be completed in about a year (JGS 2007b). As shown in Figures 11 and 12, the collapsed embankments were reconstructed using GRS RW, ensuring the drainage of ground and surface water. The waste soil that had originally been a part of the collapsed embankment will be re-used



Figure 13. Failure of road retaining wall at Agewa due to 2007 Niigataken-chuetsu-oki earthquake.



Figure 15. Failure of anchor tendons for cut-slope at construction site of Isawa dam due to 2008 Iwate-Miyagi-nairiku earthquake.



b) (by courtesy of Kashiwazaki City)

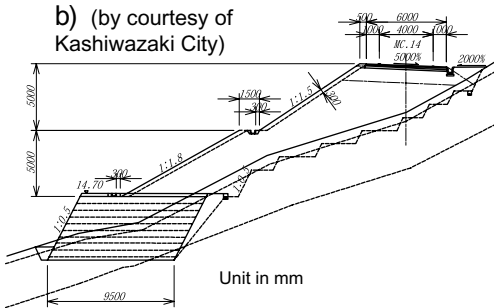


Figure 14. Geosynthetic-reinforced soil retaining wall at Agewa.



b) (by courtesy of MLIT)

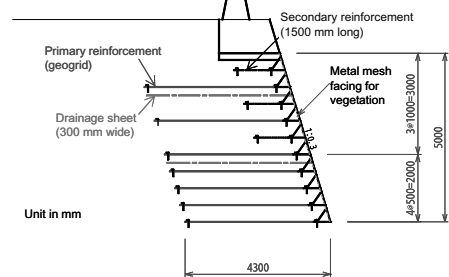


Figure 16. Geosynthetic-reinforced soil retaining wall at construction site of Isawa dam.

fully investigated. In this paper, based on the limited information that the first author could gather, several case histories are reported.

Figure 13 shows failure of a retaining wall during the Niigataken-chuetsu-oki earthquake, which had been constructed on a slope for a municipal road at Agewa, Kashiwazaki city. In contrast, a GRS RW with segmental facing panels made of metal mesh that was located at the foot of the slope could survive the earthquake as shown in Figure 14.

Figure 15 shows an anchored cut-slope at a construction site of Isawa dam, Oshu city. The anchors

with a length of 20 to 40 meters had been installed as a countermeasure against landslide movement. By the Iwate-Miyagi-nairiku earthquake, most of the tendons were broken at their free sections, and the upper parts of the broken tendons were ejected. On the other hand, a GRS RW with segmental facing panels made of metal mesh that was located on the other side of the slope survived the earthquake as shown in Figure 16.

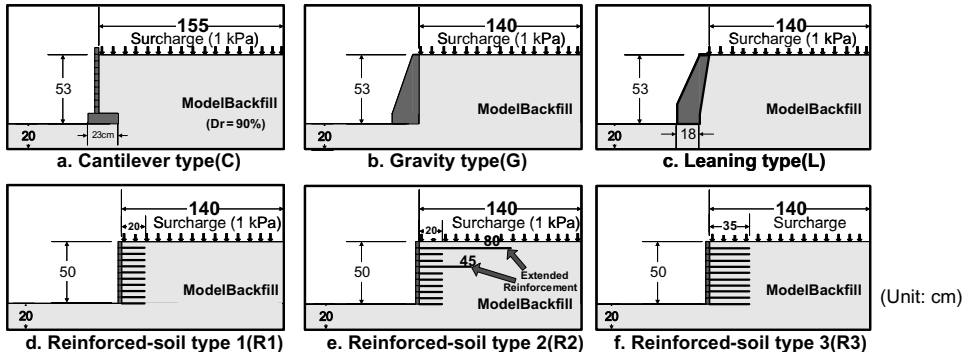


Figure 17. Retaining wall models on level ground (Watanabe et al., 2003).

3 MODEL TESTS

3.1 Test procedures

A series of relatively small-scale 1-g model shaking tests was conducted on six different types of retaining walls resting on level ground as shown in Fig. 17. The wall models were about 50 cm high and the subsoil and backfill were modeled by very dense dry sand layers. They were subjected to several sequential horizontal excitations as typically shown in Fig. 18 in 0.1 g increments. Refer to Watanabe et al. (2003) for the detailed test conditions.

3.2 Test results

Figure 19 shows the cumulative horizontal displacements near the top of each model wall. The seismic coefficient plotted in the horizontal axis is defined as the peak base acceleration during each shaking step that is normalized with the gravity. Up to seismic coefficient of about 0.4, no significant difference could be observed. However, under higher seismic loads, the residual wall displacements accumulated rapidly with the conventional retaining walls, i.e., cantilever, gravity and leaning-type ones. In contrast, the GRS RWs with a full-height rigid facing exhibited more ductile behavior, in particular with the one having partly extended reinforcements (R2 or type 2, Fig. 17e).

The reason for the less ductile behavior of the conventional retaining walls can be understood from Fig. 20. The subgrade reaction at the toe of base footing of the gravity-type wall increased sharply with the accumulation of wall top displacement. It suddenly decreased, however, after showing a peak state, suggesting a local failure due to loss of bearing capacity. On the other hand, the subgrade reaction at the heel of the base footing decreased in the beginning, followed by a slight increase with the occurrence of the local failure at the toe.

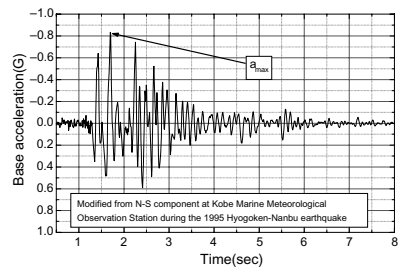


Figure 18. Typical excitation time history (Watanabe et al., 2003).

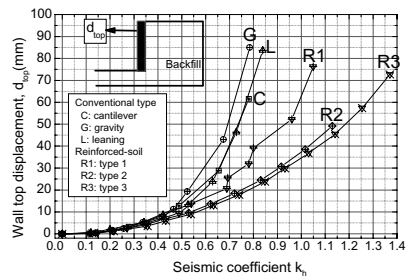


Figure 19. Comparison of residual wall top displacements (Watanabe et al., 2003).

In case of GRS RWs, as shown in Fig. 21, the tensile forces in the reinforcements measured at three different heights increased with the accumulation of the wall top displacement. Such a response of GRS RWs is the key feature for their good performance under high seismic loads. It should be noted that the mobilization of tensile force was concentrated to the uppermost long reinforcement for the type 2 wall, which could effectively resist against the overturning of the facing. Due attentions should be paid on such stress concentration.

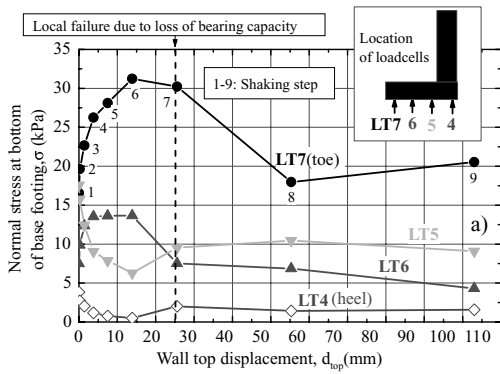


Figure 20. Footing load response of gravity-type wall model (Watanabe et al., 2003).

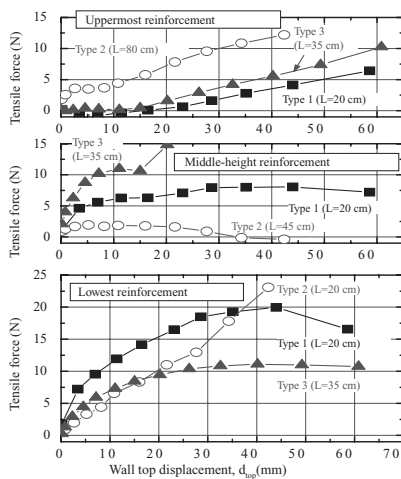


Figure 21. Reinforcement load response of GRS RWs (Watanabe et al., 2003).

3.3 Discussions on further improvements of seismic performance of GRS RWs

As typically shown in Fig. 22, shear deformation of reinforced backfill was observed in the model tests on GRS RWs, which was associated with the overturning displacement of the facing. In evaluating their residual displacements, such effects of shear deformation of reinforced backfill should be considered properly. On the other hand, the reinforced backfill has been modeled as a rigid body in many of the relevant design guidelines.

Note that, as shown in Fig. 23, the residual tilting angle of the facing of GRS RWs with full-height rigid facing could be effectively reduced by installing a sheet pile at the foot of the facing and connecting it to the facing (Nakajima et al., 2006).

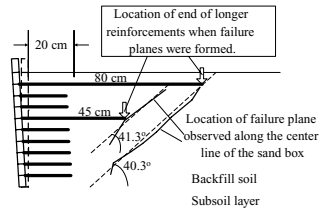


Figure 22. Shear deformation of reinforced backfill of GRS RW on level ground (Watanabe et al., 2003).

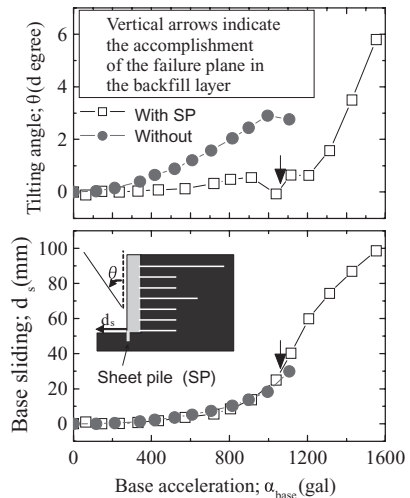


Figure 23. Comparison of residual facing displacements of GRS RWs with/without sheet pile (Nakajima et al., 2006).

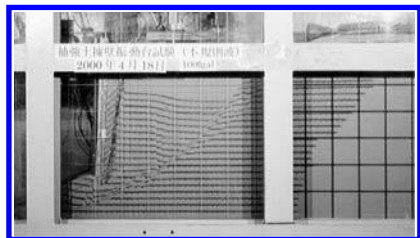


Figure 24. Full failure plane in unreinforced backfill of GRS RW constructed on slope (Kato et al., 2002).

It should be also noted that, as shown in Fig. 24, in case of GRS RW constructed on slope, a full failure plane in the unreinforced backfill and the sloped subsoil was formed rather easily (Kato et al., 2002). After the formation of such full failure plane, as shown in Fig. 25, the mobilization of the tensile forces in the reinforcement of the GRS RW on slope was reduced.

4 PERFORMANCE-BASED DESIGN STANDARD OF RAILWAY EARTH STRUCTURES IN JAPAN

4.1 Composition of the standard

The table of contents of the newly revised design standard for railway earth structures in Japan and its commentaries (RTRI 2007) is listed in Table 1.

As one of the standard construction methods, soil reinforcing techniques including GRS are adopted in chapters 7 through 10, covering a subtotal volume of 86 pages that is about a quarter of the total volume excluding the appendix. The reinforced soil wall (chapter 8) and the reinforced soil abutment (chapter 9) deal with GRS retaining walls with a full-height rigid facing. The reinforced cut slope (chapter 10) deals with retaining walls to support cut slopes that are reinforced with nailing, micropiling or doweling.

In addition, in chapter 3 on embankment, use of secondary geosynthetic reinforcements is standardized. In this report, therefore, design of embankments will be also described in sections 4.2 and 4.4. More details of the embankment design against not only the seismic action but also the rain action are reported by Shinoda et al. (2009).

4.2 Design flow of embankments

Figure 28 illustrates the flow chart of the performance-based design of embankments that is specified in the design standard (RTRI 2007). After setting up the required performance in terms of safety, serviceability and reparability, decision is made whether prescriptive measures are adopted or not.

The prescriptive measures have three different levels. Each of the prescriptive measures has been verified in advance to fulfill the corresponding performance rank, and thus no additional verification is required at the design stage.

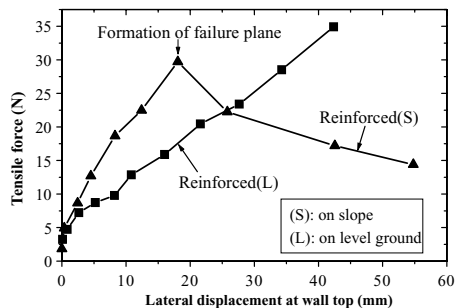


Figure 25. Reinforcement load response of GRS RWs on level ground and slope (Kato et al., 2002).

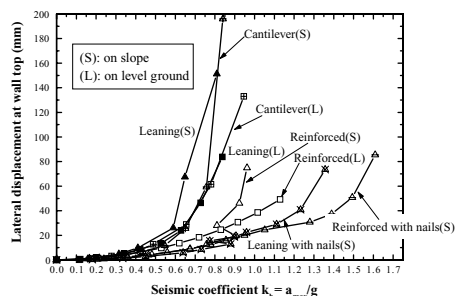


Figure 26. Comparison of residual wall top displacements (Kato et al., 2002).

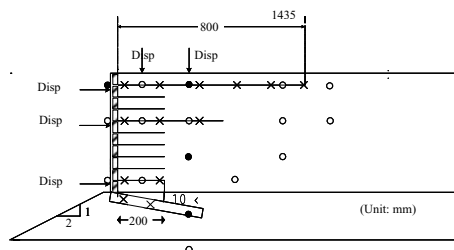


Figure 27. GRS RW model constructed on slope and reinforced with nails (Kato et al., 2002).

As shown in Fig. 26, it was followed by rapid accumulation of the wall displacement, which was the case as well with the conventional retaining wall models.

On the other hand, as also shown in Fig. 26, the GRS RW constructed on slope and reinforced with large diameter nails (Fig. 27) could exhibit substantially higher seismic stability than those without nails (Kato et al., 2002). It yielded very limited amount of residual wall displacements even at seismic coefficients exceeding 1.0. Refer to Nakajima et al. (2007) for the detailed analysis of tensile loads induced in the large diameter nail models.

Table 1. Composition of the design standard for railway earth structures and its commentaries (RTRI 2007).

Chapters	Pages
1. General	30
2. Design principles	32
3. Embankment	90
4. Cut and natural slopes	36
5. Base course	40
6. Subgrade	21
7. Reinforced soil (general)	28
8. Reinforced soil wall	17
9. Reinforced soil abutment	17
10. Reinforced cut slope	24
Appendix	365

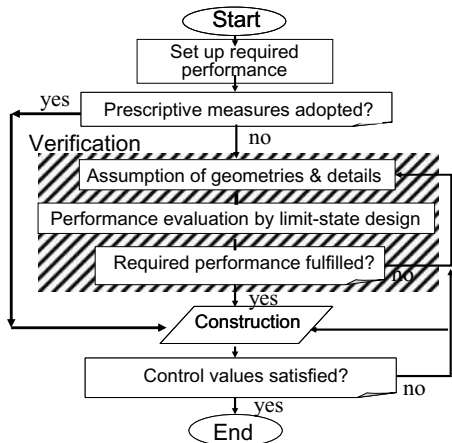


Figure 28. Flow of performance-based design of embankments.

On the other hand, if the prescriptive measures are not adopted, one needs to proceed to the verification process, including assumption of the geometries and structural details, performance evaluation based on limit-state design and confirmation of the required performance. In case the required performance is not fulfilled through the verification, one should modify the assumption and repeat the same procedures.

It should be noted that, in designing structures other than embankments, prescriptive measures are not available, and thus the verification process shall be implemented.

4.3 Required seismic performance

Table 2 summarizes the required performances of railway earth structures against two levels of design earthquake loads. In this table T_{des} is the design life of the structure. In general, the design life of a railway earth structure is assumed as 100 years.

For a level 1 earthquake load that is highly expected over the design life, it is required that all the earth structures will maintain their design functions without requiring repair work, i.e. will not exhibit excessive displacements (Performance rank III).

Against a level 2 earthquake load, which is defined previously in section 1.2, it is required that important earth structures can be restored to design function conditions with minimal repair (Performance rank II), while the other earth structures will not undergo overall instability (Performance rank I).

4.4 Prescriptive measures for embankments

When the prescriptive measures are adopted for embankments, different configurations of reinforcement arrangement as well as the slope geometry are employed depending on the performance rank.

Table 2. Performance requirements for railway earth structures in Japan (modified from Koseki et al., 2006a).

Action (design earthquake loads)	Level 1 (highly expected for T_{des})	Level 2 (maximum possible for T_{des})
Important structures	Performance I: Will maintain their expected functions with- out repair works (no excessive displacements)	Performance II: Can restore their functions with quick repair works
Others		Performance III: Will not undergo overall instability

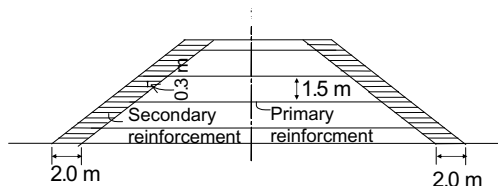


Figure 29. Cross-section of 6 m-high embankment with performance rank I specified as prescriptive measure.

For example, for a 6 m-high embankment, the primary reinforcements are used with rank I, as shown in Fig. 29 and Table 3. They are placed for the full width of the embankment at a vertical spacing of 1.5 m. With ranks II and III, on the other hand, only the secondary reinforcements are used to protect the slope for the width of 2.0 m and to enhance the specified height (= 0.3 m) of fill lift during construction. The design tensile strength of the primary and secondary reinforcements shall be 30 and 2 kN/m, respectively.

For a 6 m-high embankment, the slope shall have no berm, while its angle is varied depending on the performance rank as listed in Table 3. It should be noted that the type of the fill material and the required degree of compaction to be secured during construction are also varied depending on the performance rank.

4.5 Verification against level 1 earthquake load

As explained in section 4.2, if the prescriptive measures are not adopted, one needs to proceed to the verification process. In case of GRS retaining walls, the performance requirement for level 1 earthquake load as explained in section 4.3 is verified through stability analyses using load and resistance factors

against internal instability (Fig. 30), external instability (Fig. 31), and facing failure (Fig. 32).

Internal stability analysis is conducted with respect to base sliding and overturning. For example, the stability against base sliding is verified using the following equation:

$$\gamma_i \times \frac{H_{Rd}}{H_{Ld}} \leq 1.0 \quad (1)$$

where γ_i is the structure factor (set equal to unity in general); H_{Rd} is the response value of base sliding force; H_{Ld} is the limiting value of base sliding force.

Table 3. Configurations of 6 m-high embankment with different performance ranks specified as prescriptive measures.

	Rank I	Rank II	Rank III
Slope	1:1.8	1:1.5 (upper) 1:1.8 (lower)	1:1.5
Primary reinforcement	Yes	Basically no	No
Secondary reinforcement	Yes	Yes	Yes

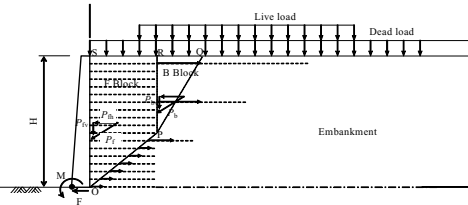


Figure 30. Modeling of GRS retaining wall for internal stability analysis.

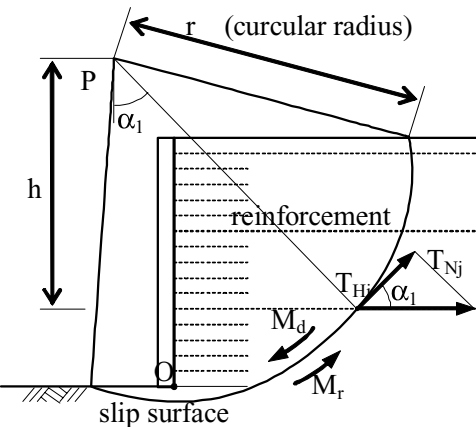


Figure 31. Modeling of GRS retaining wall for external stability analysis.

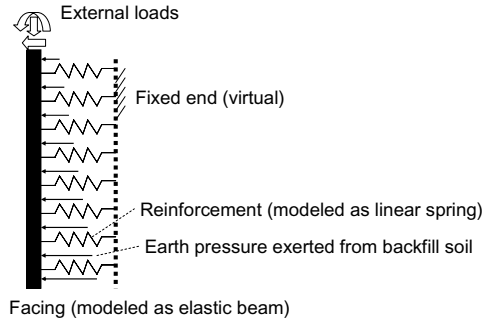


Figure 32. Modeling of facing and reinforcements.

The response value of base sliding force is evaluated as:

$$H_{Rd} = \gamma_H \times (P_{jh} + W_{EQ} + F_H) \quad (2)$$

where γ_H is the load factor (set equal to unity in general); P_{jh} is the horizontal component of the resultant force of earth pressure exerted from the backfill; W_{EQ} is the horizontal inertia force of facing; F_H is the external load applied to the top of the facing (e.g., due to the existence of noise barrier). As schematically shown in Figure 4, the resultant force of earth pressure is evaluated based on the two-wedge method.

The limiting value of base sliding force is evaluated as:

$$H_{Ld} = f_{ri} \times (\sum T_i + W_{BS} + W_{hp}) \quad (3)$$

where f_{ri} is the resistance factor (set equal to 0.80 against level 1 earthquake load); T_i is the design tensile resistance of reinforcement; W_{BS} is the design shear resistance mobilized at the bottom of facing; W_{hp} is the design horizontal resistance mobilized at the embedded part of the facing. The design tensile resistance of reinforcement is evaluated as the smaller value between the design tensile strength of reinforcement T_d (refer to Koseki et al., 2007 for its detailed derivation) and the pull-out resistance of the reinforcement T_p that is evaluated as:

$$T_p = f_{rg} \times (\sigma_{vi} \times \tan \phi \times 2l_i + c \times 2l_i) \quad (4)$$

where f_{rg} is the resistance factor (set equal to 0.80 against level 1 earthquake load); σ_{vi} is the effective vertical stress acting on the i th reinforcement; l_i is the effective length of the i th reinforcement; ϕ and c are the internal friction angle and cohesion of the backfill soil, respectively.

4.6 Verification against level 2 earthquake load

For structures with performance ranks II and III, performance requirement for level 2 earthquake loads is verified in terms of their residual deformations using Newmark sliding block analyses and other numerical

analyses. In case of GRS retaining walls, base sliding displacement of the retaining wall (Fig. 33), overturning displacement (Fig. 34), and shear deformation of the reinforced backfill (Fig. 35) are evaluated.

It should be noted that, the residual shear deformation of the reinforced backfill has not been considered in many of the other existing design codes which adopt the assumption that the reinforced backfill behaves as a rigid body.

In conducting the Newmark sliding block analysis, one needs to specify the design earthquake motions. They are specified in the design standard as shown in Fig. 36. They were obtained by applying a band-pass filter (0.3–4.0 Hz) to the design motions specified at

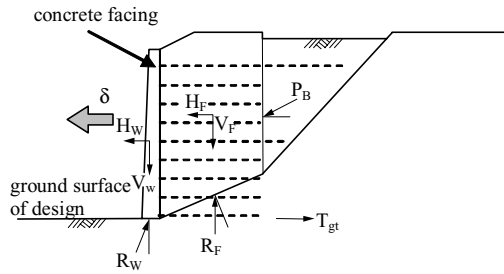


Figure 33. Modeling of GRS retaining wall for evaluation of base sliding.

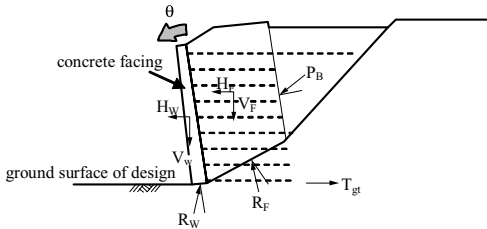


Figure 34. Modeling of GRS retaining wall for evaluation of overturning.

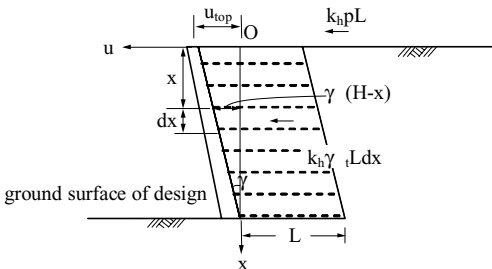


Figure 35. Modeling of GRS retaining wall for evaluation of shear deformation of reinforced backfill.

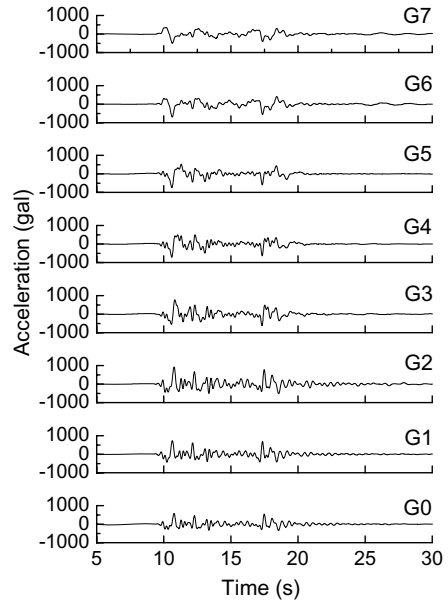


Figure 36. Time history of level 2 design earthquake motions (refer to Tables 5 and 6 for ground type classification and amplitude of maximum acceleration).

Table 4. Ground type classification based on natural period T_g (unit in seconds).

G0–G2	G3	G4	G5	G6	G7
Less than 0.25	0.25–0.5	0.5–0.75	0.75–1.0	1.0–1.5	More than 1.5

G0: Rock deposit; G1: firm base deposit; G2: Pleistocene deposit; G3: moderate; G4: moderate to soft; G5 and G6: soft; G7: very soft.

Table 5. Maximum acceleration of level 2 design earthquake motions (unit in gals).

G0	G1	G2	G3	G4	G5	G6	G7
578	732	924	779	–718	–741	–694	–501

the ground surface levels in the relevant design standard (RTRI, 1999). Depending on the natural period T_g of the ground, which is evaluated using Eq. 5 based on the profile of shear wave velocities, different wave forms and amplitudes are assigned as listed in Tables 4 and 5. The peak accelerations a_{max} are in the range between 500 and 920 gals, and the largest value of a_{max} is assigned for the G2 ground consisting mainly of Pleistocene deposits.

Table 6. Results from Newmark sliding block analyses on 6 m-high embankments with different performance ranks.

	Rank I	Rank II	Rank III	Rank III
Slope	1:1.8	1:1.5	1:1.8	1:1.5
Primary reinforcement	Yes	No	No	No
Secondary reinforcement	Yes	Yes	Yes	Yes
Residual displacement*	10.6 cm	36.0 cm	61.8 cm	96.5 cm

* Against level 2 design earthquake motion for G2 ground.

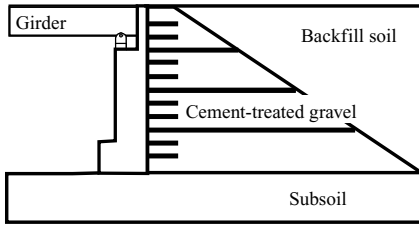


Figure 37. GRS abutment having cement-treated gravel for reinforced backfill (Aoki et al., 2005).

$$T_g = 4 \times \sum_{i=1}^N \left(\frac{h_i}{V_{Si}} \right) \quad (5)$$

where N is the total number of soil layers; h_i and V_{Si} are the thickness and the shear wave velocity of the i th layer, respectively.

For example, results from the Newmark sliding block analyses on the 6 m-high embankment with different performance ranks specified as prescriptive measures (see section 4.4) are shown in Table 6. In setting the level 2 design earthquake motion, the severest ground condition (i.e., the condition of G2 ground) was assumed. It should be noted that the embankment with performance rank II was simplified into two kinds of configurations having a uniform slope angle.

As a result, the embankment with performance rank I suffered from a residual displacement of about 10 cm, while those with performance rank II underwent residual displacements in the range of 40 to 60 cm. Further, the embankment with performance rank III suffered from a residual displacement of about one meter. Such different performances are expected when they are subjected to level 2 earthquake motion.

4.7 Seismic design of reinforced soil abutment

In chapter 9 of the design standard, design of GRS abutments having cement-treated gravel for reinforced backfill, as developed by Aoki et al. (2005) and schematically shown in Fig. 37, is described.

In their seismic design, the abutment body and the reinforced backfill are verified with respect to safety against level 1 earthquake load and reparability against level 2 earthquake load.

For example, in verifying the reparability of the abutment body, a pseudo-static non-linear push-over analysis is conducted against the inertia force of the girder, while considering the tensile reaction of the reinforcements and assuming that the reinforced backfill does not exert any earth pressure to the body.

5 CONCLUSIONS

The contents of the present paper on seismic performance of geosynthetic-reinforced soil retaining walls in Japan and their performance-based design can be summarized as follows.

1. Case histories during recent major earthquakes in Japan have revealed good performances geosynthetic-reinforced soil retaining walls. Therefore, preferred use of this type of structure has been implemented in damage rehabilitation work as well as new construction of important permanent structures.
2. Relevant model shaking tests have confirmed a) mechanisms of seismic resistance mobilization that are different depending on the structural types and b) further improved performance of new type structures using combined reinforcement systems.
3. Performance-based design procedures have been developed for railway GRS structures in Japan. They have the following features:
 - Three ranks of required seismic performance against level 1 & 2 earthquakes are assigned considering the importance of the structure. The level 2 design earthquake motions have the max. accelerations in the range of 500 to 920 gals.
 - Use of prescriptive measures is admitted for embankments. In setting the standard cross-section, use of primary and/or secondary geosynthetic reinforcements is mandated.
 - Recommendation of verification procedures is made. Against the level 2 earthquake, Newmark sliding block analysis is adopted as well as the evaluation of residual shear deformation of reinforced backfill in case of GRS retaining walls.

ACKNOWLEDGEMENTS

The authors wish to express their special appreciation to Mr. O. Matsuo, Mr. T. Sasaki and Mr. M. Mizuhashi (Public Works Research Institute), Mr. Y. Matsuda (Ishikawa Prefecture), Mr. N. Wada (Ministry of

Land, Infrastructure and Transport), Mr. S. Hamaya (Shimizu Corp.), Mr. S. Nishimura (Chuo Kaihatsu Corp.), Mr. H. Kameya, Mr. T. Kanai and Mr. K. Oozono (Oyo Corp.), Prof. J. Kuwano (Saitama University), Prof. F. Tatsuoka and Dr. T. Kiyota (Tokyo University of Science), Dr. D. Hirakawa (National Defense Academy), Dr. K. Kojima and Mr. T. Matsumaru (Railway Technical Research Institute), Mr. K. Horii and Mr. S. Morikoshi (Integrated Geotechnology Institute, Corp.), Prof. K. Konagai, Dr. R. Kuwano, Dr. S. Yamada, Ms. Y. Tsutsumi and Mr. D. Sugimoto (University of Tokyo), Dr. Y. Munaf and Mr. N. Kato (Formerly Univ. of Tokyo) for their help in preparing the manuscript, conducting the earthquake damage survey and performing the model tests that are reported in this paper.

REFERENCES

- Aoki, H., Yonezawa, T., Tateyama, M., Shinoda, M. and Watanabe, K. 2005. Development of aseismic abutment with geogrid-reinforced cement-treated backfills, *Proc. of 16th International Conf. on Soil Mechanics and Geotechnical Engineering*, 3, 1315–1318.
- Ishikawa Prefecture. 2007. Damage to toll road due to Notohanto earthquake and its rehabilitation, *Official Bulletin*, 1, 4p. (in Japanese).
- Japan Society for Civil Engineers. 2006. *Report on the 2004 Niigata Chuetsu Earthquake*, CD-ROM. (in Japanese).
- Japanese Geotechnical Society. 2007a. *Report of damage survey committee on the Niigata-ken Chuetsu Earthquake*, 518p. (in Japanese).
- Japanese Geotechnical Society. 2007b. *Compiled data on damage to highways due to the 2007 Noto-hanto Earthquake*, 79p. (in Japanese).
- Kato, N., Huang, C.C., Tateyama, M., Watanabe, K., Koseki, J. and Tatsuoka, F. 2002. Seismic stability of several types of retaining walls on sand slope, *Proc. 7th International Conf. on Geosynthetics*, Nice, 1, 237–240.
- Kitamoto, Y. Abe, H., Shimomura, H., Morishima, H. and Taniguchi, Y. 2006. Rapid and strengthened repair construction for a seriously damaged railway embankment during violent earthquakes, *Proc. 8th Int. Conf. on Geosynthetics*, Yokohama, 3, 861–864.
- Koseki, J., Tateyama, M., Horii, K., Munaf, Y. and Kojima, K. 1999. Back analyses of case histories and model tests on seismic stability of retaining walls, *Proc. 11th Asian Regional Conf. on Soil Mechanics and Geotechnical Engineering*, 1, 399–402.
- Koseki, J., Bathurst, R.J., Guler, E., Kuwano, J. and Maugeri, M. 2006a. Seismic stability of reinforced soil walls, Keynote lecture, *Proc. of 8th International Conference on Geosynthetics*, Yokohama, 1, 51–77.
- Koseki, J., Sasaki, T., Wada, N., Hida, J., Endo, M. and Tsutsumi, Y. 2006b. Damage to earth structures for national highways by the 2004 Niigata-ken Chuetsu earthquake, *Soils and Foundations*, 46(6), 739–750.
- Koseki, J., Tateyama, M. and Shinoda, M. 2007. Seismic design of geosynthetic reinforced soils for railway structures in Japan, *New Horizons in Earth Reinforcement*, Taylor & Francis, 113–119.
- Koseki, J., Tateyama, M., Watanabe, K. and Nakajima, S. 2008. Stability of earth structures against high seismic loads, Keynote Lecture, *Proc. of 13th Asian Regional Conference of Soil Mechanics and Geotechnical Engineering*, Kolkata, Vol. 2 (in print).
- Morishima, H., Saruya, K. and Aizawa, F. 2005. Damage to earth structures for ordinary railways and its rehabilitation, *Foundation Engineering and Equipment (Kiso-ko)*, 33(10), 78–83 (in Japanese).
- Nakajima, S., Koseki, J., Watanabe, K., Tateyama, M. and Kato, N. 2006. Shaking table model tests on geogrid reinforced soil retaining wall with embedded sheetpile, *Proc. of 8th International Conference on Geosynthetics*, Yokohama, 4, 1507–1510.
- Nakajima, S., Koseki, J., Tateyama, M. and Watanabe, K. 2007. Shaking table model tests on retaining walls reinforced with soil nailings, *New Horizons in Earth Reinforcement*, Taylor & Francis, 707–712.
- RTRI. 1999. *Seismic design standard for railway structures*, Railway Technical Research Institute (ed), Maruzen, 467p. (in Japanese).
- RTRI. 2007. *Design standard for railway earth structures*, Railway Technical Research Institute (ed), Maruzen, 703p. (in Japanese).
- Shinoda, M., Watanabe, K., Kojima, K., Tateyama, M. and Horii, K. 2007. Seismic stability of reinforced soil structure constructed after the mid Niigata prefecture earthquake, *New Horizons in Earth Reinforcement*, Taylor & Francis, 783–787.
- Shinoda, M., Watanabe, K., Kojima, K. and Tateyama, M. 2009. Outline of performance-based design for railway earth structures in Japan, this symposium.
- Tatsuoka, F., Tateyama, M., Koseki, J. and Uchimura, T. 1995. Geotextile-reinforced soil retaining wall and their seismic behaviour, *Proc. 10th Asian Regional Conf. on Soil Mechanics and Foundation Engineering*, 2, 26–49.
- Tatsuoka, F., Tateyama, M. and Koseki, J. 1996. Performance of soil retaining walls for railway embankments, *Soils and Foundations, Special Issue of Soils and Foundations on Geotechnical Aspects of the January 17 1995 Hyogoken-Nambu Earthquake*, 311–324.
- Tatsuoka, F., Koseki, J. and Tateyama, M. 1997. Performance of reinforced soil structures during the 1995 Hyogo-ken Nanbu Earthquake, *Earth Reinforcement*, Balkema, 2, 973–1008.
- Tatsuoka, F., Koseki, J., Tateyama, M., Munaf, Y. and Horii, N. 1998. Seismic stability against high seismic loads of geosynthetic-reinforced soil retaining structures, *Proc. 6th Int. Conf. on Geosynthetics*, Atlanta, 1, 103–142.
- Tatsuoka, F. 2003. Technical report-wall structures session, *Landmarks in Earth Reinforcement*, Balkema, 2, 937–948.
- Tatsuoka, F., Konagai, K., Kokusho, T., Koseki, J. and Miyajima, M. 2006. Special Session on the 2004 Niigata-ken Chuetsu earthquake, *Proc. of 16th International Conf. on Soil Mechanics and Geotechnical Engineering*, 5, 3279–3287.
- Watanabe, K., Munaf, Y., Koseki, J., Tateyama, M. and Kojima, K. 2003. Behaviors of several types of model retaining walls subjected to irregular excitation, *Soils and Foundations*, 43(5), 13–27.

Evaluation of spatial variations in soil stiffness using stress wave propagations

D.S. Kim, H.J. Park, J.T. Kim & N.R. Kim

Korea Advanced Institute of Science and Technology (KAIST), Daejeon, Korea

E.S. Bang

Korea Institute of Geoscience and Mineral Resources, Daejeon, Korea

ABSTRACT: In the performance based design (PBD), the great emphasis is placed on the control of structural deformation not a safety factor and the evaluation of soil stiffness, particularly spatial variation of shear wave velocity, is crucial in the site investigation for reliable PBD. In this paper, the special features of both intrusive and non-intrusive seismic methods frequently used in practice are briefly reviewed. Among those seismic methods, SPT- uphole based tomography and 2 dimensional Harmonic Wavelet Analysis of Waves (HWAW) methods for field investigations, and bender element tomography method in the centrifuge model are introduced as the potential candidates for spatial evaluation of soil stiffness. The merits of the proposed methods in the spatial evaluation of soil stiffness are discussed compared to other test results at the model sites of known dimensions and properties.

1 INTRODUCTION

The design paradigm of civil engineering structures currently moves toward the performance based design (PBD) from the traditional safety factor based design. In the PBD, the great emphasis is placed on the control of structural deformation not a safety factor in order to assure the serviceability and durability. Ground stiffness, not a strength, controls the deformation not only in the ground but in the adjacent structures. Therefore, the evaluation of deformation characteristics of geomaterials is very important in the site investigations for PBD.

It has been well known that the soil behaves nonlinearly from the small strains (Burland 1989, Kim 1991). The maximum shear modulus (G_{\max}) below the elastic threshold strain, γ_t^e , which is a fundamental stiffness in design, is usually inferred from the shear wave velocity obtained by seismic wave propagation tests. The variation in shear modulus with strain can be determined at small to intermediate strains by resonant column, torsional shear and tri-axial testing equipment and the normalized modulus reduction curve (G/G_{\max} vs. $\log \gamma$) can be found for each layer (Tatsoka & Shibuya 1992, Kim & Stokoe 1994). Because the modulus value obtained by laboratory test is affected by sampling disturbance and is difficult to be representative of the site, the reliable nonlinear stiffness variation is usually determined by combining G_{\max} obtained by field seismic test and G/G_{\max} curves from laboratory test, in which G_{\max}

converted from the shear wave velocity can be used as key soil property for the deformation analysis of soil-foundation systems.

Underground is not homogeneous and the spatial variations in soil stiffness should be considered for the reliable deformation assessment. When evaluating earthquake ground motion, it is important to model 2D or 3D soil-rock boundary in order to consider the trapped body waves (Graves 1993, Stewart et al., 2002). In the seismic performance based design of geotechnical structure, the acceptable level of damage should be specified in terms of engineering terms such as displacement and rotation (International Navigation Association 2001, Iai et al., 2008), and it is important to model the soil-structure system in 2D or 3D schemes considering spatial variations in soil stiffness. In the past, one point information of subsurface is generally obtained using boring and 1D borehole seismic tests to evaluate the design parameters, but it is not enough for the reliable estimation of deformation in the performance based design of geotechnical structures.

In this paper, the seismic site investigation methods used in practice for stiffness evaluation are reviewed. Both intrusive and non-intrusive methods are discussed considering special features of each methods, merits and demerits, applicability of spatial stiffness evaluation, etc. Among those seismic methods, SPT-based uphole method, Harmonic Wavelet Analysis of Waves (HWAW) method, Bender Tomography in centrifuge model, which are currently developed

Table 1. Intrusive methods for seismic site investigation.

Intrusive methods	Key features					Data reduction	Regions of site sampled
	Borehole	Source	Receivers	Waves			
Crosshole (Mok et al., 1988)	2 or more	Piezoelectric or mechanical impact source in the borehole	2 or 3 component geophones	S and P waves		Direct travel times	1D or 2D tomography
Downhole (Mok et al., 1989, Kim et al., 2004)	1	Hammer and plate, on the surface	3 component geophones, coupled with borehole	S and P waves		Direct method, Interval method, Refracted ray path method	1D
SPT based uphole (Bang & Kim 2007)	1	SPT sampler impact source	2 component geophones, on the surface	S and P waves		Refracted ray path method	1D or 2D tomography
Suspension PS-logging (Ohya et al., 1984)	1, Fluid-filled borehole	Mechanical source or solenoid hammer, in the borehole	2 geophones, within the fluid-filled borehole	Various propagation mode (S, P and interface waves)		Interval travel time between 2 receivers	1D

in KAIST are introduced in detail as the potential candidates for spatial stiffness evaluation. The testing setup, testing procedure, and data-reduction scheme are discussed and the merits for spatial stiffness evaluation are assessed compared to other test results at the in-situ and centrifuge model sites of known dimensions and properties.

2 REVIEW OF SEISMIC METHODS FOR STIFFNESS EVALUATION

An elastic half-space is appropriate as a model of the earth as a first approximation. By hitting the ground, the energy coupled into the ground is transmitted away by a combination of P-, S-, and R- waves. Body waves (P and S waves) propagate outward from the source along the hemispherical wave front whereas the surface (R) wave propagates along a cylindrical wave front. S waves often divide into two types, as SH and SV waves, depending on the plane of particle motion. Surface wave energy is existed mostly within a depth of one wave length and the dispersive characteristic in which waves of different wavelength propagate at different velocity, is shown in layered media. Wave propagation theory and observed phenomena should be further refined by considering a layered half-space model where the waves are reflected and refracted at the layer boundary. In the site investigation of soil layers, S and R waves are mostly used because the stiffness of the soil structure cannot

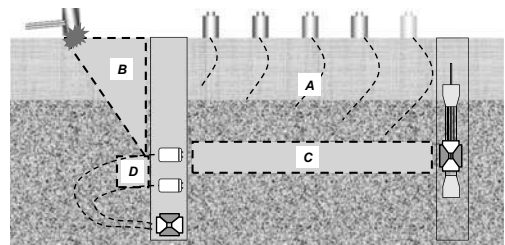


Figure 1. The ranges of site sampled during each testing; (A) Surface wave method, (B) Downhole and Uphole method, (C) Crosshole method, and (D) Suspension PS-logging methods.

be distinguished using P wave below the ground water table and the shearing mechanism during earthquake is similar to shear wave propagation. Compared to other geophysical methods, seismic method has a certain advantage of obtaining wave velocity profiles which are engineering properties directly related with soil stiffness (Richart et al., 1970, Kramer 1996).

The seismic site investigation methods can be grouped as intrusive and non-intrusive methods. The testing borehole is utilized in the intrusive method whereas the source and receivers are on the ground surface in the non-intrusive methods. Typical intrusive methods include crosshole, downhole, SPT based uphole and suspension PS-logging methods as 1D characterization and tomography methods for multi-D characterization. The special features of each intrusive

Table 2. Surface wave methods for seismic site investigation (modified from Stokoe et al., 2004).

Non-intrusive methods		Key features					
		Field testing		Evaluation of experimental dispersion curve	Determination of V_s profile		
		Source	Receivers		Forward model	Mode	Inversion
Surface wave methods	SASW (Stokoe et al., 1994)	Active impulsive or random vibration source	2 receivers are generally used	Apparent phase velocity from phase differences between 2 receivers	Dynamic stiffness matrix method	Superposed mode	Inversion analysis
	MASW (Park et al., 1999)	Active impulsive source or Passive ambient vibrations	12 or 24 channel is usually used	Swept-frequency record or frequency-wave number spectrum approach	Transfer matrix method	Fundamental and higher mode (mode separation)	Inversion analysis
	F-k method (Gabriels et al., 1987)	Active impulsive source or Passive ambient vibrations	Multiple receivers (128, 256 receivers)	Phase velocities from frequency-wave number spectrum using 2D FFT or slant stacking, Frequency domain beamforming	Transfer matrix method	Fundamental and higher mode (mode separation)	
	CSW (Matthews et al., 1996)	Steady-state harmonic source	4 to 6 receivers	Apparent phase velocity from average phase-angle slope over receiver-spread area		Superposed mode	
	HWAW (Park & Kim 2004)	Active impulsive source	2 receivers are generally used	Based on the harmonic wavelet transform to evaluate dispersive phase and group velocities.	Dynamic stiffness matrix method	Superposed mode	Iterative forward modeling
	ReMi (Louie 2001)	Passive ambient vibrations	12 to 48 receivers	Two-dimensional slowness-frequency (p-f) transform	Compound matrix method	Fundamental mode	Iterative forward modeling

method are summarized in Table 1 and the regions of site sampled during each testing are schematically shown in Figure 1.

For non-intrusive stiffness evaluation of the site, the seismic refraction and reflection methods using body waves and the spectral analysis of surface waves (SASW), multichannel analysis of surface waves (MASW), frequency-wave number (f-k) spectrum, continuous surface wave (CSW), harmonic wavelet analysis of waves (HWAW), and refraction microtremor (ReMi) methods using surface waves are frequently

utilized. The special features of each method are summarized in Table 2. Most of the methods use the active ground sources, but some methods use the passive ambient vibrations. The surface wave method which uses the dispersion characteristics in the layered media consists of three steps: field testing, evaluation of dispersion curve, and determination of V_s profile using inversion. The special features for surface wave methods in each step are summarized in Table 2.

The evaluation of 2D or 3D stiffness images is important for the assessment of deformation in the

Table 3. Seismic methods for 2D subsurface stiffness imaging.

Classification	2D stiffness imaging methods	Features
Intrusive methods	Crosshole tomography (Menke 1989, Santamarina & Fratta 2005) SPT-uphole based tomography	Ray-tracing algorithms, Various inversion techniques Travel-time tomography inversion with simultaneous iterative reconstruction technique (SIRT)
Non-intrusive methods	Seismic reflection survey (seismic interferometry) (Matsuoka et al., 2006) Seismic refraction tomography (Hayashi et al., 2001) Surface wave methods CAP-SASW method (Joh 2005) High lateral resolution MASW (Lin et al., 2008) HWAW method (Park & Kim 2001, 2004).	Signal processing technique for generating Green's function by applying cross-correlation operations Non-linear travel-time tomography consisting of ray tracing for forward modeling and simultaneous iterative reconstruction technique (SIRT) for inversion Evaluation of stiffness profile for a subgrade cross-section by the common-array-profiling technique A walk-away survey and a phase-seaming procedure for allowing wide wavelength dispersion analysis within a small spatial range Based on the harmonic wavelet transform to evaluate dispersive phase and group velocities, using maximum energy point in time-frequency map

performance based design of geotechnical structures. The features of each method are summarized in Table 3. In the borehole methods, tomography techniques are frequently utilized in practice, and among those, the SPT based uphole tomography in the field and bender tomography in the centrifuge model are discussed in this paper. In the surface wave methods, the receiver spacing becomes longer to explore the deeper soil layers and the 1D average V_s profile is usually determined with the difficulties obtaining the detailed spatial stiffness variations. To assess the 2D stiffness images, CAP-SASW method, high lateral resolution MASW method, and HWAW method are introduced by improving conventional surface wave techniques. Among those, HWAW method, recently proposed to overcome some weaknesses of existing surface wave methods, will be discussed in this paper.

3 SPT-UPHOLE BASED TOMOGRAPHY

3.1 Introduction of SPT-uphole method

The downhole method is an attractive borehole seismic method for several reasons. This method requires just one borehole and uses a simple surface source, thus it is easy to operate and relatively economical. However, in the layers of sedimentary gravels, weathered and fractured rocks frequently encountered in Korea, it is difficult to construct a test hole and to get a good coupling between the surrounding soils and the casing. In addition, the wave propagation is hindered by these layers and the substantial amount of source energy is required to acquire a discernible signal in the deep downhole test (Kim et al., 2004). Alternatively, the uphole method uses receivers on the ground surface and an underground source such as a small explosive or a mechanical source. Test result can be interpreted

similarly to the downhole seismic method. However, in practice the application of this original uphole method is somewhat uncommon, as it is difficult to generate the shear wave component underground and for this reason it is not cost effective.

A modified form of the uphole method called SPT-uphole method was introduced to obtain the V_s profile of a site cost-effectively and a schematic diagram of the method is shown in Figure 2 (Bang and Kim 2007). The standard penetration test (SPT) is the most frequently used method in a geotechnical site investigation. The impact energy generated by the SPT can be used as a source for the uphole method. The significant amount of compression and shear waves will be generated at the tip and side when the split spoon sampler is penetrated into the soil by hammering on the ground surface. The SPT is usually performed at every 1 or 1.5 meter intervals. If a series of receivers are placed on the ground surface, it would be feasible to perform the uphole test during SPT. The boring and SPT is performed in tandem; therefore, the SPT-uphole method can be performed simultaneously while boring without additional cost such as the preparation of the testing hole, casing, grouting, and sourcing work compared to other borehole seismic methods. For this reason, it is usually very simple, economical and not labor intensive.

3.2 Understanding of particle motions due to SPT source

As the sampler moves downward during the impact, it can be postulated that the shear (S) wave of the particle motion in a vertical direction (SV type) as well as compression (P) wave near the source are generated as shown in Figure 3. The P-wave component is detected mainly in a radial direction on the ground surface when

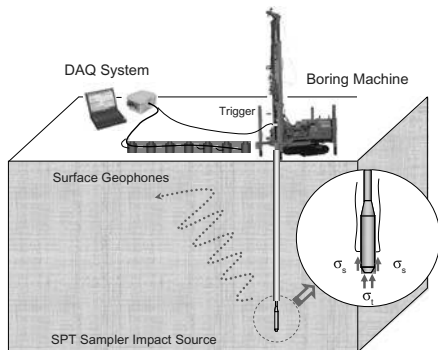


Figure 2. Schematic diagram of the SPT-uphole test.

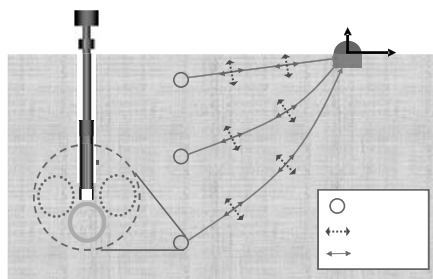


Figure 3. Prediction of particle motion at the surface generated by the SPT impact source.

the SPT source is located at a shallow depth while it is detected mainly in a vertical direction at deeper depths. In contrast, as the vertical motion of an SV-type wave changes to a horizontal motion as propagating to the ground surface due to Snell's law, the S-wave component is detected mainly in the vertical direction on the ground surface when SPT source is located at shallow depth and mainly detected in the radial direction when located at deeper depths. Specifically, the major direction of each wave motion will vary depending on the locations of the source and receiver and both vertical and radial horizontal motions are simultaneously governing the surface motion when the elastic wave is generated by the SPT sampler in the ground.

This can be well understood from the characteristics of particle motion at the ground surface obtained from numerical simulation. Figure 4 shows the particle motions in both vertical and radial horizontal directions at every case of this numerical study. The vertical distances are the testing depth and the horizontal distances are the distances from the borehole (offsets). The motion of the P-wave component is identical to the direction of the ray path and the motion of the S-wave component is perpendicular to the direction of the ray path. On the left side of Figure 4, the representative particle motions at source depths of 6 m, 15 m,

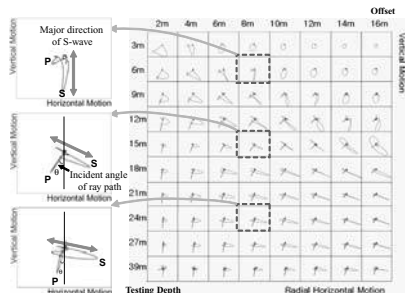


Figure 4. Characteristics of the particle motion on the ground surface in the space domain of a vertical and radial horizontal direction.

24 m and the receiver location of 8 m are enlarged. It is shown that the direction of particle motions of the P and S-waves changes according to the location of the source and receiver as discussed in Figure 3.

3.3 Tomography: testing procedure and data reduction

The SPT-uphole tomography method is a kind of borehole to surface travel time tomography and it uses impact energy during SPT as a source. The proposed method is composed of three steps. The first step is data acquisition (to obtain signals from field test), the second step is signal processing (to determine arrival travel time of shear wave), and the last step is inversion analysis (to construct subsurface imaging).

The surface geophones are placed on the ground at the selected intervals from the boring point. As more receivers are used, it will provide better results. Additionally, using two-component (radial horizontal and vertical) geophones is recommended to obtain better travel time information for a deep testing depth.

The typical signal traces of the vertical and horizontal components at each distance when the depth of source is 3 m, 18 m and 39 m are shown in Figure 5. On the right side of figure, the root mean square signals of the vertical and horizontal components in the time domain (two-component signals) are plotted. The first peak points of the shear wave in root mean square signals coincide with the first peak points of the shear wave in the particle motion space in Figure 4. From these root mean square signals, the first peak travel times can be determined in the entire depths without the need for a subjective judgment.

In order to correct the first peak travel time information to the first arrival time, the dominant frequency around first peak point of S wave is determined, then initial arrival is determined at a quarter of period ahead of peak point. As the travel times are calculated from signals with different trigger locations, a correction for the inconsistent trigger should be considered. It is highly impractical to install a trigger system at a sourcing point of the SPT; accordingly, the trigger system is

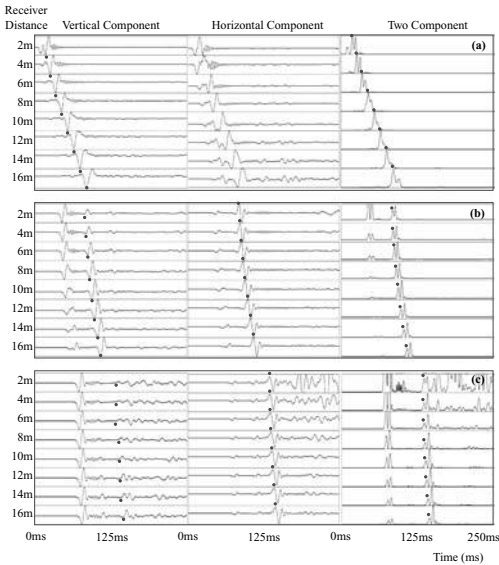


Figure 5. Signal traces at each receiver generated by a numerical simulation of the SPT-uphole method with source depth of (a) 3 m, (b) 18 m, (c) and 39 m. The dot is first peak of the shear wave component.

normally installed below the anvil. The length of the rod will change with a different testing depth and the travel time through the rod should be subtracted from the measured travel time.

The distribution of shear wave velocity is determined by travel-time tomography inversion. Many travel-time tomography programs were introduced and commercialized by geophysicists and among those GeoTomCG was used for this study (Tweeton et al., 1992). This involves modification of an arbitrary initial velocity model by repeated cycles of three steps: forward computation of model using first arrival travel times, calculation of travel time residuals, and application of velocity corrections. Inversion of travel time data was made with a variation of the SIRT algorithm (Lytle et al., 1978).

3.4 Field application

Field tests were performed to verify the applicability of SPT-uphole tomography method. Figure 6 shows the schematic diagram of SPT-uphole testing site at Kimje in Korea. All six borings were drilled to the depth of 13.5 m for the evaluation of the horizontal non-homogeneity characteristics and SPT-N values as shown in Figure 7. The measured N-value was adjusted to the value with reference energy ratio as N_{60} . To illustrate the horizontal variation of the layers, V_s distribution map was constructed by using the empirical relationship between SPT-N value and shear wave

velocity suggested by Imai et al., (1982). Figure 8 shows that the shape of layers at the site is upward inclined.

Signal traces obtained from each receiver are shown in Figure 9 with the source depth. Four vertical component geophones were used at this site. The location of each receiver was 6 m, 9 m, 12 m, 15 m from the boring point (BH-2) and the boring was performed to the depth of about 20 m especially for tomography. The travel time information of shear wave was obtained by using the peak point of the vertical component only and the first arrival times for tomography inversion were determined by the proposed scheme in section 3.3. Because only vertical component geophones were used, the signals recorded can be easily interfered with P wave component, especially at the near receivers as shown in Figure 9a. Therefore, it is recommended to use two component receivers in the field for compensating this problem by horizontal component. In this case, testing depth was not deep and only limited travel time data on receivers have interfered with

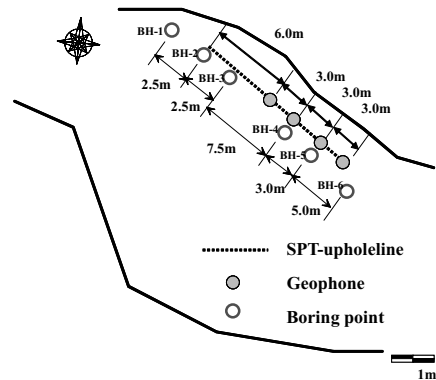


Figure 6. Schematic diagram of SPT-Uphole testing site.

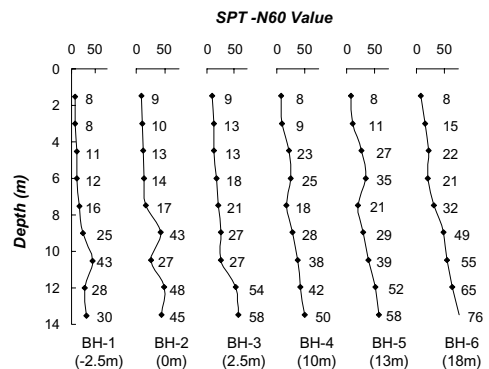


Figure 7. SPT-N values of the 6 boring holes.

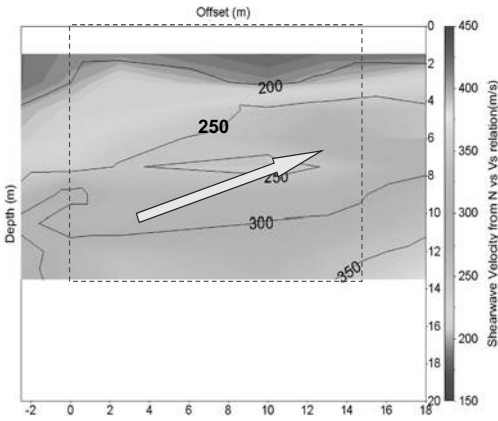


Figure 8. V_s distribution map determined by SPT-N vs. V_s empirical relationship.

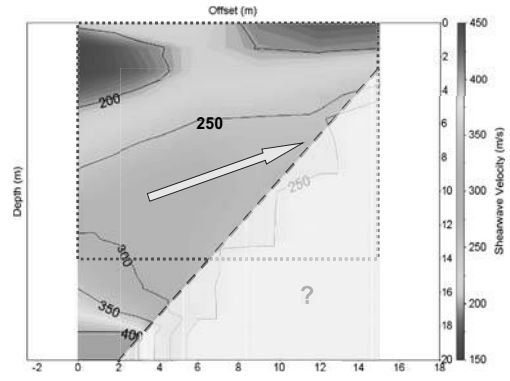


Figure 10. V_s distribution map determined by SPT-Uphole tomography method.

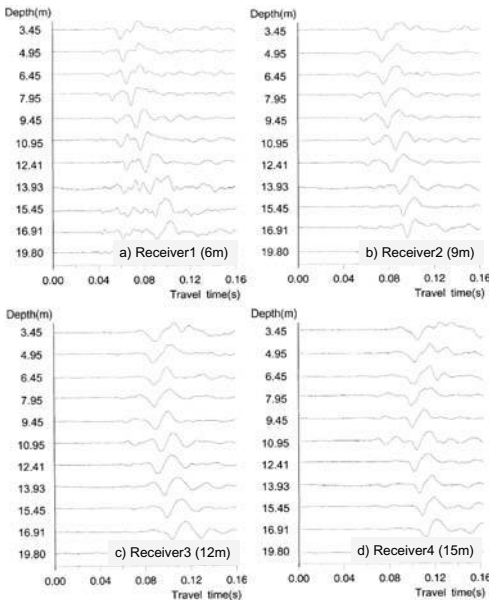


Figure 9. Signal trace at each receiver in this field application.

P-wave component and those data were excluded from tomography analysis.

The triangular shape of shear wave velocity distribution map determined by SPT-uphole tomography is shown in Figure 10. The shape of the distribution map determined by proposed method is similar to that obtained by SPT-N values. From the depth of 14 m, it is difficult to guess the horizontal variation because of the limited traces. Therefore, it is recommended to perform deeper than the depth interested to evaluate.

It can be noted that the horizontal variation of V_s in the distribution map is characterized economically using SPT-uphole tomography when comparing to the result in Figure 8. SPT-uphole tomography method shows good potential for characterization of deformation properties spatially in geotechnical engineering.

4 2D STIFFNESS IMAGING USING HAWW METHOD

4.1 HAWW method

HAWW method is based on the harmonic wavelet transform to evaluate dispersive phase and group velocities of surface wave. To apply the harmonic wavelet transform, the meaning of harmonic wavelet coefficient is interpreted from a different point of view.

The step by step procedure to evaluate the dispersive phase and group velocities was proposed (Park & Kim 2001, 2004). First, harmonic wavelet transform decompose signals obtained at receiver 1 and 2 into frequency components in time domain. And this transform determine energy and phase timefrequency maps which describe instantaneous energy and phase of frequency components with time (Fig. 11). Then, the group and phase delays of each frequency component are determined from instantaneous energy and phase information. The group delay means time corresponding to maximum energy and the phase delay is time corresponding to certain fixed phase around maximum energy time. If the distance between receiver 1 and receiver 2 is D , then the group velocity V_{gr} and the phase velocity V_{ph} at each frequency are obtained (Fig. 12). The HAWW method mainly uses the signal portion of the maximum local signal/noise ratio to evaluate the phase velocity and it can minimize the effects of noise (Park & Kim 2001).

4.2 Site characterization using HWAW method

For the site characterization, HWAW method can use two test setups; short receiver spacing setup and conventional test setup. In the short receiver spacing setup (Fig. 13), source-receiver spacing (D) is 6~12 m and receiver spacing (R) is 1~3 m.

In contrast, at the conventional test setup, source-receiver spacing is over 10 m and receiver spacing is same as the source-receiver spacing. For more accurate and detailed result, the short receiver spacing setup is preferable because of the lateral non-homogeneity of soil layer.

The proposed method uses the whole wave field information to determine dispersion curve representing whole depth from one test setup. The dispersion curve determined by HWAW method and the theoretical dispersion curve used in the inversion process consider whole wave field information in the same way. Therefore, the whole wave field dispersion curve can be used to evaluate deep soil profile (Park & Kim 2001, 2004).

Because the phase velocities vary with receiver location due to different velocities of various modes

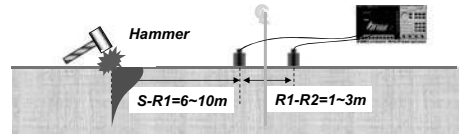


Figure 13. Test setup for HWAW method (short receiver spacing setup).

of which surface wave consists, the field testing set up should be considered in the inversion process. The array inversion in which the theoretical dispersion curve is generated at receiver locations same as field test setup was developed to consider testing setup in the inversion process (Joh 1996). Array inversion shows good performance but cause increasing calculation time and complexity in the inversion process. In the HWAW method, the single array inversion process can be possible without increasing calculation time and any complexity because the HWAW method uses just one test setup in the field. Because the HWAW method uses short receiver spacing setup, it can minimize the possibility of error due to lateral non-homogeneity and can determine detailed local soil profile (Park & Kim 2001, 2004).

By performing series of tests along testing direction, 2D subsurface stiffness imaging can be obtained by interpolating all local V_s profiles of interested region. Even though this is not a tomography but a simple interpolation job, this method can provide detailed 2D stiffness contour because receiver is close enough. So, to evaluate detailed local properties of ground and 2D stiffness image, it is recommended to use short receiver spacing setup.

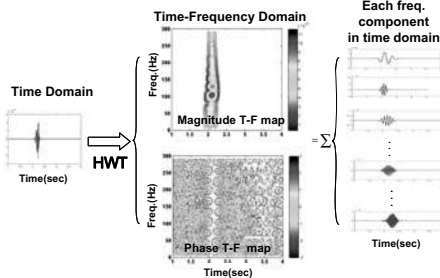


Figure 11. Decomposition of time record by harmonic wavelet transformation.

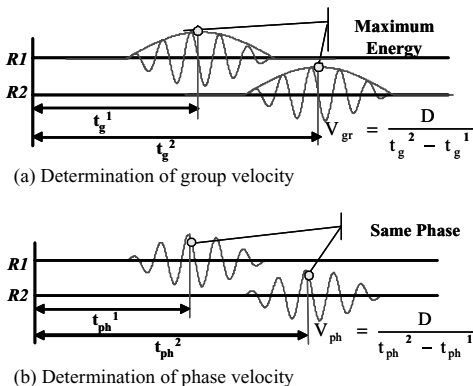


Figure 12. Determination of group and phase velocities of each frequency component.

4.3 Field applications

In order to compare HWAW results with various seismic test results widely used in geotechnical site investigation, various seismic tests including SASW, MASW, HWAW and downhole tests were performed and test results wave compared in this study.

4.3.1 Site 1

Three surface wave tests including SASW, MASW, and HWAW tests were performed with three borings (BH-1, BH-2 and BH-3) to evaluate the applicability of HWAW method at the beach site. As shown in Figure 14, the soil layers are horizontally uniform.

HWAW method was performed using short receiver spacing setup in which source to receiver spacing was 6 m and receiver to receiver spacing was 2 m. SASW and MASW tests were performed using conventional test setup. The testing setups for each surface wave tests are summarized in Table 4.

The dispersion curve by HWAW method was compared with those by SASW and MASW tests in

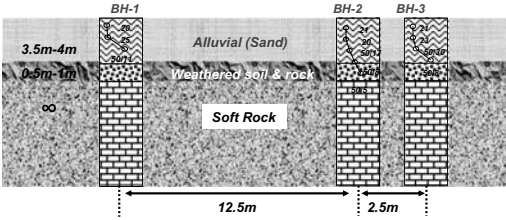


Figure 14. The profile of the site 1.

Table 4. The testing setups at site 1.

Tests	Survey line	Source offset	Receivers
SASW	64 m	2, 4, 8, 16, 32 m	2 geophones
MASW	43 m	20 m	24 geophones
HWAW	8 m	6 m	2 geophones

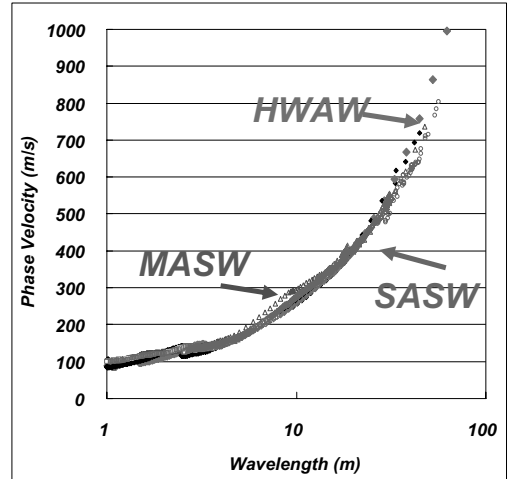


Figure 15. The dispersion curves by 3 surface wave tests.

Figure 15. With respect to the dispersion curves, it can be noted that three test results are similar over whole frequency ranges.

Compare to other surface wave methods, HWAW method provide the equivalent or better dispersion curve up to the long wave length even though the receiver spacing and survey line is short. Among surface wave methods, HWAW method shows a certain advantage and the potential to obtain detailed 2D stiffness imaging.

4.3.2 Site 2

Down-hole, SASW and HWAW were performed to evaluate applicability of 2D imaging by HWAW method and three borings (BH-1, BH-2, BH-3) were performed at site 2 (Park et al., 2007). Figure 16 shows the boring results. It is noted that soil layers are not horizontally uniform. HWAW method was performed using short receiver spacing setup in which source to receiver spacing was 6 m and receiver to receiver spacing was 2 m. SASW test was performed using conventional test setup. Down-hole test was performed to about 30 m depth at three bore-holes.

Figure 17 shows comparison of V_s profiles determined by HWAW, SASW, and down-hole test at BH-2. Although there are some differences between three results, it can be said that three V_s profiles are similar over whole depth range. The differences between HWAW and SASW method can be explained by the lateral stiffness variation of the site and differences in sampled region. V_s profiles determined by down-hole method are similar to results by surface wave method. Through these comparisons, can be verified that HWAW can give a reliable V_s profile to the deep depth properties with short receiver spacing setup.

HWAW test was also repeated shifting source and receiver setup, and total 14 dispersion curves were

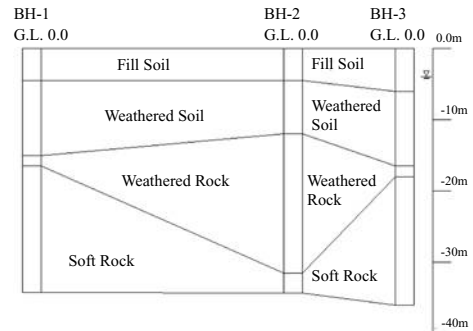


Figure 16. The geology profile of the site 2.

evaluated. Figure 18 shows the 2D V_s image which shows the horizontal irregularity, and the boundaries of weathered soil and weathered rock were assumed by the shear wave velocity contours of around 250 m/s and 600 m/s, respectively. Boring logs are also shown in the figure, and it is possible to distinguish boundaries of layers by wave velocities. It can be noted that the assumed weathered soil and weathered rock lines in the 2D V_s image accord well with 2D boring geology. The good applicability to develop 2D V_s profile using HWAW method was also verified.

4.3.3 Site 3

Site 3 is a model site which composed of four sublayers with size about 16 m × 26 m × 8.5 m ($W \times L \times H$) as shown in Figure 19 (Kim et al., 2006). Total of 140 vertical and horizontal geophones were embedded at the boundary of each layer to evaluate the dynamic material properties of each layer. Using

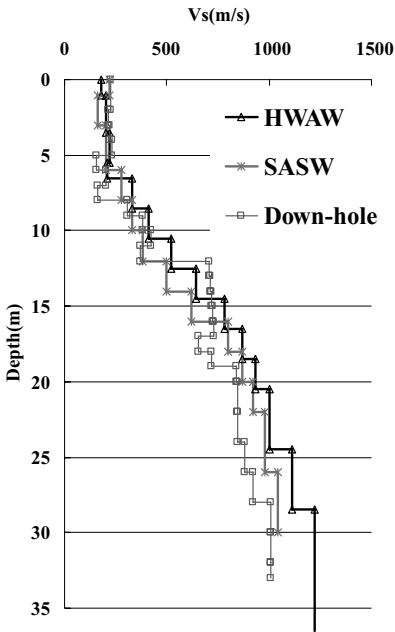


Figure 17. Comparison of V_s profiles obtained by HAW, SASW and Down-hole tests at BH-2 in site 2.

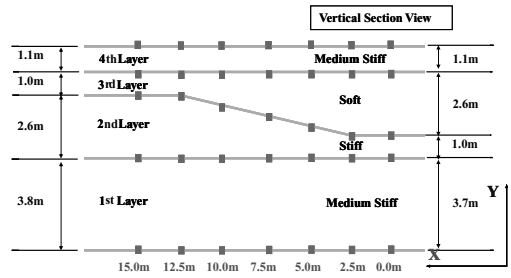


Figure 19. The geology profile of the model testing site.

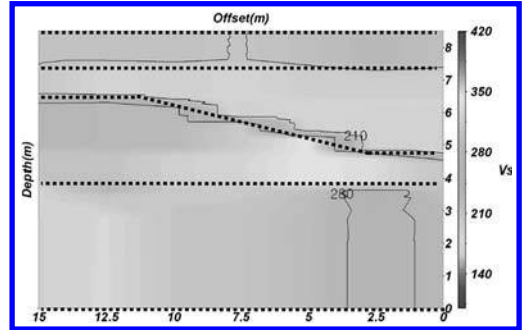


Figure 20. 2D V_s image of model testing site obtained by reference value.

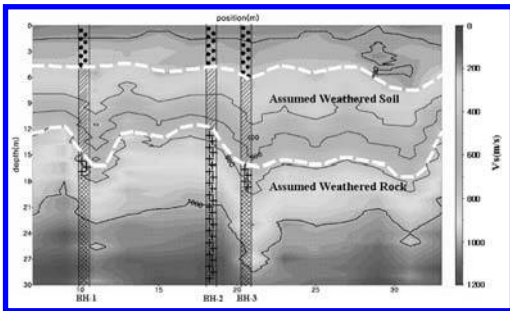


Figure 18. 2D V_s image of site 2 obtained by HAW method.

the interval travel time between embedded geophones, V_s and V_p of each layers were obtained as reference data for evaluation of various seismic tests (Fig. 20). As the surface wave methods, HAW, SASW, and MASW methods were performed along the embedded geophone line. All test sets were fitted to find V_s profile up to 8.5 m depth which is the depth of model site. HAW method was performed using 6 m of source to receiver spacing (S-R1) and 2 m of receiver to receiver spacing (R1-R2), and was repeated by shifting source and receiver setup parallel from 0 m to 15 m at 7 locations where embedded geophones were located. SASW method was performed with receiver spacing 3, 5, 10 m and the central location between two

receivers was at horizontal coordinate of 10 m. MASW method was performed using 24 channel geophones with 0.5 m receiver spacing and 4 m offset, and then also repeated along the line of embedded geophone from coordinates of 0.6 m to 12.1 m with 0.5 m interval to obtain the local V_s profiles of interested region. Down-hole test was performed at 3 boreholes with 0.5 m vertical interval and data reduction was performed using refracted ray path method (Kim et al., 2004).

Figure 21 shows comparison of representative results of four seismic tests and reference data which were determined by embedded geophones. Results of HAW method match well with reference values. V_s profile of SASW method at 10 m location represents the average V_s profile of model site using combination of several receiver spacing, so it does not match well with reference value and can't show horizontal variations of site. In case of MASW method, V_s profiles of upper layer match well with reference values, but V_s of lower layer cannot present detailed properties and horizontal variation. Since MASW method using multi-channels evaluates V_s profile averaged over total length of the array, lateral resolution decreases. Also, in small surface of model test site, due to short survey line, low frequency components of waves were not fully generated. In case of downhole test, although

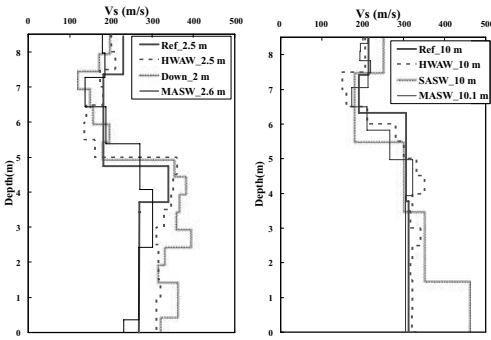


Figure 21. Comparison of V_s profiles obtained by HAWW, SASW, MASW and Down-hole tests in model testing site.

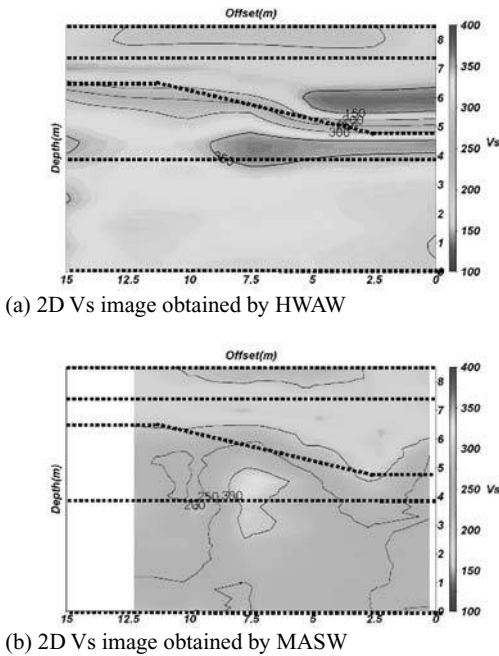


Figure 22. 2D V_s images of model testing site.

V_s profile is very similar to reference value and locally detailed, it give a point values not enough to show entire shape of 2D V_s profiles of model site.

Figure 22 shows 2D V_s images obtained by HAWW and MASW methods. 2D V_s profiles by HAWW method match well with detailed geometry and reference value of model site shown in Figure 20. As shown in Figure 22b, MASW method also provide 2D V_s profiles but the 2D image is a little different from reference value. MASW method use 24 receivers (receiver spacing: 0.5 m) and determine average V_s profile covering horizontal length of 11.5 m. On the

contrary, HAWW method uses short receiver spacing (2 m) contrary to long multi-channel receiver array of MASW, so it is possible to get locally detailed V_s profile of the entire model site. By comparing 2D image determined by reference data, the good applicability to develop 2D V_s profile using HAWW method was verified.

5 IN-FLIGHT MEASUREMENT OF V_s DISTRIBUTION IN CENTRIFUGE MODELS

There have been several methods suggested for evaluating the performance of geotechnical structures. In geotechnical engineering, model tests can play key roles because they can reflect the nature of soil characteristics by constructing the model with the same material, soil, with the prototype structures. Physical modeling using geotechnical centrifuge can offer unique capabilities in wide range of performance evaluation from small-strain soil behavior to structural failure condition.

For performance based design, the deformation behavior of geotechnical structures governs the design while current design methods usually rely on the strength of geomaterial and factor of safety. In this context, it is important to characterize the soil conditions of geotechnical systems accurately to predict deformation behavior. Shear wave velocity (V_s) can be used as a key parameter for evaluating deformation of geotechnical structures because it is highly related with deformational characteristics of soil, maximum shear modulus, G_{max} . Measuring V_s before an earthquake event or construction process provides a basic information for evaluating structural performance, and measuring V_s after events gives general information on the change of soil condition caused by earthquake or service conditions.

There have been a series of methods for measuring V_s in centrifuge models. Installation of piezoelectric oscillator (Shibata et al., 1991), a vertical array of bender elements (Goyal & Finn 1991), and a mini-air hammer (Arulnathan et al., 2000) were utilized for direct measurement of shear wave velocities. More recently, V_s measurement using a series of bender element couples at various depths was adopted for centrifuge tests before earthquake simulation to obtain V_s profile (Fu 2004), and the tomography measurement system using bender elements have been reported (Rammah et al., 2006). V_s measurement using these methods can offer important information for the deformation analysis.

In this study, an experimental setup to evaluate shear wave velocity distribution in model soil has been developed for centrifuge model tests. Piezoelectric bender elements are used for both generating and receiving shear wave signals and V_s distribution can be visualized by tomography inversion. The change

in V_s distribution before and after applying surface load is monitored during in-flight condition and it has been found that the developed system is useful for characterizing soil condition and monitoring the soil behavior.

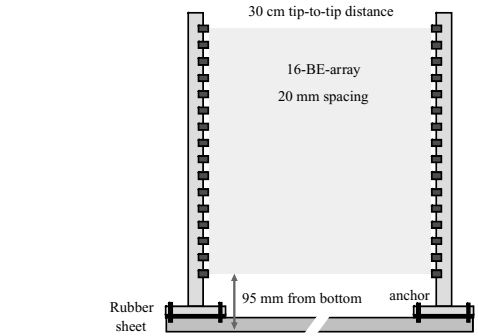
5.1 Experimental setup

Piezoelectric bender elements are widely used for measuring V_s in soil specimen. It is easy to setup and the testing mechanism is straightforward. V_s tomography measurement system using bender element arrays has been recently developed at KAIST for centrifuge testing. The purpose of this system is measuring spatial variation of V_s and G_{max} in the centrifuge testing model which is basic information in evaluating deformation behavior of soil mass.

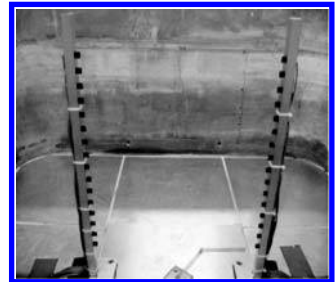
A state-of-the-art geotechnical centrifuge facility has been developed at KAIST in 2008 under Korea Construction Engineering Development Collaboratory Program (KOCED Program). The centrifuge with 5.0 m platform radius has the maximum capacity of 240 g-tons. The maximum usable payload for testing model is 2,400 kg up to 100 g acceleration and the maximum acceleration is 130 g up to 1,300 kg payload. This machine will be equipped with 4-degree-of-freedom in-flight robot and biaxial shaking table in early 2009. The main purpose of developing this facility under KOCED program is to activate physical model test activities for research and development in Korean geotechnical society and practitioners, so it will be share based operated to whoever wants to use this facility.

Figure 23 shows the physical configuration of the bender element tomography system in centrifuge models. Two arrays with 16 bender elements on each side are installed in a rectangular soil container, and each bender element is installed every 20 mm depth covering $300\text{ mm} \times 300\text{ mm}$ cross-sectional area. Parallel connection type was used for transmitter array and series connection type was used for receiver array. Parallel type is useful for generator because the amplitude is twice compared to series type and when the same voltage level is applied, series type is better as a receiver by similar reason.

The natural frequency of bender element cantilever beam affects the efficiency to detect shear wave signal. Lee & Santamarina (2005) showed that the amplitude of output signal increases when the major frequency of shear wave approaches to the natural frequency of bender element cantilever. In this study, the natural frequency of installed bender elements is selected considering the shear wave characteristics and soil conditions. Assuming that the V_s range in tomography area is from 100 m/s to 300 m/s at 50 g acceleration, the frequency range of shear wave is around 5 kHz to 15 kHz within 20 mm wavelength which is the resolution of tomography system. The cantilever length of



(a) Schematic diagram



(b) Installation

Figure 23. Bender element arrays for V_s tomography in centrifuge testing.

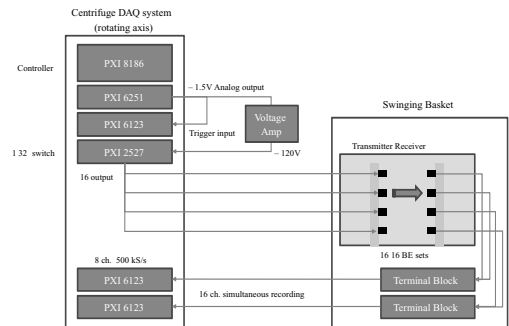


Figure 24. BE driving and measurement system in KAIST centrifuge.

bender elements is determined as 6 mm considering the frequency characteristics.

Figure 24 shows the configuration of bender element driving and measurement system installed in the centrifuge. This system is developed by modifying the data acquisition system of KAIST centrifuge. Once an analog voltage signal for driving bender element is generated from an analog-output channel, it goes to the transmitter bender element after amplified up to the maximum voltage level for the bender

element. The system starts recording the output data from 16 receiver bender elements simultaneously at 500 kS/s sampling rate when the driving signal triggers the transmitter. 16 tests at each depth are conducted by switching the driving channel connection by controlling the switch module and total 256 travel time data are obtained as a result. This travel time data is gathered from the output signal and it is used as input information for the tomography inversion process.

5.2 Testing procedure and results

Model tests are conducted to check the applicability of the tomography system in centrifuge. Homogeneous silica sand sample with uniform density is prepared using automatic sand-rainer in a rectangular container which is equipped with the bender element arrays. The sand-rainer installed at KAIST, originally developed by LCPC, France, is known that the model constructed by the equipment shows uniform and homogeneous relative density in sand layer (Garnier 2002). Relative density (D_r) in the model is 44% and travel time for tomography is measured at 40 g and 80 g acceleration levels to confirm the consistency of tomography results. Commercial software, GeoTomCG (Tronicke et al., 2001), based on SIRT algorithm was used for the tomography inversion process.

Figure 26 shows the V_s tomography image obtained at 40 g. Even if there are some errors at the edges due to the lack of ray-path information, this result shows the increase of V_s with depth or effective stress level. The tomography inversion result at 80 g shows similar trends to that of 40 g. To verify the accuracy of V_s distribution with depth, middle vertical array of tomography inversion data was collected and plotted with mean effective stress in Figure 27. Mean effective stress, σ'_m , is simply calculated from the density of sand and depth from the surface assuming the coefficient of earth pressure at rest, K_0 , is 0.5. The maximum shear modulus shows linear relationship with mean effective stress in log-log domain, which can be expected from Hardin's equation (1978), and the result from experiments at 40 g and 80 g shows consistency. These results could be compared with resonant column (RC) test result for the same soil sample with 40% relative density and it shows a good agreement.

Tomography inversion considering curved ray path must be considered in this case. While most of tests using bender elements are conducted at a short distance and element level with a uniform effective stress for entire soil mass, the effective stress in centrifuge model increases continuously with depth and it results in the variation of shear wave velocity in soil system. Therefore, the ray path for shortest travel time is not straight for relatively long travel distance. It is the same phenomenon as in the seismic refraction

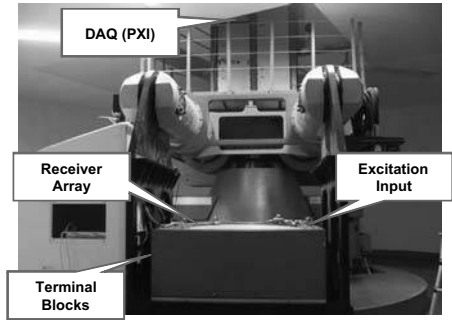


Figure 25. Geotechnical centrifuge testing setup.

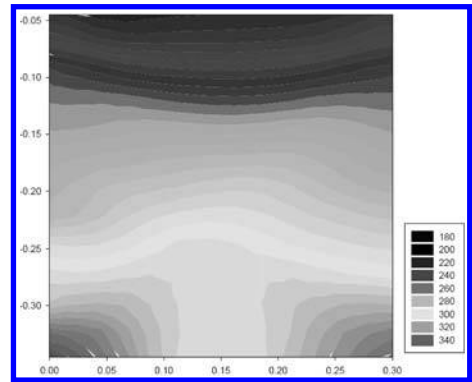


Figure 26. V_s tomography image at 40 g.

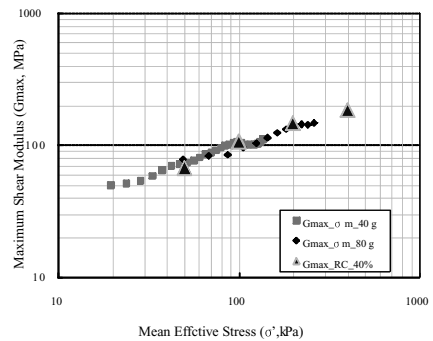


Figure 27. Maximum shear modulus with mean effective stress from tomography inversion.

method in the field. The curved ray path information of the tomography inversion for test results at 40 g acceleration is shown at Figure 28. In this result, the refracting trends are significant especially at shallow depth where wave velocity increases quickly with depth.

To verify this effect on tomography image, the result from tomography inversion data is compared with shear wave velocity calculated assuming straight ray path in Figure 29. This result shows that G_{\max} considering straight ray path is bigger than G_{\max} from curved ray path as expected because the straight travel distance is shorter than the curved one for the same travel time. This trend is significant at shallow depth with low effective stress level because the impedance ratio for the same vertical distance is bigger at shallow depth. The results from curved ray path inversion shows better agreement compared with RC test data, showing that the power, n , of mean effective stress in G_{\max} relationship, from curved ray path inversion is closer to RC test result than straight path calculation. Therefore, it is important to use appropriate testing and data reduction method considering curved ray path for tomography analysis in centrifuge model tests.

5.3 Application case: Tomography imaging under surface footing load

The purpose of V_s tomography measurement in centrifuge model is to monitor the change of soil

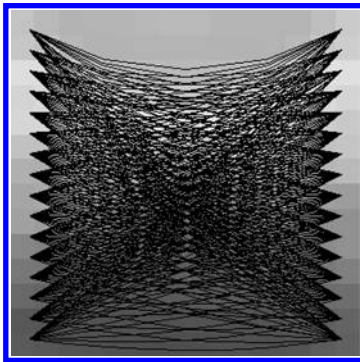


Figure 28. Tomography ray path information (40 g testing result).

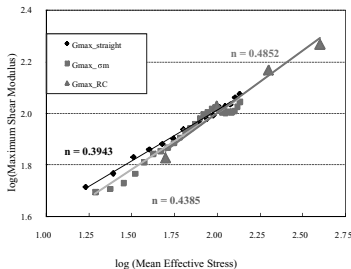


Figure 29. Comparison of results from curved ray path inversion and straight path calculation.

condition in each performance stage of geotechnical structures. This program could be used for monitoring soil condition under foundation load in order to assess its applicability for measuring V_s increase in soil mass due to additional stress development by footing. At the first trial, 100 mm diameter aluminum plate is prepared to simulate footing load at the central part of the surface and it is attached to the vertical loading equipment to measure load-settlement behavior of the foundation.

The same soil model described previously is prepared and the centrifugal acceleration is applied to 50 g. To compare the effect of footing load in the V_s distribution of soil layer, shear wave travel time is first measured without any surface load to obtain original tomography image. While controlling the vertical loading amplitude, load and settlement of the foundation was recorded and the cross sectional area was also monitored by tomography method using the bender element arrays.

Figure 30a shows the V_s tomography images for homogeneous soil sample before loaded with footing. This is the reference information for assessing the changes of V_s in soil mass due to loading condition. As the footing load increases, V_s increases at the middle part beneath the footing, as shown in Figure 30b. These phenomena can be clearly displayed by comparing the tomography image before and after loading stage. Subtracting V_s values of original condition from the V_s when the load is applied, pure increment of V_s can be obtained as shown in Figure 30c. This increase in V_s beneath footing is localized within 1.5 times of diameter of loading plate in depth, and 2 times of that in horizontal direction. This V_s increase can be interpreted as additional effective stress by footing load. Even if the distribution shape of increasing V_s is a little different from analytical solution suggested by Boussinesq (1885), it is still useful for understanding how the footing load affects the soil behavior beneath footing.

Figure 30d shows the tomography image of V_s increment obtained when 254 kPa load is removed. It shows that V_s increment remains permanently in the region that it increased by surface loading. This can be understood that void ratio decreased due to surface load and permanent settlement occurred in previous testing stage. Shear wave velocity is highly related to mean effective stress in soil, void ratio, over consolidation ratio, etc. Using this V_s increase in sandy soil due to foundation loading, vertical effective stress distribution and void ratio changes can be evaluated by adopting empirical relationship of V_s , σ'_m , and void ratio suggested by Hardin. Therefore, the soil properties such as effective stress level and void ratio changes can be evaluated by geophysical tomography method in model test and appropriate method for evaluating those properties is under developing stage.

6 CONCLUSIONS

For the performance based design, the evaluation of spatial variation of soil stiffness, particularly the shear wave velocity which is a key parameter in deformation analysis, is very important in the site investigation. Both intrusive and non-intrusive seismic methods based on stress wave propagations are frequently used in practice and those methods are reviewed considering special features, merits and demerits of each method. Among those, SPT-uphole based tomography and 2D HWA methods in the field and the bender-tomography method in the centrifuge model, currently developed in KAIST, are discussed in detail. The basic principle, testing set-up, and data reduction scheme are introduced and the advantages and applicability of the proposed methods are assessed by comparing the test results obtained by other tests at the sites of known geometry and material properties.

ACKNOWLEDGMENT

This research was supported by a fund of the Construction Research and Development Program (04 construction kernel B01-04) and KOCED Geotechnical Centrifuge Center contributed by the Korea Ministry of Land, Transport and Maritime Affairs (KMLTM). It is gratefully acknowledged.

REFERENCES

- Arulnathan, R., Boulanger, R.W., Kutter, B.L. & Sluis, W.K. 2000. New tool for shear wave velocity measurement in model tests, *Geotechnical Testing Journal* 23(4): 444–453.
- Bang, E.S. & Kim, D.S. 2007. Evaluation of shear wave velocity profile using SPT based uphole method, *Soil Dynamics and Earthquake Engineering* 27: 741–758.
- Boussinesq, M.J. 1885. Application Des Potentiels, à L'étude De L'équilibre Et Du Mouvement Des Solides élastiques, Gauthier-Villars, Paris.
- Burland, J.B. 1989. Ninth Lauritis Bjerrum Memorial Lecture: 'Small is Beautiful'—the Stiffness of Soils at Small Strains, *Canadian Geotechnical Journal* 26: 499–516.
- Fu, L. 2004. Application of Piezoelectric Sensors in Soil Property Determination, Ph.D. Thesis, Case Western Reserve University.
- Gabriels, P., Snider, R. & Nolet, G. 1987. In situ measurements of shear wave velocity in sediments with higher-mode Rayleigh waves. *Geophysical Prospecting* 35: 187–196.
- Gohl, W.B. & Finn, W.D.L. 1991. Use of piezoceramic bender in soil dynamic testing, Recent advances in Instrumentation, Data Acquisition and Testing in Soil Dynamics, *Geotechnical Special Publication* 29, K.B. Shobha & W. B. Geoffrey, eds., pp. 118–133.
- Graves, R.W. 1993. Modeling three-dimensional site response effects in the Marina District, San Francisco, California, *Bulletin of the Seismological Society of America* 83: 1042–1063.

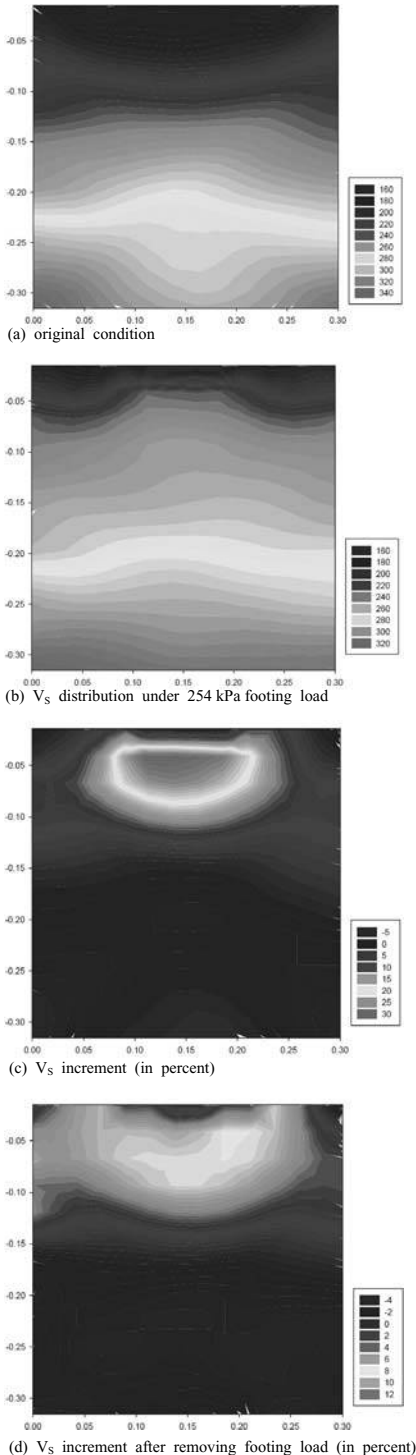


Figure 30. V_s increment due to footing load.

- Hardin, B.O. 1978. The Nature of Stress-Strain Behavior of Soils, Proceedings, *Earthquake Engineering and Soil Dynamics*, ASCE Pasadena, California, Vol. 1: 3–89.
- Hayashi, K. & Takahashi, T. 2001. High Resolution Seismic Refraction Method Using Surface and Borehole Data for Site Characterization of Rocks, *International Journal of Rock Mechanics and Mining Sciences*, 38: 807–813.
- Iai, S., Tobita, T. & Tamari, Y. 2008. Seismic Performance and Design of Port Structures, Geotechnical Special Publication No. 181—Geotechnical Earthquake Engineering and Soil Dynamics, ASCE: 2024–2039.
- Imai, T. & Tonouchi, K. 1982. Correlation of N-value with S-wave Velocity and Shear Modulus, *Proceedings of the 2nd European Symposium on Penetration Testing*, Amsterdam: 57–72.
- International Navigation Association. 2001. *Seismic Design Guidelines for Port Structures*, A.A. Balkema Publishers.
- Joh, S.H. 1996. Advanced in interpretation and Analysis Techniques for spectral analysis-of-surface-waves (SASW) measurements. Ph.D. Thesis, University of Texas at Austin.
- Joh, S.H., Jang, D.W., Kang, T.H. & Lee, I.W. 2005. Evaluation of Stiffness Profile for a Subgrade Cross-Section by the CAP (Common-Array-Profiling)-SASW Technique, *Journal of the Korean Geotechnical Society*, 21(4): 71–81.
- Kim, D.S. 1991. Deformational Characteristics of Soils at Small to Intermediate Strains from Cyclic Tests, Ph.D. Thesis, University of Texas at Austin.
- Kim, D.S., Bang, E.S. & Kim, W.C. 2004. Evaluation of various downhole data reduction methods to obtain reliable V_s profile. *Geotechnical Testing Journal*, 27(6): 585–597.
- Kim, D.S., Kim, J.T., Bang, E.S., Park, H.J. & Park, H.C. 2006. Comparative study of Seismic Field Test using Multi Layered Model Testing Site, *ASCE Geotechnical Special Publication* 149: 204–211.
- Kim, D.S., Park, H. C. & Kim, S.H. 2004. Seismic Site Characterization using Harmonic Wavelet Analysis of Wave (HWAW) Method, US-Korea Joint Workshop, Seoul, Korea: 335–346.
- Kim, D.S. & Stokoe, K.H. 1994. Torsional motion monitoring system for small-strain (10^{-5} to $10^{-3}\%$) soil testing, *Geotechnical Testing Journal*, GTJODJ, 17(1): 17–26.
- Kramer S.L. 1996. *Geotechnical earthquake engineering*, Prentice-Hall, Englewood Cliffs, N.J., 653 p.
- Lee, J.S. & Santamarina, J.C. 2005. Bender Elements: Performance and Signal Interpretation, *Journal of Geotechnical and Geoenvironmental Engineering*, 131(9): 1063–1070.
- Lin, C.P. & Lin, C.H. 2008. High lateral resolution surface wave method, The 3rd international Conference on Site Characterization, Taipei, Taiwan.
- Lytle, R.J., K.A. Dines, E.F. Laine & D.L. Lager. 1978. Electromagnetic Cross-Borehole Survey of a Site Proposed for an Urban Transit Station, UCRL-52484, Lawrence Livermore Laboratory, University of California.
- Matsuoka, T., Shraishi, K., Onishi, K. & Aizawa T. 2006. Application of seismic interferometry to subsurface imaging, *Proceedings of 10th International Symposium on RAEg*, Daejeon, Korea.
- McMechan, A. George. & Yedlin, J. Mathew. 1981. Analysis of dispersive waves by wave field transformation. *Geophysics*. 46(6): 869–874.
- Menke, W. 1989. *Geophysical Data Analysis: Discrete Inverse Theory*, Academic Press, 289 p.
- Mok, Y., Stokoe, K.H. & Wilson C.R. 1989. Use of Inverse Theory to Analyze Downhole Seismic Data, Society of Exploration Geophysicists Expanded Abstracts 8, 23.
- Mok, Y.J., Sanchez-Salinerio, I., Stokoe, K.H. & Roesset, J. 1988. In Situ Damping Measurements by Crosshole Seismic Methods, Earthquake Engineering and Soil Dynamics II Recent Advances in Ground Motion Evaluation, *Geotechnical Specialty Publication* 20: 305–320.
- Nazarian, S. & Stokoe, K.H. 1984. In situ shear wave velocities from spectral analysis of surface wave. *Proceedings of 8th conference on earthquake engineering*, S.Franisco, 31–38.
- Ohya, S., Imai, T. & Ogura, K. 1984. The Suspension P-S velocity logging system, Annual offshore technology conference, Houston, USA.
- Park, C.B., Miller, R.D. & Xia, J. 1999. Multi-channel analysis of surface waves, *Geophysics*, 64(3): 800–808.
- Park, H.C., Kim, D.S., Bang, E.S. & Kim, J.T. 2007. Seismic Site Characterization using HWAW(Harmonic Wavelet Analysis of Waves) Method, *Proceedings of 4th International Conference on Earthquake Geotechnical Engineering*, Thessaloniki, Greece.
- Park, H.C. & Kim, D.S. 2001. Evaluation of the Dispersive Phase and Group Velocities using Harmonic Wavelet Transform, *NDT&E International*, 34(7): 457–467.
- Park, H.C. & Kim, D.S. 2004. Development of Seismic Site Characterization Method using Harmonic Wavelet Analysis of Wave (HWAW) Method, *Proceedings: International site characterization (ISC-2) on Geotechnical and Geophysical Site Characterization*, Porto, Portugal, Rotterdam, Millpress: 767–774.
- Rammah, K.I., Ismail, M.A. & Fahey, M. 2006. Development of a centrifuge seismic tomography system at UWA, *Physical Modeling In Geotechnics: ICPMG '06*: 229–234.
- Richart, F.E., Hall, J.R. & Woods, R.D. 1970. *Vibrations of soils and foundations*, Prentice-Hall, Inc.
- Santamarina, J.C. & Fratta, D. 2005. *Discrete Signals and Inverse Problems*, Wiley, 364 p.
- Stewart, J.P. Chiou, S. Bray, J.D. Graves, R.W., Somerville, P.G. & Abrahamson, N.A. 2002. Ground motion evaluation procedures for performance-based design, *Soil Dynamics and Earthquake Engineering* 22(9–12): 765–772.
- Stokoe, K.H., Joh, S. & Woods, R.D. 2004. Some contributions of in situ geophysical measurements to solving geotechnical engineering problems, *Proceedings: International site characterization (ISC-2) on Geotechnical and Geophysical Site Characterization*, Porto, Portugal, Rotterdam, Millpress: 97–132.
- Shibata, T., Kita, K. & Kobayashi, S. 1991. Performance of shaking table tests and measurement of shear wave velocities in a centrifuge, *Centrifuge 91*: 391–398.
- Troncke, J., Tweeton, D.R., Dietrich, P. & Appel, E. 2001. Improves Crosshole Radar Tomography by using Direct and Reflected Arrival Times, *Applied Geophysics* 47: 97–105.
- Tweeton, D.R. 1999. GeoTomCG, Three Dimensional Geophysical Tomography, GeoTom LLC, USA.

Determining the undrained residual strength of soils from field penetration tests with some case history studies

Y. Tsukamoto

Department of Civil Engineering, Tokyo University of Science, Japan

ABSTRACT: In shifting from conventional regulation-based design to performance-based design principles in earthquake geotechnics, the role of soil investigation technologies is expected to become more important than ever before. To satisfy the practical needs in determining design soil parameters accurately enough to employ performance-based design, purpose-specific approaches might be preferred, where the choice of field and laboratory testing is given in advance in determining particular soil parameters. In the present study, the evaluation of undrained residual strength of soils from field penetration tests is examined based on laboratory triaxial tests, laboratory calibration chamber tests and some case history studies. From the outcome of laboratory triaxial tests, the undrained residual strength is examined within the framework of a steady-state concept, and then formulated with respect to the relative density. From the outcome of laboratory chamber tests on Swedish weight sounding tests, the Swedish penetration resistance is formulated with respect to the effective overburden stress and relative density. By combining these formulations, the correlation of the undrained residual strength with Swedish penetration resistance is established. Some post-earthquake reconnaissance field investigations are conducted with Swedish weight sounding tests to provide some case history studies.

1 INTRODUCTION

The experiences from recent huge earthquakes have brought about the practical considerations on the shifts from regulation-based design to performance-based design principles in designing earth structures, accompanied with the introduction of different levels of design earthquakes. In order to evaluate whether the required seismic performance would be satisfied under design earthquakes, it would be necessary in design practice to achieve more accurate estimations of strength and deformation of earth structures. In doing so, more elaborate and innovative uses of soil investigation technologies would be allowed to enter into the framework of conventionally adopted soil investigation methodologies.

The procedures for estimating the liquefaction resistance and undrained residual strength of soils have been examined extensively, in evaluating the possibility of occurrence of soil liquefaction and the stability of earth structures against flow deformation during earthquakes. The procedure for estimating the liquefaction resistance of soils has been achieved based on laboratory cyclic triaxial tests on frozen intact samples and also on field penetration tests including standard penetration tests (SPT), cone penetration tests (CPT) as well as velocity logging tests. The procedure for estimating the undrained residual strength of soils has also been examined based on laboratory triaxial tests and also on case history studies involving field

penetration tests, (Seed 1987; Seed & Harder 1990; Ishihara et al., 1990; Idriss & Boulanger 2007; and others).

One of the recent issues discussed in detail was associated with the inhomogeneity of soil layers. Particularly in the presence of a soil layer with significantly lower permeability overlying the liquefiable layer, there would be situations where the upward pore water seepage during earthquakes could lead to localized loosening of the liquefiable soil. Under these situations, it would be reasonable to assume that the undrained shear strength mobilized in the field can be much lower than that observed in laboratory tests, (Idriss & Boulanger 2007). Such a phenomenon was termed as 'water film generation' and 'void redistribution mechanisms', (Kokusho 2000; Kulasingam et al., 2004; Malvick et al., 2006; and others).

The effects of soil density, confining stress and grain composition of soils on the undrained shear strength of saturated sands have been examined extensively by using laboratory triaxial tests within the framework of a steady-state concept. On the other hand, the characterization of soil properties using field penetration tests has also recently evolved considerably, where the use of calibration chamber tests allowed the effects of state parameters such as soil density and overburden stress as well as grain composition of soils on the field penetration resistance to be examined in detail. In the present study, by combining such independent studies based on the laboratory triaxial

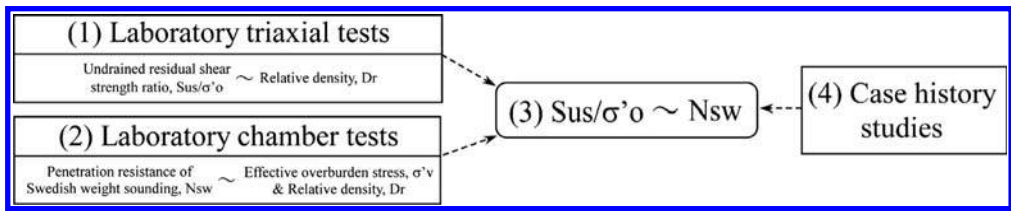


Figure 1. General layout of the present study.

		Level of shear strain, γ (%)			
		0.001	0.01	0.1	1
Type of field tests	Elastic	Velocity logging			
	Elastic-plastic	Pressuremeter			
	Plastic	Penetration tests (SPT, CPT, Swedish)			
Topics		Go	$G - \gamma$ relation	Liquefaction strength & residual strength	

Figure 2. Levels of shear strain involved in field tests.

tests on saturated silty sands and calibration chamber tests on Swedish weight sounding tests, the correlation of the undrained residual strength of silty sands with the field penetration resistance is examined in detail. The framework of the present study is illustrated as shown in Fig. 1. The advantages of adopting such a direct correlation are also discussed in detail. The levels of shear strain associated with field tests and derived soil parameters are often discussed as shown in Fig. 2. The levels of shear strain expected to be mobilized during field penetration tests are shown to be large enough to be comparable to those at residual states where the residual strength is mobilized.

2 UNDRAINED RESIDUAL STRENGTH FROM LABORATORY TRIAXIAL TESTS

2.1 Background

The undrained behaviour of saturated cohesionless soils has been investigated extensively within the framework of a steady state concept since 1970s, (Castro 1975; Castro & Poulos 1977; Finn & Byrne 1976; Poulos 1981; and others). Subsequent studies followed suit and examined the conditions of the steady state and quasi-steady state to occur on Toyoura sand, (Verdugo 1992; Ishihara 1993; Verdugo & Ishihara 1996; Kato et al., 2001; and others). The effects of anisotropic consolidation on subsequent undrained behaviour were first addressed by Chern (1985) and Vaid & Chern (1983, 1985), and discussed that instead of the effective mean principal stress, the effective major principal stress is a primary parameter in quantifying the effects of confinement on undrained

behaviour of sand. In what follows, the results of laboratory undrained triaxial tests are examined and interpreted in the framework of a steady-state concept.

2.2 Typical patterns of deformation and definition of flow condition

The typical patterns of response of anisotropically consolidated samples against undrained compression are schematically illustrated in Fig. 3.

In Figs. 3(a) and 3(b), the effective stress paths in terms of the effective mean principal stress, $p' = (\sigma'_1 + 2\sigma'_3)/3$, against the shear stress, $q = \sigma'_1 - \sigma'_3$ and stress—strain relations are shown. The specimens are isotropically consolidated at point A, and the points B, B' and B'' indicate that the specimens are anisotropically consolidated to a certain K_c -value, where $K_c = \sigma'_3/\sigma'_1$. Then the specimen is dense, it shows dilative behaviour along the points B, C and D, where the point C corresponds to the state of phase transformation, and the point D is called the steady state. The undrained residual strength is defined as the shear stress mobilised at the state of phase transformation. This dilative behaviour as a whole is categorised as “no flow”. When the specimen is loose, it shows contractive behaviour along the points B', C' and D', where the points C' and D' correspond to the quasi-steady state and steady state. In case of loose sand, the quasi-steady state and steady state coincides, and the undrained residual strength is defined at this largely deformed state. This contractive behaviour as a whole is categorised as “flow”. When the specimen is medium dense, it shows intermediate behaviour along the quasi-steady state C' and the steady state D'. Since the phase transformation takes place from contractive to dilative behaviour at point C', at which the shear stress is smaller than that at point D', the undrained residual strength is defined at the quasi-steady state C'. This intermediate behaviour is categorised as “flow with limited deformation”.

In Fig. 3(c), the relations between the void ratio, e , and the effective mean principal stress, p' are shown. In Fig. 3(d), the relations between the void ratio, e , and the axial strain, ϵ_a , are shown. It is clearly shown in Fig. 3(c) that when the specimen is dense, initially located at point B below the initial dividing line (IDL),

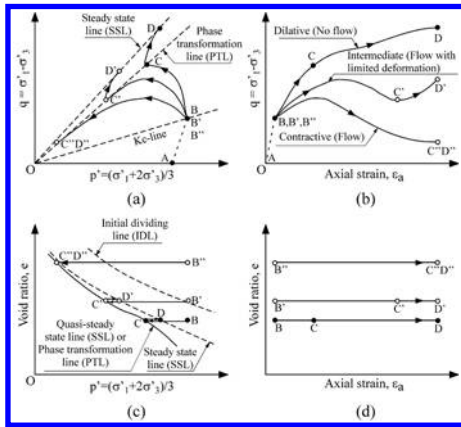


Figure 3. Schematic diagram showing typical behaviour during undrained compression.

it shows dilative behaviour. On the other hand, when the specimen is loose, initially located at point B'' above IDL, it shows contractive behaviour. When the specimen is medium dense, initially located at point B', it shows intermediate behaviour.

2.3 Characteristic lines

The steady state line (SSL) is known to be a unique line, which is found in the plot of void ratio against the effective mean principal stress at which the sand undergoes large deformation under constant void ratio, effective confining stress and shear stress, (Fig. 3). From a number of data of undrained compression tests on Toyoura sand, the plots of e against p'_{ss} are produced in Fig. 4(a). Herein, the steady state line obtained in the previous study is also plotted, (Ishihara 1993). Also found in Fig. 4(a) is another line termed as a quasi-steady state line (QSSL), at which the minimum strength is mobilised at medium to large shear strain. When the void ratio is significantly large, the steady state line and quasi-steady state line become coincident. However, at a medium to greater density, the quasi-steady state tends to occur at lower effective confining stress than the steady state, leading to the quasi-steady state line located lower than the steady state line in the $e-p'$ plot. In Fig. 4(a), the quasi-steady state line tends to deviate from the steady state line approximately at $p'_{ss} = 100$ kPa. The same set of data is rearranged and the plots of e against the effective major principal stress, σ'_{1ss} , at steady state and quasi-steady state are produced as shown in Fig. 4(b). The steady state line and quasi-steady state line can also be determined equally well in this relation.

The plots of e against p'_s at the state of phase transformation are shown in Fig. 5(a). Herein, the values of p'_s are determined at a point where the effective

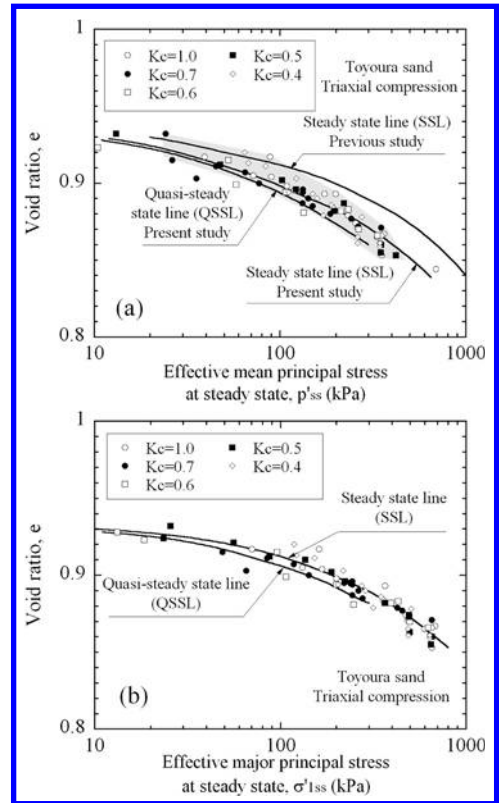


Figure 4. Steady state lines in triaxial compression (a) $e-p'$ (b) $e-\sigma'_1$.

stress path bends from leftwards to rightwards on the phase transformation line (PTL), (Fig. 3). In Fig. 5(a), by looking at the three series of data on $K_c = 1.0$ with $p'_c = 49$ kPa to 294 kPa, the correlations can be established between e and p'_s . These correlations represented by the four lines in Fig. 5(a) tend to converge into a single main line specifying the quasi-steady state or steady state line. The same set of the test data shown in Fig. 5(a) is rearranged and the plots of e against σ'_{1s} are produced as shown in Fig. 5(b). It may be possible to draw a line of phase transformation through a cluster of data points with an equal level of consistency.

The steady state line, quasi-steady state line and phase transformation lines defined above refer to the relations between the void ratio and effective confining stress for sand, which is deformed largely under undrained triaxial compression. All of these characteristic lines do not refer to the initial state prior to undrained compression. It has however been customary in soil mechanics to express the strength and deformation characteristics of soils in terms of the parameters indicating the initial state at consolidation. The characteristic line proposed in this context is what

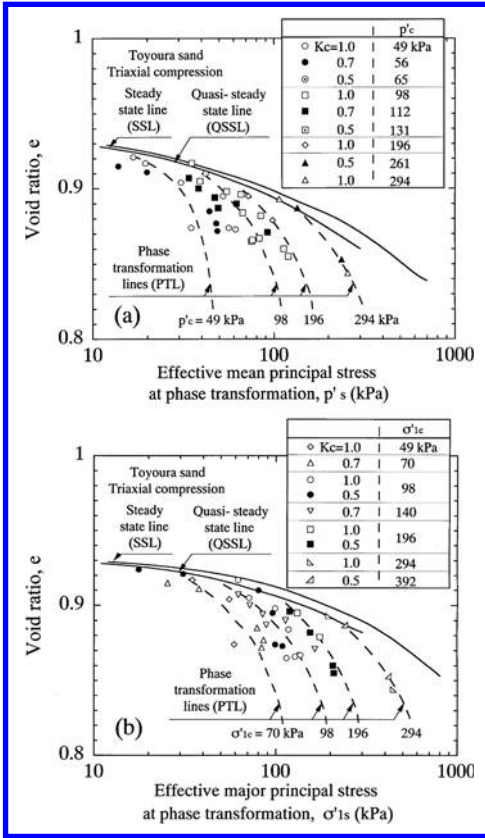


Figure 5. Phase transformation lines in triaxial compression (a) $e - p'$ (b) $e - \sigma'_1$.

is called an “initial dividing line”, (Ishihara 1993). For loose sand exhibiting contractive behaviour, the initial values of e and p'_c at consolidation are plotted with open symbols in Fig. 6(a). For medium dense to dense sand exhibiting dilative behaviour, the data are plotted with dark symbols. It is then possible to draw a line in the $e - p'_c$ plot giving the border between the clusters of open symbols and dark symbols as indicated in Fig. 6(a). The same set of the test data shown in Fig. 6(a) is rearranged and the plots of e against σ'_{1s} at consolidation are produced as shown in Fig. 6(b). It is also found possible to draw an initial dividing line with an equal level of consistency in this relation.

2.4 Undrained residual strength

The initial state ratio r_c serves as a good parameter in characterizing the response of the excess pore water pressure during undrained compression of saturated isotropically consolidated sand, (Ishihara 1993). In the present study, since the importance of the effective major stress σ'_1 in indicating confinement of soils

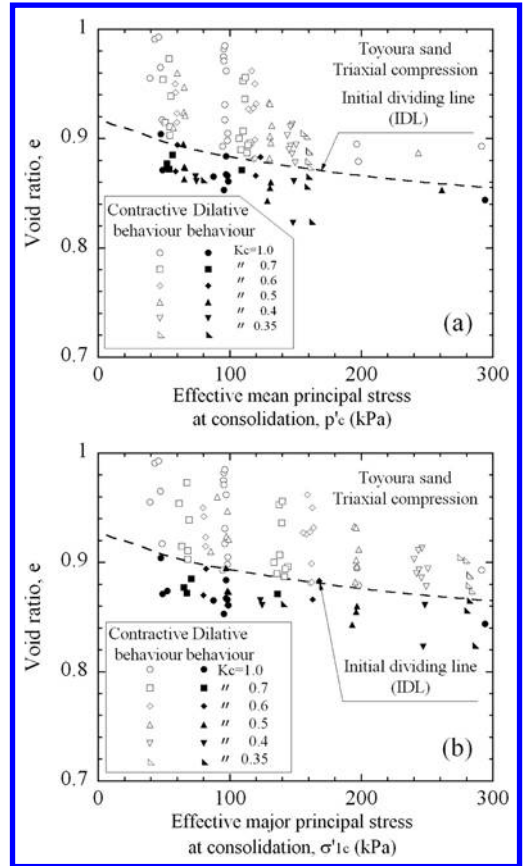


Figure 6. Initial dividing lines in triaxial compression (a) $e - p'$ (b) $e - \sigma'_1$.

is examined, the new parameter r'_c is introduced as follows, (Tsukamoto et al., 2004a),

$$r_c = \frac{p'_c}{p'_s} = \frac{1 + 2K_c}{1 + 2K_s} r'_c \quad (\text{TC}) \quad (1)$$

$$r'_c = \frac{\sigma'_{1c}}{\sigma'_{1s}} = \frac{\sigma'_{ac}}{\sigma'_{as}} \quad (\text{TC}) \quad (2)$$

$$r_c = \frac{p'_c}{p'_s} = \frac{2 + K_c}{2 + K_s} r'_c \quad (\text{TE}) \quad (3)$$

$$r'_c = \frac{\sigma'_{1c}}{\sigma'_{1s}} = \frac{\sigma'_{cc}}{\sigma'_{cs}} \quad (\text{TE}) \quad (4)$$

where $K_s = (3 - M_s)/(3 + 2M_s) = (1 - \sin \phi_s)/(1 + \sin \phi_s)$ for triaxial compression (TC), and $K_s = (3 - 2M_s)/(3 + M_s) = (1 - \sin \phi_s)/(1 + \sin \phi_s)$ for triaxial extension (TE), $M_s = q_s/p'_s$ and ϕ_s is the internal friction angle at states of phase transformation.

In Figs. 7(a) and (b), the plots of r_c against K_c and the plots of r'_c against K_c are shown for Toyoura sand, where the data points are divided into the contractive

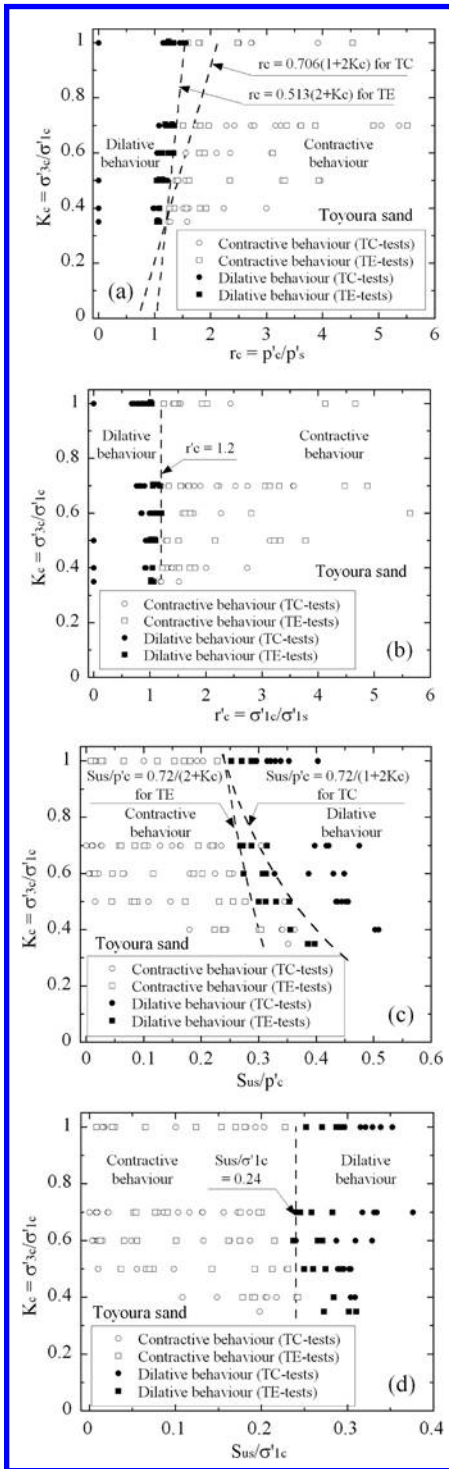


Figure 7. r_c , r'_c , S_{us}/p'_c and $S_{us}/\sigma'_{1c} - K_c$ relations (Toyoura sand) (a) $r_c - K_c$ (b) $r'_c - K_c$ (c) $S_{us}/p'_c - K_c$ (d) $S_{us}/\sigma'_{1c} - K_c$.

and dilative behaviour. It is found in Fig. 7(b) that the parameter r'_c uniquely divides the two behaviours at $r'_c = 1.2$, independent of the shearing mode of TC and TE and also of the K_c value. Assuming the constant value of r'_c in Eqs. (1) and (3), the border in the $r_c - K_c$ plots is given as a function of K_c .

With respect to the undrained residual strength ratio S_{us}/p'_c introduced by Ishihara (1993), the new undrained residual strength ratio S_{us}/σ'_{1c} is also defined in the present study as follows,

$$\frac{S_{us}}{p'_c} = \frac{q_s \cos \phi_s}{2} \frac{1}{p'_c} = \frac{M_s \cos \phi_s}{2} \frac{1}{r_c} \quad (\text{TC \& TE}) \quad (5)$$

$$\frac{S_{us}}{\sigma'_{1c}} = \frac{q_s \cos \phi_s}{2} \frac{1}{\sigma'_{1c}} = \frac{3 M_s \cos \phi_s}{2(3 + 2M_s)} \frac{1}{r'_c} \quad (\text{TC}) \quad (6)$$

$$\frac{S_{us}}{\sigma'_{1c}} = \frac{q_s \cos \phi_s}{2} \frac{1}{\sigma'_{1c}} = \frac{(3 + M_s) M_s \cos \phi_s}{2(3 + 2M_s)} \frac{1}{r'_c} \quad (\text{TE}) \quad (7)$$

In Figs. 7(c) and (d), the plots of S_{us}/p'_c and K_c and the plots of S_{us}/σ'_{1c} and K_c are shown for Toyoura sand, where the data points are divided into the contractive and dilative behaviour. Since the value of M_s is a material constant and the value of r'_c is also found to be constant, the undrained residual strength ratio S_{us}/σ'_{1c} can also be determined as a constant from Eqs. (6) and (7). The constant threshold value of S_{us}/σ'_{1c} is shown in Fig. 7(d), which forms the border between contractive and dilative behaviour. The borders given in the $S_{us}/p'_c - K_c$ relation are different between TC and TE, as shown in Figs. 7(c). The threshold value of S_{us}/σ'_{1c} dividing the two behaviours effectively corresponds to the largest undrained residual strength ratio under flow deformation.

Since the value of S_{us}/σ'_{1c} giving the border was found to be uniquely determined regardless of the K_c -value, the values of S_{us}/σ'_{1c} are plotted against the void ratio at consolidation, as shown in Fig. 8(a). The same sets of data for the other silty sands are shown in Figs. 8(b) to (d). The relations for TC and TE are found to draw different curves. By drawing the intermediate curves, the threshold values of the relative density D_r , at which the two behaviours can be separated, are shown in Figs. 8(a) to (d). The threshold value for Toyoura clean sand is found to be $D_r = 30\%$, and those for the other silty sands with non-plastic fines are found to be about $D_r = 60$ to 70% . It would imply that the ranges of the initial relative density leading to flow deformation are different among the soils, though the largest value of the undrained residual strength ratio under flow deformation is similar to each other and stays at about 0.24 to 0.26. Based on this finding, in examining the flow occurrence, it would be more preferable to determine directly the undrained residual strength of soils rather than to determine the relative density of soils.

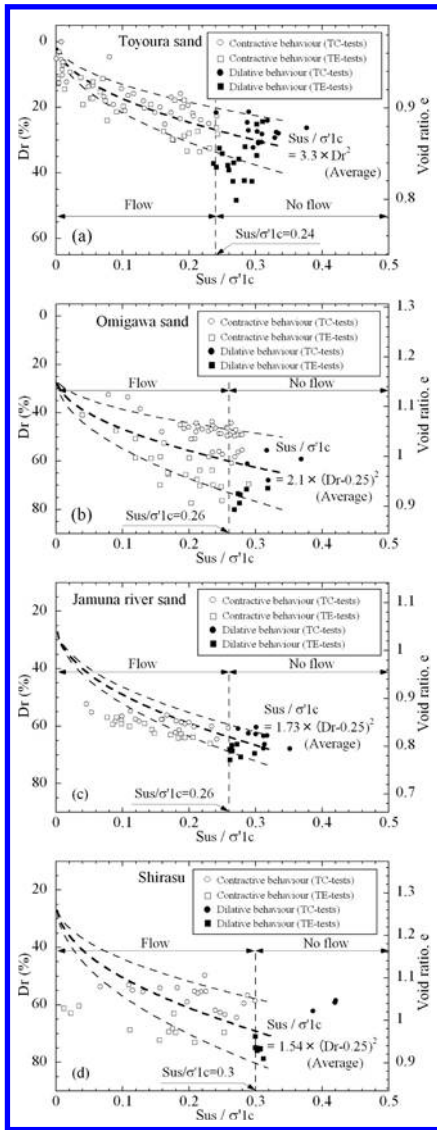


Figure 8. $S_{us}/\sigma'_{1c} - D_r$ relations (a) Toyoura sand (b) Omigawa sand (c) Jamuna river sand (d) Shirasu.

2.5 Effects of relative density

The primary findings from the outcome of the laboratory triaxial tests as described above are summarized as follows.

1. The border determining the conditions of “flow” and “no flow” can be given by a unique value of S_{us}/σ'_{1c} regardless of K_c and TC/TE modes.
2. This threshold value of S_{us}/σ'_{1c} takes a value ranging from 0.24 to 0.26 for clean sand and ordinary silty sands.

It then follows that based on the plots of S_{us}/σ'_{1c} against D_r for the four different soils shown in Fig. 8, the relation between S_{us}/σ'_{1c} and D_r are formulated as follows,

$$\frac{S_{us}}{\sigma'_{1c}} = A_{us} (D_r - D_{ro})^2 \quad (8)$$

where D_{ro} is the initial offset of the relative density. It is found in Fig. 8(a) for Toyoura clean sand that there would be no offset of the relative density in this relation, and it can be determined as $D_{ro} = 0$. On the other hand, there needs to be some offset in this relation for silty sands, as shown in Figs. 8(b) to (d). The value of $D_{ro} = 25\%$ is adopted for all the silty sands examined in the present study. Because of its compressibility, the silty sand is found to show some value of D_{ro} . The value of D_{ro} is in effect controlled by the volume compression during consolidation. For example, the void ratio changes of Omigawa silty sand during anisotropic triaxial consolidation are shown in Fig. 9. It is found that there is a sufficient amount of volume compression during consolidation. This offset of the relative density, D_{ro} , serves as a parameter which defines the lowest value of the relative density attainable under the presence of confining stress. The definition of D_{ro} is schematically illustrated in Fig. 10.

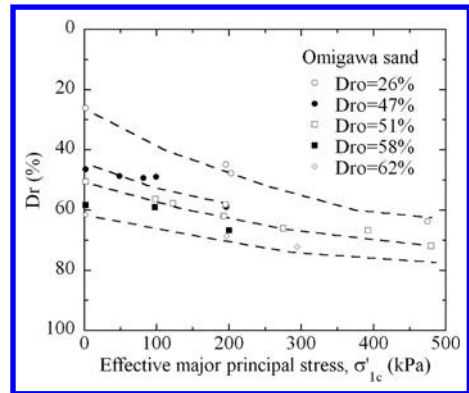


Figure 9. Consolidation lines (Omigawa sand).

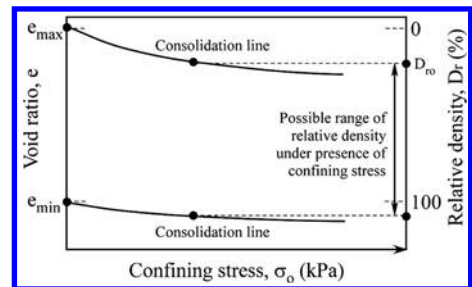


Figure 10. Schematic illustration on offset of relative density due to confining stress increase.

3 SWEDISH PENETRATION RESISTANCE FROM LABORATORY CHAMBER TESTS

3.1 Swedish weight sounding

Swedish weight sounding test has commonly been used for field inspections on road and railway embankments and residential house constructions, and has also been frequently used for earthquake reconnaissance field investigations. The testing procedure consists of static and rotational penetrations. In the first phase of static penetration, the depth of rod penetration is measured while the screw-shaped point weighing 5 kg is statically penetrated into the ground by gradually putting the weights of 2×10 kg and 3×25 kg to achieve the total weight of 100 kg, (Fig. 11). The value of W_{sw} corresponds to the current sum of weights under static penetration. In the second phase of rotational penetration, the rod is rotated by using the horizontal bar fixed at its top while holding the total weight of 100 kg. The number of half a turn necessary to penetrate the rod through 25 cm is counted and converted to the value of N_{sw} (ht/m).

3.2 Calibration chamber

The calibration pressure chamber is used in the present study, which is 78.7 cm in diameter and 92.4 cm in depth, as shown in Fig. 12. The vertical stress and horizontal stress can be applied independently to a soil sample in the chamber by inflating the rubber membranes. The dry soil sample was poured into the chamber by the method of air pluviation and tamping, and various values of the relative density, D_r , were achieved. All the soil samples were normally

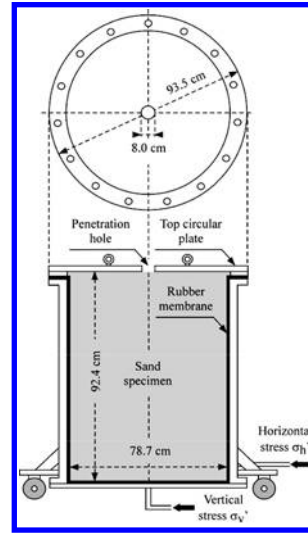


Figure 12. Calibration chamber.

consolidated with the earth pressure coefficient K_0 , ranging between 0.2 and 0.3. A series of Swedish weight sounding tests were conducted under various values of the relative density, D_r , and vertical and horizontal stresses, σ'_v and σ'_h .

3.3 Effects of relative density

The field penetration resistance is known to be affected mainly by soil density, effective overburden stress and grain composition of soils among others, (Meyerhof 1957; Liao and Whitman 1986; Skempton 1986; Ishihara 1993 & 1996; Cubrinovski and Ishihara 1999; Tsukamoto et al., 2004b; and others). In the present study, the effects of soil density and effective overburden stress on the N_{sw} -value are formulated by using the same procedure as described by Tsukamoto et al. (2004b).

Since the static penetration resistance represented by the value of W_{sw} has some influence on the rotational penetration resistance, N_{sw} , it would be reasonable to give an offset parameter with respect to the value of N_{sw} , which is equivalent to the static resistance $W_{sw} = 100$ kg. The converted overall resistance N'_{sw} is then introduced by defining this offset as α_{sw} as follows,

$$N'_{sw} = N_{sw} + \alpha_{sw} \quad (\alpha_{sw} = 40) \quad (9)$$

This is assumed to hold valid under the phase of rotational penetration, where N_{sw} is larger than 1. In the phase of static penetration, N'_{sw} is assumed to take a value less than or equal to α_{sw} in a manner that $N'_{sw} = \alpha_{sw} W_{sw}$ (kg)/100. For example, it would be $N'_{sw} = 20$ at $W_{sw} = 50$ kg.

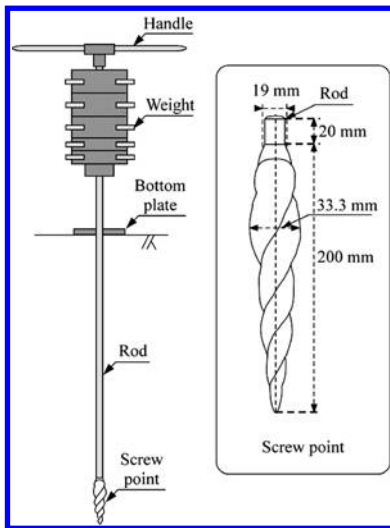


Figure 11. Equipment for Swedish weight sounding tests.

The value of N'_{sw} may then be normalized with respect to the vertical stress, and the normalized parameter of N'_{sw1} may therefore be defined as follows,

$$N'_{sw1} = N'_{sw} \sqrt{\frac{\sigma'_o}{\sigma'_v}} = N'_{sw} \sqrt{\frac{98}{\sigma'_v}} \quad (10)$$

where σ'_o is taken as 98 kPa and σ'_v is in kPa. The above equation (10) was confirmed by examining the linear relation between N'_{sw} and $\sqrt{\sigma'_v}$, (Tsukamoto et al., 2004b).

From the viewpoint of establishing the relation between N_{sw} and the undrained shear strength ratio as formulated in the equation (8), it would be preferable to normalize the value of N'_{sw1} in a manner similar to the equation (8). The plots of N'_{sw1} against D_r are produced for the four soils as shown in Fig. 13, and the following relation is also found to work well,

$$N'_{sw1} = A_{sw} (D_r - D_{r0})^2 \quad (11)$$

where the same values of D_{r0} are assumed in the equations (8) and (11). It is to note here that the chamber size effects are considered negligible and are not taken into account.

4 DIRECT CORRELATION OF UNDRAINED RESIDUAL STRENGTH WITH SWEDISH PENETRATION RESISTANCE

Since the initial effective vertical stress, σ'_{vo} , is nearly equivalent to σ'_{ic} in usual circumstances such normally consolidated sands, it would be reasonable to assume that the undrained shear strength ratio, S_{us}/σ'_{ic} can be replaced by S_{us}/σ'_{vo} . In addition, the undrained shear strength ratio S_{us}/σ'_{ic} (= S_{us}/σ'_{vo}) and Swedish penetration resistance N_{sw} were found to be formulated with respect to the relative density D_r in the same manner, as seen in the equations (8) and (11). Therefore,

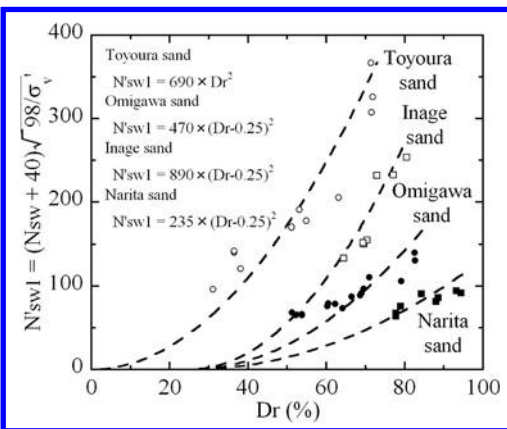


Figure 13. $N'_{sw1} - D_r$ relations.

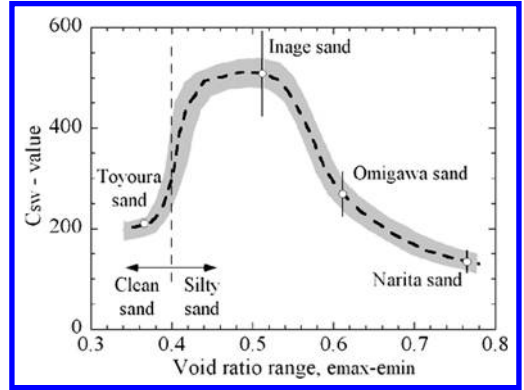


Figure 14. $C_{sw} - e_{max} - e_{min}$ relation.

the correlations of S_{us}/σ'_{vo} with N_{sw} can be derived as follows,

$$\frac{S_{us}}{\sigma'_{vo}} = \frac{N'_{sw1}}{C_{sw}} = \frac{N_{sw} + 40}{C_{sw}} \sqrt{\frac{98}{\sigma'_{vo}}} \quad (12)$$

where C_{sw} is the parameter uniquely determined for any given soil, and $C_{sw} = A_{sw}/A_{us}$. Since the state parameters influencing the soil behaviour, such as soil density and overburden stress, are all incorporated in the formulation, the value of C_{sw} would only be dependent upon the grain composition of soils.

One of the parameters that represent the grain composition of silty sands was shown to be the void ratio range, $e_{max} - e_{min}$, (Miura et al., 1997; Cubrinovski and Ishihara 1999, 2000a & 2000b). The values of C_{sw} inferred from the present study are therefore plotted against the void ratio range, as shown in Fig. 14. The void ratio range for clean sand is generally lower than 0.4, and it becomes larger as the fines content increases in the soil. The largest value of C_{sw} is found when the soil contains some fines, implying that the soil containing some fines exhibits the lowest undrained residual strength when the same value of N_{sw} is observed at a given depth.

5 SOME CASE HISTORY STUDIES

The post-earthquake field reconnaissance investigations using Swedish weight sounding tests were carried out at three locations during the recent earthquakes in Japan.

5.1 Tsukidate landslide

The rapid landslide occurred at Tsukidate, Miyagi, Japan, on a gentle slope consisting of reclaimed soil deposits for agricultural purposes, during Miyagiken-oki Earthquake on May 26, 2003, (Uzuoka et al., 2005).

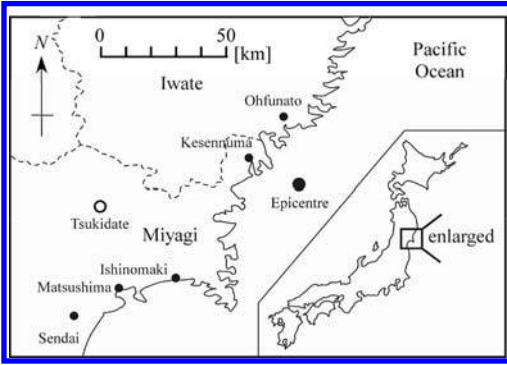


Figure 15. Location of site of landslide at Tsukidate.

The location of Tsukidate is shown in Fig. 15. The loose reclaimed soil deposits with 40 metres wide, 80 metres long and 5 metres deep were collapsed and flowed downstream on a gentle slope with 7 degrees inclination, as shown in Figs. 16(a) and (b). A series of Swedish weight sounding tests were carried out at this site, and the results of the test conducted at the original intact soil deposit close to the top portion of the collapsed area are indicated in Fig. 17. The soil deposits were from pyroclastic origin with pumice tuff, and include 36% of fines less than 0.075 mm with the mean diameter $D_{50} = 0.25$ mm. The undrained shear strength ratio, S_{us}/σ'_{vo} , of soils mobilized at this site is estimated to be about 0.12, based on the following simple expression, (Ishihara et al., 1990),

$$\frac{S_{us}}{\sigma'_{vo}} \approx \frac{S_{us}}{\gamma_t H} = \cos \alpha \sin \alpha \quad (13)$$

where H and α are the depth and angle of subsurface sliding surface. The value of S_{us}/σ'_{vo} thus estimated is also confirmed from the results of laboratory undrained triaxial compression tests conducted on the soil sample retrieved from this site and field density measurement.

5.2 Tanno flow failure

The fluidization and subsidence of gently sloped farming fields took place in Tanno area of Kitami in Hokkaido during Tokachi-oki Earthquake on September 26, 2003. The location of the site is indicated in Fig. 18. The farming field of 35 metres wide and 150 metres long subsided due to the eruption of fluidized subsurface deposits through a couple of ejection holes located downstream portions of the subsided area, as shown in Photos 1 and 2. It was found from the interview of the local people that the subsided area had been reclaimed with the deposits of local volcanic soil for agricultural purposes. The plan view and cross section of the site are shown in Fig. 19. It was found from the

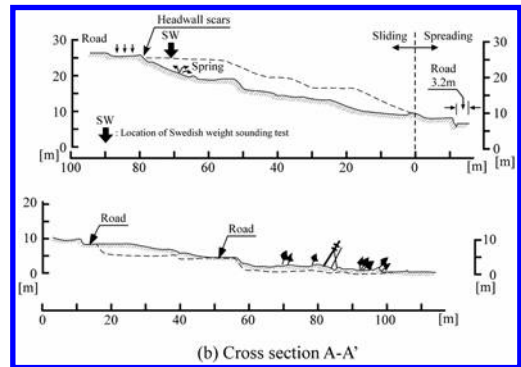
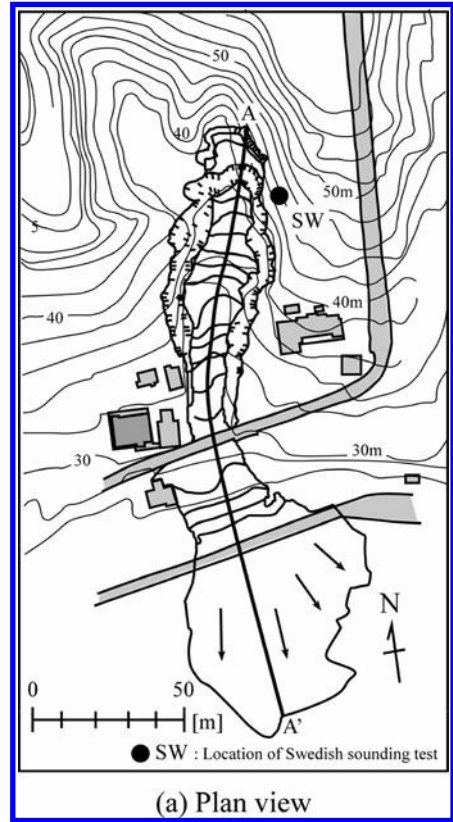


Figure 16. Post-earthquake plan view and cross section of site of landslide at Tsukidate (a) plan view (b) cross section.

site survey that the bottom surface of the fluidized subsurface deposits forms a round basin in a transverse cross section, and the fluidized deposits flowed down swinging leftwards and rightwards along the basin until they were erupted at the downstream portions of the subsided area. A series of Swedish weight sounding tests were carried out at this site, and the results of the test conducted at the original intact soil

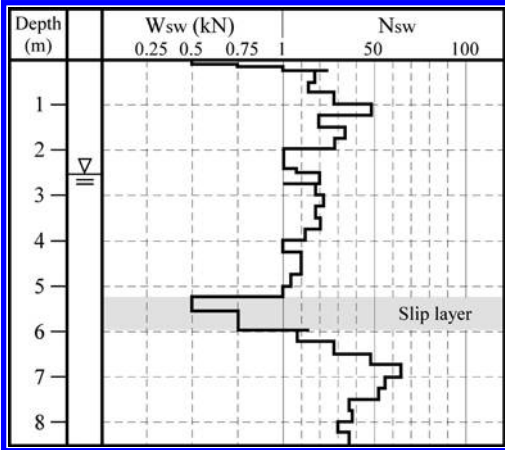


Figure 17. Results of Swedish weight sounding test at Tsukidate.



Photo 1. Looking towards upstream (Tanno).



Photo 2. Looking towards downstream (Tanno).

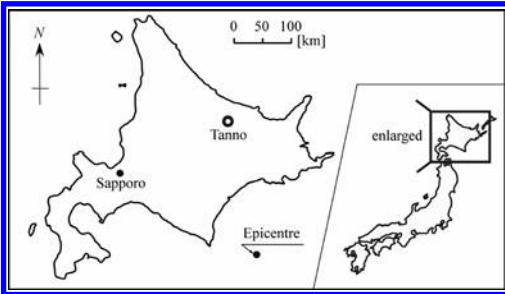


Figure 18. Location of site of landslide at Tanno.

deposit close to the top portion of the collapsed area are indicated in Fig. 20. The soil deposits were from volcanic origin, and include 28% of fines less than 0.075 mm with $D_{50} = 0.19$ mm. The undrained shear strength ratio, S_{us}/σ'_{vo} , of soils mobilized at this site inferred from the equation (13) is estimated to be as low as 0.05. The value of S_{us}/σ'_{vo} thus estimated is also confirmed from the results of laboratory undrained tri-axial compression tests conducted on the soil sample retrieved from this site and field density measurement.

5.3 Liquefaction and subsidence at Kashiwazaki

The soil liquefaction and associated subsidence and ground deformation took place at one of the regional sewage centre located near the mouth of Sabaishi river in Kashiwazaki, Niigata, during Niigataken-chuetsu-oki Earthquake on July 16, 2007. A vast amount of sand boils were observed around the buildings, and the almost entire area within the centre subsided down to about 35 cm, as shown in Photos 3 and 4. The cracks and ground deformation were also observed around the

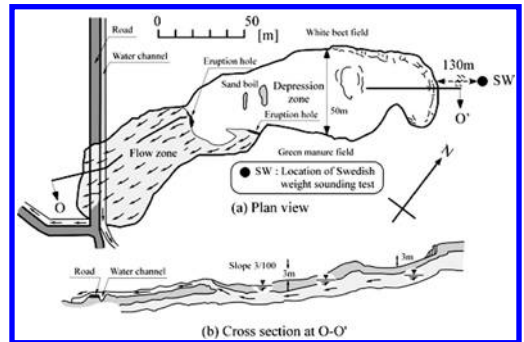


Figure 19. Post-earthquake plan view and cross section of site of landslide at Tanno (a) plan view (b) cross section.

buildings, as shown in Photos 5 and 6. The locations at which these photos were taken are indicated in Fig. 21. The soil deposits around the buildings are silty sands containing 10% non-plastic fines less than 0.075 mm. A couple of Swedish weight sounding tests were conducted at the locations indicated in Fig. 21, and the results are indicated in Fig. 22. The ground water level

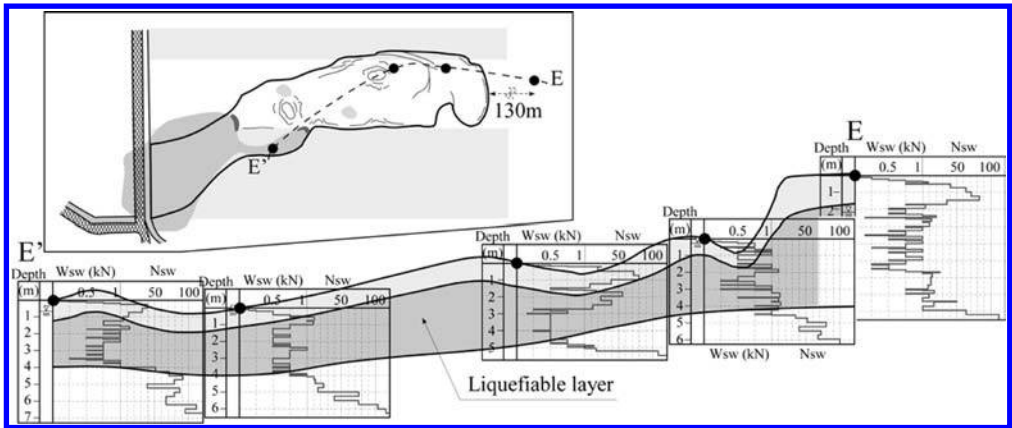


Figure 20. Results of Swedish weight sounding test at Tanno.



Photo 3. Subsidence (Kashiwazaki).



Photo 5. Crack and ground deformation (Kashiwazaki).



Photo 4. Subsidence (Kashiwazaki).

was found to be located 2 metres below the ground surface, and the loose deposits were found to prevail down to 6–7 metres below the ground surface. This field investigation would provide a good case history

study on the liquefaction-induced subsidence at level grounds, though it would provide little on the evaluation of undrained residual strength, which is examined in the present study.

5.4 Swedish penetration resistance

Based on the data derived from the case history studies as described above, the values of S_{us}/σ'_{vo} and N'_{sw1} are examined, and the values of C_{sw} are then inferred as the ratio of N'_{sw1} to S_{us}/σ'_{vo} . Since the parameter C_{sw} is considered to be only dependent on the grain composition of soils, the values of C_{sw} thus estimated are replotted on the diagram correlating the parameter C_{sw} with the void ratio range, $e_{max}-e_{min}$, as shown in Fig. 23.

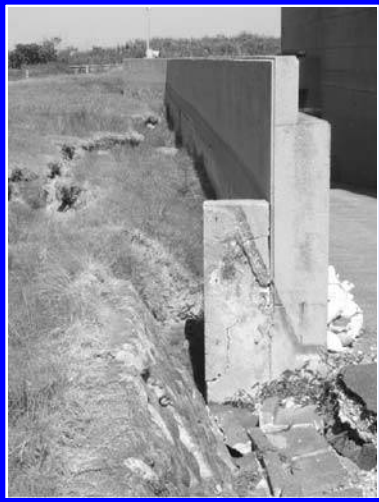


Photo 6. Crack and ground deformation (Kashiwazaki).

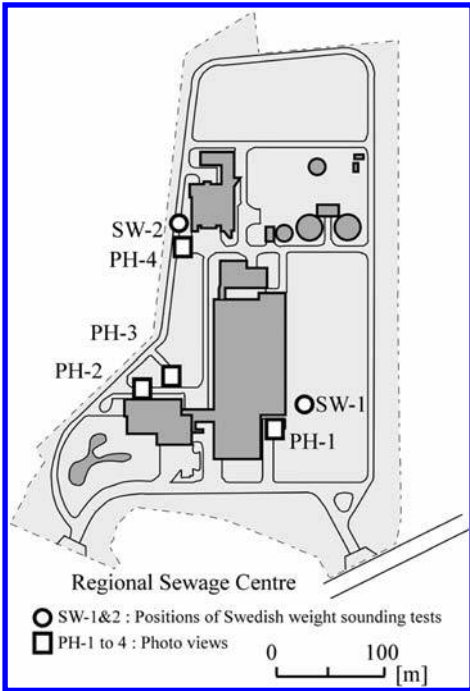


Figure 21. Location of site of subsidence and flow deformation at Kashiwazaki regional sewage center.

The plot for the site of Tsukidate is located within the range of its correlation derived from the laboratory study conducted in the present study. However, the plot for the site of Tanno is out of range probably because of its extremely low value of undrained shear

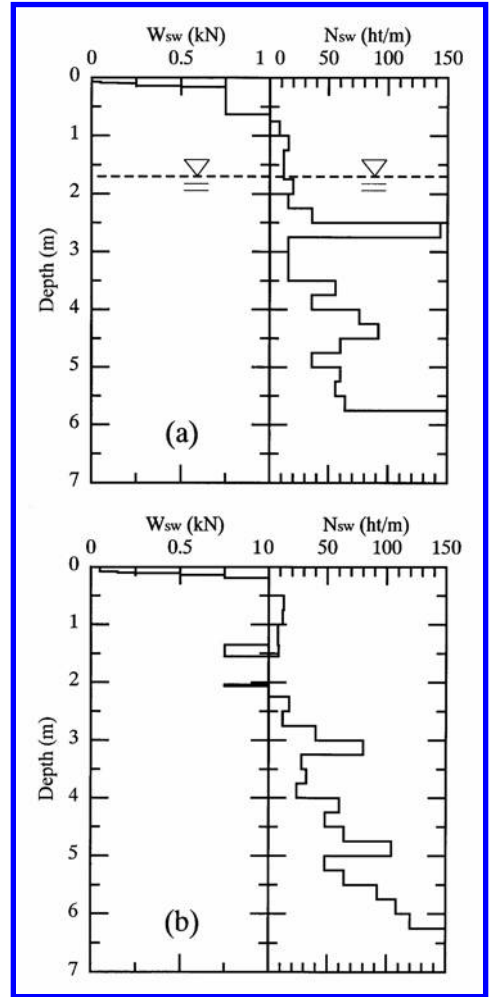


Figure 22. Results of Swedish weight sounding test at Kashiwazaki.

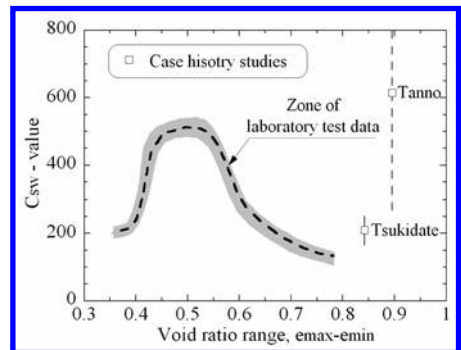


Figure 23. $C_{sw}-e_{max}-e_{min}$ relation from case history studies.

strength. It is to note here that this extremely low value was derived based on the average slope angle using the equation (13). However, as described above, the fluidized deposits seem to have flowed down swinging leftwards and rightwards along the basin from bottom to top portions, indicating that the local failure slope angle might be greater than the average angle, due to such basin effects.

6 CONCLUSIONS

The evaluation of the undrained residual strength of silty sands from Swedish weight sounding tests was examined. Based on the outcome of the laboratory triaxial tests, the undrained residual strength ratio was defined with respect to the effective major principal stress, and was formulated with respect to the relative density. Based on the outcome of the laboratory calibration chamber tests, the Swedish penetration resistance was formulated with respect to the effective overburden stress and relative density. By combining these formulations, the correlation of the undrained residual strength with Swedish penetration resistance was established. Based on some case history studies on the post-earthquake reconnaissance field investigations using Swedish weight sounding tests, the validity of this correlation was examined and found to work well.

ACKNOWLEDGEMENTS

The author would like to express his sincere appreciation to Professor K. Ishihara for his guidance and useful comments on the present study, and to Dr. S. Okada, Professor S. Yamashita and Professor A. Onoue for providing him with the opportunity to conduct field tests at Tsukidate, Tanno and Kashiwazaki. Thanks are also extended to the past and current students for their help in conducting laboratory tests and field tests described in the present study.

REFERENCES

Castro, G. 1975. Liquefaction and cyclic mobility of saturated sand. *Journal of Geotechnical Engineering Division* 101, GT6, ASCE: 551–569.

Castro, G. & Poulos, S.J. 1977. Factors affecting liquefaction and cyclic mobility. *Journal of Geotechnical Engineering Division* 103, GT6, ASCE: 501–516.

Chern, J.C. 1985. *Undrained response of saturated sands with emphasis on liquefaction and cyclic mobility*. Ph.D. thesis, University of British Columbia.

Cubrinovski, M. & Ishihara, K. 1999. Empirical correlation between SPT N-value and relative density for sandy soils. *Soils and Foundations* 39(5): 61–71.

Cubrinovski, M. & Ishihara, K. 2000a. Flow potential of sandy soils with different compositions. *Soils and Foundations* 40(4): 103–119.

Cubrinovski, M. & Ishihara, K. 2000b. Maximum and minimum void ratio characteristics of sands. *Soils and Foundations* 42(6): 65–78.

Finn, W.D.L. & Byrne, P.M. 1976. Liquefaction potential of mine tailings dams. *Proceedings of 12th International Conference on Large Dams*, Mexico City, Vol. 1: 153–177.

Idriss, I.M. & Boulanger, R.W. 2007. SPT- and CPT-based relationships for the residual shear strength of liquefied soils. *Earthquake Geotechnical Engineering*, Pitilakis, K.D. (ed.), Springer: 1–22.

Ishihara, K., Yasuda, S. & Yoshida, Y. 1990. Liquefaction-induced flow failure of embankments and residual strength of silty sands. *Soils and Foundations* 30(3): 69–80.

Ishihara, K. 1993. Liquefaction and flow failure during earthquakes. *Geotechnique* 43(3): 351–415.

Ishihara, K. 1996. *Soil behaviour in earthquake geotechnics*. Oxford Science Publications: 287–288.

Kato, S., Ishihara, K. & Towhata, I. 2001. Undrained shear characteristics of saturated sand under anisotropic consolidation. *Soils and Foundations* 41(1): 1–11.

Kokusho, T. 2000. Mechanism for water film generation and lateral flow in liquefied sand layer. *Soils and Foundations* 40(5): 99–111.

Kulasingam, R., Malvick, E.J., Boulanger, R.W. & Kutter, B.L. 2004. Strength loss and localization at silt interlayers in slopes of liquefied sand. *Journal of Geotechnical and Geoenvironmental Engineering*, ASCE 130(11): 1192–1202.

Liao, S.C. & Whitman, R.V. 1986. Overburden correction factors for SPT in sand. *Journal of Geotechnical Engineering*, ASCE 112(3): 373–377.

Malvick, E.J., Kutter, B.L., Boulanger, R.W. & Kulasingam, R. 2006. Shear localization due to liquefaction-induced void redistribution in a layered infinite slope. *Journal of Geotechnical and Geoenvironmental Engineering*, ASCE 132(10): 1293–1303.

Meyerhof, G.G. 1957. Discussion on research on determining the density of sands by spoon penetration test. *Proceedings of 4th International Conference on Soil Mechanics and Foundation Engineering*, Vol.1: 110.

Miura, K., Maeda, K., Furukawa, M. & Toki, S. 1997. Physical characteristics of sands with different primary properties. *Soils and Foundations* 37(3): 53–64.

Poulos, S.J. 1981. The steady state of deformation. *Journal of Geotechnical Engineering Division*, 107, GT5, ASCE: 553–562.

Seed, H.B. 1987. Design problems in soil liquefaction. *Journal of Geotechnical Engineering Division*, ASCE 113(8): 827–845.

Seed, R.B. & Harder, L.F. Jr. 1990. SPT-based analysis of cyclic pore pressure generation and undrained residual strength. *Proceedings of Seed Memorial Symposium*, Duncan, J.M. (ed.), BiTech Publishers, Vancouver, B.C.: 351–376.

Skempton, A.W. 1986. Standard penetration test procedures and the effects in standards of overburden pressure, relative density, particle size, ageing and overconsolidation. *Geotechnique* 36(3): 425–447.

Tsukamoto, Y., Ishihara, K. & Shibayama, T. 2004a. Evaluation of undrained flow of saturated sand based on triaxial

- tests. *Proceedings of 3rd International Conference on Continental Earthquakes*, Beijing, China.
- Tsukamoto, Y., Ishihara, K. & Sawada, S. 2004b. Correlation between penetration resistance of Swedish weight sounding tests and SPT blow counts in sandy soils. *Soils and Foundations* 44(3): 13–24.
- Uzuoka, R., Sento, N., Kazama, M. & Unno, T. 2005. Landslides during the earthquakes on May 26 and July 26, 2003 in Miyagi, Japan. *Soils and Foundations* 45(4): 149–163.
- Vaid, Y.P. & Chern, J.C. 1983. Mechanism of deformation during cyclic undrained loading of saturated sands. *International Journal of Soil Dynamics and Earthquake Engineering* 2(3): 171–177.
- Vaid, Y.P. & Chern, J.C. 1985. Cyclic and monotonic undrained response of saturated sands. *Advances in the art of testing soils under cyclic conditions, Proceedings of ASCE Convention*, Detroit, Michigan: 120–147.
- Verdugo, R. 1992. *Characterization of sandy soil behaviour under large deformation*. Ph.D. thesis, University of Tokyo.
- Verdugo, R. & Ishihara, K. 1996. The steady state of sandy soils. *Soils and Foundations* 36(2): 81–91.

The use of controlled blasting for evaluating seismic performance

S.A. Ashford & Y. Kawamata

Oregon State University, Corvallis, Oregon, USA

K.M. Rollins

Brigham Young University, Provo, Utah, USA

R.E. Kayen

United States Geological Survey, Menlo Park, California, USA

T.J. Weaver

University of Idaho, Moscow, Idaho, USA

T. Juirnarongrit

Team Consultants, Bangkok, Thailand

ABSTRACT: Over the past decade, controlled blasting techniques have been used to gain insight into the behavior of deep foundations subjected to liquefaction and lateral spreading. This paper summarizes the results of the authors' work on blast-induced liquefaction from around the world, starting with the Treasure Island Liquefaction Test (TILT) in California over 10 years ago, to more recent experiments on Hokkaido Island in Japan. Insight gained from each of the projects is discussed. While questions remain on how closely blasting replicates the process of earthquake induced liquefaction, once liquefaction is achieved, controlled blasting is a proven complement to our arsenal of techniques for physically modeling liquefaction and lateral spreading, and remains essentially the only available choice for field scale experiments.

1 INTRODUCTION

In past earthquakes, liquefaction-induced lateral spreading has caused significant damage to deep foundations, resulting in damage to a variety of super-structures, including port facilities, buildings, bridges, and utilities. Also, lateral spreading of liquefied soil has induced considerable permanent deformation of pavement, retaining walls, natural slopes, and artificial earth structures, such as road embankments and levees. Based on observations in past earthquakes, it is essential to gain better understanding of the impact of liquefaction and related lateral spreading and induced ground deformations on the behavior of foundations and structures in order to improve current design methods and prevent catastrophic failure in future earthquakes.

To develop more reliable designs, several types of research efforts on liquefaction and lateral spreading have been conducted; e.g. numerical studies, laboratory element tests, centrifuge tests, and large-or full-scale limited area 1-g shake table tests. However, these research efforts generally provide information only under assumed ideal conditions, and then, it

is also important to know behavior of liquefied and laterally spread ground in the field, i.e. at actual sites. One effective physical modeling method is the use of controlled blasting to induce liquefaction at this sites. Over the past decade, this method has been used several times in conjunction with deep foundations to gain insight on their behavior when subjected to liquefaction and lateral spreading.

In this paper, a general description of the controlled blasting method is presented, followed by several examples of projects where the authors have used controlled blasting techniques.

2 DESCRIPTIONS OF CONTROLLED BLASTING TECHNIQUES

Controlled blasting technique has been successfully performed for over 50 years in many different soil and site conditions as a densification method of loose saturated soils. Installing explosives into soils and blasting them, large impact can be generated, and it results in porewater pressure buildup, liquefaction and lateral spreading if slope or free surface exists. When

porewater pressure dissipation completes, particles of liquefied soils rearrange, and the liquefied strata settle and become denser.

Using this mechanism, controlled blasting has been used for large-or full-scale liquefaction tests. However, it is obvious that the process of liquefaction induced through controlled blasting compared to that resulting from seismic loading is quite different. In earthquake induced liquefaction, the porewater pressure is slowly increased by shear waves propagating up through the soil, while the porewater pressure is almost instantaneously increased by compression waves generated from the explosion in blast-induced liquefaction. Blasting produces higher accelerations and higher frequency ground motions than an earthquake; nevertheless, the velocity and strain levels are comparable. Because of these differences, the actual process leading up to liquefaction during an earthquake can not be simulated well by blasting, and then, soil behavior once liquefaction had been induced is usually focused on in controlled blasting liquefaction tests.

Some of controlled blasting liquefaction projects have been contributed by the authors, and briefly presented as application examples of this technique in the following chapter.

3 EXAMPLES OF CONTROLLED BLASTING LIQUEFACTION TESTS

3.1 *Treasure Island, California, USA*

The lateral load capacity of deep foundations is critically important in the design of bridge structures in seismically active regions. Estimation of deformation during and after earthquakes also becomes important as performance-based design concept gets more familiar. Although reliable design methods had been developed for the lateral capacity of piles in non-liquefied soils, information to make accurate prediction of piles that are surrounded by liquefiable soils was very short. Centrifuge studies using scaled models (e.g. Wilson et al. 2000; Dobry et al. 1996) could prove valuable insight on soil-pile interaction in liquefied soil; however, full-scale tests were necessary to verify these models, scale effect and so forth, and also to provide ground truth information. To improve our understanding of the lateral load behavior of deep foundations in liquefied soil, a series of full-scale lateral load tests had been performed at Treasure Island in San Francisco, California. The ultimate goal of this project was to develop lateral load-displacement relationships for a variety of individual piles and pile groups in liquefied sand under full-scale conditions.

Prior to a series of the lateral load pile tests, a pilot liquefaction test was performed to design specification of blasting, such as the amount of explosives, installation spacing, and forth. Site characteristics, test setup,

and examples of obtained results in the pilot test are presented herein. Details of the pilot test and the pile tests are available elsewhere (Ashford & Rollins 2002, 2004).

3.1.1 *Site characteristics*

Treasure Island is a 160-hectare manmade island in San Francisco Bay. It was constructed by hydraulic and clamshell dredging during 1936 and 1937. The loose nature of the hydraulic fill in Treasure Island site combined with a high groundwater table indicates that the site is susceptible to liquefaction. This was demonstrated in the 1989 Loma Prieta earthquake, with several sites across the island liquefying during the earthquake. Since Treasure Island is a National Geotechnical Experimentation Site, a substantial amount of geotechnical data is available in the vicinity. In addition, site-specific geotechnical investigations were carried out as part of this study. The soil profile at the pilot liquefaction test area is shown in Figure 1 in reference to the excavated surface, which is approximately 1 m below the original ground surface. It consists of hydraulically placed fill and native shoal sands to a depth 4.5 to 6 m. The hydraulic fill generally consists of loose fine sand or sandy silt with thin interbeds of lean clay underlain by sandy silts and Young Bay Mud. The water table is typically 0.5 m below the excavated ground surface. According to the Unified Soil Classification system, the sand typically classifies as SP material and generally has a D_{50} between 0.2 and 0.3 mm. The $(N_1)_{60}$ values in the sand typically ranged from 19 to 2 while the normalized cone resistance, q_{c1} ranged from 15 to 4 MPa. Using two independent correlations with $(N_1)_{60}$ and q_{c1} (Kulhawy & Mayne 1990), the relative density D_r was estimated, and its profile typically shows between 70 and 20 percent in the clean sand layers.

3.1.2 *Test setup*

The layout of blast holes and pore pressure transducers (PPT) at the pilot liquefaction test area is shown in Figure 2. Depth of PPTs is summarized in the left

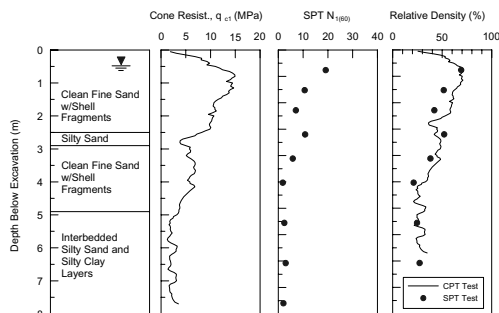


Figure 1. Soil profile at pilot liquefaction study site.

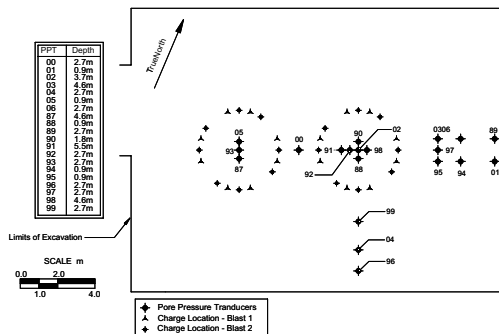


Figure 2. Test layout for pilot liquefaction study.

tale in Figure 2. Two sets of blasts were carried out to determine whether it would be possible to liquefy the site a second time. The charges were placed around the periphery of two circles each having a horizontal radius of 2.1 m. Two-part explosives, 0.5 kg TNT-equivalent charges composed of ammonium nitrate and nitromethane, were placed at a depth of approximately 3.6 m below the excavated surface and the borehole was back-filled with pea gravel. Pore pressure readings from the 20 PPTs were obtained at 1-second intervals using a computer data acquisition system. Deep foundation elements were to be placed at the center of these circles in the following pile tests.

3.1.3 Examples of test results

Two test blasts were carried out as part of the pilot liquefaction study. Three days after the first blast, additional charges were placed. In both cases, charges were detonated two at a time with a 250-millisecond delay between explosions. Although the PPTs indicated that liquefaction occurred within just a few seconds of the explosion, there was no surface manifestation of liquefaction for a period of 3 to 5 minutes in both of the tests. At this point, sand boils began to form at several of the transducer boreholes as well as at some blast holes.

An example of pore water pressure ratio (R_u) time histories is shown for a vertical PPT array at the center of the charge ring in Figure 3. The indicated depths are measured from the groundwater table, located approximately 0.5 m below the excavated surface. In this figure, the peaks of R_u showed between 90 and 100% at each of the transducers, with the exception of that at 0.9 m depth in both tests. At the 0.9 m depth, the R_u peaked at approximately 75% but then rapidly dropped to around 40%. It can be explained by higher $(N_1)_{60}$ values at shallow depth in Figure 1. For all other transducer depths, the R_u value remained above 80% for at least 4 minutes and above 60% for at least 8 minutes after the blast. Though not shown in the figure, excess pore pressure ratios in the sand were typically

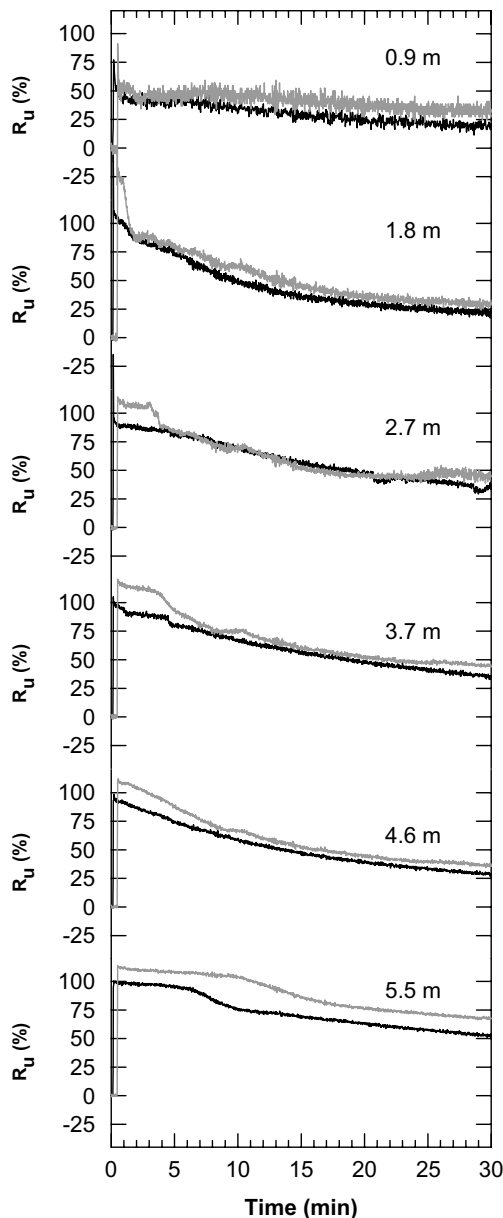


Figure 3. An array of excess pore pressure ratio time histories at the center of the charge ring (black = first blast, gray = second blast).

down to between 10 and 20% within one hour after the blast. Comparing results from the first and second tests shown in Figure 3, slightly higher values of R_u were observed in the second test than in the first test, with nearly identical dissipation rates. This confirmed that liquefaction could be induced at least twice at the

same site, as long as the time interval between blasts was relatively short (in this case, 3 days).

Ground surface settlement was monitored using lines of survey stakes spaced at approximately 0.6 m intervals through the blast area. Settlement was calculated as the change in the stake elevation between before and after the blast. Maximum ground surface settlements ranged from 25 mm for the single blast charges during the initial testing to almost 100 mm for the 16 blast points of the pilot liquefaction study (Figure 4). Our survey indicated that about 85% of the settlement occurred within about 30 minutes of the detonation.

Settlement contours for the second blasts of the pilot liquefaction study showed quite similar settlement pattern, with the greatest settlement occurring between the blast circles and extending as far as 6 to 8 m from the blast points. The zero settlement contour lies within the boundary of soil experiencing elevated pore water pressures, because of arching with the surrounding soil that did not liquefy beyond this contour. The dashed portion of the 0-mm contour line shows inferred settlements where measurements were not available.

To evaluate densification process after blasting, a series of cone penetration tests were carried out at various times. The results from CPT tests before blasting, and 42 days after a third blast are presented in Figure 5. In each figure, the profiles of the cone tip resistance and friction ratio are shown as average, the upper and lower bounds based on all CPT soundings. Comparing CPT soundings performed prior blast and 42 days after a third blast as shown in Figure 5(a) & (b), it could be found that the average cone tip resistance between 2 and 5 m depth had increased by approximately twice the pre-blast value and 2.5 times above the value two days following blasting. Similar trends are observable in the friction ratio profiles, although the changes are less significant.

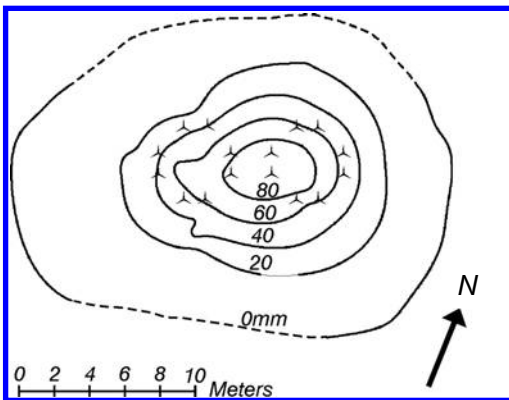


Figure 4. Settlement contours as a result of the first blast.

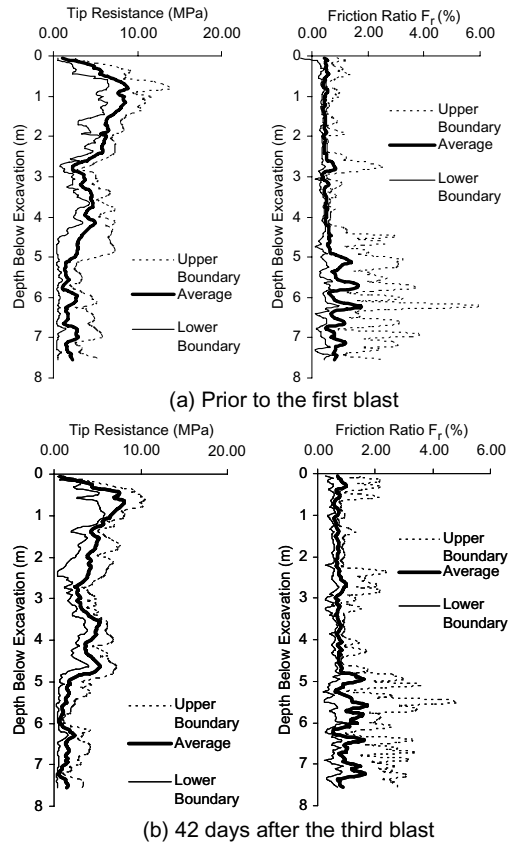


Figure 5. CPT Results at the pilot liquefaction study.

3.1.4 Summary

The results of this pilot study for the Treasure Island Liquefaction Test (TILT) demonstrated that controlled blasting techniques could be used to successfully induce liquefaction in a well-defined volume of soil in the field for full-scale experimentation. Excess pore pressures ratios (R_u) of above 90% were generated within a depth range of 1.8 m to 5.9 m and over a 12.8 m × 19.2 m surface area. R_u values typically maintained greater than 0.8 for 4 minutes and greater than 0.6 for 8 minutes. Settlement became up to 100 mm using 0.5 kg charges at 16 points. About 85% of the settlement occurred within first 30 minutes after the blast. Though not mentioned herein, the CPT resistance decrease was observed within 2 days of blasting. However, it was significantly increased after several weeks (42 days), and it could be proved that the controlled blasting techniques could improve liquefaction strength of soil.

Following the TILT pilot study, a total of 17 deep foundations were later tested under lateral loading at the site. One of the primary findings of the load tests

was the concave up nature of the back-calculated p-y curves for liquefied soil, as shown in Figure 6. This significant finding was the impetus for several additional full-scale experiments at other sites around the world.

3.2 Cooper River Bridge, South Carolina, USA

Based on the successful TILT project, another series of blasting tests was conducted at the Arthur Ravenel Bridge which now spans the Cooper River in Charleston, South Carolina. Completed in July 2005, the Ravenel Bridge has a clear span of 471 m, making it the longest cable-stayed bridge in North and South America. Results of geotechnical investigations at the site showed that liquefaction could occur to a depth of 13 m on the eastern approach to the bridge in a repeat of the 1886 Charleston earthquake (estimated M7.3). Based on the Treasure Island Liquefaction Test, full-scale blast liquefaction testing was planned as part of the foundation testing program for the new bridge. After liquefaction was induced by blasting, lateral load tests were performed using both conventional hydraulic actuators and a static loading device to evaluate lateral resistance of the large diameter drilled shaft foundations supporting the bridge superstructures. Properties of soil, test pile, test setup, and some examples of test results are provided herein, and details of this project will be published soon (Rollins et al., 2008).

3.2.1 Site characteristics

The soil profile at the test site generally consists of alluvial sands underlain by stiff to very stiff clay called

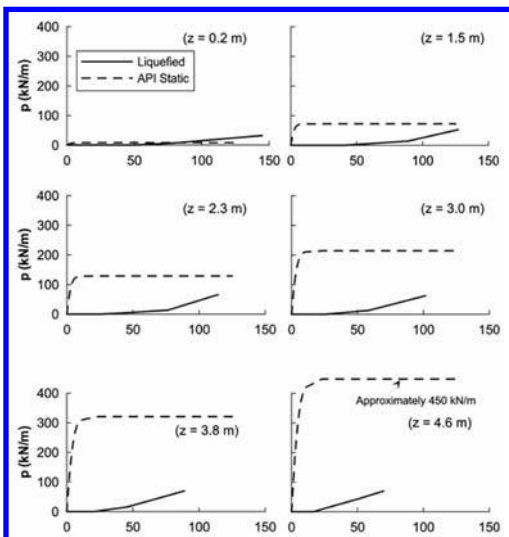


Figure 6. Back-calculated p-y curves for liquefied soil.

Cooper Marl at a depth of 13 to 14 m. Groundwater was generally within 1.5 m from ground surface, depending on tidal fluctuations. The sandy sediments of the coastal plain in South Carolina are typically loose Pleistocene age materials, and have high liquefaction potential. The representative soil profile is shown in Figure 7. In this figure, the third through fifth layers from ground surface were highly liquefiable. The third layer was loose fine sand to silty sand and extended to a depth of 7 m. The fines content varied with depth and from hole to hole in considerably wide range from 0.5 to 28%. The fourth layer lain between 7 and 10.5 m below the ground surface. This layer was typically classified as silty sand or clayey sand with higher fines content from 15 to 24%. The top of the fifth layer was at a depth of 10.5 m and extended to the top of the stiff clay layer. This layer contained fewer fines and generally classified as a loose to medium dense, poorly graded fine sand.

Using cone penetration test (CPT) results and an equation developed by Kulhawy and Mayne (1990) for clean young normally consolidated sands, the relative density (D_r) of each layer was estimated. The profile of the estimated D_r is also plotted in Figure 7. The average relative density is approximately 50% in the sand layers, and about 35% in the silty sand layer.

3.2.2 Test setup

The test shafts for the static test and the static test were 2.59 m outside diameter cast-in-steel-shell (CISS) piles. The steel casing with a thickness of 2.54 cm were installed through the sand layers and into the Cooper Marl at a depth of 16.2 m using a vibratory hammer, and then, the hole was advanced through the Marl to a depth of 46.9 m without casing. The hole was then filled with concrete using a tremie pipe. An average 30-day compressive strength of filled concrete was 370 MPa. 36 #18 bars were evenly distributed around a circle with a diameter of 2.13 m as the vertical reinforcements with confinement provided by #6 bar

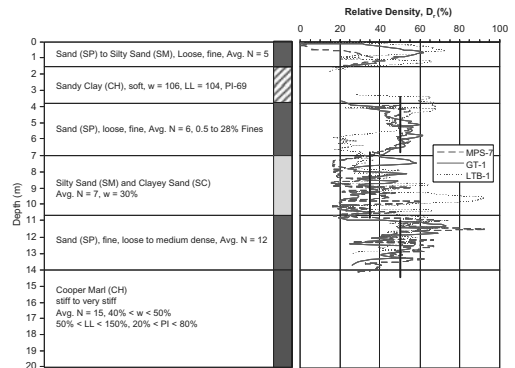


Figure 7. Soil profile for the Cooper River test site.

spirals with a pitch of 8.9 cm. A three inch concrete cover was maintained between the spiral reinforcement and the inside of the steel case.

Instrumented 0.91 m long #4 bars with strain gages were tied into the rebar cage at 10 depth intervals. At each strain gauge station, two strain gauges were mounted on opposite sides of the pile separated by a distance of about 2.1 m. The gauges were oriented to be in line with the direction of loading.

For the static actuator tests, the load was applied at a height of 0.53 m above the ground surface using two actuators setup in parallel. A reaction pile with nearly identical properties was installed approximately 8.5 m from test pile in center-to-center. Two linear potentiometers (LVDTs) were mounted to measure displacements of the pile head at heights of 0.53 m and 1.34 m above the ground surface. The lower LVDT located at the point of the load application. Four load cells on each of the two actuators provided a direct measurement of the applied load. Additional details of the static hydraulic actuator tests are provided by Rollins et al. (2005a).

For the statnamic load tests the load was applied at height of 1.31 m above the ground surface on the shaft as shown in Figure 8. The statnamic load sled weighed approximately 70 tons. Applied load and pile head deflection were measured by a load cell on the piston of the statnamic device and LVDTs mounted on the pile head, respectively. In addition, two accelerometers were attached to the pile head and a string of downhole accelerometers was installed to make measurements at eight depths within an inclinometer cast into the test shaft. Piezometers were installed at various distances and depths around the test piles in order to measure pore water pressure build-up and dissipation due to blasting. The location and depth of each piezometer for the statnamic testing are shown in Figure 9, and the similar layout was used for the static test. Three vertical arrays were installed on the circles with radii of 1.83, 7.31, and 10.36 m from the center of the test shaft. Piezometers identified with “A” and “B” in Figure 9 were standard piezoresistive and electrical resistance transducers, respectively. The electrical resistance transducers were more sensitive to damage during blasting, and in fact, several transducers closest to the explosive charges were damaged during blasting while those further from the charges provided some useful information. Additional information regarding pore pressure transducer selection, installation, and performance is provided by Rollins et al. (2005b).

Prior to the pile loading test, a pilot blasting liquefaction test was performed at a location separate from the foundation test sites for more accurate design of specification of explosives necessary to produce liquefaction. Based on the pilot test, the blast holes were placed around radii of 3.96, 4.57, and 5.18 m as shown in Figure 9. The first blast series on the inner circle used a 680 g charge at 3.05, 6.10, 9.14, and 11.73 m

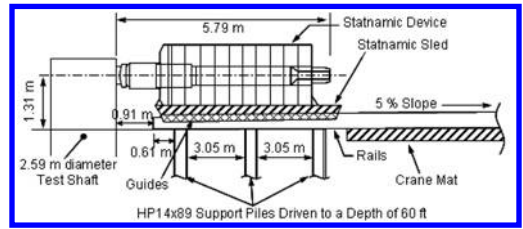


Figure 8. Test setup for lateral statnamic load tests.

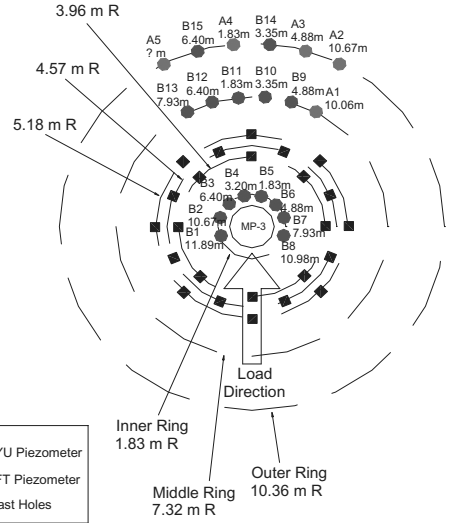


Figure 9. Plan view with layout of blast holes and piezometers.

below the ground surface. The second blast series on the middle circle used 907 g charges at depths of 4.57, 7.62, and 10.67 m, and the final blast series on the outer circle put 680 g charges at the same depths as in the first blast series. The charges and layout for the actuator test were similar. The binary explosives were a mixture of ammonium nitrate and nitro-methane, and the weights are given in equivalent weights of TNT. During each of the three blast sequences, the charges were detonated two at a time with a delay of 250 milliseconds between detonations. The blasts were started at the bottom ring and then moved upward around each subsequent ring to the top.

3.2.3 Examples of test results

Prior to the lateral load testing, the explosive charges were detonated to induce liquefaction. The excess pore water pressure ratios were developed using the readings on each piezometer and calculated effective vertical stress. A profile of the peak residual excess pore pressure ratio (R_u) for each ring of piezometers is

provided in Figure 10. The R_u values are typically between 75 and 100% in the sandy soil layers, and are bit lower in the sand clay layer at a depth from 1.5 to 3 m and in the sand layer at the bottom of the profile.

The load-deflection curves before and after the detonation of the explosive charges, are compared in Figure 11. It was obvious there is a significant decrease in stiffness after liquefaction. This stiffness reduction of pile-soil system was also observed in Treasure Island Liquefaction Test Mentioned above. Approximately 6 to 7 times more deflection was recorded at the same level of lateral load as that prior to blasting. This decrease of stiffness was somewhat less than that observed in the Treasure Island experiments with 0.31 m diameter steel pile, and it may result from the fact that the percentage of lateral resistance carried by the large diameter shaft itself is much larger than that for the smaller diameter piles. Because sand flowed into the gap behind the pile generated during loading, tensile load (negative load in Figure 11) was observed when the test pile was pulled back to its initial location.

Although not shown herein, the maximum moment for a given load after blasting increased by about 100% in comparison with the pre-blast value. Prior to blasting, the maximum moment occurred at a depth of about 6.1 m; however, after liquefaction, the maximum moment occurred near the top boundary of the Marl at a depth of 12.8 m. The profiles of

bending moment and displacement along the pile length were used to back-calculate p-y curves for the liquefied sand. These curves were in good agreement with p-y curves defined using the equation developed for the Treasure Island project (Rollins et al., 2005c) and multiplying correlation factor of pile diameter. The equation was originally developed for 0.31 m diameter piles and sands with D_r of about 50%, while sands with a D_r of about 35% were found to produce no resistance. The correlation factor for pile diameter effect was 9.2 for the 8.5 times larger diameter pile. The back-calculated p-y curves in this project were used for non-linear pushover analysis with the commercial software, LPILE plus version 5.0.12 (Reese et al., 2000). The computed load-deflection curve is presented in Figure 11 and reasonably agreed with the test results.

The measured load on the load cell in the statnamic device (F_{stn}) includes the contribution to load provided by inertia, damping, and soil resistance. The area inside the hysteresis loop in the load-deflection curve indicates magnitude of damping; i.e. large area means large damping. The damping forces can be derived by subtracting the inertial and the soil resistance for a lumped mass model from the measured statnamic force. Because the acceleration time histories were measured on the installed accel-erometers at certain depths, and then, could be converted to velocity time histories for each segment of the shaft by integrating acceleration time histories. The damping coefficient was also estimated based on the log-decrement method. Although conditions after the statnamic loading do not strictly correspond to “free-vibration” conditions, it is close enough for an estimation of the damping ratio. Based on this approach the damping ratio for the three statnamic load tests was found to be between 0.30 and 0.35. Removing dynamic effect from the statnamic test results, the interpreted static lateral resistance versus deflection curve for the second statnamic test was determined and plotted in Figure 12 with hysteresis loops for the static test. Although the curves are offset due to a difference in the initial

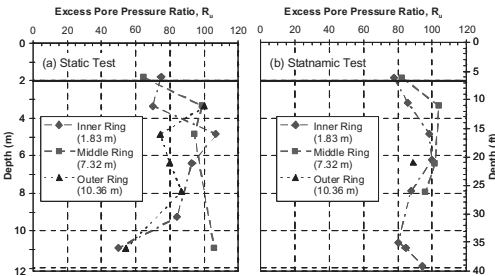


Figure 10. Profiles of the peak excess pore water pressure ratio.

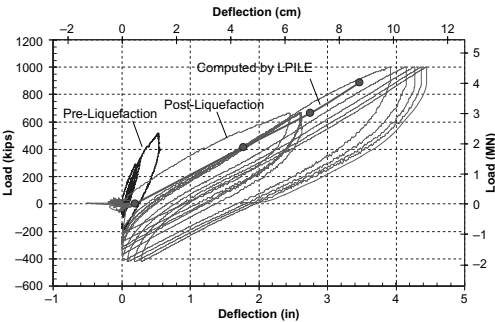


Figure 11. Lateral load-deflection curves for static load test.

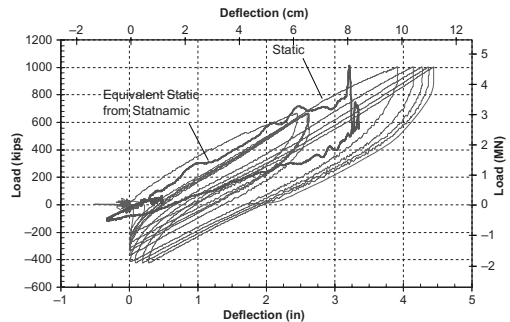


Figure 12. Comparison of lateral load-deflection curves.

starting point for the static load test, the slope of both curves is remarkably similar. In addition, the shape of the hysteresis loop for both curves is also similar. These similarities suggest that derived damping ratio from the static test is reasonable.

3.2.4 Summary

The Cooper River testing program showed that controlled blasting techniques could successfully induce liquefaction to considerable depth using several layers of charges. Furthermore, the combination of controlled blasting with the static lateral load test procedure provides useful information to evaluate the dynamic lateral resistance of full-scale deep foundations in liquefied sand.

The increased resistance provided by the 2.59 m diameter test pile could be reasonably approximated using the equations proposed for a 0.31 m diameter pile with a diameter correction factor of about 9. The interpreted static lateral resistance from the static test using a lumped mass approach was approximately the same as the static lateral resistance measured in hydraulic actuator tests on an adjacent test shaft at the same site. The damping ratio for the 2.59 m diameter drilled shaft in liquefied sand during the static testing was approximately 30 to 35%.

3.3 The Port of Tokachi, Japan

At present, two load conditions are usually considered for foundation design; that is, inertial and kinematic load conditions. The two projects mentioned above were performed to obtain better understanding for design under inertial load from seismic response of superstructure, but these tests did not account for kinematic loading from permanent ground. In light of this, several full-scale instrumented piles were subjected to blast-induced lateral spreading in experiments carried out in November and December 2001 in the Port of Tokachi on Hokkaido Island, Japan. The overall research effort of this project was lead by the Port and Airport Research Institute, Japan (PARI), with a primary objective of assessing the performance against lateral spreading of two different quay walls, which were with seismic design and traditional design which did not consider seismic effect. Totally 13 organizations, including US universities and Japanese universities and industries made joint collaboration, and installed their own specimens, such as soil-cement columns of liquefaction mitigation, and pipe lines. The test piles were installed in the zone of the traditional design quay wall where larger lateral spreading was expected. The area of the test site was about 4800 m², and about 880 kg of explosives were installed at 257 locations. More details of this project are available in the literature (e.g. Sugano et al., 2002).

3.3.1 Site characteristics

The test site is composed of man-made hydraulic fill without any ground improvement, built approximately 2 years prior to the experiment to expand port capacity by. As a result, the soil is very loose and highly susceptible to liquefaction. Figure 13 presents a typical soil profile in the vicinity of the test piles, together with in-situ test results, including standard penetration tests (SPT), penetration tests (CPT), Swedish weight sounding tests (SWS), and two downhole shear wave velocity tests. Generally, the soil profile consisted of 7.5 m of hydraulic fill, a 4-m layer of very loose to loose silty sand, underlain by a 3.5-m layer of very soft lean to fat clay with sand. 1 m of medium dense sand overlying a very dense gravel layer underlay hydraulic fill. The ground water table was approximately 1 m below the ground surface. The SPT N-values for cohesionless soils presented in Figure 12 were corrected for field procedures and overburden pressure using the method proposed by Seed and Harder (1990). The SPT N-values for the clay layer were only corrected for field procedures. Shear wave velocities of hydraulic fill was less than 100 m/s, and indicated that its soil stiffness was very low. The other soil properties, such as the relative density and friction angle of the cohesionless soils, and undrained shear strength of the clay, were estimated from the results from SPT, CPT, and SWS using correlation equations proposed in the literatures (Figure 13).

Using a US criterion (Seed and Idriss 1971), liquefaction susceptibility of the soils at the test site was

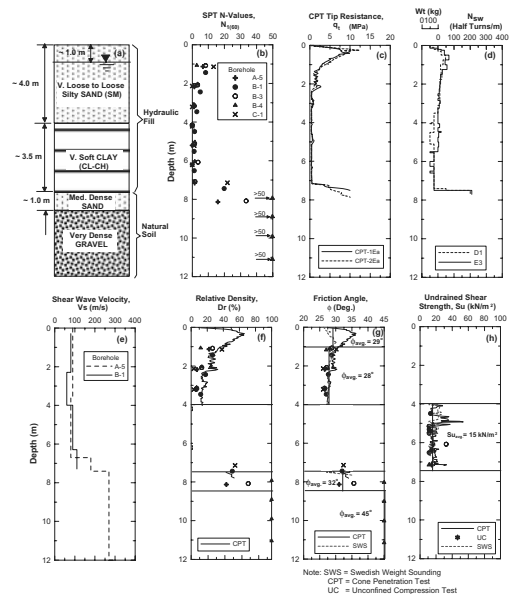


Figure 13. Typical soil profile and characteristics at the Tokachi liquefaction test site.

evaluated. As a result, it was found that the first and second sand layers below the water table are susceptible to liquefaction, while the middle clay layer is not liquefiable. In fact, the results of pile bending moments in later sections indicate that only the sand layer was liquefied, and the clay layer did not liquefy.

3.3.2 Test setup

A layout of the test site for the first experiment is shown in Figure 14(a). The water elevation in front of the quay wall was approximately +2.00 m, the same elevation as the ground water table. The quay wall was sheet pile type with tie-rods fixed to H-piles. This quay wall was designed based on a traditional Japanese design without consideration of the seismic effect. The ground surface was at elevation +3.00 m from the quay wall for 25.2 m, and began to slope upwards at 4%.

The test piles consisted of a single pile, a 4-pile group, and a 9-pile group (see Figures 14 and 15). The pile outside diameter was 318 mm with a wall

thickness of 10.5 mm, a nominal length of 11.5 m, and a yield strength of 400 MPa. Steel channels (C 75 mm × 6.92 kg/m) with a yield strength of 400 MPa were welded to the steel pipe piles for strain gage protection from damage during pile installation. Three similar free-head single piles were also installed in the area, labeled “W” in figure 15. The properties of these piles were the same as the other piles, but the pile lengths were shorter.

A diesel hammer was used for pile driving. The piles were planned to be driven full length into the ground, corresponding to about 3.0 to 3.5 m penetration into the gravel layer to obtain a degree of fixity at the pile tips. However, some of the piles could not be driven to the desired depth due to the presence of the cobbles at the final depth. As a result, the pile lengths in the groups varied between 10.2 m and 11.5 m as summarized in the table in Figure 15. In the pile groups, the piles were spaced at 3.5 pile diameters, center-to-center, corresponding to 1.11 m. The pile heads were fixed against rotation by reinforced concrete pile caps based on typical Caltrans design practice.

Explosives were placed in the 6.0 m square grid pattern as shown in Figure 14. Charges were installed at depths of 3.5 m and 7.5 m below the design ground surface. The mass of charges was usually from 3 to 5 kg, but was reduced to 2 kg near the pile specimens in order to prevent damage on the large number of

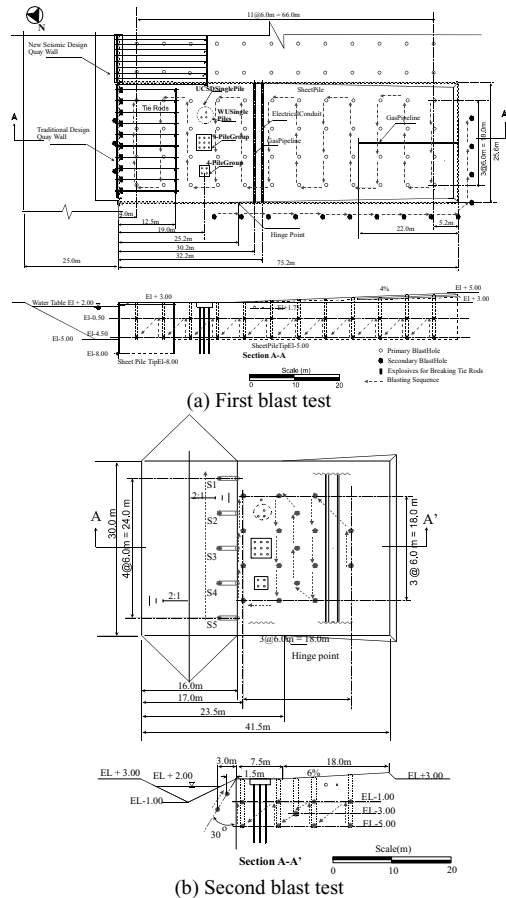


Figure 14. Site layout of Tokachi liquefaction test.

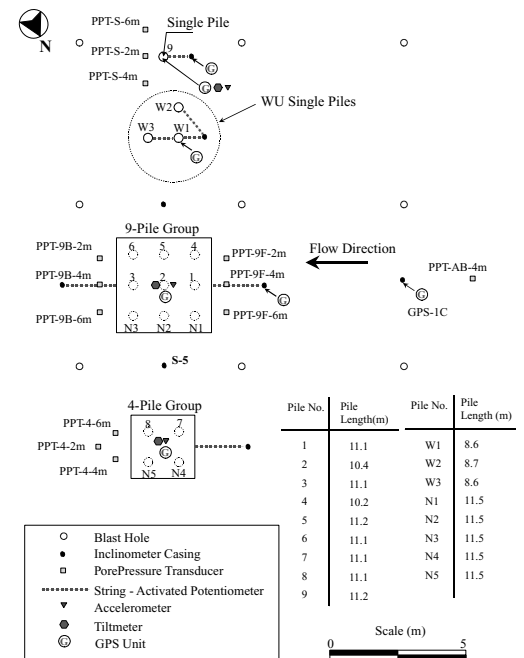


Figure 15. Plan view of test setup and instrumentations for Tokachi liquefaction test.

instruments installed in the vicinity from huge acceleration generated by blasting. The sequence of the primary blasting in the area surrounded by sheet piles is also shown in Figure 14. The blasting interval between two adjacent blast holes was approximately 0.75 seconds, with a total elapsed time of approximately 35 seconds. Immediately following the primary blasting, the secondary blasting was made by detonations of explosives placed around the perimeter of the test site with the time interval between each blast hole of 1 second. The purpose of these explosives was to liquefy the soil in the vicinity of the sheet pile to minimize boundary effects, and promote lateral spreading of soil liquefied by the primary blasting. Approximately 20 seconds after the completion of the secondary blasting, additional explosives were detonated to break the tie-rods of the quay wall, which allowed additional movement of the soil within the test area.

About one month after the first test, the second lateral spreading test was carried out with the same test piles and instrumentation from the first experiment still in place. The second blast test was performed in an attempt to induce additional ground deformations and further evaluate the performance of the piles subjected to a larger soil deformation. The test site for the second lateral spreading test was modified from the first test to make larger spreading; i.e. removing the quay wall and sheet piles surrounding the test site, and steepening the slope to 6% (Figure 14 (b)). The locations of the blast holes in the second test are shown in Figure 14 (b), and charges were installed at depths of 4.0 m and 8.0 m below the design ground surface. The amount of the charges varied from 2 kg to 4 kg. The explosives under the steep slope (S1 to S5) were detonated first, and approximately 15 seconds later, the primary blasting sequence was initiated at the rear of the embankment and proceeded sequentially towards the waterway. The weather during the second test was quite poor, with a heavy snowfall and strong wind, and then, the ground was frozen to a depth of approximately 0.20 m below the surface. The frozen ground would likely impede lateral spreading. In an attempt to mitigate this problem, jackhammers were used to break up the frozen ground into small blocks in the vicinity of the test piles.

3.3.3 Examples of test results

GPS units were used to monitor the movements of both the ground surface and test piles during lateral spreading (Turner 2002). An example time-history of soil movements on the up-slope side of the 9-pile group (GPS-1C in Figure 15) in the longitudinal, transverse, and vertical directions, is presented in Figure 16 (a), with R_u near the GPS unit (PPT-AB-4 m). It was found that, once R_u reached about 50% (at about 10 seconds after the blasting), the soil mass began to translate toward the quay wall. As the blasting approached the

GPS unit, short period responses in all directions due to blasting impacts were observed as sharp spikes on the displacement time-histories. The rate of longitudinal movement between 10 seconds and 27 seconds was fairly constant at about 1 cm/second. Beyond 27 seconds, the effect of dynamic force from the blasting was not important because the blasting past the location of the GPS unit as indicated by the insignificant movements in the transverse and vertical directions. However, the rate of movement in longitudinal direction still kept about 1 cm/second for another 5 seconds. Around 32 seconds, the lateral movement became saturated. An increase in soil movements at 40 seconds was due to the effect of secondary blasting around the sheet pile wall. Figure 16 (b) presents the displacement path of the GPS unit in the horizontal plane. This figure shows the horizontal movement mainly occurred in the longitudinal direction towards the quay wall.

In the first test, the average displacement of the soil on the up-slope side of the pile groups was approximately 30 cm, while the soil movement between groups was approximately 30% greater than that of the up-slope soil movement with a magnitude varying between 40 and 43 cm. This fact implied that the movement of the up-slope soil was impeded by the pile foundations, and then, the soil movement between the pile groups likely represented a “free-field” soil displacement with no interference from pile foundations. Longitudinal soil surface movement generally decreased with distance from the quay wall. The pile head displacement of the single pile was 32 cm, while the 4-pile group and the 9-pile group, moved about

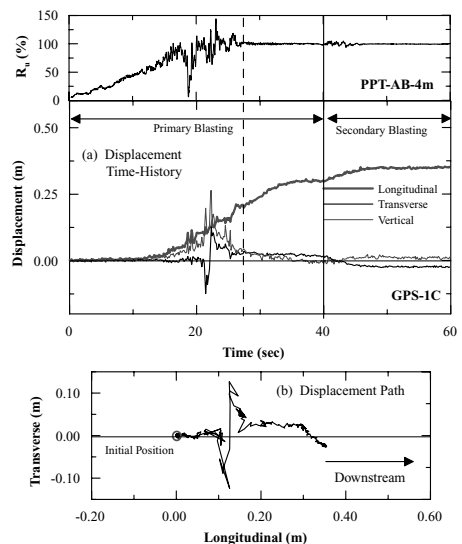


Figure 16. Time histories of pore water pressure and ground deformation at unit GPS-1C in the first test.

21 cm and 18 cm, respectively. The movements of both pile groups were approximately about 50% of the free-field soil movement in the vicinity of the test piles. The pile groups with a fixed-head condition moved less than the free-head pile due to the effect of pile head restraint in the groups contributing to resist the moment induced by the lateral soil pressure.

In the second test, the horizontal soil movements on the up-slope side were significantly lower than in the first test with an average value of 15 cm. This is likely because the soil during the second test was frozen with less susceptibility of liquefaction, and the duration of blasting was significantly shorter than in the first test. Similar to the first test, the magnitude of soil movement generally decreased with increasing distance from the waterway. Soil movement observed between the pile groups was 46 cm in maximum. The deflections of the top of the single pile, 4-pile group and 9-pile group were slightly less than in the first test with magnitudes of 28 cm, 18 cm and 16 cm, respectively.

Using the records on the strain gauges attached to the test piles, the curvatures along the length of the piles could be calculated, and the moments in the piles corresponding to maximum displacements could be determined from the moment-curvature relationship of the test piles. All the strain gauge readings were initialized to zero before each test. Assuming zero relaxation strain between the first and the second tests, the strains measured in the second test were added to those measured in the first test to obtain the total strains and curvatures, as well as the total bending moments in the second test. Though not shown herein, the lateral soil reactions were then back-calculated by double differentiating the moment data. The pile rotations and pile displacements were obtained by single and double integration of the curvature data, respectively. Since the strain data was discrete, interpolation was necessary. In this analysis, polynomials of an appropriate order were used to fit the experimental moment curves. Profiles of rotation, deflection, and moment at the end of the first and the second blast tests are summarized in Figure 17. The solid and dotted lines in the moment profiles represent curve interpolated for the first and second tests, respectively.

Because of free-head condition of the single pile, the moments at the head were zero. The maximum moment occurred around the boundary between the medium sand and the dense gravel layers at a depth of about 9 m. The moment profiles indicate that the single pile yielded during the second test with the plastic hinge length of more than 1 m. The moment was insignificant through the top 4 m of the very loose liquefied sand layer, indicating that the resultant force on the pile produced by the liquefied soil was negligible. Below the liquefied soil layer, the moment increased with depth for the next 3.5 m, through a soft clay layer. Though the R_u in this layer also reached 100%, the clay

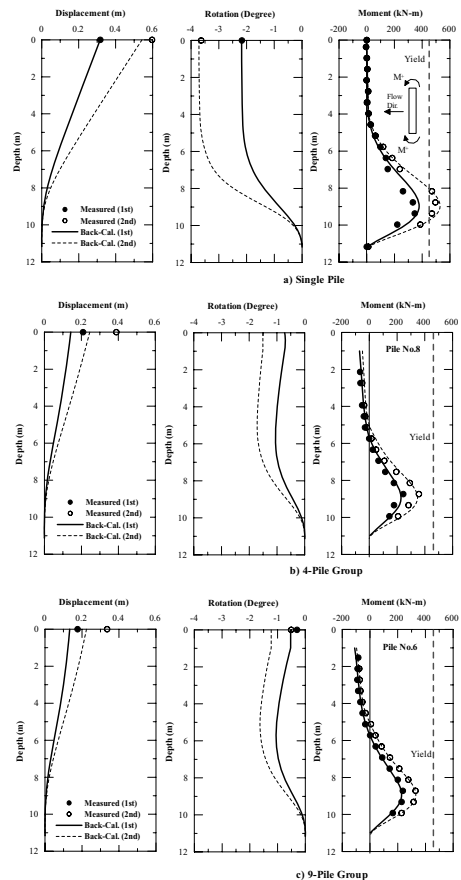


Figure 17. Profiles of displacement, rotation, and moment along the piles; a) single pile, b) 4-pilegroup, and c) 9-pile group.

layer behaved differently from the liquefied sand at the top 4 m; i.e. the positive bending moment along the pile soil began rising up in this layer, and became larger in depth. The second sand layer (-7.5 to -8.5 m) was also liquefied and may provide zero resisting force to the pile as similarly to the first sand layer, but the profiles could not verify it obviously. This is likely because this layer was so thin that very limited strain gauge data was not able to capture this phenomenon. The back-calculated pile head rotations and pile head displacements of the single pile were in good agreement with the measurements obtained from both blast tests.

The moment, calculated rotation, and deflection profiles of pile No. 8 in the 4-pile group and pile No. 6 in the 9-pile group (see Figure 14) are also presented in Figure 17. In the moment profiles obtained from the first and second experiments, negative moments were observed at the pile head. These negative moments were due to the effect of pile head restraint at the

connection between the pile head and the cap. The maximum moment occurred at a depth of 9 m below the ground surface as in the case of the single pile, but the magnitude of the maximum moment was significantly less than that of the single pile because rotational restraint at the connection. Based on the moment data, all piles in the groups did not reach at yielding, and were in elastic.

Though the maximum positive moments in the second test were greater than that of the first test, the negative moments at the pile heads in the second test were very similar to the first test. It implied that the rotational restraint at the connection was yielded in the first test, and the connection could not take larger moment any more. In fact, spalling of surface concrete at the connection was observed during excavation for inspection of in-ground condition of the piles. Slight decrease of the moment at the pile head in the second test may be due to the loss of surface concrete at the connection. The pile moment distribution between depths of 1 and 4 m, corresponding to the depth of the very loose liquefied sand layer, was approximately constant, resulting in zero reaction acting to this portion of the pile. This finding agrees well with the previous conclusion obtained from the single pile case.

The back-calculated displacement profiles of both pile groups were approximately 25% and 35% lower than the measured values for the first and second tests, respectively. This may be because some translation and/or rotation at the pile tips had occurred during the tests, while both were assumed to be zero in the back-calculation. It can be reasonable explanation because the amount of rotations at the pile tips to match the measured displacements at the pile cap of the 9-pile group was small, about 0.2 and 0.5 degrees for the first and second tests, respectively.

The back-calculated pile head rotations of the 9-pile group were significantly higher than the measured ones, especially in the second test. As mentioned above, rotational restraint at the pile-cap connection reached at yielding, and then, some rotation at the pile head underneath the pile cap was allowed resulting in a jump of rotations between the pile cap and the pile heads.

After completion of the tests, the soil surrounding the pile caps was excavated to investigate the structural damage conditions. A little concrete spalling surrounding the pile heads was observed, indicating that some rotations between the piles to the pile caps might occur as mentioned earlier. No pull-out of piles from the pile cap was observed on the connections of both pile groups though both pile groups experienced the total movements of nearly 40 cm.

3.3.4 Summaries

The Tokachi experiments demonstrated that controlled blasting could successfully induce steady permanent slope deformations as a result of pore-pressure build

up, similar to lateral spreading, with little affect on the foundations from the blasting itself.

The magnitudes of free-field soil displacements around the test piles were 40 cm for both tests. Insignificant moment along the piles in the liquefied soil layer indicated that liquefied soil layer generated negligible reaction force to the piles. The moments developed in the piles were caused by the mobile soft clay layer underlying liquefied layer, which imparted driving forces to the piles, while the dense gravel layer provided resisting forces.

Rotational restraint at the pile cap led to a stiffer response, which resulted in the smaller in-ground maximum moment along the piles, as well as smaller pile head displacement when compared to the single pile with free-head condition.

The single pile yielded at the end of the second test. The piles in both of the 4-pile and 9-pile groups remained elastic. Little concrete spalling was observed at the pile to pile cap connection at the end of the second test, indicating that some rotations between the piles to the pile caps might occur.

3.4 The Port of Ishikari, Japan

This blast-induced liquefaction experiment was carried out by PARI, Japan in the fall of 2007 to evaluate seismic performance of airport facilities, effective design of liquefaction mitigation, applicability of non-destructive evaluation methods detecting voids beneath pavement induced by liquefaction, and so forth. The location of the test site was the coastal port of Ishikari in Hokkaido Island on the northern-Sea of Japan. This research effort was mainly supported by the Ministry of Land, Infrastructure, and Transportation, of the Government of Japan. Totally, 30 research works were made by 47 research groups contributing to this project. The plan view of the test site is shown in [Figure 18](#). Oregon State University (OSU) and United States Geological Survey (USGS) were ones of participants in the project, and measured liquefaction-induced ground settlement using scanning system, called LIDAR.

Terrestrial LIDAR technology is a revolutionary tool for characterizing fine-scale changes in topography (e.g. Kayen & Collins 2005). This technology is a natural extension of laser range finder systems or electronic distance meters (EDMs) commonly used in survey applications. A laser beam systematically scanned over target areas to acquire the precise distances to objects. The laser repeatedly shot pulses of light at each rotation point of the scanner, sending light to reflect off an object and back to the scanner. The pulse hits the object and the ground scattered a portion of the light back to the scanner sensor. Timing the two-way travel time of light of each laser pulse allows for the determination of range. A spherical coordinate system is initially used to map the targets, and then

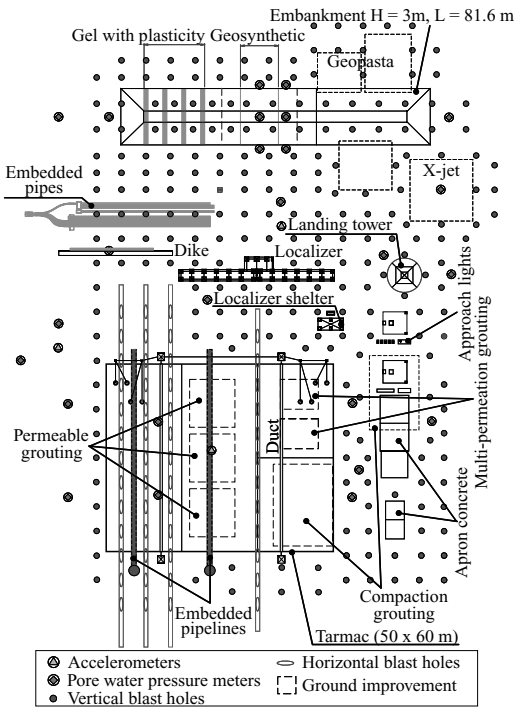


Figure 18. Site layout of Ishikari liquefaction test.

data are converted to a Cartesian scanner coordinate system centered on a scanner instrument datum.

In this paper, the LIDAR investigation and the ability to measure deformations throughout the study area are described. More information of entire project will be published in future (PARI, 2009).

3.4.1 Site characteristics

Soil profile at the test site consists of reclaimed sand dredged from Ishikari Bay underlain by alluvial soils about 5 to 6 m deep from ground surface. The reclaimed sand layer was loose with 10 to 20% of fines content and 1 to 8 of N-values. Below the reclaimed surface layer, several types of the alluvial soil layers lay; i.e. the upper and the lower alluvial sand, and the alluvial clay layers. N-values and thicknesses of this sand layer were from 3 to 12, and 1 to 5 m, respectively. In the southwestern portion of the test site, coarse gravel with 60 to 500 mm in diameter was included in the upper alluvial sand layer, and N-values of the layer widely varied from 3 to more than 50. The third layer was the 13 to 16 m thick lower alluvial sand layer with 8 to 20 of N-values underlain by the alluvial clay. The underground water table was found about 2 to 2.5 m from the ground surface. Figure 19 shows an example of boring logs in the southwestern part of the site with coarse gravel in the top alluvial sand layer.

3.4.2 Field measurement

The engineering application of LIDAR in the Ishikari liquefaction project focused on mapping the PARI tarmac test site for vertical changes of the ground. Terrestrial LIDAR technology was used for the measuring the topography of the test sites before the blast, immediately after the blast, 1 day after, two days after, three days after, and ultimately 5 months after the event.

The USGS LIDAR system used in this project is manufactured by RiegI and is based on near-infrared YAG laser transceiver. The systems are portable (the units weigh 15 kg plus the weight of accessory cables,

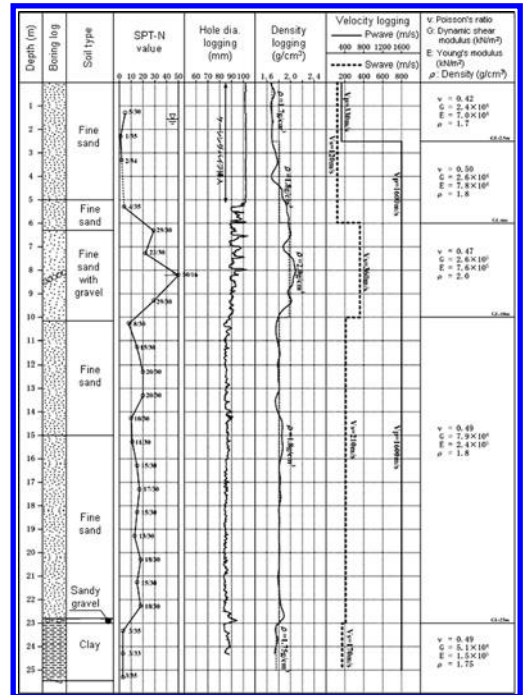


Figure 19. Typical soil profile at Ishikari liquefaction test site.



Figure 20. Scanning laser set up on the top of the embankment.

tripod, battery and laptop) and designed for the rapid acquisition of high-resolution 3-dimensional imagery. The maximum distance to targets is about 700 m for the Riegl under the best atmospheric conditions and is dependent on the reflectivity of the given target. For this study, the maximum target distance was much shorter than the maximum range of the units, and the minimum target distance is 2 m, the distance to the ground from a tripod-mounted system. The range accuracy is consistently about 15 mm for the Riegl at the range of interest in this study. The laser beam divergence angle is 3 milliradians, meaning that at a range of 10 m, the beam footprint is approximately 30 mm across. Because of the footprint size, the shots are ideally spaced 3 milliradians apart. The position of the center of the footprint is measured to a precision of 0.17 milliradians by an encoder. The angular position of the laser-pulse leaving the scanner is controlled by precise servo-motors within the units.

The USGS scanners (Figure 20) have a single scan sweep from 336° – 360° horizontally and 80° vertically for the two Riegl scanners used in the project. The scanners take several hundred thousand to several million individual x, y, z position measurements, at a rate of 8,000 points/second, and the time required for a scanning can range from 45 seconds to 6 minutes, dependent on resolution used. LIDAR systems also have the ability to collect real color object data. The USGS system records a single pixel of color for each laser footprint assigning the pixel color to each point in the point cloud. To image the tarmac surface, the scanner was mounted on an elevated platform adjacent to the test site. In general, a tripod was placed on the ground (Figure 20). However, 3-dimensional laser scanners cannot image behind objects, and the first object encountered casts a shadow over objects behind it. At low grazing-angles away from the scanner, the laser path angle decreases to only several degrees and proportionally larger shadows are cast on the ground behind the target. To minimize shadow



Figure 21. A 20 m cherry-picker used to make several scans.

zones and get full coverage of the target surface, the scanner was elevated as much as possible over the tarmac. Therefore, a cherry-picker hoist was used to elevate the scanner 20 meters above the ground for collection of some of the imagery (Figure 21).

Also, the sensor was moved around the tarmac for multiple setups because area behind objects would be shadow and multiple scans from several different view points are needed to remove shadow and make more accurate 3-dimensional imagery. Manipulation of that data is performed with specialized surface modeling software and a computer with high-graphics workstation speed and memory. The system used in this project utilizes two surface modeling software packages, I-SiTE Studio (I-Site Pty. Ltd) and RiSCAN Pro (Riegl Co.). These software packages collect the scan point-cloud data and can process multiple scans into geo-referenced surfaces. An example of image composite from multiple scans is shown in Figure 22.

3.4.3 Examples of scanned results

An oblique image of the study area immediately after the blast experiment can be seen in Figure 23 with the lower corner (to the left of the words “scan point”) of the tarmac settled and flooded with liquefied soil. In order to produce difference maps of the tarmac to measure settlements, surface models were produced from each day data set. The pre-scan LIDAR data was used as a control on the experiment to measure the ground settlement. A series of standard processing steps is followed to produce a surface model. First, the individual scans were assembled in a data folder. The coordinate system for an individual scan centers the data set about the scanner origin. Then, multiple scans are merged together by (1) assigning one scan as the fixed registered reference, with scanner origins

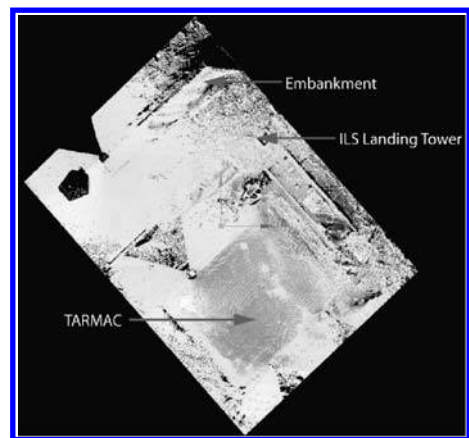


Figure 22. Laser image composite from multiple scans of the Ishikari test site.

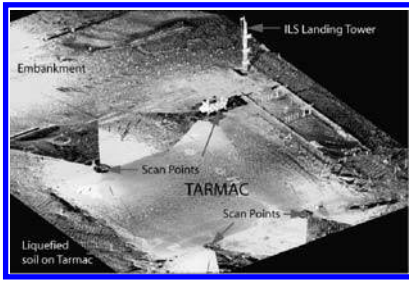


Figure 23. An oblique image with the circular no-data area below scan location.

of $x = 0, y = 0, z = 0$, and then (2) referencing the other scans to it using a least-squares “best-fit” match between scan points or reflectors. The transformation of the data from scanner coordinates to project coordinates requires a linear 3-dimensional translation of the data from one point to another, and rotation of the data. To adjust the data to a global coordinate system (e.g., WGS84), reflector targets and scanner positions in the merged data set were precisely surveyed with a differential global positioning system (DGPS) and these. Again, transformation to global coordinates requires data translation and rotation. Filters are then utilized to eliminate unwanted data. For example, filters can be used to remove vehicles, people, barricades, and vegetation to observe the bare earth. The filtered point-data can then be “segmented” to differentiate discrete surfaces from each other and from complex objects like trees and brush. When the data are filtered, surface models can be rendered. Multiple processed surfaces are used to measure change of volumes, areas, and distances.

Settlement map of the tarmac area scanned on the day of the blast experiment is shown in Figure 24. There were three distinct zones at the tarmac test site, unimproved, grouting with different depths of improvement. The southwest portion of the tarmac was unimproved ground, and suffered maximum settlements of between 0.25 m and 0.40 m. A probability distribution function (PDF) of settlements shows a peak in the range of 0.25-0.40 m for this area. The deformations in the unimproved area are not significantly effected by the perimeter of the tarmac as can be seen in the random contours at the margins of this area. The central and northeast zones were ground stabilized with compaction grouting or grout injection with different depths of improvement. Both zones had maximum benefit from the grouting in the center of the improved area, and both sections did well to minimize settlements. It implies the chemical grouting and the compaction grouting seem comparable ground improvement methods against liquefaction-induced settlement, and the deeper grouting on the bottom center had quite little benefit relative to the shallower

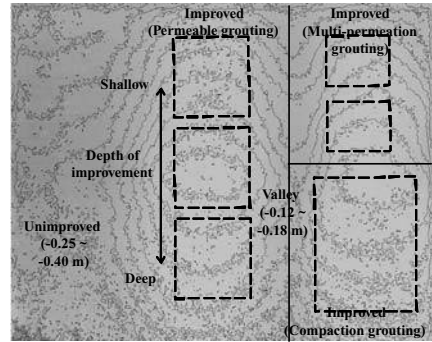


Figure 24. Settlement map of the test tarmac.

grout injection zone on the top center of the figure. In the central portion of each improved zone, the ground appears to have not settled at all. The grouted zone in the PDF is associated with the peak centered about 0.0 m and extending from +0.0 m to -0.08 m. Settlements at the perimeter of the improved areas may indicate that these areas, closer to the actual blast charges may indicate the soil beneath the center of the improved zone did not liquefy. The settlements near the margins of the improved zone may better reflect the likely settlements during an actual earthquake. The valley of settlement between the two improved ground zones probably reflects a bridging of the tarmac over the unimproved zone. In the PDF, the peak associated with this topographic valley ranges from -0.12 to -0.18 m. In the absence of the grouted zones adjacent to the valley, and the bridged tarmac, this zone should have settled more. It is possible be that voids developed beneath this zone of bridged pavement between the two improved zones.

3.4.4 Summary

While the results are still being analyses, the Ishikari project demonstrated the usefulness of Light Detection and Ranging (LIDAR) to map deformations resulting from liquefaction. Several laser scanners were deployed at the site before the blast, immediately following the experiment, and at intervals 1, day, 2 days, 3 days, and 5 months after the blast. LIDAR successfully mapped the deformations of ground due to blast-induced liquefaction at the site, and these results bear directly on the effectiveness of the ground remediation used at the site. The unimproved test site had settlements of between 0.25 m and 0.40 m, while the improved ground with injection grouting had negative settlements (uplift) of several centimeters in the center of the test area and increasing settlements to the edges of the improved zone. The tarmac behaved as a flexible mat that interacted with the liquefied soil to dampen the effect of the settlements.

4 CONCLUSIONS

Over the past decade, several full-scale experiments using controlled blasting techniques were conducted in order to study the seismic performance of pile foundations and structures subjected to liquefaction and lateral spreading. In all of the projects discussed above, controlled blasting successfully liquefied the soil and, where desired, induced lateral spreading. The response of soil and structures were measured using various types of instrumentation, with some examples of data obtained during the tests briefly described in this paper. In all cases, something new was learned from each study.

Liquefaction and lateral spreading are complex phenomena, and some questions remain on how accurately controlled blasting replicates the process of earthquake induced liquefaction. Nevertheless, the full-scale blasting experiments conducted over the past decade have proven to be reliable complement to others types of physical modeling, and is still the only effective method of gaining insight at the field level on the effect of liquefaction and lateral spreading on deep foundations.

ACKNOWLEDGMENTS

These large field experiments would not be possible without the participation and dedication of numerous researchers and staff. The authors would like to specifically acknowledge the contributions of J. Dusty Lane to the Treasure Island project, those of Nontapat Nimityongskul and Diane Minasian to the Ishikari project, and our Japanese colleagues Dr. Takahiro Sugano and Professor Masanori Hamada. The authors would also like to thank previous sponsors of this line of research, including the Pacific Earthquake Engineering Research Center, Caltrans, National Science Foundation, and several state Departments of Transportation. This current work is funded under National Science Foundation Grant No. CMMI-0728120.

REFERENCES

Ashford, S.A., Juirnarongrit, T., Sugano, T. & Hamada, M. 2006. Soil-Pile Response to Blast-Induced Lateral Spreading Part I: Field Test. *Journal of Geotechnical and Geoenvironmental Engineering*. Volume 132, Issue 2, pp. 152–162.

Ashford, S.A., & Juirnarongrit, T. 2004. Performance of Lifelines Subjected to Lateral Spreading. Report SSRP-04/18, Department of Structural Engineering, University of California, San Diego.

Ashford, S.A., & Rollins, K.M. 2002. TILT: Treasure Island Liquefaction Test: Final Report. Report SSRP-2001/17, Department of Structural Engineering, University of California, San Diego.

Ashford, S.A., & Rollins, K.M. 2004. Blast-Induced Liquefaction for Full-Scale Foundation Testing. *Journal of Geotechnical and Geoenvironmental Engineering*, Volume 130, Issue 8, pp. 798–806.

Dobry, R., Abdoun, T.H., & O'Rourke, T.D. 1996. Evaluation of pile response due to liquefaction induced lateral spreading of the ground. *Proceedings Fourth Caltrans Seismic Design Workshop*, 10 p.

Kayen, R.E., & Collins, B.D. 2005. Terrestrial LIDAR Imagery and Analysis of Hurricane Katrina Levee Failures in the City of New Orleans, *Eos Trans. AGU*, 86(52), Fall Meet. Suppl. Abstract H42C-07.

Kulhawy, F.H., & Mayne, P.W. 1990. Manual on Estimating Soil Properties for Foundation Design. Electric Power Research Institute, EL-6800 Research Project 1493-6 Final Report, pp. 2–24 and 2–33.

Independent Administrative Institution, Port and Airport Research Institute, Japan 2009, Technical Note of the Port and Airport Research Institute: Full Scale Field Experiment of Airport Facilities during Liquefaction induced by Controlled Blasting Technique. in prep.

Juirnarongrit, T. & Ashford, S.A. 2006. Soil-Pile Response to Blast-Induced Lateral Spreading Part II: Analysis and Assessment of the p-y Method. *Journal of Geotechnical and Geoenvironmental Engineering*, Volume 132, Issue 2, pp. 163–172.

Reese, L.C., Wang, S.T., Isenhower, W.M., & Arrellage, J.A. 2000. Computer program LPILE plus version 5.0 users manual, Ensoft, Inc., Austin, Texas.

Rollins, K.M., Hales, L.J., Ashford, S.A. & Camp, W.M. III. 2005a. p-y curves for large diameter shafts in liquefied sand from blast liquefaction tests. *Geotechnical Special Publication No. 145*. Ed. Boulanger, R.W. and Tokimatsu, K. ASCE, pp. 11–23.

Rollins, K.M., Lane, J.D., Dibb, E., Ashford, S.A., & Mullins, A.G. 2005b, Pore pressure measurement in blast-induced liquefaction experiments. *Transportation Research Record 1936*, *Soil Mechanics 2005*, TRB, Washington DC, pp. 210–220.

Rollins, K.M., Gerber, T.M., Lane, J.D., & Ashford, S.A. 2005c. Lateral resistance of a full-scale pile group in liquefied sand. *Journal of Geotechnical and Geoenvironmental Engineering*, ASCE, Vol. 131(1), pp. 115–125.

Rollins, K.M., Bowles, S., Hales, L.J. & Ashford, S.A. 2008. Static and Dynamic Lateral Load Tests in Liquefied sand for the Cooper River Bridge, Charleston, South Carolina. *The Sixth National Conference of Bridges and Highways*. Charleston.

Sugano, T., Kohama, E., Mitoh, M., & Shiozaki, Y. 2002. Seismic Performance of Urban, Reclaimed and Port Areas—Full Scale Experiment at Tokachi Port by Controlled Blasting Technique. *The Earthquake Engineering Symposium Proceedings*, Vol. 11, pp. 901–906.

Turner, L.L., 2002. Measurements of Lateral Spread Using a Real Time Kinematic Global Positioning System. *California Department of Transportation Division of New Technology & Research*, 94 p.

Wilson, D., Boulanger, R., & Kutter, B. 2000. Observed seismic lateral resistance of liquefied sand. *Journal of Geotechnical and Geoenvironmental Engineering*, ASCE, 126(10), pp. 898–906.

Lessons learned from sampling and CPT in silt/sand soils

A.B. Huang

National Chiao Tung University, Hsin Chu, Taiwan

ABSTRACT: Recent studies on the liquefaction behavior of sand and silt mixtures have covered a wide range of gradations. The term silt/sand or M/S is proposed as an inclusive abbreviation of soils that can span from clean sand, silty sand to pure silt. Earlier studies related to M/S soils have concentrated mostly on laboratory tests using reconstituted specimens. The author used Laval and gel-push sampler to retrieve high quality M/S samples at test sites in Central and Southern Taiwan. Piezo-cone penetration tests (CPTU) were conducted at the test sites concurrent with the field sampling. Results from natural undisturbed samples and field CPTU showed that the effects of fines are much less significant than what have been revealed from reconstituted soil specimens or field observations. CPTU in heterogeneous alluvial soil can be a drained test even with high fines contents. The age of natural soil deposit may reduce or nullify the effects of fines as we have learned from laboratory tests using freshly reconstituted specimens.

1 INTRODUCTION

Studies on the effects of fines (soil particles passing #200 sieve) on cyclic behavior of granular soils have included a wide spectrum of gradations that span from clean sand, silty sand, clayey sand, sandy silt to pure silt. The unified soil classification of these soils can vary from SP, SW-SM, SM, SM-SC to ML, depending on the amounts and characteristics of the fines. The term silt/sand (M/S) is proposed to serve as an abbreviated term to describe inclusively, granular soils with a possibility of some cohesion and wide range of gradations.

Researchers have generally agreed that as fines contents exceed 5%, the relative density ceased to be a reliable index to predict liquefaction potential (Seed et al., 1985; Ishihara, 1993). There is still a lack of consensus as to what role the fines contents plays in relation to liquefaction. Some studies showed that the fines content has a stabilizing effect, while others indicate no effect, and still others claim a destabilizing effect. The situation is more complicated when the cyclic strength of M/S soils is inferred from in-situ test results under the framework of simplified procedure. The available correlations used in the simplified procedure are empirically derived mainly from field observations of soil behavior following earthquakes. There can be uncertainties in the observations such as depth of liquefied deposit and acceleration magnitudes.

In comparison with clean sands (fines contents less than 5%), studies on liquefaction of M/S soils have been relatively limited. These studies have mostly been concentrated on laboratory tests on reconstituted specimens. The M/S specimens were often made

of mixtures of clean quartz (e.g., Ottawa) sand with crushed silica, kaolin or other types of natural silt. These mixtures of sand and fines, or gap graded artificial soils have been compared to those of coarse and fine spherical grains (Lade et al., 1998), or a binary packing. Based on the binary packing, Thevanayagam et al. (2002) proposed a series of void ratio indices that relate the active grain contacts (i.e., the soil skeleton) to threshold fines contents. For M/S soils under the same void ratio, and fines content below the threshold value, cyclic strength decreases with fines content. This trend is reversed when fines content exceeds the threshold. As the diameter ratio of the coarse grains over that of the fine grains exceeded approximately 7, one can expect a bilinear correlation between the minimum void ratio (e_{\min}) and fines content. The e_{\min} reaches its lowest value as the fines content approaches 30%, as conceptually described in Figure 1.

Figure 1 implies that as fines content approaches 30%, the binary packing becomes unstable unless the grain mixture is in a denser state (hence lower void ratio). Thus the threshold fines content should correspond to that when the packing is at its least stable state, provided the M/S soil gradation is close to binary. Some of the studies on artificial silty sand specimens, mostly of silica in nature, have demonstrated that the threshold fines content, generally ranged from 25 to 45% (Koester, 1994; Polito, 1999; and Xenaki & Athanasopoulos, 2003). The tests on artificial, gap graded soil samples provided a scientific basis to describe the potential trend of M/S soil behaviors and their relationship with fines contents. It is questionable however, if soils with blends of these kinds of mineral contents and gap gradations exist in natural soil deposits. There has been convincing evidence

to demonstrate that how the M/S specimens were reconstituted can significantly affect their undrained strengths (Huang et al., 2004; Yamamuro & Wood, 2004). Studies have also showed that regardless of fines contents, the reconstituted specimens are not able to duplicate the stress-strain and strength behavior of natural M/S soils (Ishihara, 1993; Høeg et al., 2000; Huang & Huang, 2007).

Due to the cost and difficulties involved in undisturbed sampling in cohesionless soils, the cyclic resistance ratio (CRR) required for liquefaction potential assessment has been inferred from empirical correlations between CRR and field test results under the framework of simplified procedure (Youd et al., 2001). The cone tip resistance (q_c) has been an important option among the available field test results used in the simplified procedure. The CRR- q_c correlations have generally been established according to field observations. Although different in magnitude and/or format, most available CRR- q_c correlations for silty sand suggest that a given CRR should correspond to a lower q_c or q_{cIN} (q_c normalized to an effective vertical stress, σ'_v of 100 kPa) as fines content increases (e.g., Stark & Olson, 1995; Robertson & Wride, 1998). Thus, an adjustment of q_{cIN} is required when CPT is used for liquefaction potential assessment in silty sand under the simplified procedure. Despite of the significant impact of fines content adjustment on the outcome of liquefaction potential assessment, little explanation has been offered to justify such adjustment (Ishihara, 1993; Youd, 2001).

In his earlier research efforts, the author performed a series of laboratory tests using Mai Liao Sand (MLS). The natural MLS with a total weight over 10 metric tons was washed through a #200 sieve to separate the coarse from fine particles and then kiln dried. Soil specimens were reconstituted by mixing sieved MLS with desirable fines contents. The laboratory tests performed included undrained monotonic and cyclic triaxial tests and calibration chamber cone penetration tests on specimens with fines contents ranged from 0 to as much as 50%. MLS represents a typical M/S soil deposit in Central Western Taiwan. The sand particles originated from grinding of shale, slate and sand stone as these rocks were washed away from the central mountain range towards the Taiwan Strait. Due to the nature of parental rock, MLS grain shapes are mostly flaky. Affected by its mineral contents, the MLS is significantly more compressible than typical clean quartz sand reported in literature (Huang et al., 1999). The cyclic strength of reconstituted MLS decreased consistently as the fines contents increased from 0 to 50% (Huang et al., 2004). By comparing the CRR, shear wave velocity (V_s) from triaxial tests and q_c from CPT calibration tests in reconstituted specimens with comparable fines contents, density and stress states, it was possible to verify the CRR- q_c as well as CRR- V_s correlations by direct comparisons for

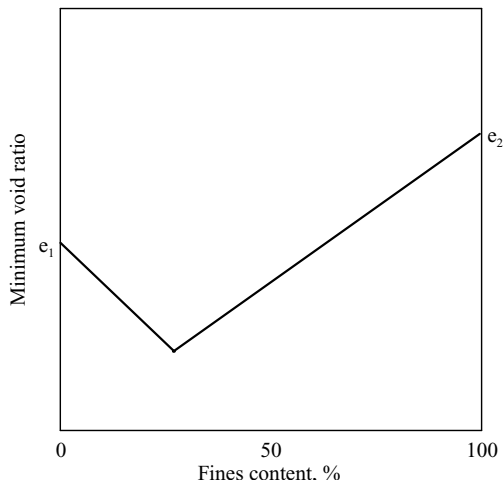


Figure 1. Effects of fines on void ratios (after Lade et al., 1998).

MLS (Huang et al., 2005). The results showed that the effects of fines on CRR- q_c and CRR- V_s correlations are significantly less than what has been suggested in currently available simplified procedures (Youd et al., 2001). Results from tests on MLS also suggest that the fines content affects the CRR- q_{cIN} correlation mainly through its influence on the drainage conditions during CPT (Huang et al., 2005). For tests in MLS with fines content, FC = 0 and 15%, CPT was essentially drained. The q_{cIN} adjustment became significant only when the fines started affecting the drainage conditions in CPT. The laboratory calibration of CRR- q_{cIN} correlation in MLS suggested that a more effective q_{cIN} adjustment scheme should be based on CPT drainage conditions rather than fines content.

Campanella et al. (1981) demonstrated the partial drainage characteristics of piezo-cone penetration tests (cone penetration tests with pore pressure measurement, CPTU) in clayey silt. By reducing the penetration rate from 20 mm/sec to 0.2 mm/sec, the pore pressure induced by cone penetration was significantly reduced. This penetration rate reduction resulted in a twofold increase of the effective q_c . The less pore pressure generation was apparently due to higher level of consolidation when penetration rate was reduced. The rate of consolidation for soil surrounding a cone tip is inversely proportional to the square of the cone diameter (Robertson et al., 1992). Therefore, changing the cone diameter can also duplicate the effects of penetration rate. McNeilan & Bugno (1984) reported their experience of CPT in offshore California silts. There was a 2 to 5 minute delay for recycling the underwater jacking unit when pushing the cone from seabed. At the start of the subsequent push, temporarily greater q_c and sleeve friction,

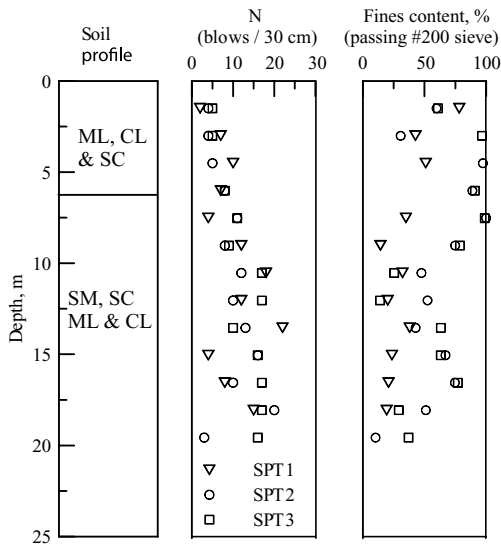


Figure 2. Soil profile at the Yuan Lin test site.

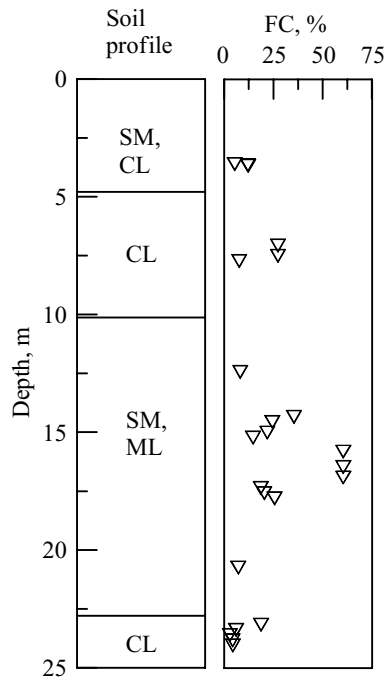


Figure 3. Soil profile at the Kao Hsiung test site.

f_s were measured. The increase in q_c and f_s were referred to as setups by McNeilan & Bugno (1984). The setup generally diminished with further penetration. For the duration of delay between recycling the jacking unit in their offshore CPT, silt and sandy silt had the most significant setups while CPT in clayey silt had essentially no setup. McNeilan & Bugno (1984) indicated that CPT may be considered drained when the hydraulic conductivity of the surrounding soil exceeded 10^{-3} cm/sec. For CPT in soils under the same density and stress states, the q_c value decreased as CPT became partially drained and eventually reached a stabilized value when CPT became undrained with hydraulic conductivity in the range of 10^{-6} – 10^{-7} cm/sec. The reason for setups is that partial drainage caused a lowered q_c due to pore pressure accumulation. The 2 to 5 minute delay was long enough for the sandy silt to dissipate pore pressure and increase its strength against cone penetration or generate the setup. The same delay time was not sufficient for clayey silt to allow significant pore pressure dissipation and thus no measurable setup in the subsequent penetration. For onshore CPTU, the delay can be allowed for as long as it takes to complete a pore pressure dissipation test. In this case, the existence of setup following the dissipation test can be used to evaluate the silty nature of the surrounding soil had the CPTU is indeed partially drained.

Because of the controversies on the issues of fines content effects and the importance of testing M/S soils in its undisturbed or natural state, the author embarked on a series of attempts to obtain undisturbed soil samples and evaluate characteristics of

Table 1. Physical properties of YLS and KHS.

Soil	Yuan Lin Soil (YLS)			Kao Hsiung Soil (KHS)			
FC, %	18	43	89	5	21	22	61
G_s	2.72	2.73	2.75	2.74	2.71	2.70	2.73
L.L., %	21–40			Non-plastic			
P.L., %	8–28			Non-plastic			

field CPTU in M/S soils. A test site was established in Yuan Lin Township of Central Taiwan and another test site in Kao Hsiung City of Southern Taiwan. As shown in Figures 2 and 3, the soil deposit at both test sites were characterized by a wide range of fines contents, well suited for the terminology of M/S soils. Tables 2 and 3 describe the basic physical properties and mineral contents of the soil grains, respectively. For more details of the test sites, geological background and physical properties of Yuan Lin Soil (YLS) and Kao Hsiung Soil (KHS), please refer to Huang & Huang (2007) and Lee et al. (2006). The paper describes the practical techniques developed for taking undisturbed samples in saturated M/S soils and field CPTU at the test sites. The implications in the characterization of M/S soils for liquefaction potential assessment and other related performance based geotechnical engineering analysis are discussed in light of these studies.

Table 2. Mineral contents of YLS and KHS.

Yuan Lin Soil (YLS)				
Mineral	Quartz	Clinochlore	Muscovite	Feldspar
Coarse,%	62-70	13-16	12-14	3-8
Mineral	Muscovite	Clinochlore	Quartz	Feldspar
Fines,%	39-51	28-38	12-28	1-4
Kao Hsiung Soil (KHS)				
Mineral	Slate	Quartz	Siltstone	Sandstone
Coarse,%	61-84	1-28	6-20	0-3
Mineral	Illite	Clinochlore	Quartz	Feldspar
Fines,%	30-66	22-26	5-32	4-16

2 UNDISTURBED SAMPLING IN M/S SOILS

Attempts of taking high quality samples of cohesionless soils from below ground water table can be traced back by at least half a century (Singh et al., 1982). Challenges involved in taking good quality sand samples include prevention of the loss of sample during withdrawal and damaging soil structure during transportation. These challenges are formidable unless the samples were taken near the ground surface or by block sampling. Many techniques have been experimented over the years with different levels of success. Yoshimi et al. (1977) is believed to be the first among the more recent attempts in developing practical procedures of ground freezing and dry coring for sand sampling. A column of sand is frozen in situ and then cored out of the ground surface. Freezing of the bottom of sampling tube to prevent loss of a saturated sand sample during withdrawal was used by the US Corps of Engineers (Singh et al., 1982). Ishihara & Silver (1977) reported their efforts of taking large diameter Niigata sand samples under ambient temperature. Upon withdrawal, the sample was allowed to drain freely for a period of 12-24 hours and then frozen by spraying the sampling tube with liquid nitrogen. Researchers from Japan and North America have generally considered in situ ground freezing (Hoffman et al., 2000) and coring to be a superior method for obtaining undisturbed samples of sand.

Provided drainage is not impeded and no change in void ratio occurs during freezing, the in situ structure can be reserved. Studies have indicated that this structure preservation is possible if free drainage is allowed in at least one direction during freezing (Singh et al., 1982). The reservation of soil structure is further enhanced if freezing is conducted under a confining stress (Yoshimi et al., 1977).

For M/S soils, especially when fines contents are high, drainage can be significantly impeded in the field. Ground freezing in M/S soil with high fines content is prone to void ratio change due to heaving.

Also, ground freezing is very costly in comparison with regular boring and piston sampling procedure. In an effort to develop more cost effective techniques to obtain high quality samples in M/S soils, the author used Laval sampler and a gel-push sampler. In both cases, the soil samples were taken under ambient temperature. The Laval sampler was used to retrieve M/S soils at the Yuan Lin test site. The gel-push sampler was used at the Kao Hsiung test site to take M/S soil samples. Details of the field sampling and sample preservation/packaging procedures are given in the following sections.

2.1 Laval sampling

The Laval sampler as schematically described in Figure 4 was developed at Laval University (La Rochelle et al., 1981), originally for taking high quality samples in sensitive clay. The sampler is made of two main parts; a sampling tube and an overcoring tube. To take a sample, the drill rig pushes the sampling tube into the bottom of the borehole while rotating the overcoring tube. The steel teeth and cutters were located at 20 mm behind the bottom of the sampling tube. During penetration, the head valve was kept open to allow drill mud circulation and thus removal of soil cuttings. The Laval sample can be 450 to 550 mm long. After a waiting period of 5 to 30 minutes, the head valve was closed and the bottom of the sample sheared by rotating the inner rod. The sample was then retrieved to the ground surface.

A Longyear 38 drill rig was used to prepare the borehole and operate the Laval sampler. The boreholes were extended by a 330 mm diameter fishtail device. The soil cuttings were removed with a mud flow that

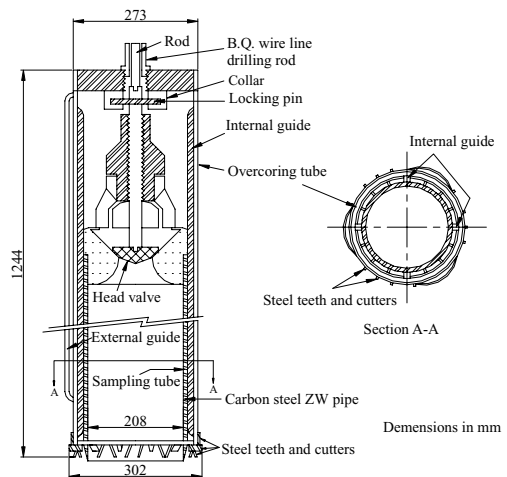


Figure 4. Schematic view of the Laval sampler (after La Rochelle et al., 1981).

consisted of a mixture of bentonite and barite. The density of the drill mud was maintained between 1.1 and 1.3 times that of water. After reaching the sampling depth, the fishtail device was removed from the borehole to give room for the Laval sampler.

Samples taken from soil layers expected to have medium or high fines contents were extruded on site. The sample was cut with a wire saw into 120 to 180 mm long segments and placed on a pre-waxed wooden board. The sample along with the wooden board was then wrapped in three layers of wax and two layers of plastic film. The sealed samples were kept in a moisturized container during transportation and laboratory storage.

The samples taken from soil layers expected to have low fines contents (fines contents less than 30%) remained in the sampling tube and kept vertical until it was completely frozen. A procedure referred to as the unidirectional freezing reported by Konrad et al. (1995) was followed to solidify the sample without causing volume change. The soil along with the sampling tube was placed in a Styrofoam lined wooden box and gradually frozen from top of the sample by dry ice at -80°C . A backpressure equal to the water head within the sample was applied by means of nylon tubing connected to the bottom of the sample to ensure that no water can drain under gravity. The bottom drainage and backpressure assured pore water drainage only due to water volume expansion during freezing. The amount of expelled water and temperature at the bottom of the soil sample were monitored as the freezing progressed. The freezing process took 15 to 24 hours, upon which the temperature at the bottom reached below 0°C . Figure 5 depicts a record of time versus expelled water volume and temperature measured at the bottom a soil sample. The frozen samples were stored in a freezer during shipping and laboratory storage until the time of shearing test.

2.2 Gel-push sampling

The gel-push sampler developed in Japan (Tani & Kaneko, 2006; Lee et al., 2006) as schematically shown in Figure 6 is a modified version from a 75 mm Osterberg piston sampler (also known as a Japanese sampler). A skid mount drill rig was used to perform the drilling and sampling operation. Bentonite drill mud was used to stabilize the borehole. Sand sample was taken by pushing the gel-push sampler as typically done for piston sampling in clays. Because of the high frictional resistance in granular soils, it is usually not possible to retrieve sand sample by pushing. The gel-push sampler injects a water soluble polymeric lubricant (the gel) from the sampler shoe to facilitate push sampling. A shutter located at the tip of the sampler remained open during pushing. A slight reverse motion by injecting water into the gel chamber triggers the closure of the shutter before the sample

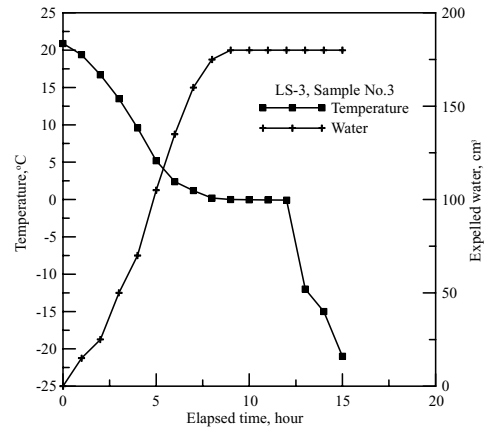


Figure 5. Water volume expelled and temperature variation with time.

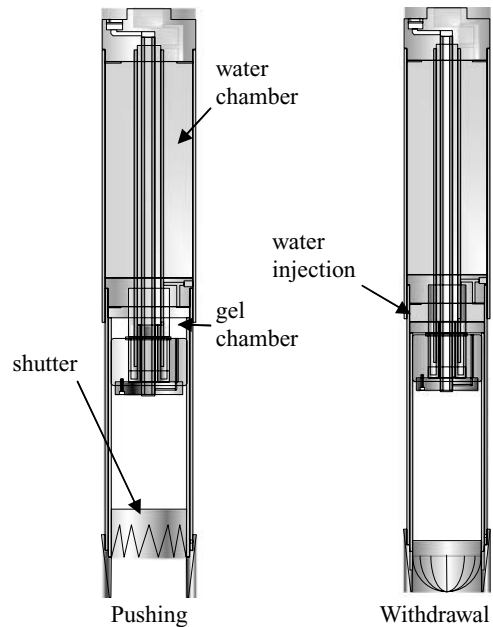


Figure 6. Schematic views of the gel-push sampler (after Lee et al., 2006).

is retrieved. The closed shutter prevents the sample from falling during withdrawal. Upon withdrawal of the sampling tube above ground, the ends of the tube were sealed with Styrofoam plugs. No freezing was conducted for the samples. The sampling tubes were stored in a well cushioned container for transportation. An accelerometer was attached to the sampling tube where the acceleration readings were continuously recorded during shipping.

3 LABORATORY TESTS ON UNDISTURBED M/S SAMPLES

3.1 Laboratory tests on laval samples

The laboratory tests included a series of cyclic triaxial tests, with shear wave velocity measurements using bender elements. The frozen Laval samples were kept in a freezer under -20°C . Cutting of the frozen sample by sawing and coring could induce enough heat to thaw the sample and cause significant disturbance. To minimize disturbance, the frozen sample was first surrounded by dry ice to lower the temperature to -50°C . The frozen Laval sample was then cut to obtain two, 170 mm long sections using a band saw, while surrounding the sample with dry ice. Four, 70 mm diameter specimens were cored from the 170 mm long section. The specially designed coring device had its cutter teeth slightly smaller than the tube to create a gap between the specimen and the tube during coring. Small holes drilled on the side of the core tube facilitate venting of the soil cuttings generated by the coring. Upon coring the specimen height was trimmed down to 140 mm by a hand saw. A small slot of 1.5 mm wide, 12 mm long and 5 mm deep was cut at the top and bottom of the trimmed specimen to give room for the insertion of bender element. The specimen was kept frozen during this preparation stage. Thawing took place after the specimen was seated in the triaxial cell, under a confining stress of 20 kPa and cell water temperature of 5°C . The pore water under a controlled temperature of 8 to 10°C was forced to enter the specimen from the bottom under a back pressure of 10 kPa. The thawing process lasted approximately 1 hour. The amount of water absorbed by the specimen and the change of specimen height were monitored during the thawing process.

The triaxial specimen taken from Laval samples was saturated under a back pressure of 500 kPa. Pore pressure parameter B values obtained after saturation had a minimum value of 0.99. Upon saturation, the specimens were isotropically consolidated under an effective confining stress (σ'_c) of 100 kPa. Because of the relatively high compressibility of the soil specimens and absorption of water in the thawing process (for the frozen specimens), the amounts of pore fluid coming in and out of the specimens were recorded. At the end of triaxial test, the whole specimen was used to determine the water content. The post consolidation water content or void ratio (e), to be used in the analysis of test data, was back calculated from the end-of-the-test water content measurement.

Upon triaxial tests on undisturbed specimens, soil specimens cut from the same Laval sample (i.e., same borehole and depth) were dismantled, fully mixed and oven dried to make reconstituted specimens. The reconstituted specimens were prepared using the moist tamping (MT) and water sedimentation (WS) methods.

All reconstituted specimens were saturated under a back-pressure of 500 kPa and had a minimum B of 0.95. The MT and WS specimens were made in an attempt to match the void ratio of the corresponding Laval samples. In most cases, however, the reconstituted specimens had void ratios lower than those of the Laval samples. For the non-frozen Laval samples, the 170 mm sections were cut by a wire saw. Four, 70 mm diameter and 140 mm high triaxial specimens were trimmed by hand using a wire saw and a knife, from each section. Slots on top and bottom of the specimens were cut to give room for the bender elements.

Figure 7 shows a comparison of shear wave velocity, V_s taken from the cyclic triaxial test specimens and those from different field measurements, normalized with respect to σ'_v or V_{s1} . V_{s1} is computed as described by Andrus & Stokoe (2000) where

$$V_{s1} = V_s \left(\frac{p_a}{\sigma'_v} \right)^{0.25} \quad (1)$$

p_a is a reference pressure of 100 kPa. The field shear wave velocity measurements included P-S logging and seismic piezo-cone penetration tests (SCPTU). The depths of the V_{s1} from Laval samples (LS) are in reference to those where the samples were taken. For laboratory measurements using bender elements, $V_s = V_{s1}$ as the specimens were under an effective confining stress (σ'_c) of 100 kPa, which is also isotropic ($\sigma'_c = \sigma'_v$). Although there were some scattering among the field measurements, the laboratory V_{s1} values are comparable to those of field measurements.

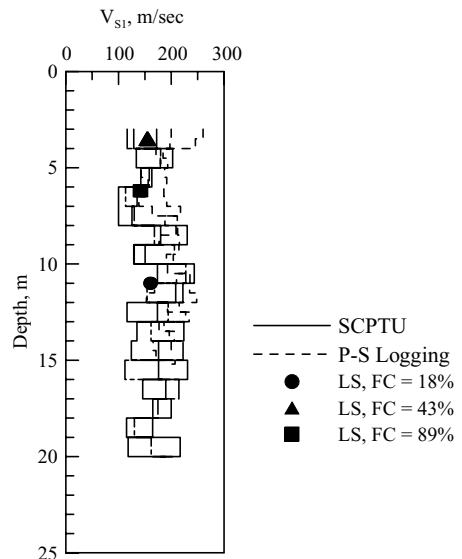


Figure 7. Comparison of laboratory and field V_{s1} measurements in YLS.

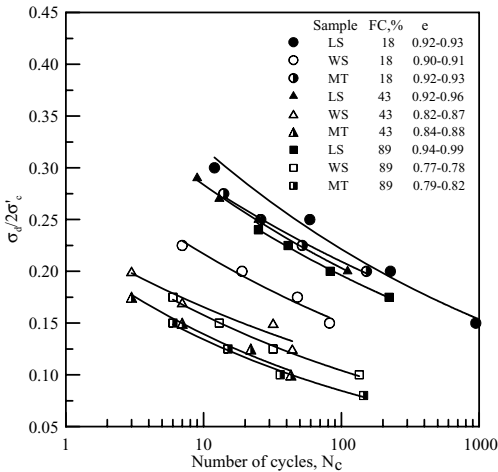


Figure 8. Cyclic resistance of the YLS.

The discrepancies of V_{s1} values from different sources may well be due to differences in shearing modes and applied lateral stress for the case of bender element tests.

Upon V_s measurement, the soil specimen was then subjected to a cyclic deviator stress, σ_d in axial direction at 0.1 Hz. Three to five cyclic triaxial tests were performed using a uniform sinusoidal loading condition with various $\sigma_d/2\sigma'_c$ ratios. Figure 8 depicts the cyclic triaxial test results in terms of the $\sigma_d/2\sigma'_c$ versus the number of cycles (N_c) that produces an axial strain of 5% in double amplitude. For comparison purpose, a cyclic resistance ratio (CRR) is defined as the interpolated $\sigma_d/2\sigma'_c$ that corresponds to N_c of 20. For the LS specimens, the CRR decreased by 13% as the FC increased from 18 to 89%. In the case of WS and MT specimens, the decrease of CRR was 29 and 55%, respectively as the FC increased from 18 to 89%. The reconstituted specimens had lower CRR than that of the corresponding LS specimens. For FC = 18%, the CRR of MT specimens was higher than that of WS specimens. This trend is reversed as the FC = 43 and 89%.

Figure 9 compiles the relative values of CRR and V_{s1} taken from tests reported above, as a function of fines content for specimens prepared by different methods. The relative values are presented as ratios of the parameter normalized with respect to the same parameter from tests using 18% fines content specimens. The results show that for the two types of parameters compared, LS specimens had the least sensitivity to fines contents. The most exaggeration of the effects of fines came from the MT specimens. The discrepancies among specimen preparation methods existed even with the significant differences in void ratios among the reconstituted specimens. The fines

content effects for non-LS specimens may be even more significant, had the void ratios of the reconstituted specimens with FC = 43 and 89% could be made as high as those of 18%.

3.2 Laboratory tests on gel-push samples

The soil sample extruded out of the gel-push sampler was trimmed to a diameter of 70 mm to fit the triaxial testing device and remove a shell of soil that was impregnated by the gel during field sampling. The trimmed soil specimen was inserted directly into a rubber membrane lined sample holder. The design of the sample holder shown in Figure 10 follows that of Dharma & Sanin (2006), where a layer of sponge was placed between the rubber membrane and the metal split mold. The sponge was compressed initially by the application of vacuum to give room for insertion of the soil specimen. Upon release of vacuum, the sponge

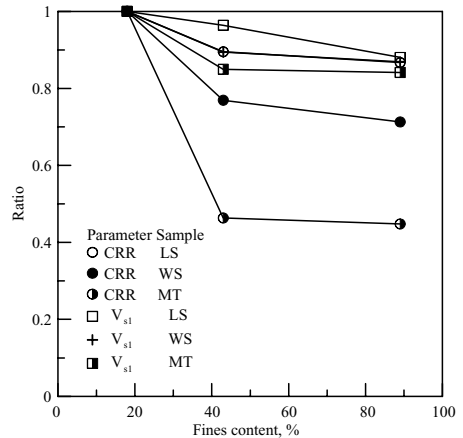


Figure 9. Relative values as a function of FC.



Figure 10. The sample holder.

expansion provides a confining stress on the granular soil specimen until the specimen is seated in the triaxial cell and vacuum resumed through the drainage lines. By maintaining the confining stress the sample holder minimizes the chance of disturbance during triaxial test set up.

A series of isotropically consolidated cyclic triaxial tests and K_0 consolidated undrained axial compression triaxial tests (CK₀U-AC) were conducted on gel-push samples. All triaxial specimens were consolidated to σ'_v comparable to the in situ overburden stress. The V_s value of the specimen upon consolidation was measured in the triaxial cell with bender elements. Figure 11 compares the V_s measurements from bender elements and those from the field seismic

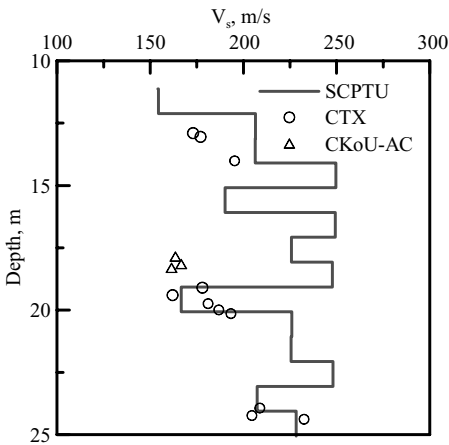


Figure 11. Comparison of V_s between the bender element and SCPTU measurements (after Lee et al., 2006).

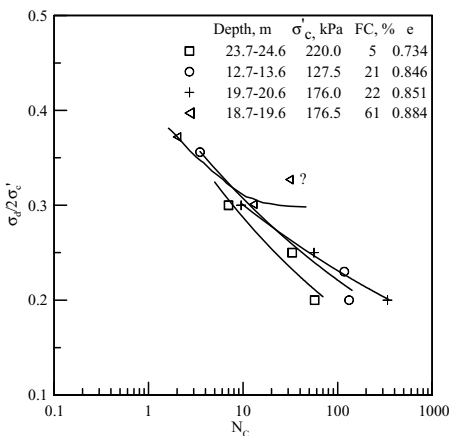


Figure 12. Cyclic resistance of the KHS (after Lee et al., 2006).

cone penetration tests (SCPTU). For the most part, the laboratory V_s falls within or close to the range of those from SCPTU at comparable depths. The cyclic triaxial test followed after the V_s measurement. Results of the cyclic triaxial tests are shown in Figure 12.

4 FIELD PIEZO-CONE PENETRATION TESTS

Considering the importance in detecting the drainage conditions during cone penetration in M/S deposits, attempts were made in the field tests to ascertain the drainage conditions associated with cone penetration. A series of piezo-cone penetration tests (CPTU) using a standard cone (cone cross sectional area = 10 cm²) penetrating at 20 mm/sec (the standard CPTU), a large cone (cone cross sectional area = 15 cm²) penetrating at 20 mm/sec (the large CPTU), and a standard cone penetrating at 1 mm/sec (the slow CPTU) were conducted at the Yuan Lin test site. The pore pressure element was located immediately behind the cone face, at the u_2 position. Profiles of CPTU results that include friction ratio, $R_f (= f_s/q_c \times 100\%)$ from tests at Yuan Lin site are shown in Figure 13. The results indicated no significant differences in q_c among three types of CPTU, considering drastic differences in cone size and/or penetration rate. Because of the time consuming nature, slow CPTU was conducted only in depth levels where Laval samples were taken. The u_2 values from large CPTU were mostly identical to those from the standard CPTU. The u_2 in slow CPTU matched well with the hydrostatic pressure u_0 , indicating that 1 mm/sec was slow enough to allow the penetration induced pore pressure to fully dissipate and reach equilibrium in most parts with the surrounding hydrostatic pressure.

The R_f values from slow CPTU were consistently higher than those of standard and large CPTU. No consistent correlation between the increase in R_f and soil fines contents could be identified. During CPTU, the soil element ahead of the cone tip experiences an increase in mean normal stress as the cone tip approaches. This increased stress is released as the soil element passes the base of the cone face and thus a reduction in lateral stress against the friction sleeve immediately behind the cone tip. In a slow CPTU, more time is allowed for the soil element to creep towards the friction sleeve and develop higher lateral stress against the friction sleeve and thus higher f_s . This creeping is believed to be the main cause of the increase in f_s or R_f when cone penetration rate was reduced from 20 to 1 mm/sec as the change in penetration rate did not have significant effects on q_c .

Profiles from standard and slow CPTU performed at Kao Hsiung site are shown in Figure 14. The slow CPTU was conducted from 9.8 to 25 m, the same depth range where gel-push samples were taken at Kao Hsiung site. The results in terms of q_c , u_2 and R_f

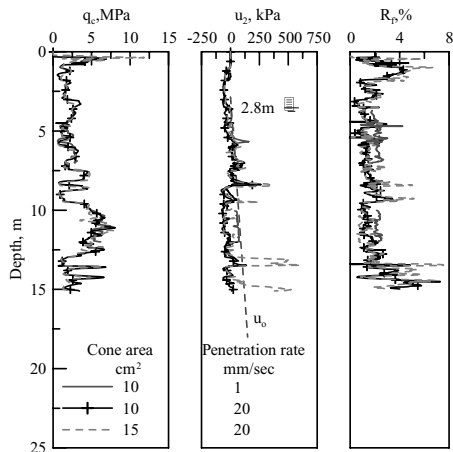


Figure 13. Profiles from CPTU at Yuan Lin test site.

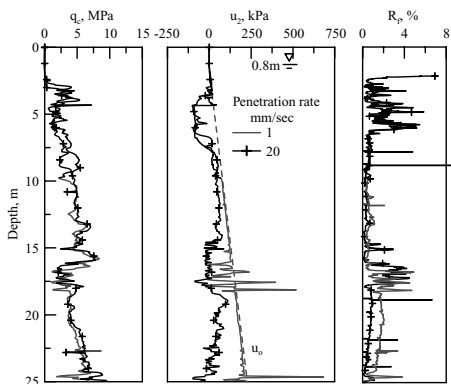


Figure 14. Profiles from CPTU at Kao Hsiung test site.

and their relationship with penetration rates are very similar to those from Yuan Lin site. No significant differences in q_c and u_2 were noticed from CPTU with a 20 times difference in penetration rate.

At Yuan Lin site, the standard CPTU was coupled with pore pressure dissipation tests from 3.5 to 12.5 m, at 1 m intervals. The same was included in the standard CPTU at Kao Hsiung site from 9.8 to 20.8 m. In a pore pressure dissipation test, the cone penetration was suspended while u_2 was continuously recorded until it reached equilibrium with u_0 . Figures 15 compares parts of the q_c profiles obtained from the field CPTU at two test sites and those from CPTU in reconstituted MLS specimens in a calibration chamber. The field data are the enlarged segments of the corresponding profiles included in Figures 13 and 14. This enlargement allows the change in q_c and its relationship with pore pressure dissipation tests to be visualized.

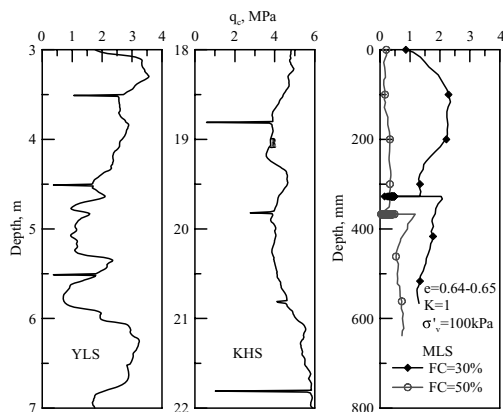


Figure 15. Comparison between field and laboratory q_c profiles.

The MLS specimens with fines contents at 30 and 50% were prepared by MT method where the sand and fines were fully mixed. The MLS specimen was saturated under a back pressure of 300 kPa during CPTU calibration test. A pore pressure dissipation test was conducted in MLS at 300–400 mm depth in the calibration chamber. For CPTU in MLS, there were distinct setups as referred to by McNeilan & Bugno (1984) or significant increase in q_c immediately following the pore pressure dissipation test or the start of the subsequent push. For the field CPTU where the fines contents could exceed 50%, the pore pressure dissipation tests were basically evidenced by a sharp decrease (due to suspension of the cone penetration) and regain of q_c values as penetration resumed, without significant setups.

The laboratory results on MLS indicate that at fines contents above 30%, CPTU behaved as a partially drained test. The effects of partial drainage were demonstrated by the presence of significant setups following a pore pressure dissipation test. The field CPTU at both test sites were close to drained conditions even when the fines contents reached as high as 89%. The drastic differences between CPTU in laboratory prepared, well mixed silty sand and natural silt/sand in the field are likely due to the heterogeneity existed in natural soil. It is believed that the presence of closely spaced free draining sand layers made the field CPTU behave as a drained test in a silty soil mass.

5 IMPLICATIONS IN LIQUEFACTION POTENTIAL ASSESSMENT FOR M/S SOILS

The above described tests in YLS and KHS offered a database to evaluate the $CRR-q_{cIN}$ correlations based

on tests that involved natural soil samples. Under the framework of simplified procedure, both CRR and q_{cIN} are normalized with respect to σ'_v of 100 kPa or one atmospheric pressure. The soil deposits at Yuan Lin and Kao Hsiung test sites were assumed to be normally consolidated with ratio of effective horizontal stress, σ'_h over σ'_v , $K = 0.5$ in the field. The inference of CRR under anisotropic stress conditions from isotropically consolidated cyclic triaxial tests (CRR_{CTX}) followed the procedure by Ishihara (1996) as,

$$CRR = CRR_{CTX} \frac{1 + 2K}{3} \quad (2)$$

For YLS, the CRR_{CTX} conducted under σ'_c of 100 kPa on LS specimens, as included in Figure 8 were used. For KHS, the CRR_{CTX} obtained from cyclic triaxial tests on gel-push specimens shown in Figure 12 were used to infer CRR using Equation 2. The average value of q_c from comparable depths where the undisturbed samples were taken was normalized as:

$$q_{cIN} = \left[\frac{q_c}{P_{a2}} \right] \left[\frac{P_a}{\sigma'_v} \right]^{0.5} \quad (3)$$

where

P_a = one atmosphere in the same units as σ'_v

P_{a2} = one atmosphere in the same units as q_c

Figure 16 plots the $CRR-q_{cIN}$ correlation of MLS according to laboratory cyclic triaxial tests and CPTU performed in a calibration chamber, reported by Huang et al. (2005) and those from field CPTU and cyclic triaxial tests on natural YLS and KHS. The $CRR-q_{cIN}$ data points have the following characteristics:

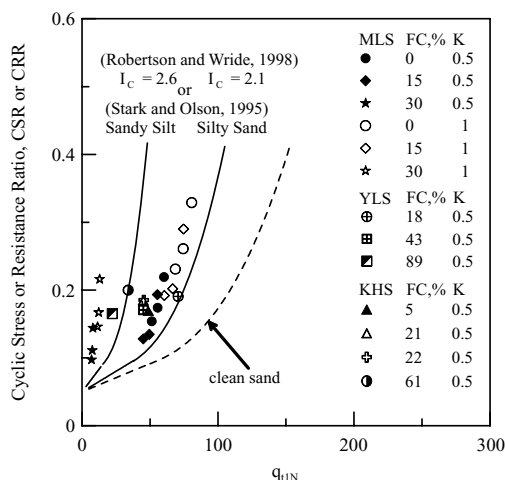


Figure 16. The $CRR-q_{cIN}$ correlations from tests on MLS, YLS and KHS.

- All data points fell to the left of the $CRR-q_{cIN}$ correlation that corresponded to $FC = 15\%$ according to Stark & Olson (1995), and soil behavior index, $IC = 2.1$ according to Robertson & Wride (1998).
- For the wide range of fines contents involved in the field and laboratory tests on YLS and KHS, there was a general trend that the $CRR-q_{cIN}$ data points moved to the left as fines content increased. This trend was consistent with those suggested in the available $CRR-q_{cIN}$ correlations shown in Figure 16.
- The effects of fines according to tests in natural YLS and KHS were less significant than those suggested by tests using the artificial MLS specimens. At much wider range of fines contents, the lateral spread of $CRR-q_{cIN}$ data points based on tests in YLS and KHS shown in Figure 16 was less than those from tests using the reconstituted MLS specimens or suggested by the available $CRR-q_{cIN}$ correlations.

The fines content adjustment reflects two aspects in the $CRR-q_{cIN}$ correlations; the first aspect deals with the differences in mineral contents and/or grain characteristics between sand and fines; and the second aspect deals with the change in drainage conditions in CPTU resulted from the increase in fines contents. Ishihara & Harada (2008) demonstrated the differences in $CRR-q_{cIN}$ correlations among clean sands due to variations in mineral contents and/or grain shapes. The data presented in this paper have shown that the field CPTU conducted in YLS and KHS can all be considered as drained tests, regardless of the fines contents. Except for those of $FC = 61$ and 89% , the $CRR-q_{cIN}$ data points from YLS and KHS clustered closely with those from MLS with $FC \leq 15\%$ where CPTU was also drained. The fines in a silt/sand mixture are more likely to have higher contents of softer minerals as indicated in Table 2 and Huang et al. (2004). MLS, YLS and KHS have similar geological origin and contain relatively soft sand grains as demonstrated in their mineral contents. These similarities explain why the available $CRR-q_{cIN}$ data points from MLS, YLS and KHS gathered in a rather narrow range, except for the cases where FC exceeded 50% , and as long as the CPTU remained drained. Provided the CPTU remained drained, the soft minerals or their higher contents cause the $CRR-q_{cIN}$ correlations to move to the left. This is likely the reason for the $CRR-q_{cIN}$ data points with FC in excess of 50% to locate to the left and away from the cluster of all the $CRR-q_{cIN}$ data points from drained CPTU and with less fines contents.

The data presented by Amini & Qi (2000) have demonstrated that the stratification in silty sand does not have significant effects on the cyclic strength. The data presented herein however, demonstrated that the stratification in silt/sand soil can have significant

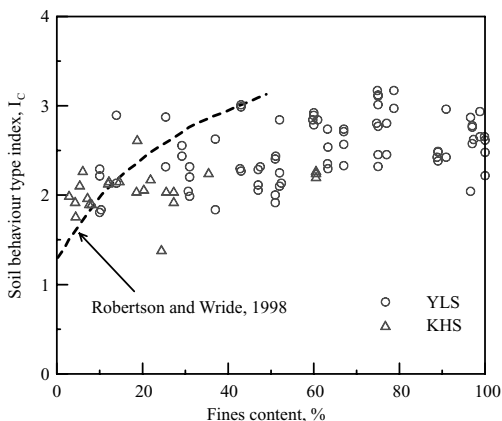


Figure 17. Comparison between I_c and fines contents.

impact on the drainage conditions of CPTU. The lack of free drainage would cause q_c to be much reduced and thus the $CRR-q_{cIN}$ correlations to move to the left.

Figure 17 compiles the available soil behaviour index, I_c (Robertson & Wride, 1998) values and their relationship with fines contents from field CPTU at Yuan Lin and Kao Hsiung sites. Figure 17 shows that the available data are rather scattered and have I_c mostly in the range of from 1.8 to 3.0. This trend does not seem to follow the empirical correlation between I_c and FC as proposed by Robertson & Wride (1998) which was restricted for $FC < 50\%$. The results indicate that the inference of fines content based on I_c may lead to significant and/or unpredictable error at least for the M/S soils tested.

6 CONCLUDING REMARKS

Studies performed by the author allowed direct comparisons among fines contents, CRR and q_{cIN} to be made for typical M/S soils in Taiwan. The studies involved laboratory tests on reconstituted and undisturbed natural soil samples and field CPTU as well as laboratory calibration chamber CPTU. These studies raised serious questions regarding the validity of the current understanding of how the fines affect the cyclic resistance and its estimation based on CPTU following the framework of simplified procedure. For the natural M/S soils reported herein, the effects of fines on cyclic strength and $CRR-q_{cIN}$ correlations are not nearly as significant as what have been reported.

The author postulate that the effects of fines on a freshly reconstituted specimen, destabilizing or not, may have been reduced or nullified by age. This is why, aged natural M/S soils showed significantly less effects of fines contents as indicated in Figure 9. The available data to support the above postulation are

limited. To ascertain if indeed the effects of fines are much reduced in natural M/S soils would require further tests on undisturbed samples. The Laval and gel-push samplers can make undisturbed sampling much more cost effective than the conventional ground freezing procedure. It is strongly recommended that the geotechnical profession should take advantage of these new developments and start performing tests on undisturbed samples on a routine basis. Conclusions made based on reconstituted specimens should be scrutinized with great care.

Significant adjustment in the $CRR-q_{cIN}$ correlation is called for if the fines contents are sufficient enough to cause the CPTU to be partially drained and thus q_c substantially reduced. In alluvial deposit where the silt/sand soils are often stratified, the CPTU can be a drained test even with substantial fines contents due to the presence of closely spaced free draining soil layers. While the stratification may not cause significant differences in cyclic strength of the silt/sand soil, its impact on cone tip resistance because of the change in drainage conditions may not be negligible. The drainage conditions in CPTU can be determined using pore pressure dissipation tests or by changing the rate of penetration. Had the drainage conditions remained the same, the amount of fines content adjustment should be associated with and limited to the effects caused by differences in mineral contents and/or grain characteristics between fines and sand. The ignorance of free draining nature of CPTU in stratified alluvial silt/sand soils may lead to excessive fines content adjustment and result in over estimation of safety factor against soil liquefaction.

The mixture of fines with sand can make the fines content adjustment complicated in many ways. The potential differences in mineral contents and/or grain shapes between fines and sand particles are important aspects that cause the shifting of $CRR-q_{cIN}$ correlations. The characteristics and magnitude of such shifting are apparently soil and site dependent. Local calibrations would be highly desirable to establish a fines content adjustment scheme and to account for the effects of mineral contents and/or grain shapes between fines and sand particles. These calibrations should be made based on direct comparisons of laboratory and field test results.

ACKNOWLEDGEMENTS

Parts of the research presented in the paper were funded by the National Science Council of Taiwan, ROC under contracts 97-2221-E-009-128, 96-2221-E-009-005, 95-2221-E-009-202 and 94-2221-E-009-043. Field sampling at Kao Hsiung test site was funded by Taiwan Construction Research Institute, Taipei, Taiwan. The author gratefully acknowledges their support.

REFERENCES

- Amini, F., & Qi, G.Z., 2000. Liquefaction testing of stratified silty sands. *Journal of Geotechnical and Geoenvironmental Engineering, ASCE* 126(3): 208–217.
- Andrus, R.D., & Stokoe, K.H., II, 2000. Liquefaction resistance of soils from shear-wave velocity. *Journal of Geotechnical and Geoenvironmental Engineering, ASCE* 126(11): 1015–1025.
- Campanella, R.G., Robertson, P.K. & Gillespie, D. 1981, "In-situ testing in saturated silt (drained or undrained?)", *34th Canadian Geotechnical Conference, Fredericton, New Brunswick*.
- Dharma, D., & Sanin, M.V., 2006. New sample holder for the preparation of undisturbed fined-grained soil specimens for laboratory element testing. *Geotechnical Testing Journal, ASTM* 29(3): GTJ12699.
- Høeg, K., Dyvrik, R., & Sandbaekken, G. 2000. Strength of undisturbed versus reconstituted silt and silty sand specimens. *Journal of Geotechnical and Geoenvironmental Engineering, ASCE* 126(7): 606–617.
- Hofmann, B.A., Segoo, D.C., & Robertson, P.K. 2000. "In situ ground freezing to obtain undisturbed samples of loose sand." *Canadian Geotechnical Journal* 126(11): 979–989.
- Huang, A.B., Hsu, H.H., & Chang, J.W. 1999. The behavior of a compressible silty fine sand. *Canadian Geotechnical Journal* 36(1): 88–101.
- Huang, Y.T, Huang, A.B., Kuo, Y.C., & Tsai, M.D. 2004. A laboratory study on the undrained strength of a silty sand from Central Western Taiwan. *Soil Dynamics and Earthquake Engineering* 24(9–10): 733–743.
- Huang, A.B., Huang, Y.T., & Ho, F.J. 2005. Assessment of liquefaction potential for a silty sand in central western Taiwan. *XVth International Conference on Soil Mechanics and Geotechnical Engineering*: 2653–2657, Osaka, Japan.
- Huang, A.B., & Huang, Y.T. 2007. Undisturbed sampling and laboratory shearing tests on a sand with various fines contents. *Soils and Foundations* 47(4): 771–781.
- Ishihara, K. 1993. Liquefaction and flow failure during earthquakes. *Geotechnique* 43(3): 351–415.
- Ishihara, K., & Silver, M.L. 1977. Large diameter sand sampling to provide specimens for liquefaction testing. *9th International Conference on Soil Mechanics and Foundation Engineering, Special Session 2*, Tokyo, Japan: 1–6.
- Ishihara, K. 1996. Soil behavior in earthquake geotechnics. Clarendon Press, Oxford, UK: 350p.
- Ishihara, K., & Harada, K. 2008. Effects of lateral stress on relations between penetration resistances and cyclic strength to liquefaction. *The 3rd International Conference on Site Characterization*, Taipei: 1043–1050.
- Koester, J.P. 1994. The influence of fines type and content on cyclic strength. Prakash S & Dakoulas P, editors. *Ground-failures under seismic conditions. ASCE Geotechnical Special Publication* 44.: 17–33.
- Konrad, J.M., St-Laurent, S. Gilbert, F., & Leroueil, S. 1995. Sand sampling below the water table using the 200 mm diameter Laval sampler. *Canadian Geotechnical Journal* 32: 1079–1086.
- Lade, P.V., Liggiio, C.D., & Yamamuro, J.A. 1998. Effects of non-plastic fines on minimum and maximum void ratios of sand. *ASTM Geotechnical Testing Journal* 21(4): 336–347.
- La Rochelle, P., Sarraihl, J., Tavenas, F., Roy, & Laroueil, S. 1981. Causes of sampling disturbance and design of a new sampler for sensitive soils. *Canadian Geotechnical Journal* 18(1): 52–66.
- Lee, W. F., Liao, H. J., & Ishihara, K. 2006. A study on engineering properties of Kaohsiung silty sand. (in Chinese), Internal Research Report, Taiwan Construction Research Institute, Taipei, Taiwan: 204 p.
- McNeilan, T.W., & Bugno, W.T. 1984. Cone penetration test results in offshore California silts. *Symposium on Strength Testing of Marine Sediments: Laboratory and In-Situ Measurements*, San Diego, ASTM STP 883: 55–71.
- Polito, C.P. 1999. The effects of nonplastic and plastic fines on the liquefaction of sandy soils, Ph.D. Thesis, Virginia Polytechnic Institute and State University, Blacksburg, Virginia.
- Robertson, P.K., & Wride, C.E. 1998. Evaluating cyclic liquefaction potential using the cone penetration test. *Canadian Geotechnical Journal* 35: 442–459.
- Seed, H.B., Tokimatsu, K., Harder, L.F., & Chung, R.M. 1985. Influence of SPT procedures in soil liquefaction resistance evaluation. *Journal of Geotechnical Engineering, ASCE* 111(2): 1425–1445.
- Stark, T.D., & Olson, S.M. 1995. Liquefaction resistance using CPT and field case histories. *Journal of Geotechnical Engineering Division, ASCE* 121(12): 856–869.
- Singh, S., Seed, H.B., & Chan, C.K. 1982. Undisturbed sampling of saturated sands by freezing. *Journal of the Geotechnical Engineering Division, ASCE* 108(2): 247–264.
- Tani, K., & Kaneko, S. 2006. Method of recovering undisturbed samples using water-soluble thick polymer. (in Japanese) Tsuchi-to-Kiso, *Journal of Japanese Geotechnical Society* 54(4): 145–148.
- Thevanayagam, S., Thenthan, T., Mohan, S., & Liang, J. 2002. Undrained fragility of clean sands, silty sands, and sandy silt. *Journal of Geotechnical and Geoenvironmental Engineering, ASCE* 128(10): 849–859.
- Xenaki, V.C. & Athanasopoulos, G.A. 2003. Liquefaction resistance of sand-silt mixtures: an experimental investigation of the effect of fines. *Soil Dynamics and Earthquake Engineering* 23: 183–194.
- Yamamuro, J.A. & Wood, F.M., 2004. Effect of depositional method on the undrained behavior and microstructure of sand with silt. *Soil Dynamics and Earthquake Engineering* 24(9–10): 751–760.
- Yoshimi, Y., Hatanaka, M., & Oh-Oka, H. 1977. A simple method for undisturbed sand sampling by freezing. *9th International Conference on Soil Mechanics and Foundation Engineering, Special Session 2*, Tokyo, Japan: 23–28.
- Youd, T.L., Idriss, I.M., Andrus, R.D., Arango, I., Castro, G., Christian, J.T., Dobry, R., Liam Finn, W.D., Harder Jr., L.F., Hynes, M.E., Ishihara, K., Koester, J.P., Liao, S.S.C., Marcuson III, W.F., Martin, G.R., Mitchell, J.K., Moriwaki, Y., Power, M.S., Robertson, P.K., Seed, R.B., & Stokoe II, K.H. 2001. Liquefaction resistance of soils: summary report from the 1996 NCEER and 1998 NCEER/NSF workshops on evaluation of liquefaction resistance of soils. *Journal of Geotechnical and Geoenvironmental Engineering, ASCE* 127(10): 817–833.

Satisfaction and dissatisfaction of port facilities designer facing to the performance based design methodology

T. Sugano & S. Miyata

Port and Airport Research Institute, Japan

ABSTRACT: Performance objectives are expressed as an acceptable level of damage, typically categorized as one of several performance levels, such as immediate occupancy, time required for restoration or collapse prevention, given that ground motion of specified severity is experienced. Factors affecting the accurate evaluation of deformation to port facilities during earthquakes by means of finite element analysis are introduced through two case studies. Not only agreement of liquefaction strength curve with test result but also well agreement of excess porewater pressure generation near liquefaction and development of strain must be required in the element test because two analyses that have the same liquefaction strength but different excess porewater pressure generation and strain characteristics resulted in non-negligible difference of residual deformation. Experience or judgment of the engineer in determining liquefaction parameter affects prediction of residual deformation. Then, notes to be taken care in evaluating liquefaction parameters are introduced based on the case study. Finally, discussion is extended to in-situ measurement of space and mechanical properties of the ground and damage investigation for the development of performance-based design.

1 INTRODUCTION

Design specification of port facilities (Japan Port and Harbour Association 1999) moved fundamental design concept from conventional specification design to performance-based design in April 2007. According to the new design specification, both performance requirement and specific safety guideline are specified to each type of facilities, and designers are required to satisfy them. Although the procedure which proves whether they are correct or not is not written definitely in the design specification, it is clear that reliable method must be used in order to fulfill accountability.

Deformation of a structure is listed as an examination of reference against level-2 ground motion, the strongest earthquake motion expected at the interested site. According to the recommendation of the design specification (Japan Port and Harbour Association 1999), reliable numerical analysis and/or model test is recommended to evaluate it. In the engineering practice at present, computer program FLIP (Iai et al., 1990), a earthquake response analysis computer program based on effective stress, is frequently used as a tool to evaluate deformation partly because it has been used in the engineering practice of the design of port facilities and partly because it is known that FLIP succeeded to explain damage to port facility in the past earthquakes (Iai et al., 1996).

FLIP employs, so called, multi-spring model for shear deformation, which has a characteristic to consider rotation of principal stress direction, and stress

path model for excess porewater pressure generation under undrained condition; it computes excess porewater pressure generation of soil under undrained condition. Five parameters are used to express undrained behavior under earthquakes, which will be called as liquefaction parameters in this paper.

Excess pore water pressure generation reduces effective stress. As a result, shear stiffness decreases with decrease of effective stress, and deformation increase. Therefore, if shear deformation of liquefied layers has dominant effect on the deformation characteristics of whole structure, choice of the value of liquefaction parameters becomes a key issue in evaluating the deformation of the structure.

In this paper, we show fundamental strategy to evaluate liquefaction parameters, and some notes to determine them based on the result of case studies.

2 METHODS TO EVALUATE LIQUEFACTION PARAMETERS

FLIP uses five parameters, w_1 , p_1 , p_2 , c_1 and S_1 , or six parameters if phase transform angle ϕ_p is counted as one parameter. Details of the parameters are described in Morita et al. (1997) and are explained briefly in the following.

Parameter w_1 controls excess porewater pressure generation expressed as a function with respect to plastic work. The larger w_1 value increases liquefaction strength or reduces excess porewater pressure generation.

Parameter p_1 controls speed of excess porewater pressure generation when excess porewater pressure ratio (ratio of excess porewater pressure to initial effective mean stress) is less than 0.6. Smaller p_1 value results in higher speed of excess porewater pressure generation.

Parameter p_2 controls speed of excess porewater pressure generation when excess porewater pressure ratio is larger than or equals to 0.6. Smaller p_2 value accelerates excess porewater pressure generation at high porewater pressure.

Parameter c_1 defines minimum shear stress ratio (shear stress amplitude under liquefaction strength test divided by initial effective mean stress) of liquefaction strength curve. As c_1 becomes larger, decrease of shear stress ratio at large number of loading cycles becomes smaller.

Finally, parameter S_1 is used to stabilize numerical analysis. It must be closer value to zero, and 0.005 or similar has been used in the engineering practice.

Values of these parameters are evaluated by trial-and-error procedure to agree liquefaction-strength curve with that by liquefaction strength test if liquefaction strength test by means of undrained cyclic triaxial test or hollow cylinder torsional shear test is conducted with undisturbed samples retrieved at the site.

It is also important not only to adjust liquefaction strength curve but also to consider excess porewater pressure generation the transient state to liquefaction and to consider development of shear strain.

If in-situ sample cannot be obtained in such a case that soil improvement will be made, for example, they are evaluated from equivalent or target SPT- N value and fines content based on simplified method to determine parameters (Morita 1997). It is, however, noted and recognized that excess porewater pressure generation and development of strain characteristics obtained by the analysis may not represent those of in-situ soil.

3 NOTES TO SET LIQUEFACTION PARAMETERS

As described in previous paragraph, liquefaction parameters are evaluated so that liquefaction strength curve agrees with test result, but it does not ensure that liquefaction characteristics can be well reproduced.

Figure 1 shows schematic figure of Rokko Island RF3 pier damaged during the 1995 Hyogoken-nambu (Kobe) earthquake. Past investigation (Inagaki et al., 1996) discussed parameters used in the analysis and proved accuracy of analysis. In this report, effect of different set of liquefaction parameters on the result of the analysis is introduced.

Two sets of parameters are used in the examination. Two sand layers are liquefiable in this model; the one is reclaimed sand in the backfill ground and the other is

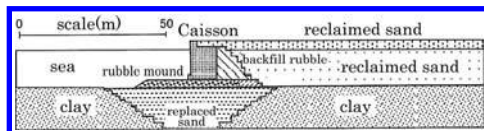


Figure 1. Analyzed model and soil profiles.

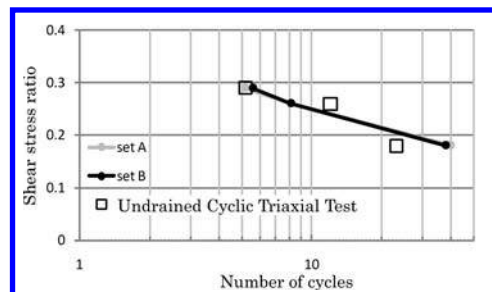


Figure 2. Comparison of liquefaction strength curve.

replaced sand beneath the caisson. For simplicity, liquefaction parameters for replaced sand are chosen as parameters. Both the NS and UD components of acceleration recorded at GL-32 m in Port Island during the 1995 Kobe earthquake is used as input wave.

The set of liquefaction parameters used in the analysis is as follows:

Parameter set A

Liquefaction parameters are the ones used in the past investigation. These parameters are evaluated so that liquefaction curve agrees with that of undrained cyclic triaxial test of in-situ undisturbed samples by means of frozen sampling technique. The test result is shown in Figure 2 with result of simulation.

Parameter set B

Liquefaction parameters are re-evaluated so that the liquefaction strength becomes same as that of set A, but transient process of excess porewater pressure generation and development of strain is out of consideration; parameters are identified only focusing on agreement of liquefaction strength, which makes time to determine parameters small.

Identified parameters are shown in Table 1. Considering the meaning of parameters described in the preceding, excess porewater pressure easily generates by set B at high excess porewater pressure region.

Other conditions such as Rayleigh damping, mechanical property of soil, etc. are set same in both analysis; difference is only liquefaction parameters of the replaced sand beneath the caisson. Method and notes

Table 1. Liquefaction parameters.

Parameter	Phase transform angle	w_1	p_1	p_2	c_1	S_1
set A	30°	9.0	0.6	0.9	1.8	0.005
set B	30°	16.0	0.5	1.9	1.4	0.005

for evaluating liquefaction parameters are described in CDIT (1997).

Result of simulation of liquefaction strength test is shown in Figure 2 with test result. Both liquefaction strength curves agree to each other as intended. It indicates that there is not unique set of liquefaction parameters to express the liquefaction strength.

Figure 3 shows residual deformation by two analyses and Figure 4 shows a time history of the caisson top horizontal displacement. Although both models show same liquefaction strength, displacements differ significantly; displacement at the top of the caisson by set B liquefaction parameters is about 1.5 times larger than that by Set A liquefaction parameters for both horizontal and vertical components. Deformations of seabed just in front of the caisson are also different to each other. In addition, as shown in the time history of tilt of the caisson in Figure 5, residual displacements of the caissons do not agree.

In order to investigate the reason of the difference, time histories of the excess porewater pressure and shear strain of the element shown as a hollow circle in Figure 3, and stress-strain curve of the element are shown in Figures 6 and 7, respectively.

As seen in Figure 6, shear strain accumulates towards the sea, which indicates that displacement of the caisson was mainly caused by the liquefaction of replaced

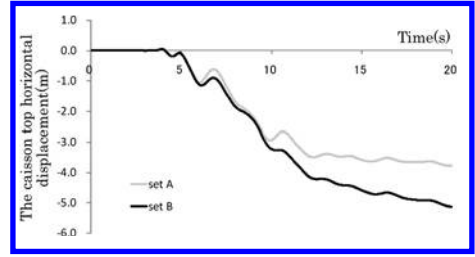


Figure 4. Time history of the caisson top horizontal displacement (–:seaward).

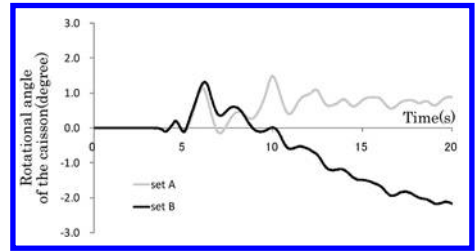


Figure 5. Time history of rotational angle of the caisson (+:CCW).

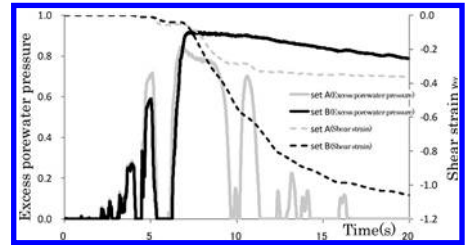


Figure 6. Excess porewater pressure/share strain time history.

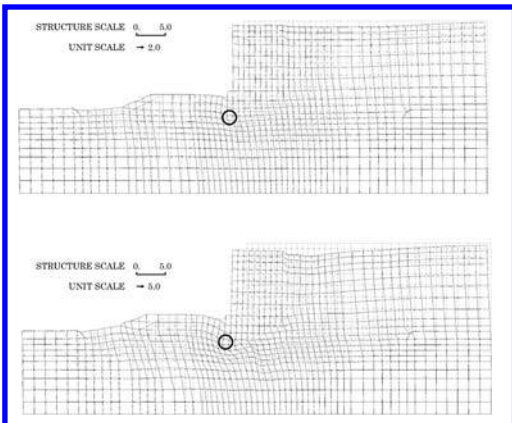


Figure 3. Residual deformation.(Upper: set A; Lower: set B; ○: Compared elements).

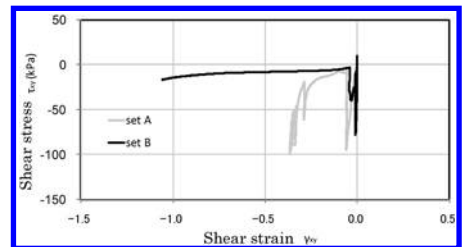


Figure 7. Shear stress-strain relationship.

sand. Rate of increase of shear strains and development of excess porewater pressure are different to each other, especially in the latter half of the analysis. It result in the larger decrease of shear stiffness in Set B analysis than that in set A analysis as is shown

in Figure 7. It is clear that this difference of shear stiffness or shear strain of the liquefiable layer caused significant difference of analyses. It is again noted that liquefaction strength are same in both cases.

Then a question arises that what is the relevant procedure to evaluate liquefaction parameters? The following procedures are recommended ones at present.

- Check that time histories of axial strain, excess porewater pressure, etc. during liquefaction strength test can be reproduced by numerical analysis.
- Ensure that liquefaction strength curve defined by 1, 2, 5 and 10 percent of double amplitude axial strain is well simulated.

It may require, however, many man-powers because the procedure to determine the value of liquefaction procedure is a trial-and-error procedure. Therefore, increase of target behavior requires more time to evaluate liquefaction parameters. A more simple procedure is encouraged to be developed in the future.

At the same time, discussions must be required whether conventional liquefaction strength test is a relevant method to grasp the dynamic property of liquefiable soil or not. Discussion is also made whether simulation of the analysis using the parameters that are evaluated based on liquefaction strength test is relevant or not. These indicate that improvement to evaluate liquefaction parameters in FLIP may be possible. It is to be noted and is important in the performance based design that the all the obtained information must be reflected in the design.

4 OTHER COMMENTS

The followings are issues to be considered in the practical analysis.

4.1 Characteristics of reclaimed soil

The reclaimed soil is not homogeneous, and its mechanical property scatters. Borehole investigation are frequently made in several tens meters distance, but this distance may not be relevant to grasp the soil profiles and mechanical property. It is strongly encouraged to improve resolution in space or to develop a relevant non-destructive examination procedure against the ground.

4.2 Modeling of improved soil

It is sometimes difficult to control mechanical property of improved soil constant. If it scatters, a question arises that small numbers of check borehole test can represent the whole behavior of the improved area. It is not realistic to make laboratory test of undisturbed samples because it requires longer construction duration.

The accuracy of checking by means of effective stress earthquake response analysis etc. against remediated and non-remediated facilities is in practical level.

4.3 High accuracy of checking

At present, two-dimensional analysis is predominant, whereas actual structure is in three-dimension. As shown in Figure 8, for example, displacement of the quay wall scatters along the shore. Then how can accuracy of two-dimensional analysis be evaluated. Both three-dimensional effect and non-homogeneous nature of mechanical property are supposed to cause scatters of displacement of the quay wall.

It is also noted that separation of construction joint and that between caissons is difficult to consider in the two-dimensional analysis.

Accuracy of resolution by in-situ soil investigation is not the same order with that of the FE analysis of mesh size; that by in-situ test is much larger than the size of FE mesh.

4.4 Method of reconnaissance of earthquake damage

Reconnaissance of earthquake damage has been conducted within the framework of conventional design such as seismic coefficient method.

Reconnaissance must be made, however, within the framework of the performance based design. In other

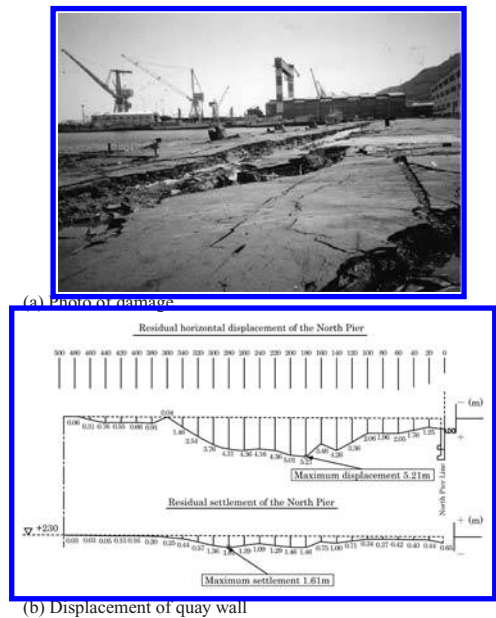


Figure 8. Damage to sheet pile quay wall at Hakodate Port during the 1994 Hokkaido-nansei-oki earthquake.

words, it becomes necessary to evaluate damage or check items quantitatively.

In the case of seismically reinforced port facility, horizontal displacement, settlement and tilt angle of the quay wall have been measured. Under the new design concept, however, measurement must be made from the point of mooring of a vessel, cargo handling, and transport. If transport by means of track is necessary, bump of an apron will become one of the important indices. It becomes also important to estimate volume of soil to fill the bump of the apron when emergency recovery works.

In addition, reconnaissance must be made not only to the damaged facilities as conventional reconnaissance is made, but also to the non-damaged or slightly damaged facilities.

5 CONCLUDING REMARKS

Based on the lessons from the damages past earthquakes, especially, the 1995 Hyogoken-Nambu earthquake, a seismic performance based design methodology was introduced. In order to assess and evaluate the seismic performance, new simulation techniques need to be introduced in the technical standards for port facilities in Japan. However, in practice, it is not easy to incorporate simulation techniques such as dynamic analyses and model tests.

To brush up the seismic performance based design methodology, it is still necessary to collect actual case history data as well as model test data and numerical simulation data, and feed them back to practice with appropriate interpretation.

REFERENCES

- Japan Port and Harbour Association (ed.) 1999. *Technical standards and commentaries for port and harbour facilities*. Japan Port and Harbour Association (in Japanese).
- Iai, S., Matsunaga, Y. & Kameoka, T. 1990. Strain space plasticity model for cyclic mobility. *Report of Port and Harbour Research Institute* 29(4): 27–56.
- Iai, S., Sugano, T., Ichii, K., Morita, T., Inagaki, H. & Inatomi, T. 1996. Performance of caisson type quay walls. The 1995 Hyogoken-Nambu Earthquake,—Investigation into Damage to Civil Engineering Structures—. Japan Society of Civil Engineers: 181–207.
- Morita, T., Iai, S., LIU, H., Ichii, K. & Sato, Y. 1997. Simplified Method to Determine Parameter of FLIP. *Technical Note of Port and Harbour Research Institute* 869: (in Japanese).
- Inagaki, H., Iai, S., Sugano, T., Yamazaki, H. & Inatomi, T. 1996. Performance of caisson type quay walls at Kobe port. *Soils and Foundations. Special Issue on Geotechnical Aspects of the January 17, 1995 Hyogoken-Nambu Earth-quake*: 119–136.
- Coastal Development Institute of Technology (CDIT) (ed.) 2007. *Port facilities design case collection*, Coastal Development Institute of Technology 1: (in Japanese).

Academics and practitioners discussion session

Evaluating seismic performance of earth structures and soil-structure systems

R.W. Boulanger

Department of Civil & Environmental Engineering, University of California, Davis, CA, USA

ABSTRACT: This Academics-Practitioner discussion session on evaluating the seismic performance of earth structures and soil-structure systems will include presentations by four international experts and be followed by open discussions. The presentations and discussions will address uncertainties in the analysis models being used to evaluate seismic performance of important earth structures or soil-structure systems in various regional/international practices and their importance to performance-based earthquake engineering design.

1 SESSION OVERVIEW

1.1 *Focus*

This Academics-Practitioner session will focus on discussing analysis models that are being used to evaluate seismic performance of important earth structures and soil-structure systems in various regional/international practices and how the uncertainties or limitations in such models are, or should be, accounted for in performance-based earthquake engineering design.

The panelists were asked to set the stage for the session by describing:

1. the analysis models that are commonly used on larger or more critical projects for an earth structure or soil-structure system of their choosing, and
2. the perceived modeling uncertainties and how those modeling uncertainties are either minimized or accounted for in practice.

There are numerous issues that warrant discussion with regard to these two questions. Some examples of questions that will be discussed are:

- What are the major limitations in the models being used, including any physical mechanisms that are not adequately modeled?
- What level of validation is expected or available for the modeling methods commonly used?
- How is the uncertainty in the input ground motions commonly addressed?
- How are modeling uncertainties viewed relative to uncertainties from other sources—e.g., site characterization—and how are these uncertainties accounted for in regional design practices?

The continued advancement of performance-based design in geotechnical earthquake engineering practice will benefit from the international discussion of perspectives on these and other issues. In this regard,

the subsequent sections of this paper provide a few thoughts related to these issues.

1.2 *Panelists*

The panel is comprised of four prominent experts representing a balance of practitioners and academicians from different countries. The panelists are:

Dr. Ernest Naesgaard of Naesgaard Geotechnical Ltd., Canada—Topic: Bridge foundations
Professor Kyriazis Pitilakis of Aristotle University, Greece—Topic: Shallow immersed tunnels and underground metro stations
Dr. Robert Pyke of Arcadis, USA—Topic: Embankment dams and levees
Professor Nozomu Yoshida of Tohoku Gakuin University, Japan—Topic: Underground structures and quay walls.

1.3 *Session organization*

The session will begin with each panelist making a 10 minute presentation that responds to the questions and issues posed above. The remainder of the session time will be devoted to open discussion from the floor and panel.

The session arrangements were facilitated by the session Secretary, Dr. Kentaro Tabata of E-Defense, NIED, Japan.

2 EVALUATING SEISMIC PERFORMANCE

2.1 *Probabilistic approach*

Performance-based evaluation and design principles have advanced considerably in recent years. The form that performance-based principles have taken varies

with the type of structure, its importance, and the region.

The performance-based earthquake engineering (PBEE) methodology advanced by the Pacific Earthquake Engineering Research Center (PEER) over the past decade involves a formal probabilistic treatment of the key aspects that affect the final decision making, which can require integrating seismological, geotechnical, structural, economic, and socio-political aspects of the problem. A probabilistic analysis requires considerable effort to complete in sufficient detail to be useful, and thus its main uses are either in application to large important projects, in developing simpler performance-based guidance, or in evaluating the relative merits of new technologies or approaches. In many situations, there is insufficient information to confidently establish distributions for some of the key relationships (e.g., system fragilities, repair costs, downtime). In such situations, the uncertainty in the final output of the analysis (e.g., deaths, dollars, downtime) can be very large. Nevertheless, the process still offers a couple of valuable attributes. One advantage is that it provides great insight by forcing the analysis/design team to recognize the dominant sources of uncertainty and the dominant factors driving the final decisions. They also provide the advantage that they can then be used in sensitivity studies to probe the benefit that would be obtained by buying additional information—if you spent additional engineering resources to reduce the uncertainty in a given aspect of the problem (e.g., more site characterization, more detailed analysis), how much would it affect the final decision variables (e.g. the mean annual frequency of exceeding some level of losses). An important benefit of the last ten years of PEER activities has been that the research community developed an ability to better communicate across disciplines in terms that they could relate to, such that multidisciplinary teams could more quickly come to consensus on the issues that were of greatest concern on specific projects, whether that may be the hazard characterization, the nonstructural contents of a building, or the post-earthquake inspection process, for example.

2.2 Selection of analysis models

The selection of an appropriate analysis model is an important step in a performance-based evaluation or design. The analyst or designer must decide what the dominant mechanisms are that need to be modeled, and then choose an analysis method that can reasonably approximate those mechanisms. Does the model need to be 1-, 2- or 3-dimensional? What degree of nonlinearity is involved? How important are interfaces, coupled flow, large deformations, compliant boundaries, etc? For some problems, even our most sophisticated analysis models can have significant limitations in capturing or approximating certain

behaviors. For example, void redistribution and water film formation due to liquefaction in layered soil profiles are mechanisms that we currently cannot model confidently enough for design applications.

For important structures, it is often worthwhile evaluating the performance using two or more analysis methods. For example, the performance of earth dams with liquefaction concerns within the embankment or foundation are often first analyzed using an equivalent linear dynamic response program to evaluate liquefaction triggering, followed by limit equilibrium slope stability analyses to evaluate post-earthquake stability or yield accelerations, and Newmark sliding block analyses to evaluate potential displacements for stable slopes. As warranted, the next level of analysis may be performed using nonlinear dynamic analysis methods that may include total stress-based constitutive models and then effective stress-based constitutive models, with and without the effects of pore water pressure redistribution during and after shaking. The systematic comparison of analysis results as the methodology becomes progressively more complex provides a check on the reasonableness of the analysis results (often identifying the need for revisions or corrections), greater insight into the effects of various mechanisms or behaviors, and thus improved confidence regarding which results can be used as the primary basis for decision making.

2.3 Validation of models

The issues of validation and verification of numerical methods are numerous, and so only a couple of points are commented on herein. For engineering applications, it is essential to have some prior evaluation of any nonlinear deformation analysis method's ability to reproduce the essential features of seismic response for closely related case histories and/or physical model tests. There are numerous examples of centrifuge models being used to evaluate numerical methods, but a couple of recent high profile examples in North America include their use to investigate uplift mechanisms for tunnel tubes surrounded by liquefiable fills. In these cases, the centrifuge models were essential for providing confidence that the deformation mechanisms were understood and that the numerical methods were capable of recreating those mechanisms.

For both the physical and numerical models, it is essential to be able to perform a sufficient number of tests and sensitivity analyses to gain the insights necessary for confident decision making. There are numerous examples in the literature where it has been relatively easy for a numerical method to be calibrated to recreate most aspects of the response of any one physical model test, but the systematic evaluation of a nonlinear deformation analysis method against a set of several physical model tests provides

far greater insights into the limitations or uncertainties in predicted responses.

Lastly, the documentation of nonlinear deformation analyses for engineering application need to be sufficiently transparent for meaningful reviews by independent parties. This requires, as a minimum, providing detailed documentation of the numerical modeling procedures, examples of the constitutive model calibrations and responses to element loading conditions (e.g., direct simple shear), and sufficient measures of the numerical models responses (element responses, deformations, pore pressures, etc.) to facilitate the review process.

2.4 *Uncertainties in inputs*

The specification of input ground motions and the site characterization are often two of the largest course of uncertainties in evaluating seismic performance of earth structures. The selection or development of ground motion time series requires expertise in seismology and in the features of motions important to a specific structure. Methods for scaling time series to match or approximate design spectra, and whether those spectra should be uniform hazard, scenario, or conditional mean spectra, are all important considerations. This continues to be an area where additional research and guidance for practice are needed.

Site characterization and the development of idealized cross-sections with assigned engineering properties are often the most important steps in evaluating performance of earth structures. For example, issues related to the characterization of gravelly soils or intermediate soils can dominate the selection of engineering properties and thus the outcome of deformation analyses. A recent performance evaluation

of an earth dam illustrated the role of site characterization. One consultant determined that the shell materials were liquefiable, assessed their strengths by correlation to SPT penetration resistances, and then predicted crest displacements exceeding 10 m during design earthquake loading. A subsequent consultant greatly expanded the site characterization effort, concluded the shell materials were not liquefiable, and predicted crest displacements more on the order of 1 m. The point is not necessarily which consultant is correct, but rather that the differences in their predicted displacements were directly due to fundamental differences in the assumed soil properties and not to major differences in their numerical methods.

3 CONCLUDING REMARKS

There are considerable challenges that remain to be addressed in the further development of PBEE design practices, but as Samuel Butler (1612–1680) commented:

“Life is the art of drawing sufficient conclusions from insufficient premises.”

It is hoped that the international discussions in this Academics-Practitioner session will contribute to the continued advancement of performance-based design in geotechnical earthquake engineering as a means for making sufficient conclusions despite insufficient premises.

Geotechnical performance-based seismic design for bridge foundations—a Western Canada perspective

Ernest Naesgaard

Naesgaard Geotechnical Ltd., Bowen Island, B.C., Canada

ABSTRACT: Performance-based seismic design criteria are being used for the seismic design of large bridges in British Columbia. Typically there are three or four design levels with varying performance requirements. The determination of the earthquake induced soil and structure displacements is the key challenge for the geotechnical designer. To do this he uses a variety of design methods and tools varying from simple empirical procedures to complex coupled effective stress dynamic analyses. The complex analyses can give much insight and allows the effectiveness of design modifications, ground improvement, etc. to be quantified. However experienced users and much judgment are still required.

1 INTRODUCTION

In Western Canada (British Columbia) there have been four large new bridges and several seismic upgrades of existing large bridges in the last decade. The seismic design is typically largely carried out using performance based philosophy. The performance criteria are usually specified as damage limits to the bridge when subjected to design earthquakes representative of a range in probability of exceedance. Seismic damage to bridge foundations and superstructure is generally caused by differential deformations. The challenge for the designer is to quantify those deformations for the various specified design scenarios.

This challenge is often compounded by large bridges being located across river valleys where soil conditions are often poor. Liquefiable loose sands, compressible and weak silts and clays, and miscellaneous fill soils are common. Large bridges are commonly supported on pile or drilled shaft foundations and interaction between foundation and weak soil predominates much of bridge foundation design practice.

Typical geotechnical seismic design tasks include:

- ground response analyses to obtain site specific design motions and design spectra,
- foundation capacity assessment,
- foundation stiffness assessment (foundation springs), and
- soil deformation assessment with and without soil-structure interaction.

2 EARTHQUAKE MOTIONS AND PERFORMANCE CRITERIA

Most of the new large bridges are Lifeline structures and designed for three or four performance

Table 1. Typical seismic design levels and performance criteria.

Design earthquake		
Return period	Probability of exceedance	Performance criteria
475 years	10% in 50 years	elastic behavior & minimal or no damage
975 years	5% in 50 years	plastic deformations allowed but with repairable damage
2475 years	2% in 50 years	non-collapse but extensive damage permitted
deterministic subduction event		non-collapse but extensive damage permitted

levels. Typical criteria are as indicated in the table 1.

Typically three to four outcropping firm ground earthquake record sets (each with three orthogonal directions of motions) are selected for each seismic design level. In past projects these records have often been modified by fitting them to uniform hazard probabilistic design spectra; however current trends appear to be to only scale the records so they match the uniform hazard spectrum at select periods of interest. The design motion is probably the item of greatest uncertainty in the seismic design process.

3 GROUND RESPONSE ANALYSES

Typically one dimensional ground response analyses are usually carried out for key pier locations for each of the various seismic design levels. Equivalent-linear analyses using variants of the program SHAKE are standard practice; however non-linear total stress and

effective stress models using FLAC, D-MOD, or other programs are becoming more frequent. Selection of site specific spectra typically involves significant judgment and both mean and/or enveloping values may be considered. Incoherence due to seismic wave travel past the structure is considered on some projects.

Ground response results are sensitive to the chosen model parameters and a standard procedure for validating and calibrating ground response models, especially non-linear and effective stress models, is an area which deserves further work. Perhaps increasingly available down-hole arrays data can be used for this purpose.

4 FOUNDATION STIFFNESS

Typically a 3D structural model is developed for the superstructure and the foundations are modeled with axial, lateral, and rotational springs. Foundation stiffness (springs) are typically obtained using P-Y approaches and programs such as L-PILE and GROUP. Generally published procedures and correlations are used to estimate the P-Y curves and little effort is made to validate the models to site specific conditions. Ranges of approximately one-half to double calculated stiffness values are often considered in design.

The same model that is used to develop the foundation stiffness parameters is also often used to transfer calculated seismic loads from the superstructure back into the piles to obtain pile design loads, stresses and displacements. The affect of kinematic, earthquake induced, ground displacements on the pile foundations has traditionally been assessed independently from inertial loading from the structure although current practice is starting to consider combinations of both kinematic and inertial loading effects as suggested by Boulanger et al. 2007.

5 GROUND DISPLACEMENTS AND SOIL-STRUCTURE INTERACTION

Determining earthquake induced ground displacement and their interaction with the bridge foundations is one of the key tasks for the design team. When the soils are not liquefiable deformations are often relatively small and reasonable estimates of ground displacements can be made using "Newmark" type procedures or by carrying out dynamic analyses using relatively simple elastic plastic constitutive models. However if soil liquefaction is triggered then much larger displacements, lateral spreading, and possibly flow failure may occur. The later scenario is typically assessed by a combination of both traditional empirical procedures

where the various segments are uncoupled and detailed dynamic soil and soil-structure interaction analyses using complex constitutive models.

The traditional uncoupled methods would include simplified "Seed and Idriss" type liquefaction triggering analysis, post-earthquake consolidation settlement estimates using procedures such as those proposed by Ishihara and Yoshimine, flow slide potential assessment using empirical residual strengths with limit-equilibrium slope analyses and lateral spreading displacement analyses such as those proposed by Youd. Displacements from these simplified methods have a high degree of uncertainty and error bands of one-half to double are likely optimistic.

Two-dimensional dynamic soil and soil structure interaction analyses are carried out for most of the local large bridge projects. Both coupled effective stress (UBCSAND) and total stress (UBCTOT) constitutive models are used within the program FLAC for potentially liquefiable cohesionless soils. Non-linear-plastic (UBCHYST) or linear-plastic (Mohr Coulomb) models are typically used for non-liquefiable silt and clayey soils. The UBCSAND constitutive model has been calibrated to emulate the behavior from an extensive set of drained and undrained simple shear laboratory tests and validated by comparing calculated to actual response from several centrifuge tests. The program has also been shown to be able to capture the seismic displacements of the Upper San Fernando dam, and the post-shaking flow failure of the Lower San Fernando dam.

A key part of the FLAC/UBCSAND analyses on large projects is calibrating the model to trigger liquefaction in the correct number of cycles and to give the proper post-liquefaction stress-strain response. This is typically done by exercising a single element model with material parameters taken from various elements in the large model and adjusting calibration factors until a reasonable match is obtained.

Pile foundations and other structures are often included in the numerical models with 3D behavior being emulated by the use of non-linear springs (analogous to P-Y and T-Z springs) between the pile structural elements and soil mesh.

The 2D dynamic numerical model can give much insight. Complex deformation patterns and failure modes can be observed and the effects of ground densification and foundation modifications can be quantified. There are many approximations and assumptions in this type of analyses and significant uncertainty in calculated displacements. An error band of one-half to double the best estimate displacement is again probably being optimistic. Experienced users and much judgment in selecting reasonable parameters and interpreting the results are required.

Prediction of behavior of underground structure and quay wall during earthquake

Nozomu Yoshida

Tohoku Gakuin University, Tagajo, Japan

1 INTRODUCTION

Underground structure and quay wall have common features in the performance during earthquakes. The predominant factor in the design of these structures is earth pressure from the surrounding soil. In this sense, they are similar to earth retaining structures such as retaining wall. The difference between them is that stability is primary interest for retaining wall whereas displacement is required in these structures.

The Mononobe-Okabe formula has been used in earth structures. It is, however, known that earth pressure by this formula is very large. Researches have pointed out it gives larger earth pressure than tests or numerical analyses. This estimation may not be true; the Mononobe-Okabe formula will give reasonable earth pressure if the mechanism that is assumed a priori occurs. It indicates that such mechanism hardly occurs in the actual situation, and it makes the problem complicate; we need to evaluate not only final stage but also transient state to failure.

2 UNDERGROUND STRUCTURE

Before the 1995 Hyogoken-nambu (Kobe) earthquake, damage to underground structures was very difficult to find except small liner structure such as water and gas pipelines. This situation changed at the Kobe earthquake. Large scaled underground structure such as subways and underground cities were collapsed or significantly damaged. The earthquake motion was much larger than that expected in the design specification. After the Kobe earthquake, therefore, design earthquake load was increased or level-2 ground motion, the largest earthquake motion expected at the site or similar, came to be considered. Since Kobe earthquake was an inland earthquake and duration of the inland earthquake is very long, sometimes more than 1,000 years. It can occur, therefore, even if there is no report of earthquakes.

The most significant damage was that of the Daikai subway station where center columns were completely collapsed and the ground surface subsided for more

than 1 meter. Not a few mechanisms have proposed to explain the damage to the Daikai subway station, such as shock wave, inertia force by vertical motion as well as horizontal load from surrounding ground. It is usual that several mechanisms can explain the cause of the damage. It is, therefore, important to examine that the same mechanism can explain undamaged or slightly damaged structures that is similar to the damaged structure. In this sense, it is important to gather data not only significantly damaged structures but also undamaged or slightly damaged structure.

It is also important to distinguish the mechanism that triggered the damage and that finally collapsed the structure. In many cases, gravity force is responsible to cause the final damage. However, if there was not the former or trigger mechanism, the structure was not collapsed. It is, therefore, important to find the first or triggering mechanism. It also indicates that actual mechanism may not be found when looking at the final collapsed shape.

As briefly explained in the case history volume (Yoshida, 2009), numerical analysis of the Daikai subway station and the Nagata station, which is a neighboring station and is similar structure but was damaged only slightly, indicates that difference of degree of damage comes from only 0.8 cm relative displacement between the top and the bottom of the structure. This is the accuracy required in the analysis. In order to respond this requirement, behavior of soil should be accurately grasped.

3 QUAY WALL

Lots of quay walls were damaged during the 1995 Kobe earthquake, resulting in displacement of the caisson up to several meters towards the sea and subsidence and horizontal displacement in the backfill ground. It caused damage to underground structures. It is noted, however, that these damage to the quay wall is not general feature. It is more frequent that a caisson is placed on the good ground, and displacement of these caissons was small in the past earthquakes. The caisson in the Kobe city was, however, placed on the replaced

sand because foundation ground was soft Holocene clay and there is no doubt that behavior of this replaced sand strongly affects the movement of the caisson. The triggering mechanism is not the same in both structures. In addition, a sheet pile is also used as quay wall. The mechanism of damage to the sheet pile quay wall and to caisson quay wall with good foundation seems similar. The earth pressure from the backfill ground is responsible.

Among the damage to these types of structures, that at the Akita port damaged by liquefaction during the 1983 Nihonkai-chubu earthquake or similar was solved by FEM by three studies (Shiomi, 1989; Iai, 1989; Ohya, 2009). These analyses seemed to succeed to explain the mechanism of damage. It may be because displacement at the top of the quay wall is constrained by tie rod and anchored pile placed at the unliquefied backfill ground. It means that this case is a fairly simple case like liquefaction in rigid boxed sand.

In the case that there is no tie rod or support block, however, the problem becomes more difficult. Small difference may result in different displacement. For example, displacement of the sheet pile quay wall at the Showa bridge site where the bridge fell down during the 1964 Niigata earthquake is affected by the drainage condition (Wang, 2000) although undrained condition is frequently assumed in the liquefaction analysis.

As seen in this example, mechanism may not be the same even in the same types of structures, but change depending on boundary condition.

4 INDICES OF SOIL PROPERTY

In both types of structures, it is recognized that behavior of soil at large strains has predominant effect on damage to the structure. At present, however, conventional method to grasp the dynamic and liquefaction property of soil does not seem to be sufficient.

Since behavior of soil is very complicated, behavior that has predominant effect is retrieved in each field of soil mechanics. In addition, in order to make treatment easy, one index is frequently used in one behavior. For example, liquefaction strength is represented as shear stress ratio under 15 or 20 cycles of loading. We should begin to discuss whether what is the relevant method to identify material property. It may be different from conventional one because situation that the engineer faces seems quite different compared with the past.

The key issues are behavior at middle strains and very large strains. The dynamic deformation characteristics test is limited up to shear strain of about 0.5% at maximum for sand based on Japanese conventional method because hysteresis loop does not stabilize nor increases as cycle at large strains.

On the other hand, liquefaction strength test measures behavior at several percents (double amplitude axial strain of 5%, for example). Therefore, data from 0.5% to several percent is completely missing.

In addition, behavior after the onset of liquefaction is also not obtained in the engineering practice, but it is required in predicting the performance of the structure when surrounding ground liquefies.

At present, the liquefaction strength curve is usually an important target to evaluate parameters of constitutive model. As Sugano (2009) will report in this symposium, however, post liquefaction behavior and residual displacement is different in two analyses using the same computer code but have different parameters of constitutive model although the liquefaction strength curves are identical.

5 CONCLUDING REMARKS

There are not a few data on damage to the structures discussed here, although many of them come from Japan. Under the performance based design, the design is not based on complete failure but transient state to failure for underground structure. The behavior of soil has predominant effect on the behavior of the structure. The method to identify the soil property is short and data of soil behavior from middle to very large strains is missing at present.

REFERENCES

- Fujii, Y., Hatanaka, M., Shiomi, T. and Tanaka, Y. (1989): Liquefaction analysis of seawall during 1983 Nipponkai-chubu earthquake, *Proc., 2nd U.S.-Japan Workshop on Liquefaction, Large Ground Deformation and Their Effects on Lifelines*, Technical Report NCEER-89-0032, pp. 322–335.
- Iai, S. and Kameoka, T. (1989): Initial stress and residual deformation—effective stress analysis of anchored sheet pile quaywall, *Proc., 2nd U.S.-Japan Workshop on Liquefaction, Large Ground Deformation and Their Effects on Lifelines*, New York, Technical Report NCEER-89-0032, NCEER, pp. 161–175.
- Ohya, Y. (2009): A study on numerical analysis of liquefaction and liquefaction-induced flow for practical use, *theses submitted to Tohoku Gakuin University*.
- Sugano, T. (2009): *submitted to this symposium*.
- Yoshida, N. (2009): Damage to Subway Station during the 1995 Hyogoken-nambu (Kobe) earthquake, *Case study volume of this symposium*.
- Wang, J., Sato, M., Yoshida, N., Kurose, H. and Ozeki, K. (2000): Liquefaction analysis of seawall structures under both drained and undrained conditions, *Proc., 12th World Conference on Earthquake Engineering*, Auckland, New Zealand, Paper No. 1300.

Evaluation of the seismic performance of embankment dams and levees

Robert Pyke

Arcadis, Walnut Creek, California, USA

ABSTRACT: The precise forward prediction of the seismic performance of embankment dams and levees remains a challenge. This contribution outlines five issues which impede our ability to make precise forward predictions. These issues do not necessarily prevent rational evaluations of existing structures or the safe design of new structures but they do mean that it is difficult, if not impossible, to implement true performance-based design at this time. A workaround is suggested that might be called the continued or renewed use of engineering judgment.

1 INTRODUCTION

The use of performance-based design, and other advanced concepts such as lowest life cycle cost, are important to the future of civil and geotechnical engineering. However, blind application of these concepts may result in catastrophic misjudgments and failures similar to the collapse of the financial markets involving mortgage-backed securities which resulted not from faulty mathematics but from faulty assumptions. With respect to embankment dams and levees, performance-based design requires that the probability of various degrees of deformation in response to multiple levels of loading be assessed. The probability of “failure” does not necessarily have to be determined explicitly but since the consequences side of the equation is highly nonlinear around the point of “failure”, unless that singularity can be pin-pointed with some accuracy, the overall approach is limited. Evaluation of the performance, under both static and seismic loadings, of slopes in general, and of embankment dams and levees in particular, in terms of expected deformations, rather than just a factor of safety, has long been a goal in geotechnical engineering and the growing interest in performance-based design gives a further push in that direction, but delivery on the promise of more rational design procedures will require addressing the five issues that are discussed in the following paragraphs. In the case of levees there are additional issues including how to handle analysis of a linear structure which may be quite variable along its length and for which seepage rather than slope stability issues may dominate.

2 LACK OF CASE HISTORIES

The importance of learning from case histories is being discussed in another session at this conference.

Its importance here is that calibration and validation of the analytical techniques that are required as part of a performance-based design requires multiple, extraordinarily well-documented case histories. It is relatively easy it is to get good agreement in a single back-calculation but what we need is enough forward predictions in a bank so that analytical techniques can be tested for their accuracy in future earthquakes. Because of the infrequency and unpredictability of earthquakes, this will take time, as will the development of well-documented databases that might allow the use of empirical relationships to predict performance.

3 EVALUATION OF IN SITU PROPERTIES

While it is now becoming more common to explicitly quantify the uncertainty in soil properties in both static and seismic analyses, experience to date with attempts to do this in US nuclear practice have shown that the greatest uncertainty involved is the necessary correction of modulus reduction and damping curves derived from laboratory tests to field conditions. This impacts the potential accuracy of both equivalent linear and nonlinear analyses. Until reliable data on the changes in in-situ properties with strain level under multi-directional shaking is developed, this uncertainty will continue to exist.

4 SHORTCOMINGS OF SOIL MODELS

The development of the models of complex soil behavior that are required to conduct meaningful analyses of deformations under seismic loadings is a difficult task. The challenge is to construct models that are sophisticated enough to follow real soil behavior but also simple enough that other engineers can readily

understand them. They also need to be tested in at least two different ways. First they need to be able to replicate elements tests conducted with complex, cyclic loadings. Then they also need to be checked against the results of either or both of 1g or centrifuge model tests. Recent research has emphasized the latter and neglected the former. One particular feature of soil behavior that has been neglected is the tendency of an element of soil to accumulate deformation in the direction of the initial shear stress when subjected to even a symmetrical cyclic stress. Models that include kinematic hardening or comply with the Cundall-Pyke hypothesis do this, but many other models, including those that comply with Masing's hypothesis, do not. While it may be possible to match the results of a limited number of centrifuge tests with models that do not have this characteristic, the more general validity of such models for forward predictions is extremely questionable.

5 MISSING MECHANISMS IN ANALYTICAL MODELS

Existing mathematical models that are used to represent embankment dams and levees are generally numerical models of a continuum, albeit one that has different properties in different regions. However, at some point excessive deformation results in localization and the development of one or more shear surfaces. For levees, where the dominant mode of failure results from under or through seepage, piping and erosion, a continuum model maybe be able to model changes in pore pressures and flow rates during a seismic event but it cannot model the most common mode of actual failure of levees under "static" conditions.

6 SENSITIVITY TO INPUT MOTIONS

A recent study conducted by the author in association with the University of California, Davis, has shown

that if a soil model is utilized that does properly accumulate deformations in the direction of the initial shear stress, the results become much more sensitive to the general character, and especially the duration, of the input motions that are used. Thus, design motions which are derived using statistical averages of large bins of records, such as may be required to support the more elegant implementations of performance-based engineering may yield results that are widely at variance with the results using input motions representing more site-specific scenario events. Indeed, the trend that the author discerns away from full probabilistic analyses towards use of scenario events undercuts the more formal implementations of performance-based engineering.

7 CONCLUSIONS

While full implementation of performance-based design remains a worthy goal, it remains true that because of various simplifications and limitations that will always apply, the purpose of analyses in geotechnical engineering is not to make precise predictions but is to gain insight. Thus the notion that we can use powerful digital computers alone to optimize designs using performance-based engineering tools is questionable. However, such tools can still be used to provide insight and, when coupled with advanced analog computers that are proficient at pattern-matching, i.e. the human brain, performance-based engineering concepts should help guide us to more rational and economical designs.

Seismic design of shallow immersed tunnels and underground metro stations

K. Pitilakis

Aristotle University of Thessaloniki, Greece

ABSTRACT: The aim of the proposed panel is to present for discussion several open or/and less elaborated issues regarding the seismic design of shallow immersed rectangular tunnels and underground constructions of large dimensions like metro stations and underground parking stations.

1 INTRODUCTION

Immersed shallow tunnels are long structures crossing often particularly unfavorable soil conditions. The transversal and longitudinal seismic design of these structures are quite demanding while the available analytical methods are rather simplified with several open questions regarding the safe design of several parts (i.e. joints, asynchronous motion, site effects including liquefaction and remedial measures) as well as the way of modeling SSI effects. Construction details play an important if not crucial role in the overall design and response. The input motion characteristics including ground shaking and imposed ground strains (transient and permanent) along the structure are determinants of the design safety. Modeling uncertainties are in general more important compared to other sources of uncertainties—e.g., site characterization—because for these important structures safety margins are more severe and strict while the geological, geotechnical and geophysical campaigns are often quite extensive and complete compared to above ground structures. However the uncertainties on the modeling of seismic ground response considering 1D, 2D, or even 3D effects, basin effects, non-linear and elastoplastic soil behavior, liquefaction and liquefaction induced phenomena, may be quite important. Consequently the decision making process is a crucial parameter for the design. It must be also emphasized that in principle the problem is anticipated in case-by-case.

On the other hand the underground metro stations are large box type structures often of several tenths of meters deep and wide and hundred of meter long. The design practice of this kind of complex large dimension structures for earthquake shaking, including ground discontinuities (i.e. faults), is still based on rather disputable modeling principles. For example simplified pseudo-static analysis is usually applied with seismic earth pressure and other inertial type loads, which are inspired from above ground structure and retaining walls available methods

(i.e. Mononobe-Okabe method). This is in contradiction with the physical problem governed by the demand of the structure to sustain safely imposed seismic ground deformations and displacements. Moreover the distribution of seismic earth-pressures for these depths (probably > 20 m) is not well known and the conventional M-O approach cannot be applied. The development of dynamic shear stresses along the faces of the structures is another complex problem which has to be solved respecting the physics and the nature of the complex ground and structural response.

Finally the input motion characteristics including the effects of incoherent, asynchronous motion and the spatial variability of site effects are also in this case an important challenge for the designers. This may affect the transversal design of the structure but also the design in the longitudinal direction and in particular the design of the joints. In the case of immersed tunnels the role of the joints (GINA gaskets) is a crucial part of the global design and safety.

2 ISSUES FOR DISCUSSION

Based on the available design models and methods that are commonly used in practice for the transversal and longitudinal seismic design of immersed rectangular tunnels and underground metro stations, the panel presentation of the hot points will discuss the following issues:

- i. The perceived modeling uncertainties, accuracy and bias for immersed tunnels and metro stations.
- ii. How modeling uncertainties can either be controlled, minimized or accounted for in practice.
- iii. Which are the major limitations of commonly used models and methods, including physical mechanisms that are not adequately modeled.
- iv. Site characterization, ground motion characteristics and associated uncertainties.

- v. Realistic hierarchy of relative importance of different sources of uncertainties and compromises, with respect to engineering practice needs.

The discussion—for both immersed rectangular shape tunnels and large deep metro stations—is addressed in particular on the following subjects:

a. Modeling in the transversal direction

- conventional pseudo-static inertial type analysis
- “racking” type modeling
- full 2D dynamic analysis
- hybrid modeling with imposed seismic ground deformations, considering also SSI effects
- selection of representative soil profiles along the axis
- input motion characteristics including complex site effects and liquefaction
- impedance factors for SSI analysis
- dynamic and geostatic earth-pressures
- seismic shear stresses along the slabs and the vertical diaphragm walls

- incoherent ground motion in the two horizontal directions
- relative importance of seismic loads to the static loads (for the metro stations only).

b. Longitudinal response and design of immersed rectangular tunnels

- longitudinal response of long structures and design principles
- incoherent ground motion and apparent velocity
- design of GINA joints
- impedance factors for the longitudinal modeling
- impact of the differential longitudinal permanent ground displacements.

The aim of the panel discussion is to highlight the complexity of the problems encountered in the design of these kinds of structures, to discuss the reasonable compromises that could be made from engineering point of view, for a safer, scientifically sound and economic design, and finally to open the panel discussion on few of the items introduced.

The role of soil properties in performance-based design

M. Maugeri & S. Grasso

Department of Civil and Environmental Engineering, University of Catania, Italy

ABSTRACT: Performance-Based Design (PBD) is a more rational approach, particularly in seismic environments. In this approach it is relevant the performance required to structures and to geotechnical works, as well as the geotechnical constitutive models used to predict the performance. The parameters of the constitutive models are related in turn to soil properties. So soil properties are a key point for Performance-Based Design. Questions arising are: (i) which are the more relevant soil properties to solve a specific PBD geotechnical problem? (ii) which are the more relevant model parameters and how they can be evaluated and/or correlated to soil properties? (iii) which is the role of the soil parameters uncertainty in Performance-Based Design? An answer to these questions is given in this paper, outlining the potential offered by the new advanced in-situ and laboratory tests and discussing the performance required by some geotechnical works.

1 INTRODUCTION

To link soil properties to the performance evaluation, we need to specify which one of the performance parameters is more relevant; i.e. in the case of shallow foundations, limitation to: vertical total or differential settlement, horizontal displacement, rotation of the building, to avoid a significant uplifting. Also a limitation on the performance must be linked not only to serviceability limit state, but also to the cost of recovering of tilting in the case of building rotation and/or the cost of the maintenance of repairing the cracks of the building in the case of excessive differential settlements. This last aspect of the maintenance is outside the aim of this paper, which is focused on the relation between soil parameters and related performance parameters of Performance-Based Design of geotechnical works. The selected soil properties could in turn be correlated to model parameters, depending on soil constitutive models of elementary soil volume and on geotechnical models selected for the design of the geotechnical work. Finally it is outlined the role of the uncertainty of soil parameters, due to different in-situ and laboratory equipment used, on the performance response of some geotechnical works and thus on the Performance-Based Design. Also the soil properties are relevant for the evaluation of seismic action and consequently on the PBD of geotechnical works.

2 MORE RELEVANT SOIL PROPERTIES FOR SEISMIC STABILITY OF PHYSICAL ENVIRONMENT AND PERFORMANCE BASED DESIGN

2.1 *Soil properties relevant for site response*

Preliminarily to Performance-Based Design there is a need to know the seismic action. In general the loads to be sustained by the structure is given by Regulations. In the case of seismic action the seismic loads to be sustained by the structure is depending on soil properties of foundation soil by means of the analysis of local site response. Which are the soil properties to be considered for the analysis? And which is depth at which site investigations must be extended? According to many Regulations, the more relevant soil properties for the evaluation of site response are: shear modulus, damping and unit weight. The shear modulus can be evaluated by the theory of elasticity by means of measurement of shear waves velocity. According to many International Codes, the recommended depth of investigation is 30 m. Also some codes, as the earthquake engineering European Code (CEN EC8, 2003), suggests to evaluate the average shear waves velocity in the upper 30 m of soil, for the evaluation of the coefficient S of site amplification of the maximum acceleration at the bedrock. Some authors (i.e. Assimaki and Kausel, 2001) suggest that

the site investigations must be extended at least at 100 m depth. In the past was very difficult to take shear waves velocity measurements at a depth greater than 30 m. But now by means of new advanced in-situ tests (Stokoe et al., 2005) it is possible to detect the shear waves profile at a depth even greater than 100 m.

It has been observed (Idriss, 2008) that the average shear waves in the upper 30 m of soil (V_{S30}) is not a representative parameter for site amplification evaluation. Soil amplification factors given by codes (i.e. CEN EC8, 2003), based on V_{S30} , are average values. These values (ranging between 1.00–1.35, in the cases of EC8) could underestimate very much the local site amplification. In the case of the microzonation of the city of Catania, soil amplification ranges between 0.8 up to 4.0 with a maximum acceleration ranging between 0.15 g and 0.80 g (Maugeri & Grasso, 2008). Bigger accelerations, more than 1.0 g, have been evaluated for some small areas of Catania city by Faccioli et al. (2002), while according to the new Italian Regulations (D.M. 14/01/08, 2008) it should be ranging between 0.225 g and 0.390 g. Perhaps the most critical uncertainties on the overall processes of Performance-Based Design is linked with the estimation of seismic loads to be applied to the given structures. By the way the maximum design accelerations, as far as the knowledge has been improved in the last 35 years, has been increased from 0.20–0.30 g in '70 s up to 0.60–0.80 g nowadays (Figure 1), according to Ishihara (2008).

Site response analysis depends also on damping, which can be evaluated by laboratory tests, with some uncertainties as will be reported in the follows.

2.2 Soil properties relevant for seismic slope stability

The Performance-Based Design must take preliminary into account the stability of inclined foundation soil.

In this case also a topographic amplification factor must be taken into consideration. Santucci De Magistris et al. (2008) reported that the maximum soil

amplification was 2.7 for a slope with an inclination of about 10° located at San Giuliano Di Puglia (Italy) where, during the Molise earthquake of October 31, 2002 ($M = 5.4$), a primary school building collapsed causing the death of 27 children. Cavallaro et al. (2008) for the Monte Po landslide located in Catania (Italy) quoted the stratigraphic amplification factor of about 1.5 and the topographic amplification factor of about 1.2, for a total amplification factor of about 1.8 for a slope with an inclination of about 13° . According to the Eurocode 8 (CEN EC8, 2003) the topographic amplification factor for a slope angle less than 15° could be neglected. The performance required for the stability of a slope during seismic action, is the maximum acceptable displacement. It must be related to the structure surrounding the slope; i.e. $D = 5$ cm allowable displacement for slope movement in a urbanized area; $D = 10$ cm allowable displacement for slope movement in a non urbanized area (Jibson R.W. & Keefer D.K., 1993). For the evaluation of the maximum acceptable displacement it can be used a Newmark (1965) approach. The most relevant soil properties for using this approach are the dynamic peak friction angle ϕ (new landslide) or residual angle (reactivated landslide) for drained conditions and the undrained cohesion C_u for undrained conditions. The Newmark approach has been modified by Biondi and Maugeri (2005), taking into account the degradation index t (Cavallaro et al., 2001), for undrained resistance due to cyclic load for clay slope. In Figure 2 is reported the influence of the index degradation parameters on the displacement accumulated on the slope during cyclic loading.

Year	70	75	80	85	90	95	00	05	10	15
Seismicity	200–300 gal		400–500 gal			600–800 gal				
Nuclear power facilities	Equivalent Liner analysis									Strengthening
Structures (Buildings, Bridges)	Pseudo static analysis	Linear analysis	Non-linear analysis			Vibration control Isolation				
Geotechnics (Liquefaction, Landslide, Soil structure interaction)	Pseudo-static analysis ($F_s > 1.2$)		<ul style="list-style-type: none"> Equivalent linear analysis Effective stress-based analysis 			<ul style="list-style-type: none"> Permanent displacement analysis Performance-based design Hazard map.Risk map 				

Figure 1. Increasing demand from seismicity and geotechnical performance-based design (after Ishihara, 2008).

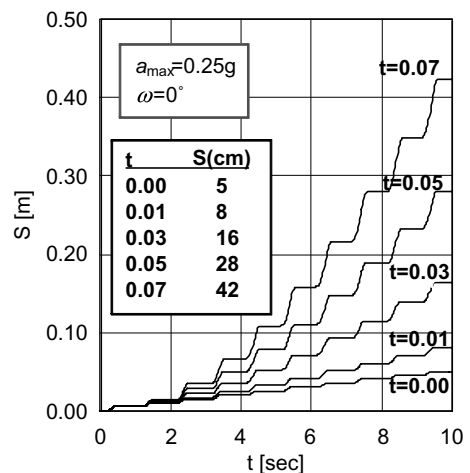


Figure 2. Soil displacement in relation to the value of the index degradation parameters.

Biondi et al. (2000), take into account the increasing of pore pressure Δu during an earthquake for sandy slope by means of empirical correlations. In this case the key soil parameter is the relative density D_r . In Figure 3 it is possible to see that large deformation occurs for loose sand (Biondi et al., 2002).

2.3 Soil properties relevant for liquefaction analysis

The Performance-Based Design must take preliminary into account the occurrence of liquefaction phenomena. The liquefaction phenomena are generally analysed by means of the evaluation of the cyclic resistance ratio (CRR) which must be greater than the cyclic stress ratio (CSR). Empirical correlations are generally used for the evaluation of CSR and CRR. The CRR evaluation is almost based on empirical correlations with SPT, CPT and V_s (Idriss and Boulanger, 2004). V_s could be measured by Down Hole, Cross Hole, SASW and others (MASW, SWM, Re.Mi., SSRW, CSW, etc) and more recently by the new Seismic Dilatometer Marchetti Test (SDMT) (Monaco et al., 2005). In Figure 4 are reported the results of a Dilatometer Test on sandy soil located on

the shore line of the Catania city (Italy). In Figure 5 are reported the CSR and CRR evaluated by empirical correlations based on SPT and CPT results.

CRR based on SPT is at some depths greater than CSR. The same occurs for CPT. Figure 6 reports CRR evaluated by empirical correlations based on V_s and K_D measured by the new Seismic Dilatometer

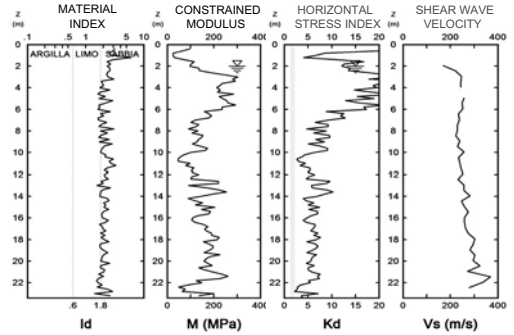


Figure 4. SDMT soil properties results relevant for liquefaction analysis.

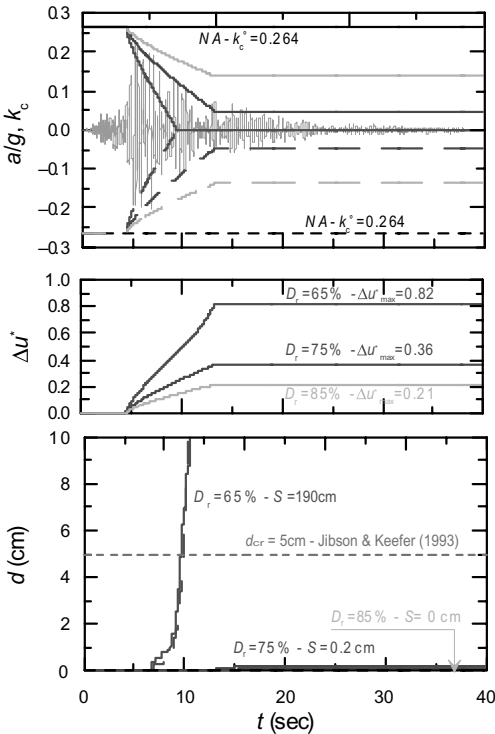


Figure 3. Soil displacement in relation to the value of relative density parameter D_r .

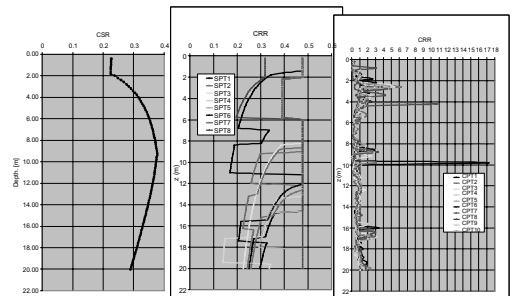


Figure 5. Comparison between CSR and CRR evaluated by SPT and CPT, for Catania (Italy) shore line sand.

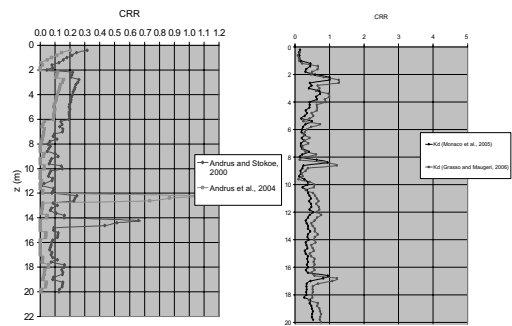


Figure 6. Evaluation of CRR by V_s (very low values) and K_D (much higher values), for Catania (Italy) shore line sand.

Marchetti Test (SDMT). The results show that the CSR is greater than CRR based on Vs almost at each depth. While CSR is lower than CRR based on K_D measurements. So the potential liquefaction is very high using Vs, high using SPT and CPT and is low using K_D . Vs seems to be not appropriate parameter also because it is not able to detect the upper rigid crust while it is clearly captured by K_D measurements.

3 MODEL PARAMETERS REQUIRED FOR THE CONSTITUTIVE MODELS USED FOR PBD OF GEOTECHNICAL WORKS

3.1 *Relevant soil parameters for the performance required to geotechnical works*

After evaluating the stability of foundation soil against slope instability and liquefaction, the design procedure must check the performance required to geotechnical works: shallow foundations, pile foundations, retaining wall, quay wall, reinforced retaining wall, anchored diaphragms, embankments, dams, landfills, pipelines, etc. The performance required at the ultimate limit state is to satisfy the limit equilibrium, checking the bearing capacity and horizontal sliding for soil and normal and shear stress and moment in the foundation. The performance required at the serviceability limit state are reported in the follows for the main typology of geotechnical works.

For shallow foundations vertical settlements, horizontal displacement and foundation rotation, including uplifting (Gazetas, 2006), must be checked. The evaluation of these performance can be made by experimental, theoretical and numerical modeling. The fundamental soil parameter for the evaluation of the performance of shallow foundation is the soil stiffness $k(N/m^3)$. Soil stiffness depends indeed on soil-structure interaction, so it is possible to define K_z and $K_y(N/m)$, to evaluate vertical and horizontal displacement and $K_{yz}(Nm)$ to evaluate foundation rotation. According to Gazetas (1991), analytical expression of K_z , K_y and K_{yz} are given in function of soil properties shear modulus G and normal modulus E or Poisson ratio ν . For seismic conditions, the key parameter is the soil impedance K_z^{dyn} , K_y^{dyn} and K_{yz}^{dyn} which are function of the soil stiffness and damping C . For pile foundations vertical settlement, horizontal displacement and rotation at the head of the pile must be checked; horizontal displacement and bending moment along the pile must be checked for inertial and kinematic soil-pile interaction. The fundamental soil parameter for the evaluation of the performance of pile foundation are the soil stiffness $k(N/m^3)$ for static conditions and the soil impedance K^{dyn} for seismic conditions (Gazetas, 1991), for the evaluation of inertial interaction. For the evaluation of kinematic soil-pile interaction particularly for layered soil a key

parameter is the ratio between the shear modulus of the soil layers, according to the solution given by Mylonakis (2001) and by Cairo et al. (2008). For retaining walls horizontal displacements and rotations must be checked on the basis of the static and dynamic earth trust, according to Caltabiano et al. (2005), taking into account the inertial forces on the wall and on the wedge, as rotations develop, and by means of a pseudo-dynamic procedure based on modified Newmark analysis for PBD (Biondi et al., 2009), taking into account also the change of the system geometry, as displacements develop. In any case, the relative density state parameter D_r is a key point for the evaluation of the earth trust and then for the evaluation of PBD for earth retaining walls.

3.2 *Soil properties for simple constitutive models*

The simplest and perhaps the more used constitutive model is the linear elastic model. This model is characterised by only three soil parameters: G , E , ν . These parameters are linked by the elastic theory, so only two are independent. In general G and ν are measured ($\nu = \epsilon_x/\epsilon_z$) and E is obtained by: $G = E/2(1 + \nu)$. Using the elastic non linear model, the decreasing of elastic soil parameters with the normal soil deformation ϵ , the shear deformation γ and the volumetric deformation ϵ_v , must be evaluated.

Another very simple constitutive model much used by practitioners is the perfectly-plastic model. This model in drained conditions is characterised by the soil parameters cohesion c and friction angle ϕ (Mohr Coulomb model), in undrained conditions is characterised by c_u (Tresca model). At large deformations the friction angles ϕ is decreasing from peak values to residual values (ϕ_{res}). ϕ_{res} is a key parameter for the evaluation of the reactivation of old landslides, particularly for clayey soils with clay particles load-oriented.

The viscous modulus is characterised by the damping coefficient C ; the damping ratio $D = C\omega/2G$ is in general measured by laboratory tests (see next chapter). This very simple model is very useful to use for dynamic analysis. In general visco-elasticity is not appropriate on its own for describing actual soil response, but visco-elastic element is often included within more sophisticated elastic-plastic models.

3.3 *Soil parameters for advanced constitutive models*

Among the more advanced constitutive models perhaps one of the more used elasto-plastic constitutive model is Cam Clay model (Schofield and Wroth, 1968). The Cam Clay model is characterised by six parameters. two of them are elastic parameters: bulk modulus K , shear modulus G ; four are plastic parameters: slope of critical state line (λ), intercept for critical-state line (ν_λ) at $p = 1$ kPa, slope of swelling

lines (k), critical-state angle of friction (ϕ_{cv}). The Cam Clay model is implemented in many commercial codes and can be used by practitioners. Another constitutive model implemented in many commercial codes is the Drucker-Prager (1952) model with capping. This model is characterized by nine parameters, described and evaluated in Figure 7 for Leighton Buzzard clay.

Among the more advanced elasto-plastic constitutive models, it can be used the Severn-Trent model (Gajo and Wood, 1999), recently implemented by Abate et al. (2008) in the ADINA code. This model is characterized by ten model parameters, two of which are elastic soil parameters (ν and G) and eight are plastic parameters. Among plastic parameters, three are of clear physical meaning (λ , ν_λ and ϕ_{cv}), and can be evaluated by routine laboratory tests; five are model parameters with not always clear physical meaning. These last can be evaluated by trial and errors procedure from triaxial tests. In Figure 8 is reported the evaluation by trial and errors of the parameter R for Leighton Buzzard sand. In Figure 9 are described and reported all the model parameters of the Leighton Buzzard model for the Leighton Buzzard sand. Model

ν	Poisson's ratio	0.3
G	elastic shear modulus $G = CG_0$	2197
J	slope of critical-state line in v -lnp plane	0.03
ν_j	intercept for critical-state line in v -lnp plane at $p = 1$ kPa	1.969
J_{cv}	critical-state angle of friction	40°
R	Ratio of sizes of yield surface and strength surface	0.1
A	Multiplier in flow rule	0.9
k_d	State parameter contribution in flow rule	2
B	Parameter controlling hyperbolic stiffness relationship	0.0016
k	Link between changes in state parameter and current strength	1

Figure 9. Model parameters and their evaluation by Severn-Trent constitutive model for Leighton Buzzard sand.

ν	Poisson's ratio	0.3
G	elastic shear modulus	2197
ρ	soil density	1.54
α	material constant related to the angle of shearing resistance	0.204
k'	material constant related to cohesion and to the angle of shearing resistance	0.3
W	Link between p and ϵ_v	-0.13
D'	Intersection of the elliptical cap with the p axis	$7.25 \cdot 10^{-4}$
L'	intersection of the elliptical cap with the failure envelope	0
R'	ratio of the major to the minor axis of the elliptical cap	2

Figure 7. Model parameters and their evaluation by cap-hardening Drucker-Prager constitutive model for Leighton Buzzard sand.

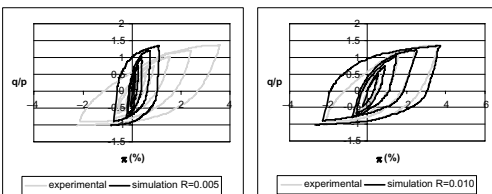


Figure 8. Evaluation of parameter R by comparison between experimental test results and numerical simulation by Severn-Trent model.

parameters with clear physical meaning are in general also soil parameters and their values could be very significantly for PBD. Model parameters with non physical meaning could be in some cases less relevant.

4 INFLUENCE OF UNCERTAINTIES OF SOIL PROPERTIES ON PERFORMANCE BASED DESIGN

4.1 Uncertainties due to spatial variation

From previous paragraphs the soil properties relevant to PBD are reported in Figure 10. These soil properties are affected by spatial variability due to soil heterogeneity along vertical and horizontal direction. To take into account the effect of spatial variation of soil properties a comprehensive number of boreholes extended at a representative depth and a comprehensive number of undisturbed samples must be taken from boreholes. Also a comprehensive number of in-situ tests must be performed. In Figure 11 are reported the stratigraphy and the V_s profile of three borings in the city of Catania, where soil heterogeneity is very pronounced.

In this situation about 1200 borings were used for the geotechnical modeling of the soil at the Catania city. The investigated urban area of Catania is about 45 km^2 , so the average density is about of 25 boreholes for each km^2 ; in the city centre there is a higher density of about 250 boreholes for each km^2 . In figure 12 are reported the spatial variation of the values of the shear modulus G_0 at different sites of the city of Catania.

The values of G_0 at depth are ranging between 50 and 400 MPa for clay sites (Piana di Catania and Via Stellata) and between 500 and 1200 MPa for volcanic

$E_0; E_u$	Initial Young modulus	$c'; c_u$	Cohesion
$E(\epsilon)$	Young modulus variation	ϕ'	Shear strength angle
G_0	Initial shear modulus	ϕ_{cv}	Shear strength angle at constant volume
$G(\gamma)$	Shear modulus variation	ϕ_r	Residual shear strength angle
D_0	Initial damping ratio	λ	slope of <i>critical-state line</i> in <i>v-lnp</i> plane for loading
$D(\gamma)$	Damping ratio variation	v_λ	intercept for <i>critical-state line</i> in <i>v-lnp</i> plane at $p=1$ kPa
ν	Poisson ratio	k	Slope of unloading-reloading line in <i>v-lnp</i> plane
V_s	Shear wave velocity	\square	Weight per unit volume
V_p	Normal wave velocity		
D_r	Relative density		

Figure 10. The most common soil properties to be evaluated by in-situ and laboratory tests.

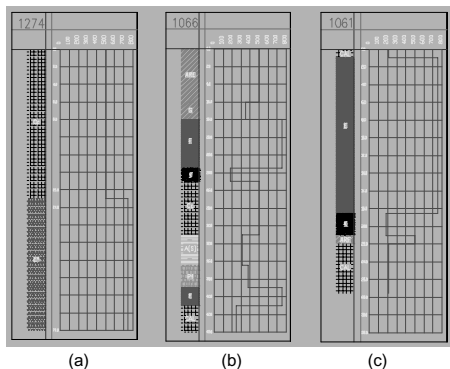


Figure 11. Heterogeneity of the soil of the city of Catania. Soil stratigraphy and V_s profiles: (a) soft soil over fractured lava; (b) lava layers interbedded on soft soil; (c) lava over soft soil.

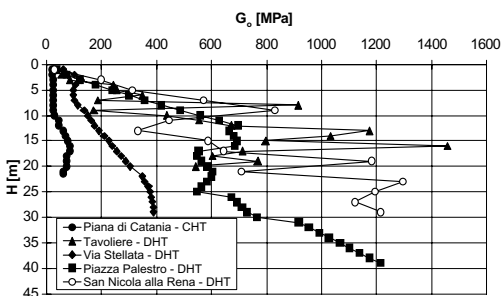


Figure 12. Heterogeneity of the soil of the city of Catania: G_0 profiles measured by similar test typologies (D-H and C-H tests) at different sites.

sand and lava sites (Tavoliere, Piazza Palestro and San Nicola alla Rena).

Similar considerations can be made for other soil properties as V_s , G_0 , c_u , c' and ϕ_{cv} . Soil non linearity, given by $(E\epsilon)$, $(G\gamma)$, $\nu(\epsilon)$ and $(D\gamma)$, is discussed in the following paragraphs.

4.2 Uncertainties due to different in-situ and laboratory equipment

Soil properties can be measured by in-situ and laboratory tests. As far as shear modulus G_0 is concerned, generally in situ evaluation based on V_s measurements is greater than the laboratory measurement based on resonant column tests (RCT) and cyclic loading torsional shear tests (CLTST). Some differences occur also using different laboratory equipments. In figure 13 the differences of G_0 evaluation by means of RCT and CLTST is about 15%.

Even bigger differences occur for the evaluation of the damping ratio D . In figure 14 the differences of D evaluation by means of RCT and CLTST is very significant. At small strains the damping ratio evaluated by RCT tests is ranging between 3% (by Method of amplitude decay) and 4% (by Steady-state method), while the damping ratio evaluated by CLTST tests is about 1%. This scatter is due to shear rate, which is ranging between 1 and 5000% for minute for CLTST tests, while it is about 1000 times bigger for RCT tests. The high shear rate reached during RCT test is much greater than that reached during a destructive earthquake and it leads to higher values than those given by CLTST tests, particularly for damping ratio.

By the way, damping ratio values obtained by old resonant column equipment were even bigger than about 10% for 0.01% shear strain (Seed & Idriss, 1970). This result could be caused also by damping phenomena in the apparatus; because of this result,

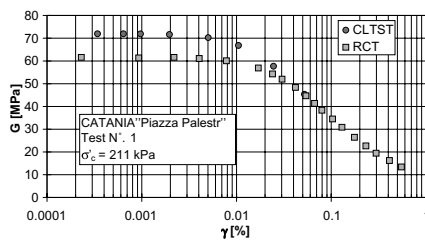


Figure 13. $G(\gamma)$ evaluation by RCT and CLTST tests for the volcanic sand at Catania Piazza Palestro site.

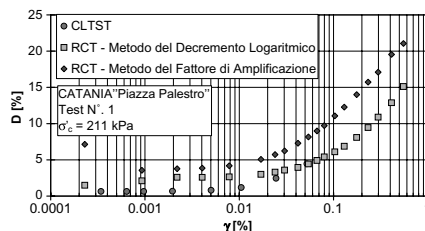


Figure 14. $D(\gamma)$ evaluation by RCT and CLTST tests for the volcanic sand at Catania Piazza Palestro site.

typical soil damping chosen by practitioners is 10%, while it is more realistic to use a damping ratio equal to 5% or less.

A further very relevant soil parameter is the Young modulus E . Generally, G and ν are measured; the latter measured by cyclic loading triaxial test (CLTxT) and multiloading triaxial tests (MLTxT). This procedure gives some uncertainties on the E values. A more precise evaluation of E value can be made by a CLTxT with double ball bearing (Cavallaro & Maugeri, 2004), as reported in figure 15. In figure 16 the evaluation of ν value by the same triaxial apparatus is reported.

Among soil parameters reported in figure 10, a key parameter for performance-based design of geotechnical works is the relativity density D_R , that is a state parameter. This parameter can be evaluated by empirical correlations by SPT, etc, but these correlations show big scatter. More reliable values can be evaluated by D-H tests, by measuring V_s and V_p (Foti & Lancellotta, 2004).

4.3 Uncertainties due to test sensitivity and repeatability

When soil properties are detected by in-situ tests, in general they are evaluated by means of empirical correlations. These correlations show some scatter, so to

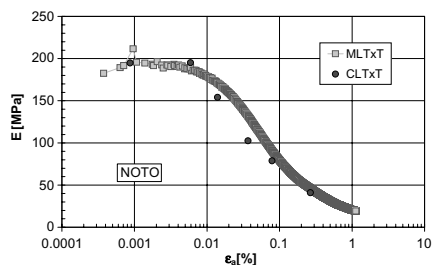


Figure 15. $E(\varepsilon_a)$ evaluation by CLTxT and MLTxT tests for the Noto (Italy) clay.

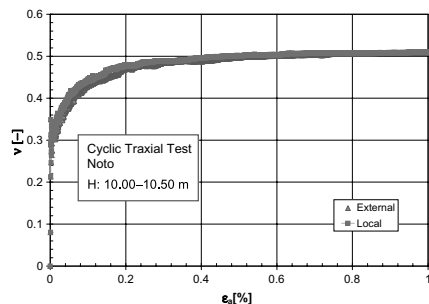


Figure 16. $\nu(\varepsilon_a)$ evaluation by CLTxT and MLTxT tests for the Noto (Italy) clay.

evaluate soil properties for PBD it is better to use more than one correlation (redundancy of data is preferable). Soil parameters directly measured by in-situ tests show an accuracy of data and repeatability which depend on the type of apparatus used and the procedure followed for the measurement. For instance the evaluation of V_s by C-H test is more accurate than that evaluated by D-H test; in turns the V_s evaluated by SDMT is more accurate than that evaluated by C-H test. In addition SDMT is very useful to practitioners because it gives many other parameters for PBD.

As regards laboratory tests, almost the new apparatus has a higher sensitivity, but repeatability can be suffered by test procedure, particularly for remoulded samples. Also undisturbed samples, when affected by some disturbance, even if it is very light, could be in some cases influencing the evaluation of soil properties for PBD. Other uncertainties could arise from the interpretation of experimental results. In some cases the different results interpretation of in-situ tests and lab tests could lead to uncertainties on PBD. For instance different interpretation for a test pile leads to different evaluations of G_0 and limiting shaft friction (f_s) and so to different evaluation of pile settlements due to negative skin friction. Using different model with the same soil parameters G_0 and f_s , the evaluated settlements are quite similar. It can be concluded that the influence on the results due to different soil models is less than the influence due to different evaluation of soil properties (Maugeri & Castelli, 1996).

5 CONCLUSION

Dynamic soil properties such as V_s , ($G\gamma$), ($D\gamma$), are relevant for the assessment of seismic actions to geotechnical works. There is an increasing demand to resist to high seismic action and PBD is the only rational answer to this demand. For PBD we use constitutive models based on model parameters which can be linked in some cases to soil parameters; in some other cases they can be evaluated by laboratory tests or by in-situ tests (i.e. pile tests) by trial and errors. The interpretation of these laboratory and in-situ tests is a key point for evaluating reliable soil properties and model parameters. The uncertainty of soil properties due to spatial variation, different in-situ and laboratory equipment and sensitivity and repeatability of tests is discussed. It is concluded that a proper evaluation of soil parameters is indeed a key point for PBD.

REFERENCES

- Abate G., Caruso C., Massimino M.R., & Maugeri M. 2008. Evaluation of shallow foundation settlements by an elastoplastic kinematic-isotropic hardening numerical model

- for granular soil. *Geomechanics and Geoengineering*, Vol. 3(1), pp. 27–40. ISSN: 1748-6025.
- Assimaki D. & Kausel E. 2001. An equivalent linear algorithm with frequency—and pressure dependent moduli and damping for the seismic analysis of deep sites, Proc. 10th SDEE Conference, Drexel University, Philadelphia, October.
- Biondi G., Cascone E., Maugeri M., & Motta E. 2000. Seismic response of saturated cohesionless slopes. *Soil Dynamics and Earthquake Engineering*, Vol. 20 n° 1–4, pp. 209–215.
- Biondi G., & Cascone E., & Maugeri M. 2002. Flow and deformation failure of sandy slopes”. *Soil Dynamics and Earthquake Engineering*, vol. 22, pp. 1103–1114.
- Biondi G., & Maugeri M. 2005. Effect of cyclic behaviour of soils on seismic response of clay slopes. Proc. of the Satellite Conference on Recent Developments in Earthquake Geotechnical Engineering. Osaka University Nakanoshima Center, Osaka City, Japan, September 10, 2005, pp. 263–270.
- Biondi G., Cascone E. & Maugeri M. 2009. Equivalent and critical acceleration coefficients for displacement-based seismic analysis of gravity retaining walls. Proc. First International Conference on Performance-Based Design In Earthquake Geotechnical Engineering Tokyo 15–18 June 2009.
- Cairo R., Conte E., & Dente G.R., 2008. Nonlinear seismic response of single piles. Atti del convegno “2008 Seismic Engineering International Conference MERCEA’08”, Reggio Calabria and Messina (Italy), 8–11 July, 2008.
- Caltabiano S., Cascone, E., & Maugeri, M. 2005. A procedure for seismic design of retaining walls. Chapter XIV in: *Seismic Prevention of Damage: A Case Study in a Mediterranean City*. M. Maugeri Editor. WIT Press, Southampton (UK).
- Cavallaro A., Ferraro A., Grasso S., & Maugeri M., 2008. Site Response Analysis of the Monte Po Hill in the City of Catania. Proceedings of International Conference commemorating the 1908 Messina and Reggio Calabria earthquake. Reggio Calabria, Italy 8–11 July, 2008.
- Cavallaro A., Lo Presti D., & Maugeri M. 2001. The degradation behaviour of Fabriano soil during cyclic loading. *Italian Geotechnical Journal*, vol. 35, n. 2, 2001.
- Cavallaro A., & Maugeri M. 2004. Modeling of cyclic behaviour of a cohesive soil by shear torsional and triaxial tests. Proc. of the International Conf. On Cyclic Behaviour of Soils and Liquefaction Phenomena, Bochum, Germany, March 31–April 02, 2004.
- CEN EC8. 2003. Design of structures for earthquake resistance—Part 1: General rules, seismic actions and rules for buildings. European Prestandard, ENV 1998, Eur. Com. for Standard., Brussels.
- D.M. 14/01/08. 2008. *Technical Regulations for Buildings*. Gazzetta Ufficiale Repubblica Italiana, 04-02-08 (in Italian).
- Drucker D.C. & Prager, W. 1952. Soil mechanics and plastic analysis for limit design. *Quarterly of Applied Mathematics*, vol. 10, no. 2, pp. 157–165.
- Gajo A & Muir Wood, D. 1999. Severn-Trent sand: a kinematic hardening constitutive model for sands: the qp formulation. *Geotechnique*, 49 (5): pp. 595–614.
- Gazetas G. 1991. Foundation vibrations. *Foundation Engineering Handbook*, (H.Y. Fang., ed.), Van Nostrand Reinhold, New York, NY, 553–593.
- Gazetas G. 2006. Shallow and deep foundation soil-structure interaction. Chapter 7 in: General Report. Proc. of the Athens Workshop on Geotechnical evaluation and application of the seismic Eurocode EC8. January 20–21, 2006.
- Idriss I.M. 2008. Use and abuse of V_{s30} in assessing the effect of local site conditions on earthquake ground motion. Proceedings of International Conference commemorating the 1908 Messina and Reggio Calabria earthquake. Reggio Calabria, Italy 8–11 July, 2008.
- Faccioli E. Pessina V. & Vecchiotti M., Risk-UE WP2 meeting 23–25 Jan 2002, Barcellona.
- Foti S. & Lancellotta R. 2004. Soil porosity from seismic velocities. *Geotechnique* 54, No. 8, 551–554.
- Idriss I.M. & Boulanger R.W. 2004. Semi-Empirical Procedures For Evaluating Liquefaction Potential During Earthquakes. 11th International Conference on Soil Dynamics & Earthquake Engineering (ICSDEE) and The 3rd International Conference on Earthquake Geotechnical Engineering (ICEGE). January 7–9, 2004 Berkeley, California, USA.
- Ishihara K., 2008. Challenges in perspectives in geotechnics for intense earthquake shaking. Proceedings of International Conference commemorating the 1908 Messina and Reggio Calabria earthquake. Reggio Calabria, Italy 8–11 July, 2008.
- Jibson R.W. & Keefer D.K. 1993. Analysis of the seismic origin of Landslides: examples from the New Madrid seismic zone. *Geological Society of America Bulletin*, Vol. 105, No. 4, pp. 521–536.
- Maugeri M. & Castelli F. 1996. Discussion on: Negative skin friction on piles in layered soil deposits. *Journal of Geotechnical Engineering*. ASCE, vol. 122, No. 12.
- Maugeri M. & Grasso S., 2008. Seismic Microzonation Studies and Site Response Analysis in the City of Catania. International Geological Congress 2008. August 6–14, 2008 Oslo.
- Mylonakis G., 2001. Simplified model for seismic pile bending at soil layer interfaces. *Soils and Foundations*, vol. 41 n° 4, pp. 47–58.
- Monaco P., Marchetti, S., Totani, G. & Calabrese, M. 2005. Sand liquefiability assessment by Flat Dilatometer Test (DMT). Proc. XVI ICSMGE, Osaka, 4, 2693–2697.
- Newmark N.M. 196E. effects of earthquakes on dams and embankments. *Geotechnique*. Vol. 15, No. 2, pp. 139–160.
- Pitilakis K., 2004. Site effects: recent theoretical and experimental studies. Implications to seismic codes. Invited Lecture. Proc. of the XI Italian National Conference on Earthquake Engineering. Genoa, January 25–29, 2004.
- Santucci De Magistris F., D’Onofrio A., Penna A., Puglia R., Silvestri F. 2008. Some open questions in seismic microzonation. Proceedings of International Conference commemorating the 1908 Messina and Reggio Calabria earthquake. Reggio Calabria, Italy 8–11 July, 2008.
- Schofield A. & Wroth P. 1968. *Critical state soil mechanics*. Mc Graw Hill, 1968, 310 p.
- Seed H.B. & Idriss I.M. 1970. Soil moduli and damping factors for dynamic response analysis. Report No. EERCT 70–10, Earthquake Engineering research Centre, University of California, December 1970.
- Stokoe II K.H., Rathje E.M., Meng F.Y., Wood S., & Wong I. 2005. Deep Vs profiling and non linear soil studies with the NEES Texas Large Mobile Shakers. *Geo-Frontiers*, Austin, Texas, January 23–26, 2005.

Role of soil investigation in performance based design

A.M. Kaynia

Norwegian Geotechnical Institute, Oslo, Norway

ABSTRACT: The focus of this discussion is on i) seismic response of slopes, and ii) seismic soil-structure interaction (SSI) for large structures such as gravity-based structures. The two most governing parameters for performance assessment in these problems are the shear modulus and the cyclic shear strength of the soil. This discussion addresses two questions: i) the most suitable equipments to measure the soil parameters, and ii) the uncertainties in the evaluation of the soil parameters by the specific equipment. In regions with moderate to strong seismicity, earthquakes could represent large loads in geotechnical designs such as in slopes. Use of traditional methods such as quasi-static stability analyses often leads to unrealistic solutions. Allowing for a PBD in which one computes the earthquake-induced strains and displacements and evaluates them against permissible levels is a realistic alternative. An important element in this discussion is the role of site investigation and the adopted methods together with the uncertainties in the interpreted soil parameters.

1 BACKGROUND

The focus of this discussion is on the following two Performance-Based Design (PBD) problems encountered often in geotechnical earthquake engineering: 1) seismic response of slopes, and 2) seismic soil-structure interaction (SSI) for critical and large structures, such as gravity-based structures (GBS), under severe earthquake loading. The two most governing parameters for these problems are the shear modulus and its variation with shear strain, and the cyclic shear strength of the soil. These parameters are essential in calculating the earthquake-induced lateral displacements in slopes as part of the assessment of co-seismic and post-seismic slope instability, and lateral permanent displacement of the structures. The earthquake criteria for most critical structures, such as most off-shore projects, call for design for earthquakes with large return periods of the order of several thousand years. Even in regions with moderate seismicity, such return periods correspond to large earthquake loads. Use of traditional methods such as quasi-static stability analyses often leads to unrealistic solutions. Allowing for a PBD in which one computes the earthquake-induced strains and displacements and evaluates them against permissible values is a realistic alternative. The designer is then confronted with the question of the reliability of the predicted nonlinear response, and the question that arises often is how to bracket the response.

An important element in this discussion is the role of site investigation and the adopted methods together with the uncertainties in the interpreted soil parameters. Some of these questions are briefly discussed in the following sections.

2 SOIL INVESTIGATION ISSUES

2.1 *Suitable equipments to measure shear modulus and shear strength of soils*

Both the shear modulus and shear strength can be measured in situ and in the lab with fairly good accuracy. The cyclic shear strength in the lab can be determined using the direct simple shear (DSS) and triaxial equipments. For long slopes and large GBSs, however, the non-linear response is often dominated by the shear response of the soil; therefore, the most suitable test is the DSS. Use of Bender Elements in the DSS apparatus, in addition, makes this apparatus capable of measuring the small-strain shear modulus. Alternatively, one could use the resonant column test which in addition to small-strain shear strain provides a measure of the damping. Variations of the shear modulus and damping at larger strains can be obtained from the cyclic DSS tests.

In the field, one of the best equipments for estimating the shear strength and shear modulus is believed to be the CPT. This in situ testing technique provides the following information and has the related advantages (e.g. Lunne et al., 1997):

- Continuous profile
- Several parameters are measured as follows and can be combined for enhanced interpretation
 - Layering and soil identification in each layer
 - Strength and deformation characteristics through theoretical and empirical interpretation schemes
 - Permeability and coefficient of consolidation through pore pressure dissipation tests

- Shear wave velocity and hence small-strain shear modulus, G_{\max} , from addition of seismic cone (SCPT)
- Empirical methods for direct assessment of liquefaction potential
- The tests are well standardized and good quality data can be obtained if one adheres to these standards
- Cost effective—one can determine several profiles in one day.

2.2 Uncertainties in the evaluation of soil parameters

This section focuses on the same two equipments mentioned in the preceding section.

In a DSS test, as in most other tests, the largest uncertainty is due to sample disturbance. Sample disturbance is caused by several factors, including

- Preparation and drilling of borehole (relevant for down-hole mode sampling only)
- Penetration of the tube into the soil
- Stress relief
- Handling, transportation and storage of the sample

Neglecting the effects of sample disturbance usually results in strength and deformation parameters that are on the low side; however, in some cases, the derived strength may be too high. Extensive research has therefore been done to quantify the degree of sample disturbance (see, for example, Lunne and Andersen, 2007).

Other sources of uncertainty are specimen preparation (trimming, reconstituting from disturbed samples, specimen non-homogeneity), controlling height (both in active height control and locked height), and testing procedures (including different standards).

The uncertainties are potentially larger with determination of the shear modulus and damping in the resonant column test beyond the small-strain range. Moreover, there is the issue of isotropic (apparatus limitation) versus anisotropic stress conditions in the test which affects the results.

The CPT is a field test and thus represents other sources of uncertainties compared to lab testing. The following constitute the most important sources of CPT uncertainties (Lunne et al. 1997):

- Measurement of sleeve friction for CPTU is still uncertain and less reliable compared to measured cone resistance and pore pressure.
- Interpretation methods for sands are mostly valid for predominantly quartz, low compressibility type material, fine to medium, uniform sands that are un-aged.
- In some soil types interpretation are quite uncertain, especially sands with high fines content, silty material, and compressible sands like calcareous material.

2.3 Role of soil parameter uncertainties on the solution of geotechnical PBD

Both of the parameters mentioned above (that is, stiffness and shear strength) have potentially large impacts on the estimation of the forces and displacements and the nonlinear responses in PBD. Low values of the shear strength generally result in larger slumping/downslope movement in the slope and larger sliding/permanent lateral displacement of the structure. Similarly, high values of the shear modulus of the soil result in larger accelerations in the soil and larger forces in the structure.

Failure in capturing the true soil behaviour beyond the peak strength results in additional uncertainties in predicting the soil response. Figure 1 illustrates an example (Kaynia, 2009). The figure shows the time history of the shear strain at 5 m depth in an 11-degree submarine slope under the Imperial Valley earthquake scaled to $PGA = 0.5$ g on the bedrock. The soil column is 150 m deep with constant shear strength equal to 5 kPa in the top 5 m and increasing 1.25 kPa/m with depth. The figure compares the results for perfectly plastic soil response after the peak shear strength against a strain-softening behaviour. The residual shear strength is attained at shear strain 5% and is 80% of the cyclic shear strength. Larger differences are expected for more brittle behaviour of the soil.

To account for the uncertainties in the shear modulus, some codes specify a lower and an upper estimate of the shear modulus from the best-estimate shear modulus profile (e.g. lower and upper estimated profiles equal to 2/3 and 3/2 times best estimate profile according to ASCE 4–98). Alternatively, one can establish a probability distribution for the shear modulus. Following the same principle, one could establish a probability distribution for the shear strength of the soil. The probability of failure of the slope, or probability of the displacements (in slope or under the structure) exceeding a pre-defined value based on an acceptable performance, can be estimated by following the principles of probability theory, for example

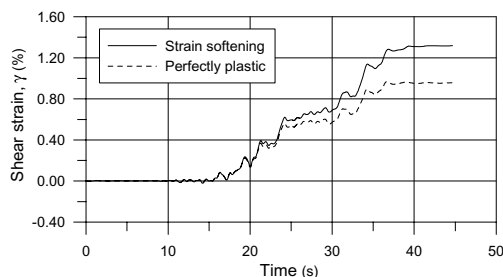


Figure 1. Example of effect of strain softening on seismic response of slope.

through Monte Carlo simulations. In such analyses, one might also incorporate the information about the seismic hazard as is done in a rigorous probabilistic approach such as the one proposed by PEER.

REFERENCES

- Lunne, T., Robertson, P.K. & Powell, J.J.M. 1997. “*Cone Penetration Testing in Geotechnical Practice*”, E & FN Spon, London, UK.
- Lunne, T. & Andersen, K.H. 2007. “Soft clay shear strength parameters for deepwater geotechnical design”. Keynote address, *Proc., 6th Int. Offshore Site Investigation and Geotechnics Conference; Confronting New Challenges and Sharing Knowledge*, 151–176, 11–13 September 2007, London, UK.
- Kaynia, A.M. 2009, “*Quiver*—a numerical code for simulation of one-dimensional seismic response of slopes”, NGI research report 20071851-1.

Role of soil investigation in performance-based design

S.L. Kramer

University of Washington, Seattle, Washington, USA

ABSTRACT: Performance-based seismic design offers the potential for more rational and consistent design of structures in different seismic environments. Performance-based design frameworks that characterize uncertainty in ground motions, soil-structure response, physical damage, and loss estimation offer the potential for illustration of the effects of uncertainty in soil properties on various aspects of performance. Increased uncertainty will tend to increased expected levels of response, damage, and loss for a given hazard level (or return period). It is important to recognize that different soil parameters will have different effects on uncertainty, and that other sources of uncertainty may contribute as much or more to the overall estimate of performance. Nevertheless, it is always desirable to reduce uncertainty to the greatest practical extent, and performance-based concepts provide a framework in which the potential benefits of additional investment in soil investigation can be investigated and documented. The use of such procedures can provide the opportunity for geotechnical engineers to illustrate and quantify the benefits of such investments.

1 INTRODUCTION

The implementation of performance-based design (PBD) requires that geotechnical and structural engineers be able to predict the performance of structures or facilities of interest in advance of earthquake shaking with reasonable accuracy. This requirement leads to two natural questions—what constitutes “performance,” and what constitutes “reasonable accuracy?” General answers to these questions are difficult to provide because each structure and each site are likely to be different, sometimes in ways that can strongly influence performance.

Structural and geotechnical performance can be described in terms of response, physical damage, and loss levels. It can be useful to divide cases of interest into those in which ground failure (meaning the development of significant permanent deformations) occurs or does not occur. It should be noted, however, that many PBD frameworks consider multiple ground motion hazard levels, the lowest of which may be unlikely to produce permanent deformations and the highest of which are likely to cause significant permanent deformations. When ground failure does not occur, the primary role of the soil profile is to amplify/de-amplify incoming ground motions and to interact in some manner with the foundations and structure. When ground failure does occur, response (e.g., the settlement of a slab-on-grade foundation), physical damage (e.g., the width, depth, and spacing of cracks in that foundation), and loss (e.g., the cost of repairing the cracks) can all be affected by the soil.

The purpose of a subsurface investigation is to define the geometry and material properties of all significant soil units whose behavior could affect the performance of the structure of interest. The investigation should be designed with consideration of the characteristics of the structure of interest. It is important to know the fundamental period (and, desirably, the periods of any important higher modes), height, ductility, and anticipated foundation type(s) of the structure before beginning the subsurface investigation. Although the subsurface investigation may take place in a relatively small area, the larger-scale geometry of the area surrounding the site must be determined—tall and/or flexible structures may, for example, be influenced by longer-period surface waves that may propagate within a basin whose dimensions far exceed those of the site. With this as background, comments in regards to a couple of the questions posed to the discussion session panelists can be offered:

1.1 *Which are the most relevant soil parameters to solve a specific PBD geotechnical problem?*

As alluded to previously, questions like this must ordinarily be addressed on a case-by-case basis since details associated with the site and the structure can strongly influence performance. There are, however, some general statements that can be made.

At sites where ground failure is not expected, either due to weak ground motions or strong soils, evaluation of site response and soil-foundation-structure interaction are the two geotechnical tasks that most

strongly affect performance estimation. The site response problem will generally be most sensitive to the stiffnesses and geometries of the major soil units. Geotechnical practice typically uses the low-strain shear modulus, G_{max} , to “anchor” the soil model in a response analysis, and that parameter is best determined from measured shear wave velocity, V_s . It is important to characterize shear wave velocity all the way down to the “half-space” assumed to exist below the modeled profile in most site-response programs; experience from past earthquakes has shown that velocities have varied more than engineers frequently anticipated and that that variation contributed to the response in a way that was not captured in the analyses. Defining transitions in V_s between layers of different stiffness can also be important. Damping characteristics can become important, but usually have a second-order effect on response compared to soil stiffness.

A number of investigations of the effects of uncertainty in soil properties on site response (e.g., Faccioli, 1976; Whitman and Protonotarios, 1977; Costantino *et al.*, 1993; Silva, 1993, 1997a; Electric Power Research Institute, 1993; Hwang and Huo, 1994; Lee *et al.*, 1998; Tsai, 2000) have been reported in the literature. Bazzurro and Cornell (2004) investigated nonlinear response of sandy and clayey sites considering uncertainty in soil properties and record-to-record variability in earthquake ground motions. Performing the analyses with base case soil profiles and suites of soil profiles with randomized soil properties showed that the average amplification factor was affected very little by the modeled uncertainty in soil properties (Figure 1a), and that the uncertainty in amplification factor was modestly increased (mostly at low frequencies) by uncertainty in soil properties. In all cases, the overall uncertainty was dominated by record-to-record variability. Analyses conducted at the University of Washington showed similar results. Figures 2 and 3 show tornado diagrams for a site analyzed with different ground motions and randomized soil properties; the effects of uncertainty in ground motion intensity, IM , can be seen to exceed those associated with specific soil properties. Of the soil properties, uncertainty in soil stiffness contributed most strongly to overall uncertainty—at lower periods (Figure 2), the modulus reduction and damping behavior were more influential than shear wave velocity; at longer periods (Figure 3), that relationship was reversed.

When ground failure is anticipated, the parameters that control permanent deformation also become important—however, it should be noted that G_{max} (or V_s) remains important. In the absence of liquefiable soils, characterization of the shear strength of the major soil units, particularly the softer and weaker units, is important for estimation of permanent deformations. For liquefiable soils, characterization of the density is critical since it will strongly affect pore

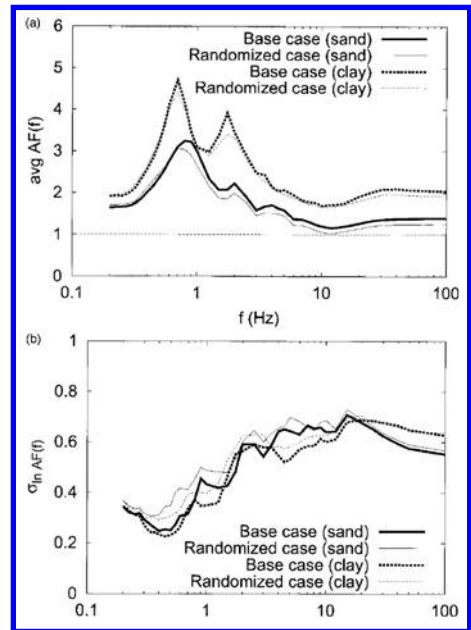


Figure 1. Results of site response analyses with and without soil parameter uncertainty: (a) mean amplification factor, and (b) log standard deviation of amplification factor (Bazzurro and Cornell, 2004).

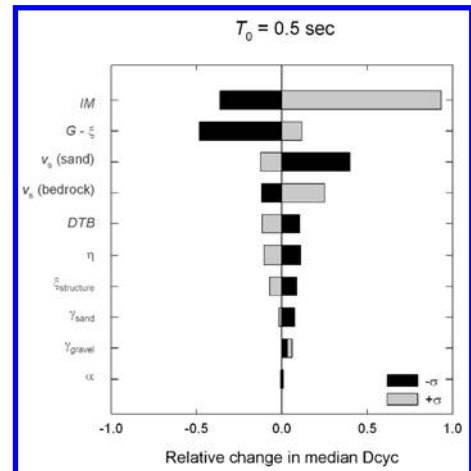


Figure 2. Tornado diagram illustrating relative influence of different parameters on median drift of nonlinear structure with 0.5 sec fundamental period.

pressure generation characteristics and residual strength. Measurement of insitu densities is extremely difficult, and so proxies such as SPT and CPT resistance are usually used for that purpose. CPT data offers the important benefit of improved spatial resolution,

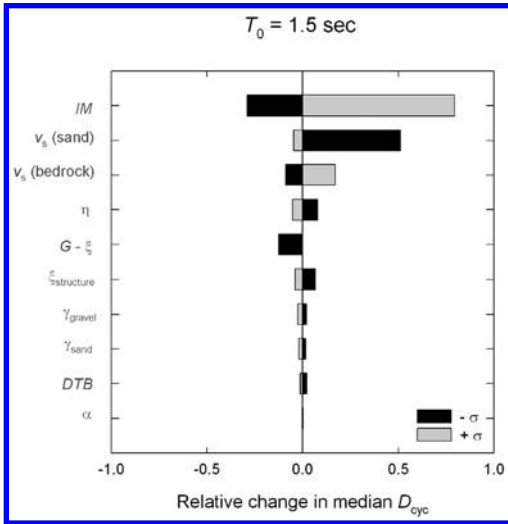


Figure 3. Tornado diagram illustrating relative influence of different parameters on median drift of nonlinear structure with 1.5 sec fundamental period.

so the potential for missing thin seams of liquefiable soil is reduced. Because the development of flow slides can be strongly affected by the presence of zones of low permeability material, particular emphasis on detecting such zones, even when very thin, should be made. When soft silty materials exist by themselves or within loose sands, laboratory testing may be required to characterize their potential for cyclic softening and strength loss.

1.2 What is the role of the soil parameter uncertainties on the solution of geotechnical PBD?

Uncertainty in soil parameters will lead to uncertainty in performance estimates, whether performance is characterized at the response, damage, or loss level. It should be recognized, however, that there are four primary sources of uncertainty in a complete, risk-consistent PBD procedure—uncertainty in ground motion, in response given ground motion, in damage given response, and in loss given damage. The uncertainty in soil parameters will certainly affect uncertainty in response estimates (given ground motion) and likely have some effect on damage (given response).

Although the uncertainties that geotechnical engineers deal with routinely are greater than those typically encountered by structural engineers, a number of studies have shown that uncertainties in ground motions have a significantly greater effect on estimated losses than all of the other primary sources

of uncertainty. These studies, however, have typically assumed that the soil deposits are “well-behaved,” i.e., that the mean (or median) values of geotechnical parameters are well-established, and have focused on the effects of variability about those means (or medians). Put differently, they assume that no significant characteristic of the soil profile has been “missed” in the subsurface investigation. They also assume that uncertainties of the significant parameters are well-understood.

Geologists and geotechnical engineers recognize very well that small details, e.g. a pre-existing failure surface, a thin seam of loose sand or silt, or a thin clay layer acting as a flow barrier can lead to radically different behavior under cyclic loading conditions. Also, the uncertainty in a number of important aspects of soil behavior—liquefaction, for example—is not well understood at present.

An example of the effects of uncertainty on seismic performance can be seen in the results of a recent study. Kramer et al. (2008) performed a detailed analysis of a pile-supported highway bridge crossing an area underlain by liquefiable soils. The bridge was designed for consistency with California Department of Transportation (Caltrans) standards and modeled using the OpenSees computer program. A schematic illustration of the bridge is shown in Figure 4. The liquefiable soils can be seen to be thicker below the right side of the bridge than the left side, and to be underlain by a layer of clay on the left side.

The site is clearly susceptible to liquefaction hazards, principally in the form of lateral spreading and settlement of the loose, saturated sands beneath the abutments. The OpenSees analyses were able to model the liquefiable soil and its interaction with the piles and bridge structure (Figure 5). The lateral spreading caused the soils beneath the abutments to move toward the center of the bridge, thereby imposing significant bending demands on the foundations and the bridge piers nearest the two abutments; the movement of the abutments caused the entire bridge deck to displace some 20 cm to the left.

Working within the PEER framework for performance evaluation, a series of engineering demand parameters (measures of system response) were related to a series of damage measures (measures of physical damage resulting from excessive levels of response). The damage measures were then related, based on standard construction estimating procedures and discussions with Caltrans personnel, to repair costs. This allowed estimation of the costs associated with different levels of ground shaking (Figure 6) that included the effects of uncertainty in response, damage, and loss. This relationship could then be combined with a seismic hazard curve to produce a repair cost curve (Figure 5). The curves shown in Figures 6 and 7 are marked with factors that illustrate the effects of reducing uncertainty in loss given ground motions; such

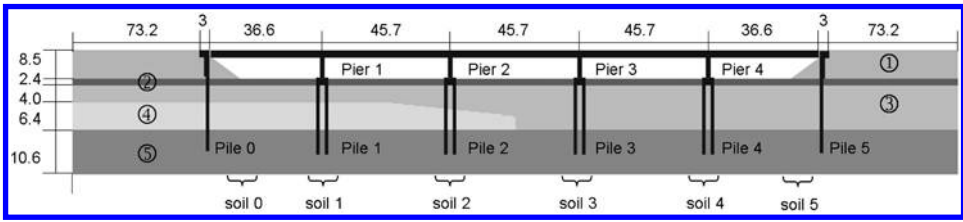


Figure 4. Bridge configuration (dimensions in meters).

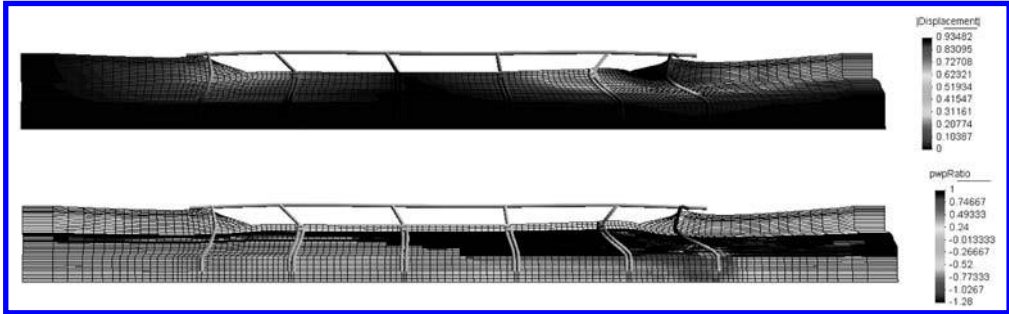


Figure 5. Horizontal and vertical displacements of bridge and pore pressure ratio in soil following earthquake—Erzincan motion. Displacements magnified by factor of 20.

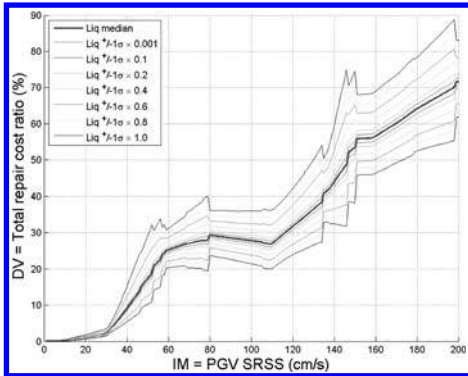


Figure 6. $DV|IM$ relationship for liquefaction case with different fractions of actual uncertainty.

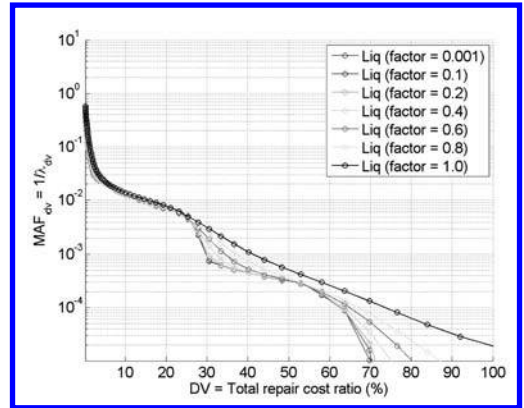


Figure 7. Effects of different levels of uncertainty in $DV|IM$ on loss hazard for liquefaction case.

reductions could include reductions in uncertainty of soil properties, response modeling, damage modeling, and loss modeling. The effects of such reductions in uncertainty can be seen in Figure 7, however, to be strongly dependent upon return period. At return periods less than about 200 years, reductions in uncertainty have virtually no effect on repair costs; under these conditions, liquefaction is not triggered and the uncertainty in repair cost is dominated by uncertainties in ground motions. At longer return periods, however, reductions in uncertainty can be seen to lead to

reductions in estimated repair cost for a given return period.

Analyses such as these offer the potential for estimating the effects of uncertainties in soil properties on the overall performance, as expressed in terms of estimated repair costs, of a structure. They can be used to estimate the value, in terms of reduced repair costs, of the more extensive subsurface investigations that may be required to reduce uncertainty in soil properties.

SUMMARY

The organizers of the panel discussion have raised a number of interesting issues and questions for practitioners adopting PBD concepts. A thorough, detailed, and extensive soil investigation will lead to more reliable and economic designs by reducing the potential for encountering unanticipated modes of response and/or permanent deformation, and by reducing the uncertainty in soil parameters that lead to increased response, damage, and loss hazards. PBD frameworks can be used to identify parameters for which additional investigation may lead to reduced losses, and to quantify the benefits of such additional investigation.

REFERENCES

- Mackie, K., and Stojadinovic B, 2007. Performance of Benchmark Bridge Structures, *ASCE Structures Congress*, Long Beach, CA.
- Costantino, C.J., C.A. Miller, and E. Heymsfield (1993). Site specific seismic hazard calculations at deep soil sites, in *Proc. of the 4th U.S. Department of Energy Natural Phenomena Hazards Mitigation Conf.*, LLNL CONF-9310102, 199–205.
- Electric Power Research Institute (1993). Guidelines for site specific ground motions, Rept. TR-102293, Vol. 1–5, Palo Alto, California.
- Faccioli, E. (1976). A stochastic approach to soil amplification, *Bull. Seism. Soc. Am.* **66**, 1277–1291.
- Hwang, H.H.M., and J.-R. Huo (1994). Generation of hazard-consistent ground motion, *J. Soil Dyn. and Earthquake Eng.* **13**, 377–386.
- Kramer, S.L., Arduino, P., and Shin, H.-S. (2008). “Using OpenSees for performance-based evaluation of bridge on liquefiable soil,” Report No. 2008/07, Pacific Earthquake Engineering Research Center, Berkeley, California, 222 p.
- Lee, R., W.J. Silva, and C. A. Cornell (1998). Alternatives in evaluating soil- and rock-site seismic hazard (abstract), *Seism. Res. Lett.* **69**, 81.
- Silva, W. (1997a). Description and validation of the stochastic ground motion model, prepared for Brookhaven National Laboratory, Associated Universities, Inc., Upton, New York.
- Silva, W. (1997b). Earthquake ground motion database, Pacific Engineering and Analysis, El Cerrito, California.
- Toro, G. (1993). Probabilistic model of soil-profile variability, in *Guidelines for Determining Design Basis Ground Motions*, Schneider, J.F. (Editor), Electric Power Research Institute, EPRI TR-102293, Vol. 2, Appendix 6A.
- Whitman, R.V., and J.N. Protonotarios (1977). Inelastic response to site modified ground motions, *J. of Geotech. Eng. Div., American Society of Civil Engineers* **103**, 1037–1053.

Relevant soil investigations and laboratory tests to estimate liquefaction-induced deformation of structures

S. Yasuda

Tokyo Denki University, Saitama, Japan

ABSTRACT: In the performance-based design, it is necessary to define ultimate limit, repairable limit and serviceable limit. In the liquefaction problem, these limits must be expressed by deformation of structures, such as settlement of buildings, uplift of underground structures and horizontal displacement of quay walls. Three grades of estimation methods for liquefaction-induced deformation; empirical methods, static (residual) analyses and dynamic (seismic response) analyses, have been developed. In the static and dynamic analyses, stress-strain relationship, permeability and coefficient of volume compressibility of liquefied soil must be determined by soil investigations and laboratory tests. Then relevant soil investigations and tests to evaluate liquefaction-induced deformation are discussed.

1 INTRODUCTION

Very strong shaking caused severe damage to structures during the 1995 Kobe earthquake. Many buildings, bridges, and houses collapsed. The Japan Society of Civil Engineering organized a technical committee to investigate new design concepts that could withstand very strong shaking after the earthquake. This committee suggested basing earthquake-resistant design on two types of ground motion: Level 1 earthquake motion, which is likely to strike a structure once or twice while it is in service, and Level 2 earthquake motion, which is very unlikely to strike a structure during the structure life time, but when it does, it is extremely strong.

In the current design for liquefaction, assessment of liquefaction potential is done first. Then the acceptability of the likely degree of damage is roughly judged and, if necessary, appropriate countermeasures are selected. However, in general, the degree of damage expected from liquefaction is not evaluated because it is difficult to evaluate. In the design under Level 1 earthquake motion, it is not always necessary to judge the degree of damage because it is easy to improve the ground not to liquefy under this level of shaking. On the contrary, liquefaction cannot be prevented by current countermeasures under the Level 2 earthquake motion, because the critical soil density at which liquefaction occurs, increases with the increase of earthquake motion. Therefore, it is necessary to introduce a new design concept based not on the occurrence of liquefaction but on the likely degree of damage to structures. This new design concept, so called performance-based design, is rational and will be used for not only for Level 2 earthquake motion but also normal ground shaking.

In the performance-based design for liquefaction-induced deformation, two items must be decided: allowable deformation or displacement of structures, and relevant method to estimate the deformation.

2 ALLOWABLE DEFORMATION OR DISPLACEMENT OF STRUCTURES

Allowable values of liquefaction-induced deformation or displacement of structures must be determined by considering the several conditions: i) serviceability of the structure after earthquakes, ii) importance of the structure, iii) consequential damage to other facilities and iv) difficulty of restoration.

In river dikes, critical condition of the dikes is not to cause overflow after earthquakes as schematically shown in Figure 1(a). In road embankments, emergency vehicles must run just after earthquakes. For example differential settlement between embankments and bridges must be within the allowable value for the vehicles, as shown in Figure 1(b).

In spread foundations, liquefaction causes not only uniform settlement but also differential settlement of structures. Therefore, two items: average settlement and tilting angle of the structures, must be considered. The author and his colleagues studied the allowable



Figure 1. Critical conditions for river and road embankments.

Structure	Deformation or displacement	Upper limit of allowable value		
		0	1	2 (m)
River dike	Settlement			
Road or railway embankment	Settlement			
House or building	Settlement			
Sewage manhole	Uplift			
Quay wall	Horizontal movement			

Figure 2. Rough upper limit of allowable deformation.

Table 1. Comparison of three grades of estimation methods of liquefaction-induced deformation.

Methods		Accuracy	Cost
Empirical methods	Moderate	Low	
Analytical methods	Static	Fairly good	Comparatively low
	Dynamic	Good	High

angle of inclination for timber houses during the 2000 Tottoriken-seibu earthquake in Japan and found that the allowable angle for inhabitants was less than about 1/100.

Underground structures such as sewage manholes and pipes are uplifted due to liquefaction. The uplift of manholes prevents not only the flow of sewage water but also road traffic. Especially high uplift of manholes from the surface of roads blocks the traffic of emergency vehicles just after an earthquake. In actual, a car collided with a floated manhole and crushed in Nagaoka City during the 2004 Niigataken-chuetsu earthquake as shown in Figure 2. The author and his colleagues researched the allowable uplift for the passage of fire engine trucks by hearings from about 900 fire stations and showed that the allowable floatation is about 13 cm and 23 cm for narrow and wide roads, respectively

Quay walls tilt and move toward sea due to liquefaction. Large movement or inclination of quay walls prevents to bring ships and unload goods.

Allowable values must be determined by considering several conditions mentioned before. However, roughly speaking, upper limit of the liquefaction-induced allowable deformation or displacement for each structure may be the values shown in Table 1.

3 ESTIMATION METHODS FOR LIQUEFACTION-INDUCED DEFORMATION

Estimation methods for liquefaction-induced deformation of structures and ground are classified into three grades: empirical methods, static (residual

deformation) analyses and dynamic (seismic response) analyses. Accuracy and cost are different among these grades as shown in Table 1. In the selection of estimate method, it is necessary to consider the accuracy, the cost and the upper limit of the allowable deformation or displacement shown in Figure 2.

1. Empirical methods

Empirical correlations between severity of liquefaction and deformation of structures can be used to estimate deformation of structures. One example is shown in Figure 4 which is the relationship between the settlement of river dikes near Nagoya City during the 1944 Tohankai earthquake and liquefaction potential, P_L at the settled dikes. Settlement of some river dikes can be estimated roughly by using this relationship. However, estimated deformation is not accurate. For example, if $P_L = 10$, settlement of a river dike is estimated with the range of 0.5 m to 2 m.

2. Static analyses

Several static (residual deformation) analytical methods have been developed. For example, in an analytical program "ALID (Yasuda et al., 2003)" it is assumed that residual deformation occurs due to the reduction of shear modulus of liquefied soils. In the first step of the analysis, stress in the ground before earthquake is calculated by static FEM based on the stress-strain relationships of not-liquefied soils. The deformation of the ground due to liquefaction is calculated in the second step by static FEM again, based on the stress-strain relationship of liquefied soils.

3. Dynamic analyses

Many dynamic (seismic response) analytical methods have been developed recently. In Japan, joint analyses of a building that settled during the Niigata earthquake were carried out by eight program codes in 1992. Estimated settlements were smaller than the actual settlement, because all the codes could not apply to large strain. Subsequently, those computer codes were modified to consider large strain. Joint analyses for the settlement of raft foundation were carried out again in 2003 in Japan (Harada et al., 2004). A hypothetical model of ground beneath a storage tank was used for the analyses. The storage tank is 10 m in diameter and 12 m in height. Six dynamic analysis methods; STADAS2, LIQCA, DIANA, STADAS, FLIP and NUW2, and one static analysis method, ALID were applied. Soil condition of the model ground was similar as the ground in Port Island where liquefaction occurred during the Kobe earthquake. Figure 4 shows relationships between vertical displacement of the tank and maximum acceleration of input wave. As shown in this figure, large settlements of the order of several ten centimeters could be evaluated by these codes. However, the results



Figure 3. A car that collided with an uplifted manhole in Nagaoka City (Tech. Com. on the Sewer Earthquake Countermeasures, 2005).

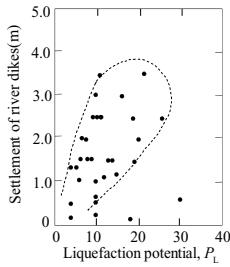


Figure 4. Relationship between P_L and settlement of river dikes.

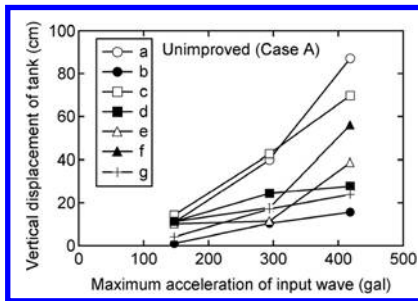


Figure 5. Relationship between acceleration and settlement of the model tank analyzed by 7 analytical methods.

analyzed by the different analytical methods vary significantly, even though the same liquefaction strength is expected. The main reason for this variation is, even though liquefaction strength curves for a particular strain level are fitted, analyses do not always give acceptable results under wide range of strain.

4 RELEVANT SOIL INVESTIGATIONS AND TESTS FOR THE ANALYSIS OF LIQUEFACTION-INDUCED DEFORMATION

In the static and dynamic analyses, stress-strain relationship, permeability and coefficient of volume

compressibility of liquefied soil must be determined by soil investigations and laboratory tests. Relevant soil investigations and tests must be different in each method. Then, the Japan Geotechnical Consultants Association surveyed the relevant soil investigations and tests by hearing from researchers who have developed analytical methods in this year. Table 2 shows the surveyed analytical programs. Eleven dynamic methods and one static method, which are widely used in Japan, were selected. Following three questions were asked:

1. minimum required soil investigations and tests,
2. frequently performed soil investigations and tests, and
3. desired soil investigations and tests.

Figure 6 to 8 show histograms of the relevant soil investigations and tests. Followings are noted:

- a. Many researches answered that the minimum required soil investigations and tests are SPT and grain size analysis as shown in Figure 6. A few researchers listed PS logging and undrained cyclic triaxial or torsional tests for liquefaction.
- b. SPT, grain size analysis, PS logging, undrained cyclic triaxial or torsional tests for liquefaction or shear modulus and triaxial compression test are frequently performed as shown in Figure 7.
- c. Special tests such as undrained monotonic shear test after cyclic shear test, drain test after cyclic shear test, permeability test in horizontal and vertical directions, drain tests after undrained cyclic shear test are added as the desired soil investigations and tests as shown in Figure 8.

In addition several investigations and tests to develop from now were proposed from the researchers:

- i. reliable and economic undisturbed sampling technique such as GS sampling, instead of freezing sampling,
- ii. special tests to measure the behavior of liquefied soil under large strain level,
- iii. in-situ tests to induce liquefaction, and
- iii. special tests to measure viscous damping.

Table 2. Surveyed analytical programs.

Classification	Name of program
Dynamic analyses	• DIANA • DIANA-J2 & TDAP III
	• DYNFLOW • EFFECT • FLIP
	• HiPER • LIQCA • Mu-DIAN
	• NUW2 • STADAS • STADAS II
	• ALID
Static analysis	• ALID

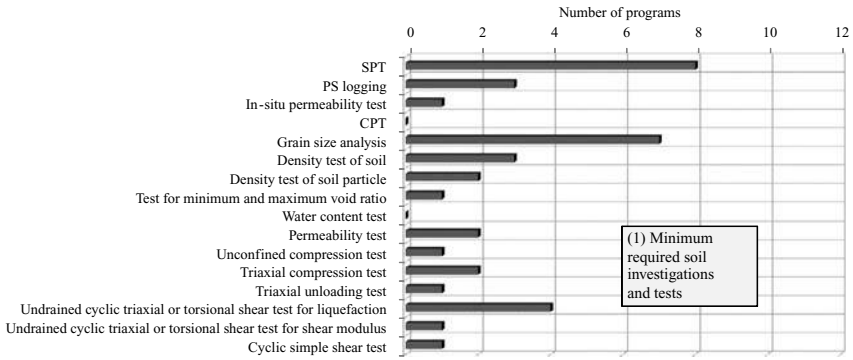


Figure 6. Histogram of minimum required soil investigations and tests.

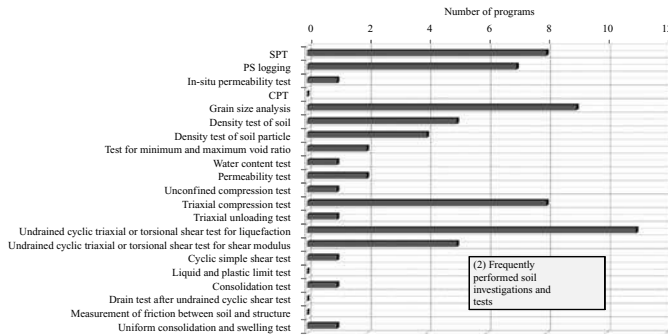


Figure 7. Histogram of frequently performed soil investigations and tests.

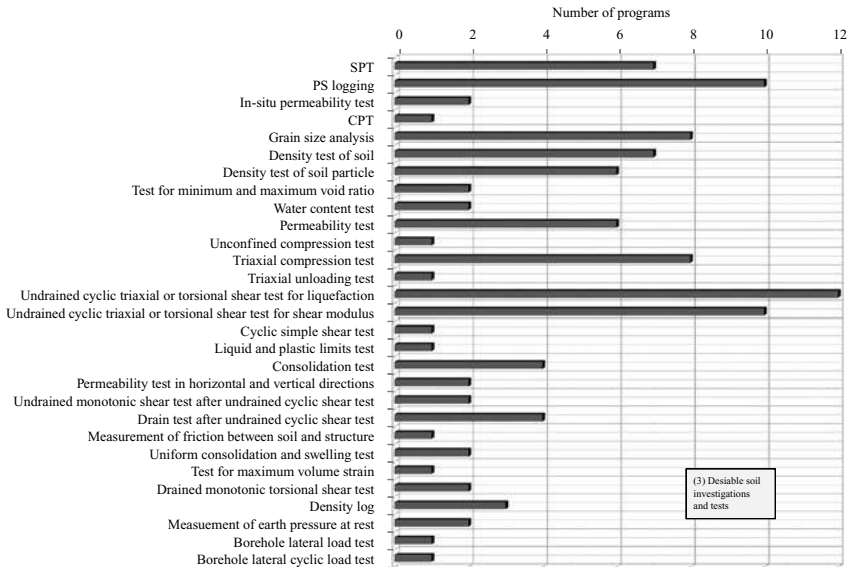


Figure 8. Histogram of desirable soil investigations and tests.

5 CONCLUDING REMARKS

Relevant soil investigations and tests to evaluate liquefaction-induced deformation are discussed. More studies on in-situ special tests, undisturbed sampling techniques and laboratory special tests are needed to obtain stress-strain relationship, permeability and coefficient of volume compressibility of liquefied soil.

strong earthquake, *Proceedings of the 3rd International Conference on Earthquake Geotechnical Engineering*, Vol., 156–566.

Yasuda, S., Ideno, T., Sakurai, Y., Yoshida, N. and Kiku, H. 2003. Analyses for liquefaction-induced settlement of river levees by ALID, *Proc. of the 12th Asian Regional Conference on SMGE*, 347–350.

REFERENCES

Harada, K., Yasuda, S., Yoshida, N., Sato, M. and Sento, N. 2004. Comparative study on the effectiveness of compaction as a countermeasure against liquefaction during a

Discussion session on performance criteria for designing geotechnical structures

S. Iai

Disaster Prevention Research Institute, Kyoto University, Kyoto, Japan

1 PRINCIPLES IN PERFORMANCE-BASED DESIGN

Following ISO23469 Seismic actions for designing geotechnical works, principles in performance-based design may be summarized as follows:

1.1 *Purposes and functions*

In designing geotechnical works, the purposes and functions are defined in accordance with broad categories of use such as commercial, public and emergency use.

1.2 *Performance objectives for seismic design*

Performance objectives for seismic design of geotechnical works are generally specified on the following basis, depending on the expected functions during and after an earthquake:

- serviceability during and after an earthquake: minor impact to social and industrial activities, the geotechnical works may experience acceptable residual displacement, with function unimpaired and operations maintained or economically recoverable after temporary disruption;
- safety during and after an earthquake: human casualties and damage to property shall be minimized, geotechnical works that are an essential part of a facility handling hazardous materials or a post-earthquake emergency facility shall maintain full operational capacity, and geotechnical works shall not collapse.

The performance objectives also reflect the possible consequences of failure.

1.3 *Reference earthquake motions*

For each performance objective described in (2), reference earthquake motions are specified for evaluating seismic performance of the geotechnical works as follows:

- for serviceability during or after an earthquake: earthquake ground motions that have a reasonable

probability of occurrence during the design working life;

- for safety during or after an earthquake: earthquake ground motions associated with rare events that may involve very strong ground shaking at the site.

1.4 *Performance criteria and limit states*

Performance criteria are generally specified by engineering parameters that characterize the response of geotechnical works to the reference earthquake motions. These engineering parameters are specified considering the design working life.

The engineering parameters depend on the process for verifying that the performance criteria have been met. The importance of the facility differentiates the level of performance objectives. These issues are taken into account in the formulation of the performance criteria.

The seismic performance of geotechnical works can be described with reference to a specified set of limit states. These limit states are

- serviceability limit state during or after an earthquake: a limit state for satisfying serviceability during and after an earthquake, and defined by an acceptable state of displacement, deformation, or stress, and
- ultimate limit state during or after an earthquake: a limit state for satisfying safety requirements during and after an earthquake, and defined by a state with appropriate margin against collapse.

More than one serviceability limit state may be introduced. For example, if one serviceability limit state is defined as the state with no residual displacements, another serviceability limit state may be defined as the state with an acceptable residual displacement and operation of the facility recoverable after minimum disruption with reasonable cost for repair.

In conventional seismic design of geotechnical works based on the equivalent static method, a seismic coefficient has been used to achieve both serviceability and safety during and after an earthquake. However, as a result of case histories of seismic damage during

the 1990s, limitations of conventional seismic design have been recognized widely. The performance-based approach can be an alternative approach to overcome these limitations.

2 PERFORMANCE CRITERIA AND THE ISSUES FOR DISCUSSION

The principles in performance-based design reviewed in the previous chapter clearly indicates that the performance criteria are defined within a hierarchical structure that consists of four elements; (1) purposes and functions, (2) performance objectives for seismic design, reflecting the possible consequences of failure, (3) reference earthquake motions, and (4) performance criteria and limit states, that are specified considering the design working life and the method for evaluation of performance. Because the performance objectives for seismic design reflect the possible consequences of failure, the importance of the facility differentiates the level of performance objectives.

In conventional seismic design of geotechnical works based on the equivalent static method, the consequences of failure are taken into account in terms of a factor specified in accordance with broad categories of importance. In the performance-based design, the consequences of failure may be evaluated through a more sophisticated methodology. For example, acceptable levels of damage shown in Table 1 are specified by a combination of structural and operational damage. In this example, the consequences of failure are categorized into structural and operational aspects. Consequence of failure due to structural damage may be relatively easily evaluated based on the cost and time needed for repair of damaged structures. However, consequence of failure due to operational damage needs much more elaborate analysis, including systemic and financial analysis by viewing a geotechnical structure as a component of a larger infrastructure system. More studies are required on this issue at the current state of development in the performance-based design. New proposals or examples on this issue are invited for the discussion session.

Another issue that may be more easily accessible from the expertise of geotechnical engineering is in the next level of hierarchy for specifying the performance criteria. This issue includes (1) determination of the most appropriate engineering parameters that characterize the response of geotechnical works, considering the availability and reliability of the methodology used for performance evaluation. It is obvious that choice of engineering parameters depends on the specific type of geotechnical structures. The choice of the methodology might be dependent on the importance of geotechnical structures. New proposals and examples on this aspect of issue are also invited for the discussion session.

Table 1. Acceptable level of damage in performance-based design*.

Acceptable level of damage	Structural	Operational
Degree I: Serviceable	Minor or no damage	Little or no loss of serviceability
Degree II: Repairable	Controlled damage**	Short-term loss of serviceability***
Degree III: Near collapse	Extensive damage in near collapse	Long-term or complete loss of serviceability
Degree IV: Collapse****	Complete loss of structure	Complete loss of serviceability

* Considerations: Protection of human life and property, functions as an emergency base for transportation, and protection from spilling hazardous materials, if applicable, should be considered in defining the damage criteria in addition to those shown in this table.

** With limited inelastic response and/or residual deformation.

*** Structure out of service for short to moderate time for repairs

**** Without significant effects on surroundings.

3 EVALUATION OF UNCERTAINTY IN THE PERFORMANCE-BASED DESIGN

While safety should be one of primary performance objectives for ordinary buildings, serviceability and economy become higher priority issues for ordinary geotechnical structures. For these structures, a methodology based on the principle of minimum life-cycle cost may be ideal (e.g. Sawada, 2003). This methodology is emerging and will be eventually adopted as the state-of-practice in the coming decade.

Life-cycle cost is a summation of initial construction cost and expected loss due to earthquake induced damage. Probability of occurrence of earthquake ground motion (i.e. earthquake ground motions with all (or varying) return periods) is considered for evaluating the expected loss due to earthquake induced damage. The life-cycle cost also includes intended maintenance cost and cost for demolishing or decommissioning when the working life of the structure ends.

When evaluating serviceability through life-cycle cost, failure of a geotechnical structure is defined by the state that does not satisfy the prescribed limit states typically defined by an acceptable displacement, deformation, or stress. If a peak ground motion input to the bottom boundary of soil structure systems is used as a primary index of earthquake ground motions, probability of failure $F_F(a)$ at peak ground motion a is computed considering uncertainty in geotechnical and structural conditions. A curve described by a function $F_F(a)$ is called a fragility curve. Probability of occurrence of earthquake ground motions is typically defined by a slope (or differentiation) of a function

$F_H(a)$ that gives annual probability of exceedance of a peak ground acceleration a . A curve described by a function $F_H(a)$ is called a seismic hazard curve.

Given the fragility and seismic hazard curves for a port structure, annual probability of failure of the port structure P_1 is computed as follows:

$$P_1 = \int_0^{\infty} \left(-\frac{dF_H(a)}{da} \right) F_F(a) da \quad (1)$$

If a design working life is T years, probability of failure of the port structure over the design working life is given by

$$P_T = 1 - (1 - P_1)^T \quad (2)$$

If loss due to earthquake induced damage associated with the prescribed limit state is designated by c_D , expected loss over the design working life of a port structures C_D is given by

$$C_D = P_T c_D \quad (3)$$

Thus, the life-cycle cost C_{LC} is given by adding initial construction cost C_I , maintenance cost C_M and demolishing cost C_{END} as

$$C_{LC} = C_I + C_D + C_M + C_{END} \quad (4)$$

This is generalized further by introducing more than one serviceability limit state.

As demonstrated for liquefaction hazard evaluation by Kramer *et al.* (2006), the probability evaluated by Eqs.(1) and (2) is a consistent index of hazard and the conventional approach based on the return period prescribed in design provisions and codes can be either too conservative or unconservative depending on the site. Expected loss evaluated by Eq.(3) is an index that reflects the consequence of failure. Life-cycle cost evaluated by Eq.(4) is an index that properly reflects the trade-off between initial cost and expected loss. The design option that gives the minimum life-cycle cost is the optimum in terms of overall economy. Thus, the optimum design has a certain probability of failure given by Eq.(2). This probability is not prescribed by an authority (such as 10% over 50 years) but rather determined as a result of the minimum life-cycle cost procedure. The probability of failure can be large if a consequence of failure in meeting the performance

criteria, as measured by seismic loss c_D , is minor. The probability can be small, however, if a consequence of failure, as measured by c_D , is significant. Thus, the minimum life-cycle cost procedure reflects the possible consequences of failure and, thereby, satisfies the principles in performance objectives in the ISO guidelines described in the previous section. New proposals and examples on this aspect of issue are also invited for the discussion session.

4 SUMMARY AND CONCLUSIONS

The issues to be discussed during the discussion session may be summarized as follows:

1. How to evaluate the consequence of failure for defining the performance objectives during and after earthquakes?
2. How to determine the most appropriate engineering parameters that characterize the response of geotechnical works for specifying performance criteria?
3. How to deal with the uncertainty in seismic design of geotechnical structures?

Answers to these questions will be most beneficial for establishing the performance-based design of geotechnical structures.

REFERENCES

- Iai, S. (2005). "International standard (ISO) on seismic actions for designing geotechnical works—An overview." *Soil Dynamics and Earthquake Engineering*, 25: 605–615.
- Kramer, S.L., Mayfield, R.T. and Anderson, D.G. (2006). "Performance-based liquefaction hazard evaluation: implications for codes and standards." *8th U.S. National Conference on Earthquake Engineering*, San Francisco, Paper No. 888.
- Sawada, S. (2003). *A new look at Level 1 earthquake motions for performance-based design of civil engineering structures*: Japan Society of Civil Engineers. <http://www.jsce.or.jp/committee/eec2/taishin/index.html>

Risk measures in design of geotechnical structures

G.J. Rix

Georgia Institute of Technology, Atlanta, Georgia, USA

ABSTRACT: Two potential improvements to the use of life-cycle cost in performance-based design of geotechnical structures are presented. The first recognizes that earthquake-induced losses may occur at any time during the design life of the structure, and thus the time value of money should be taken into account by using the present value of the life-cycle cost. The second proposed improvement is an alternative definition of risk based on the dispersion (e.g., variance or standard deviation) of the life-cycle cost rather than the mean value. This approach results in an “efficient frontier” of design options that users may choose from depending on their definition of risk and tolerance for risk.

1 INTRODUCTION

One of the issues to be discussed in the session on Performance Criteria for Designing Geotechnical Structures is how to deal with uncertainty in seismic design of geotechnical structures. Iai (2009) has summarized an approach based on the life-cycle cost of structures subjected to earthquake loads (Sawada 2003). The life-cycle cost is the sum of the initial construction cost, maintenance cost, demolition or decommissioning cost, and the cost (i.e., loss) due to earthquake-induced damage. The design alternative that minimizes the expected value of the life-cycle cost is preferred.

In this brief paper, two proposed enhancements to the life-cycle cost procedure are presented.

2 LIFE-CYCLE COST METHOD

For the sake of completeness, the life-cycle cost method described by Iai (2009) is summarized herein. The annual probability of failure for a structure is:

$$p_f = \int_y p_f(y) \left(\frac{-d\lambda(y)}{dy} \right) dy \quad (1)$$

where $p_f(y)$ is the annual probability of failure conditional on the ground motion parameter y and $\lambda(y)$ is the seismic hazard curve (i.e., the mean annual rate of exceedance of y).

Each year in the design life of the structure is a Bernoulli trial with probability of failure p_f . Thus, the probability mass function (PMF) of the number of failures n during the design life of the structure (T years) is given by a binomial distribution:

$$p(n|T, p_f) = \frac{T!}{n!(T-n)!} p_f^n (1-p_f)^{T-n} \quad (2)$$

The expected value of the total direct and indirect losses associated with failure may be expressed as:

$$E[C_D] = E[nc_D] = c_D E[n] = c_D p_f T \quad (3)$$

where $E[n]$ denotes the expected value and c_D is the deterministic loss associated with an individual failure.

As noted earlier, the life-cycle cost is the sum of the initial construction cost (C_I), maintenance cost (C_M), demolition and decommissioning cost (C_{end}), and earthquake-induced losses (C_D):

$$C_{LC} = C_I + C_M + C_{end} + C_D \quad (4)$$

The expected value of the life-cycle cost is simply the sum of the expected values of each term:

$$E[C_{LC}] = E[C_I] + E[C_M] + E[C_{end}] + E[C_D] \quad (5)$$

The objective is to minimize the expected value of the life-cycle costs (i.e., least mean cost). Further information is available in Werner (1998) and Wen and Kang (2001a; Wen and Kang 2001b).

3 TIME VALUE OF MONEY

One potential improvement to this approach is to recognize that three of the four costs in Equation 4 occur at different times throughout the design life of the structure. In order to objectively compare costs that occur over time, it is necessary to calculate the present value of these costs. Given a cost incurred in t years in the future, the present value of the cost is:

$$C_{PV} = C_t (1+r)^{-t} \quad (6)$$

where r is the discount rate. Thus, the present value of the demolition and decommissioning costs at the end of the design life is:

$$E[C_{end, PV}] = E[C_{end}] (1+r)^{-T} \quad (7)$$

If we assume that the maintenance costs are equal from year to year, the present value of the series of costs is:

$$E[C_{M,PV}] = E[C_M] \frac{1 - (1+r)^{-T}}{r} \quad (8)$$

Finally, it may be shown that the present value of a series of random values such as the earthquake-induced losses in each year is:

$$E[C_{D,PV}] = E[C_D] \frac{1 - (1+r)^{-T}}{r} \quad (9)$$

The initial construction costs, of course, do not need to be discounted. Thus, the expected value of the life cycle cost accounting for the time value of money may be obtained by substituting Equations 7–9 into Equation 5.

4 DISPERSION OF LIFE-CYCLE COST

A traditional definition of risk in engineering problems is the product of *probability* and *consequence* (Baecher and Christian 2003). Using this definition, the expected value (Eq. 3) is a measure of the risk associated with earthquake-induced losses during the design life of the structure. Likewise, Equation 5 is a measure of the risk associated the life-cycle cost. As such, minimizing the life-cycle cost may also be viewed as minimizing the risk.

An alternative definition of risk is the dispersion (i.e., aleatoric uncertainty) about the expected value (Levy 2006). Typically, the variance or standard deviation is used as measures of risk in this context. Large values of the variance or standard deviation of the life-cycle cost are likely to be considered “risky” by some stakeholders. The use of dispersion as a measure of risk has its basis in the pioneering methods of financial investment analysis developed by Markowitz (1952) and Sharpe (1964).

For simplicity, let us assume that the variance of the losses due to earthquake-induced damage is large compared to the other costs in Equation 4. Hence, we may write:

$$Var[C_{LC}] \approx Var[C_D] \quad (10)$$

The variance of the earthquake-induced costs is equal to the variance of the binomial distribution:

$$\begin{aligned} Var[C_D] &= Var[nc_D] \\ &= c_D^2 Var[n] \\ &= c_D^2 T p_f (1 - p_f) \end{aligned} \quad (11)$$

Like expected costs, the variance should also be discounted for costs that occur in the future. It may be shown that the present value of the variance of the earthquake-induced losses is:

$$Var[C_{D,PV}] = c_D^2 T p_f (1 - p_f) \frac{1 - (1+r)^{-2T}}{r(2+r)} \quad (12)$$

Additional discussion on the use of dispersion as a measure of risk in civil infrastructure and natural hazards applications is contained in Taylor and Werner (1995), Werner (1998), and Alesch et al. (2002).

5 ILLUSTRATIVE EXAMPLE

To illustrate these ideas, a simple example involving earthquake-induced permanent displacements of an infinite slope is presented. The seismic hazard curve for peak ground acceleration (*pga*) is given by the following expression (Cornell et al. 2002; McGuire 2004):

$$\lambda(pga) = 5 \times 10^{-5} pga^{-3} \quad (13)$$

The probability of failure conditional on the peak ground acceleration is defined using an expression derived by Bray and Travarasou (2007) for the probability that the seismically-induced displacement will exceed 1 cm, which is considered by Bray and Travarasou to be the minimum displacement of engineering significance:

$$\begin{aligned} P(D > 1 \text{ cm}) &= \Phi[-1.76 - 3.22 \ln(k_y) \\ &\quad + 3.52 \ln(pga)] \end{aligned} \quad (14)$$

where k_y is the yield coefficient and Φ is the standard normal cumulative distribution function. This expression is based on Equation 3 in Bray and Travarasou for $T_s = 0$ (i.e., an infinite slope). Note that “failure” could be defined in terms of larger displacements without loss of generality. In this example, the yield coefficient is considered to be a design parameter that could be varied by changing the slope angle among other parameters affecting k_y . Once the integration in Equation 1 is performed, the annual probability of failure can be expressed as a function of the yield coefficient as shown in Figure 1.

To calculate the life-cycle cost, several simplifying assumptions are made. The initial construction cost is given by:

$$E[C_I] = 1.0 + 0.5k_y \quad (15)$$

where the second term reflects the additional cost associated with constructing a slope with a higher yield coefficient. The expected value of the loss due

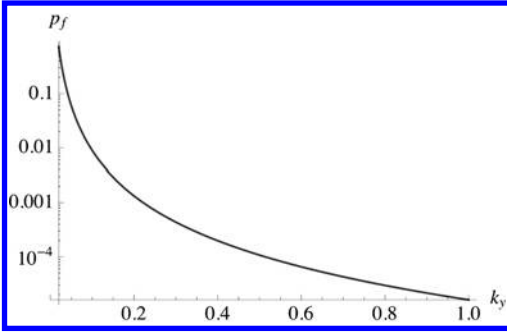


Figure 1. Annual probability of failure.

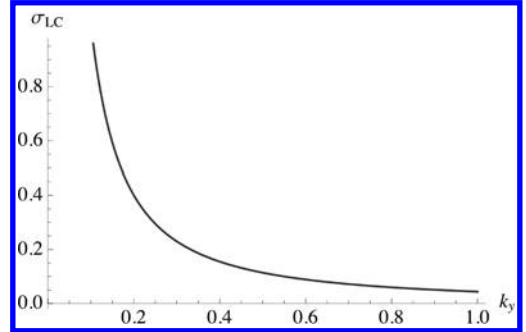


Figure 3. Standard deviation of total cost as a function of yield coefficient.

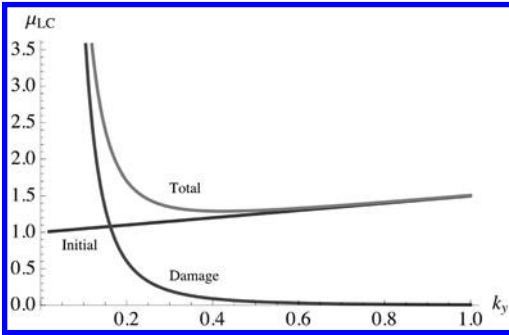


Figure 2. Expected value of initial construction cost, earthquake-induced damage, and total cost as a function of yield coefficient.

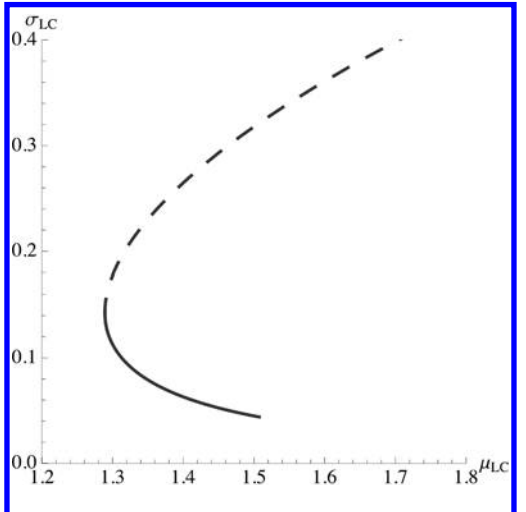


Figure 4. Standard deviation vs. mean value of total cost.

to earthquake-induced damage is equal to 50% of the initial construction cost:

$$c_D = 0.5C_I \quad (16)$$

The design life of the slope (T) is 50 years and an annual discount rate of 5% is used for the time value of money. Finally, maintenance and demolition costs are neglected because they are assumed to be independent of the yield coefficient selected for design and thus do not affect the outcome of the risk analysis.

With these assumptions, the expected values of the initial construction cost and the earthquake-induced losses may be calculated using Equations 3, 5, and 9. The results are shown in Figure 2. As anticipated, increasing the design yield coefficient increases the initial construction costs, but it significantly decreases the expected value of the earthquake-induced loss. The expected value of the life-cycle (i.e., total) cost reaches a minimum at $k_y = 0.42$. The corresponding mean total cost is 1.29.

The variance (or standard deviation) of the life-cycle cost may be calculated via Equation 12. A plot of

the standard deviation is shown in Figure 3. Note that the standard deviation of the life-cycle cost decreases significantly with increasing k_y .

Additional insight can be gained by plotting the standard deviation of the life-cycle cost as a function of the mean value as shown in Figure 4. The dashed portion of the curve corresponds to values of k_y that are less than the value at which the mean life-cycle cost is a minimum (i.e., $k_y = 0.42$). For this range of values, both the mean and standard deviation of the life-cycle cost are high. The solid portion of the curve defines the “efficient frontier” where a trade-off exists between the mean and standard deviation of life-cycle cost. Some decision-makers may choose to minimize the mean cost. However, others may be willing to accept higher mean costs in exchange for reducing (or minimizing) the standard deviation of the

life-cycle cost. There is no single best option, and the decision will depend on the user's definition of risk and their risk tolerance.

6 CONCLUSIONS

The use of life-cycle costs helps to achieve the objectives of performance-based design by properly representing the possible consequences of failure. Two improvements have been presented: (1) accounting for the time-value of money over the design life of the structure and (2) defining risk as the dispersion of the life-cycle cost rather than the mean value. The latter results in an "efficient frontier" of design alternatives that users may choose from based on their definition of risk and risk tolerance.

ACKNOWLEDGEMENTS

This material is based on work supported by the National Science Foundation under Grant Nos. CMS-0530478 and CMS-0402490. Any opinions, findings, and conclusions or recommendations expressed in this material are those of the authors and do not necessarily reflect the views of the National Science Foundation.

REFERENCES

Alesch, D.J., Nagy, R., and Taylor, C.E. (2002). "Seeking Criteria for the Natural Hazard Mitigation Investment Decision." *Acceptable Risk Processes: Lifelines and Natural Hazards*, C.E. Taylor and E. VanMarcke, eds., American Society of Civil Engineers, Council on Disaster Reduction and Technical Council on Lifeline Earthquake Engineering Monograph No. 21, Reston, VA, 160–184.

Baecher, G.B., and Christian, J.T. (2003). *Reliability and Statistics in Geotechnical Engineering*, John Wiley & Sons, Chichester, West Sussex, England.

Bray, J.D., and Travasarou, T. (2007). "Simplified Procedure for Estimating Earthquake-Induced Deviatoric Slope Displacements." *Journal of Geotechnical and Geoenvironmental Engineering*, 133(4), 381–392.

Cornell, C.A., Jalayer, F., Hamburger, R.O., and Foutch, D.A. (2002). "Probabilistic basis for 2000 SAC Federal Emergency Management Agency steel moment frame guidelines." *Journal of Structural Engineering*, 128(4), 526–533.

Iai, S. (2009). "Discussion session on performance criteria for designing geotechnical structures." International Conference on Performance-Based Design, Tokyo, Japan, June 15–18.

Levy, H. (2006). *Stochastic Dominance: Investment Decision Making Under Uncertainty*, Springer, New York.

Markowitz, H.M. (1952). "Portfolio selection." *Journal of Finance*, 7(1), 77–91.

McGuire, R.K. (2004). *Seismic Hazard and Risk Analysis*, Earthquake Engineering Research Institute, Oakland, CA.

Sawada, S. (2003). "A new look at Level 1 earthquake motions for performance-based design of civil engineering structures." Japan Society of Civil Engineers.

Sharpe, W.F. (1964). "Capital asset prices: A theory of market equilibrium under conditions of risk." *Journal of Finance*, 19(3), 425–442.

Taylor, C.E., and Werner, S.D. (1995). "Final Report, Proposed POLA 2020 Acceptable Seismic Risk Procedures with Demonstration Application to Pier 300 Wharf, Port of Los Angeles, San Pedro, CA." Dames & Moore, Inc.

Wen, Y.K., and Kang, Y.J. (2001a). "Minimum building life-cycle cost design criteria. I: Methodology." *Journal of Structural Engineering*, 127(3), 330–337.

Wen, Y.K., and Kang, Y.J. (2001b). "Minimum building life-cycle cost design criteria. II: Applications." *Journal of Structural Engineering*, 127(3), 338–346.

Werner, S.D. (1998). "Seismic Guidelines for Ports." Technical Council on Lifeline Earthquake Engineering, American Society of Civil Engineers, Reston, VA.

Determining criteria for seismic performance of earth structures

I. Towhata

University of Tokyo, Tokyo, Japan

ABSTRACT: This paper concerns a methodology for determination of seismic performance criteria which are relevant for future earthquake resistant design of geotechnical structures. Although many people are talking recently about the need for seismic performance-based design, one of its major difficulties lies in the decision of performance criteria. Considering the lack of rational approach to this problem, the author classifies geotechnical structures into three categories, for which different ideas of criteria are proposed. The basic idea therein is that negative effects to the public should be made as small as possible, irrespective of the category of structures. Two major issues are the allowable restoration time and minimization of the life cycle cost.

1 CURRENT SITUATION

The classical philosophy of earthquake resistant design, which is based on the static seismic coefficient and the factor of safety, had been successful since its introduction to practice in 1920s. This situation, however, started to change because of the increasing demand for safety and the increasing intensity of design earthquakes. The latter was particularly significant because the limited shear strength of geotechnical materials could not sustain the increased magnitude of design earthquake forces, resulting in seismic factor of safety less than unity.

The performance-based design principle (*PBD*) is a newly proposed alternative. *PBD* allows the seismic factor of safety less than unity. There are two goals to be achieved in *PBD*. The one is the development of practically useful tool for prediction of seismic performance, and the other is the decision of a critical seismic performance; if the predicted performance exceeds this critical one, the proposed design is not accepted. While neither goal is easily achieved, the present paper addresses mainly the latter issue.

2 BASIC REQUIREMENTS

It is essential that any design principle fully considers the people's recent demand for safety. While safety used to mean that of life and probably that of properties, the recent situation adds to them the reduction of economic loss, quick recovery from seismic damage, and securing continuity of business. The recent trend is particularly important because the quality of post-earthquake life is, in the recent advanced society, substantially affected by those new safety issues.

As far as geotechnical structures are concerned, the extent of earthquake-induced damage and the seismic performance are expressed by the residual deformation. The greater deformation reduces the function/operation of the structure more significantly, makes longer the duration time for restoration, and increases the economic loss. It is fortunate that seismic damage of embankments and other geotechnical structures has killed few people. Most earthquake victims have been killed by collapse of weak buildings, failure of natural slopes, and tsunamis. Hence, *PBD* needs to assess the residual deformation as precisely as possible within practically affordable costs and, moreover, to determine the extent of allowable residual deformation.

A precise assessment of residual deformation is not an easy task. Besides the complexity of advanced numerical tools, behavior of soils under cyclic undrained loading in two- or three-dimensional manner is often more complicated than existing constitutive models concern. Another difficulty is the reliability of in-situ soil investigations. Problems in undisturbed soil sampling and nonuniformity of natural soil deposits are not yet solved.

The present paper considers that the above-mentioned difficulties in performance assessment will not be fully solved in near future. Hence, the results of analysis should be regarded as an index calculation, which becomes greater when the real seismic deformation is more significant. This attitude is reasonable because the performance cannot be predicted precisely unless the true acceleration input is accurately predicted, which is impossible.

The critical deformation during earthquake is difficult to decide. It is proposed herein to decide as an alternative the critical restoration time. If the deformation is too big to be restored within this critical

time, the design should be revised. In other words, *PBD* should aim to minimize the negative effects to the public, which are both direct and economic ones.

In the following sections, geotechnical structures will be classified into three groups, which are namely ordinary structures, important ones, and extremely important ones.

3 PERFORMANCE CRITERIA

3.1 Ordinary structures

Low embankments of local roads, quays of small harbors, and most river levees belong to this group. Since construction budget are limited, advanced soil investigation and numerical analyses are not feasible. Hence, preparedness for damage and quick restoration has been sought for. Most river levees have not been designed against earthquakes because flooding and earthquake would not come together.

In case *PBD* is introduced, the residual deformation has to be assessed. This task can be simply performed by referring to a table prepared by running Newmark sliding block analogy on many typical cross sections. Input soil parameters are determined on the basis of simple soil parameters such as degree of compaction. Different deformation is obtained for different static factor of safety and different magnitude of design earthquake motions. Then the required restoration time is assessed and compared with the critical time. Probably the critical time would be a few weeks to months. However, when the concerned structure belongs to a network that has an alternative structure, the critical time can be longer.

3.2 Important structures

This group consists of national motorways, most railways, access to bridges, and big harbors. Because these structures are unlikely to have alternative choices, the allowable restoration time is short. It is important that these structures play key roles in the post-earthquake rescue and restoration activities. If this is the case, the allowable restoration time is very short, or even immediately after a quake, at least one lane of a road has to maintain its function.

Towhata et al. (2008 & 2009) showed how to rationally determine the allowable deformation. According to them, first the size of an affected area should be determined, and second the allowable restoration time is decided. Both decisions are easier than direct decision of the allowable deformation. Consequently, the allowable deformation is determined. It seems that the reasonable restoration time is within one month.

3.3 Extremely important structures

Intercity expressways, trunk railways, and international harbors are included in this group. Although

attempts have been made to carry out *PBD* on these structures, it appears that the critical residual deformation has been determined by engineering judgment, without a rigorous methodology.

For these structures, the economic damage has to be taken into account. The restoration time should not be so long as to cause fatal economic damage to the concerned community. In this regard, the life cycle cost (*LCC*) principle should be aimed in near future. *LCC* is a summation of the initial cost (C_i), the maintenance cost (C_m), and the seismic loss (C_e);

$$LCC = C_i + C_m + C_e \quad (1)$$

It is aimed to minimize *LCC* by spending the optimum amount of money on the initial construction. Since *LCC* methodology is probabilistic, the uncertainty in input earthquake motion and variation of soil properties are taken into account.

Towhata et al. (2008 & 2009) attempted to carry out *LCC* principle. The findings therein were

- Uncertainties in intensity of earthquakes and variation of soil properties are taken into account.
- Uncertainty of earthquake motion is more significant than that of soil properties.
- Although economic damage is still difficult to assess, it is the key factor that governs the optimum design option.
- The *LCC* optimum design may be different from what conventional factor-of-safety approach suggests.

ACKNOWLEDGMENT

The studies introduced in the present text were previously conducted in an activity of the earthquake engineering committee of Japan Society for Civil Engineers as well as with a financial support by NEDO of Japanese Government. The authors deeply appreciate those assistances.

REFERENCES

- Towhata, I., Yoshida, I., Suzuki, S., & Ishihara, Y. 2008. Life cycle cost evaluation for seismic performance-based design of geotechnical structures, 12th *IACMAG*, Goa, India.
- Towhata, I., Yoshida, I., Ishihara, Y., Suzuki, S., Sato, M., & Ueda, T. 2008. On design of expressway embankment in seismically active area with emphasis on life cycle cost, accepted by *Soils and Foundations*.

Integrated design of structure-foundation systems and performance based design

M.J. Pender

University of Auckland, New Zealand

1 INTRODUCTION

These notes are concerned with the earthquake resistant design of foundations, both shallow and deep, for buildings and bridges in situations where liquefaction is not a risk. The ideas presented herein are part of the background to the thesis work of Wotherspoon (2009) and Toh (2008).

The main thrust of the comments is that performance based design of foundations needs to be linked with the performance based design of the super incumbent structure; in other words the complete system, foundation and structure, needs to be considered as a single entity. It is envisaged that this might be achieved by considering the responses of numerical models of the whole system using design earthquake motions as input.

The process suggested in the above paragraph requires a close working together of the geotechnical and structural teams involved in the design. This may not be common practice in some, or even many, parts of the world. A statement in the FEMA 356 document (Federal Emergency Management Agency 2000) cautions against handling uncertainty by specifying lower bounds on soil stiffness and strength values. If the actual values are greater than those assumed, then the real design actions may be larger than those estimated. The FEMA document requires that the basis for assignment of property values needs to be fully explained in geotechnical reports. This suggests that the geotechnical work is completed well before the structural design commences. This separation of activities is not what is envisaged herein, rather it is suggested that the essence of performance based design of foundation-structure systems is a close working together of the structural and geotechnical teams.

Much of our exploration of integrated design concepts has been done with the Ruaumoko software (Carr 2004) modified where necessary to incorporate foundation modelling.

Performance based design, at least in part, must involve working within criteria for satisfactory post-earthquake permanent displacements. Where are these performance displacement criteria to come from?

This is not clear at present. Possible sources of insight might be criteria for acceptable differential settlements of structures. In other words if post earthquake differential settlements are within accepted bounds for structural differential displacements then, presumably, the performance is satisfactory. Limitations on permanent rotations of tall structures may be another source of allowable displacement criteria. Allowable relative movements between foundations and service connections are another. In as much as interstorey drift is affected by foundation response, then there may be further insight here. Finally, spacing between adjacent buildings and prevention of contact during earthquake response might be another source of acceptable permanent displacement criteria. These are offered here as comments in lieu of recognised residual deformation criteria.

In the remainder of these notes examples of integrated design will be discussed briefly.

2 SHALLOW FOUNDATIONS

Although shallow foundations can sustain moment, this is expensive in that larger foundations are needed for a given vertical load. In the case of a framed building on shallow foundations the ground floor column bases may transfer moments to the foundations during earthquake loading. It is obvious that more economical shallow foundation sizes are possible if the column-footing connections are pinned. Pender (2007) illustrated this and also demonstrated that the additional lateral displacements induced in the structure because of the pinned connections are quite modest. Considering the moment distribution in the ground floor column, it is apparent that when the column-footing connections are fixed the moments at the top and bottom of the column are of roughly equal magnitude. But for the pinned connection there is no moment at the footing and the magnitude of the moment at the top of the first storey column is about double that of the previous case. Thus geotechnical design assumptions may have a significant effect on structural performance.

The paper by Pender et al. (2009) at this conference explores another aspect of shallow foundation behaviour, namely the possibility of using the permanent displacement at the end of the earthquake as a performance criterion. This has long been done with regard to the performance of slopes and gravity retaining walls. Even though it is likely that acceptable permanent displacements of slopes will be greater than those for walls, which in turn will be greater than those of shallow foundations, consideration of the validity of shallow foundation post-earthquake displacement is still merited. In the Pender et al. (2009) paper the dynamic response, measured in a centrifuge, of a model tower structure on a shallow foundation is compared with computed outputs from three different numerical models. It is seen, that from the point of view of design analysis, all three models give a reasonable prediction of the response.

3 PILED FOUNDATIONS

We have also looked at modelling the response of framed structures supported on piles, one pile below each column. In this case the pile head—column connections are also connected by tie beams. Ruaumoko modelling (Wotherspoon 2009) shows that with appropriate bending stiffness for the tie beams, it is possible to “optimise” the moment distribution in the bottom storey columns and the piles so that roughly the same magnitude of maximum moment occurs at the top and bottom of the column and in the pile shaft below. This is another example of an insight that is a fruit of the developing integrated models of the structure-foundation system.

4 DISCUSSION QUESTIONS

- i. Is the suggestion made above that a teamwork approach is necessary to achieve the best outcome for performance based design of structure foundation systems feasible?

- ii. It goes without saying that the numerical model of the structure-foundation system needs to be based on high quality site investigation data. What is the best strategy for obtaining such information?
- iii. Following on from (ii), is the approach suggested in the FEMA 356 document—obtaining a best estimate of the ground stiffness and then checking the response at twice and half this stiffness—realistic for performance based design?

REFERENCES

- Carr, A.J. 3D RUAUMOKO: inelastic three-dimensional dynamic analysis program, University of Canterbury—Department of Civil Engineering, Christchurch, NZ, 2004.
- Federal Emergency Management Agency “Prestandard and Commentary for the Seismic Rehabilitation of Buildings—FEMA 356”. Washington D.C, 2000.
- Pender, M.J “Seismic design and performance of surface foundations”, Chapter 10, Earthquake Geotechnical Engineering, K.D. Pitalakis (ed), Springer, pp. 215–241, 2007.
- Pender, M.J., Toh, J.C.W., Wotherspoon, L.M., Algie, T.B., and Davies, M.C.R. “Earthquake induced permanent displacements of shallow foundations—performance based design”, IS-Tokyo 2009.
- Toh, J.C.W. “Performance based aseismic design of shallow foundations”, ME thesis, University of Auckland, 2008.
- Wotherspoon, L.M. “Integrated modeling of Structure—Foundation systems”, PhD thesis, University of Auckland, 2009.

Learning from geotechnical earthquake engineering case histories

J.D. Bray

University of California, Berkeley, CA, USA

ABSTRACT: Earthquake engineering is an experience-driven field. Documenting and sharing the key lessons learned from major earthquake events around the world contributes significantly to advancing research and practice in earthquake engineering. The importance of detailed mapping and surveying of damaged areas cannot be overemphasized, as it provides the base data of well-documented case histories that drive the development of many of the design procedures used by engineers. Many engineering methods are based on observations from past earthquakes. Field observations are particularly important in the field of geo-engineering, because it is difficult to replicate in the laboratory soil deposits built by nature over thousands of years. Much of the data generated by a major earthquake is perishable and therefore must be collected within a few days of the occurrence of the earthquake. Thus, geo-engineers should be prepared to investigate the next large earthquake and to learn from it.

1 INTRODUCTION

There have been major findings and subsequent advances in engineering and scientific understanding in the aftermath of significant earthquakes in urbanized and industrial areas. Past earthquakes that have significantly influenced earthquake engineering include the 1906 San Francisco, 1923 Kanto, 1964 Niigata, 1964 Alaska, 1971 San Fernando, 1985 Mexico City, 1989 Loma Prieta, 1994 Northridge, 1995 Hyogoken Nambu, 1999 Kocaeli, and 1999 Chi-Chi earthquakes. Much of the data and information generated by an earthquake is perishable. Therefore, it must be collected immediately following the event. The removal of earthquake debris during recovery operations and restoration of means of transportation and lifelines quickly obscures observable significant damage, and hence it obscures critical data that could advance the state-of-the-art in earthquake engineering.

Fortunately, severe hazards that have the potential to kill people and destroy infrastructure occur relatively infrequently. Hence, they are referred to as “extreme events.” However, they occur frequently enough with the capacity for such severe consequences that society cannot ignore them. Instead, we must learn from them and develop the understanding that will allow us to evaluate and mitigate the effects of future earthquakes.

2 SIGNIFICANCE OF EARTHQUAKE ENGINEERING RECONNAISSANCE

Documenting and compiling the key lessons learned from earthquake events constitutes an important task

for advancing research and practice in geotechnical earthquake engineering. For example, the Seismic Hazards Mapping Act, which became operative in the State of California in 1991, is a model for identifying and mitigating potential earthquake hazards. The stated purpose of the Act is “to protect public safety from the effects of strong ground shaking, liquefaction, landslides, or other ground failure, and other hazards caused by earthquakes” (California Division of Mines and Geology 1997). The California State Mining and Geology Board, Geological Survey, and advisory committees are implementing this legislation with the assistance of the U.S. Geological Survey and with the benefit of the results from prior research from the U.S. National Earthquake Hazards Reduction Program. The successful implementation of these types of laws and regulations is of paramount importance to society.

Many of the current guidelines utilized in efforts such as the California Hazard Mapping Program, however, are poorly defined regarding the effects of strong shaking (especially in the near-fault region), liquefaction and ground failure and their effects on building performance, seismically induced landslides, and the effects of surface faulting on structural systems and lifelines. For example, a key element of California’s Seismic Hazards Mapping Act is to identify zones containing potential liquefaction/ground failure hazards and to require review of design and mitigation measures in these zones. The recommended evaluation/mitigation guidelines for ground failure hazards are largely based on the “simplified” empirical methods delineated in Youd et al. (2001), yet many of the methods proposed in Youd et al. (2001) are based on data from earthquakes that occurred before

1985. Clearly, these and other “standard” procedures require re-evaluation and updating as important case histories emerge.

The results of recent studies of soil liquefaction, especially those involving soils with a significant amount of fines, have been largely motivated by observations of liquefaction and ground softening documented by reconnaissance teams after recent earthquakes in Turkey and Taiwan. For example, the careful documentation of liquefaction following the 1999 Kocaeli earthquake (Bray and Stewart 2000) provided much of the data that advanced the profession’s understanding of liquefaction/ground softening of fine-grained soils, and led to important new criteria for evaluating the liquefaction potential of these soils (e.g., Bray and Sancio 2006). Observations of the liquefaction/softening of soils with fines in Taiwan by Stewart (2001) have supported research by Chu et al. (2004) on the liquefaction of fine-grained soils as well. Additional case histories are required to enhance the profession’s understanding of other earthquake phenomena, such as the effects of ground softening, ground failure, and ground movement on structures. Important advancements are possible through research of these effects in future earthquakes worldwide.

The geo-engineering profession has a rich tradition of understanding the need to develop and to apply new technologies and techniques that document in detail the effects of earthquakes on urban infrastructure. Because of the significant experience of geo-engineers in documenting the effects of earthquakes and because of their leadership in implementing new technologies in reconnaissance activities, geo-engineers are uniquely poised to work with other professionals to document the effects of earthquakes and to advance earthquake engineering through learning the lessons made apparent through these disasters.

3 GEO-ENGINEERING RECONNAISSANCE METHODS

The last ten years represent a time of unprecedented advancement in the technologies used to document earthquake damage. For example, during this period the Geo-engineering Extreme Events Reconnaissance (GEER) Association has been a leader in developing applications of emerging technologies that have proven useful in documenting the effects of earthquakes (<http://www.geerassociation.org/>). The innovative use of personal digital assistants (PDAs) to record earthquake damage resulting from the 1999 Kocaeli, Turkey earthquake allowed engineers to collect systematically and analyze carefully observations in a consistent manner. The ground based LIDAR (Light Detection And Ranging) mapping system proved useful in documenting ground failure resulting from the 2004 Niigata-ken Chuetsu, Japan earthquake before

reconstruction efforts erased physical evidence that proved critical to understanding the potential failure mechanisms involved at many sites with ground failure (e.g., Kayen et al., 2006).

The data and information that can be collected by post-earthquake reconnaissance teams includes high quality digital photographs of damage from aircraft and from the ground. All observations can now be documented digitally and positioned accurately using GPS (Global Positioning System) coordinates allowing integration of reports and detail as shown in Figure 1. Aerial photographs taken after the event can be compared to those from existing databases to help define damage patterns that can provide invaluable insights (e.g., Bray and Stewart 2000).

Besides photographic documentation that records visual images of damaged and undamaged facilities and systems, advanced techniques, such as LIDAR, can be used to help document more completely ground deformation across wide areas (Kayen et al., 2006). Ground-based LIDAR has been used successfully to document ground failure in several earthquakes as well as after other extreme events. For example, aerial photography and ground-based LIDAR were used to document the Shiroywa (White Rock) landslide that resulted from the shaking of the 2004 Niigata-ken Chuetsu, Japan earthquake (see Figure 2). This large landslide adversely impacted a major road and bridge that was adjacent to it (Rathje et al., 2006).

Remote sensing, via spaceborne or airborne sensors, is another tool that has emerged as a crucial component of documenting the effects of natural disasters, including earthquakes. Remote sensing represents the acquisition of data using sensors not in direct physical contact with the area being investigated, and includes optical satellite imagery, synthetic aperture



Figure 1. Map showing GPS-located incidents of liquefaction in the south of downtown Seattle area, and photographs of sand liquefaction resulting from the 2001 Nisqually, Washington earthquake at one location (N47.58487° W122.33980°; 03/02/2001; Bray et al., 2001). Geo-engineers were able to accurately locate areas of liquefied ground using hand-held GPS devices. Data were available one week after the earthquake.



Figure 2. The reconnaissance for the 2004 Niigata Ken Chuetsu earthquake in Japan provided geo-engineers an opportunity to use new technologies in their field studies. Aerial photography and terrestrial LIDAR were used to document earthquake-induced landslides, such as the Shiroya Slide, which is shown here (Rathje et al., 2006).

radar (SAR), and LIDAR. Commercial optical satellites routinely obtain sub-meter imagery that can be used to assess the geographical distribution of earthquake damage. Satellite imagery is georeferenced to standard cartographic projections, and thus observations from the imagery can be fused with ancillary information such as geologic maps, topographic maps, or any other information that has been georeferenced. Very high resolution (VHR) satellite imagery was used to document the distribution of landslides from the 2004 Niigata-ken Chuetsu earthquake and to investigate the influence of geologic, topographic, and seismic conditions on the observed failures (Rathje et al., 2006).

SAR represents an active remote sensing technique in which the reflections of transmitted radar signals are measured. Because of the active source, SAR can acquire imagery at night or through clouds, which are attractive features for acquiring data as quickly as possible after an earthquake. In addition to the collected imagery, SAR data allows for advanced analytical techniques, such as radar interferometry (InSAR), which can provide precise measurements of ground deformation. Specifically, InSAR has been successful in measuring aseismic and coseismic slip across faults (e.g., Sandwell et al., 2002) and documenting the spatial and temporal distribution of landslide movements (Hilley et al., 2004).

Detailed mapping is possible with differential GPS devices, such as total stations, as illustrated by the survey of ground deformation associated with surface fault rupture observed after the 1999 Chi-Chi earthquake as shown in Figure 3. The importance of detailed mapping and surveying of damaged areas relative to general damage surveys cannot be overemphasized, as they provide the data for well-documented case histories that drive the development of many of the empirical procedures used in geotechnical earthquake engineering practice. Geologic maps, topographic maps, soil reports, and damage reports can be collected from various sources to help complete the picture of what happened and prepare for later

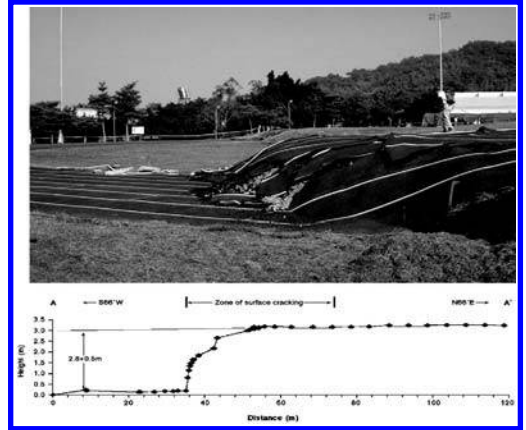


Figure 3. Detailed mapping of surface fault rupture from the 1999 Chi-Chi, Taiwan earthquake that shows 2.8 m of vertical offset over a 20 m wide zone of deformation. This information is being used to develop mitigation design strategies for engineered systems, such as buried pipelines, that must cross active faults (Kelson et al., 2001).

support studies that allow the profession to discern why it happened.

Field observations, detailed mapping and measurements, and remote sensing technologies provide diverse data at different spatial scales, temporal scales, and spatial dimensions, yet together they offer opportunities to develop more comprehensive observations of earthquake damage. Additionally, the fusion of observations from different sources can lead to more comprehensive assessments of failure mechanisms and earthquake effects. The data can also be integrated with other types of geospatial information, such as geologic maps, topographic maps, and Shakemaps of ground motion, to explore the relationships between earthquake damage and these important conditions. This integration is facilitated by the fact that currently all damage observations, whether made in the field or via remote sensing techniques, are georeferenced to standard cartographic projections using GPS.

Existing techniques can also be better utilized in a coordinated manner to obtain quantitative data on ground failure and building performance after an earthquake. For example, using a modified version of the Coburn and Spence (1992) rapid survey of structural damage and the ground failure index presented in Bray and Stewart (2000), reliable data was obtained before damaged buildings were razed or repaired. These data (an example is shown in Fig. 4) proved to be invaluable for focusing later in-depth studies. These data allowed investigators, such as described in Sancio et al. (2002), to correlate the occurrence of ground failure with particular ground conditions, as illustrated in Figure 5.

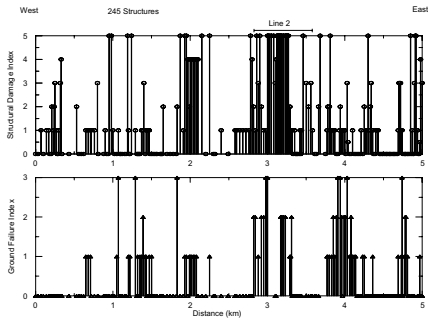


Figure 4. Record of Structural Damage Index, which Ranges from D0 (no observed damage) to D5 (complete collapse of a story or building), and Ground Failure Index, which Ranges from GF0 (no observable ground failure) and GF3 (significant building penetration of more than 25 cm or 3 degrees tilt) on Line 1 in Adapazari, Turkey (Bray and Stewart 2000).

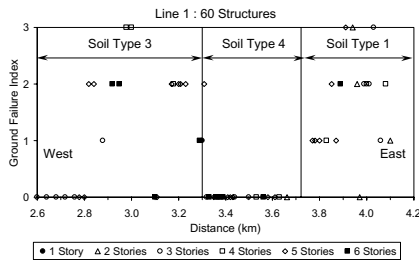


Figure 5. Correlation of Ground Failure and Soil Type on Line 1 in Adapazari, Turkey. Soil Types 1 and 3 contain liquefiable silt deposits, but Soil Type 4 does not. (Sancio et al., 2002).

4 CONCLUSIONS

The documentation of the geotechnical effects of the of the 1999 Kocaeli, Turkey earthquake in Youd et al. (2000), of the 2007 Pisco, Peru earthquake in Rodriguez-Marek et al. (2007), and of the 2007 Niigata-Chuetsu Oki earthquake in Kayen et al. (2007), among other fine efforts, are great examples of what effective post-earthquake geo-engineering reconnaissance can accomplish. These efforts succeeded in large part because of the value geotechnical engineers place on learning from earthquakes and on developing well-documented case histories that form the cornerstone of understanding for the profession.

ACKNOWLEDGMENTS

This material is based upon work supported by the National Science Foundation (NSF) through the

Geotechnical Engineering Program under Grant Nos. CMMI-0323914 and CMMI-0825734. Any opinions, findings, and conclusions or recommendations expressed in this material are those of the authors and do not necessarily reflect the views of the NSF. The Geoengineering Extreme Events Reconnaissance (GEER) Association is made possible by the vision and support of the NSF Geotechnical Engineering Program Directors: Dr. Richard Fragaszy and the late Dr. Cliff Astill. GEER members also donate their time, talent, and resources to collect time-sensitive field observations of the geotechnical effects of extreme events.

Many of the concepts and techniques described in this paper are the products of the efforts of the GEER Steering Committee (SC) members, which includes David Frost and Ellen Rathje, who serve as Co-Chairs of the SC, and J.P. Bardet, R. Kayen, N. Sitar, and L. Youd. The GEER Association is described further at its organizational website: <http://www.geerassociation.org/>.

REFERENCES

Akai et al. 1995. "Geotechnical Reconnaissance of the Effects of the January 17, 1995, Hyogoken-Nanbu Earthquake, Japan," N. Sitar, ed., *Earthquake Engineering Research Center*, Report No. UCB/EERC-95/01, University of California, Berkeley, July 1995.

Bray, J.D., and Stewart, J.P., 2000. "Damage Patterns and Foundation Performance in Adapazari," Chapter 8 of the *Kocaeli, Turkey Earthquake of August 17, 1999 Reconnaissance Report*, in *Earthquake Spectra Journal*, Suppl. A to Vol. 16, EERI, pp. 163–189.

Bray, J., Sancio, R., Kammerer, A., Merry, S., Rodriguez-Marek, A., Khazai, B., Chang, S., Bastani, A., Collins, B., Hausler, E., Dreger, D., Perkins, W., and Nykamp, M., 2001. "Some Observations of Geotechnical Aspects of the February 28, 2001, Nisqually Earthquake in Olympia, South Seattle, and Tacoma, Washington," March 8, < <http://peer.berkeley.edu/nisqually/geotech/index.html> >.

Bray, J.D., and Sancio, R.B., 2006. "Assessment of the Liquefaction Susceptibility of Fine-Grained Soils," *J. of Geotechnical and Geoenvironmental Engineering*, ASCE, Vol. 132, No. 9, pp. 1165–1177.

California Division of Mines and Geology, 1997. *Guidelines for Evaluating and Mitigating Seismic Hazards in California*, Department of Conservation, State of California, Special Publication 117.

Chu, D., Stewart, J., Lee, S., Tsai, J.S., Lin, P.S., Chu, B.L., Seed, R., Hsu, S.C., Yu, M.S., and Wang, M., 2004. "Documentation of soil conditions at liquefaction and non-liquefaction sites from 1999 Chi-Chi (Taiwan) earthquake," *Soil Dynamics and Earthquake Engineering*, V. 24, pp. 647–657.

Coburn, A., and Spence, R., 1992. *Earthquake Protection*. John Wiley & Sons, West Sussex, England.

Hilley, G., Burgmann, R., Ferretti, A., Novali, F., and Rocca, F., 2004. "Dynamics of Slow-Moving Landslides from Permanent Scatterer Analysis," *Science*, 304, pp. 1952–1955.

- Kayen, R., Pack, R., Bay, J., Sugimoto, S., and Tanaka, H., 2006. "Terrestrial-LIDAR Visualization of Surface and Structural Deformations of the 2004 Niigata Ken Chuetsu, Japan, Earthquake," in *Earthquake Spectra* Journal, Suppl. S1 to Vol. 22, EERI, pp. S147–S162.
- Kayen, R., Collins, B., Abrahamson, N., Ashford, S., Brandenberg, S., Cluff, L., Dickenson, S., Johnson, L., Tanaka, Y., Tokimatsu, K., Kabeyasawa, T., Kawamata, Y., Koumoto, H., Marubashi, N., Pujol, S., Steele, C., Sun, J., Tsai, B., Yanev, P., Yashinsky, M., and Yousok, K., 2007. "Investigation of the M6.6 Niigata-Chuetsu Oki, Japan, Earthquake of July 16, 2007," U.S. Geological Survey, Open-File Report 2007–1365, version 1.0.
- Kelson, K., Bray, J., Cluff, L., Harder, L., Kieffer, S., Page, W., Perkins, W., Rix, G., Roblee, C., Sitar, N., Wells, D., Wright, R., and Yashinsky, M., 2001. "Fault-Related Surface Deformation," Chapter 3 of the *Chi-Chi, Taiwan, Earthquake of September 21, 1999 Reconnaissance Report*, in *Earthquake Spectra* Journal, Suppl. A to Vol. 17, EERI, pp. 19–36.
- Rathje, E.M., Kayen, R., and Woo, K.-S., 2006. "Remote Sensing Observations of Landslides and Ground Deformation from the 2004 Niigata Ken Chuetsu Earthquake," *Soils and Foundations*, Japanese Geotechnical Society, 46(6), pp. 831–842.
- Rodriguez-Marek, A., Hurtado, J.A., Cox, B., Meneses, J., Moreno, V., Olcese, M., Sancio, R., and Wartman, and J., 2007 "Preliminary Reconnaissance Report on the Geotechnical Engineering Aspects of the August 15, 2007 Pisco, Peru Earthquake," GEER Association Report No. GEER-012, August.
- Sancio, R.B., Bray, J.D., Stewart, J.P., Youd, T.L., Durgunoglu, H.T., Onalp, A., Seed, R.B., Christensen, C., Baturay, M.B., and Karadayilar, T., 2002. "Correlation Between Ground Failure And Soil Conditions In Adapazari, Turkey," *Soil Dynamics and Earthquake Engineering* Journal, October–December 2002, V. 22 (9–12), pp. 1093–1102.
- Sandwell, D., Sichoix, L., and Smith, B., 2002. "The 1999 Hector Mine earthquake, Southern California: Vector near-field displacements from ERS InSAR," *Bulletin of the Seismological Society of America*, 92(4): 1341–1354.
- Stewart, J.P. (Coordinator), Chu, D., Seed, R., Ju, J.-W., Perkins, W., Boulanger, R., Chen, Y.-C., Ou, C.-Y., Sun, J., and Yu, M.-S. (Contributors) (2001) "Soil Liquefaction," Chapter 4 of the *Chi-Chi, Taiwan, Earthquake of September 21, 1999 Reconnaissance Report*, in *Earthquake Spectra* Journal, Suppl. A to Vol. 17, EERI, 2001, pp. 37–60.
- Youd, T.L., Idriss, I.M., Andrus, R.D., Arango, I., Castro, G., Christian, J.T., Dobry, R., Finn, W.D. Liam, Harder, Jr., L.F., Hynes, M.E., Ishihara, K., Koester, J.P., Liao, S.S.C., Marcuson, III, W. F., Martin, G.R., Mitchell, J.K., Moriwaki, Y., Power, M.S., Robertson, P.K., Seed, R.B., and Stokoe, II, K.H., 2001. "Liquefaction Resistance of Soils: Summary Report from the 1996 NCEER and 1998 NCEER/NSF Workshops on Evaluation of Liquefaction Resistance of Soils," *Journal of Geotechnical and Geoenvironmental Engineering*, ASCE, Vol. 127, No. 10, pp. 817–833.
- Youd, T.L., Bardet, J.P., and Bray, J.D., 2000. *Kocaeli, Turkey Earthquake of August 17, 1999 Reconnaissance Report*, in *Earthquake Spectra* Journal, Suppl. A to Vol. 16, EERI.

The role of remote sensing in documenting landslide and ground failure case histories for performance-based seismic design

E.M. Rathje

University of Texas at Austin, Austin, TX, USA

ABSTRACT: The use of advanced technologies in earthquake reconnaissance has become more prevalent over the last decade. In particular, remote sensing technologies have demonstrated their potential to improve the documentation of earthquake-induced landslide and ground failure phenomena. Continued advances in remote sensing will lead to further use of these technologies and the more accurate documentation of case histories for performance-based seismic design.

1 INTRODUCTION

The main goals of earthquake reconnaissance are to identify and document important case histories that can improve our seismic design methods and predictive models. Performance-based design imposes an additional criterion on the documenting of case histories—the quantification and direct measurement of the system's performance.

Advanced technologies are starting to play an important role in earthquake reconnaissance because they can provide important observations and measurements that could not be obtained before. In fact, one of the primary objectives of the Geoen지니어ing Extreme Events Reconnaissance (GEER) Association (formerly the Geo-Engineering Earthquake Reconnaissance Association) is to employ innovative technologies for post-event reconnaissance. Other organizations have also taken advantage of advanced technologies (e.g., Earthquake Engineering Research Institute, EERI).

Remote sensing represents a group of imaging techniques that provide geospatial information about an area, generally from a spaceborne, airborne, or tripod platform. The remote sensing techniques that have predominantly been used in earthquake studies are optical satellite imagery, synthetic aperture radar (SAR), and light detection and ranging (LIDAR). These technologies collect data using different sensing approaches and at different spatial scales such that they provide different information about the area being investigated. Rathje and Adams (2008) provide an overview of remote sensing techniques and their application to earthquake studies.

Remote sensing has been used in several earthquake reconnaissance efforts sponsored by GEER and EERI. This paper describes some of these efforts within the context of documenting case histories of earthquake-induced landslides and ground failure.

The opportunities for remote sensing in the future are also discussed.

2 PREVIOUS USES OF REMOTE SENSING

2.1 2004 Niigata-Ken Chuetsu Earthquake

The 2004 Niigata-Ken Chuetsu Earthquake ($M_w = 6.6$) in Japan induced severe landsliding in the uplands region close to the epicenter (e.g., Kieffer et al., 2006, Rathje et al., 2006, Toyota et al., 2006). Very high resolution (VHR) optical satellite imagery (submeter) was used by the GEER/EERI team during reconnaissance to plan reconnaissance efforts and was used after reconnaissance to develop an estimate of the landslide distribution throughout the entire uplands area (Carr 2009). The development of accurate inventories of earthquake-induced landslides is an important endeavor for evaluating seismic landslide hazard maps, which are typically based on slope performance as quantified by sliding block displacement.

Airborne LIDAR was used after this earthquake to document the post-earthquake geometries of some of the largest landslides (T. Kokusho, personal communication), and terrestrial LIDAR was used (Kayen et al., 2006) to image other slope failures (Figure 1). These data provide detailed failure geometries that can be used to evaluate our analytical predictions of earthquake-induced landslide deformations.

2.2 2007 Pisco, Peru Earthquake

The 2007 Pisco, Peru Earthquake ($M_w = 8.0$) caused significant soil liquefaction along the coast of central Peru and GEER supported a targeted geotechnical reconnaissance of this event (Rodriguez-Marek et al., 2007). During the earthquake a large lateral spread, approximately 3-km long, occurred on a marine

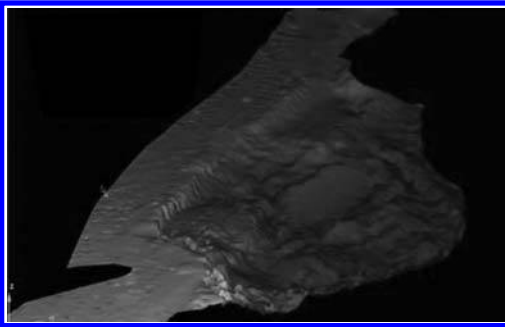


Figure 1. 3D digital terrain model of a slope failure from the 2004 Niigata-ken Chuetsu earthquake (Kayen et al., 2006).

terrace near the town of Canchamana. At its midpoint, the cumulative lateral displacement (obtained from adding up the widths of tension cracks) totaled more than 5 m (Meneses et al., 2009). However, due to the size of the feature, it was difficult to spatially quantify the magnitude of the displacements in the field and to discern if the entire marine terrace moved as a coherent lateral spread toward the ocean. Therefore, pre- and postearthquake VHR satellite imagery was used to evaluate the extent and variability of lateral displacements across the marine terrace. Preliminary satellite image analyses confirmed significant lateral movement (as much as 6 m) along portions of the marine terrace (Figure 2; Dr. Brady Cox, personal communication). However, there is reason to question the absolute validity of the results (in particular the directions of the displacement vectors) because of various technical concerns and uncertainties. A more refined satellite image analysis plan is currently being implemented to address the deficiencies revealed in the preliminary analyses (Cox, personal communication).

2.3 2008 Wenchuan Earthquake

The 2008 Wenchuan Earthquake ($M_w = 7.9$) in China represents another earthquake that induced significant landslides and a GEER/EERI reconnaissance team was tasked to the field (Frost et al., 2009). In this earthquake the landslides occurred over an area over 20,000 km² in size, as compared to an area of less than 100 km² for the Niigata-Ken Chuetsu earthquake. Because of the large area affected, both moderate resolution (15–30 m LANDSAT) and VHR (sub-meter) optical satellite imagery was used to identify the locations of earthquake-induced landslides (Carr 2009).

An area of approximately 30,000 km², centered about the fault rupture zone, was analyzed using LANDSAT imagery. Change detection analysis of pre- and post-earthquake imagery was performed to identify landslides based on areas of stripped vegetation. Cloud cover and haze were pervasive in the

post-earthquake imagery, such that the longer wavelength mid-infrared band was used in analyses because of its ability to better penetrate the adverse atmospheric conditions. The LANDSAT analysis provided a large-scale evaluation of the landslide distribution across the entire affected area. These results identified the hardest hit areas, which were further investigated with VHR imagery.

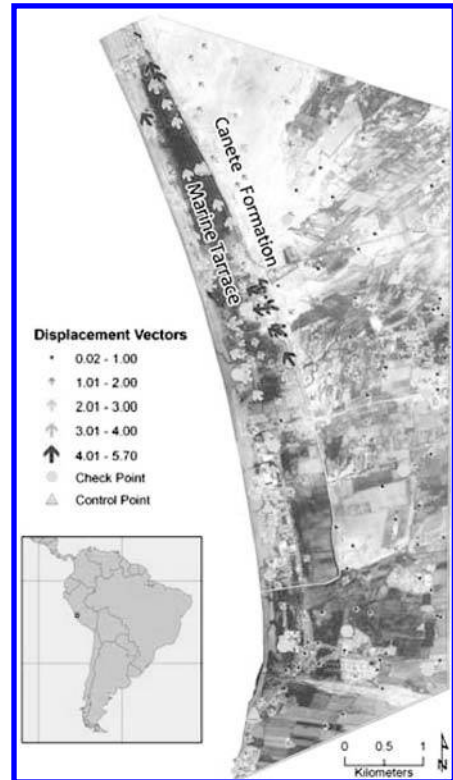


Figure 2. Displacement vectors obtained from preliminary satellite image processing of the Canchamana lateral spread (Cox, personal communication).



Figure 3. Pre- and post-earthquake VHR satellite imagery of landslides and building damage induced by the 2008 Wenchuan earthquake in the town of Ying Xiu, Sichuan Province, China.

Figure 3 shows the pre- and post-earthquake VHR satellite imagery from the town Ying Xiu, located in the epicentral area. Ying Xiu was one of the hardest hit areas, with some areas experiencing landslide concentrations of 100%. The VHR imagery clearly shows the significant damage to this area and this data is currently being used to develop an accurate inventory of the earthquake-induced landslides from this earthquake.

3 FUTURE OPPORTUNITIES

3.1 Higher resolution data

The commercial satellite imagery industry is strong and several new VHR sensors are coming online. Recently launched sensors include GeoEye-1, which collects panchromatic data at 0.4 m and multispectral data at 1.65 m, and WorldView-1, which collects panchromatic (grayscale) data at 0.5 m. WorldView-2 has plans to collect panchromatic data at 0.5 m and multispectral data at 1.8 m. Data from these new sensors will play an important role in documenting the effects of future earthquakes.

Currently, our ability to evaluate seismic landslide hazard mapping methodologies is hampered by the limited validation data that is available. The most comprehensive landslide inventory from an earthquake comes from the 1994 Northridge earthquake (Jibson et al., 2000), but few other inventories exist. Inventories of earthquake-induced landslides are not often developed for earthquakes with significant landslides because the cost of traditional landslide surveys is too high. Developing landslide inventories from VHR satellite imagery can fill this gap, and higher resolution data with more geospatial accuracy will lead to more accurate inventories. As a result, satellite imagery will allow us to develop landslide inventories for any earthquake around the globe that induces significant landslides. Increasing the number of landslide inventories available to validate our seismic landslide prediction methods will lead to improved seismic landslide maps.

3.2 Deformation measurements

An exciting opportunity related to landslides and ground failure involves deriving accurate deformation measurements from remote sensing data. SAR interferometry (InSAR) and optical imagery correlation have been used to monitor various types of ground deformation, from coseismic fault slip (Fiegl et al., 2002) to landslide creep (Delacourt et al., 2007) to land subsidence (Buckley et al., 2003). Figure 2 represents one of the first attempts to apply this type of analysis to lateral spread deformation. The higher resolution optical satellites, coupled with higher resolution SAR

satellites (e.g., TerraSAR-X and Cosmo-SkyMed with 1 m resolution), will allow for more accurate measurements of deformation from remote sensing. These measurements will allow us to significantly increase the number of ground failure case histories in which we have detailed measurements of movements. These data will lead to better and improved models for predicting deformations of landslides and ground failure.

ACKNOWLEDGMENTS

Various entities have contributed to this work and made it possible to purchase the remote sensing imagery. GEER is supported by the National Science Foundation under Grants CMMI-0323914, 0825734, 0825507, and 0825760. The study of the landslides from the Niigata-Ken Chuetsu earthquake was supported by the U.S. Geological Survey under Grant 07HQGR0152. The U.S. Geological Survey also facilitated access to commercial and government satellite imagery for the 2008 Wenchuan Earthquake which was made available through activation of the International Charter—Space and Major Disasters.

REFERENCES

- Buckley, S.M., P.A. Rosen, S.Hensley & B.D. Tapley 2003. Measurement of land subsidence in Houston, Texas by radar interferometry and constrained by extensometers. *Journal of Geophysical Research*, Vol. 108, No. B11.
- Carr, L. 2009. *The Application of Remote Sensing for Mapping Earthquake-Induced Landslides Caused by the 2008 Wenchuan, China and 2004 Niigata-Ken Chuetsu, Japan Earthquakes*, M.S. Thesis, University of Texas at Austin.
- Delacourt, C., Allemand, P, Berthier, E., Raucoules, D., Casson, B., Grandjean, P., Pambrun, P., & Varel, E. 2007. Remote-sensing techniques for analysing landslide kinematics: a review. *Bulletin de la Societe Geologique de France*, 178(2): 89–100.
- Fiegl, K., Sarti, F., Vadon, H., McClusky, S., Ergintav, E., Durand, P., Burgmann, R. Rigo, A., Massonnet, D., & Reilinger, R. 2002. Estimating Slip Distributions for the Izmit Mainshock from Coseismic GPS, ERS-1, RADARSAT, and SPOT Measurements. *Bulletin of Seismological Society of America*, 92(1): 138–160.
- Frost, D., Qiu, T., Carr, L., Rathje, E., Turel, M., Sun, J., Huang, M., Hashash, Y., Huang, R., Li, Z., & Bardet, J. 2009. *Reconnaissance and Assessment of Selected Geo-Engineering Consequences of May 12, 2008 Magnitude 7.9 Wenchuan Earthquake, Sichuan Province, China*. GEER Association Report No. GEER-016.
- Jibson, R.W., Harp, E.L., & Michael, J.A. 2000. A Method for Producing Digital Probabilistic Seismic Landslide Hazard Maps. *Engineering Geology* 58: 271–289.
- Kayen, R., Pack, R., Bay, J., Sugimoto, S., and Tanaka, H., 2006. Ground-LIDAR visualization of surface and structural deformation of the Niigata Ken Chuetsu, 23

- October 2004, earthquake. *Earthquake Spectra* 22(S1): S147-S162.
- Kieffer, D.S., Jibson, R., Rathje, E.M., and Kelson, K. 2006. Landslides Triggered by the Niigata Ken Chuetsu, Japan, Earthquake of October 23, 2004. *Earthquake Spectra*, Earthquake Engineering Research Institute, 22(S1): S47-73.
- Meneses, J.F., Franke, K.W., Cox, B.R., Rodriguez-Marek, A., & Wartman, J. (2009). Performance-Based Evaluation of a Massive Liquefaction-Induced Lateral Spread in a Subduction Zone. *IS-Tokyo 2009—International Conference on Performance-Based Design in Earthquake Geotechnical Engineering—From Case History to Practice*, Tokyo, Japan.
- Rathje, E.M., Kayen, R., & Woo, K.-S. 2006. Remote Sensing Observations of Landslides and Ground Deformation from the 2004 Niigata Ken Chuetsu Earthquake. *Soils and Foundations*, Japanese Geotechnical Society, 46(6): 831–842.
- Rathje, E.M., & Adams, B.J. 2008. The Role of Remote Sensing in Earthquake Science and Engineering: Opportunities and Challenges. *Earthquake Spectra*, Earthquake Engineering Research Institute, 24(2): 471–492.
- Rodriguez-Marek, A., Hortado, J., Cox, B., Meneses, J., Moreno, V., Olcese, M., Sancio, R., & Wartman, J. 2007. *Preliminary Reconnaissance Report on the Geotechnical Engineering Aspects of the August 15, 2007 Pisco, Peru Earthquake*. GEER Association Report No. GEER-016.
- Toyota, H., Wang, J., Nakamura, K., & Sakai, N. 2006. Evaluation of Natural Slope Failures Induced by the 2004 Niigata Ken Chuetsu Earthquake. *Soils and Foundations*, Japanese Geotechnical Society, 46(6): 727–738.

Landslides induced by Earthquake and their subsequent effects—lessons learned from the Chi-chi earthquake, 1999

M.L. Lin, K.L. Wang & T.C. Kao

Department of Civil Engineering, National Taiwan University, Taipei

ABSTRACT: The Chi-Chi earthquake struck central region of Taiwan on September 21, 1999, with a local magnitude of 7.3, which induced extensive landslides covering a total area of more than 8000 ha. In this paper, the effects of the ground motion of the Chi-Chi earthquake on the landslides and characteristics of the landslide are examined. Finally, the effects of the earthquake on triggering of subsequent landslides and the variation of the threshold rainfall following the Chi-Chi earthquake are discussed.

1 INTRODUCTION

The Chi-Chi earthquake struck central region of Taiwan on September 21, 1999, with a local magnitude of 7.3, had caused severe ground failures and loss of lives and properties. The earthquake was triggered by the faulting action of the Chelungpu fault, which is a shallow thrust east-dipping fault moving westward. The focal depth of the earthquake was only 8 km releasing a tremendous amount of energy near the ground surface. The fault rupture length was 105 km and the maximum peak horizontal ground acceleration was about 1g, where the maximum peak vertical ground acceleration was 0.7 g. The PGA contour of motion caused by the main shock is shown in Figure 1. The maximum horizontal displacement was about 9 m, and the maximum vertical displacement was about 6 m near the north-end of the fault where it turned eastward. With such strong ground motion and

large displacements, various types of ground failure occurred causing significant amount of damages and loss. Among all types of failure, landslides covered the most significant extents and caused tremendous loss and profound effects (NCREC, 2000). A follow-up investigation based on the aero-photo and SPOT satellite images taken before and after the earthquake by the Council of Agriculture identified more than 21,900 items of pixel variation with a total area of more than 8,600 hectare as shown in Figure 2. In this paper, the characteristics of the landslides induced by the earthquake are discussed, and the effects of ground motion and subsequent events are examined.

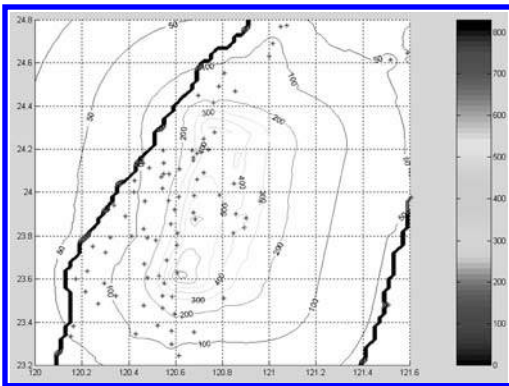


Figure 1. The distribution of horizontal peak ground acceleration of the Chi-Chi earthquake (in gal).

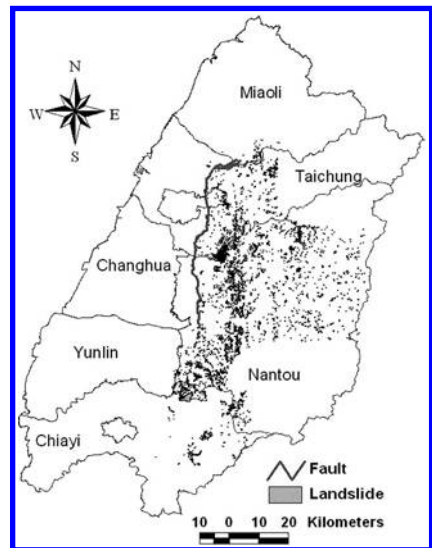


Figure 2. Distribution of identified landslide caused by Chi-Chi earthquake using SPOT images (Lin et al., 2002).

2 CHARACTERISTICS OF THE LANDSLIDES

Based on the data from the field reconnaissance (NCREE, 2000), most of the landslides induced by the earthquake were with small to medium scales, and about 70% of the landslides had area smaller than 4000 m². The distribution of different types of failure reported is as shown in Figure 3. In Figure 3 the debris slide is the most encountered failure type which accounts for 63% of the failure, while toppling and rock fall is the second with 22%. Distribution of the failed slope angle is as shown in Figure 4. The landslides with slope angle larger than 45° account for 90% of all cases, which suggests that the slope with high slope angle has higher landslide potential. The results of large percentage of high slope angle are quite consistent with the distribution of the failure types of the slope, because typically the debris slide and toppling/rock fall would occur on steep slope. The field observation also confirm that the most common type of slides were shallow slides on the steep slope occurring near the crest. The weather condition before the Chi-Chi earthquake was fairly dry without much precipitation as illustrated in the record of the Sun-Moon-Lake rain gage station close to the epicenter in Figure 5. Thus it is unlikely to have significant cases of deep-seated slides for lacking of ground water pressure effects.

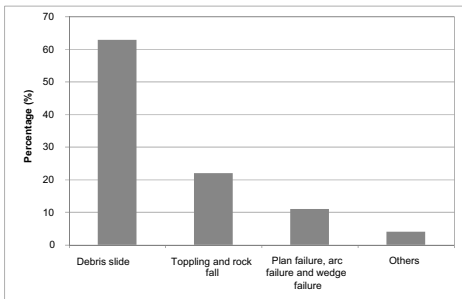


Figure 3. The distribution of failure types of landslides.

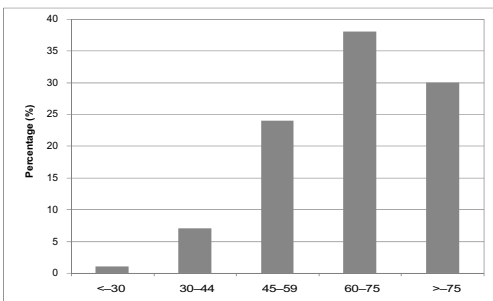


Figure 4. The distribution of slope angle of landslides.

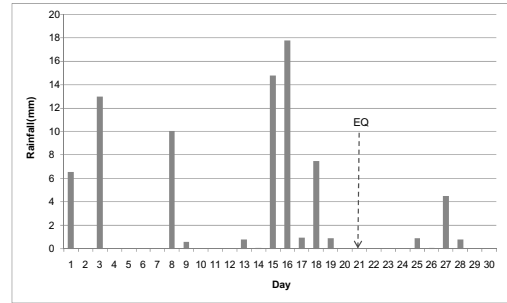


Figure 5. The precipitation record of September, 1999 of the Sun Moon Lake rain gauge station, the Central Weather Bureau.

3 THE EFFECTS OF GROUND MOTION ON THE LANDSLIDES

In order to understand the effects of the ground motion on the landslides, the ground acceleration at each landslide site was determined based on interpolation of records of nearby strong motion stations. The distribution of the mean horizontal peak ground acceleration and vertical peak ground acceleration of each event were plotted with respect to the slope angle in Figures 6 and 7, respectively. It was found that the effects of the ground motion were significant and relatively independent of the slope angle, and there appeared to be threshold accelerations for both the vertical and horizontal ground motions. From Figures 6 and 7, the threshold of vertical peak acceleration is approximately 70 gal with slope angle larger than 20°, and the threshold of horizontal peak acceleration is approximately 100 gal with slope angle larger than 20°. Both threshold peak ground accelerations appear to be constants and relatively independent of the slope angle with slope angle larger than 20°. For both cases, the threshold accelerations increase with decreasing slope angle when slope angle become smaller than 20°. However, with smaller slope angle the landslide typically occurred with high ground acceleration. One significant event with slope angle smaller than 20° occurred, i.e. the Tsaoling dip-slope landslide. The landslide was dominated by the geological structure and with slope angle of 12 ~ 14°. Close examination revealed that the high vertical ground acceleration played an important role in causing the landslide. Similar results were drawn upon analysis of several other events. The effects of the high vertical acceleration can be observed comparing Figures 6 and 7 as the distribution of ground acceleration in both directions are about the same magnitude.

The attenuation of the peak ground acceleration with respect to the hypocentral distance for vertical motion and horizontal motion were plotted in Figures 8

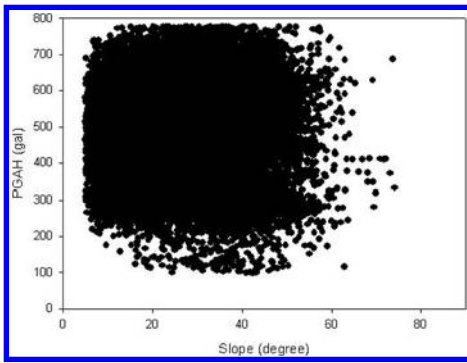


Figure 6. The distribution of horizontal peak ground acceleration versus slope angle.

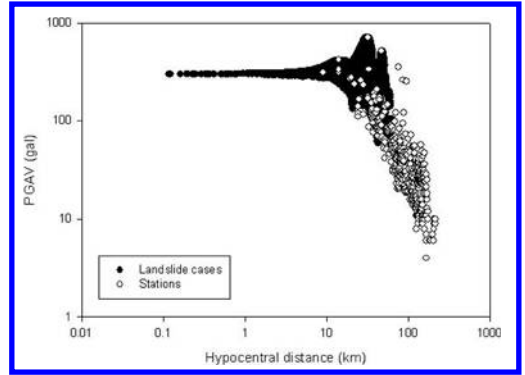


Figure 9. The distribution of vertical peak ground acceleration versus hypocentral distance.

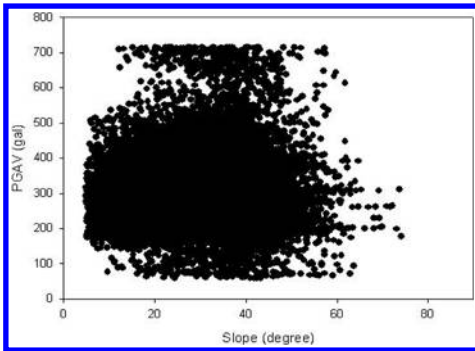


Figure 7. The distribution of vertical peak ground acceleration versus slope angle.

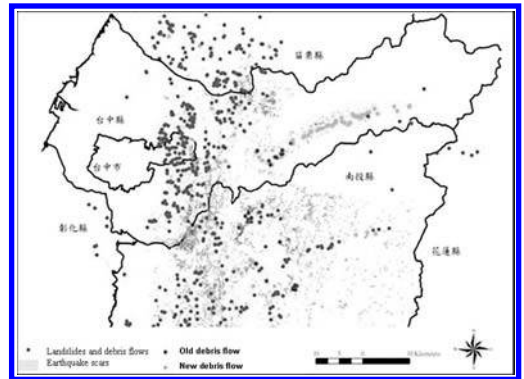


Figure 10. Landslides and debris flows induced by typhoon Mindule in 2004 versus landslides induced by the Chi-Chi earthquake (Lin et al. 2004).

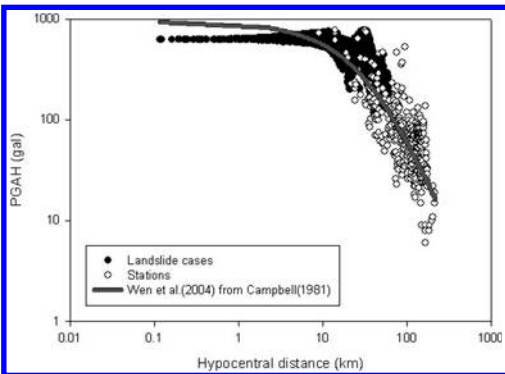


Figure 8. The distribution of horizontal peak ground acceleration versus hypocentral distance.

and 9, respectively. Generally, the attenuation of ground motion in both directions of the landslide events followed the same trend of attenuation recorded by the free field strong motion stations, and located in the range with larger ground motion and closer to

the epicenter. The two small peaks observed in both Figures 8 and 9 appeared to be affected by the large ground displacement caused by the faulting action and the triggered events (Shin, 1999). Such effects appeared to be more significant on the vertical ground motion than the horizontal ground motion due to the large upward displacement of the hanging wall side near the fault. Based on the previous discussions, the ground motion appeared to be the most important factor causing landslides during the Chi-Chi earthquake, and the effects of the vertical peak ground acceleration were quite significant. Comparing the ground motion of landslide events to the ground motion recorded by the strong motion stations, the distribution of the main group of events fell in the similar trend as ground motion recorded by the strong motion stations. However, it was found that the landslide events appeared to locate in the ranges with higher ground motion, and typically with high vertical acceleration.

4 EFFECTS OF THE LANDSLIDES ON SUBSEQUENT EVENTS

Due to the severe slope failures caused by the Chi-Chi earthquake, it is likely that new landslides, rock falls, and debris flow may be easily triggered by other earthquakes or rainfall. In 2001, typhoon Toraji caused severe landslide and debris flow hazard in Central Taiwan, and it was found that most of the landslides and debris flows occurred at locations of previous landslides induced by the Chi-Chi earthquake. In 2004, typhoon Mindule caused severe landslide and debris flow hazard in the Central Taiwan area. The reconnaissance (Lin, et al., 2004) indicated a close relationship between the hazard induced by the typhoon Mindule and landslides induced by the Chi-Chi earthquake as shown in Figure 10. For both typhoon events, it was found that the extent of failures of many reactivated landslides and debris flows increased significantly. Case histories of 14 debris flow torrents with known recurring records were documented for major typhoon

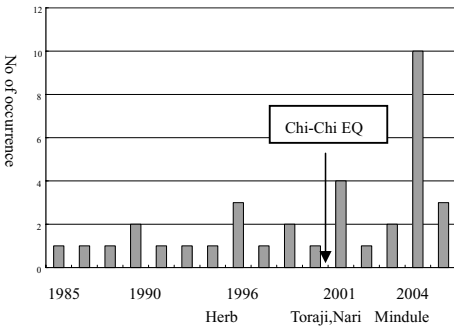


Figure 11. Number of debris flow occurrences of 14 torrents during major typhoon events (data from SWBC 2002).

events from 1985 to 2004 as shown in Figure 11. Noted that the number of debris flow occurrence increased significantly after the Chi-Chi earthquake, and the recurring period of severe events decreased. Two watersheds severely impacted by the earthquake i.e. the Ta-Chia River watershed, and the Chen-You-Lan River watershed were selected for further analysis. The landslides caused by the Chi-Chi earthquake together with the landslides caused by subsequent typhoon Toraji, and typhoon Mindule were shown in Figure 12. It was found that the number of reactivated landslides by subsequent typhoon events were significantly. In Ta-Chia River watershed the reactivated landslides took up about 30% of landslides induced by both typhoons Toraji and Mindule. In Chen-You-Lan River watershed the reactivated landslides took up about 55% and 33% of landslides induced by typhoons Toraji and Mindule, respectively. Comparison of the reactivated landslides and landslides induced by the Chi-Chi earthquake revealed that the landslides caused by the earthquake occurred near the crest of the slope due to the characteristic of seismic load and ground amplification. Subsequently, the landslide scars and open cracks would easily lead to landslide reactivation in the lower part of the slope profile by heavy rainfall of typhoons where ground water infiltrates and accumulates, and then debris and heavy rainfall lead to triggering of debris flow as illustrated in Figure 13.

5 VARIATION OF THRESHOLD RAINFALL OF LANDSLIDE FOLLOWING CHI-CHI EARTHQUAKE

Severe landslides along the Puli-Wushe highway in the May River watershed were induced by the Chi-Chi earthquake and followed by reactivated landslides and debris flow. The May River watershed is

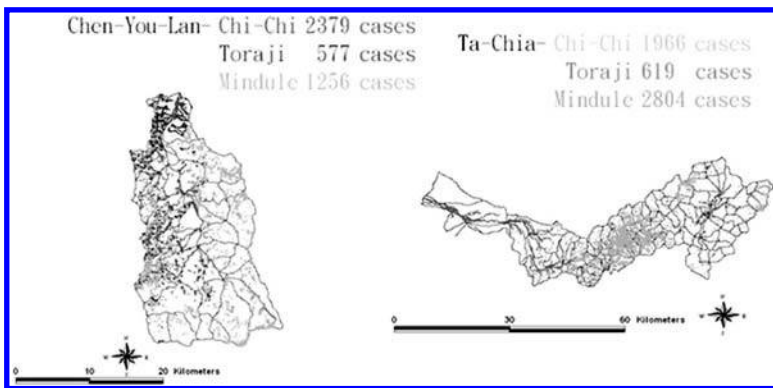


Figure 12. The landslide events caused by the Chi-Chi earthquake 1999, typhoon Toraji 2001, and typhoon Mindule 2004 in Chen-You-Lan River watershed and Ta-Chia River watershed.

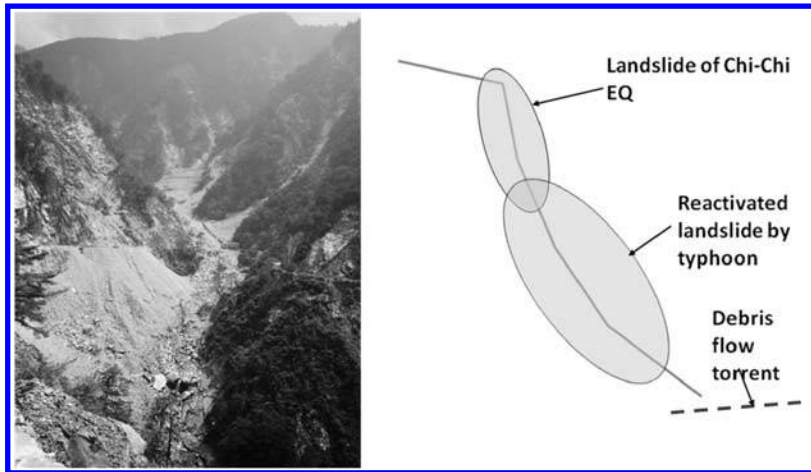


Figure 13. Illustration of reactivation of landslides and triggering of debris flows following the earthquake induced landslides; showing in the left is a landslide case in the Ta-Chia River watershed.

located between the Ta-Chia River watershed and Chen-You-Lan River watershed, and the cases are presented for discussions of the variation of threshold rainfall following the Chi-Chi earthquake. The first event immediately after Chi-Chi earthquake is the rainfall in February 2000, followed by typhoon Toraji in 2001, typhoon Mindulle in 2004, and the most recent typhoon Sinlaku in 2008. The landslide hazard events occurred during the period from 1999 to 2008 are shown in the hill shaded map in Figure 14 following time sequential order. Observing the figure, the landslide hazards at most sites occur repeatedly after the Chi-Chi earthquake. In order to discuss the variation of the rainfall for triggering of landslide hazard along Puli-Wushe highway following the Ch-Chi earthquake, the rainfall records of the nearby Ren-Ai rain gage station of selected events are used and the total accumulated rainfall and the maximum 24 hrs accumulated rainfall of all the events are plotted in Figure 15 following time sequence. In Figure 15, it is found that the triggering accumulated rainfall and the maximum 24 hrs accumulated rainfall increase gradually with time after the Chi-Chi earthquake. More events were analyzed using the maximum rainfall intensity versus the total accumulated rainfall as plotted in Figure 16, and it is found that the rainfall intensity versus accumulated rainfall of time sequential events can be grouped into two distinct lower bounds. The lower bounds can be treated as the minimum thresholds for causing landslides, and it starts with much lower threshold immediately after the earthquake, and then moves toward the upper right as time elapses, which suggests increasing rainfall is required for triggering of landslide hazard. Both Figures 15 and 16 suggest that the threshold rainfall for triggering of

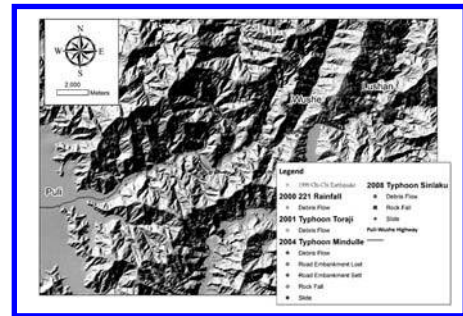


Figure 14. The hill shaded map along Puli-Wushe highway in May River watershed and the landslide hazard events.

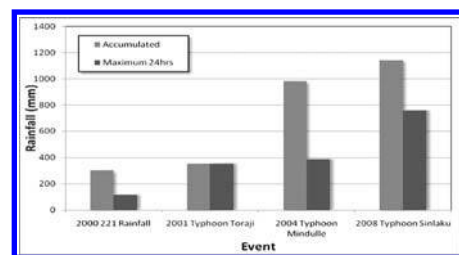


Figure 15. The variations of the total and maximum 24 hrs accumulated rainfall at Ren-Ai station of selected landslide hazard events in time sequence following Chi-Chi earthquake.

the landslide hazard increases with time after Chi-Chi earthquake, and the slopes in the May River watershed gradually become more stable as time proceeds.

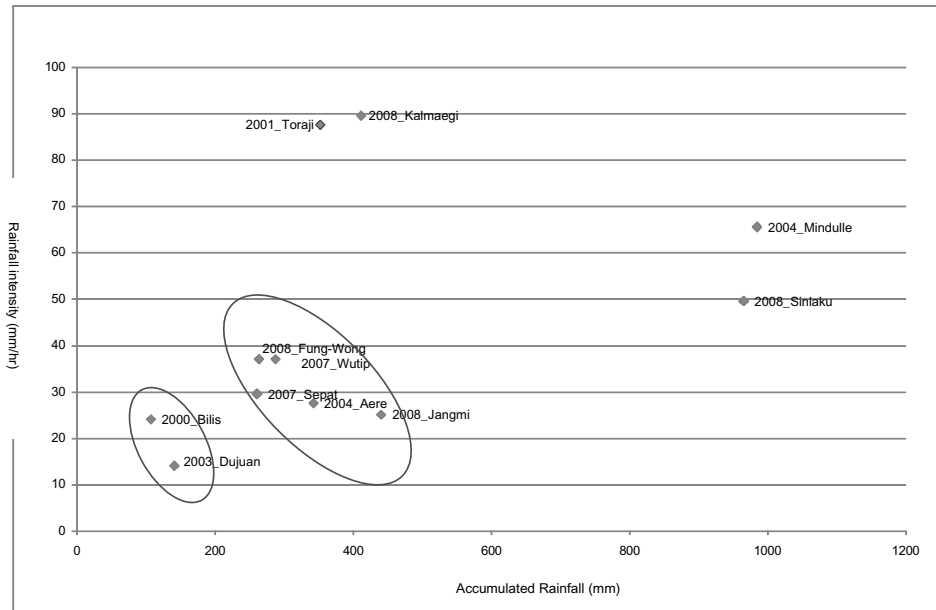


Figure 16. The maximum rainfall intensity versus accumulated rainfall of Ren-Ai gauge station of the selected events.

6 CONCLUSIONS

In 1999 the Chi-Chi earthquake struck central Taiwan and caused extensive landslide hazard. Based on the analysis of ground motion data of the identified landslide events, it is suggested that the ground motion is the most important factor for causing landslides, and the vertical peak ground acceleration has a significant effect. The threshold peak ground acceleration observed is approximately 70 gal in vertical direction, and 100 gal in horizontal direction. A large magnitude earthquake such as Chi-Chi earthquake could cause extensive landslides with cracks and fissures, which could lead to activation of the subsequent landslides and triggering of debris flows. It is expected that the effects would be prolonged but in a diminishing rate. The triggering rainfall of landslide hazard appeared to increase gradually with time after the Chi-Chi earthquake, suggesting the slopes in the study area gradually become more stable as time proceeds. However, efforts are still required in order to reduce such effects of secondary hazard in the near future.

REFERENCES

Huang, C.Y., Lin, C.W., Chen, W.S., Chen, Y.G., Yu, S.B., Chia, I.P., Lu, M.D., Hou, C.S., & Wang, Y.S., 1999. Seismic Geology of the Chi-Chi Earthquake, *Proceedings, International Workshop on the September 21, 1999 Chi-Chi Earthquake*, 25–42.

Lin, M.L., Chen, T.C., & Chen, L.C., 2002. The Geotechnical Hazards and Related Mitigation after Chi-Chi Earthquake, *Proceedings, Disaster Resistant California Conference, City of Industry, California, USA*.

Lin, M.L., Chen, C.H., Lin, M.L., Chen, H.Y., Lin, C.C., & Hsue, M.H. 2004. Reconnaissance of the Hazard Induced by Typhoon Mindulle in Ta-Chia River Watershed, *the magazine of the Chinese Institute of Civil and Hydraulic Engineering*, Vol. 31, No.4, pp.19–25.

Lin, M.L., & Kao, J.J., 2005. The Threshold Displacement of Landslides Caused by Chi-Chi Earthquake, *International Symposium on the Potential, Risk, and Prediction of Earthquake-induced Landslides, Taipei, Taiwan*.

Lin, M.L., & Tung, C.C., 2004. "A GIS-Based Potential Analysis of the Landslides Induced by the Chi-Chi Earthquake", *Engineering Geology*, 71, 63–77.

Lin, M.L., Wang, K.L., & Chen, T.C., 2000. Characteristics of the Slope Failure Caused by Chi-Chi Earthquake, *Proceedings of International Workshop on Annual Commemoration of Chi-Chi Earthquake, III-Geotechnical Aspect*, 199–209.

NCRE, NAPHM, and Taiwan Geotechnical Society, 1999. *Reconnaissance report of the geotechnical hazard caused by Chi-Chi earthquake*, National Research Center on Earthquake Engineering, Taiwan, 111p.

Shin, T.C., 1999. Chi-Chi Earthquake-Seismology", *Proceedings, International Workshop on the September 21, 1999 Chi-Chi Earthquake*, 1–14.

Wen, K.L., Jan, W.Y., Chang, Y.W., Chen, K.T., & Jian, J.S. 2004. Site effects on strong motion of Taiwan area, *Report, Central Weather Bureau, Report No. MOTC-CWB-93-E-09*.

2008 Wenchuan 8.0 earthquake of China

Characteristics of disasters induced by the Wenchuan 8.0 earthquake and lessons learnt from it

L.M. Wang, Z.J. Wu & X.M. Zhong

Lanzhou Institute of Seismology, China Earthquake Administration, Lanzhou, China

ABSTRACT: On May 12, 2008, a great earthquake with a magnitude 8.0 occurred in the Wenchuan County, Sichuan Province, China. The main shock was widely felt by the people in 30 provinces of China, 6 of which were seriously affected. The strong shaking not only caused enormous buildings and houses collapsed or seriously damaged, but also triggered more than 12,000 landslides, collapses and mudflows, which dammed more than 30 quake lakes. According to the authority statistics, more than 87,000 people were killed and 374,000 people injured. The direct economic loss reaches 845 billion Chinese Yuan, which is about 124 billion USD. In this paper, the characteristics of damage of buildings, houses, infrastructures and lifeline were described, which including reinforced concrete buildings, brick-concrete buildings, the bottom reinforced concrete buildings, brick-wood houses and adobe-wood houses, highways and railways, bridges, dams, electricity supply, water supply, gas supply and communication system. The secondary disasters induced by the earthquake, such as landslides, rolling rocks, seismic settlement and liquefaction were investigated and introduced. The distribution characteristics of both ground motion and faults rupture caused by the earthquake were presented.

1 INTRODUCTION

On May 12, 2008 at 14:28, a great earthquake with a magnitude 8.0 occurred in the Wenchuan County, Sichuan Province in China. The Epicenter locates at the place of latitude N31.021 and longitude E103.367, and the focal depth is 14 Km. The earthquake caused tens of thousands of deaths and hundreds of billions RMB in losses, and it has become the worst earthquake event to occur since new China established in 1949, except the Ms 7.8 Tangshan Earthquake in 1976. The distribution of casualties and economic loss in the Sichuan and the other regions around it is listed in Table 1. The event occurred along the Longmen fault, where the Diexi Earthquake with magnitude 7.5 occurred in 1933, and two other earthquakes both with magnitude of 7.2 occurred in the Songpan County within one week in 1976.

The earthquake affected large areas, which includes 30 provinces and municipals in China. The seriously damaged areas include Sichuan, Gansu and Shaanxi Provinces. The earthquake had an extremely high intensity over a large affected area with sustained impact, and the epicentral intensity is XI on Chinese Intensity Scale at the Beichuan County and Yingxiu Town of Wenchuan County. The earthquake intensity zone is shown in Figure 1, provided by the Chinese Earthquake Administration (CEA). As of October 21, 2008, a total of 34417 aftershocks had been observed

Table 1. Distribution of casualties and economic loss in the Sichuan and the other regions around it in China.

Region	Dead	Injured	Missing	Loss (10 ⁹ US\$)
Total	69209	374498	18194	130.87
Sichuan	68696	360236	18194	121.31
Gansu	368	10171		6.70
Shaaxi	122	3379		2.86
Chongqing	18	637		
Yunnan	1	51		
Henan	2	7		
Hubei	1	17		
Hunan	1			

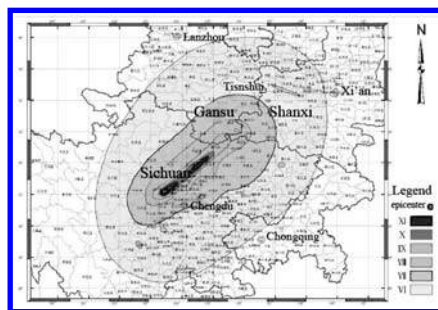


Figure 1. Earthquake intensity zone (Chinese scale), provided by the Chinese Earthquake Administration (CEA).

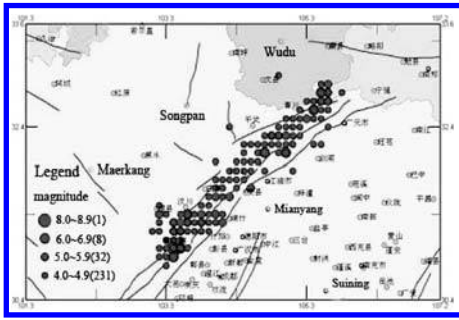


Figure 2. Distribution of aftershocks with magnitude above 4 (From the China Earthquake Networks Center (CENC)).

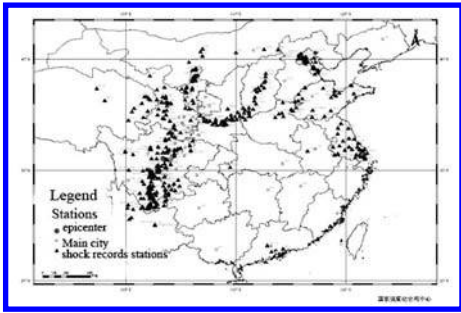


Figure 3. Stations that observed the main shock records around the epicenter in China (From the China Strong Motion Networks Center (CSMNC)).

(CENC, 2008). Figure 2 shows the distribution of aftershocks with magnitude above 4, including the main shock of the earthquake.

2 THE DISTRIBUTION OF GROUND MOTION ACCELERATION

There are hundreds of stations of strong ground motion located in the quake-hit areas. However, tens of the observation stations and instruments in the heavily quake-hit area were damaged, 398 stations of them recorded valuable information on strong ground motion. Figure 3 shows the stations that observed the main shock records in China. The largest one was obtained at Wolong station in Dujiangyan City as shown in Figure 4. Among the three components, the largest one was the EW horizontal one, and the maximum acceleration, velocity and displacement is 959.1 gal, 50.1 cm/s and 12.7 cm respectively. The distributions of strong ground motion of the horizontal components (EW, NS) and vertical components (UP) around the epicenter are shown in Figure 5, Figure 6 and Figure 7.

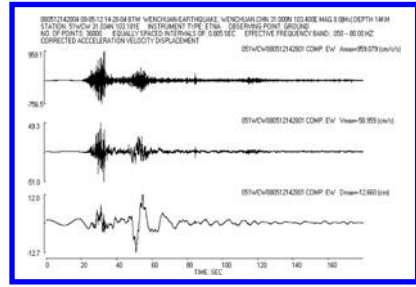


Figure 4. Ground strong motion obtained at Wolong station in Dujiangyan City (From the top to bottom are acceleration, velocity and displacement respectively.) (From the China Strong Motion Networks Center (CSMNC)).

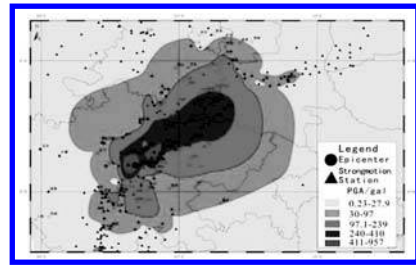


Figure 5. Distribution of strong ground motion of the horizontal components (EW) (From CSMNC).

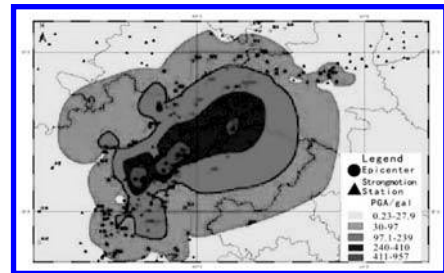


Figure 6. Distribution of strong ground motion of the horizontal components (NS) (From CSMNC).

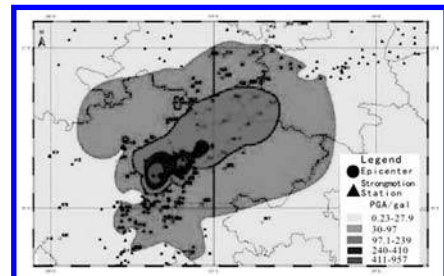


Figure 7. Distribution of strong ground motion of the vertical components (UP) (From CSMNC).

3 CHARACTERISTICS OF DAMAGE OF BUILDINGS AND HOUSES

There are five kinds of buildings and houses in the quake-hit area, the Sichuan, Gansu and Shaanxi Province, which includes reinforced concrete buildings, brick-concrete buildings, the bottom reinforced concrete buildings, brick-wood houses and adobe-wood houses. The characteristics of damage of these buildings and houses are described as following.

3.1 Reinforced concrete buildings

The reinforced concrete buildings mainly locate in the cities and towns of the heavily affected area, and which were proper seismic design and high-quality construction. Even in towns with almost complete destructions, there were always a few RC buildings that did not suffer heavy damage, except the buildings located at a place where a fault rupture crossing. Figure 8 shows a standing building in the Dongfang Steam Turbine Works located in Hanwang town, which was damaged during the earthquake. Field investigation proved that the first and second floors were sheared damage to the walls, however the beams and columns did not damaged and the structure could be used after repairs. Figure 9 shows a business building in Hangwang town. Note the walls of this building were collapsed but the frame kept in good situation. Most of the reinforced concrete buildings have a good performance during the great earthquake shocking, in which the main frame did not collapse.

3.2 Bottom reinforced concrete buildings

The bottom reinforced concrete buildings are also located in cities and towns of the quake-hit region.



Figure 8. A standing building in the Dongfang Steam Turbine Works located in Hanwang town.



Figure 9. A businesses building in Hangwang town.



Figure 10. A five floors building in Dujiangyan City.



Figure 11. The building with the top floor destroyed in Guangji town of Mianyang City.

In general, the first floors were constructed by reinforced concrete and the upper floors were brick-concrete contracture. Figure 10 shows a five floors building in Dujiangyan City. The second floor was sheared to damage and the upper floors were minor damage to the walls. Figure 11 shows a building which the top floor was destroyed in Guangji Town of Mianyang City.



Figure 12. Completely collapse of a school building in Yingxiu town of Wenchuan County. (From Gao Mengtan).



Figure 14. The Weather Bureau of Longnan City in Wudu District.



Figure 13. A building in Beichuan County, which the first floor was destroyed and the upper floors were heavily damaged.



Figure 15. Completely collapse of a school building in Yingxiu town of Wenchuan County. (From Gao Mengtan).

3.3 Brick-concrete buildings

The brick-concrete buildings have low seismic resistance, especially the buildings with precast slabs. The intensities were 10 and 11 at the heavily affected area, which was much higher than specified by the building design codes for Wenchuan and Beichuan County. Therefore, 90% of the brick-concrete buildings collapsed or were heavily damaged in Sichuan Province. A great number of people were died due to the collapses of brick-concrete buildings with precast slabs. Figure 12 shows the complete collapse of a school building in Yingxiu Town of Wenchuan County. Figure 13 shows a building which the first floor was destroyed and the upper floors heavily damaged in Beichuan County.

In the heavily quake-hit area in Gansu Province, which the intensities were 8 and 9, most of the brick-concrete buildings kept standing but were damaged. The upper floors were damaged worse than the floors below. Figure 14 shows a building of the Weather Bureau of Longnan City in Wudu District, where the intensity was 8. The top floor of the building was sheared to damage badly, and this building was removed later.



Figure 16. A building in Beichuan County, which the first floor was destroyed and the upper floors were heavily damaged.

3.4 Brick-wood houses and adobe-wood houses

The brick-wood houses and adobe-wood houses locate in the rural area in Sichuan, Gansu and Shaanxi Province. The current design code does not cover buildings in rural areas in China, making these buildings vulnerable when an earthquake occurs. These kinds of houses have a very low level of earthquake resistance and most of them were built before 2000.

Almost all of these houses collapsed in the region with intensity of 10 and 11, causing a huge number of casualties and loss as shown in Figure 15. In the area with intensity of 8 and 9 of Longnan City in Gansu Province, The brick-wood houses and adobe-wood houses which located at the top mountain or mountainside were collapsed. Figure 16 shows the completely destroyed village of Haoping village in Wudu District of Longnan City.

4 THE CHARACTERISTICS OF DAMAGE TO INFRASTRUCTURES AND LIFELINE

In the heavily quake-hit area, many types of infrastructures and lifeline engineering structures suffered damages to different extents, such as highway and railway, bridge, dam, electricity supply, water and gas supply, and communication system.

4.1 Highway and railway

Many highways were destroyed by the main shock and the secondary disasters induced by the great earthquake, such as landslides and rolling rocks. Figure 17 shows the Duwen highway connecting the Dujiangyan City and the Wenchuan County, which was opened for traffic on May 11, 2008 and destroyed by the main shock completely on May 12, 2008. It had only operated for 1 day. Figure 18 shows a subsidence with 10 m long and 3 m wide in the G212 highway, which connects Gansu Province and Sichuan Province in Wenxian County, Gansu Province. Moreover, the earthquake caused damage to railways. The railway track deformed and a freight train overturned at the Yinghua Town, Shifang City. No. 109 tunnel of Baocheng railway, which connects the Baoji City and the Chengdu City, was damaged by a landslides caused by the earthquake as shown in Figure 19. A train contained airplane gasoline was getting across the tunnel when the main shock occurring. The train had fired and stopped the traffic of the railway a few days.

4.2 Bridge

There were more than 400 bridges damaged by the huge earthquake, which included simply supported beam, steel truss, suspension and arch bridges. Some of them were collapsed or seriously damaged in the turn section and the rupture zones due to failure or dislocation of the piles and foundation. The combination effect of ground surface rupture and main strong shaking caused the damage to bridges. Figure 20 shows the damage to Xiaoyudong Bridge, which was 187 m long and operated for traffic in 1999. A few bridges were damaged by after-shocks. Figure 21



Figure 17. Duwen highway, which connects the Dujiangyan City and the Wenchuan County, was completely destroyed.



Figure 18. A subsidence with 10 m long and 3 m wide in the G212 highway.



Figure 19. No. 109 tunnel of Baocheng railway was damaged by a landslides caused by the earthquake. (From Du Zezhong).

shows a bridge in Wenxian County, which was completely destroyed by the after-shock with magnitude of 6.1, occurred on August 5.

4.3 Dam

The damage to dams was not serious, that could seem to be due to the big dams were designed for a seismic



Figure 20. Damage to the Xiaoyudong Bridge.



Figure 22. Settlement of 30 cm at the top the dam of the Zipingpu reservoir.



Figure 21. Luoxuangou Bridge, which connects the Wenxian County of Gansu Province and the Guanyuan City of Sichuan Province, in Wenxian County.



Figure 23. Damage to the Bikou reservoir in Wenxian County.

intensity of 8 in the quake-hit area. Zipingpu reservoir is one of the largest reservoirs along the Mingjiang River, which has a rock-fill dam with a concrete cover plate, and the height of it is 156 m and length 663 m. The hydropower plant has been working well since the main shock occurring. Figure 22 shows a settlement of 30 cm at the top the dam. Figure 23 shows the Bikou reservoir in Wenxian County, which was damaged slightly by the earthquake.

4.4 Power, water and gas supply

The power supply was stopped in the seriously quake-hit area at the several beginning days of the main shock. More than 100 transmission towers were damaged. Some transmission towers and power substations were found to be damaged as shown in Figure 24 and Figure 25. Water and gas supply was not seriously damaged during our survey. Figure 26 shows a water supply pipe was broken after the earthquake.

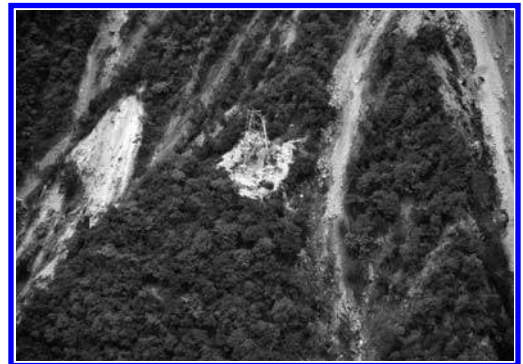


Figure 24. A power transmission tower was damaged. (From Xinhuanet, 2008).

4.5 Communication system

All communication with the outer world of the seriously quake-hit area had been stopped a few days by the main shock. Even in Lanzhou City, 505 km away from the epicenter, the communication was congested

5 THE GEOTECHNICAL DISASTERS INDUCED BY THE EARTHQUAKE

5.1 Faults rupture

The great earthquake occurred along the Longmen fault locating at the southern part of the famous south-north seismic belt, which has an up bound magnitude of 7.3 for potential seismic sources on the zonation map in China (Wang, 2008). The main ground rupture is more than 200 km long through the science survey for the earthquake organized by CEA, and the secondary rupture is about 50 km in length. The maximum vertical dislocation is 6.4 m and the horizontal dislocation 5.5 m respectively. The fault is a left lateral thrust one, and the north-west plate uplifted during the main shock. Figure 28 shows the spread of the ground rupture of the earthquake. Figure 29 shows the uplifted of a county road in Hongkou, Dujiangyan City. Figure 30 shows a rupture crossed between two buildings of the Bailu high school. During the survey in the quake-hit areas (see Fig. 31), it was found that the fault rupture completely destroyed buildings



Figure 25. A power substation was damaged in Yingxiu Town, Wenchuan County.



Figure 26. A water supply pipe was broken after the earthquake (From Yuan Yifan, 2008).



Figure 27. A set of communication cables was pulled down.

in the first time and stopped about 1 hour. Figure 27 shows a set of communication cables was pulled down.

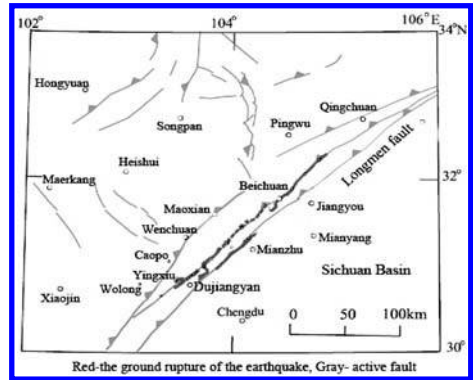


Figure 28. Spread of the ground rupture (red line) caused by the earthquake.



Figure 29. Uplifted of a county road in Hongkou, Dujiangyan City.



Figure 30. A rupture crossed between two buildings of the Bailu high school.



Figure 32. The photos before and after the quake lake formed. (Taking time: the left, 2006-05-14, the right, 2008-05-22) (From Xie Lili, 2008).



Figure 31. The fault rupture crossed the Beichuan county. (Towards to SW).



Figure 33. More than 7000 people were buried by the huge landslides induced by the main shock in Beichuan County.

and houses within 50 m, seriously damaged within 100 m, medium damage within 150 m and kept in good condition beyond 200 m.

5.2 *Quake Lake*

There were 34 Quake lakes found in the affected area, because of rocks plugged the Qingshui River and its branch, the Hongshi River. The largest one is the Tangjia Mountain quake lake, which had a dam with 82.8 m in height and 220 m in length. The quake lake could flood more than 1.3 million people lower downstream, including people in the Beichuan County, the Shifang and Deyang city etc. The photos before and after the quake lake formed are as shown in Figure 32.

5.3 *Landslides, rolling rocks and mud-rock flow*

Landslides, rolling rocks and mud-rock flow were the three main types of secondary geotechnical damage. Many places were seriously affected by huge landslides, slope collapses, rolling rocks and mud-rock



Figure 34. Rolling rocks crashed a bus and caused 10 people died in Wenxian County, Gansu Province.

flows after the main shock. It caused the destruction of constructions, infrastructures, buildings and houses, which brought a great number of deaths and injuries. More than 7000 people were buried by huge landslides in Beichuan County (see Fig. 33) induced by the main shock. Figure 34 shows rolling rocks, which crashed



Figure 35. A mud-rock flow buried a village in the Jiufeng Mountain, Pengzhou City.



Figure 37. Earthquake settlements occurred at a farmland in Qingshui County, where the intensity was 6.



Figure 36. A liquefied site in a farmland in Wudu District, Longnan City, Gansu Province.

a bus and caused 10 people died in Wenxian County, Gansu Province. Figure 35 shows a mud-rock flow buried a village in Jiufeng Mountain, Pengzhou City.

5.4 Liquefaction and settlements

There were total 38 liquefied sites found in the quake-hit area of Sichuan and Gansu Province. Liquefaction caused damage widely to houses, buildings, farmlands, fish pounds, irrigation channels, underground wells, bridges, and roads etc. It was observed that liquefaction developed in sand and gravel, and some of them were sand with medium size. Some buildings were damaged due to liquefaction. It is unexpected that liquefaction was developed in silt and gravel deposits in the sites with low earthquake intensities. Figure 36 shows a liquefied site in a farmland in Wudu District, Longnan City, Gansu Province. Some seismic settlements were found in losses regions of Gansu Province. Figure 37 shows the seismic settlements occurred at a farmland in Qingshui County, where the intensity was 6.

6 LESSONS LEARNT FROM THE GREAT WENCHUAN EARTHQUAKE

Some lessons learnt from the earthquake were summarized as follows: (1) The collapses of brick-concrete buildings with precast slabs was the first reason that caused the biggest number of deaths and injuries by the huge earthquake. This kind of buildings was not built according to current seismic design. However, most of buildings with well seismic design and good construction quality indeed did not damage even though encountering much stronger ground motion as expected (see Fig. 38). (2) Most of the reinforced concrete buildings, in the seriously affected area, had a good performance during the Earthquake, in which the main frame did not collapse. (3) Large-span rooms and staircases were the weak parts of buildings, many of them collapsed. The construction idea of “Strong columns and weak beams” for houses and buildings didn’t been come true in the affected areas. Actually, most of columns of the buildings in the quake-hit area damaged first, instead of beams. (4) Many bridges were collapsed or seriously damaged in the turn section and the rupture zones due to failure or dislocation of the piers and foundation. (5) Landslides were the typical secondary disasters caused more than 8000 people died. The new sites for reconstruction in villages and towns should be evaluated in terms of seismic safety. (6) The effect of site amplification on damage was remarkable at the sites at deep losses and the top of mountains, which was observed in Gansu Province. The higher the landform, the worse the quake disaster is. The earthquake intensity at the top of mountains is about 1 degree higher than that of valleys. Figure 39 shows the different displacements of wood columns of two adobe-wood houses, which locate at the same mountain and very close. The left house locates at the top of mountain, and the right one at the valley,



Figure 38. The new village in Wudu District, Longnan City, Gansu Province.



Figure 39. Different displacements of wood columns of two adobe-wood houses in Haoping village, Wudu District, Longnan City.

which is about 150 meters lower than the left one. The displacement of the left one was 5 cm, the right 1 cm. The deeper layer of losses, the more serious the damage. The Qingyang City of Gansu Province, where the losses layer is very deep, 669 km away from the epicenter of the huge earthquake. However, the damage to the city was serious. (7) It is unexpected that liquefaction was developed in silt and gravel deposits in the sites with low earthquake intensities.

7 CONCLUSIONS

1. The most efficient and reliable methods, which are currently available for relieving the casualties and

loss caused by earthquake, are reasonable seismic prevention, formal seismic design and good construction quality for buildings and infrastructures. The buildings and infrastructures designed according to the present Chinese code for seismic design of buildings had obviously better performance under the effects of the Wenchuan great earthquake than those without seismic design.

2. Among buildings with various kinds of structures, reinforced concrete buildings had the best seismic performance, and then the bottom reinforced concrete buildings, brick-concrete buildings, the brick-wood houses respectively and adobe-wood houses had the worst performance.
3. Most of death toll was caused by both Collapses of brick-concrete buildings and geotechnical disasters, especially the landslides and rolling rocks induced by the earthquake.
4. Seismic capability of houses, public infrastructures for both farmers and town citizens should be improved in China. Sites for construction in buildings and houses should be evaluated in terms of seismic safety.
5. The effect of site amplification on ground motion was remarkable in terms of the field damage investigation.
6. The fault rupture completely destroyed most of the buildings and houses within 50 m, seriously damaged within 100 m, medium damage within 150 m and in good shape beyond 200 m.

ACKNOWLEDGMENT

The authors thank to Prof. L.L. Xie, Prof. Y.F. Yuan and Prof. Y.Q. Wu for their providing some related data and help in the field investigation. The paper is supported by the basic research fund of the Earthquake Predict Institute, CEA.

REFERENCES

- China Earthquake Networks Center (CENC), 2008, China Earthquake Networks Center Data.
- Z.F. Wang, 2008. A preliminary report on the great Wenchuan earthquake. *Earthquake Engineering and Engineering Vibration*, 2008, Vol. 7, No. 2.

Damage investigation and analysis of buildings in Southern Gansu province during 2008 Wenchuan earthquake

Longzhu Chen¹, Wei Liu^{1,2} & Hongwang Ma¹

¹ *Institute of Engineering Safety and Disaster Prevention, Shanghai Jiao Tong University, Shanghai, China*

² *Department of Civil Engineering, Ningbo Institute of Technology, Zhejiang University, Ningbo, Zhejiang Province, China*

Zhijian Wu

Lanzhou Institute of Seismology, CEA, Lanzhou, Gansu Province, China

ABSTRACT: The behavior of buildings in Gansu province that suffered severe structural damage during the 2008 Wenchuan Earthquake is investigated. Real analyses are described in attempt to identify the reasons of the building damage, which are supported by scene photographs and engineering drawings. The results indicate that seismic damage of rural buildings is very different from that of urban buildings. Generally, the construction of rural buildings does not follow the seismic design code, which leads to serious damage even in low-intensity seismic areas. Urban buildings, on the other hand, generally satisfy the seismic-design requirements. The buildings designed properly survived the earthquake with light or moderate damage. Investigation shows that severe damage of urban buildings is mostly caused by the effect of poor construction quality, improper design and selection of construction sites. However, the ground motions and the structural responses vary dramatically with the practical seismic intensity. The real intensity in these disaster regions lies between 6 and 9 degree, while the design intensity is 8 degree. So the observed failures and data can be used to demonstrate whether the current design methods could satisfy the Three-Level performance fortification target in China. At the end of this paper, advice for seismic fortification and post-earthquake rebuilding are given.

1 INTRODUCTION

A devastating earthquake of magnitude $M_s = 8.0$ occurred in Wenchuan at 14:28 local time on May 12, 2008. The epicenter of main shock was located at 31.021N and 103.367E, with its focus 14 km below. Wenchuan earthquake was the largest instrumentally recorded event since the Tangshan earthquake on July, 28, 1976 in China. The impact of the earthquake was catastrophic, and the serious damage area reached more than 100,000 square km. It was strongly felt in an extensive area of the whole country and was felt as far as in Thailand, Vietnam, Philippines and Japan. Damage from Wenchuan earthquake is widespread with the most impact in Sichuan. Gansu is the second affected province, which is adjacent to Shanxi in the east and to Sichuan in the south. The heavy disaster area, located in the south and east of Gansu, involve 46 counties and over 600 villages. In Gansu, the earthquake resulted in 365 deaths, more than 7595 injuries, and more than 113,500 square km damage area. It is very difficult to estimate the total economical loss. The direct economical loss may be estimated as approximately 6.2 billion USD (Wang & Wu 2008).

After the earthquake, a joint seismic damage investigation group consisted of experts from Lanzhou Institute of Seismology, CEA and Shanghai Jiao Tong University. From June 3 to June 8, 2008, investigation group visited the southern area of Gansu, including Tianshui, Wushan, Wudu and Wenxian (Fig. 1). Results of these in-situ investigations on structures are presented in this paper. A description of damage to different structural types of the existing buildings is presented, along with explanations of the various factors that caused it. Since seismic damage of rural buildings is very different from that of urban buildings, this paper introduces structure damage in two parts: rural building damage and urban building damage. Finally, advice for seismic fortification and post-earthquake rebuilding are proposed.

2 INTENSITY DISTRIBUTIONS

After the earthquake, China Seismological Bureau organized specialists to carry out macro-seismic damage investigation in Sichuan, Gansu, Shanxi, Chongqing, Yunnan, and Ningxia etc. The coverage area is about 500,000 square km with 4150 investigation

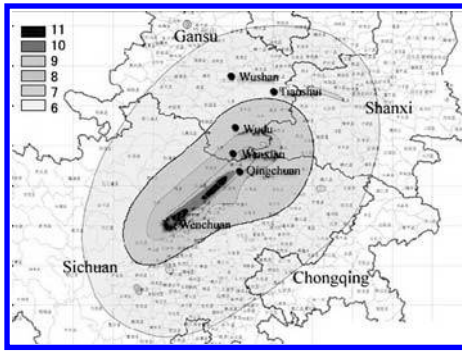


Figure 1. Intensity distribution of the Wenchuan earthquake. (modified from website of China Earthquake Administration).

Table 1. Strong motion record at five stations in Gansu.

Station	Epicentral distance (km)	EW direction (gal)	NS direction (gal)	Vertical direction (gal)
Wenxian	249	180	180	168
Wudu	304	173	158	107
Tanchang	316	91	108	59
Minxian	400	71	45	25
Lanzhou	560	38	40	22

sites. Based on the field survey data, the map of intensity distribution of Wenchuan earthquake was announced on September 2, 2008 (Fig. 1). According to the map of intensity distribution, intensity of the investigated regions in Gansu is determined: intensity of Wenxian is 7~9 degree; intensity of Wudu is 7~8 degree; intensity of Wushan and Tianshui is 6 degree (Chinese standard). Moreover, Wenchuan earthquake was recorded by several accelerographs of the national permanent strong motion network in Gansu, which were installed, serviced and monitored by Lanzhou Institute of Seismology, CEA. Table 1 shows the amplitudes of three components of seismic acceleration in several areas.

3 STRUCTURE DAMAGE

3.1 Rural building

In the rural area of Gansu, local construction materials, such as brick, gravel or stone, are widely used for saving the construction cost. According to the combination of these materials, the rural buildings in Gansu can be roughly distinguished into three categories (Zhang et al., 2006):

- i. Buildings with load-bearing adobe (stone, brick) wall and wooden roof

- ii. Buildings with in-fill adobe (brick) wall and load-bearing wooden frame
- iii. Masonry structure buildings

Among them, the first and second categories occupied more than 80% in rural areas.

3.1.1 Buildings with load-bearing adobe (stone, brick) wall and wooden roof

This type of rural building was generally self-built without sound seismic design and construction. It had the most widespread damage throughout southern Gansu, resulting in the largest number of casualties. The most common damages were: total collapse, falling of roof, wall rupture, wall crash, building inclination, separation of orthogonal walls, pulling out of purlin and so on.

Load-bearing wall is generally constituted with adobe brick, rammed-earth, or heaped gravel, which has low tensile strength but heavy weight. The mortar used in the load-bearing wall is mainly composed of plaster and straw, which has not sufficient strength to provide tight adherence between the bricks or gravels when subjected to lateral loads. Besides, the buildings are general lack of effective link between walls and roof truss, or wall and wall. Therefore, the integrity of this structural system is poor. Under the action of slight seismic force, these buildings could sustain moderate shaking without heavy damage. However, the structural system of this building type shows very low strength under strong seismic actions. In 8 degree and above 8 degree area, this type building generally sustained partial or complete collapse (Fig. 2). And the same serious damage was found on the summit of hills which was located in the 7 degree area (Fig. 3).

3.1.2 Buildings with in-fill adobe (brick) wall and load-bearing wooden frame

The residential wood-frame buildings, generally constructed after 1980s, are often has "four beams plus eight columns". Due to the fine mechanical behavior of wood frame, this type of buildings presents good seismic performance with better integrity and ductility. It is noteworthy that the load-bearing wooden frame would not collapse even with the total collapse of in-fill walls. It is the so-called "walls collapse but structures don't". The main reasons for the wall damage are the low strength of wall material and the absence of effective connection between walls and wooden frame. In regions with 7 degree and 8 degree, the most common damages were: diagonal crack in the wall, wall rupture, partial collapse of in-fill wall, and displacement of wooden column base etc. And in regions with 9 degree, the most common damage were: slide of roof, outward topple and fall of gable, falling of roof, dislodgement of the in-fill wall, and failure of the connection to foundation etc (Fig. 4).



Figure 2. Stone wall collapse in Wenxian town (8 degree zone).



Figure 3. Adobe wall collapse in Haoping village, Wudu (7 degree zone).

3.1.3 Masonry structure buildings

Masonry structure buildings in the rural area of Gansu were always self-built without rational design and construction, and showed poor seismic performance. But because of small building size, simple structural systems and regular plane-upright arrangement, completely collapse of these non-engineered masonry buildings was hardly found. The main damage observed in this type of buildings was: falling of eaves or parapet, vertical or horizontal cracking of wall, X-shaped crack of wall, serious deformation of window and door, local buckling, etc. Survey shows that the most important reasons of the damage were: deficiency of seismic concept design and seismic fortification measures. It was observed that the buildings constructed under the guide of Gansu Provincial Construction Department have not been practically affected by the seismic action. On the contrary, the buildings without enough seismic provisions, such as constructional column or ring beam, are damaged seriously.

Based on extensive post-earthquake site inspections, the main technical reasons of structural damage in masonry structure buildings are briefly discussed below:



(a) Partial collapse of walls



(b) Building collapse

Figure 4. Damage of adobe (brick) wall and wooden frame bearing structure building in Bikou town, Wenxian (9 degree zone).

i. Buildings lack of constructional column and ring beam

A 2-storey masonry structure house in Bikou area, Wenxian was investigated. Field observation shows the damage of this house was very serious with the falling of roof, the partial collapse of walls, separation of orthogonal walls, and collapse of staircase (Fig. 5). Investigation on the structure of this house shows it only had constructional columns in the first storey without tie bar embed between constructional column and walls. Moreover, the so-called ring beam was discontinuous at the junction. Therefore, the nominal constructional columns and ring beams can not achieve the effective binding between walls and combine the whole structure into integrity. Besides, pitched roof truss was put directly on the wall without effective tie.

ii. Building lack of regularity

Irregular buildings of poor design are widely constructed in southern Gansu. This type of buildings generally has low load bearing capacity, especially to the lateral loads. A 2-storey rural house of irregular structure is shown in Fig. 6. This house was characterized of a large-size overhanging and flexible roof.



(a) Front view



(b) Back view

Figure 5. Heavily damaged masonry residence in Bikou area, Wenxian (9 degree zone).



Figure 6. Residence in Zhongmiao, Wenxian (9 degree zone).

Therefore, the damage mainly occurred in the 2nd storey (Fig. 6).

A three-storey masonry residential building, built in the 1990s, was located in Qinchuan adjacent to Wenxian. The structure has constructional columns at the outside wall corners, continuous ring beams on each floor, and reinforced concrete floors and roof. But this building still suffered serious seismic damage, which focused on the wall of lateral elevation and the inner walls connected with it as shown in Figures 7a, b. The main reasons are: (a) shape of this

building was complicated with the top floor retracted and some outside walls removed for opening of large entrance doors; brick column between doors (Fig. 7b) had small section area and formed a weak location. The earthquake action concentrates weak location easily. When the earthquake occurred, this brick column and the inner wall connected with it were destroyed seriously at first. Then failure of this brick column immediately enlarged the span of upper beam and accelerated damage of upper walls. Therefore, for the masonry structure with complex load-bearing system in high seismic intensity, it is not enough to reach the earthquake resistant requirements only with general constructional measures.

iii. Buildings with load-bearing walls made of small hollow concrete blocks

A large number of masonry structures, with the load-bearing walls composed of small hollow (2 holes) concrete blocks, commonly met in the wider Wenxian area. These buildings were damaged severely during Wenchuan earthquake. Wide X-shaped cracks (width of 3~12 mm) were developed and accompanied with the horizontal offset of the walls (Fig. 8). This damage is mainly due to the misuse of non-bearing hollow walls as load-bearing walls, the lack of core column (or constructional column) and ring beams, poor construction quality, and the deficiency of reliable joint between roof and wall.



(a) Lateral elevation



(b) Narrow wall between entrance doors and the inner wall connected with it

Figure 7. Residence in Yaodu, Qingchuan (9 degree zone).



(a) The deficiency of reliable joint between roof and wall



(b) Serious damage at corner of the wall



(c) A small hollow concrete block

Figure 8. Residence in Xiaojia, Wenxian (9 degree zone).

3.2 Urban building

Almost all the buildings in urban area are designed and constructed in according to seismic code. Investigation results indicated that seismic building damage in urban were much lighter than that in rural. In Gansu, majority of the urban building behaved in a satisfactory way. Urban buildings, be designed and constructed strictly according to seismic code, show a good seismic behavior and could satisfy the Three-Level performance objectivity.

However, various failures observed in urban can be attributed rather to poor design, bad construction, unreasonable adding storey or reconstruction and so on. Hence, the following description of damage to urban buildings is organized on this basis.

3.2.1 Buildings with unreasonable adding storey or reconstruction

Wudu PC Standing Committee Building was a three-storey (four stories partially) masonry structure. It was built in 1980s, and added a storey of reinforced concrete frame on the original roof in 1990s. The earthquake severely damaged the entire building (Fig. 9). It was observed that the quality of masonry was poor, the stairway had no anti-seismic strengthen measure, and no effective joint between the adding frame column and in-fill wall. However, unreasonable adding storey was the main cause of serious seismic damage. Because the original part of the structure is masonry and the upper new adding part is frame, the force-transferring path of the entire building was not clear. Up to now, seismic code has not definite seismic fortification measures to treat this complex structural system, so it is not appropriate to be used.

Wenxian Traditional Chinese Medicine Hospital was built in 1990s. It is a four-storey building (five stories partially) with L-shaped plan, and it is connected with staff building by an additional corridor. Moreover, a brick house, without any anti-seismic



(a) Story-addition on the roof, X-shaped crack of exterior wall



(b) X-shaped crack of interior wall

Figure 9. Wudu PC Standing Committee Building (7 degree zone).



Figure 10. Storey-addition on the roof of Wenxian Traditional Chinese Medicine Hospital (8 degree zone).

measures, was put up on the roof. Due to the complex structural systems, the building was damaged seriously during Wenchuan earthquake. It was worth mentioning that the added brick house nearly collapsed with serious inclination and separation of orthogonal walls (Fig. 10).

3.2.2 Buildings with unreasonable horizontal and vertical arrangement

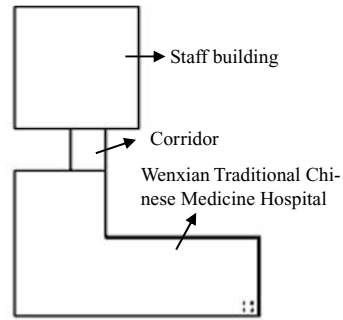
Wenxian Traditional Chinese Medicine Hospital mentioned in 3.2.1 has great asymmetry and irregularities of plane and elevation, which lead to a strong torsion response. This made the walls, far from rotation center, damaged seriously (Fig. 11).

3.2.3 Building pounding damage

Wudu Traffic Bureau Building, constructed in 1987, was a three-storey masonry structure. Main building was completely separated from the staircase with a 10 mm separation gap, filled with strawboard. As the practice intensity was 7 degree in Wudu town, it was rather seldom to find even medium damage in masonry buildings of this region. But the separation gap of Wudu Traffic Bureau Building was too narrow to accommodate the relative motions of adjacent buildings. Serious pounding occurred during Wenchuan earthquake (Fig. 12). Moreover, pounding made the damage of staircase to a greater extent than that of main building.

Wenxian government building, a 9-storey reinforced concrete frame structure, was built in 1990s. The building has two seismic joints with the width of 180 mm, which satisfied the requirement of seismic code. In this region, real intensity and fortification intensity are all 8 degree, and building has not been practically affected by the seismic action. The only damage observed was: falling of seismic joint strip (Fig. 13), and some light horizontal cracking which separated frame beams and masonry.

In Wenxian, a primary school's teaching buildings consists of several masonry structures, which constructed in different years. Figure 14a shows the

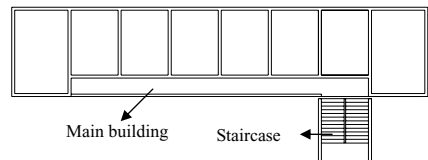


(a) Plane layout



(b) Heavily damaged walls far from rotation center

Figure 11. Wenxian Traditional Chinese Medicine Hospital (8 degree zone).



(a) Plane layout



(b) joint between main building and staircase

Figure 12. Wudu Traffic Bureau Building (7 degree zone).

plan layout of several buildings. Among them, Building A in middle was constructed in 1987, Building B located in left side was constructed in 1998, and building C located in right side was constructed in 2006. Subsequently, two smaller building D and E were constructed behind them. These buildings were built in contact with each other closely. Exterior walls of building A, B and C have about 500 mm separation,



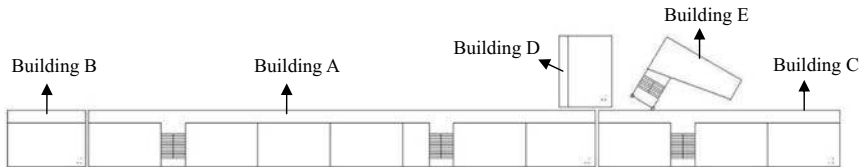
Figure 13. Seismic joint of Wenxian government building (8 degree zone).

but the roof, corridor floors and corridor sideboards have virtually no separation (Fig. 14). Exterior walls of building D also has no separation with the corridor sideboards of building B and C, and the columns of building E even embedded in the corridor sideboard of building C. Unfortunately, very little consideration was given to their separation design to preclude pounding.

The buildings pounded at the floor level of the adjacent buildings, and the corridor sideboard above the pounding level collapsed. The clear pattern of damage above the pounding level suggests that pounding may have contributed to this catastrophic event.

4 SITE AMPLIFICATION EFFECT

Most buildings in the villages of Gansu were built on the hills. The structural damage on the summit of a hill was more severe than that on the foot of a hill. It has been proved by plenty of macroscopic seismic examples that seismic damage would be aggravated due to the complicated topography in loess region. The complicated topography includes: development on the slope, isolated-protruding spur, and the upper edges of the high-steep slope (namely edges of tableland and high terrace). This research shows again that the seismic amplification effect occurs not only along the height of the hills, but in the hillside regions at the same height.

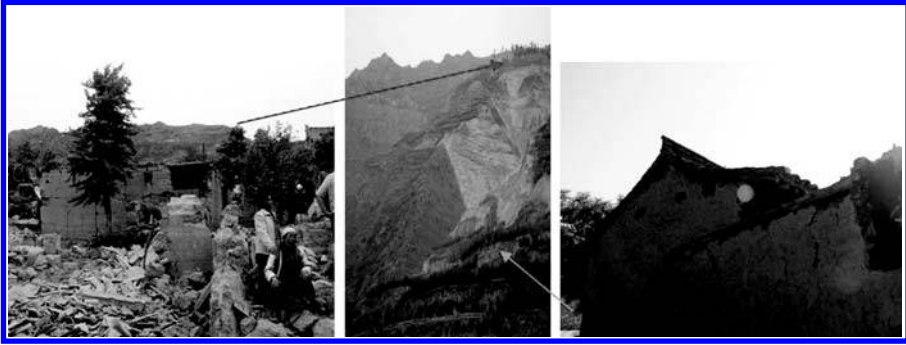


(a) Plane layout



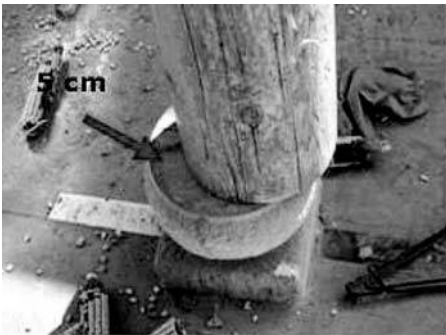
(b) Joints between Building A and B; (c) Joints between Building C and E; (d) Damage of corridor sideboard

Figure 14. A primary school's teaching buildings, in Wenxian (8 degree zone).

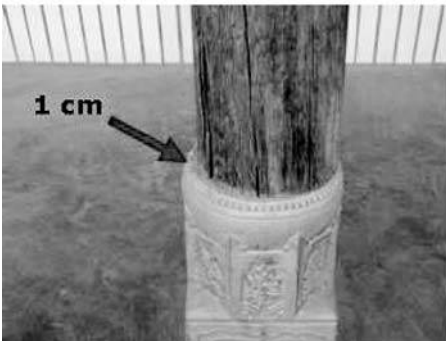


(a) Haoping Village, Wudu; (b) Liujiapo village, Wudu

Figure 15. Comparison of the seismic damage of adobe buildings in Haoping village and Liujiapo village.



(a) Haoping village, Wudu



(b) Liujiapo village, Wudu

Figure 16. Comparison of wooden column base dislocation in Haoping village and liujiapo village.

they are all one-storey building with similar geometric size and plane layout. Therefore, it can be derived that these adobe buildings have close natural periods, so do these wooden frame buildings. But the same type structure suffered very different seismic damage in two villages. Adobe buildings in Haoping village were almost all complete collapsed. At the same time, adobe buildings in Liujiapo village suffered a less severe seismic damage presented as wall rupture, wall crash and separation of orthogonal walls (Figs 15a, b). Damage of wooden frame buildings in two villages were also different, Figure 16 shows the different dislocations of wooden column base in two villages. As known, properties of ground motion, soil and structure affect the damage level of structures during an earthquake. Since the similar structure has same soil conditions and close natural periods, influence of ground seismic intensity on the degree of building damage is very significant. It indicated that seismic action on the summit of hill was much heavier than that on the foot of hill.

Microtremors of ground were observed by the seismograph. According to the analysis of collected data, predominant frequencies of foundation are: 1.85 Hz in Haoping village and 3.85 Hz in Liujiapo village, respectively. It indicated that terrain has a significant effect on the spectrum characteristics of strong ground motion.

5 COMMENTS ON THE EXISTING SEISMIC FORTIFICATION TECHNOLOGY

Haoping village (1811 m altitude, at the summit of hill) and Liujiapo village (1485 m altitude, in the hillside) are located on the same hill in Wudu County (Fig. 15). Adobe buildings and wooden frame buildings are the main building forms in both villages. Due to the local traditional building habits,

Since the establishment of Republic China, several great earthquakes have taken place in our country. The 1975 Haicheng earthquake, predicted successfully, resulted in sudden building collapse to more than 2734 square km area of building, and the 1976 Tangshan earthquake devastated the whole Tangshan city in ruins. Since that, high attention has been paid on

the building seismic fortification by the government. Based on experiences and lessons from Tangshan earthquake, the old seismic code was significantly modified and Code GBJ 11-89 for seismic design of buildings was formally promulgated in 1989. Now, the present seismic code is Code GB50011-2001 for seismic design of buildings, which have more ductile detailing and other improvements.

The 12 May 2008 Wenchuan earthquake has larger earthquake intensity than Tangshan earthquake. It is the most significant earthquake since 1949, because of its high ground motions and strong destruction to extensive area. According to incomplete statistics, Wenchuan earthquake resulted in more than 80,000 casualties, more than 30 million square m collapsed buildings, and more than 120 million square m damaged buildings. The grievous loss makes people concern and query widely to the building seismic fortification. But great magnitude and high intensity of earthquake, which far exceed the level of seismic fortification, are the main reasons for serious earthquake disasters in Sichuan Province with the most seismic impact. So we should not rashly negate the existing seismic design method only due to the enormous disasters.

Three-level Performance Fortification Objectives and Two-Stage Seismic Design Method have been specified in seismic code since 1989(GBJ11-89 1989 & GB50011-2001 2001). Three-level Performance Fortification Objectives are: structure should not be damaged or can continue to service when suffered to frequently occurred earthquake lower than seismic fortification intensity about 1.5 degree; structure may be damaged when suffered to earthquake equivalent to seismic fortification intensity, but can continue work after common repair; structure should not collapse or be damaged to seriously endanger people's life when suffered to rare earthquake higher than seismic fortification intensity about 1 degree, namely, no failure for minor earthquake, repairable for moderate earthquake and no collapse for strong earthquake. The objectives are implemented by the Two-Stage Seismic Design Methods, which with the first stage of bearing capacity checking computation and the second stage of elastic-plastic deformation checking, combined with seismic concept design of buildings and fortification measures.

The seismic fortification intensities of the investigated regions in Gansu Province are all 8 degree, while the real intensities are 6~9 degrees (Table 2). This means, investigated buildings in 7 degree areas should not be damaged; buildings in 8 degree areas should continue to work after repair, and investigated buildings in 9 degree areas should not collapse. Thereupon, the observed seismic damage could be used to demonstrate whether the current design methods could satisfy the Three-Level performance fortification target in China. It was found that most urban

Table 2. Real intensity in Wenchuan Earthquake and fortification intensity in the investigated regions.

Location	Real intensity	Fortification intensity	Design basic acceleration of ground motion
Tianshui	6	8	0.30 g
Wushan	6	8	0.20 g
Wudu	7, 8	8	0.20 g
Wenxian	7~9	8	0.20 g

buildings were multistoried buildings and only a very small part of them were high-rise buildings in these investigated regions. Urban buildings in Wushan and Tianshui experienced very light damages, and those in Wudu suffered slight damages. However, urban buildings in Wenxian developed rather more serious damages but didn't collapse. The survey showed that buildings with sound seismic design and construction all have a well seismic behavior, and the distributions of building damages have good agreement with seismic fortification objectives. On the other hand, serious damage and collapse occurred in those buildings which suffered from design error, poor construction quality, and improper selection of the structural system. So the present seismic codes play very important roles in disaster prevention and reduction.

Although no collapsing with strong earthquake is required compulsively by seismic code, only small amount of important buildings are required to be checked with seismic collapse calculation. Actually, large amount of ordinary buildings achieved this purpose not by collapse calculation but by seismic concept design of buildings and seismic fortification measures. In this earthquake, collapsed buildings mostly belong to ordinary buildings. So how to improve the structure performance of preventing collapse is needed to be studied further, which puts forward new demands to Two-Stage Seismic Design Methods.

6 CONCLUSIONS

Damages in Gansu from the Wenchuan earthquake occurred mainly on the vast rural and mountain areas, where buildings were mostly self-built without seismic design. On the contrary, urban building suffered relatively light damages. Through the investigation and analysis on the building seismic damages in Gansu, Some conclusions and advice would be drawn as follows:

1. Code for seismic design of buildings is an important basis to ensure the anti-seismic ability of structures. The fortification intensity of the survey regions are all 8 degree, while the real intensity are 6~9 degree. As a result, seismic damage in

these regions could reflect the resistance capacity for minor earthquake, moderate earthquake, and strong earthquake. Investigation shows that urban structures, designed and constructed strictly according to Chinese seismic code, could basically meet with Three-level Performance Fortification Objectives.

2. It is urgent to improve the ability of building's seismic fortification in the countryside. Severe seismic damage, such as casualties and building collapse, almost all occurred in the countryside. China has paid high attention on seismic fortification of urban building and has obtained good results since Tangshan earthquake. But less attention is paid to the extensive rural buildings due to the economic backwardness of countryside. Moreover, vast rural buildings were self-built without sound seismic design and construction. This grievous disaster is an important warning for us that seismic fortification of countryside construction should be highly emphasized. Anti-seismic measures of rural buildings should be based on the local realities, and should be the focus of seismic research. Up to now, new-countryside construction has obtained good results in some areas of Gansu Province. It should be promoted to more extensive regions.
3. Study on the seismic damage and control measures of mountain area should be enhanced. Lots of earthquake affected area of Gansu is located in mountain area, whose seismic disasters were more serious than plain area. Seismic disaster of mountainous area is very complicated. Vast mountain landslide and dilapidation result in more casualties and more destroyed buildings. Seismic amplification effect, due to mountain landform, aggravates the damage of seismic. So people always underestimate the destructive power caused by earthquake in mountainous area. Therefore, seismic disaster of this area should be highly valued and become one of the key earthquake research fields in Gansu.
4. Important roles of seismic fortification measures should be highly emphasized. Two-Stage Seismic Design Method is composed of two parts: seismic calculation and seismic fortification measures. And fortification measures mainly include: site selection, structural form selection, determination of structure system, and details of seismic design for increasing structure ductility. It was observed that one of the most important reasons of the seismic damage is the deficiency of seismic knowledge and negligence of seismic fortification measures, such as improper selection of load-bearing systems, improper setting of seismic joint, improper

setting of constructional column-beam system, and loose tie between wall and column etc. For large amount of ordinary buildings, seismic concept design of buildings and seismic fortification measures play a vital role to achieve Three-level Performance Fortification Objectives. Because of this, great attention should be paid to seismic fortification measures.

5. It is suggested that some rural structure systems should be abolished in high intensity region. Rural buildings of Gansu have various forms. Among them, buildings with load-bearing adobe wall, in general, suffered catastrophic hazards in high intensity region. Survey shows that almost all the adobe buildings sustained complete collapse in the 9 degree areas. Due to the seismic amplification effect, the same damage was found on the summit of hills which located in the 7 degree areas. With an inherent weakness in the structural system, adobe building shows poor seismic performance under strong seismic actions. So it is suggested that adobe building should be abolished in the 8 degree and above 8 degree regions.

ACKNOWLEDGMENTS

The authors acknowledge the Seismological Bureau of Gansu Province and Shanghai Jiao Tong University for providing travel arrangements to conduct the earthquake reconnaissance. The authors are also thankful to Professor Aiguo XIN and Professor Ai-lan CHE of Shanghai Jiao Tong University, and Mr. Weipeng GE and Mr. Hengzhi WANG of Lanzhou Institute of Seismology, CEA for their valuable review comments.

REFERENCES

- GBJ11-89 Code for seismic design of buildings [S]. Beijing: China Architecture and Building Press, 1989 (in Chinese).
- GB50011-2001 Code for seismic design of buildings [S]. Beijing: China Architecture and Building Press, 2001 (in Chinese).
- Wang Lan-min, Wu Zhi-jian. Wenchuan Ms 8.0 earthquake and its damage in Gansu Province [R]. Lanzhou: Lanzhou Institute of Seismology, CEA, June, 2008.
- Zhang Shoujie, Wan Lanmin, Wu Jianhua, et al. Present Situation of Seismic Safe Rural Project and Countermeasures of Earthquake Resistance Protection for Village Buildings in Gansu Province [J]. Technology for Earthquake Disaster Prevention, 2006, 1(4): 345~352.

Earthquake damages of earth-wood buildings during the Wenchuan Ms 8.0 earthquake

Rendong Qiu, Zhongxia Yuan & Qiang Wang
Lanzhou Institute of Seismology, Lanzhou, China

ABSTRACT: Based on field investigation on earthquake damages caused by Wenchuan Ms 8.0 of 12 May 2008 on low-cost earth-wood buildings, studies are carried out on feature of earthquake damage, vulnerability of these structures. First, the earth-wood buildings are classified and their characteristics are discussed. The earth-wood buildings in South Gansu are mainly fall into two categories: adobe structures and rammed earth structure, with either full wood frame or wood roof. The investigation shows though these buildings commonly suffered damages, but there are substantial differences depending on of site condition and structure characteristics. Scenes of most buildings in a street completely collapsed, but some adobe structure buildings were remained are not uncommon. The characteristics and the mechanism of damages for each kind of buildings are examined. Furthermore, experiences and lessons on seismic disaster prevention and reduction are suggested the quality management of rural buildings is emphasized.

1 INTRODUCTION

On May 12, 2008 at exactly 14:28:01, a huge earthquake with magnitude 8 on the Richter scale hit Wenchuan County of the Sichuan Province in China. The aftermath are tens of thousands of deaths and hundreds of billions RMB in loss, making it the worst earthquake event ever in China since the Ms 7.8 Tangshan Earthquake in 1976. The fault where the Great Wenchuan Earthquake occurred is located at the southern part of the south—north seismic belt in China, and no precursor information was observed by the newly completed China Geophysical and Geochemical Network. It appeared to be a totally unexpected event that resulted in tremendous losses of life and property and caused huge social disruption. The major features of this event are summarized as follows:

1. High intensity, large affected area

The event occurred in the continental block interior, and is of shallow source at around 14 km depth. Almost all Chinese provinces are affected by the sustained impact of the event except Jilin, Heilongjiang and Xinjiang. More than 15 million rooms collapsed during the earthquake. Even weeks after the main shock, millions of people in the affected area are still living under a continuing threat that includes several potential geological disasters.

2. Epicenter is located at the seismic belt

From the historical record, a total of eight earthquakes with magnitudes larger than M7 occurred within 200 km of the epicenter of the present event, the largest being the 1933 M7.5 Diexi Earthquake in Mao County, Sichuan Province.

3. Weak seismic safety standard of the buildings in the remote mountain area

The buildings are vulnerable in the rural areas. The typical buildings are built with stone masonry walls or rammed earth, which have very low seismic resistance in the surveyed area. The results demonstrated a great number of buildings collapsed or were damaged, especially near the epicenter.

4. Vulnerability of schools and hospitals

There are many observations from the field. The first is the vulnerability of schools and hospitals. The main shock occurred during the day on Monday, and the deaths and injuries basically occurred in crowded public places of regions, i.e., schools, hospitals and office buildings.

5. The relief work is very difficult

The relief work is very difficult, both because of frequent aftershocks (Zifa 2008) and mountainous terrain. Bad weather and serious geological hazards caused by the earthquake further aggravated the difficulty of the relief work. Most of the heavily-hit zones are located in the mountain, where access is very difficult due to transportation and communication interruptions.

2 THE DAMAGE FEATURES OF THE EARTH-WOOD BUILDINGS AND ITS ANALYSIS

Earth and wood are the oldest and most widely used building materials. Around 30% of the world's population lives in earth-wood-made construction (Houben and Guillard 1994). Approximately 50% of the population

in developing countries, including the majority of the rural population and at least 20% of the urban and suburban population, live in earthen dwellings. This type of construction has been used mainly by low-income rural populations. Adobe is low-cost, in the south-east parts of the Gansu province, where timber is more readily available, buildings made up of wooden beams and mud are mainly used. Adobe structures are generally self-made because the construction practice is simple and does not require additional energy consumption. Skilled technicians (engineers and architects) are generally not involved in this type of construction.

In addition to its low cost and simple construction technology, earth-wood construction has other advantages, such as excellent thermal and acoustic properties. However, the earth are vulnerable to the effects of natural phenomena such as the earthquakes. Traditional earth-wood construction responds very poorly to earthquake ground shaking, suffering serious structural damage or collapse, and causing a significant loss of life and property. Seismic deficiencies of the construction are caused by the heavy weight of the structures, their low strength, and brittle behavior. During strong earthquakes, due to their heavy weight, these structures develop high levels of seismic forces they are unable to resist, and therefore they fail abruptly. Typical modes of failure during earthquakes are: severe cracking and disintegration of walls, separation of walls at the corners, and separation of roofs from the walls, which, in most cases, leads to collapse.

A few hours after the occurrence of the Wenchuan earthquake, the Institute of Lanzhou Seismology (Earthquake Administration of Gansu Province), which is belong to the China Earthquake Administration (CEA), sent its first expert team to the field of south-east Gansu province, which is affected by the event seriously. They work on different fronts, from search and rescue, loss estimation, and damage survey. The author also went out to the field fifteen days after the event, and visited most of the heavily damaged areas in Gansu, including Kangxian, Huixian, Chengxian, Tianshui, Wudu and Wenxian (The location of the study area is showed in Figure. 1).

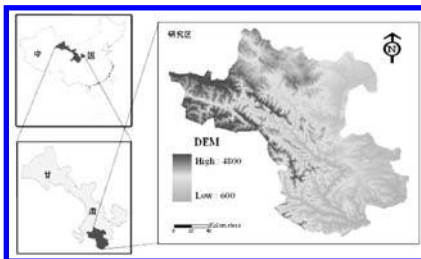


Figure 1. Location of the study area.

2.1 Typical damaged earth-wood buildings and its photos



Figure 2. Collapsed building caused by the serious damage of the earth walls, the walls are fragile.



Figure 3. Cracking and separation of adobe walls' corner.



Figure 4. Roof truss collapse caused by the less lap length of the wood roof.



Figure 5. Roof truss collapse caused by the less lap length of the wood roof.



Figure 6. The collapses caused by the inclination of the wall.



Figure 10. The collapses caused by the collision between the beams and the columns.



Figure 7. The collapses caused by the deformation of the building structure.



Figure 11. Good seismic behavior for the wood structure and bad seismic behavior for the earth wall.



Figure 8. The crest tiles slides down from the top of the building's roof.



Figure 9. The collapses caused by the serious damages of the foundation.

2.2 Analysis for the damaged earth-wood buildings based on three types

The earth-wood buildings are vulnerable when subjected the earthquake loads. The typical buildings are built with stone masonry walls, adobe or rammed earth, which have very low seismic resistance in the surveyed area. The earth-wood buildings were classified as the three types based on the bearing structure, the wood frame bearing structure, the earth wall bearing structure and the earth-wood composite bearing structure.

2.2.1 The damaged mechanism for the wood frame bearing structure

The wood frame bearing structure buildings have good flexibility, and the natural period difference between the wood frame structure and the bedrock is large, so the structure has a good seismic resistance (Figure. 7, Figure. 11). The connection of the wood frame is the stress concentration and force transfer position. If beams and columns are sufficiently strong and flexible, braced and tied together to work as units, wooden frame structure can resist the lateral forces induced by earthquakes. On the other hand, if beams and columns are not strong and flexible enough, braced and tied together not very well, the wooden frame structure can't resist the lateral forces (Figure. 5). For example, Lack of proper connections between the main

load-carrying elements of the building are some of the major shortcomings in this type of construction. Low strength is the other reason because do the corrosion of the wood during a long historic time.

2.2.2 *The damaged mechanism for the earth wall bearing structure*

Low strength earth-made wall buildings are weak against earthquakes, and should be avoided in high seismic zones (Figure. 2). The other reason for the collapse of these buildings was caused by poor bonding strength of mortar. The position of the connection between walls and the roof is the stress concentration position. The position may fracture when the conjunction measures of walls and the roof are improper. Therefore, light and well-connected roof should be employed.

2.2.3 *The damaged mechanism for the earth-wood composite bearing structure*

Although the spaces between the timber frame may be filled with adobe, brick or simply left vacant, the wooden skeleton of the house can stand on its own as a self-supporting system. When occurred earthquakes, the movement behavior of the rammed earth, adobe walls and the wood frame is not consistent, because of their different material stiffness. The earth-wood connection parts are damageable during the collision process. The collision between earth and wood is the first reason for the wall's crack. The crack propagation process can lead to the damage of the building's roof or induced the deformation of the walls (Figure. 8, Figure. 10).

2.3 *Other reasons for the damaged earth-wood buildings*

The damage of the foundation can cause the collapse of the earth-wood buildings. The walls' deformation or crack caused by the damage of the foundation is very serious especially in the rural mountain area (Figure. 9). The other reason is the effect of topography on house damage. In the investigation, some earth-wood buildings were destroyed seriously at the hillside or top, otherwise, some buildings are very well after the event at the foot of mountains.

3 SUGGESTIONS

Since the brittle nature of these buildings is the major cause for collapse of buildings and loss of lives, there is a need to introduce remedial measures in the construction of such buildings.

Suggestion 1: The horizontal bands are helpful in tying the walls together at the junctions and also in preventing the growth of vertical cracks and in-plane shear cracks (Coburn and Hughes 1995).

Suggestion 2: The aspect of seismic hazard should be taken into account in the early stages of the conceptual design of a building. The initial conceptual design are as follows:

1. Structure should be simple, transmission of the seismic (inertia) forces to the ground should be direct and clear (Tolles and Kimbro 2002),
2. Torsion resistance and stiffness should be ensured (main structural elements should be placed symmetrically nearby periphery of the building),
3. Structural elements should be appropriately connected with floor systems or diaphragms (which have to have sufficient in-plane stiffness),
4. Building should have adequate foundation.

Suggestion 3: Flat and firm dry site, good quality construction, light and well-connected roof, horizontal and vertical reinforcement.

4 CONCLUSIONS

Earth-made adobe is a low-cost, readily available construction material manufactured by local communities. The earth-wood structures are generally self-made because the construction practice is simple and does not require additional energy consumption. Skilled technicians (engineers and architects) are generally not involved in this type of construction.

However, adobe structures are vulnerable to the effects of natural phenomena such as earthquakes. Due to its low cost, earth-wood construction will continue to be used in high-risk seismic areas of the world. Development of cost-effective building technologies leading to improved seismic performance of earth-wood construction is of utmost importance to the substantial percentage of the global population that lives in these buildings.

REFERENCES

- Coburn, A. & Hughes, R. 1995. Technical Principles of Building for Safety. Intermediate Technology Publications, London, UK.
- Houben, H. & Guillaud, H. 1994. Earth Construction—A Comprehensive Guide. ITDG Publishing, London, UK.
- Tolles, E.L. & Kimbro, E.E. 2002. Planning and Engineering Guidelines for the Seismic Stabilization of Historic Adobe Structures, GCI Scientific Program Reports, The Getty Conservation Institute, Los Angeles, CA.
- Zifa, W. 2008. A preliminary report on the great Wenchuan earthquake. Earthquake Engineering and Engineering Vibration.: 7(2) 225–234.

Review on geotechnical hazard caused by Wenchuan 8.0 earthquake

Z.X. Yuan

Lanzhou Institute of Seismology, China Earthquake Administration, Lanzhou, China

ABSTRACT: The Wenchuan 8.0 earthquake affected a large part of mountainous Sichuan, Gansu and Shaanxi provinces. Due to local terrain conditions, there are a huge number of disastrous geotechnical hazards which exacerbated situations in affected area. In this paper, based on site investigation mainly in South of Gansu and its vicinity, these geotechnical hazards are carefully analyzed to determine the main reason and typical mechanism of them. In certain cases, laboratory tests are given as further proof. It is found that not only there is strong ground motion during main shock of Wenchuan earthquake, but also the ground motions during aftershocks have substantial effect. In addition, the long extension of rupture of the earthquake fault, sustained strong ground motion caused serious safety risk for slope and ground as well. Through examination of the main factors of geotechnical hazard, the reasons are concluded. In the end seismic risk reduction measures are also proposed.

1 INTRODUCTION

Geotechnical hazards have contributed much to the huge damages caused by the Wenchuan 8.0 earthquake on May 12th, 2008. The mountainous terrain of the earthquake affected area was the hotbed of various type of geotechnical hazard during not only the main shock but also the aftershocks.

With some of the extraordinary scenes, the geotechnical hazard has been estimated to account for 1/3 of all death. In Beichuan, geotechnical hazard caused the highest death rate. Nearly ten thousand lives lost and buildings buried by landslides or smashed by falling rocks is a common scene. It is reported that nearly 13000 sites are identified with landslides and other type of geotechnical hazard in the earthquake affected area.

2 ABOUT THE WENCHUAN 8.0 EARTHQUAKE

The epicenter of Wenchuan earthquake located at Yingxiu Village in Southeast of Wenchuan county. Actually, the site borders with Dujiangyan City (Figure 1).

Although the neighboring areas such as Songpan, Pingwu are of high seismicity in records, the Longmen Mountain Faults is not very active and thought to be with modest seismic risk based on known evidences and records, which turned out to be incomplete for Longmen Mt. Faults with long return period.

The earthquake intensity map is given as Figure 2 (From CEA website.)



Figure 1. The epicenter and faults of Wenchuan earthquake.

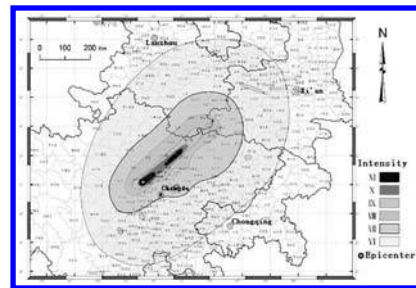


Figure 2. Intensity map of Wenchuan Earthquake.

With rupture faults extends more than 300 km, Wenchuan earthquake affected much wider area than previous disastrous Tangshan Earthquake. Geotechnical hazard is found in all areas with intensity from XI to VI.

3 AN OVERVIEW ON GEOTECHNICAL HAZARD

The most common geotechnical hazard is: ground fissure, landslides, rockfall and ground failure. Other types of geotechnical hazard such as seismic settlement and liquefaction are also identified, but they accounts for very small portion of earthquake damage.

3.1 Ground fissure

Except from fault raptures, ground fissures are mostly found in slopes and level ground of soft soil. Ground fissure is results of combined effect of strong ground motion and low shear strength of slop or ground. With downward potential, slopes developed fissures easily under earthquake ground motion, especially; the top of slop is prone to ground fissure development.

Figure 3 is ground fissure found at the slopes North to Baishuijiang Bridge in Shazhou Village of Qinchuan Country (In intensity IX area). The ground fissure has maximum width of 20 cm and maximum differential height of 30 cm and extends for approximately 300 meters. Series of ground fissures developed in parallel on the site with South-North orientation. Some of the ground fissures clearly indicate signs of landslide development (Figure 4).

Due to strong ground motion, ground fissures are also developed on level ground of soft/loose soil (Figure 5). Figure 5 is in Guochuan Village of Qingshui County in Gansu Province, where intensity is VI, and nearly 400 Km from nearest rapture fault in Qingchuan County in Sichuan Province.

When ground fissure passes by a building, the consequence is usually disastrous. In Figure 6 a ground fissure passes by a building on the slope to the south of Baishuijiang Bridge in Shazhou County of Sichuan Province. The two storey masonry building partially collapsed.

3.2 Landslide

Landslide is by far the most extensive distributed and the most hazardous geotechnical hazard in Wenchuan



Figure 3. Ground fissure developed on slope.

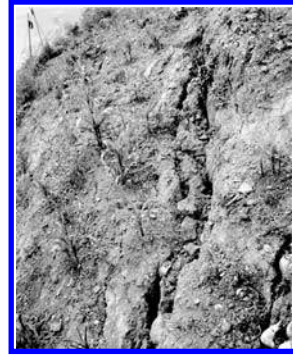


Figure 4. Ground fissure indicates landslide development.



Figure 5. Ground fissure developed in soft soil ground.



Figure 6. Ground fissure contributing to partially collapse of a masonry building.

earthquake. Landslide not only buried home, but also blocked rivers and roads to result in a chain of indirect loss and secondary hazard.

The city town of Beichuan County, where half of the nearly twenty thousands urban population lost their lives, is the most landslides stricken area.

From Figure 7 and 8, It can be found that a fairly number of buildings were buried or crashed by large



Figure 7. Beichuan Country before earthquake.



Figure 8. Beichuan Country after earthquake (Intensity XI).



Figure 9. Buildings in landslide debris.

scale of landslides. Figure 9 shows some of the buildings in debris of landslides.

The most affected area with intensity from VIII to XI has humid weather and the terrain is mountainous. Either the rocks are weathered quite badly, or there developed a thick layer of colluvial deposit. Consequently, there is readily material and condition for development of landslide. For this reason there is no shortage of scenes with series of larger scale landslides (Figure 10 and Figure 11).

A single landslides can be over one million cubic meters in volume. Figure 12 is a huge landslide along Dujiangyan-Wenchuan highway. It is more than 400 m wide and more than 500 m long. The highest relative altitude of the mountain in view is from 500–600 m.

Although the scale and frequency are of modest, many landslides developed in area with intensity



Figure 10. Larger scale landslides around Zipingpu Reservoir in Dujiangyan of Sichuan Province (Intensity X, In front: Miaoziping Bridge of Dujiangyan-Wenchuan Expressway).



Figure 11. Larger scale landslides in Bikou, Wenxian County in Gansu Province (Intensity X).

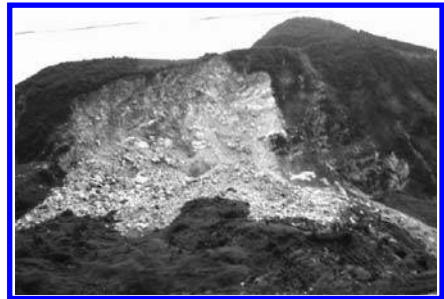


Figure 12. Huge landslides along Dujiangyan-Wenchuan highway (Intensity X).

of VI. Figure 13 is a larger loess landslide caused by Wenchuan earthquake in Yuquan Village, Qincheng district in Tianshui (Intensity VI, around 450 Km from epicenter).

3.3 Rockfall

Rockfall is the geotechnical hazard second only to landslides in term of loss of life. Hundreds or even more than one thousands vehicles were smashed by falling rocks along the highway, on streets and even in backyard.

Rockfalls are mostly found in area with intensity of IX and above and badly weathered rock slope. The size of rockfalls is quite striking. Figure 14 is a comparison of size of a fallen rock with a bus. In fact,



Figure 13. Loess landslides in area with intensity VI.



Figure 14. A comparison of size of fallen rock with a bus (Qingchuan county, intensity IX).



Figure 15. Building damaged by rockfall in Wenchuan.

rockfall with size to that of a car are not uncommon. Not only the strong main shock but also numerous after shocks caused rockfalls which can be dangerous for both building and human.

The speed of rocking is also very high. The rockfall smashed buildings and even sometimes reached the 2nd or the third floor.

3.4 Seismic settlement and liquefaction

Seismic settlement and liquefaction are not among major geotechnical hazard, because of the site condition. But they are found in many places.

In site with intensity VI, seismic settlement in loose Loess ground developed. The settlement in Figure 15 is nearly one meter. The gully is about 12 m depth from ground.



Figure 16. Loess seismic settlement in Guochuan Village, Qingshui county of Gansu province (Intensity VI).



Figure 17. Liquefaction in Yuanba Village in Wenxian county.

Liquefaction is mostly found in lowland near river. Figure 16 shows liquefaction of sand in Yuanba Village in Wenxian county of Gansu province, where intensity is VIII.

4 DISCUSSION

Geotechnical hazard accounts for a substantial loss in terms of both life and property. The strong ground motion, the mountainous terrain and badly weathered rocks are all factors contributed to such huge geotechnical disasters.

However, to prevent geotechnical hazard in such scale is economically forbidden, particular for single family. A practical way is to build collective dwellings with careful site selection, effective ground treatment and measures to reduce geotechnical hazard. Some of the current human occupancies have to be abandoned.

REFERENCES

- The intensity map of Wenchuan Earthquake, <http://www.cea.gov.cn> Official website of China Earthquake Administration, 2008.
- Report of earthquake loss evaluation, Earthquake Administration of Gansu Province, 2008.
- L.M. Wang, Loess Soil Dynamics, 2003, Press of Seismology, Beijing.

Application of micro tremor observation on disaster investigation in the quake-hit area of Gansu province by the Wenchuan great earthquake

Z.J. Wu, J.J. Sun & H.Z. Wang

Lanzhou Institute of Seismology, China Earthquake Administration (CEA), Lanzhou, China

A.L. Che & L.Z. Chen

Shanghai Jiao Tong University, Shanghai, China

ABSTRACT: The Wenchuan great earthquake, which measured at Ms 8.0 and Mw 7.9, occurred on May 12, 2008 in Sichuan province of China. The earthquake caused enormous death toll and economic loss in China. Gansu province was the secondly seriously-hit region. The buildings, lifeline engineering and infrastructures were damaged badly, and secondary disasters were serious and wide. In order to investigate the damage characteristics and mechanism of buildings and secondary disasters induced by the earthquake, and to service reconstruction, many field teams for disaster investigation were practiced. Our group of 12 persons, 6 from Shanghai Jiaotong University (SJU) and 6 from Lanzhou Institute of Seismology (LIS), CEA, had investigated damage to buildings and secondary geologic disaster in the south of Gansu Province in June, 2008. The micro tremor measurements were surveyed at some typical ground sites and building structures. It is confirmed that the test results agree well with the structural damages, and there are obvious amplification effects at higher ground site than that at the lower one.

1 INTRODUCTION

The Ms 8.0 great earthquake occurred in the Wenchuan area, Sichuan Province on May 12, 2008. It caused a great number of death toll and huge damage to economy loss. Gansu and Shaanxi were the two provinces suffered damage less than Sichuan Province, which was the most seriously quake-hit area by the Earthquake. The epicenter is 167 km away from the southern boundary of Gansu, 407 km away from the Tianshui City of Gansu, 507 km away from the Lanzhou City (the capital city of Gansu Province), and 669 km away from the Qingyang City, the most northern city of Gansu. The huge Earthquake affected the whole area of Gansu Province and hit 52 counties (districts) of 10 cities (states), in which more than 600 towns in 46 counties (districts) of 8 cities(states) was swept severely. The whole disaster area spreads 110,000 km², with 15,169,131 people affected, about 203,640,395 families hit, 369 deaths caused and 10171 people injured. The earthquake caused great damages to rural houses, educational and healthy buildings, and lifeline engineering, meanwhile, it also caused serious secondary geotechnical disasters.

The serious quake-hit area of Gansu Province locates in the southeast of Gansu, which is to the west of Shaanxi, to the north of Sichuan, and locates in the crossed area of the Qinba Mountain Area, the Qinhai-Tibet Plateau and the Loess Plateau. The whole area gradually lowers from northwest to southeast, which

generates complicated landform with both mountains and valleys.

There are three main purposes for LIS and SJU coproceeding this investigation in Gansu earthquake disaster region from 3 to 9 of June, 2008 as following. Firstly, to search the characteristics and damage mechanisms of the building structure after shock; Secondly, to survey the features how the earthquake induces geotechnical disasters; Thirdly, to recommend a much better way serving the reconstruction after the earthquake.

This investigation based on the prior-period of the earthquake hazard assessment conducted by the Gansu Earthquake Administration. We selected typical towns, buildings and secondary geotechnical disaster region as key investigated objects. The secondary geotechnical disasters investigation concludes rock types, damage characteristics and mechanism analysis, micro tremor observation, and taking photos.

The building investigation covered rural and urban buildings of the downtown in Tianshui City and the Wushan County, the Wudu district and Wen County of the Longnan City, and buildings of the Yaodu town in Qingchuan County of Sichuan Province as well. The methods in buildings investigation includes structure types, damage-suffering characteristics, micro tremor observation in ground soil and structures, and photos taken for damage features. The geotechnical disasters investigation includes landslides, collapses, rolling rocks along the G212 Highway connecting the

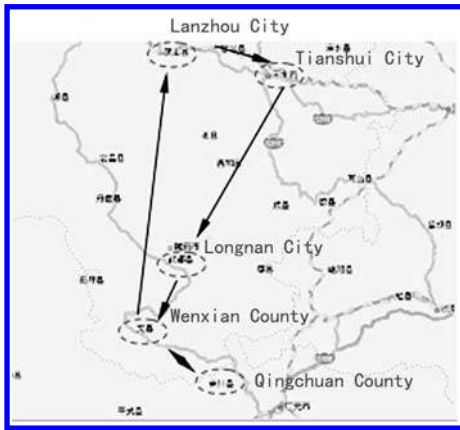


Figure 1. Investigation route.

Wenxian County of Gansu and the Qingchuan County of Sichuan, along the road between the Wen County and Jiuzhaigou County of Sichuan, and the landslide in the Wushan County, Gansu Province. Fig. 1 shows the investigation route.

2 MICRO TREMOR MEASUREMENTS

It is well known that the micro tremor observation is one of the most convenient methods to investigate the dynamic characteristics of the surface ground and structure. The micro tremor is a kind of geophysics prospecting and drilling information, which is of abundant intention such as the information of soil site and engineering geological condition and so on. The frequency characteristics of micro tremor can be obtained by a spectral analysis of its signals, which can be used to probe into dynamical characteristics of the structure and/or the soil of measuring area (Che, 2006, Guo, 1999, Jiang, 1997, Peng, 2000, Xia, 2001). The observed signals are analyzed by the fast Fourier transform method (FFT).

2.1 Measuring equipment and data acquiring

The measuring equipment is a kind of handy seismometer (SPC-35F: VSE-15D velocity seismometer, distinguishability 16Bit, made by Vibration-Measuring Corporation of Tokyo, Japan). The frequency of the detector ranges is between 0 Hz and 70 Hz. Table 1 lists the main measuring parameters of the micro tremor equipment.

While investigating, the disturbing of people and energy source should be avoided and the ground sites should be as flat as possible. The records of the horizontal and vertical components of short-period micro tremors are obtained using a three components

Table 1. Parameters of the micromotion instrument.

Model	Seismograph portable(SPC-35F: VSE-15D model velocity instrument)
Vibration measurement	Velocity:100 m kine and 10 m kine, resolution 10 μ kine,frequent range 0.1~70 Hz Acceleration:10 gal and 100 gal; frequent range 0.1~70 Hz Displacement:100 μ m and 10 μ m;frequent range 0.1~70 Hz
Frequency	1000 Hz, 500 Hz, 200 Hz, 100 Hz, 50 Hz, 20 Hz, 10 Hz, 5 Hz, 1 Hz



(a) Haoping village, Wudu District, Longnan City



(b) Liujiapo village, Wudu District, Longnan City



(c) Jiuzhaigou County, Sichuan Province

Figure 2. Three ground sites of observation.

high-sensitive seismometer, which has a natural period in one second. The device measures two horizontal components (EW and NS) and a vertical one (UD) for ground micro tremor, two horizontal components (long axis and shot axis) and a vertical one (UD) for building micro tremor, respectively. It is designed to record at a sampling rate of 100 Hz for 5 minutes, and a total of 30000 measurements are recorded.

2.2 *Micro tremor measurements for ground site*

The micro tremor measurements spots of ground sites in the survey are listed as follows, the Haoping Village, Wudu District, Longnan City (N 33°26.57, E 104°58.92; elevation, 1811 m) and Liujiapo Village (N 33°27.18, E 104°58.47; elevation, 1485 m), which locates at the hillside of the same mountain with Haoping Village, and landslide in Jiuzhaigou County, Sichuan Province (N 33°26.57, E 104°58.92; elevation, 1811 m). (See Fig. 2)

2.3 *Micro tremor measurements for structures*

The micro tremor measurements spots of structures in the survey are listed as follows, the buildings of the People’s Congress of Wudu District (four-floor brick-concrete building), the Transportation Bureau (three-floor brick-concrete building), and the Government of Wudu District (six-floor reinforced concrete building) (See Fig. 3). Fig. 4 shows the sample of selected data.

3 ANALYSIS FOR MICRO TREMOR OF GROUND SITES

3.1 *Proceeding methods of measurements*

As Fig. 5 shows, the analyzing method for the micro tremor observation data is called the fast Fourier transform (FFT). The frequency characteristics of micro tremor can be obtained by a spectral analysis of its signals, which can be used to probe into dynamical characteristics of the structure and/or the soil of measuring area. The observed signals are analyzed by FFT method. The potential noise sources such as machinery, vehicles traffic or pedestrians, near the seismometer are avoided during the measurement time of 5 minutes. And from the recorded data of micro tremor measurements, five sets of 2048 digital data at lower noise periods are selected to use for FFT analysis. The velocity Fourier amplitude spectra, spectra ratio and relative variation amplitude are computed.

3.2 *Predominant frequencies determination of ground sites*

3.2.1 *Analyzing Methods*

The main purpose of investigating the ground by micro tremor observation is to obtain the amplitude of micro



(a) Observation sites at the People’s Congress of the Wudu District (the top one is at the ground floor, and lower the third floor)



(b) Observation sites at the Transportation Bureau of Wudu District (the top one is at the ground floor, and lower the second floor)



(c) Observation sites at the building of the Government of the Wudu District (the top one is at the ground floor, and lower the fifth floor)

Figure 3. Three observation sites for structures.

Table 2. Predominant frequency of each observation site.

observation point	Haoping village, Wudu county	Liujiapo village, Wudu county	Jiuzhaigou langslides
Predominant frequency (Hz)	1.86	3.81	3.22

tremor and the predominant frequency. One of the popular method nowadays is the Nakamura Method (H/V).

The Nakamura Method refers to obtain tri-component Fourier frequency spectra, to divided the 2 horizontal components(NS, EW) by the vertical component(UD), and get the transfer function of the ground and the predominant frequency. The advantage of this method lies in simply and quickly solving the problem.

3.2.2 Analyzing results

Fig. 6 shows the analyzing results by H/V. Mostly H/V obtain many peak amplitudes, and every amplitude is not predominant due to the loud environmental noises and close velocities of shear waves between soil

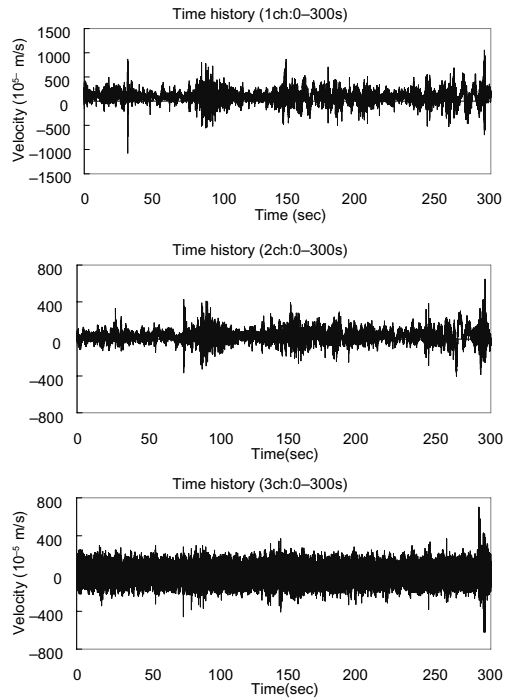


Figure 4. Examples of the collected data.

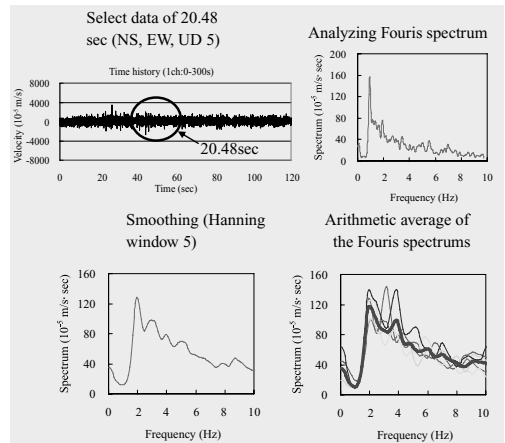


Figure 5. Fouris analysis.

layers testified. Tab. 2 lists the predominant frequencies of the observation spots.

As we can see from the testing results of the predominant frequencies, the result of Haoping Village, which is on the top of the mountain, is about 1.86 Hz, while Liujiapo Village, locates at the same mountain 300 m below, and the landslide in the Jiuzhaigou County, is

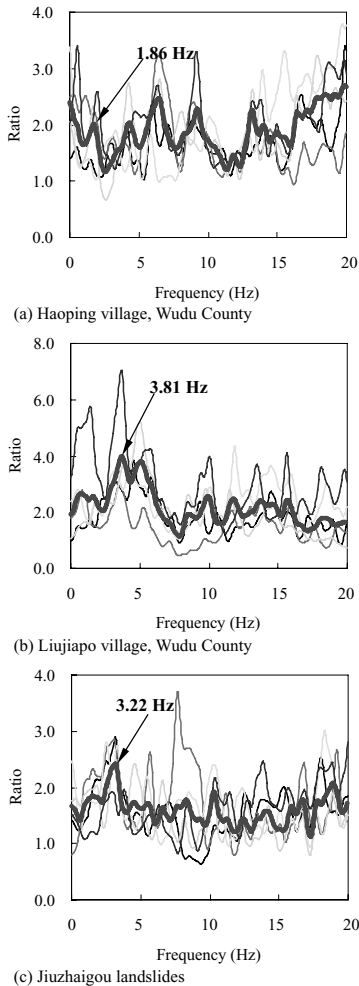


Figure 6. Nakamura method (H/V) analysis results.

3.81 Hz and 3.22 Hz respectively. In this case, the preliminary conclusion may be that the ground of the Haoping Village is mainly relatively loosening accumulative soil layer, which may enlarge the earthquake effect obviously.

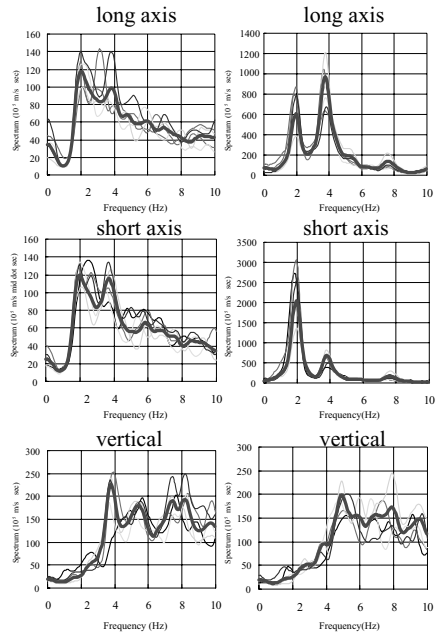
4 ANALYSIS FOR MICRO TREMOR OF STRUCTURES

4.1 *Predominant frequencies determination of the structure*

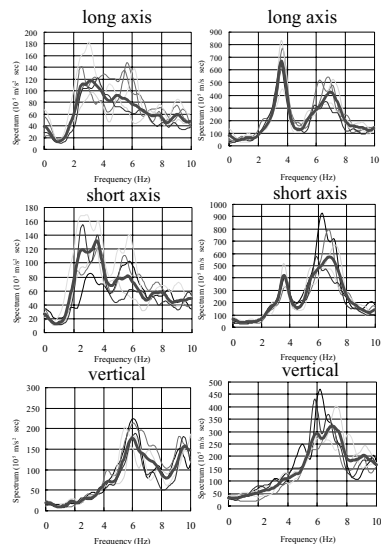
The detector was set horizontally on the top and ground floor of the building for obtaining the micro tremor signals along long-axis, short-axis and vertical-axis respectively. Fig. 7 shows the frequency spectra

of micro tremor of top and ground floor in every building. Fig. 8 shows the predominant frequencies of the three buildings in three components (two horizontal and one vertical).

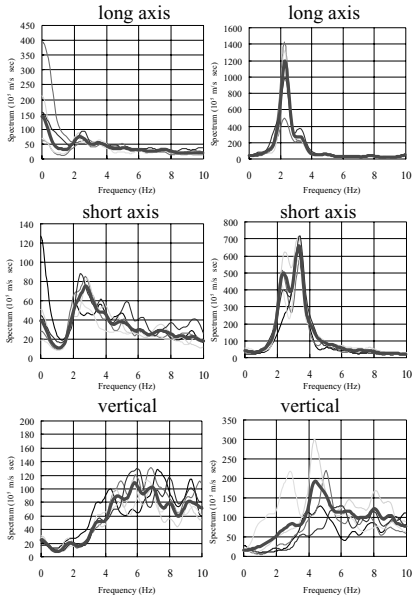
As show in Fig. 7 and Fig. 8, the 1, 2, 3 order characteristic value of the building can be obtained through



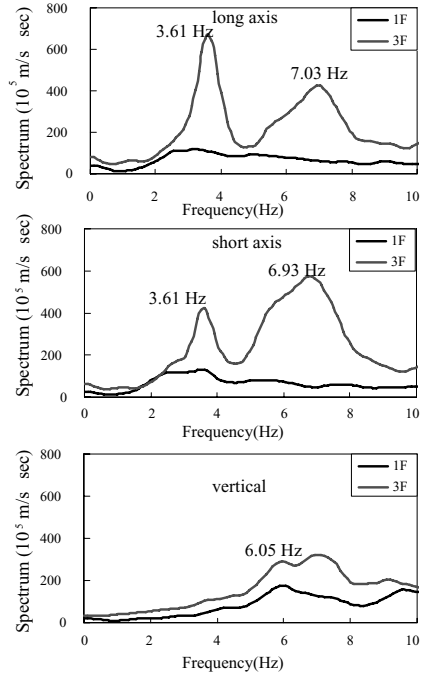
(a) The People's Congress of the Wudu District (Left is bottom floor, Right is top floor)



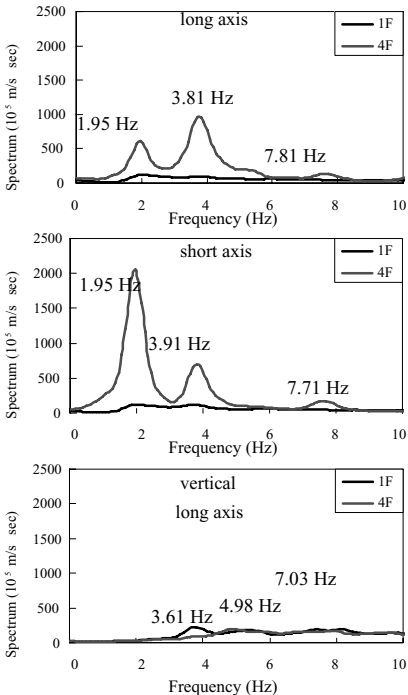
(b) The Transportation Bureau of the Wudu District (Left is bottom floor, Right is top floor)



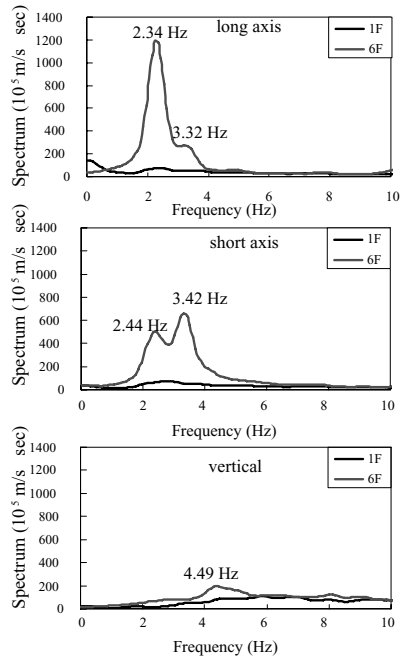
(c) The Government of the Wudu District
(Left is bottom floor, Right is top floor)



(b) The Transportation Bureau of the Wudu District



(a) The People's Congress of the Wudu District



(c) The Government of the Wudu District

Figure 8. Predominant frequency of micro motion in long axis, short axis and vertical component for the three buildings.

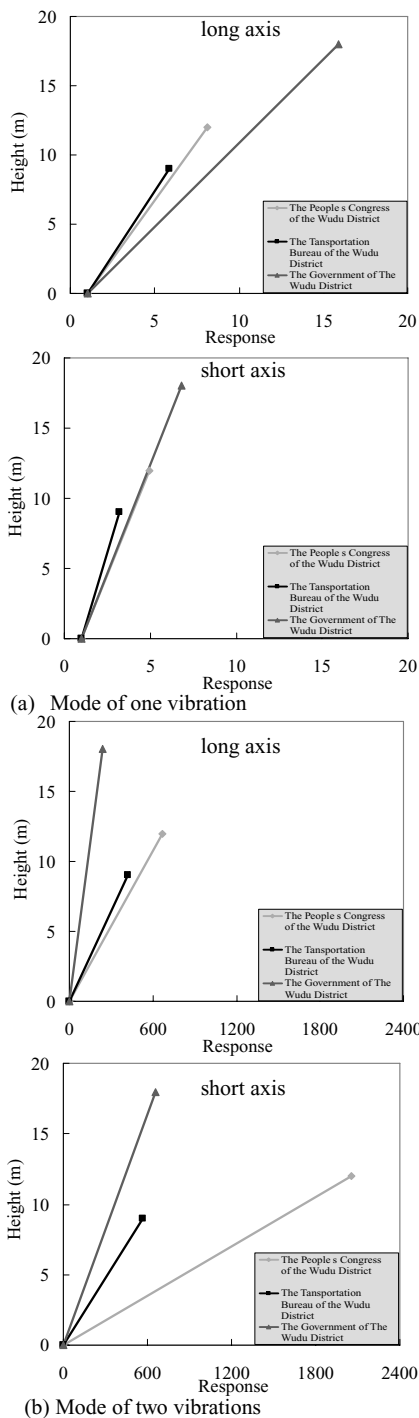


Figure 9. Dynamic response mode of bottom and long axis, short axis of top structure (the red is the People's Congress of Wudu, the black is the Transportation Bureau of Wudu and the green is the Government of Wudu).

the micro tremor observation. At the building of the People's Congress of Wudu District, the natural frequencies in 1, 2, 3 order are 1.95 Hz, 3.8 Hz, and 7.8 Hz respectively, while the results in 1, 2 order of buildings of the Transportation Bureau and the Government are 3.6 Hz, 7.0 Hz, and 2.3 Hz, 3.3 Hz respectively.

4.2 The determination of dynamic response modal

Fig. 9 shows the dynamic response modal along both long axis and short axis on the top and ground floor of the three structures. According to the analysis of the testing results, the first and second order of the vibration modal are obtained, so that we can conclude the first order modal response along the long-axis is more obvious than that along the short-axis. The responses for the first and second order modal of the three buildings decrease progressively as follows, the People's Congress, the Transportation Bureau, and then the Government of Wudu District, which is consistent with the real damage to the buildings caused by the great earthquake.

The building of the People's Congress of the Wudu District, which was built in the 1980's, it was a 3-floor brick-concrete structure, and was damaged seriously by the main shock. According to our survey, it was poor in the construction quality at the wall, strengthened measures of the staircases, and the connection between walls and pillars. And the building was removed later. The Transportation Bureau is a 3-floor brick-concrete building built in 1987, the main body and staircases were two separated parts, but there was no aseismatic joint between two parts. They crashed seriously and damaged during the quake. The Government building is a 6-floor reinforced concrete building. The building only caused slightly damage.

5 CONCLUSIONS

1. The predominant frequencies of the Haoping Village and Liujiapo Village, which locate at the same mountain with an altitude difference in 326 m, are 1.86 Hz and 3.891 Hz respectively. The soil layer of the ground in the Haoping Village is a mainly relatively loosening accumulative layer, which the effect on earthquake amplification may be more obviously.
2. At the building of the People's Congress of Wudu District, the natural frequencies in 1, 2, 3 order are 1.95 Hz, 3.8 Hz, and 7.8 Hz respectively, while the results in 1, 2 order of buildings of the Transportation Bureau and the Government are 3.6 Hz, 7.0 Hz, and 2.3 Hz, 3.3 Hz respectively.
3. The responses for the first and second order modal of the three buildings decrease progressively as following, the People's Congress, the Transportation

Bureau, and then the Government of Wudu District, which is consistent with the real damage to the buildings caused by the great earthquake.

ACKNOWLEDGMENT

The authors thank to Prof. Ma Hongwang, Ms. Liu Wei, Mr. Ge Weipeng and Zhaoliang for their strong support in field investigation. The paper is supported by the basic research fund of the Earthquake Predict Institute, CEA.

REFERENCES

A.L. Che, T. Iwatate, X.R. Ge, Study on the applicability of frequency spectrum of micro-tremor and dynamic characteristics of surface ground in Asia area, Journal of Zhejiang University SCIENCE, 2006, Vol.7, No.11, 1856–1863.

- M.Z. Guo, L.L. Xie, E.G. Gao, et al. Review for analysis of site response by microtremors [J]. World Earthquake Engineering, 1999, 15(3): 14–19. (in Chinese).
- T. Jiang. Study on microseism and its application to earthquake engineering [J]. World Earthquake Engineering, 1997, 13(4): 41–46. (in Chinese)PENG Yuanqian, LU Zheng, LI Xueying, et al. The application for the pulsant predominant period of the subsoil in engineering seismics [J]. North China Earthquake Sciences, 2000, 18(4): 61–68. (in Chinese).
- X. Xia, Z.W. LIU, M.Z. Guo, et al. A review of microtremor study in engineering site rating [J]. Earthquake Engineering and Engineering Vibration, 2001, 21(4): 18–23. (in Chinese).

Application of micro tremor observation on investigation of geological hazard induced by the great Wenchuan earthquake in Sichuan province

A.L. Che, J.H. Qi & X.P. Wu

School of Naval Architecture, Ocean and Civil Engineering, Shanghai Jiaotong University, China

T. Iwatate, M. Yoshimine, Y. Oda, Q.W. Ma & F. Zhang

Tokyo Metropolitan University, Tokyo, Japan

Z.J. Wu

Lanzhou Institute of Seismology, Chinese Earthquake Administration, Lanzhou, China

ABSTRACT: The Wenchuan great earthquake, which measured at Ms 8.0 and Mw 7.9, occurred on May 12, 2008 in Sichuan Province, China. The earthquake caused enormous death toll and economic loss in China. The Sichuan Province was the most seriously quake-hit region. The buildings, lifeline engineering and infrastructures were damaged badly, and secondary disasters were serious and wide. An effective ground investigation method was required to provide information for hazard investigation and post-earthquake reconstruction. In order to investigate the damage characteristics and mechanism of secondary disasters induced by the great earthquake, and to service reconstruction, many field teams for disaster investigation were practiced. Our group of 12 persons, 5 from Shanghai Jiaotong University (SJU) and 7 from Tokyo Metropolitan University, had investigated damage to buildings and secondary geologic disaster in the north of the Sichuan Province in July, 2008. The micro tremor measurements were surveyed at some typical ground sites including landslide and Longmen mountain fault as well. It is confirmed that the test results are useful for the geological hazard investigation.

1 INTRODUCTION

On May 12 of 2008, the Wenchuan Ms 8.0 earthquake occurred along the Longmen mountain tectonic belt, which locates at the eastern margin of the Qinghai-Tibet Plateau in Sichuan Province and has an up bound magnitude of 7.3 for potential seismic sources on the zonation map in China. The thrust-dextral slip of Beichuan-Yingxiu fault, which is one of the three sub-faults of the Longmen belt, led to the Wenchuan Ms 8.0 earthquake. The depth of epicenter is 14 km. The earthquake caused great damages to rural houses, educational and healthy buildings, and lifeline engineering, and it also caused serious secondary geotechnical disasters. The Sichuan Province suffered great damages, especially, the super-strong ground motion caused surface cracking directly and secondary geological hazards (such as landslides, landslips and rolling stones) destroyed the civic structures.

The field investigation and survey was preceded in the quake-hit region along the Longmen belt, in the Sichuan Province, from 4 to 7 of August, 2008, to survey the features how the earthquake induced geotechnical disasters, and tried to recommend a better way serving the reconstruction after the earthquake occurred. We selected typical towns, buildings

and secondary geotechnical disaster regions as key investigated objects along the Longmen mountain fault. The secondary geotechnical disasters investigation concluded damage characteristics and mechanism analysis, micro tremor observation, and taking photos as well. Fig. 1 shows the investigation sites along the Longmen fault.

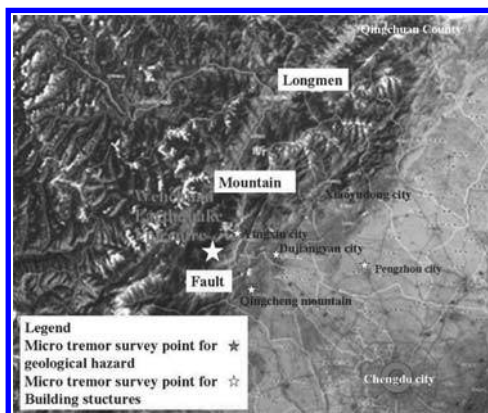


Figure 1. Investigation sites.

The micro tremor is one of the most convenient methods to investigate the dynamic characteristics of the surface ground (Yamanaka, et al., 1996). The method has been widely used in the recent years for there low cost, easy operation, also, it gives the dynamic property of the ground, i.e. the predominant frequency (f), which is used as a parameter in the field of geotechnical earthquake engineering. We applied the micro tremor survey for geological hazard investigation where the great Wenchuan Earthquake occurred. The micro tremor was conducted in landslides of the Qingchuan County and faults in the Xiaoyudong Town for geological hazard. Fig. 1 shows the investigation sites of micro tremor that we surveyed in the quake-hit area in the Sichuan Province. We analyzed the dispersion of the recorded data and then estimated the predominant frequency of the ground by FFT method. All of these have provided a more dependable basis for serving the reconstruction after the earthquake.



Figure 2. Land slides and quake lake along the Qinzu River and the Hongguang River.

2 GEOLOGICAL HAZARDS INVESTIGATION IN RESEARCH AREA

2.1 *The Qingchuan County and landslides*

The Qingchuan County locates at the northern end of the Yingxiu-Beichuan fault, which occupies 150 km length in the County. There are two seismic belts throughout the county, the bigger one is from Yingxiu Town to Qingchuan County, and the smaller one is at north side of this seismic belt. The highest elevation of the county is 3837 m, and more than 90% of the land is steep cliffs.

The earthquake intensity, caused by the main shock, in the Qingchuan County was IX (Chinese intensity scale), and it suffered thousands of aftershocks, the biggest one with a magnitude of Ms 6.4 occurred in 16:21, May 25. A large number of geological disasters such as landslides, landslips, rolling stones, and mud-rock flow and quake lakes occurred in the county, at the same time, groundwater was also faced with the potential of contamination. Figure 2 shows the landslides and Quake Lake formed by landslide-induced reservoirs along the Qinzu River and the Hongguang River.

2.2 *The Longmen Mountain belt and the rupture in the Xiaoyudong Town*

The Longmen fault is composed by three sub-faults, which are the Guanxian-Jiangyou fault, Yingxiu-Beichuan fault and Wenchuan-Maoxian fault. The Longmen fault continuously endures pressure from both the Pacific Plate and the Indian Plate, which implies that the area has a high level of seismicity. In 1933, a magnitude 7.5 earthquake occurred in



(a) The standing brick-concrete building near the rupture



(b) The brick-concrete building was sheared to damage at the first floor near the rupture

Figure 3. Surface rupture in the Xiaoyudong town and the damages to the buildings.

the same area at a place called Diexi. In 1976, two earthquakes, both with magnitudes of 7.2, occurred in the Songpan area within one week, resulting in a death toll of over 800 (Wang, 2008).

The fault where the great earthquake occurred is located at the southern part of the Yingxiu-Beichuan fault.

Near the Xiaoyudong Town of Pengzhou City (see Fig. 1), there was a NW trending surface rupture zone with 6 km length and 5 to 20 m width. It was mainly composed of bend-slip fold in the surface, and showed a SW to NE thrusting and strong left-rotated mechanism. Along the rupture zone, there was generally a 1 to 2 m vertical dislocation and 1 to 3 m left-rotated horizontal dislocation, which showed that the amount of left-rotated horizontal dislocation was equal to or slightly larger than the amount of vertical dislocation. Seismic fault dislocated riverbed, terraces, roads, buildings and so on, formed continuous extension of the fault scarp and accompanied by left-rotated displacement. Figure 3 shows the surface rupture in the Xiaoyudong Town and the damages to the buildings.

3 FIELD OBSERVATIONS

It is well known that the micro tremor observation is one of the most convenient methods to investigate the dynamic characteristics of the surface ground and structure. And it is a kind of geophysics prospecting, in a degree it may provides drilling information, which is of abundant intention such as the information of soil site and engineering geological condition and so on. The frequency characteristics of micro tremor can be obtained by a spectral analysis of its signals, which can be used to probe into dynamical characteristics of the soil of measuring area (Che, 2006; Guo, 1999; Jiang, 1997; Peng, 2000; Xia, 2001). The observed signals are analyzed by the fast Fourier transform method (FFT).

At the research area, the micro tremor observation was conducted at the landslide of the Qingchuan City the axis of the dam, which total length is about 12 km. The data are acquired on a 23 m survey line with a receiver interval of 1 m for each measurement point, and the interval of measurement points is 100 m. So the total numbers of measurements are about 120 (Fig. 2), and surface rupture zone in the Xiaoyudong Town.

3.1 Measuring equipment and data acquiring

The measuring equipment is a kind of handy seismometer (SPC-35F: VSE-15D velocity seismometer, distinguish ability 16Bit, made by Vibration-Measuring Corporation of Tokyo, Japan). The frequency of the detector ranges is between 0 Hz and 70 Hz. Table 1 lists the main measuring parameters of the micro tremor equipment.

While investigating, the disturbing of people and energy source should be avoided and the ground sites should be as flat as possible. The records of the horizontal and vertical components of short-period micro tremors are obtained using a three components high-sensitive seismometer, which has a natural period in one second. The device measures two horizontal components (EW and NS) and a vertical one (UD) for micro tremor respectively. It is designed to record at a sampling rate of 100 Hz for 5 minutes, and a total of 30000 measurements are recorded.

3.2 Micro tremor observations in the Qingchuan County

The micro tremor observations spots of ground sites in the survey was conducted at the landslides site surrounding the Qinzhu river and the Hongguang river, and the landslides induced quake lake as well. The data were acquired through two survey lines with a 30° angle, which were A-line with 5 observation points and B-line with 7 points, and the interval of measurement points was 10 m. The total numbers of measurements were 12. Fig. 4 shows the location of the two survey lines.

Table 1. Parameters of the Micro tremor instrument.

Model	Seismograph portable (SPC-35F: VSE-15D model velocity instrument)
Vibration measurement	Velocity: 100 m kine and 10 m kine, resolution 10 μ kine, frequent range 0.1~70 Hz Acceleration: 10 gal and 100 gal; frequent range 0.1~70 Hz Displacement: 100 μ m and 10 μ m; frequent range 0.1~70 Hz
Frequency	1000 Hz, 500 Hz, 200 Hz, 100 Hz, 50 Hz, 20 Hz, 10 Hz, 5 Hz, 1 Hz



Figure 4. Measurement points in Qingchuan County.



Figure 5. Measurement lines in the Xiaoyudong Town.

3.3 Micro tremor observations in the Xiaoyudong Town

The micro tremor observation spots of ground sites in the survey were conducted at the fault zone in the Xiaoyudong Town. The data were acquired by two parallel survey lines which were normal to the fault. There were a A-line with 9 points and a B-line with 10 points, and the interval of measurement points is 10 m as well, the total numbers of measurements are 19. Fig. 5 shows A-line and B-line in the Xiaoyudong Town.

4 ANALYSES AND RESULTS

4.1 Proceeding methods of measurements

As shown in Fig. 6, the analyzing method for the micro tremor observation data is called the fast Fourier transform (FFT). The frequency characteristics of micro tremor can be obtained by a spectral analysis of its signals, which can be used to probe into dynamical characteristics of the structure and/or the soil of

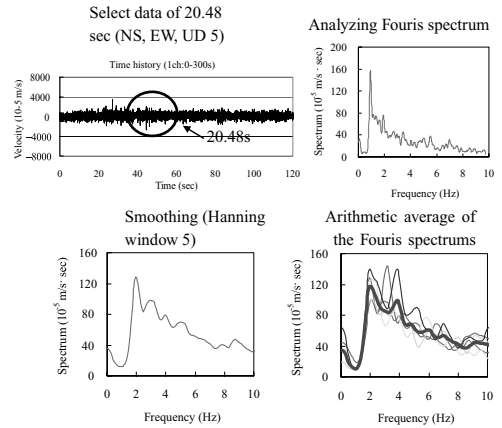


Figure 6. Procedure of the Fast Fourier transforms analysis.

measuring area. The observed signals are analyzed by FFT method. The potential noise sources such as machinery, vehicles traffic or pedestrians, near the seismometer are avoided during the measurement time of 5 minutes. And from the recorded data of micro tremor measurements, five sets of 2048 digital data at lower noise periods are selected to use for FFT analysis. The velocity Fourier amplitude spectra, spectra ratio and relative variation amplitude are computed.

4.2 Predominant frequencies determination of ground sites

4.2.1 Analyzing methods

The main purpose of investigating on ground by micro tremor observation is to obtain the amplitude of micro tremor and the predominant frequency. One of the popular methods nowadays is the Nakamura Method (H/V).

The Nakamura Method refers to obtain tri-component Fourier frequency spectra, to divide the 2 horizontal components (NS, EW) by the vertical component (UD), and get the transfer function of the ground and the predominant frequency. The advantage of this method lies on simply and quickly solving the problem.

4.2.2 Analyzing results in the Qingchuan County

Fig. 7 shows the analyzing results of survey line-B for landslides, in the Qingchuan County, by the Nakamura Method (H/V). The predominant frequency of the ground shows obvious peak amplitudes, it is 3.9 Hz in the observation spot. It can be considered that the soil layer is overburden by the landslide, and the predominant frequencies are the dynamic characteristic of the overburden.

Figure 8 shows the predominant frequencies along the observed directions. The total observed length is

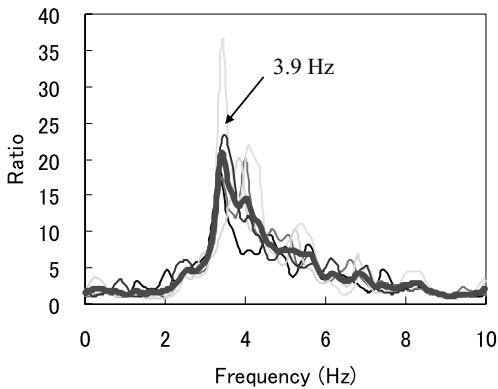


Figure 7. An example of Nakamura method (H/V) analysis results (Line-B) (The blue thick line indicates arithmetic average of the other five Fourier spectrums).

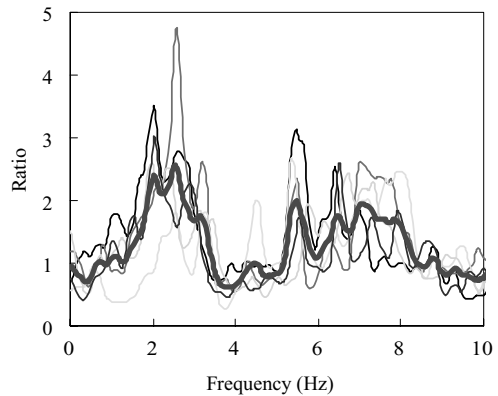


Figure 9. Nakamura method (H/V) analysis results (Line-A) (The blue thick line indicates arithmetic average of the other five Fourier spectrums).

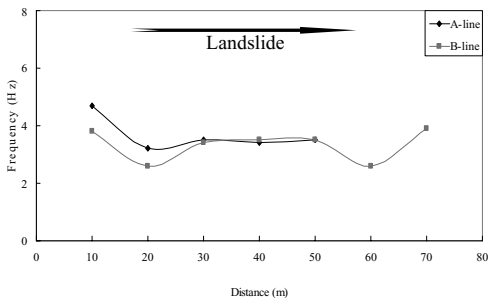


Figure 8. Predominant frequencies along the observed directions.

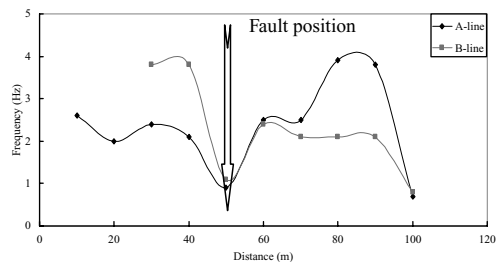


Figure 10. Predominant frequencies along the observed directions.

60 m, and the predominant frequencies of both Line-A and Line-B are 2.6 Hz~4.7 Hz. It is well known that the predominant frequencies are related to the thickness of the overburden, therefore the changing of the predominant frequencies of the site also shows the trending of the thickness of the overburden.

4.2.3 Analyzing results in the Xiaoyudong Town

Fig. 9 shows the analyzing results by H/V. Mostly, H/V obtain unobvious peak amplitudes, and the amplitude is not predominant due to the loud environmental noises and close velocities of shear waves between soil layers testified. Figure 10 shows the predominant frequencies along the observed directions. The total observed length is 90 m, and the predominant frequencies of both Line-A and Line-B are 0.9 Hz~3.9 Hz, and it is a sudden change in both Line-A and Line-B when the fault is across. The predominant frequencies of the observation spots, which was normal to the fault in the Xiaoyudong Town, show a converse response, which agree with the trend of fault well.

5 CONCLUSIONS

The predominant frequencies of the ground were calculated from the observed survey, and the relationship between the results and the hazard investigations was estimated. To study the application of the method on geological hazard investigation, a series of field experiments and analyses were carried out. The main results are as follows.

1. The predominant frequencies of the landslide in the Qingchuan City show obvious peak amplitudes, it can be considered that the soil layer is overburden by the landslide and the predominant frequencies are the dynamic characteristic of the overburden.

The total observed length is 60 m, and the predominant frequencies of both Line-A and Line-B are 2.6 Hz~4.7 Hz. It is well known that the predominant frequencies are related to the thickness of the overburden, therefore the changing of the predominant frequencies of the site also shows the trending of the thickness of the overburden.

2. The predominant frequencies of the spots along the survey lines, which were normal to the rupture in Xiaoyudong city, show sudden change in both Line-A and Line-B when the fault is across. The converse response well agrees with the trend of fault.

REFERENCES

- A.L. Che, T. Iwatate, X.R. Ge, Study on the applicability of frequency spectrum of micro-tremor and dynamic characteristics of surface ground in Asia area, *Journal of Zhejiang University SCIENCE*, 2006, Vol.7, No. 11, 1856–1863.
- M.Z. Guo, L.L. Xie, E.G. Gao, et al. Review for analysis of site response by microtremors [J]. *World Earthquake Engineering*, 1999, 15(3): 14–19. (in Chinese).
- T. Jiang, Study on microseism and its application to earthquake engineering [J]. *World Earthquake engineering*, 1997, 13(4): 41–46. (in Chinese).
- X. Xia, Z.W. Liu, M.Z. Guo, et al. A review of microtremor study in engineering site rating [J]. *Earthquake Engineering and Engineering Vibration*, 2001, 21(4): 18–23. (in Chinese).
- Y. Nakamura 1989. A method for dynamic characteristics estimation of subsurface using micro tremor on the ground surface. *OR or RTR1*, 30, 25–33.
- Y.Q. Peng, Z. Lu, X.Y. Li, et al. The application for the pulsant predominant period of the subsoil in engineering seismics [J]. *North China Earthquake Sciences*, 2000, 18(4): 61–68. (in Chinese).
- Z.F. Wang. A preliminary report on the great Wenchuan earthquake [J]. *Earthquake Engineering and Engineering Vibration*, 2008, Vol.7, No. 2: 225–234. (in English).

*Special discussion session—
future directions of performance-based design*

Perspectives in geotechnics for vastly strong earthquake shaking

K. Ishihara

Chuo University, Tokyo, Japan

Over the last 30 years, there have been remarkable progresses in sophistication of instruments and strengthening of observation network for recording strong motions during earthquakes. In Japan there is a network of stations called K-Net consisting of about 1000 high-precision recorders placed on the ground surface with a spacing of 25 km × 25 km throughout the country. Another set of recording stations called KiK-net has also been established in which about 700 sites are installed with instruments both on the ground surface and on the bed rocks. Thus, the coverage of areas was widened and precision improved greatly to capture motions throughout the country during any scale of earthquakes.

As a consequence, the magnitude of recorded accelerations has increased remarkably year after year, as demonstrated in Fig. 1. At the time of the Tokachi-Oki earthquake in 1968, the peak horizontal ground acceleration recorded was 225 gal in the port of Hachinohe north of Japan, but it jumped up to a value of 891 gal at the time of the 1995 Kobe earthquake. Since then, the network of recording stations were strengthened and at the time of the most recent earthquake in 2008, the peak recorded acceleration reached a value as high as 4022 gal in combined 3-D absolute peak acceleration. Since earthquakes are natural phenomena, it seems unlikely that the intensity of motion itself has in fact increased so dramatically, particularly in recent times. The strong motions must have occurred in long geological past. However, once they are recorded, it is not permissible to ignore them. From the engineering point of view, the increase in the recorded motions is to be recognized as an advent of a strong demand dictating that the design for structures and facilities be correspondingly made to cope with such an increased level of seismicity. Thus, engineers are confronted with new challenges as to how to come up with effective and still economically feasible concepts and procedures.

Shown in Table 1 are the evolutions with time regarding capacity evaluation in terms of design concepts and methods of analysis in response to the increasing demand.

In the design and practice of nuclear power facilities, the accelerations for input motions had been set at a high value from the early period and equivalent linear analysis procedures have been used. The major

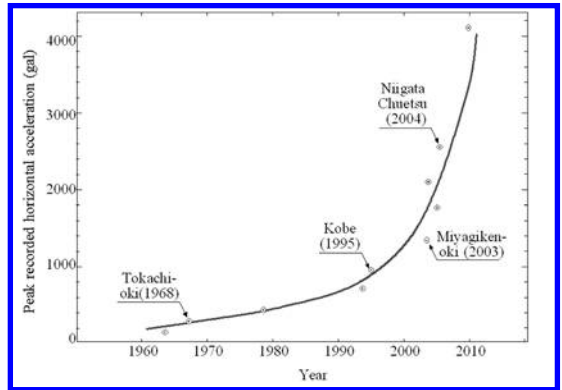


Figure 1. Increasing trend of recorded horizontal accelerations during recent earthquakes in Japan.

Table 1. Evolution in demand versus capacity in the seismic design.

Year	1970	75	80	85	90	95	00	05	10	15
Seismicity	200-300 gal		400-500 gal			600-800 gal		1500 gal		
Nuclear power facilities	Equivalent Linear analysis								Strengthening	
Structures (Buildings, Bridges)	Pseudo-static analysis			Linear analysis			Non-linear analysis			
				Vibration control Isolation						
Geotechnics (Liquefaction, Landslide, Soil structure interaction)	Pseudo-static analysis ($F_s \geq 1.2$)			Equivalent linear analysis			Permanent displacement analysis			
				Effective stress-based analysis			Performance-based design			
<ul style="list-style-type: none"> • Hazard map, Risk map 										

efforts being undertaken in Japan for the nuclear facilities after the 2007 October earthquake is further strengthening of the ground surrounding foundations and water-intake facilities.

In the field of structural engineering, the pseudo-static method was employed until around 1970, but linear analysis procedure using computer codes has become a common practice. This was followed by the non-linear analysis from early 1980. On the other hand, theory and practice was developed for the structural control and vibration isolation from around 1980s.

Although this technique is an outgrowth from general demand to reduce the damage, it is also viewed as being of additional help to cope with the very strong shaking during earthquakes.

In the area of geotechnical engineering, pseudo-static analysis has long been used to evaluate levels of safety of embankments and dams against an external force due to seismic shaking. Subsequently equivalent linear analysis procedure had been developed and, used for instance, for assessing local amplification characteristics of soil deposits and also for evaluating deformations developed in earth structures. With the evolution of the constitutive laws characterizing soil deformations, response analysis procedures based on effective stress principle has been developed and put into practical use. This method consists in evaluating gradually decreasing effective confining stress and reflecting it on the decrease in stiffness and strength as seismic excitation proceeds with time. Thus, this method is considered to reflect actual situations more precisely in which large acceleration is suppressed by softening of soils, but accompanied in turn with large deformations. The development of response analysis based on the effective stress principle has provided new concepts and means for the advances of design methodologies based on large and residual deformations. With these tools, what is called the performance-based design was vastly enhanced, as indicated in Table 1. The large acceleration corresponding to a large shear stress supposedly in excess of strength will make soils deformed largely and the criteria for specifying an allowable deformation will become a major yardstick for the design of soil deposits and earth structures subjected to an intense shaking during earthquakes.

Another countermeasure to reduce the risk of damage due to soil failure would be to prepare local zoning maps as indicated in Table 1 and to enhance preparedness amongst residents for possible distress caused by soil failures. Efforts are being made in this direction by local governments in Japan to reduce risk of damage by large earthquakes.

Consequences of strong shaking during earthquakes to instability of the ground have been recognized widely as liquefaction of saturated sands and ensuing flow failure and settlements. However, there have

been other types of damage in recent earthquakes which have not been properly addressed. The following is just examples of such new problem areas.

The occurrence of significant settlements of the ground composed of well-compacted partly saturated silty sand fills has never been identified and reported in the literature. In the premise of the nuclear power station in Kashiwazaki, the settlement of the order of 30–50 cm did actually take place, at the time of the Niigata Chuetsu-Oki Earthquake of 2007.7.16, accompanied by local distortions or offsets on the ground surface. This appears to have accrued as a result of extraordinarily strong shaking of the order of 1,000 gals in acceleration, inducing a peak cyclic stress ratio of 0.8–0.9 in dynamic loading. Thus, even partly saturated soils developed settlements. The behaviour of partly saturated soils subjected to intense cyclic loads seems to be a new subject area.

The depression developed in the vicinity of vertical walls of the buildings in the nuclear power station suggested that there might have been gradual clogging of the openings by surrounding soils during the repetition of shaking, which must have conducted to an increase in earth pressure on the wall. This phenomenon may be cited as ratcheting action. There was another place in the area of equally strong shaking where the sea walls were damaged due to the increased horizontal thrust which might have resulted from the ratcheting phenomenon. It may thus be mentioned that the ratcheting soil movement around the wall could lead to a greatly increased earth pressure which would not be able to be explained by the conventional concept. Thus, a new challenge will crop up regarding earth pressure evaluation induced by strong shaking during earthquakes. There are other problems which will be manifested by large earthquakes in future. Geotechnical engineers are requested to keep an eye to ground-associated damage in any earthquakes in future. Capturing novel items of problems and addressing them properly should be taken as responsibilities of those involved in geotechnical works related to earthquakes.

Seismic behaviour of geotechnical structures—Past, present and future

Pedro S. Sêco e Pinto

Laboratório Nacional de Engenharia Civil, Lisbon, Portugal

ABSTRACT: This paper begins with the background of earthquake geotechnical engineering history divided in 4 periods. The performance based seismic design is addressed and after a brief introduction to earthquake hazard the topics slope stability, potentially liquefiable soils, earth retaining structures, soil-structure interaction, embankment dams, underground structures, solid waste landfills are discussed. The topics that deserve more consideration and can be considered new challenges are pointed out. Finally my vision and lessons for tomorrow are presented.

*I am very busy
I have already begun with my survey
And I began to write my next error.*

Bertolt Brecht

1 INTRODUCTION

When I was invited to prepare this paper for the *Special Plenary Session by Honorable Experts on Future Directions of PBD* I felt very honoured, but soon became worried and still remain so, because I am not sure what is expected. Due to space limitations I will remain general and in the First Part a brief background of earthquake geotechnical engineering history will be given. In the Second Part I will try to highlight the current Performance Based Design situation. In the Third Part I will address the new challenges that we are facing and in the Fourth Part I will give my personal vision.

2 BACKGROUND OF EARTHQUAKE GEOTECHNICAL ENGINEERING HISTORY

Pre-Historic (before 1940)—This period was characterized by the development of historical earthquakes and Paleoseismicity, the use of empirical methods, the knowledge was primary and parcelled. The measurement of the destructiveness of the earthquake was based in human reaction and observed damage and use of Mercalli scale. Investigation of the earthquake induced damage due to Great San Francisco earthquake (1906) was performed by Sano (1916). In the early 20th century there were discussions on whether or not a big earthquake would hit Tokyo area, what unfortunately occurred on 1st September, 1923. For the assessment of seismic behavior of retaining

walls Mononobe & Matsuo (1929) and Okabe method (1924) was proposed.

Classic Period (1940–1983) with the attempt to organize as scientific discipline, records of typical earthquakes e.g. El-Centro earthquake (1940), the use of magnitude for the physical measure of size of the earthquake and several scales based on the amplitude of seismograph records. After Niigata and Alaska earthquakes in 1964 the first studies of liquefaction evaluation of sands and silty sands came out. Use of geophysical tests namely refraction tests, up-hole and downhole tests. Use of laboratory cyclic tests namely resonant column tests, simple shear tests and triaxial tests for soil behavior and definition of shear modulus and damping ratio. Developments of pseudo-static methods for embankments (Ambraseys, 1960) and simplified methods for assessment of displacements (Newmark, 1965, Sarma, 1975, Makdisi & Seed, 1977). Implementation of codes in total stress SHAKE in 1971 and QUAD 4 in 1974.

Modern Period (1983–1995) characterized by the definition of seismic action using strong ground motions parameters PGA, PGV and PGD, response spectra and use of deterministic and probabilistic methods. Development of laboratory and field tests with more automation in operation, more accurate measurements, reduced costs in maintenance and production of data processing techniques with high resolution and degree of reliability, use of seismic arrays and SASW. Use of physical models e.g. shaking table, reaction walls, centrifuge tests, calibration chambers and prototype tests. Proposals for liquefaction assessment of gravel materials were presented. Developments of mathematical models for dynamic analysis and codes in effective stress using plasticity models e.g. DIANA, DYNAFLOW, TARA among others. First stage of development of codes and standards. Lessons from Mexico earthquake (1985), Loma Prieta

earthquake (1989) and Northridge earthquake (1994) were taken into account.

Actual Period (after 1995) with the implementation of cyclic triaxial tests and torsional shear tests. Combination of laboratory and field tests to assess design parameters. Development of more realistic coupled models, using boundary elements and discrete elements, incorporating non linear behavior, ageing, thermal effects and 3D analyses. Verification, calibration and validation of computer codes. Prediction of residual strength and allowable deformation of soils exploring aerial photographs. Implementation of instrumentation and monitoring to assess seismic behavior of structures. Great emphasis on diffusion of knowledge by journal, conferences, codes of practice and development of networks. Use of case histories for a better understanding of seismic behavior of structures and calibration of predictions. Developments of techniques for remediation and rehabilitation of structures.

3 PERFORMANCE BASED DESIGN

3.1 Introduction

To the author knowledge the first application of performance based seismic design was for nuclear powerplants in 1971 where 2 levels of seismic action were considered (USAEC, 1973; IAEA, 1972).

After a brief introduction to earthquake hazard the following topics slope stability, potentially liquefiable soils, earth retaining structures, soil-structure interaction, embankment dams, underground structures, solid waste landfills will be addressed. Due space limitations offshore structures, breakwaters, machine foundations and shallow foundations will be kept out.

3.2 Earthquake hazard zonation

In general the national territories are divided by the National Authorities into seismic zones, depending on the local hazard. The World List is a good example.

In Eurocode 8 (1998a), in general, the hazard is described in terms of a single parameter, i.e. the value a_g of the effective peak ground acceleration in rock or firm soil called “design ground acceleration” expressed in terms of: a) the reference seismic action associated with a probability of exceeding (P_{NCR}) of 10% in 50 years; or b) a reference return period (T_{NCR}) = 475 years. For the design two basic requirements are defined: (i) Non collapse requirement (ultimate limit states) i.e. after the occurrence of the seismic event the structure shall retain its structural integrity, with respect to both vertical and horizontal loads, and adequate residual resistance, although in some parts considerable damage may occur, (ii) Minimization of damage (serviceability limit state) after seismic actions with high

probability of occurrence during the design life of the structure some parts can undergo minor damage without the need of immediate repair. The structure shall be designed and constructed without the occurrence of damage and the associated limitations of use, the costs of which would be disproportionately high in comparison with the costs of the structure itself. The seismic action to be taken into account for the “damage limitation requirement” has a probability of exceedance, of 10% in 50 years and a return period of 95 years.

The structures following EC8 are classified in 4 importance categories related with the size, value and importance for the public and on the possibility of human losses in case of collapse. To each important category an important factor is assigned. The important factor $\gamma_f = 1.0$ is associated with a design seismic event having a reference return period of 475 years. The importance category varying I to IV (with the decreasing of the importance and complexity of the structure) are related with the importance factor γ_f assuming the values 1.4, 1.2, 1.0 and 0.8, respectively.

Since the doctrine proposed by Aristotle (384–322 B.C) in his book *Meteorologica* that earthquakes were produced by dried exhalations (spirits or winds) in caves inside the earth and later the explosive theory was adopted by Newton in his book *Optics* (1718), the modern scientific ideas consider the earthquake a natural phenomenon. Within this framework the tectonic conditions should include tectonic mechanisms, location and description of faults (normal, stryke and reverse) and estimation of fault activity (average slip rate, slip per event, time interval between large earthquake, length, directivity effects, etc), these factors are important to assess the involved risk.

The current practice is the deterministic approach in which the seismic evaluation parameters were ascertained by identifying the critical active faults which show evidence of movements in Quaternary time (ICOLD, 1998).

To assess if there is the potential for a significant amount of surface displacement trenches are excavated with 3 to 4 meters deep and 30 to 50 meters long and should be inspected and log the exposures geologic features. Recently a fault investigation method other than trenching has been developed, called the long Geo-slicer method in which long iron sheet piles with a flat U-shaped cross section are driven into an unconsolidated bed, iron plate shutters are inserted to face these iron sheet piles and the piles and shutters are pulled out to take undisturbed samples of strata of a certain width.

When active faults are covered with alluvium geophysical explorations such as seismic reflection method, sonic prospecting, electric prospecting, electromagnetic prospecting, gravity prospecting and radioactive prospecting can be used.

3.3 Slope stability

For the natural or artificial slopes a verification of ground stability to ensure safety or serviceability under the design earthquake should be performed.

The following methods of analysis: (i) dynamic analysis, using finite elements; (ii) rigid block models; and (iii) simplified pseudo-static methods can be used.

Pseudo-static method shall not be used for soils that develop high pore water pressure or significant degradation of stiffness under cyclic loading.

The performance based design evaluates the residual deformation/displacement and the calculated values at the end of the earthquake are compared with the allowable values (Towhata, 2008).

Amplification factors for the seismic action to incorporate the topographic effects and particularly for slopes with height greater than 30 m are recommended.

3.4 Potentially liquefiable soils

Empirical liquefaction charts are given with seismic shear wave velocities versus SPT values to assess liquefaction.

The new proposals integrate: (i) data of recent earthquakes; (ii) corrections due the existence of fines; (iii) experience related with a better interpretation of SPT test; (iv) local effects; (v) cases histories related to more than 200 earthquakes; and (vi) Bayesian theory.

For liquefaction assessment by shear wave velocities two methodologies are used: (i) methods combining the shear wave velocities by laboratory tests on undisturbed samples obtained by tube samplers or by frozen samples; (ii) methods measuring shear wave velocities and its correlation with liquefaction assessment by field observations.

It is important to refer that Eurocode 8 (1998)-Part 5 considers no risk of liquefaction when the ground acceleration is less than 0.15 in addition with one of the following conditions: (i) sands with a clay content higher than 20% and a plasticity index > 10 ; (ii) sands with silt content higher than 10% and $N_1(60) > 20$; and (iii) clean sands with $N_1(60) > 25$.

For post liquefaction strength relationships between SPT and CPT tests and residual strength were proposed by several authors.

Also to assess the settlement of the ground due to the liquefaction of sand deposits there are some proposals based on the knowledge of the safety factor against liquefaction and the relative density converted to the value of N_1 .

The new trend for performance based design is to consider 2 levels of seismic actions and to analyse the situation when the limit of force balance is exceeded for high intensity ground motions associated with a very rare seismic event.

The remedial measures against liquefaction can be classified in two categories (TC4 ISSMGE, 2001);

INA, 2001): (i) the prevention of liquefaction; and (ii) the reduction of damage to facilities due to liquefaction.

For the selection of the remedial measure it is important to consider: (i) Potential efficiency; (ii) Technical feasibility; (iii) Impact on structure and environmental; (iv) Cost-effectiveness; and (v) Innovation.

The methods: (i) soil grouting using calcifying bacteria; (ii) confinement wall; (iii) soil cementation and solidification by deep mix method; (iv) permeable grouting; and (v) sand compaction pile to prevent soil liquefaction are getting very popular.

3.5 Earth retaining structures

For the pseudo-static analysis of rotating structures the seismic coefficients can be taken as (Eurocode 8, 1998b):

$$k_h = \alpha_{gr} \gamma_f S / g \cdot r \quad (1)$$

$$k_v = \pm 0,5k_h \text{ when the ratio } \alpha_{vg}/\alpha_{gr} \text{ is greater than } 0.6 \quad (2)$$

$$k_v = \pm 0,33k_h \text{ otherwise} \quad (3)$$

where α_{gr} is the reference peak ground acceleration for class A ground, S is the soil parameter, γ_f is the importance factor of the structure and the factor r takes the values listed in Table.

For saturated cohesionless soils susceptible to develop high pore pressure the r factor should not be taken larger than 1.0, and the safety factor against liquefaction should not be less than 2 (see Table 1).

Development of methods to assess the displacements exploring Newmark (1965) model, Richard-Elms (1979) model and Nadim-Whitman (1984) model and considering solutions in pure translation, pure rotation and translation and rotation simultaneous.

In performance based design the acceptable level of damage should be specified in engineering terms such as displacements, limit stress state, and ductility/strain based on the function and seismic response of the structure. Two levels of earthquakes are used: (i) Level 1 (L1)—the level of earthquake that occur during the life-span and (ii) Level 2—the level of earthquake

Table 1. Factor affecting the horizontal seismic coefficient.

Type of retaining structure	r
Free gravity walls that can accept a displacement $d_r \leq 300 \alpha S(\text{mm})$	2
As above with $d_r \leq 200 \alpha S(\text{mm})$	1.5
Flexural r.c. walls, anchored or braced walls, r.c. walls founded on vertical piles, restrained basement walls and bridge abutments.	1.0

associated with infrequent rare events that involve very strong ground shaking (Iai & Tobita, 2005).

3.6 Soil-Structure Interaction

In general for the Soil-Structure Interaction (SSI) the design engineers ignore the kinematic component, considering a fixed base analysis of the structure, due the following reasons: (i) in some cases the kinematic interaction may be neglected; (ii) aseismic building codes, with a few exceptions, e.g. Eurocode 8, do not refer it; and (iii) kinematic interaction effects are more difficult to assess than inertial forces,

There is strong evidence that the SSI plays and important role in slender tall structures, structures founded in very soft soils and structures with deep foundations. The Eurocode 8 states: "Bending moments developing due to kinematic interaction shall be computed only when two or more of the following conditions occur simultaneously: (i) the subsoil profile is of class D, S_1 or S_2 , and contains consecutive layers with sharply differing stiffness; (ii) the zone is of moderate or high seismicity, $\alpha > 0.10$; and (iii) the supported structure is of important category I or II.

The stability of footings for the ultimate state limit design criteria shall be analyzed against failure by sliding and against bearing capacity failure.

Piles and piers shall be designed to resist the following action effects: (i) inertia forces from the superstructure; and (ii) kinematic forces resulting from the deformation of the surrounding soil due the propagation of seismic waves.

The complete solution is a 3D analysis very time demanding and it is not adequate for design purposes. The decomposition of the problem in steps implies: (i) the kinematic interaction involving the response of the base acceleration of the system considering the mass of superstructure equal to zero; (ii) the inertial interaction that involves the computation of the dynamic impedances at the foundation level and the dynamic response of the superstructure. Several techniques have been explored namely lumped (discrete) models (elementary boundaries, viscous boundaries and consistent boundaries), special techniques (superposition boundary, extrapolative algorithms) and boundary integral equation methods.

The use of inclined piles is not recommended to absorb the lateral loads of the soils. If inclined piles are used they must be designed to support axial as well as bending loads.

The investigation methods for pile foundation damage are: (i) direct visual inspection, (ii) the use of borehole camera inspection and (iii) pile integrity test. The ground deformation can be investigated by visual survey and GPS survey.

3.7 Embankment dams

For medium embankment dams a conventional pseudo-static analysis method was used to evaluate the seismic behavior of dams (Ambraseys, 1960; Seed and Martin, 1966), but for dams over 100 m high a dynamic analysis including computational analysis (modal analysis), model tests, field measurements and prototype tests was performed (ICOLD, 1975).

Simplified methods to compute displacements were proposed by Newmark (1965), Sarma (1975) and Makdisi and Seed (1977). For embankment dams a value of 5% axial strain was used as allowable deformation.

Later ICOLD (1983) has proposed 2 levels for seismic activity, namely MCE (Maximum Credible Earthquake) considering a return period of 500–1000 years and DBE (Design Basis Earthquake) for a return period of 145 years, with a probability of exceeding in 100 years less than 50%.

ICOLD (1989, 2002) has considered 3 levels of seismic action, namely: MDE (Maximum Design Earthquake), MCE (Maximum Credible Earthquake) and OBE (Operating Basis Earthquake). Four hazard classes were defined, namely: Low with $PGA < 0.10$ g, Moderate with $0.10 < PGA < 0.25$ g, High with $PGA > 0.25$ g (no active faults within 10 Km) and. Extreme with $PGA > 0.25$ g (active faults within 10 Km). ICOLD has introduced the potential risk of dam associated with capacity, height, evacuation requirements and potential downstream damage considering these 4 hazard classes.

3.8 Underground structures

Due to the myth that underground structures have a good resistance against shaking in many design specifications aseismic design is not usually considered. The reasons for this believe are: (i) the rock mass surrounding the tunnel has considerable stiffness to avoid tunnel shape changes; and (ii) it is considered that the tunnel follow the soil movements.

From a careful case histories study on underground structures behaviour during earthquakes occurrences the following failure mechanisms can be selected: (i) Sliding or shear distortion of surrounding massif or foundation or both; (ii) Failure and collapse of the ceiling slab of stations; (iii) Disruption of underground structure by major fault movement in foundation; (iv) Differential tectonic ground movements; (v) Piping failure through cracks induced by ground motions; (vi) Large ground deformation due liquefaction; and (vii) Separation of construction joints on side walls at the intersection between the underground and ground surface sections in soft ground.

The principal pipe failures are: (i) rupture due to axial tension; (ii) local buckling due to axial compression; and (iii) flexural failure.

The countermeasures to mitigate seismic damage to pipelines include high strength or high ductibility materials for the pipelines, use of joints to allow expansion/contraction or rotation, methods to isolate the pipeline from ground movements and methods to reduce ground movements.

Models based in f.e.m have been used for non linear analyses with Ramberg-Osgood relationship for life-lines. Due the spatial development it is important to simulate the faults movements.

3.9 Performance of solid waste landfills during earthquakes

The key point on seismic response of solid waste landfill is the dynamic response of geomembranes liners, because the eventual failure of the base liner and the cover liner systems cause the loss of landfill serviceability and the environmental damages due to water and air pollution.

The Code of Federal Regulations (USEPA, 1994) requires that the new municipal solid waste landfills to be designed for a maximum horizontal acceleration with a 10% or 2% probability of exceedance in 50 years considering a return period of 475 years or 2475, respectively. The sliding displacement prediction is important to assess the performance of solid waste landfills. The shear strength properties of waste landfills are not easily determined since the physical composition of the mixture makes it unsuitable for the conventional laboratory strength testing.

The allowable value for the calculated permanent seismic displacement of geosynthetic liner systems is 150 to 300 mm. The upper value of 300 mm is appropriate for simplified analyses which use upper bound displacement curves for generic Newmark displacement charts, residual shear strength and/or simplified seismic analyses. The lower value 150 mm is more appropriate for more sophisticated analyses and formal Newmark displacement analyses. The knowledge of interaction between waste and structures is still poor and mainly limited to field observations.

4 NEW CHALLENGES

The following topics deserve more consideration and can be considered new challenges:

4.1 Earthquake hazard zonation and strong motions

Dense recording GPS arrays with sampling rate allow determining deformation rates in seismic active regions. Intrinsic properties of rock at depth have to be obtained in situ by deep drilling into active faults. Computational with high resolution model for stress and deformations in communicating fault systems should be developed. A better exploration

of microtremors technique, directivity effects and attenuation laws is needed.

4.2 Slopes

(i) Assessment of the residual strength of the soil; (ii) Guidelines to assess the rock slopes stability; (iii) Analyses of mass movements; (iv) Mitigation methods; (v) Analyses to assess amplification effects and comparison between 3D with 2D analyses.

4.3 Liquefaction

i) The use of Becker hammer and geophysical tests to assess the liquefaction of gravelly materials; ii) Determination of residual strength of soil; iii) Evaluation of liquefaction consequences and post earthquakes displacements; iv) Mitigation methods with use of microorganisms.

4.4 Retaining structures

(i) Design methods for the computation of permanent displacements that allow the couple computation of rotation and translation movements should be referred; (ii) The permanent displacements should be related with the height of the wall; (iii) Due the good behavior of geogrid—reinforced soil retaining walls in comparison with reinforced concrete cantilever retaining walls, during the occurrence of earthquakes, these structures should be favored.

4.5 Soil-Structure Interaction

i) The influence of pile cap; ii) The incorporation of the non linear behavior of the materials in the methods of analysis; iii) The instrumentation of the piles for design purposes; iv) Analysis of piles group effect.

4.6 Embankment dams

(i) Coupled models with non linear analyses and pore water pressure generation and dissipation models; (ii) Hydrodynamic effects of reservoir associated with dynamic foundation-structure interaction (Seco e Pinto, 2001); (iii) Failure of tailing dams that currently reach more than 200 m high and reservoirs with more than one billion tons of slimes due the occurrence of liquefaction and the increase of the resistance due to ageing effects of the deposits.

4.7 Underground structures

i) For underground pipelines two extreme cases needed to be analyzed: soil liquefaction and fault movements and landslides. To minimize the effect of an imposed displacement and to introduce maximum flexibility in the system the following actions are

taken: use of joints to allow expansion/contraction or rotation, methods to isolate the pipeline from ground movements and methods to reduce ground movements.

4.8 *Solid waste landfills*

i) A better characterization of dynamics properties of solid landfills; ii) A better understanding of landfill-structure interaction in order to predict displacements.

4.9 *New materials*

Use of steel slag materials (recycling materials) to increase lateral resistance of pile and equipments using fiber optics.

4.10 *Team work*

Today there is a need to work in large teams exploring the huge capacity of computers to analyze the behavior of complex structures. Innovative methods and new solutions require high reliable information and teams integrating different experts, namely seismologists, geologist, geophysics, geotechnicians and structures engineers.

5 MY VISION—LESSONS FOR TOMORROW

The actual tendency is to prepare unified codes for different regions but keeping the freedom for each country to choose the safety level defined in each National Annex. The global safety factor was substituted by the partial safety factors applied to actions and to the strength of materials. Also the lessons learned from the seismic behavior of geotechnical structures are important for the revision of existing design codes. The performance based design that is incorporated in recent codes needs further discussion related the allowable displacements for the 2 levels of seismic action.

The objective of reducing the earthquake motion transferred to the structure through the foundation by developing cost effective methods, innovative constructive techniques for soil improvement and soil reinforcement is getting increased attention. Case histories provide a unique opportunity to interplay the theory with practice.

One very important question to be discussed is: (i) How to improve the relations between the users: relevant authorities, clients and designers? and (ii) how to implement in practice that codes may not cover in detail every possible design situation and it may require specialized engineering judgment and experience? It is hoped that the contributions to be presented by the participants of this Conference, in the next years, will help to clarify several questions that still remain without answer.

The death and destruction due to earthquakes in developing countries given by the news rise the question about the efficiency of the assistance programs and if they have reached the right people. The learned lessons from earthquakes have shown that it is important to implement: (i) earthquake codes in rural and in urban communities; (ii) instructions for building in rural areas safe houses, schools, hospitals and other infrastructures; (iii) guidelines related to the actions to be implemented before, during and after these events; (iv) government education programs about the perception of risk, the cost/benefit aspects of mitigation measures. As an example after the collapse of buildings due Lisbon earthquake (1755) the wooden structure or cage (“gaiola”) embedded in the walls was implemented. A full scale model was built and the efficiency of the structure was tested and this experiment was considered the first dynamic essay.

A joint effort between Owners, Decision-Makers, Researchers, Consultants, Professors, Contractors and General Public to face this challenge is needed.

It is important to understand the concepts of vulnerability and resilience. Vulnerability is associated with two dimensions, one is the degree of loss or the potential loss and the second integrates the range of opportunities that people face in recovery. This concept received a great attention from Rousseau and Kant (1756). Resilience is a measure of the system's capacity to absorb recover from a hazardous event. Includes the speed in which a system returns to its original state following a perturbation. The capacity and opportunity to recolonize or to change are also key dimensions of disaster resilience. The purpose of assessing resilience is to understand how a disaster can disturb a social system and the factors that can disturb the recovery and to improve it.

It is important to stress that a better understanding of geotechnical structures during the occurrence of earthquakes can only be achieved by a continuous and permanent effort in order to be up-to-date with the last developments in earthquake engineering. It is important that engineers educate themselves and the Public with scientific methods for evaluating risks incorporating the unpredictable human behavior and human errors in order to reduce disasters.

From the analysis of past incidents and accidents occurred during the earthquakes it can be noticed that all the lessons have not deserved total consideration, in order to avoid repeating the same mistakes. We need to enhance a global conscience and develop a sustainable strategy of global compensation how to better serve our Society. The recognition of a better planning, early warning, quality of evacuation that we should take for extreme events which will hit our civilization in the future. Plato (428–348 BC) in the *Timaeus* stressed that destructive events that happened in the past can happen again, sometimes with large time intervals between and for prevention and protection

we should followed Egyptians example and preserve the knowledge through the writing.

The none recognition for the engineers work is lacking since the past, e.g. the Egyptian King Cheops has his name linked with the great pyramid, a master piece engineer work, but the history does not record the name of the engineer. It is important to interact with the Society and General Public and to explain that the concern for man and fate has been always the core interest of the engineer profession, in order that the creations may be taken as a blessing for the Society.

The engineers should have competence, devotion and honesty. All of us possess the resources we need to achieve what we want if only we have the self-confident to try. We face challenges we can overcome them, not though by being special, but by co-operating and helping each other along the way. We should never forget the 7 Pillars: Practice, Precedents, Principles, Prudence, Perspicacity, Professionalism and Prediction. Following Thomas Mann we should enjoy the activities during the day, but only by performing those will allow us to sleep at the night. We should never forget the contribution of Voltaire and the book *Candide* published in 1759, after the Lisbon earthquake (1755), for the change from the intellectual optimism and potential fatalism that is a necessary condition for the construction of future scenarios in a risk analysis context.

The main components of risk management are risk assessment (risk analysis and risk evaluation), risk mitigation and control (risk reduction, emergency actions) and decision (Seco e Pinto, 2002).

Also it is important to narrow the gap between the university education and the professional practice, but we should not forget that Theory without Practice is a Waste, but Practice without Theory is a Trap. Kant has stated that *Nothing better that a good theory, but following Seneca Long is the way through the courses, but short through the example*. I will add through a careful analysis of Case Histories.

REFERENCES

- Ambraseys, N.N. 1960. The seismic stability of earth dams. *Proc. 2nd World Conference on Earthquake Engineering*, Tokyo, Vol.II, pp. 331–336.
- Eurocode 8. 1998. Design provisions for earthquake resistance of structures. Part 1.
- Eurocode 8. 1998. Design provisions for earthquake resistance of structures- Part 5: Foundations, retaining structures and geotechnical aspects.
- I.A.E.A. 1972. Earthquake guidelines for reactors siting. *Technical reports series n° 139*, Vienna, Austria.
- Iai, S. & Tobita, T. 2005. Performance—based approach for designing remediation of liquefaction. *Proc. of Geot. Earthquake Engineering*. Satellite Conf. TC4 pp. 14–21.
- ICOLD. 1975. A review if earthquake resistant design of dams. *Bulletin 27*.
- ICOLD. 1983. Seismicity and dam design. *Bulletin 46*.
- ICOLD. 1989. “Selection seismic parameters for large dams—Guidelines”. *Bulletin 72*.
- ICOLD. 1998. Neotectonics and dams. Guidelines and case histories. *Bulletin 112*.
- ICOLD. 2002. Earthquake design and evaluation of structures appurtenant to dams, *Bulletin 123*, Committee on Seismic Aspects of Dam Design, ICOLD, Paris.
- INA (International Navigation Association). 2001. *Seismic Design Guidelines for Port Structures*, 474 p.
- Kant, I. 1756. Writings on the Lisbon earthquake. Portuguese edition of the three essays about earthquakes published in Konigsberg, Almendina, 135 p.
- Makdisi, F.I. & Seed, H.B. 1977. A simplified procedure for estimating earthquake induced deformations in dams and embankments. *Report n° EERC 79–19*. University of California, Berkeley.
- Mononobe, N, & Matsuo, H. 1929. On the determination of earth pressure during earthquakes, *Proc. World Engineering Conference*, Vol. 9, 177–185.
- Nadim, F. & Whitman, R.V. 1984. Coupled sliding and tilting of gravity retaining walls during earthquakes. *Eight World Conference on Earthquake Engineering*, Vol. 3.
- Newmark, N.M. 1965. Effects of earthquakes on dams and embankments. *Geotechnique*, Vol. 15, n°2, 139–160.
- Okabe, S. 1924. General theory on earth pressure and seismic stability of retaining wall and dam. *Proc. JSCE*, Vol. 10, N°6, 1277–1330.
- Richard, R. Jr. & Elms, D.G. 1979. Seismic Behaviour of gravity retaining walls. *Journal of the Geot. Eng. Div., ASCE*, Vol. 105, GT 4. April.
- Sano, T. 1916. Seismic resistant design of buildings (Part 1 and Part 2) N° 83. *Report of Shinsai Yobo Chosa Kai* (Research Institute for Mitigation of Earthquakes Disasters).
- Sarma, S.H. 1975. Seismic stability of earth dams and Embankments. *Geotechnique*, Vol 25, n° 4, 743–76.
- Sêco e Pinto, P.S. 2001 Dam engineering- Earthquake aspects. Special Lecture. *Proc. of 4th ICSDEE*, San Diego, CD.
- Sêco e Pinto, P.S. 2002. Some Reflections about risk analysis of geotechnical structures. *Proc. of 12th Danube-European Conference Geotechnical Engineering*, Passau. 41–46.
- Seed, H.B. & Martin, G.R. 1966. The seismic coefficient in earth dam design. *JSMFD, ASCE*, Vol. 92, SM3, 59–83.
- TC4 ISSMGE, 2001. Case Histories of Post-Liquefaction Remediation. Committee on Earthquake Geotechnical Engineering.
- Towhata, I. (2008). *Geotechnical Earthquake Engineering*, Springer.
- U.S.A.E.C. 1973. Design response spectra for seismic design of nuclear powerplants. *Regulatory Guide 1.60*.
- USEPA, 1994. RCRA Subtitle D (258) Seismic design guidance for Municipal Solid Waste Landfill Facilities, Final Draft. United States environmental Protection Agency.
- Voltaire 1759. *Candide*. Oeuvres completes, 9, vol., edit. Moland, Paris 1877.

Some emerging issues in performance based design

W.D. Liam Finn

University of British Columbia, Vancouver, BC, Canada

ABSTRACT: Recent developments in performance based design are presented and reviewed in the broader context of probabilistic performance based earthquake engineering. The focus is on the components of the system that impact design: New concepts regarding selection of ground motions, the necessary number of input motions, the concept of the conditional mean spectrum, the frequency distribution of the response measure and the utility and cost effectiveness of performance based design. The new approach is illustrated by a case history involving development of a probabilistic approach to the assessment of the seismic stability of slopes intended for residential development in British Columbia, Canada. The case history illustrates clearly the utility and cost effectiveness of performance based design.

1 INTRODUCTION

Performance based design (PBD) is based on tolerable displacement criteria and has become part of practice in geotechnical earthquake engineering, since 1989 (Finn 1990). It has been widely used for developing cost-effective remediation strategies for embankment dams with foundations or slopes susceptible to liquefaction under design seismic loadings. There are two crucial requirements for implementing PBD: acceptable performance criteria and a reliable method of analysis. For embankment dams the criterion of acceptable performance is specified by tolerable displacements, such as allowable settlement of the crest. A nonlinear dynamic analysis is essential because soil behaves as a nonlinear solid under strong shaking. If significant seismic pore water pressures are developed during shaking, the analysis must be based on effective stresses.

Analogous developments occurred in structural earthquake engineering except that the potential performance of a structure was evaluated using static pushover analysis. In this analysis the forces simulating the first mode force distribution of the structure were applied with monotonically increasing amplitude and the response of the structure was described by various response parameters; inter-storey drift, inter-storey drift angle or roof drift. Drift limits were established for various functional requirements ranging from minor, easily repairable damage to life safety and to the ultimate limit for collapse prevention. Pushover analysis was also used for bridges.

In recent years the Pacific Earthquake Engineering Research (PEER) Center at the University of California at Berkeley has made performance based design the major focus of research. The work of researchers from the universities associated with the center has led

to the rapid evolution of PBD into the more general field of Performance Based Earthquake Engineering (PBEE) in which PBD is still the major component. PBEE has four major components: seismic demand, structural response, damage assessment and evaluation of consequences in terms of fatalities or financial costs. Each of these components is probabilistically based.

The major developments in PBEE have occurred over the last six years and some of these that being adopted into practice are reviewed in the next section. The review will focus on those developments with direct relevance to PBD in geotechnical earthquake engineering and will be limited to the specification of seismic demand and the characterization of structural response. The application of PBEE in geotechnical earthquake engineering are illustrated by a case history involving the evaluation of the seismic stability of slopes slated for residential development which are subjected to low probability ground motions.

2 SOME MAJOR DEVELOPMENTS IN PBEE

Two developments in PBEE, incremental dynamic analysis (IDA) and the conditional mean spectrum- ϵ , will be reviewed. Both of these are currently being introduced into geotechnical practice in assessing the seismic safety of the critical structures of a major utility such as intake towers and embankment dams.

2.1 *Incremental dynamic analysis, IDA*

In structural engineering static pushover analysis has been used to provide a continuous picture of structural response to incremental increases in the first mode distribution of inertial forces over the complete range

of behavior from elastic response to final collapse. Incremental dynamic analysis, IDA, is a method of providing a similar continuous picture of the dynamic response (Vamsatsikos and Cornell 2005). A simplified version of the IDA procedure has been proposed to establish priorities for retrofit of 800 schools in British Columbia. In this procedure 20 ground motions are selected that match a uniform hazard design spectrum that has a probability of exceedance of 2% in 50 years. Each motion is scaled linearly on peak ground acceleration (PGA) to give a set of motions with the same frequency content, but varying in PGA from lower to higher than the 2% in 50 years PGA. The resulting sets of motions are used as input motions to a generic model of a school building type e.g. wood frame. The average PGA causing the structural type to reach the ultimate limit state defined by a specified drift ratio is considered the critical intensity. The probability of this critical PGA being exceeded is taken as an approximation to the probability of structural collapse. PGA is not a good scaling parameter but it is simple and considered adequate for a rough screening of schools to establish preliminary retrofit priorities to get the retrofit process underway. The IDA procedure below will be adopted for future evaluation of retrofit priorities.

The spectral acceleration, $Sa(T_1)$, of a structure at the first mode period is usually taken as the measure of seismic demand on the structure. The target $Sa(T_1)$ for design, $Sa(T_1)_d$, is determined by a probabilistic seismic hazard analysis. A set of ground motions are selected that are considered appropriate for the site and each motion is scaled linearly with respect to $Sa(T_1)$ to give a range in seismic demand below and above $Sa(T_1)_d$. Dynamic analysis of a structure is conducted using as input motions the suite of scaled motions for any one of the original design suite of motions. The results can be plotted as $Sa(T)$ versus displacement. Similar plots can be drawn from the results of analyses using all the other motion sets as input. Multi-record IDAs are necessary because IDA results can be highly dependent on the individual acceleration record. The results of multi-record IDA analyses can be used to determine the mean and standard deviation of the displacement response to a given $Sa(T)$ input or the distribution of $Sa(T)$ associated with a specific displacement. These distributions, coupled with the probabilistic seismic hazard, provide a basis for the probabilistic evaluation of a seismic design. As applied to the school retrofit study referred to earlier, the multirecord IDA analyses would yield the probability of failure and provide a sound basis for priority ranking of schools for retrofit.

This kind of multi-record analysis is very different from the deterministic approach used so far in the application of PBD to dams in geotechnical earthquake engineering where the behavior of the dams has been evaluated by only one or two ground motions. IDA is

clearly a very computationally intensive process and therefore is only justified for critical structures such as dams, important bridges and buildings housing critical facilities.

2.2 Conditional mean spectrum— ε

In probabilistic PBEE the intensity of shaking is characterized by an intensity measure (IM) and the response of the structure by an engineering demand parameter (EPD). In most PBEE applications the spectral acceleration with 5% damping at the first elastic period of the structure, $Sa(T_1)$, is selected as the IM and the EPD is characterized by some appropriate measure of response such as maximum crest settlement in the case of an embankment dam or interstorey drift in the case of a structure. $Sa(T_1)$ for design is obtained from a probabilistic seismic hazard analysis (PSHA). Disaggregation of the hazard gives the mean magnitude, \bar{M} , the average distance, \bar{R} , and the scaling parameter $\bar{\varepsilon}$ that cause the occurrence of the design spectral acceleration, $Sa(T_1)_d$, at period T_1 . The parameter $\bar{\varepsilon}$ is a measure in standard deviations of the difference between the mean spectral response corresponding to \bar{M} and \bar{R} and the design spectral value. This definition can be generalized to any record not just the one with the design spectral acceleration at T_1 . The mean spectral values and standard deviations at different periods can be determined using \bar{M} and \bar{R} in an appropriate attenuation relation such as Abrahamson and Silva (1997).

Spectral shape affects the response of multidegree-of-freedom non-linear structures for two reasons. First the higher modes of the structure may affect response significantly and the shape of the spectrum controls the spectral accelerations at the higher modes relative to the first mode. Secondly as behavior becomes non-linear the fundamental period increases, bringing into play the contribution at a longer period. Baker and Cornell (2005) have demonstrated that ε affects the spectral shape of a ground motion record and that its effect is at least as significant as M and R , the parameters that traditionally have controlled the selection of records for analysis. Now it is equally important to take ε into account when selecting ground motions.

A simple approximate procedure for constructing a design spectrum that reflects the effects of M , R and ε , called the conditional mean spectrum - ε , which can be implemented on a spread sheet has been presented by Baker and Cornell (2006). Conditional mean spectra for a site in Van Nuys, California with exceedance rates of 2% and 50% in 50 years for a structure with $T_1 = 0.8s$ are shown in Figure 1.

The conditional spectrum has some useful properties. The spectral ordinates are always less than the uniform hazard spectrum, UHS, for the hazard level associated with $Sa(T_1)_d$ resulting in less conservative designs. The conditional spectrum is representative of

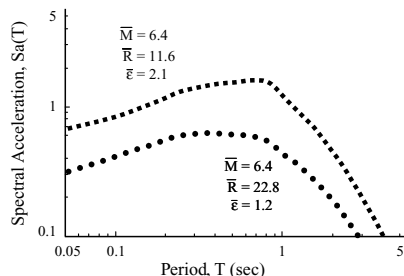


Figure 1. Mean conditional response spectra for a site in Van Nuys, California given $Sa(0.8s)$ values with exceedance rates of 2% and 50% in 50 Years (after Baker and Cornell, 2006).

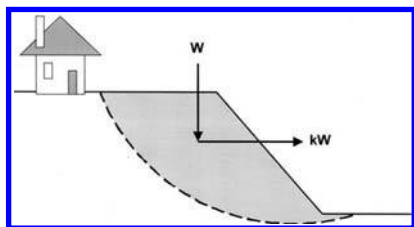


Figure 2. Pseudo-static seismic slope stability analysis.

ground motions from an earthquake event. The uniform hazard spectrum is not. The higher frequencies in the UHS are representative of smaller closer earthquakes. The longer periods are associated with larger farther earthquakes. When using the conditional spectrum for design, ground motions are selected from a large database such as the PEER database that match the conditional spectrum (PEER 2007). Because these motions reflect the effects of M , R and ϵ these motions have the property that they show little bias and have lower dispersion in the response variable than the traditional method where record selection is based on M and R . Reduced dispersion means that fewer motions are required to develop reliable statistics on response. The conditional spectrum has only recently been adopted for evaluating the seismic safety of dams by a major public utility. Initial reaction to the use of the spectrum is very favorable.

3 CASE HISTORY OF PROBABILISTIC PBD

3.1 Background

In 2005 the National Building Code of Canada (NBCC 2005) adopted design ground motions with a 2% chance of being exceeded in 50 years. This change resulted in about a doubling of peak ground accelerations (PGA) compared to the PGA associated with the

Table 1. PGA hazard in Canadian cities, NBCC 1995 and 2005.

Median frequency of exceedance	Vancouver	Toronto	Montreal
10% in 50 yrs NBCC 1995	0.24	0.08	0.20
2% in 50 yrs NBCC 2005	0.46	0.20	0.43

design ground motions in the previous code (NBCC 1995) as shown in Table 1.

The impact of the increases in ground motions on geotechnical engineering practice depends on the type of design. Conventional procedures for assessing liquefaction potential and slope stability have been based traditionally on peak ground acceleration. Designs based on these procedures have been strongly and directly affected by the increased peak ground accelerations. Sites and structures which would have been safe under the old code may now be considered unsafe for the new hazard levels. Geotechnical engineers and their clients have been expressing concerns about the great impact of the changes in ground motions on projects.

The impact on seismic slope stability makes an interesting case history. Following the adoption of the NBCC 2005 design motions by the province of British Columbia (BC) in the BC building code (BCBC 2006) in 2006, sites on slopes slated for residential development failed to be approved for the use intended that would have been considered safe under the previous code. Developers and municipalities were understandably upset by this abrupt turn of events and appealed to the BC government for relief. The government responded by issuing provincial regulation M268 in December 2006 restoring the 10% in 50 years motions for slope stability assessment as a temporary measure and setting up a task force on seismic slope stability (TFSSS) under the direction of the Association of Professional Engineers and Geologists of British Columbia (APEGBC) to study the issues and make recommendations for future action. The writer is a member of the task force. The TFSSS approach to assessment of slope stability is described herein. A later extension by the writer is described in which procedures recommended by the TFSSS are coupled with reliability analysis to allow uncertainties in soil properties and seismic input to be taken into account in a probabilistic assessment of slope displacement.

3.2 BC Practice

In BC, the most common method currently used to carry out seismic slope stability analysis is the pseudo-static limit equilibrium method. In this method, earthquake loading is represented by a constant horizontal force, kW , applied to the centre of gravity of

the potential sliding mass, as shown in Figure 1. W is the weight of the sliding mass and the coefficient, k , is called the seismic coefficient.

There is, however, no generally accepted method in BC practice for selecting seismic coefficients for slopes. From a limited survey of BC practice, the TFSSS found seismic coefficients in the range $0.5 \text{ (PGA)} \leq k \leq 1.0 \text{ (PGA)}$, where PGA is the peak ground acceleration.

The choice of $k = 1.0 \text{ (PGA)}$ may be very conservative as shown by the acceleration time history in Figure 2. The PGA occurs only for an instant and most of the record indicates accelerations much less than the maximum. The PGA has no significant impact on the response of the slope to shaking by the time history. Therefore the TFSSS recommends the use of $k = \text{PGA}$ only as a preliminary screening tool. If $FS \geq 1.0$, when $k = \text{PGA}$ is used in a pseudo-static limit equilibrium slope stability analysis, no further stability analyses are required.

3.3 Slope performance during shaking

Newmark (1965) revolutionized concepts of seismic slope stability by pointing out that just because the factor of safety occasionally fell below $FS = 1.0$ during earthquake shaking, it did not necessarily mean slope failure. He proposed that the total displacement accumulated during the times when the factor of safety was less than $FS = 1.0$ be used as the index of slope

performance during an earthquake and he developed simple procedures for calculating the displacements.

Permanent displacements can occur in a slope during an earthquake only if the shear stresses generated by the earthquake exceed the shearing resistance of the slope. The horizontal force required to bring the slope to the condition of incipient displacement is shown in Figure 3 as $F = k_y W$ where k_y is the seismic yield coefficient, a special value of the seismic coefficient that just allows slip or yielding in the slope. The yield coefficient, $k_y = a_y/g$, where, $a_y =$ yield acceleration and $g =$ the acceleration of gravity.

Figure 4 is a segment of a typical earthquake shaking record to an enlarged scale. Slope displacements can initiate whenever the ground acceleration, 'a', exceeds the yield acceleration, a_y . The total slope displacement at the end of earthquake shaking is the sum of the incremental slope displacements generated each time the ground acceleration exceeds the yield acceleration. Newmark (1965) calculated these displacements by considering the sliding mass of soil to be rigid. He also provided charts for estimating the maximum displacements. These charts were based on the small selection of strong ground motion records available at the time. In present practice, slope displacements are also estimated by direct calculation using design ground motions as input to the Newmark (1965) sliding rigid block computational model or by using a model that takes the flexibility of the slope into account.

Makdisi and Seed (1978) improved the Newmark model for application to embankment dams by taking into account the flexibility of the embankment and the amplification of ground motions on passing up through the embankment. They developed charts relating slope displacement to earthquake magnitude and the ratio of the seismic coefficient k to yield coefficient k_y . On the basis of Makdisi and Seed (1978) data, Seed (1979) recommended values of k in the range 0.1–0.15 depending on earthquake magnitude, M , for the analysis of the slopes of earth dams. For example the Seed procedure calls for $k = 0.15$ and a factor of safety $FS \geq 1.15$ for an earthquake with $M = 8.25$. This value of k is associated with

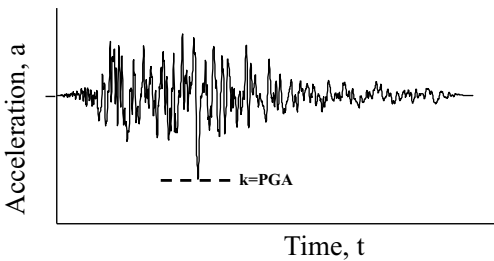


Figure 3. $k = \text{PGA}$, can be a very conservative estimate of k .

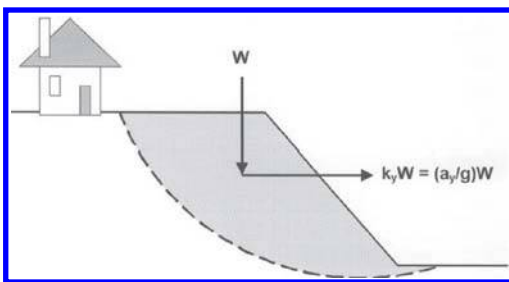


Figure 4. The condition of incipient displacement under k_y .

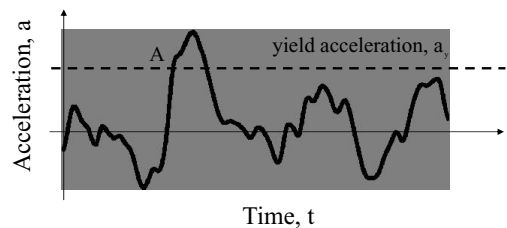


Figure 5. Displacement is initiated when ground acceleration exceeds yield acceleration.

a maximum allowable displacement of 100 cm. Los Angeles County subsequently modified this procedure to a single k value with $k = 1.15$ and $FS \geq 1.0$ (Blake et al. 2002). Hynes-Griffin and Franklin (1984) recommended using $k = 0.5(PGA)$. This value of k is also based on a maximum allowable slope displacement of 100 cm. It is important to note that these generally accepted methods for selecting a seismic coefficient in U.S. practice for embankment dams are based on slope displacement criteria. The two procedures recommended here by TFSSS are also based on a criterion of acceptable slope response during an earthquake expressed in terms of allowable displacement. These methods, to be acceptable for general use, had to be conceptually simple and easy to apply.

4 PBEE: PROBABILISTIC ASSESSMENT OF SLOPE DISPLACEMENT (METHOD 1)

The TFSSS reviewed recent developments in methods of seismic slope stability analysis and selected a new approach based on the concept of tolerable displacements. The method is based on the work of Bray and Travarasou (2007). They conducted approximately 55,000 Newmark type slope displacement analyses involving eight different slope configurations, ten different yield accelerations for each slope configuration, and 688 different recorded ground motions from the PEER (2007) data base. From a regression analysis of the resulting slope displacements, they developed an equation for estimating the median slope displacement along a slip surface with a conditional probability of exceedance of 50%, if the design ground motion occurs. When this probability is combined with 2% probability of exceedance of the ground motions in 50 years, the absolute probability of the median displacements being exceeded is 1% in 50 years (approximately 1/5000). The median displacement is selected as the controlling slope displacement because of the low absolute probability of exceedance.

Bray and Travarasou's equation slope displacement, D , greater than 1 cm is:

$$\begin{aligned} \ln(D) = & -1.10 - 2.83 \ln(k_y) - 0.333 (\ln(k_y))^2 \\ & + 0.566 \ln(k_y) \ln(S(1.5T_s)) \\ & + 3.04 \ln(S(1.5T_s)) \\ & - 0.244 (\ln(S(1.5T_s)))^2 + 1.5T_s \\ & + 0.278(M - 7) \pm \varepsilon \end{aligned} \quad (1)$$

The displacement D is due to shearing along the slip surface and has both vertical and horizontal components.

T_s is the initial fundamental period of the potential sliding mass prior to the seismic event, ($0.05s < T_s < 2.0s$) and, for a slope such as shown in Figure 1, is estimated by:

$$T_s = 4H/V_s \quad (2)$$

where H is the average height and V_s is the average shear wave velocity of the potential sliding mass. Site investigations for most residential developments do not typically include measurements of shear wave velocity, but estimates can be inferred from standard penetration test or cone penetration test data (Sykora and Koester 1988).

In Equation 1, ε is a normally distributed random variable with a mean of zero and a standard deviation $\sigma = 0.66$ and M the moment magnitude of the earthquake under consideration. The term $S(1.5T_s)$ is the spectral acceleration at the site for the period of $(1.5T_s)$. It is given by $S(1.5T_s) = F^*Sa(1.5T_s)$ where $Sa(1.5T_s)$ is the spectral acceleration for firm soil conditions and F is the amplification factor for the site class. Values of F , as a function of site class and period, and $Sa(1.5T_s)$, for periods $T = 0.2, 0.5, 1.0$ and 2.0 , are provided in NBCC 2005. Values of $Sa(1.5T_s)$ for other periods can be interpolated linearly from the values provided in NBCC 2005. Bray (2007) suggested that a value of $T_s = 0.33$, giving a spectral period $(1.5T_s)$ of 0.5 , would be adequate for general use. The TFSSS recommends this value but an engineer is not precluded using a slope specific T_s , when he considers it more appropriate. S decreases with increasing values of period and therefore the general value $S = 0.5$ will become more conservative as the slope period increases beyond $T_s = 0.33$. For periods shorter than $0.33s$, $S(T_s)$ increases. In such cases the designer may wish to use a slope specific period.

The ground motions specified by NBCC 2005 are probabilistic. Therefore the PGA is not associated with any particular earthquake magnitude but reflects the contributions of all earthquake magnitudes considered in the probabilistic seismic hazard analysis. The designer has to select an appropriate magnitude. The TFSSS recommends using the modal magnitude. This is the magnitude making the largest contribution to the PGA. Site specific values of modal magnitudes may be obtained from the Geological Survey of Canada. Since the modal magnitudes for BC sites are rarely much larger than $M = 7.0$, it is suggested that $M = 7.0$ may be used for all sites.

The parameter k_y is the yield coefficient ($0.01 < k_y < 0.5$) and is best determined by iterative analyses using commercially available computer programs. Simplified equations for calculating k_y may be found in Bray et al. (1998). Bray and Travarasou (2007) point out that "the primary issue in calculating k_y is estimating the dynamic strength of the critical strata within the slope." Since k_y is assumed to be a

Table 2. Displacements estimated using Equation 1.

Slope Location	H (m)	M	Ts (s)	PGA			S _a (T)			k _y	D (cm)
				(g)	0.2	0.5	1.0	NBCC 2005	0.2		
Nanaimo	30	7	0.35	0.50	1.0	0.69	0.35	0.17	13		
Duncan	22	7	0.31	0.54	1.1	0.74	0.37	0.49	2		
Victoria	13	7	0.23	0.61	1.2	0.82	0.38	0.52	2		

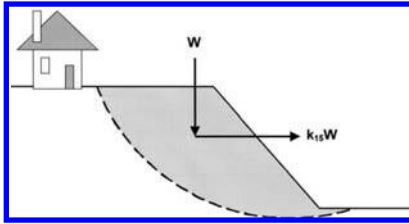


Figure 6. Pseudo-static analysis with an inertia force equivalent to 15 cm of displacement.

constant during earthquake shaking, the earth materials in the slope cannot undergo significant strength loss. The selection of appropriate shear strength should follow best current practice. An extensive discussion of the dynamic strength of soil, may be found in Blake et al. (2002) and Duncan and Wright (2005).

The TFSS recommends a displacement of 15 cm or less as a tolerable slope displacement along the slip surface for use with the Bray and Travasarou (2007) method in most cases. This guideline is based on experience with wood frame construction and is predicated on the residential building being located back from the slip surface. The objective is to avoid the slip surface daylighting within or behind the building.

As examples of the use of Equation 1, displacements were estimated for soil slopes located in Nanaimo, Duncan, and Victoria, BC, being considered for development. Slope properties were provided by the geotechnical engineers involved in the projects. As shown in Table 2, the calculated median slope displacements (D) are relatively small (2 cm to 13 cm). Using a maximum allowable displacement of 15 cm, these slopes may be considered suitable for residential development. Note that, in these examples, site specific site periods, T_s, are used rather than the general value of 0.33. The applicable values for S(1.5T_s) are obtained from the listed NBCC 2005 values in Column 6 by interpolation.

Conventional pseudo-static slope stability analysis, with 2% in 50 year ground motions and k = PGA, shows all three slopes to have FS < 1.0 and therefore, typically would be considered unsuitable for residential development. Even for k = 0.5 (PGA), the Nanaimo slope would have a k = 0.25 which

Table 3. Comparison of k₁₅ with k = 0.5 (PGA).

Slope Location	H (m)	K ₁₅	K = 0.5 (PGA)
		2% in 50 yrs	10% in 50 yrs
Nanaimo	30	0.16	0.11
Duncan	22	0.18	0.15
Victoria	13	0.20	0.18

is greater than the yield acceleration, and would be considered unsuitable for residential development. The PBD approach using displacement analysis in conjunction with a criterion for tolerable displacement provides a more flexible and less conservative approach to evaluating slope stability for residential development than the factor of safety approach.

5 PSEUDO-STATIC ANALYSIS USING A SLOPE DISPLACEMENT-BASED SEISMIC COEFFICIENT (METHOD 2)

To continue to allow the use of pseudo-static slope stability analysis and yet retain the advantages of using a displacement criterion, the TFSS asked Bray (2007) to provide a seismic coefficient that would be compatible with the recommended limiting displacement of 15 cm of displacement, k₁₅, (Fig. 5).

Bray estimated this value of k to be that given by:

$$k_{15} = (0.006 + 0.038M) S(0.50) - 0.026$$

with $S(0.50) < 1.5g$ (3)

This regression equation is valid only for a spectral period of 0.5s. Therefore slope specific periods cannot be used with this equation.

M is the moment magnitude of the earthquake. As in the case of Equation 1, modal magnitude, M = 7.0, and spectral acceleration, S(0.50), are acceptable for general use but the designer is not precluded from using a site specific modal magnitude, obtainable from the Geological Survey of Canada.

Values for k₁₅ were estimated for the three slopes in Table 3. The k₁₅ values for 2% in 50 year ground motions, and k values for k = 0.5 (PGA) for 10% in 50-year ground motions, are also shown in Table 3. The values of the slope displacement-based seismic coefficient (the k₁₅ values) corresponding to 2% in 50-year ground motions are slightly larger, and therefore somewhat more conservative, for these cases, than the seismic coefficient used in association with 10% in 50-year ground motions, when k = 0.5 PGA.

If the pseudo-static analysis, using the slope displacement-based seismic coefficient k₁₅ (Fig. 5) gives a factor of safety FS ≥ 1.0, the slope may be considered suitable for residential development.

6 ANALYSIS WITH UNCERTAINTY IN VARIABLES

Slope displacement $D > 1$ cm is given by Bray and Travararou (2007) as

$$\ln(D) = f[S(T), k_y, T_s, M] \pm \varepsilon \quad (4)$$

where $S(T)$ = spectral acceleration at the period $T = 1.5T_s$; k_y = yield coefficient; T_s = initial period of the potentially sliding mass and M = earthquake magnitude. These variables are treated as deterministic by Bray and Travararou (2007) in their Equation 1 for evaluating D . The error term, ε , is the uncertainty in the displacements for deterministic values of the other independent variables and has a normal distribution with a mean of 0.0 and a standard deviation of 0.66.

The performance function for probabilistic analysis of the likelihood that some limiting displacement D_{lim} is exceeded for specified uncertainties in the variables is given by the performance function:

$$G = \ln(D_{lim}) - \ln(D) \quad (5)$$

D_{lim} is some specified limiting displacement and D is the displacement calculated using the Bray and Travararou (2007) Equation 3, taking into account the probabilistic variations in the controlling parameters.

Reliability analysis of the Austrian Dam in California was conducted using the program RELAN (Foschi et al. 2007), in which the performance function G had been inserted. This dam was one of many case histories analyzed by Bray and Travararou (2007) in validating their method for estimating seismic displacement of slopes.

The variations in slope parameters were prescribed as follows. The spectral values in NBCC 2005 have a lognormal distribution with a standard deviation

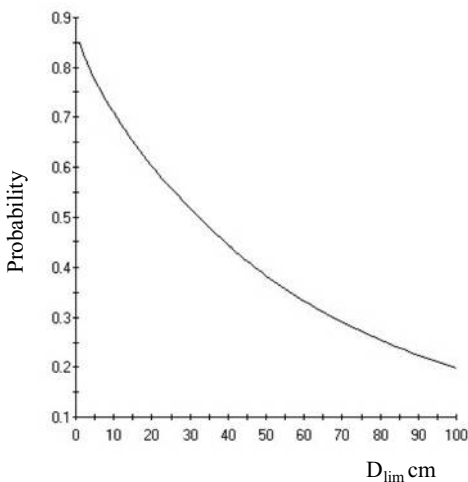


Figure 7. Probability of exceeding displacement D_{lim} .

of 0.7. A standard deviation of 0.3 was assumed for magnitude M . Standard deviations equivalent to 20% of the deterministic values used by Bray and Travararou (2007) in their analysis of the dam were assumed for the other variables, k_y and T_s , reflecting the difficulty in defining shear strength and slope period accurately. The latter three variables were assumed to have normal distributions.

The analyses were conducted using both first and second order statistical analysis to assess the impact of uncertainty in the independent variables controlling D . In this application the difference between first and second order analyses was negligible.

The observed displacement of the slope of the Austrian Dam was 50 cm during the 1989 Loma Prieta Earthquake. The results of the RELAN analysis are shown in Figure 6 which shows the conditional probabilities of exceedance of prescribed displacements D_{lim} . The observed displacement of 50 cm is predicted to have a probability of exceedance of 38% for the specified variations in seismicity and slope parameters. Bray and Travararou (2007) estimated the 84% displacement to be 70 cm. RELAN estimates that this displacement has a probability of exceedance of 30% for the specified uncertainties in the controlling parameters.

7 CONCLUDING REMARKS

Full scale IDA analysis has not yet been adopted in geotechnical earthquake engineering except for the few cases cited where the results of analyses of generic models were of wide applicability to other cases. The use of the conditional mean spectrum- ε has been adopted by a major public utility as a design spectrum and as a basis for the selection of ground motions for seismic response analyses that have low bias and least dispersion. The use of this spectrum is likely to increase.

Two methods for determining whether a slope is suitable for residential development, when subjected to 2% in 50-year design ground motions are recommended.

- Method 1 involves calculating the median slope displacement with parameters that reflect slope properties and local seismicity (Equation 1). This slope displacement has an absolute probability of exceedance of approximately 1/5000 for BC design ground motions. This method was extended to take into account uncertainties in the parameters.
- Method 2 is based on pseudo-static (limit equilibrium) seismic slope stability analysis, similar to current practice, but uses a slope displacement-based seismic coefficient, k_{15} , that is equivalent in its effect to adopting a tolerable slope displacement of

15 cm, when the slope is subjected to design ground motions.

- Based on experience with wood frame residential construction, a displacement of 15 cm is considered to be acceptable.

REFERENCES

- Abrahamson, N.A. and Silva, W.J. (1997). Empirical response spectral attenuation relations for shallow crustal earthquakes. *Seismological Research Letters*; 68: 1275–1284.
- BCBC (BC Building Code) 2006. Published by the Office of Housing and Construction Standards, BC Ministry of Forests and Range.
- Baker, J.W. and Cornell, C.A. (2005). Vector-valued ground motion intensity measure consisting of spectral acceleration and epsilon. *Earthquake Engineering and Structural Dynamics*; 34: 1193–1217.
- Baker, J.W. and Cornell, C. Allen. (2006). Spectral shape, epsilon and record selection. *Earthquake Engineering and Structural Dynamics*; 35:1077–1095.
- Blake, T.F., Hollingsworth, N., Bray, J.D., and Stewart, J.P. 2002. Recommended Procedures for Implementing of DMG Special Publication 117, Guidelines for Analyzing and Mitigating Landslide Hazards in California, Southern California Earthquake Center, University of Southern California, Los Angeles, CA.
- Bray, J.D. 2007. Private communication to TFSSS.
- Bray, J.D., Rathje, E.M., Augello, A.J., and Merry, S.M. 1998. Simplified seismic design procedures for geosynthetic-lined solid waste landfills. *Geosynthetic. Int.*, 5(1–2), 203–235.
- Bray, J.D., and Travasarou, T. 2007. Simplified procedure for estimating earthquake-induced deviatoric slope displacements. *Journal of Geotechnical and Environmental Engineering*, ASCE, Vol. 153, No. 4. pp. 381–392.
- Duncan, J.D., and Wright, S.G. 2005. *Soil strength and slope stability*, Wiley, Hoboken, N.J.
- Finn, W.D. Liam (1990). Analysis of Post-liquefaction Deformations in Soil Structures. Proceedings, H. Bolton Seed Memorial Symposium, BiTech Publishers Ltd., Vancouver, BC, Canada.
- Foschi, R.O., Li, H., Zhang, J., Folz, B., and Yao, F. 2007. RELAN and IRELAN V8.0: Software Packages for Reliability Evaluation and Performance-Based Design, Department of Civil Engineering, University of British Columbia, Vancouver, B.C. Canada, V6T 1Z4.
- Hynes-Griffin, M.E., and Franklin, A.G. 1984. Rationalizing the Seismic Coefficient Method. Miscellaneous Paper GL-84-13, United States Army Engineers, WES, Vicksburg, MS.
- Makdisi, E., and Seed, H.B. 1978. Simplified procedure for estimating dam and embankment earthquake-induced deformations, *Journal of Geotechnical and Environmental Engineering*, ASCE, Vol. 104, No. 4, pp. 381–392.
- Newmark, N.M. 1965. Effects of earthquakes on dams and embankments, *Geotechnique*, 15(2) pp. 139–160.
- NBCC (National Building Code of Canada) 1995. Published by the National Research Council of Canada, Ottawa.
- NBCC (National Building Code of Canada) 2005. Published by the National Research Council of Canada, Ottawa.
- PEER 2007. Pacific Engineering Research Center Strong Motion database, <http://peer.berkeley.edu/smcat>.
- Sykora D.W., and Koester J.P. 1988. Review of existing correlations between dynamic shear resistance and standard penetrations in soils, *Proceedings, Earthquake Engineering and Soil Dynamics II - Recent Advances in Ground Motion Evaluation*, ASCE Geotechnical Engineering Division, Park City, Utah.
- Vamsatsikos, Dimitrios and Cornell, C. Allen (2002). Incremental dynamic analysis. *Earthquake Engineering and Structural Dynamics*; 31: 491–514.

Short comment on site specific earthquake ground motion characteristics for performance based design

A. Ansal & G. Tönük

Bogazici University, Kandilli Observatory & Earthquake Research Institute, Bogazici

For a site-specific assessment of performance levels for Immediate Occupancy, Life Safety and Collapse Prevention, seismic hazard analysis need to be conducted to assess design earthquake characteristics on the foundation level with respect to the selected exceedance levels for 2% 10% and 50% for 50 years respectively. The analysis may be considered as composed of statistically independent two consecutive stages that can be evaluated separately.

The first stage is the estimation of design earthquake characteristics on the rock outcrop based on seismic hazard study for all performance levels. The second stage is the estimation of design earthquake characteristics on the ground surface based on the geotechnical, geological and topographical conditions. Both of these stages involve various degrees of uncertainties.

A probabilistic approach may be adopted to evaluate the uncertainties involved in the above mentioned two stages of the earthquake hazard analysis. The overall exceedance probability is determined by assigning the identical probability levels to both stages. Thus site-specific peak ground acceleration and acceleration design spectrum may be calculated with respect to overall exceedance probability of 2% 10% and 50% for 50 years corresponding to Immediate Occupancy, Life Safety and Collapse Prevention performance levels respectively.

As an example at one site in Istanbul, 16 real acceleration time histories compatible with the earthquake hazard in terms of probable magnitude ($M = 6.5-7.5$), epicenter distance ($20 \leq R \leq 30$ km) and fault mechanism (strike slip) recorded on stiff site conditions with average shear wave velocities larger than $V_s 30 \geq 420$ m/s were selected as the probable input acceleration time histories from the PEER strong motion data bank (<http://peer.berkeley.edu>).

The main purpose was to account as much as possible for the variability arising from the differences in the source characteristics observed in the acceleration time histories.

The selected input acceleration time histories were scaled with respect to the peak ground horizontal accelerations calculated from the earthquake hazard study (0.36 g and 0.67 g corresponding to Life

Safety and Immediate Occupancy performance levels, respectively) and were used as input for site response analysis. The acceleration response spectra calculated for these records, the average acceleration spectra corresponding to Life Safety and Immediate Occupancy are shown in Figure 1. However, it may be more in line with the performance base design to assume that at each period the variation of the spectral accelerations can be modeled by normal distribution to estimate acceleration response spectra corresponding to 10% exceedance in the case of Life Safety and 2% exceedance in the case of Immediate Occupancy as shown in Figure 1.

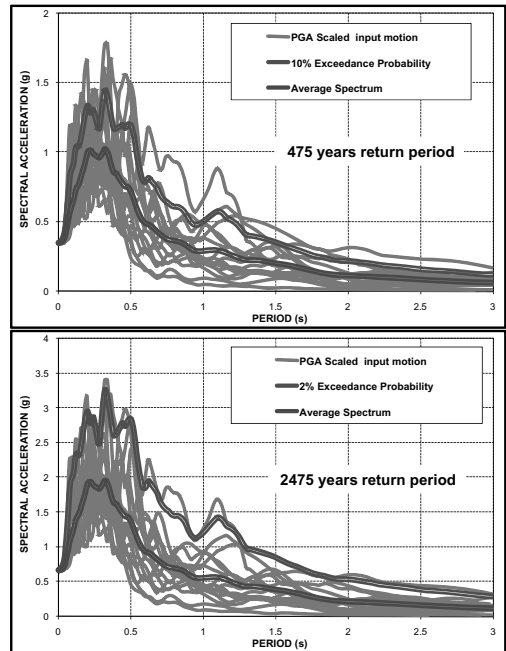


Figure 1. Acceleration response spectra for PGA scaled acceleration time histories, the average, 10% and 2% exceedance level spectra with respect Collapse Prevention and Immediate Occupancy Performance levels.

PBD in earthquake geotechnical engineering and energy-based design

T. Kokusho

Civil Engineering Department, Chuo University, Tokyo, Japan

Despite long lasting efforts, PBD has not yet been established sufficiently in geotechnical engineering practice. Seismically induced ground deformation essential to performance design is not easy to evaluate mainly because, in contrast to superstructures, the ground is 3-dimensional continuum with tremendous spatial variability and its stress-strain relationship is strongly nonlinear with dilatancy effect. However, a rapid development in practical and reliable PBD in geotechnical engineering is badly needed not only for foundation design but also for superstructures resting on incompetent soils.

In Table 1, the backgrounds of Performance-Based Design in earthquake geotechnical engineering is summarized in terms of Social background, Technical background, Technical requirements and Technical difficulties to overcome.

One of the important requirements for PBD in geotechnical engineering is the establishment of the performance criteria to comply with the performance of buildings or civil structures in terms of ground displacement. Then the next major challenge is to shift from the limit state calculations based on acceleration or its modified seismic coefficients to deformation-based calculations using design ground motions. More and more numerical methods incorporating time-histories or spectra of input motions as well as soil nonlinearity are already in practice.

However, uncertainties involved in such analytical tools seem to become considerable as seismic input motions get stronger and soil nonlinearity gets greater. It is particularly true under current circumstances where seismic ground motions observed during recent destructive earthquakes are getting larger and design codes designate higher ground motions.

In contrast to the conventional limit design, uncertainties involved in the PBD become considerable in terms of seismic input, large-strain soil properties, parameters in numerical analyses, etc, which almost inevitably attracts designers from the deterministic method to probabilistic approach.

Probabilistic approach is also preferred because of its accountability to general public to attain social acceptance of projects. However, the results should be carefully scrutinized whether or not the probability is based on sufficient and reliable statistical database.

One of the most significant uncertainties may be the seismic design input. We cannot forget in simulating design earthquake motions in time/spectrum domain that we still do not know much about earthquakes and considerable uncertainties may be involved in deciding recurrence time of less frequent extreme events, fault mechanisms such as asperity and directivity.

Another significant uncertainties which geotechnical researchers in particular have to reduce is those in physical modeling of soil performance, which tend to be enormous as seismic input motions get stronger and soil nonlinearity gets greater. Continuous models in the finite element method cannot enough reproduced discontinuous deformations along slip planes/shear zones, while discrete models such as those in the discrete element method seem to be similar to numerical experiments without proper design philosophy. We should make more efforts to develop simpler methods with appropriate designer's philosophy based on fundamental physical principles such as the preservation of energy. In any case, case

Table 1. Background to PBD in earthquake geotechnical engineering.

Social background	Preparedness to extreme events Accountability to different group of people Economy and rationalization of design
Technical background	Increasing ground motion, observed and required. Development of numerical methods Development of probabilistic design
Technical requirements	Decision of performance criteria by displacement Quantifying uncertainties on PBD Quantifying uncertainties on PBD Validation of PBD by case histories & model tests
Technical difficulties to overcome	Probability evaluation of extreme events Better input parameters for seismic performance Modeling of failure including strong nonlinearity Grasping variability of soil profile & properties

histories with well-documented observation data are really important as a benchmark to verify the reliability of these design tools.

A key for better performance predictions is to choose better seismic input parameters with which seismic response of a system can be evaluated reliably. In probabilistic performance-based design, we need to develop a hazard curve and a fragility curve as a function of a certain input parameter such as PGA or PGV. It should be pointed out that the high accelerations recorded in recent earthquakes did not necessarily result in high structural or geotechnical damage. For instance, during the 1971 San Fernando earthquake and 1994 Northridge earthquake in USA, the PGA of 1.0 G and 1.8 G did not make significant structural damage in the surrounding area. During the 2004 Niigataken Chuetsu earthquake in Japan, the acceleration of 1.7 G in Tokamachi again did not produce so much damage as anticipated. Other than these, there are quite a few similar cases where no significant damage occurred under PGA nearly or larger than 1 G. It indicates that the acceleration may not be a proper parameter to govern the deterioration of structures or soils compared to other parameters such as particle velocity. There are a couple of indices to represent seismic performance of structures based on spectrum or time-history of ground motions such as Housner's spectral intensity (1952) and Arias Intensity (1970). These are based on the response of one-degree-of-freedom system and include some additional considerations on structures.

In PBD, as already mentioned, seismically induced displacement, instead of seismically induced force, is the key to decide the performance criteria. The acceleration directly controls force-equilibrium but only indirectly determines the displacement through dynamic response. Velocity is increasingly used in place of acceleration because it is believed to be closely related to seismic energy. Then, why don't we use the wave energy supplied to structures. The energy has clear advantage in PBD because it is the product of the displacement and the force and related to structural performance more directly than other parameters.

Based on a postulate that dominant seismic motions propagate in the vertical direction by SH waves, energy flux \bar{E} and the accumulated energy E can be defined as Eqs. (1) and (2), respectively (Kokusho and Motoyama, 2002);

$$\bar{E} = \frac{dE}{dt} = \rho V_s \left(\frac{du}{dt} \right)^2 \quad (1)$$

$$E = \rho V_s \int \left(\frac{du}{dt} \right)^2 dt \quad (2)$$

where ρ = soil density, V_s = S-wave velocity and du/dt = particle velocity of the soil. Note that du/dt in Eqs. (1) and (2) is the particle velocity not directly of recorded motions but of upward traveling waves.

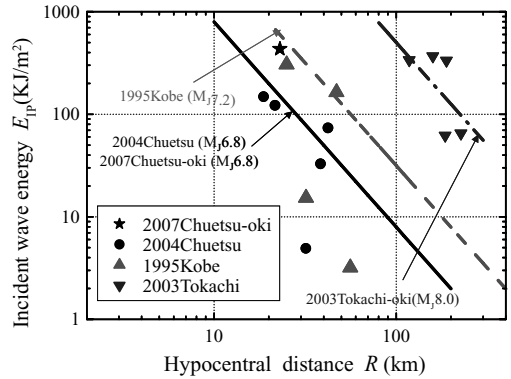


Figure 1. Incident seismic wave energy at base rock evaluated from vertical array records and compared with simple equation based on spherical energy radiation.

Therefore, it is essential to separate a measured motion at a point into upward and downward waves in order to evaluate the energy.

If a set of horizontal soil layers is assumed to behave as linear materials, upward and downward waves at any point can be calculated from a surface record based on the multiple reflection theory, from which the flow of the energy is readily evaluated. During strong earthquakes, seismic motions at the ground surface in soft soil sites are influenced by soil nonlinearity, which should be considered in evaluating the energy. If vertical array records are available, the separation of upward and downward waves from measured motions at two different underground levels is possible based on the multiple reflection theory (Kokusho and Motoyama, 2002), from which subsurface energies or energy flux can be readily calculated.

For superstructures with small damping and small ductility, the energy flux may serve a design parameter, for which the time history of ground motion is necessary. In contrast, the accumulated energy may be sufficient without time history for soil structures such as slopes, dams, retaining walls, etc., in which residual deformation by cyclic loading is essential for structural performance.

Thus, seismic wave energy is basically calculated as a square of particle velocity times soil impedance. This indicates that, even if the same particle velocity is measured, at A and B-site for example, the energy is twice larger at A if the impedance is twice larger at A than B (Kokusho et al. 2008). This effect is not clearly identified in the present seismic design practice.

Kokusho and Ishizawa (2007) indicated by using vertical array seismic records during recent strong earthquakes in Japan that the input energy per unit horizontal area, E_{IP}/A , evaluated by Eq. (3) in a bedrock of about 100–300 m deep can be approximated by the following equation assuming a spherical energy radiation.

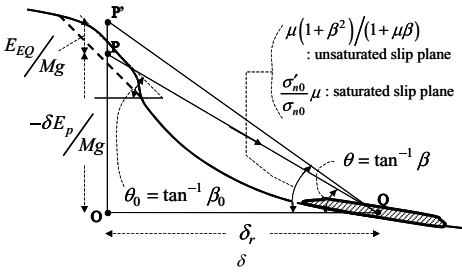


Figure 2. Schematic diagram how to evaluate travel distance δ_r in seismically induced slope failure based on wave energy.

$$E_{IP}/A = E_0/(4\pi R^2) \quad (3)$$

Here, R is the hypocenter distance, and E_0 is the total wave energy in the unit erg ($1 \text{ erg} = 10^{-10} \text{ kJ}$), which is assumed to radiate from the hypocenter. The energy E_0 is determined using the empirical equation by Gutenberg (1955)

$$\log E_0 = 1.5M + 11.8 \quad (4)$$

where M is the earthquake magnitude using the Richter scale. Fig. 1 indicates incident energies per unit area E_{IP}/A calculated from the vertical array records at bedrock during recent strong earthquakes in Japan, which are found mostly consistent with the empirical formula by Eqs. (3) and (4) shown with straight lines (The Japanese Earthquake Magnitude, M_J , was used here to compute E_0 because the Richter magnitude and the Japanese magnitude are almost equivalent), despite simple assumptions in the energy evaluation without characterizing fault mechanisms such as fault dimension, directivity, asperity, etc.

Earthquake energy E_{EQ} , that is transmitting into the upper layer, can be computed by subtracting from the input energy E_{IP} the energy reflected downward into the bedrock due to the impedance contrast at layer boundaries. The energy flow in the surface layers can be easily computed based on the 1-D multi-reflection analysis of SH wave. If actual ground conditions are approximated as a two-layers system and all the energy E_{EQ} transmitting into the upper layer is assumed to be absorbed due to widespread geotechnical failure such as liquefaction or slope slide, then the energy ratio E_{EQ}/E_{IP} may be formulated as;

$$E_{EQ}/E_{IP} = 4\alpha/(1+\alpha)^2 \quad (5)$$

where α is the impedance ratio of the upper layer to the bedrock (Kokusho et al. 2007).

Thus, the accumulated input energy during the earthquake may be readily computed for engineering purposes if the earthquake magnitude and the focal distance are given. In this case we do not need any time history, which makes uncertainties associated with seismic input very much reduced.

As an example in which the accumulated energy may be able to serve as an appropriate input parameter instead of acceleration for geotechnical problems, let me briefly introduce the travel distance evaluation of seismically failed slope. The detailed theoretical basis of the evaluation method is available in other literatures (Kokusho and Ishizawa 2007).

Fig. 2 shows a schematic view of a slope in which a center of gravity of sliding soil mass moves from P to Q during seismically induced failure. Let β denote a global inclination of a straight line PQ different from the initial slope inclination β_0 , and μ average mobilized friction coefficient over the travel distance. The drop height PO ($-\delta E_p/Mg$, in which $-\delta E_p$; potential energy change, Mg ; weight of failed slope) divided by the horizontal distance OQ (δ_r) corresponds to the global inclination β of the slope, hence,

$$\frac{-\delta E_p/Mg}{\delta_r} = \beta \quad (6)$$

On account of the earthquake energy, the pre-earthquake centroid can be considered to rise up by E_{EQ}/Mg , from P to P' . If the slip plane is assumed unsaturated (Kokusho and Ishizawa 2008), the inclination of the line $P'Q$, or the ratio of the height $P'O$ expressed as $(-\delta E_p/Mg + E_{EQ}/Mg)$ to the horizontal displacement (δ_r), OQ , can be expressed as;

$$\frac{-\delta E_p/Mg + E_{EQ}/Mg}{\delta_r} = \mu \frac{1 + \beta^2}{1 + \mu\beta} \quad (7)$$

Consequently, the procedure for the travel distance evaluation is:

1. Determine the dimension and weight of a potential sliding soil mass and its centroid P .
2. Determine the mobilized friction coefficient μ .
3. Evaluate the earthquake energy E_{EQ} .
4. Locate Point P' , which is by E_{EQ}/Mg higher than P .
5. Starting at Point P' , draw a line having an inclination of $\mu(1 + \beta^2)/(1 + \mu\beta)$, until it intercepts the slope surface (Point Q). Then from the geometry of the slope, δ_r can readily be obtained.

This very simple procedure may be conveniently used to evaluate the run-out distance for seismically induced slope failure. This kind of energy approach may be able to serve as a simple yard stick to compare with sophisticated analytical results.

Thus, as a key for better performance predictions, the seismic wave energy may be able to serve as a better seismic input parameter, in addition to conventional PGA or PGV, with which seismic response of ground and geotechnical structures can be evaluated more reliably.

REFERENCES

- Arias, A. (1970): A measure of earthquake intensity. *Seismic Design for Nuclear Power Plants*. Massachusetts Institute of Technology Press, Cambridge, 438–483.
- Gutenberg, B. (1955): The energy of earthquakes, *Quarterly Journal of the Geological Society of London*, Vol. CXII, No. 455, 1–14.
- Housner, G.W. (1952): Intensity of ground motion during strong earthquakes, California Institute of Technology, Earthquake Res. Lab.
- Kokusho, T. and Motoyama, R. (2002): Energy dissipation in surface layer due to vertically propagating SH wave, *Journal of Geotechnical and Geoenvironmental Engineering*, ASCE, Vol. 128, No. 4, 309–318.
- Kokusho, T., Motoyama, R. and Motoyama, H. (2007): Wave energy in surface layers for energy-based damage evaluation, *Soil Dynamics & Earthquake Engineering* 27, 354–366.
- Kokusho, T. and Ishizawa, T. (2007): Energy approach to earthquake-induced slope failures and its implications, *Journal of Geotechnical and Geoenvironmental Engineering*, ASCE, Vol. 133, No. 7, 828–840.
- Kokusho, T. and Ishizawa, T. (2008): Energy-based evaluation of earthquake-induced slope failure and its application, *Geotechnical Special publication No. 181, Geotechnical Earthquake Engineering and Soil Dynamics*, GEO Institute, ASCE, (CD-publication).